

Earth Sciences, History of

Naomi Oreskes

University of California, San Diego

- I. Earth History and Geological Time
- II. Extinction, Evolution, and the Age of the Earth
- III. Continental Drift and Plate Tectonics
- IV. Oceanography, Meteorology, Seismology, and Planetary Sciences
- V. Historiographic Reflections

GLOSSARY

Asthenosphere A region of the earth's upper mantle at a depth of approximately 75–150 km, characterized by low mechanical strength, attenuation of seismic shear waves, and partial melting. The term was coined in the 1910s by geologist Joseph Barrell to describe the zone in which isostatic adjustment occurs and basaltic magmas are generated. With the development of plate tectonics in the 1960s, the asthenosphere is now understood as the plastic zone over which the rigid plates move.

Bathymetry Measurement of ocean depths.

Benioff zones Zones of intermediate and deep-focus earthquakes, dipping 30°–45° from the ocean toward the continents, described by seismologist Hugo Benioff in the 1950s. While Benioff interpreted them as fault planes along continental margins, these zones are now understood to mark the locations where oceanic crust is subducted beneath continental margins at convergent plate margins.

Fennoscandian rebound In the early nineteenth century, farmers and fishermen observed that the shorelines

and coastal islands of Scandinavia were rising. In the early twentieth century, this uplift was recognized as a regional phenomena encompassing Norway, Sweden, and Finland, resulting from landscape adjustment to post glacial conditions. During the Pleistocene period, the land had sunk under the weight of glacial ice. When the ice melted, the land began to rebound in a gradual process, still continuing today.

Geognosy A term introduced in the eighteenth century by German mineralogist Abraham Gotlob Werner to denote factual knowledge of rocks, minerals, and their spatial relations, without reference to theoretical interpretation.

Geosynclines Regions bordering the continental margins where thick sequences of shallow-water sedimentary strata accumulated, and subsequently were compressed and folded into mountain belts. The concept was developed in the nineteenth century by geologists James Dana and James Hall, Jr., to account for the features of the American Appalachians, and in the United States it became the generally accepted explanation for the origins of mountains prior to plate tectonics. However, it was never widely accepted elsewhere.

Isostasy The theory that the earth's crust floats in hydrostatic equilibrium within a denser, fluid or plastic substrate.

Orogenesis The theory or study of mountains and their origins.

Uniformitarianism The principle, articulated by nineteenth century British geologist Sir Charles Lyell, that geological history can be explained by reference to presently observable processes. In his now-classic work, *Principles of Geology* (1830), Lyell argued that past geological processes were the same in rate, intensity, and kind as those currently in operation, and earth history was not progressive (*substantive uniformitarianism*). Many geologists were unconvinced by Lyell's arguments for constant rates and intensity, but enthusiastically adopted uniformitarianism as a methodological program of interpreting the geological record by analogy with modern environments and events (*methodological uniformitarianism*). In the twentieth century, uniformitarianism was often said to be the fundamental guiding principle of modern geology.

ALTHOUGH THE TERM “geology” did not come into widespread use until the nineteenth century, interest in geological phenomena dates back at least to the ancient Greeks. Historian Mott T. Greene has suggested that the battle between Zeus and Kronos in Hesiod's *Theogony* is a description of the eruption of the volcano at Thera in the fifteenth century BC. No doubt the inhabitants of the ancient world were fearful of the volcanoes and earthquakes that intermittently threatened their existence. No doubt also they paid heed to the earth materials used for the construction of their cities, art, pottery, and weaponry.

Explicit speculations on the causes of earthquakes, volcanoes, lightning, and floods are found in the writings of Ionian philosophers such as Thales, Anaximander, and Xenophanes (c. sixth century BC). Earthquakes and floods feature in Plato's *Timaeus* in the account of the disappearance of Atlantis; in *Meteorologica* Aristotle (384–322 BC) discusses the processes responsible for changing the earth's surface. In the Roman world, the natural historian Pliny the Elder was killed in the 79 AD eruption of Vesuvius that destroyed Pompeii. In the medieval period, interest in rocks and minerals is recorded in the lapidaries of European and Arabic scholars.

Interest in geological matters flourished in the late fifteenth and early sixteenth centuries, when the growing commercial and intellectual activity of Renaissance Europe stimulated demand for minerals and building materials and curiosity about natural objects encountered through travel and trade. Among Leonardo da Vinci's

(1452–1519) multitude of interests was a fascination with earth materials. As an architect and engineer supervising excavations, he recognized the similarity of fossils with living forms and interpreted rock strata as evidence of a progressive earth history in which terrestrial regions were previously inundated. Da Vinci also advanced one of the earliest recorded estimates of the duration of a geological process: 200,000 years for the Po River to lay down its alluvial plain.

Leonardo's interest in strata exposed in building sites was paralleled by Georgius Agricola's (1494–1555) interest in the rocks of the mining districts of Saxony. Best known for *De Re Metallica*, his influential treatise on ore deposits, mining techniques, and mineral processing, Agricola also wrote extensively on physical geology, subsurface fluid flow, mineralogy, fossils, and the causes of geological features. He proposed that mineral veins were precipitated from circulating fluids, and suggested that sequences of geological events could be interpreted from the structural relations of rocks and minerals.

The realization that materials could be introduced into rocks after their formation advanced the study of ore deposits but confounded the study of fossils. Renaissance naturalists used the term *fossil* to refer to any object dug up from rocks, and there was considerable dispute over whether they were the remains of past life or had grown *in situ*. Much of the debate hinged on the degree of similarity between fossil and living forms. Conrad Gesner's (1516–1565) *On Fossil Objects* was the first text to include systematic woodcuts explicitly comparing fossils with living organisms. In the late sixteenth century, the advent of copper engraving enabled naturalists to produce illustrations of great clarity and detail. Together with the development of museum collections and private “cabinets” of specimens, this innovation facilitated communication among specialists, who increasingly acknowledged the similarity between some fossil and living forms. The organic origins of fossils remained disputed, however, in part for lack of an account of how the fossils got inside the rock.

I. EARTH HISTORY AND GEOLOGICAL TIME

A. From Stratigraphy to Earth History

The first scientific account of sedimentation and stratigraphy is credited to Niels Stensen, better known as Nicholas Steno (1638–1686). As physician to the Grand Duke of Tuscany, Ferdinand II, Steno dissected a shark that fisherman brought ashore in 1666 and was struck by the similarity between the shark's teeth and the “tongue-stones” of naturalists' discussions. He concluded that tongue-stones

were petrified teeth, preserved in soft mud, later hardened into rock. From this insight he developed the law of superposition: that stratified rocks are precipitated in horizontal layers, oldest at the bottom; tilted rocks have been disrupted by later events. Therefore, a sequence of historical events could be inferred from the structural relations of rocks. In England, Steno's work was furthered by Robert Hooke (1635–1703). In one of the first uses of microscopy in paleontology, *Micrographia* (1665), Hooke had compared the fine structure of fossil and living wood as demonstration of the organic origins of fossils. Drawing on Steno, he argued persuasively for the preservation of organic remains by sedimentary processes. But how long did such processes take?

Traditionally, scholars had assumed that earth history and human history were coextensive, and texts were reliable sources of evidence about natural historical events such as the Biblical flood. Most saw little reason to doubt the work of Archbishop James Ussher, who placed the origins of the world at 4004 BC on the basis of textual evidence, or Thomas Burnet (1635–1715) whose *Sacred Theory of the Earth* (1680) integrated natural and supernatural explanation to account for the physical features of the earth's surface and the literary record provided by scripture. This view was challenged by George Buffon (1707–1788), who argued for human history as only the last of seven epochs preserved in the stratigraphic record. Buffon argued that the study of human history had to be decoupled from earth history, and rocks rather than texts were the relevant source of information about the latter. Inspired by Leibniz, he experimented with cooling globes to obtain an estimate of the age of the earth of several tens of thousands of years.

The eighteenth century scholar who most advanced naturalistic study of earth history was the German mineralogist Abraham Gottlob Werner (1749–1817). Hailing from a family associated with ironworks, Werner was educated at the Bergakademie Freiberg, where he then built his career. Students came from across Europe to hear his famed lectures (including later luminaries Leopold von Buch, Alexander von Humboldt, and Friedrich Mohs), and Freiberg became the most celebrated school of geology in the world. In his systematic mineralogy, Werner laid the foundations of the system of identifying minerals by their external characteristics still used by field geologists today. He also introduced the concepts of geognosy—knowledge of rock masses, their mineral contents, and their spatial relations—and formations. Challenging taxonomic tradition, he argued that rocks should be grouped by their mode and time of formation, even if they looked different, thereby providing a basis for regional correlation.

Werner divided the rock record into five basic formations: primitive, transition, flötz, alluvial, and volcanic. At

the start of geological time, perhaps one million years ago, the earth was entirely fluid. The first three units formed by progressive precipitation, with the least soluble materials forming the primitive rocks, the most soluble forming the flötz (which included such obviously soluble materials as salt and gypsum). The fossil content became more abundant and complex with time, suggesting that plant and animal life began to flourish as the waters gradually receded. Structural dislocations were attributed to periods of stormy conditions, and lithological variations were attributed to spatial and temporal heterogeneity in the ocean from which the materials precipitated. Above the three aqueous formations were the alluvial materials, formed by erosion and redeposition of the earlier sequences, and the volcanic rocks, pumice and lava, formed from burning coal beds in the flötz. Not all rocks were given a chemical interpretation, but all were given superficial origins.

Neptunism was subsequently discredited in the debate over the origins of basalt, leading later writers to caricature Werner's theory and dismiss his contributions. This is a mistake. By enabling correlation between distant locales, Werner's formation concept made it possible to talk about earth history in a global manner. Formations became the organizing principle of stratigraphy, inspiring scores of geologists in the early nineteenth century to take up systematic field mapping. One example is William Maclure, who produced the first geological map of the United States in 1809.

The proof of the igneous origins of basalt is properly credited to the French geologist, Nicolas Desmarest (1725–1815), who, in explaining the basalts of Auvergne, articulated the principle of uniformity generally associated with his Scottish contemporary, James Hutton (1726–1797). In fact, many French and German geologists in the late eighteenth century interpreted geological patterns by reference to observable processes of sedimentation, erosion, and volcanism; by late century the habit of examining modern environments for interpretive analogues was established. Hutton, however, elevated this practice into a unifying methodological precept, linked to a steady-state theory of earth history.

A polymathic founding member of the Royal Society of Edinburgh and avid Newtonian, Hutton believed that rocks recorded the “natural history” of the earth: as monuments recorded human history and their functions could be understood by comparison with contemporary edifices, so ancient rocks could be understood by comparison with processes presently operating on the earth's surface. Sedimentary rocks formed by erosion and redeposition of terrestrial materials, but this implied that an earlier generation of rocks had been exposed at the surface. How? Hutton's answer, presented in his *Theory of the Earth* (1795), was a geological cycle of deposition, burial, heating, melting,

expansion, uplift, erosion, and deposition again. But erosion and deposition were scarcely detectable; their rates of operation were nearly vanishingly slow. So Hutton concluded that geological time must be “indefinite,” prompting his famous description of earth history as bearing “no vestige of a beginning, no prospect of end.”

Hutton and Werner have commonly been cast as antagonists, in part because their theories diverged on the question of whether earth history was progressive or steady state. But there was an important commonality: a shared emphasis on the primacy of fieldwork as the methodological tool to unravel earth history through the structural relations of rocks. In the nineteenth century geological field work came to prominence, culminating in the establishment of the geological time scale.

B. The Geological Time Scale

In 1835, the British Geological Survey was founded under Henry Thomas De la Beche (1796–1855), reflecting an increased governmental interest in the materials fueling the industrial revolution: coal, limestone, iron, tin, copper, and lead. The Survey was preceded and complemented by the work of private land surveyors, such as William Smith (1769–1839), who pioneered the use of fossil assemblages to distinguish lithologically similar units, and produced the first geological map of England in 1815. Complementing economic motivation, academic natural theologians such as William Buckland (1784–1856) and Adam Sedgwick (1785–1873) pursued field geology as a means to know God through his works, while gentlemen-scientists such as Roderick Murchison (1792–1871) adopted natural history an appropriate vocation for men of independent means. The task of geological reconstruction was facilitated by the British Isles’ remarkably complete and largely undeformed sequences. Field mapping flourished; by midcentury geologists had reconstructed the sequence of rock units across Great Britain, Europe, and portions of North America, and defined the geological time scale in use today.

Geological mapping established that earth history was marked by distinctive rocks with characteristic fossil assemblages. However, in any one place only fragments of the whole record were found, and gaps were commonly associated with structural dislocations where rocks were tilted or folded like putty. It seemed logical, even obvious, to interpret these gaps and dislocations as the result of cataclysmic events such as the Lisbon earthquake of 1756, the Etna eruption of 1669, or the Biblical flood. Challenging this view, Charles Lyell (1797–1875) revived Hutton’s interpretive reliance on observable processes and promoted it as the basis for geological explanation. In *Principles of*

Geology (1830), he argued the view later dubbed uniformitarianism: that the accumulation of incremental change, operating in the past at the same rate and intensity as in the present, was sufficient to explain the transformations of the geological record. It was not merely that the laws of nature were temporally and spatially uniform—any Newtonian would have accepted that—but also that the processes themselves were uniform. Study of modern analogues was therefore both necessary and sufficient for understanding past geological process. While the details of Lyell’s position were hotly argued by his contemporaries, particularly the assertion of constant rates of change, the uniformitarian framework was widely accepted. Many would later call it the central methodological principle of geology.

The uniformitarian reading of geological time was far greater than any literal or even semiliteral interpretation of the Old Testament might allow, thus contributing to a more flexible interpretation of religious doctrine. Geological knowledge also facilitated the exploitation of earth materials, warranting the expansion and institutionalization of the science. By the late nineteenth century, academic departments and government surveys had been established across Europe and the United States.

II. EXTINCTION, EVOLUTION, AND THE AGE OF THE EARTH

A. The Fact of Extinction

With the establishment of geological time, historian Paolo Rossi notes, fossils “become the clocks that can measure the long time periods of natural history.” The newly established geological time periods were partly defined by their distinctive fossil assemblages. Most notably, the ends of geological eras—Paleozoic, Mesozoic, Cenozoic—as well as the ends of the periods—Cambrian, Permian, Cretaceous, etc.—were marked by the disappearance of one or more major species.

Extinction had often been addressed in the context of divine providence: Why would God destroy his own work? Why would he create imperfect forms? Initially, many paleontologists thought that seemingly missing creatures might still be lurking in the depths of oceans and the interiors of uncharted terrains. However, as increasing numbers of fossils were discovered and their relations to living forms scrutinized, this explanation became increasingly untenable. In his 1796 paper “*On the Species of Living and Fossil Elephants*,” the French paleontologist and comparative anatomist George Cuvier (1769–1832) demonstrated that the fossil “elephants” (mammoths) of Siberia were distinct from living forms. The fact of the extinction of

mammoths and many other species, from belemnites to ammonites, was soon accepted.

This led to a new scientific question: Why did species go extinct? And where did new species come from? It was increasingly clear that new species appeared at intervals in the fossil record as surely as some old ones had disappeared, and these changes provided a metric by which to measure geological time. Cuvier recognized three explanatory options: destruction, modification, or migration. Seeing no direct evidence of modification in the fossil record, he opted for destruction followed by migration: rapid marine transgressions had destroyed the faunal assemblages of earlier periods, after which species migrated in from elsewhere. Drawing on the political events of his own time, he called these periods revolutions. These natural revolutions were not necessarily sudden or violent, but they were major transformations in which old species vanished, new ones appeared.

B. From Revolution to Evolution

The question of modification of species was taken up by Jean-Baptiste Lamarck (1744–1829) and later more successfully by Charles Darwin (1809–1882). A follower and later a friend of Lyell, Darwin was deeply influenced by his argument for the efficacy of small changes accumulated over geological time. This became the foundation for his theory of the origin of species by natural selection. By analogy with a presently observable process—artificial selection by breeders—Darwin conceptualized a mechanism of natural evolutionary change. Uniformitarianism provided theoretical justification for a gradualist interpretation of faunal change in the absence of direct evidence. Darwin famously attributed the “missing links” to gaps in the fossil record, and most geologists concurred. By the end of the nineteenth century, the fact of evolution (if not the mechanism of it) was widely accepted. This fact hinged in turn on a very old earth.

But how old was old? Most geologists spoke in qualitative terms. Werner had described the great duration of geological time “in contrast to which written history in only a point.” Hutton had called geological time “indefinite”; others spoke of its “limitless stores.” Uniformitarianism inspired attempts at quantification: Darwin used modern sedimentation rates to estimate the time for the deposition of the Weald (a unit of the lower Cretaceous) at 300 million years—implying an earth age of hundreds of billions. Irish geologist John Joly (1857–1933) used the salt concentration of modern rivers to calculate how long it would take to salinize the world’s oceans. His result: 90 million. While the rigor of Joly’s calculations appealed to some, many geologists intuitively felt it was too low. Most preferred billions to millions.

C. Millions or Billions?

Geologists’ conviction in a prodigiously old earth was radically challenged in the late nineteenth century by British physicist William Thomson, later Lord Kelvin (1824–1907). Kelvin revived an idea earlier proposed by Buffon that the earth’s age could be deduced on the principle of a cooling sphere. Drawing on the Kant–LaPlace nebular hypothesis, that the solar system had formed by condensation from a gaseous cloud, and applying Fourier’s theory of heat transfer, Kelvin calculated the time required for the earth to cool to its present temperature at no more than 20–40 million years. If uniformitarianism implied otherwise, then uniformitarianism must be wrong, and geological practice based on a fallacy. Moreover, Darwin’s theory of the origin of species by natural selection must also be wrong, resting as it did on the premise of eons of time.

This was a profound challenge. Some geologists tried to adjust themselves to Kelvin’s numbers; some sought a compromise or defended the geological view. Darwin suggested that the rate of evolution might be faster than he had supposed. The debate was resolved in the early twentieth century on the geological side by the discovery of radiogenic heat, which mooted Kelvin’s starting premises. (Today it is further mooted by the theory of cold accretion of the terrestrial planets.) By 1913, British geologist Arthur Holmes (1890–1965) had used U–Pb ratios to demonstrate that Precambrian rocks were at least 2 billion years old. In the 1930s, the development of the mass spectrometer by Alfred Nier (1911–1994) made it possible to differentiate lead isotopes, pushing calculations upward toward 3 billion. In 1953, American geochemist Clair Patterson (b. 1922) used iron–nickel meteorites to determine primeval lead ratios, producing the presently accepted earth age of 4.55 billion years.

III. CONTINENTAL DRIFT AND PLATE TECTONICS

A. The Origin of Mountains: Thermal Contraction

Geologists in the eighteenth and nineteenth century made great advances in documenting earth history and explaining the origins of sedimentary rocks; they were less successful in accounting for the origins of mountains, earthquakes, and igneous processes. In Europe, mountains had often been viewed as frightening and dangerous places, but they also contained many valuable mineral deposits. In the early nineteenth century, they attracted increasing artistic attention as sites of great natural beauty, cultural attention as potential sites of human conquest, and political attention as a barriers to expansion. They attracted

scientific attention as well. How were they formed? What caused their spectacular structural features? What made the earth move?

Most nineteenth-century theories of orogenesis invoked terrestrial contraction as a causal force. In Europe, Austrian geologist Edward Suess (1831–1914) popularized the image of the earth as a drying apple. Like Kelvin, Suess built on the premise of secular cooling. Drawing on the earlier theories of Léonce Elie de Beaumont (1798–1874) and Henry De la Beche, he proposed that the earth contracted as it cooled, and mountains resulted from crustal wrinkling in response. Initially, the crust was continuous, but it broke apart as the earth's interior shrank, and the collapsed portions formed the ocean basins. With further cooling, the remaining elevated portions (the continents) became unstable and collapsed to form the next generation of ocean floor; what had formerly been ocean now became dry land. This explained the presence of marine deposits on land (which had puzzled da Vinci), and the interleaving of marine and terrestrial materials in the stratigraphic record. Suess's theory also explained the widely known similarities of fossil assemblages in parts of India, Africa, and South America by attributing them to an early period when these continents were still contiguous. He called this ancient supercontinent Gonawanaland.

In North America, a different version of contraction theory was developed by James Dwight Dana (1813–1895), famous at the age of 24 for his *System of Mineralogy*, which comprehensively organized minerals according to their chemical affiliations. (First published in 1837, a version is still in print today.) Drawing on his understanding of the chemical properties of minerals, Dana suggested that the earth's continents had formed first, when minerals with relatively low fusion temperatures such as quartz and feldspar had solidified. Then the globe continued to cool and contract, until the high temperature minerals such as olivine and pyroxene finally solidified: on the moon, to form the lunar craters, on earth, to form the ocean basins. Continued contraction after solidification caused surface deformation. The greatest pressure was experienced at the boundaries between the oceanic and continental blocks, explaining the localization of mountains (particularly the Appalachians). Because continents and oceans were understood as permanent features of the globe, Dana's version of contraction came to be known as permanence theory.

In North America, permanence was linked to the theory of geosynclines, developed by Dana and James Hall (1811–1889), State Paleontologist of New York and the first President of the Geological Society of America (1889). Hall suggested that materials eroded off the continents accumulated in the adjacent marginal basins, causing the basin to subside. Subsidence allowed more

sediments to accumulate, causing more subsidence, until finally the weight of the pile caused the sediments to be heated, lithified, and by some mechanism not elucidated, uplifted into mountains. Dana modified Hall's view by arguing that thick sedimentary piles were not the cause of subsidence but the result of it. Either way the theory provided a concise explanation of how thick sequences of shallow-water rocks could form.

B. Continental Drift as Alternative to Contraction Theory

In the early twentieth century, contraction theory was refuted by three independent lines of evidence. First, field mapping in the Swiss Alps and the North American Appalachians demonstrated hundreds of miles of shortening of strata, which would require impossibly huge amounts of terrestrial contraction to explain. Second, geodesists studying the problem of surface gravitational effects showed that the surface mass associated with mountains was counterbalanced by a mass deficit within or beneath them. Mountains were held aloft not by their internal strength, but by floating—a concept called isostasy. Continents and oceans were not interchangeable, because continents could not sink to form ocean basins. Third, physicists discovered radiogenic heat, which refuted the premise of secular cooling. With contraction no longer axiomatic, earth scientists were motivated to search for other driving forces of deformation. Many did; Alfred Wegener (1880–1930) is the most famous.

Primarily known as a meteorologist and author of a pioneering textbook on the thermodynamics of the atmosphere (1911), Wegener realized that paleoclimate change could be explained if continents had migrated across climate zones, and the changing configurations of continents and oceans periodically altered climate patterns. However, continental drift was more than a theory of paleoclimate change. It was an attempt at unification of disparate elements of earth science: on one hand, the paleontological evidence that the continents had once been connected; on the other, the geodetic evidence that they could not be connected in the way Suess had imagined. Wegener's answer was to reconnect the continents by moving them laterally.

Wegener's theory was widely discussed in the 1920s and early 1930s. It was also hotly rejected, particularly by Americans who labeled it bad science. The standard explanation for the rejection of Wegener's theory is its lack of a causal mechanism. But this explanation is false. There was a spirited and rigorous international debate over the possible mechanisms of continental migration. Much of it centered on the implications of isostasy: if continents floated in a denser substrate, then this substrate had to be plastic or fluid, and continents should be able to

move through it. The Fennoscandian rebound—the progressive uplift of central Scandinavia since the melting of Pleistocene glacial ice—provided empirical evidence that they did, at least in the vertical direction and at least in the Pleistocene. But here the cause of motion was known: the weight of glacial ice and the pressure release upon its removal. What force would cause horizontal movement? And would the substrate respond comparably to horizontal as to vertical movement? Debate over the mechanisms of drift therefore concentrated on the long-term behavior of the substrate, and the forces that could cause continents to move laterally. Various proposals emphasized the earth's layered structure, which allowed for decoupling of the continental layer from the one beneath.

John Joly linked the problem of continental drift to the discoveries in radioactivity. He had demonstrated that pleochroic haloes in mica were caused by radiation damage from tiny inclusions of U- and Th-bearing minerals, proving that radioactive elements were ubiquitous in rocks. Then radiogenic heat was also ubiquitous, and as it built up it would melt the substrate. During these molten periods the continents could move under the influence of small forces that would otherwise be ineffectual.

Joly's theory responded to a geophysical complaint against a plastic substrate: that the propagation of seismic waves indicated a fully solid and rigid earth. More widely credited was the suggestion of Arthur Holmes that the substrate was partially molten or glassy. Underscoring arguments made by Wegener, Holmes emphasized that the substrate need not be liquid, only plastic. Furthermore, it might be rigid under high strain rates (during seismic events) yet be ductile under the low strain rates prevailing under most geological conditions. If it were plastic in response to long-term stress, then continents could move within it. Holmes's driving force was convection currents in the mantle. He argued that the midocean ridges were the sites of upwelling convection currents, where continents had split, and the ocean deeps (geosynclines) were the sites of downwelling currents, where continents were deformed as the substrate descended. Between the ridges and the trenches, continents were dragged along in conveyor-like fashion.

C. The Rejection of Continental Drift

Arthur Holmes's papers were widely read and cited; many thought he had solved the mechanism problem. However, opposition to drift was nonetheless for that, particularly in the United States, where reaction to Wegener's theory was harshly negative, even vitriolic. Evidently more was at stake than a matter of scientific fact.

Three factors contributed to the American animosity to continental drift. One, Americans were widely com-

mitted to the method of multiple working hypotheses, and Wegener's work was interpreted as violating it. For Americans, right scientific method was empirical, inductive, and involved weighing observational evidence in light of alternative explanatory possibilities. Good theory was also modest, holding close to the objects of study. Most closely associated with the University of Chicago geologist T. C. Chamberlin (1843–1928), who named it, the method of multiple working hypotheses reflected American ideals expressed since the eighteenth century linking good science to good government: Good science was antiauthoritarian, like democracy. Good science was pluralistic, like a free society. If good science provided an exemplar for good government, then bad science threatened it. To American eyes Wegener's work was bad science. It put the theory first, and then sought evidence for it. It settled too quickly on a single interpretive framework. It was too large, too unifying, too ambitious. Features that were seen as virtues of plate tectonics were attacked as flaws of continental drift.

Continental drift was also incompatible with the version of isostasy to which Americans subscribed. In the late nineteenth century, two accounts of isostatic compensation had been proposed: John Henry Pratt (1809–1871) attributed it to density variations, George Biddell Airy (1801–1892) attributed it to differences in crustal thickness. Until the early twentieth century, there had been no empirical confirmation of the concept beyond the original evidence that had inspired it, nor any means to differentiate the two explanations. Then American geodesists John Hayford (1868–1925) and William Bowie (1872–1940) used the Pratt model to demonstrate that isostatic compensation was a general feature of the crust. By making the assumption of a uniform depth of compensation, they were able to predict the surface effects of isostasy to a high degree of precision throughout the United States. At first, their work was hailed as proof of isostasy in general, but in time, it was viewed as confirmation of the Pratt model in particular. However, if continental drift were true, then the large compressive forces involved would squeeze the crust, generating thickness differentials. Continental drift seemed to refute Pratt isostasy, which had worked for Americans so well, and because it had worked, they had come to believe was true. Rather than reject Pratt isostasy, they rejected continental drift.

Finally, Americans rejected continental drift because of the legacy of uniformitarianism. By the early twentieth century, the methodological principle of using the present to interpret the past was deeply entrenched in the practice of historical geology. Many believed this to be the *only* way to interpret the past, and that uniformitarianism made geology a science, for without it what proof was there that God had not made the Earth in seven days,

fossils and all? Historical geologists routinely used faunal assemblages to make inferences about climate zones, but on drift-based reconstructions, continents placed in the tropics did not necessarily have tropical faunas, because the reconfiguration of continents and oceans might change things altogether. Wegener's theory raised the specter that the present was not the key to the past—it was just a moment in earth history, no more or less important than any other. This was not an idea Americans were willing to accept.

In North America, the debate over continental drift was quelled by an ad hoc explanation of the faunal evidence. In 1933, geologists Charles Schuchert (1858–1942) and Bailey Willis (1857–1949) proposed that the continents had been intermittently connected by isthmian links, just as the isthmus of Panama connects North and South America and the Bering Land Bridge once connected North America to Asia. The isthmuses had been raised up by orogenic forces, subsided under the influence of isostasy. This explanation was patently ad hoc—there was no evidence of isthmian links other than the paleontological data they were designed to explain. Nevertheless, the idea was widely accepted, and a major line of evidence of continental drift undercut. In 1937, South African geologist Alexander du Toit (1878–1948) published *Our Wandering Continents*, a comprehensive synthesis of the geological evidence of continental drift, but it had little impact in North America.

D. Plate Tectonics

In the late 1930s, Dutch geodesist Felix Vening Meinesz (1887–1966) and American Harry Hess (1906–1969) applied the idea of convection currents to explain downwarpings of the oceanic crust associated with gravity anomalies in the Caribbean and the Dutch East Indies. However, this work was cut short by World War II. In the 1950s, continental drift was revived by British geophysicists working on rock magnetism as a means to investigate the earth's magnetic field, one group at Imperial College led by P. M. S. Blackett (1897–1974), and one at Cambridge (later at Newcastle) led by S. Keith Runcorn (1922–1995).

Both groups found evidence that rocks had moved relative to the earth's magnetic poles, so either the continents or the poles had moved. Initially geophysicists were more receptive to the idea of polar wandering, but by the late 1950s comparative evidence from India and Australia pointed in the direction of differentially moving continents. Inspired by these results, Harry Hess revisited convection currents as driving force for continental motion, and proposed the hypothesis Robert Dietz (1914–1995) dubbed sea floor spreading. Hess suggested that mantle

convection drives the crust apart at midocean ridges and downward at ocean trenches, forcing the continental migrations in their wake. Hess interpreted the oceanic crust as a hydration rind on serpentinized mantle; Dietz modified this to generate oceanic crust by submarine basalt eruptions. Dietz's interpretation was later confirmed by direct examination of the sea floor.

Meanwhile American researchers, Richard Doell (b. 1923), Brent Dalrymple (b. 1937) and Allan Cox (1923–1987) were studying a different aspect of rock magnetism: the record of reversals in the earth's magnetic field. Detailed field studies of basaltic lava flows convinced them that reversals were not an artifact of cooling or laboratory procedures. In fact, one could construct a chronology of paleomagnetic reversals—a geomagnetic time scale. Magnetic reversals plus seafloor spreading added up to a testable hypothesis, proposed independently by Canadian Lawrence Morley and British geophysicists Frederick Vine (b. 1939) and Drummond Matthews (1931–1997): If the seafloor spreads while the earth's magnetic field reverses, then the basalts forming the ocean floor will record these events in the form of a series of parallel "stripes" of normal and reversely magnetized rocks. Since World War II, the United States Office of Naval Research had supported seafloor studies for military purposes, and large volumes of magnetic data had been collected. American and British scientists quickly set to work examining these data, and by 1966 the Vine and Matthews hypothesis had been confirmed.

At this point, many workers turned to the problem. Among the most important were J. Tuzo Wilson (1908–1993), who thought of another test of the theory. The midocean ridges were repeatedly offset by faults; the slip direction on these faults would be one direction if seafloor spreading were taking place, the opposite if it were not. Wilson called the latter transform faults, as they transformed one segment of a spreading ridge into another. Seismic data analyzed by Lynn Sykes (b. 1937) at the Lamont–Doherty Geological Observatory confirmed the existence of transform faults.

Sykes's Lamont coworkers, Walter Pitman (b. 1931) and James Heirtzler (b. 1925), used paleomagnetic data to refine the reversal time scale, and confirm that the patterns on either side of the mid-Atlantic ridge were symmetrical. In 1967–1968, these various lines of evidence were independently synthesized by Daniel P. McKenzie (b. 1942) and Robert L. Parker (b. 1942) working at the Scripps Institution of Oceanography, and by Jason Morgan at Princeton University. Both showed that existing data could be used to analyze crustal motions as rigid body rotations on a sphere. The result became known as plate tectonics, which by the early 1970s had become the unifying theory of the earth sciences.

IV. OCEANOGRAPHY, METEOROLOGY, SEISMOLOGY, AND PLANETARY SCIENCES

A. Historical Background

Oceanography, meteorology, seismology, and planetary science have only recently received sustained historical attention. One reason is itself historical: these are young sciences. The earth's surface permitted scientific study sooner than the other parts. Anyone could pick up a rock or a fossil and begin to develop a collection, but it required instruments, financing, and often national or international cooperation to study the oceans, atmosphere, and earth's interior. The distant planets were even less accessible.

Prior to the late nineteenth century, oceanographic and meteorological questions were commonly understood as issues of geography, and investigations were piggybacked on expeditions that were not primarily scientific. Seismology began to flourish around the same time in conjunction with earthquake studies and the development of precise seismographs. Early in the twentieth century, it grew substantially, first through its application to petroleum exploration, later more dramatically through its application to nuclear test ban verification. Planetary science similarly developed in a limited way in the early century with the construction of powerful reflecting telescopes, and then much more fully in conjunction with the U.S. and Soviet space programs.

B. Oceanography

Oceanography is the oldest of the ancillary earth sciences, with its links to navigation and exploration, colonialism and trade. In the seventeenth century, members of the British Royal Society compiled sea temperatures; Isaac Newton (1642–1727) and Edmund Halley (1656?–1743) theorized the astronomical cause of tides. In the eighteenth century, British sea captain James Cook (1728–1779) recorded tides and temperatures during his voyages.

Currents were obviously important to navigation, and most early workers thought they were driven by density differences—hence attention to surface temperature. In the early nineteenth century, scientists began to consider other factors. English surveyor James Rennell (1742–1830) suggested the role of winds in driving surface currents, while the German polymath, Alexander von Humboldt (1769–1859), promoted the idea that sinking of cold water in high latitudes could drive deep circulation. Many ship voyages therefore included some measurements of salinity, temperature, surface currents, and soundings. The founding of systematic bathymetry is generally credited to Matthew Fontaine Maury (1806–1873), who pioneered

this work at the U.S. Navy Hydrographic Office, but resigned from federal service during the American Civil War.

The voyage of H. M. S. *Challenger* (1872–1876) was the first explicitly oceanographic expedition. Lasting three and a half years and covering 110,000 km, the expedition took thousands of soundings, measurements of temperature and salinity, and biological and bottom sediment samples. The results (published in 50 volumes) provided the first systematic description of the oceans. The data demonstrated the existence of the abyssal plains at approximately 5 km depth, the constancy of the proportion of salts in seawater, and the variation of deep-water temperature. The detection of a systematic temperature difference between the eastern and western half of the Atlantic Ocean was first suggestion of the existence of a mid-Atlantic Ridge. Dredging the seafloor revealed the predominance of calcareous oozes and red clays, quite unlike terrestrial sediments, providing an early argument against the interchangeability of continents and oceans. Among the biological results, 3225 new species were discovered, including many at great depths, disproving the idea that ocean depths were devoid of life.

Toward the end of the century, interest in oceanography received impetus from Arctic explorers, particularly Scandinavians Fritjof Nansen (1861–1930) and Roald Amundsen (1872–1928?). In the *Fram* expedition (1893–1896), Nansen completed the first drift across the Arctic, discovering that the ice drift diverged 45° from prevailing wind directions. Suspecting the Coriolis force [articulated by French natural philosopher Gaspard Coriolis (1792–1843), but as yet unapplied to ocean dynamics], Nansen proposed the problem to a young Swedish oceanography student, Wagn Ekman (1874–1954), who demonstrated mathematically that the drift was indeed consistent with wind-driven circulation modified by the Coriolis effect—dubbed the “Ekman spiral.” Amundsen repeated the Arctic drift on the *Maud* (1918–1925) with improved instruments permitting better measurement of wind and current directions, and confirmed Ekman’s results.

Ekman’s work became a cornerstone of the “dynamic oceanography” developed by Bjørn Helland-Hansen (1877–1957), Johan Sändström (1874–1947), and Harald Sverdrup (1888–1957). Using temperature and salinity data to determine a density field, one deduced a pressure field, and from this, ocean currents. However, mathematical treatment relied on accurate data; thus the development of dynamic oceanography also depended on improved instrumentation. Chief among these was the “Nansen bottle.” In response to problems encountered on the *Fram*, Nansen invented a self-sealing insulated bottle to collect deep-water samples and measure their temperatures *in situ* with a pressure-protected thermometer. The

Nansen bottle was widely used until the development of the bathythermograph for temperature measurement in the 1940s, and electronic techniques for salinity measurement in the 1960s.

Oceanography also benefited from international cooperation. Alarmed by declining fish stocks, Swedish oceanographer Otto Pettersson (1848–1941) spearheaded the creation of *The International Council for the Exploration of the Seas* (ICES) in 1902, in the hope of stemming further losses through improved scientific understanding. From Germany, the *Meteor* expedition (1925–1927) confirmed the existence of deep-water circulation from north to south in the northern hemisphere and middepth flow south to north in southern hemisphere, while Albert Defant (1884–1974) published the first German textbook of the dynamic method, *Dynamische Ozeanographie* (1929) and George Wust (1890–1977) demonstrated that calculations of the Gulf Stream based on dynamic method matched empirical measurements.

Dynamic oceanography was brought to the United States by Harald Sverdrup, who had sailed with Amundsen on the *Maud*. Together with Martin Johnson (1893–1984) and Richard Fleming (1909–1990), Sverdrup authored the first comprehensive textbook of oceanography in English, *The Oceans* (1942). Perhaps the single most influential book in the history of oceanography, it framed the agenda for oceanographic research for several decades. Together with Walter Munk (b. 1917), Sverdrup developed the methods used to predict surf conditions for amphibious landings during World War II.

After World War II, oceanography flourished in the United States as the U.S. Office of Naval Research (ONR) provided abundant funding for research relevant to subsurface warfare and communication. Munk and Henry Stommel (1920–1992) improved prediction of ocean circulation by adding friction and detailed wind data. This work explained how wind-driven circulation leads to intensification of currents on the western sides of oceans in the northern hemisphere (eastern sides in the southern hemisphere), helping to explain phenomena such as upwelling currents and El Niño events. Stommel also predicted the existence of abyssal circulation involving the sinking of cold water at high latitudes, as suggested by Humboldt, now thought to be of major importance in controlling the earth's climate. The ONR also supported investigations of the structure of the seafloor and oceanic crust, including the paleomagnetic studies that demonstrated seafloor spreading.

Postwar advances in isotope geochemistry, headed by American chemist Harold Urey (1893–1981) and geochemist Harmon Craig (b. 1926), led to the recognition that O¹⁸/O¹⁶ ratios in fossil foraminifera could be used to measure paleotemperatures. The results revealed many

more temperature fluctuations than previously recognized from lithological evidence. Cesare Emiliani (1922–1995) linked these fluctuations to Milankovitch cycles—small variations in earth's orbit on a time scale of 20–100,000 years—providing the first widely accepted theoretical account of the cause of the ice ages.

C. Meteorology

Natural philosophers in the seventeenth and eighteenth century sporadically investigated atmospheric phenomena, but systematic meteorology developed in the nineteenth century when forecasters began to organize weather data to predict storms. This advance hinged on the telegraph, which permitted forecasters to integrate geographically dispersed information. It also hinged on the military value of weather forecasts, which in the United States were sent alongside military communications.

In the late nineteenth century this empirical tradition was criticized by researchers who hoped to reduce meteorological systems to physics and hydrodynamics. Leading the effort was Norwegian physicist Vilhelm Bjerknes (1862–1951), whose polar front concept gave physical interpretation to the behavior of storm systems and the interaction of air masses. Bjerknes was an inspired teacher; among his students he counted the pioneers of dynamic oceanography, who applied Bjerknes's principles and methods to the movement of water masses. As oceanography received support in part for its application to fisheries and navigation, so meteorology grew with the development of the aeronautics industry.

Bjerknes believed that the behavior of weather systems could be deterministically calculated, much as one could compute advance positions of planets by knowing their orbits and initial conditions. This problem was taken up in midcentury by British mathematician Lewis Fry Richardson (1881–1953), who pioneered the use of digital computers in weather forecasting. Richardson achieved great improvements in short-term forecasting, but the hope of a deterministic science of meteorology was dashed by the work of Edward Lorenz (b. 1917), who discovered that small changes in initial conditions could create very large perturbations in meteorological models. This realization—dubbed the “butterfly effect”—was a key element in the development of chaos theory.

In the late twentieth century attention shifted from weather to climate, as researchers developed General Circulation Models to understand the effect of altered atmospheric chemistry caused by burning of fossil fuels. Just as telegraph communication was critical to nineteenth-century empirical forecasting, the development of high-speed digital computers has been critical to twentieth-century climate modeling. However, given the complexity

of the climate system and its interrelation with ocean circulation, the goal of accurate prediction of climate change remains a task for the future.

D. Seismology

As in meteorology and oceanography, scientific seismology required accurate instrumentation and synthesis of geographically dispersed data, which began to develop in the midnineteenth century. Early seismic investigations focussed primarily on earthquake occurrences; one of the earliest comprehensive catalogs was compiled by Irish engineer, Robert Mallet (1810–1881), who also coined the term *seismology* and developed an early design for an electromagnetic seismograph, later developed in Italy by Luigi Palmieri (1867–1896). In 1862, Mallet undertook a detailed investigation of the 1857 Basilicata (Naples) earthquake ($M \cong 7$), mapping the distribution of ground motion based on damage, and in the process inventing the term and concept of isoseismal lines.

Fear of earthquake damage provided the major incentive for government support of seismology in the nineteenth century; in Japan, the Meiji government recruited several British engineers to study seismology and seismic hazard. In 1878, John Milne (1850–1913) was hired at the Imperial College of Engineering, where he began detailed investigations of earthquake ground motions, improved seismograph design, and helped to establish the Seismological Society of Japan, the first national society of its kind. He also developed a rivalry with fellow expatriates Thomas Gray (1850–1908) and James Ewing (1850–1935), engineering professors at Tokyo University. Using a modified version of Milne's horizontal-pendulum seismograph, Gray and Ewing obtained high-quality records of earthquake ground motion. In 1895 Milne returned to Britain to establish the first world-wide seismic recording network, with financial support from the British Association for the Advancement of Science. With 30 stations world-wide, Milne's network remained the most extensive until the creation of the World Wide Standard Seismic Network (WWSSN) in 1960 (see below).

Seismograph design was also pursued in Germany, where Emil Wiechert (1861–1928) developed the inverted-pendulum sensor in 1904—widely used throughout the first half of the twentieth century—and in Russia, where B. B. Golicyn (Galitzin) (1862–1916) developed a sensitive design based on electrodynamic sensors and photographically recording galvanometers, in 1906. The development of high accuracy instruments enabled seismologists to differentiate between various “phases” of earthquake arrivals, which were soon related to different kinds of earthquake waves with different velocities and travel paths. Seismology now began to develop along

two distinct lines: determining the internal structure of the earth based on arrival times, and understanding the mechanism of earthquakes and wave propagation.

The initial use of arrival times to deduce internal structure is often credited to R. C. Oldham (1858–1936), the Director of the Geological Survey of India, who discovered in 1900 that shock waves from earthquakes came in two pulses: an early (P or Primary) wave and a later (S or secondary) wave. Because they were traveling at different rates, the difference in their arrival times must be proportional to the distance to the source, and one could triangulate to determine the earthquake epicenter. In addition, Oldham found that the velocities increased with distance traveled, suggesting that the waves were traveling faster in the earth's deeper portions. Therefore, one could use seismic velocities to determine the earth's interior density. On this basis, he suggested that the earth might contain an iron core.

This line of investigation was taken up vigorously by Wiechert and his students, particularly Beno Gutenberg (1889–1960). Wiechert is credited with the first accurate solution to the problem of deducing seismic wave velocities from travel times; Gutenberg used this to determine the radius of the core: 2900 km. Oldham had suggested the core might be liquid; proof of this came from Sir Harold Jeffreys (1891–1989), who provided the rigorous mathematical treatment to rule out alternative interpretations, and Danish seismologist Inge Lehmann (1888–1993), who demonstrated that seismic data were most consistent with a twofold structure: a liquid outer core and a solid inner core.

With the confirmation of the earth's core, it became clear that the earth had a three-layer structure—crust, mantle and core—but the depth to the mantle was not known. In the 1950s, Anglophone scientists realized it had already been identified by Croatian seismologist Andrija Mohorovicic (1857–1936), who in 1909 discovered the discontinuity in seismic waves under the continents at a depth of about 45 km that now bears his name. However, the core–mantle distinction was confounded by Gutenberg's discovery of the attenuation of S-waves in a region below the crust, at a depth of about 80 km. Gutenberg suggested this was a of partial melting, which he called the asthenosphere—borrowing the term coined by geologist Joseph Barrell (1869–1919) to describe the weak zone in which isostatic compensation occurred. It was not until the 1960s that this idea was generally accepted, when the distinction between the lithosphere and asthenosphere became a foundation of plate tectonics.

Seismologists in the twentieth century also studied the mechanisms of earthquakes themselves. As in Japan, seismology in the United States was motivated primarily by seismic hazard. Drawing on evidence from the devastating

1906 San Francisco quake, Johns Hopkins professor Harry Fielding Reid (1859–1944) developed elastic rebound theory: that strain builds up slowly in rocks, which then break suddenly along faults. While the association of earthquakes with surface faults seems obvious in retrospect, this connection was not always accepted prior to Reid's work. Meanwhile Gutenberg had moved to the United States, where he collaborated with Caltech colleague Charles Richter (1900–1985) to develop the magnitude scale that bears the latter's name.

Attention to earthquakes themselves led to renewed interest in their spatial distribution, and in the 1930s, Japanese seismologist Kiyoo Wadati (1902–1995) discovered that deep focus earthquakes are almost entirely restricted to narrow zones dipping steeply under the continental margins. In the 1950s, this was rediscovered by Hugo Benioff (1899–1968), and “Benioff zones” were soon recognized as slabs of oceanic lithosphere subducting under continental lithosphere at plate margins.

Two other concerns contributed to the development of seismology in the twentieth century: petroleum exploration and nuclear test ban verification. In the first half of the century, seismic refraction and reflection techniques were developed for the analysis of shallow crustal structure to identify petroleum traps. In the second half of the century, seismology was greatly boosted by the demand for identification of nuclear weapons tests. In 1960, the United States established the World Wide Standard Seismic Network, with over 100 stations world wide, under project Vela-Uniform, to distinguish nuclear blasts from natural seismic events. This program was further boosted by the 1963 Limited Test Ban treaty, which made seismic verification essential to treaty enforcement. While developed for political reasons, the WWSSN produced greatly improved location of earthquake foci and analysis fault-plane mechanisms, which proved critical to the modern understanding of earthquakes as indicators of plate motions.

E. Planetary Science

The principal development of planetary science came with the U.S and Soviet space programs. While information had been gleaned through telescopic study going back to Galileo's study of the moons of Jupiter, space probes and manned space flight yielded a cornucopia of information about the other planets. Among the many important results of the space program were the confirmation of composition of the Moon and its age (the same as the earth), the multiple moons of Jupiter, the rings of Neptune, and the discovery that Pluto may not be a planet at all. From the perspective of the earth sciences, the two most important conceptual developments are the recognition of the geo-

logical importance of impact cratering, and the absence of plate tectonics on other planets.

The Apollo lunar missions greatly increased scientific understanding of the lunar craters, proving after decades of debate that they were impact rather than volcanic craters. In addition, the various space craft returned showing the effects of thousands of tiny impacts from cosmic dust and micrometeorites. The resulting resurgence of interest in meteorite impacts on earth led to the suggestion by Eugene Shoemaker (1928–1997) and Robert Dietz that meteorite impacts had been important forces in geological and evolutionary history. In the early 1980s, Walter Alvarez (b. 1911) and coworkers discovered the existence of a thin layer of Ir-rich sediment at the Cretaceous–Tertiary (K–T) boundary. Interpreting this as the remains of an impact event, they proposed that the mass extinction of dinosaurs, ammonites, and other species at the K–T boundary could be thus explained. While impacts as a general cause of mass extinction has not been proven, most geologists now accept that a massive meteorite impact—and its associated effects on ocean and atmospheric chemistry—was the primary cause of the demise of the dinosaurs. Similar large impacts may well have played a role in the other mass extinctions of earth history.

While the Apollo missions showed that lunar features were relevant to understanding earth processes, studies of Venus and Mars have shown that tectonics there are very different than on earth. Venus has enormous volcanoes, far greater than any on earth, and appears to be dominated by plume tectonics rather than by plate tectonics. Mars likewise has volcanoes and rifts, but no evidence of lateral crustal motion. In our solar system, it appears that only earth has plate tectonics.

V. HISTORIOGRAPHIC REFLECTIONS

Given the importance of the earth sciences for industry, transportation, communication, and warfare, and for understanding the planet we live on, it is remarkable that historians have paid so little attention. Perhaps the utility of the earth sciences has made them seem less worthy to historians enamored of a pure science ideal. Perhaps the highly international and cooperative nature of advances in oceanography and seismology have made these sciences harder to idealize by those searching glory through national scientific accomplishments. In addition, the military connections of these sciences, particularly in the twentieth century, have made the documentary record difficult to uncover.

Nor do the earth sciences fit models of scientific advance that celebrate the role of individual genius and accomplishment, crucial experiments, conceptual revolutions, or

advance through reductionism. Meteorology is a case in point: Bjerknes went far in his efforts to reduce forecasting to principles of physics, but he also reached a roadblock that involved more than lack of computational power. Advances in the earth sciences have been as much a function of improved communication and data collection as of improved theory. Often theory has followed advances in instrumentation and data-processing rather than the other way around.

The enormous need for data collection in these sciences has in the past confused historians who have mistaken their methods for “naïve empiricism,” and dismissed them as primitive and uninteresting. But the earth sciences are less primitive than they are complex; like the systems they study, they are not easily reduced to simple formulations. Rather than understand them as naïve, we might understand them as big science—requiring substantial institutional support—before the term “big science” existed. Today, large-scale data collection remains central to the earth sciences. As remote sensing permits the creation of synoptic images of earth systems, and as computer models give us new means of investigating these systems, the traditional methods of field mapping and data analysis find renewed importance as “ground-truth” for these images and models.

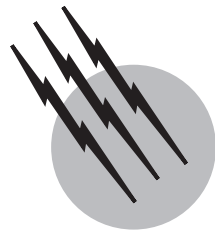
The rise of computer modeling in the earth sciences has also raised the question of prediction in the earth sciences. Many people believe that the goal of science is prediction and control, and from this perspective the earth sciences look like failures. But prediction and control have only rarely been viewed as primary purposes in the earth sciences. When prediction and control were on the scientific agenda—as in earthquake prediction or weather control—often they were placed there by government patrons, such as military officials wishing to manipulate weather to strategic advantage. Scientists may or may not have shared these aspirations; whether they did is a historical question. Rather than assume all sciences share the goals of prediction and control, it would be better to ask, What were the goals of the earth sciences? Often, the primary goal was to develop an explanatory framework of processes that were clearly too large and too powerful to control. From this perspective, the earth sciences in the twentieth century have proved a conspicuous success.

SEE ALSO THE FOLLOWING ARTICLES

CLIMATOLOGY • EARTH'S CORE • EARTH'S MANTLE • GEOLOGIC TIME • METEOROLOGY, DYNAMIC • PLATE TECTONICS • PHYSICAL OCEANOGRAPHY • PLANETARY GEOLOGY • SEISMOLOGY, OBSERVATIONAL • SEISMOLGY, THEORETICAL • SOLAR SYSTEM, GENERAL • VOLCANOLOGY

BIBLIOGRAPHY

- Agnew, D. C. (in press). In “IASPEI International Handbook of Earthquake and Engineering Seismology,” Chap. 1. Academic Press, San Diego.
- Bowler, P. J. (1992). “The Norton History of the Environmental Sciences,” New York, W. W. Norton.
- Brush, S. G. (1996). “A History of Modern Planetary Physics: Vol. 1, Nebulous Earth; Vol. 2, Transmuted Past; Vol. 3, Fruitful Encounters,” Cambridge University Press, New York.
- Burchfield, J. D. (1990). “Lord Kelvin and the Age of the Earth,” 2nd ed., The University of Chicago Press, Chicago.
- Doel, R. E. (1996). “Solar System Astronomy in America: Communities, Patronage and Inter-Disciplinary Research,” Cambridge University Press, New York.
- Ellenberger, F. (1996). “Histoire de la Geologie,” A. A. Balkema, Rotterdam.
- Fleming, J. R. (1998). “Historical Perspectives on Climate Change,” Oxford University Press, New York.
- Friedman, R. M. (1989). “Appropriating the Weather: Vilhelm Bjerknes and the Construction of a Modern Meteorology,” Cornell University Press, Ithaca, NY.
- Greene, M. T. (1992). “Natural Knowledge in Preclassical Antiquity,” The Johns Hopkins University Press, Baltimore.
- Laudan, R. (1987). “From Mineralogy to Geology: The Foundations of a Science, 1650–1830,” The University of Chicago Press, Chicago.
- Le Grand, H. E. (1988). “Drifting Continents and Shifting Theories,” Cambridge University Press, New York.
- Oldroyd, D. (1996). “Thinking about the Earth: A History of Ideas in Geology,” Athlone Press, London.
- Oreskes, N. (1999). “The Rejection of Continental Drift: Theory and Method in American Earth Science,” Oxford University Press, New York.
- Rossi, P. (1984). “The Dark Abyss of Time: The History of the Earth and the History of Nations from Hooke to Vico” (L. G. Cochrane, trans.), The University of Chicago Press, Chicago.
- Rudwick, M. J. S. (1985). “The Meaning of Fossils: Episodes in the History of Paleontology,” 2nd ed., The University of Chicago Press, Chicago.
- Rudwick, M. J. S. (1985). “The Great Devonian Controversy: The Shaping of Scientific Knowledge among Gentlemanly Specialists,” The University of Chicago Press, Chicago.



Evaporites

Peter Sonnenfeld

University of Windsor

- I. Environment of Evaporite Formation
- II. Continental Evaporites
- III. Marine Evaporites

GLOSSARY

- Archean eon** Time before about 2450 m.y. BP (million years before present).
- Arid** Climate with an evaporation rate exceeding the rate of atmospheric precipitation throughout the year.
- Clastics** Transported fragmental products of weathering (e.g., sands, silts, clays).
- Coriolis effect** Apparent deflection of moving air (specifically, any moving body) to the right in the northern hemisphere and to the left in the southern hemisphere.
- Endorheic basin** Depression in the land surface with water inflow and no surface outflow.
- Holocene** Time since the last ice age or the last 8,000 years BP.
- Horse latitudes** Subtropical high pressure belt, about 30–35° away from the equator, seasonally migrating with the sun about 5°.
- Neogene** Either a period of the Cenozoic era, spanning the last 25 m.y. BP or the younger portion of the Tertiary period, 25–1.8 m.y. BP.
- Permian** Last period of the Paleozoic era, 280–225 m.y. BP.
- Proterozoic eon** The time interval between about 2450–570 m.y. BP.
- Pseudomorph** A mineral crystallizing in the form of the mineral it replaces.

Salt dome, diapir A salt plug or stock, rising several kilometers above the mother lode, piercing, upwarping, and fracturing overlying sediments.

Semiarid Climate with an evaporation rate seasonally exceeding the rate of atmospheric precipitation.

Zeolite Group of hydrous aluminum silicates akin to feldspars that occur as secondary minerals and are characterized by easy loss of water of hydration.

EVAPORITES are rocks composed of chemically precipitated minerals derived from naturally occurring brines concentrated to saturation either by evaporation or by freeze-drying. They form in areas where evaporation exceeds precipitation, especially in a semiarid subtropical belt and in a subpolar belt. Evaporite minerals can form crusts in soils and occur as bedded deposits in lakes or in marine embayments with restricted water circulation. Each of these environments contains a specific suite of minerals.

Bedded marine evaporites comprise the bulk of ancient evaporitic rocks. They form in basins with broad shelves that act as preconcentrators of the brine and permit gypsum to crystallize out. The excess brines are able to exit as bottom outflow, as seepage through the basin floor, or to gather in rapidly subsiding deeper parts, where eventually halite precipitates. Further concentration brings about a

saturation for compounds that rise upon cooling and thus precipitate on the basin slopes. Clastics and organic matter may be swept into the basin and either dissolve in the brine, form separate laminations, or be swept into the subsurface. Eventually, precipitation rates catch up with subsidence rates and the basin fills up, the water surface area and with it evaporation losses are reduced, the inflow slows down, the salinity of the brine is reduced, and a reverse sequence of evaporite minerals is deposited. Beds of less soluble minerals follow upon beds of more soluble ones, effectively protecting them from dissolution. Compressional pressures acting on deeply buried salt bodies can deform these into salt pillows and eventually into salt domes that pierce through overlying beds.

I. ENVIRONMENT OF EVAPORITE FORMATION

Evaporites form in a narrow range of environmental conditions of temperature, atmospheric humidity, and air pressure. Basin location, orientation, and shape also play a decisive role. Evaporite minerals form in a 130° range of temperatures from -55°C , when water and solute go into a solid phase simultaneously (the eutectic point), to about 75°C when brines dry out by crystallizing completely (the eutonic point) before their density reaches 1.40 g/cm^3 . Seawater contains 92 water molecules per ion. This is reduced to 4.5 molecules per ion before halite starts precipitating and to 3 molecules at the eutonic point, when the solution dries out. Salt precipitation is thus the result of a deficiency of free water molecules to act as a solvent.

There are only two ways of concentrating a brine, by freeze-drying and by evaporation. Freeze-drying is restricted to areas of extensive winter frosts and inadequate atmospheric precipitation (i.e., to some arid or semiarid polar and high-altitude mountain regions). It produces groundwater-derived crusts and efflorescences in soils and around lake shores. Freezing of sea-water extracts water, but any remaining liquid easily diffuses into the ocean. As the water temperature is lowered, the clusters of liquid water molecules become larger, and thus the amount of hydrogen bonding available to other cations increases sharply. Consequently, the lower the temperature of formation, the greater is the number of water molecules attached to a crystal lattice and the more readily the mineral will convert in time to a less-hydrated variety. Moreover, hydrated evaporite minerals are not very soluble, and thus the rate at which they precipitate increases. Rising salinity counteracts the hydration, because it raises the hygroscopy of the brine and with it lowers the temperature range in which anhydrous minerals become stable.

Evaporation is only possible where the relative humidity of the air (the partial vapor pressure in the air) is lower than the vapor pressure of the fluid. The evaporative water loss from a brine surface is a function of the difference between relative humidity of the air and the vapor pressure of the brine surface; this difference decreases as the brine concentrates. According to Raoult's law, introducing further solute reduces the mole fraction of water molecules in a solution. Consequently, to lose any more water, saturated brines need a much higher vapor pressure than dilute ones or a lower water vapor saturation (relative humidity) of the air. In addition, the surface tension of the brine increases linearly with its molarity, making it progressively more difficult for water molecules to escape. The rate of evaporation from a solution saturated for sodium chloride is reduced by about 30%, from a solution saturated for potassium chloride, about 50% of that from a freshwater surface.

Brine saturation by evaporation occurs in areas of inadequate atmospheric precipitation (rain, dew, snow) and runoff (rivers, creeks, groundwater discharge), allowing the rate of evaporation to exceed the rate of replenishment (water deficit). Although evaporation rates are very high in equatorial regions, the daily rains counteract excessive water losses of land plants. In the other extreme, in polar regions, the vapor pressure of cold seawater is too low to allow for a significant evaporative concentration in a marine bay.

The water deficit becomes significant only where the amount of rain and with it the runoff decrease. That is to say,

$$E/t - (R + P)/t = D \quad (1)$$

where E/t is the evaporative water loss per unit of time, R/t the runoff and P/t the atmospheric precipitation per unit of time, and D the water deficit. Such water deficit is generated wherever descending air heats up adiabatically and decreases its relative humidity. Descending air occurs on the leeside of mountain ranges and on a larger scale in the subtropical high pressure belt (the horse latitudes). In both hemispheres the main belt with a deficit in the water budget straddles the horse latitudes and veers poleward from west coasts of continents. These are the areas of sparse, discontinuous desert or steppe vegetation, of evaporitic crusts in soils, and of hypersaline lakes, often located in endorheic basins. However, they are also areas of occasional flash floods due to a great variability in the amount of annual rainfall. Most of the massive marine evaporite accumulations of the past are confined to ancient semiarid areas with pronounced dry and wet seasons.

There seems to be a distinct relationship between cooler periods in the earth's history to extensions in the arid belt, a widening of the subtropical horse latitudes, and high

rates of evaporite accumulation. In contrast, peaks in coal formation correlate with low points in evaporite production. In the last ice age, maxima in aridity coincided with colder winters and cooler summers, yet lagged slightly behind maxima in glaciation.

Evaporite minerals form in four environments:

1. On a small scale in a series of microenvironments, such as at mine outlets, in tunnels, and lava caves, as encrustations that rarely exceed a few cm in thickness. Such occurrences are known in almost all climatic belts.
2. As groundwater-derived crusts and efflorescences in semiarid soil horizons and in polar, temperate, and subtropical climates.
3. As lacustrine deposits in semiarid and arid polar, temperate, and subtropical climates.
4. As precipitates in marine embayments in semiarid subtropical climates.

Groundwater-derived crystals and crusts of evaporite minerals are known from the dawn of earth history, the Archean era. Bedded marine evaporites derived from evaporation of an exposed brine surface formed only since the Proterozoic era. The earliest gypsum or anhydrite beds are about 1.7–1.8 billion years (b.y.), but the earliest halite and potash beds only about 0.7–0.8 b.y. old.

II. CONTINENTAL EVAPORITES

A. Groundwater-derived Crystals and Crusts

Both groundwater-derived evaporites and lacustrine deposits are very dependent in their mineralogy on the composition of the source waters and on the water temperature. In arid and semiarid lands, both in polar and subtropical regions, groundwater rises by capillary action through the aerated zone of soils and evaporates. It is charged with a variety of dissolved weathering products, which upon evaporation precipitate. They form either individual crystals or aggregates fused together with soil components into a firm crust. The progressive concentration of groundwater by evaporation leads to a precipitate of calcite followed by gypsum. Sulfate ions can enter the groundwater through oxidation of sulfide minerals in an aqueous environment; they generate gypsum crusts in steppe soils, because the calcium sulfate is the least soluble of all the sulfates. Halite precipitates only where there is a sufficient supply of chloride ions.

The more soluble components are capable of traveling farther and leapfrogging over less soluble ones; commonly a carbonate cement is overlain by a gypsum crust that marks the depth of wetting in a leached soil horizon, and

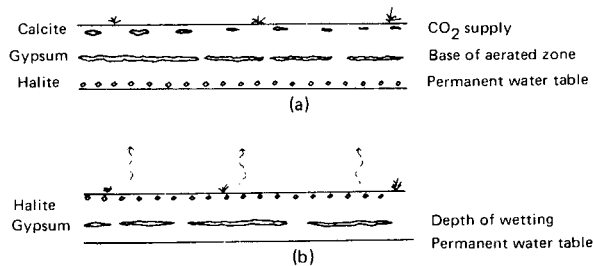


FIGURE 1 Precipitated crusts in semiarid soils; (a) downward leaching to a deeper water table and (b) capillary suction from a shallower water table. [Reprinted with permission from Sonnenfeld, P. (1984). In "Brines and Evaporites," Academic Press, Orlando. Copyright 1984 Academic Press.]

halite effloresces at the surface to be largely blown away by the wind. If seawater wets a soil at the high-water level, only to recede with the ebb, the water seeping into the soil will form an opposite sequence with halite encrustations below gypsum crusts. We can thus derive the direction of water movement from the relative position of crusts (Fig. 1).

Groundwater seeping toward a depression, particularly one filled with a lake fed by groundwater springs, will deposit evaporite minerals in concentric belts around the lake, with the most soluble minerals found closest to the lake shore. The slower the groundwater movement and the more dilute the brine initially, the larger are the crystals formed in the soil.

The contribution of marine sodium declines in polar soils landward, and weathered-out calcium and magnesium become the more important cations; likewise, chloride minerals decrease in frequency landward, while sulfates and nitrates increase in the same direction. Calcium, magnesium, bicarbonate, and sulfate ions also predominate in subtropical lakes unless there is some subsurface leaching of ancient evaporite deposits. Phosphates are rare and appear to be mutually exclusive with sulfates, while iodides and chlorates are unknown in evaporitic environments. Both nitrates and iodates occur only in areas of extreme aridity (i.e., in polar soils or in subtropical deserts with less than 10 mm of annual rainfall) and then only in surface exposures; neither iodates nor nitrates are known as buried ancient deposits. Formation of the nitrate deposits, known in almost all deserts, is not yet well understood. They are said to be derived from capillary evaporation of groundwater that may have picked up volcanic emanations or from atmospheric nitrogen oxides dissolved in dew and fog. However, rutile, common in desert soils, can act as a catalyst in the nitrogen cycle to combine atmospheric nitrogen with chemisorbed water to form ammonia, which is redistributed by daily fog. The nitrates accumulate only where the soil is insulated from groundwater by a halite crust and dissolve where buried below the water table of formation waters.

Depressions that are episodically filled by rains, by rising groundwater, or by storm tides from a nearby sea are called sebkhas. Continental sebkhas, also called playas, are either periodically inundated by flash floods or are fed by groundwater rising to the surface. Paralic sebkhas are either supratidal plains fed only by storm tides or shallow coastal lagoons still connected to the sea by a very narrow neck. All sebkhas are characterized by a net dominance of detrital fragments, a deficiency of calcite and dolomite, lattice imperfections in strontium-enriched anhydrites, and a presence of gypsum and other evaporite minerals only as encrustation within the soil.

A specialized environment for the formation of euhedral gypsum crystals or nodular aggregates is the strata beneath the ocean floor. The precipitation is induced by sulfur-oxidizing bacteria that consume dispersed organic matter. They can turn pyritiferous clays into gypsiferous ones.

B. Lacustrine Evaporites

Lacustrine evaporites accumulate only in basins with insufficient drainage, particularly closed or endorheic basins, often fed by a groundwater influx. Some of these have little or no relief and feeble rates of subsidence (e.g., the Chad Basin in Africa), others are tectonic basins with rapid subsidence and great relief. Because of the great diversity of solutes carried in waters of continental origin, a great number of minerals can form that are then classified by the dominant anion.

The sequence of precipitates somewhat differs in polar lakes from that in the subtropical zone because of the greater hydration potential in cold temperatures. For instance, gypsum does not precipitate in the presence of sodium bicarbonate carried by groundwater; calcium carbonate and sodium sulfate form instead. Mirabilite and thenardite are found wherever the brine approaches freezing temperatures in the winter, at which time the bicarbonate solubility increases drastically. Seawater concentrated by evaporation precipitates gypsum at 4.5-fold concentration; concentrated by freeze-drying it yields mirabilite, the hydrated sodium sulfate, already at 4-fold concentration. Mirabilite is also common in supraglacial and periglacial meltwater lakes, where it is derived from redissolved thenardite, the anhydrous sodium sulfate. Bloedite, the hydrated sodium-magnesium sulfate, crystallizes in cold lakes even before halite saturation is reached. Seawater concentrated by evaporation precipitates halite at 10-fold concentration, concentrated by freeze-drying; below -23°C , it precipitates hydrohalite, the hydrated form of sodium chloride, at 8-fold concentration.

Lakes outside the polar regime concentrate their brines by evaporation in the summer. Only in rare cases is there precipitation by freeze-drying in the winter, because the latter produces a less concentrated brine that can redis-

solve the precipitate when the ground warms up. A vertical and horizontal zonation of precipitates develops in that the most soluble compounds travel the farthest.

If the source waters are highly carbonated, either by redissolution of limestone, or from rotting plant material, they precipitate first calcite and even monohydrocalcite. Among the three anhydrous calcium carbonate minerals, vaterite is built into some gastropod shells but eventually converts to aragonite. Aragonite is the preferred precipitate of many marine organisms, calcite of lacustrine ones. In time, however, all aragonite, whether inorganically precipitated or built into shells and skeletons, converts to calcite. Aragonite of Mesozoic age is very rare, pre-Permian aragonite is unknown. Calcium carbonates as rocks are called limestones.

Because of the lower calcium/sodium ratio in terrestrial runoff compared to seawater, the progressive concentration of brines in alkaline lakes leads then to a preferential precipitation of sodium and compound sodium–calcium carbonates. All the hydrated species of minerals in this group are unstable and either convert in time to anhydrous varieties or redissolve (Table I). They are found exclusively in lacustrine environments. Soda lakes form mainly on bedrock composed of crystalline rocks or polymictic, feldspathic or argillaceous sandstones; magnesium-rich brines form where carbonated groundwater comes in contact with basic igneous rocks.

Magnesite is the only form of pure magnesium carbonate and is found in lacustrine environments either precipitated directly or as a bacterial alteration product of calcite. It can also be found along the rims of marine lagoons and sebkhas with a considerable influx of continental waters. Dolomite, the calcium-magnesium double carbonate, is found in a few instances near the interface between groundwater discharge and seawater influx as cryptocrystalline soft paste that eventually hardens into a very fine-grained rock, quite different in appearance from sucrosic dolomites that are evidently secondary after limestone. Whether this dolomite is truly primary or calcite converted within a season to dolomite is not always clear.

Many such hypersaline lakes develop a high alkalinity and a high pH sufficient to dissolve any swept-in silicates. These may be precipitated as framework silicates in the zeolite group (e.g., sodium–aluminum silicate minerals hydrated to a varying degree) found in several lakes in north central Africa. Hydrated calcium–aluminum silicates or calcium–sodium aluminum silicates are also known but are much rarer. However, the mineral stability is ephemeral: in time the minerals are progressively dehydrated and turn into authigenic feldspar crystals, or the sodium and alumina are leached out and they convert into members of the opal group and hence into a variety of quartz or chert. If the source waters are rich in dissolved silica, a series of hydrous silica compounds (related to

TABLE I Lacustrine Carbonates

Kalichinite	KHCO_3
Fairchildite	$\text{K}_2\text{CO}_3 \cdot \text{CaCO}_3$
Buetschliite	$\text{K}_2\text{CO}_3 \cdot \text{CaCO}_3 \cdot 2\text{H}_2\text{O}$
Thermonatrite	Na_2CO_3
Soda (natron)	$\text{Na}_2\text{CO}_3 \cdot 10\text{H}_2\text{O}$
Nahcolite	NaHCO_3
Wegscheiderite	$\text{Na}_2\text{CO}_3 \cdot 3\text{NaHCO}_3$
Trona	$\text{Na}_2\text{CO}_3 \cdot \text{NaHCO}_3 \cdot 2\text{H}_2\text{O}$
Nyerereite	$\text{Na}_2\text{CO}_3 \cdot \text{CaCO}_3$
Shortite	$\text{Na}_2\text{CO}_3 \cdot 2\text{CaCO}_3$
Pirssonite	$\text{Na}_2\text{CO}_3 \cdot \text{CaCO}_3 \cdot \text{H}_2\text{O}$
Gaylussite	$\text{Na}_2\text{CO}_3 \cdot \text{CaCO}_3 \cdot 5\text{H}_2\text{O}$
Burbankite	$\text{Na}_2\text{CO}_3 \cdot (\text{Ca}, \text{Ba}, \text{Sr}, \text{La}, \text{Ce})_4(\text{CO}_3)_4$
Eitelite	$\text{Na}_2\text{CO}_3 \cdot \text{MgCO}_3$
Northupite	$\text{Na}_2\text{CO}_3 \cdot \text{MgCO}_3 \cdot \text{NaCl}$
Tychite	$\text{Na}_4\text{Mg}_2(\text{CO}_3)_2(\text{SO}_4)_3$
Bradleyite	$\text{Na}_3\text{PO}_4 \cdot \text{MgCO}_3$
Dawsonite	$\text{NaAl}(\text{OH})_2\text{CO}_3$
Burkeite	$\text{Na}_2\text{CO}_3 \cdot 2\text{Na}_2\text{SO}_4$
Hanksite	$\text{Na}_{22}\text{K}(\text{CO}_3)_2(\text{SO}_4)_9\text{Cl}$
Siderite	FeCO_3 with Mg : Fe under .05
Sideroplesite	(Mg, Fe) CO_3 with Mg : Fe = 0.5–.30
Pistomesite	(Mg, Fe) CO_3 with Mg : Fe = .30–1.0
Mesitite	(Mg, Fe) CO_3 with Mg : Fe = 1–3
Breunerite	(Mg, Fe) CO_3 with Mg : Fe = 3–20
Magnesite	MgCO_3 with Mg : Fe over 20
Barringtonite	$\text{MgCO}_3 \cdot 2\text{H}_2\text{O}$
Nesquehonite	$\text{MgCO}_3 \cdot 3\text{H}_2\text{O}$
Lansfordite	$\text{MgCO}_3 \cdot 5\text{H}_2\text{O}$
Artinite	$2\text{MgCO}_3 \cdot \text{Mg}(\text{OH})_2 \cdot 3\text{H}_2\text{O}$
Dypingite	$4\text{MgCO}_3 \cdot \text{Mg}(\text{OH})_2 \cdot 3\text{H}_2\text{O}$
Hydromagnesite	$3\text{MgCO}_3 \cdot \text{Mg}(\text{OH})_2 \cdot 3\text{H}_2\text{O}$ or $4\text{MgCO}_3 \cdot \text{Mg}(\text{OH})_2 \cdot 4\text{H}_2\text{O}$
Huntite	$3\text{MgCO}_3 \cdot \text{CaCO}_3$
Dolomite	$\text{MgCO}_3 \cdot \text{CaCO}_3$
Calcite, aragonite	CaCO_3
Monohydrocalcite	$\text{CaCO}_3 \cdot \text{H}_2\text{O}$
Trihydrocalcite	$\text{CaCO}_3 \cdot 3\text{H}_2\text{O}$
Pentahydrocalcite	$\text{CaCO}_3 \cdot 5\text{H}_2\text{O}$
Ikaite	$\text{CaCO}_3 \cdot 6\text{H}_2\text{O}$

opal) are precipitated. They are all unstable and convert in time to anhydrous silica cement or to some variety of chert. The complete conversion to chert may take several million years, but none of the complex hydrous silica compounds common in dried-out Neogene lake beds are known from more ancient sediments.

Further concentration of a lacustrine brine stripped of carbonate ions leads to the precipitation of sulfates or of corresponding magnesium compounds. The sulfate ions can form sodium, magnesium, and calcium sulfates but only after the progressive concentration has stripped the

brine of nearly all carbonate and bicarbonate content ([Table II](#)). Gypsum does not precipitate in the presence of sodium bicarbonate; instead, calcite and mirabilite, the hydrous sodium sulfate, or thenardite, the dehydrated sodium sulfate, are formed.

Potassium is screened out of the groundwater by sorption and ion exchange, resulting in a substantial enrichment in sodium cations. In a very few instances, potassium sulfate minerals are found in lacustrine environments, wherever the groundwater is especially enriched in potassium and has no opportunity to turn some clay into illite. Iron sulfates do not form either crusts or bedded deposits; they occur almost exclusively as halos around weathering sulfides. Upon dissolution in an aqueous environment, they become bivalent iron-organic complexes.

Chlorine content of igneous and metamorphic rocks is minimal. Wherever groundwater contains significant quantities of chloride anions, these are usually due to contamination by discharging calcium chloride enriched formation waters or to dissolution of ancient marine or lacustrine chloride deposits ([Table III](#)). Circulating groundwater can easily dissolve precipitated chlorides and deliver them to the nearest surface flow; the occurrence of salt creeks or salt rivers is, therefore, quite common even outside the arid belt.

Reprecipitation of these solutes leads to secondary, non-marine chloride deposits that display all the aspects of marine evaporite deposits. However, such evaporite sequences show no evidence of any connection to a coeval ocean and most of the time do not exhibit the complete marine succession of evaporites, either being devoid of calcium sulfates or of potash deposits. Being redeposited and recrystallized, the bromine/chlorine ratio in recycled evaporite deposits is but a fraction of that found in similar marine deposits. Such interior salt basins are found in Europe, Asia, Australia, and North America. Mesozoic and Cenozoic salt accumulations in both North Dakota and Arizona appear to be in this category. For example, the Great Salt Lake appears to derive its salt content from a leaching of Jurassic salts from the Wasatch Range.

Borates form a great variety of hydrated minerals that are common as nests in both lacustrine and marine evaporites, wherever there is either a syngenetic or an epigenetic volcanic source of boron nearby. Boron is also liberated out of the decomposing lattice of swept-in muscovite flakes. On occasion it leads to the formation of a few slivers of authigenic tourmaline.

III. MARINE EVAPORITES

Marine evaporites constitute by far the largest volume of evaporite deposits. None of them were formed in the open ocean where currents induce thorough mixing and prevent

TABLE II Evaporitic Sulfate Minerals

Mineral	Formula	Sp. gr.	Mineral	Formula	Sp. gr.
<i>Lacustrine sulfates:</i>					
Celestite	SrSO ₄	3.971	Hanksite	2Na ₂ CO ₃ ·9Na ₂ SO ₄ ·KCl	2.570
Polyhalite	K ₂ SO ₄ ·2CaSO ₄ ·MgSO ₄ ·2H ₂ O	3.000	Burkeite	Na ₂ CO ₃ ·2Na ₂ SO ₄	2.570
Anhydrite	CaSO ₄	2.980	Uklonskovite	NaOH·MgSO ₄ ·2H ₂ O	2.450
Glauberite	Na ₂ SO ₄ ·CaSO ₄	2.850	Gypsum	CaSO ₄ ·2H ₂ O	2.330
Bassanite	CaSO ₄ ·H ₂ O	2.761	Bloedite	Na ₂ SO ₄ ·MgSO ₄ ·5H ₂ O	2.280
Thenardite	Na ₂ SO ₄	2.698	Hydroglauberite	5Na ₂ SO ₄ ·3CaSP ₄ ·6H ₂ O	1.510
Aphthitalite	Na ₂ SO ₄ ·3K ₂ SO ₄	2.656	Mirabilite	Na ₂ SO ₄ ·10H ₂ O	1.490
Bruckerite	2Na ₂ SO ₄ ·CaSO ₄ ·2H ₂ O				
<i>Marine sulfates:</i>					
<i>Ca-sulfates:</i>	(decreasing calcium content)		<i>Ammonium sulfates:</i>		
Anhydrite	CaSO ₄	2.980	Boussingaultite	(NH ₄) ₂ SO ₄ ·MgSO ₄ ·6H ₂ O	1.723
Bassanite	CaSO ₄ ·H ₂ O	2.761	<i>Mg-sulfates:</i>	(decreasing magnesium-content)	
Gypsum	CaSO ₄ ·2H ₂ O	2.330	Kieserite	MgSO ₄ ·H ₂ O	2.570
Goergeyite	K ₂ SO ₄ ·5CaSO ₄ ·H ₂ O	2.770	Sanderite	MgSO ₄ ·2H ₂ O	1.757
Glauberite	Na ₂ SO ₄ ·CaSO ₄	2.850	Leonhardite	MgSO ₄ ·4H ₂ O	
Polyhalite	K ₂ SO ₄ ·2CaSO ₄ ·MgSO ₄ ·2H ₂ O	3.000	Allenite	MgSO ₄ ·5H ₂ O	
Syngenite	K ₂ SO ₄ ·CaSO ₄ ·H ₂ O	2.597	Sakiite	MgSO ₄ ·6H ₂ O	
<i>Sr-sulfates:</i>	(decreasing strontium content)		Epsomite	MgSO ₄ ·7H ₂ O	1.677
Celestite	SrSO ₄	3.971	<i>Na-sulfates:</i>	(increasing sodium content)	
Kalistrontite	K ₂ SO ₄ ·SrSO ₄	3.320	Aphthitalite	Na ₂ SO ₄ ·3K ₂ SO ₄	2.656
<i>K-Mg sulfates:</i>	(decreasing potassium content)		Bloedite	Na ₂ SO ₄ ·MgSO ₄ ·5H ₂ O	2.280
Kainite	4KCl·4MgSO ₄ ·11H ₂ O	2.190	Loeweite	6Na ₂ SO ₄ ·7MgSO ₄ ·15H ₂ O	2.423
Langbeinite	K ₂ SO ₄ ·2MgSO ₄	2.829	Vant'hoffite	3Na ₂ SO ₄ ·MgSO ₄	2.694
Picromerite	K ₂ SO ₄ ·MgSO ₄ ·6H ₂ O	2.150	D'ansite	9Na ₂ SO ₄ ·MgSO ₄ ·3NaCl	2.650
Leonite	K ₂ SO ₄ ·MgSO ₄ ·4H ₂ O	2.201	Thenardite	Na ₂ SO ₄	2.698

the formation of brines of increased salinity. All of the marine evaporites originated in lagoonal embayments or marginal seas. Polar marine embayments, even where ice-bound, do not develop hypersalinity or brine concentrations conducive to evaporite precipitation, because melt-

ing ice readily produces a surplus in the water budget and with it an estuarine (fjord-type) water circulation. The low rates of evaporation in cold climates cannot counteract this surplus. The formation of marine evaporites is thus restricted to subtropical lagoons, where high evaporation

TABLE III Evaporitic Chloride Minerals

Chlorides in marine environments			
Halite	NaCl	Sylvite	KCl
Carnallite	KCl·MgCl ₂ ·6H ₂ O	Bischofite	MgCl ₂ ·6H ₂ O
Tachyhydrite	CaCl ₂ ·2MgCl ₂ ·12H ₂ O	Rinneite	FeCl ₂ ·3KCl·NaCl
Chlorides in polar lacustrine environments			
Halite	NaCl	Sylvite	KCl
Hydrohalite	NaCl·2H ₂ O	Carnallite	KCl·MgCl ₂ ·6H ₂ O
Antarcticite	CaCl ₂ ·6H ₂ O		
Rare accessory minerals			
Sal Ammoniac	NH ₄ Cl	Baeumlerite	CaCl ₂ ·KCl
Chloraluminite	AlCl ₃ ·3H ₂ O	Erythrosiderite	FeCl ₃ ·2KCl·H ₂ O
Rokuehnite	FeCl ₂ ·2H ₂ O	Molysite	FeCl ₃
Douglasite	FeCl ₂ ·KCl·2H ₂ O or FeCl ₂ ·2KCl·2H ₂ O		

rates produce a water deficit counteracted by an antiestuarine circulation.

A. The Entrance Barrier

Carl Ochsenius (1888) was the first to suggest that for evaporite precipitation a lagoon must have an entrance sill to restrict water circulation, as bays with unrestricted access maintain salinities only marginally higher than the open sea. He envisaged a continuous inflow to maintain a supply of brine to prevent the basin from drying out.

Otto Krull in 1917 and many other investigators thereafter augmented the Ochsenius model of a barred basin by assuming a surface inflow and a concurrent bottom outflow that was somewhat slowed by friction against entrance floor and walls and by drag against surface inflow (Fig. 2). Barriers principally serve to retard the removal of salt by any outward flowing bottom current, and in so doing, cause the basin waters to become progressively saltier. The width, depth, and configuration of the entrance strait thus plays an important role in determining the rate of bay water concentration. If the outflow were to carry out more solute per unit of time than was delivered by the inflow, the saline waters in the bay would gradually freshen.

The depth of the interface between inflow and outflow is only a function of the length of a strait to its total depth; the lower this interface, the less brine can escape. The inflow sets up an interface with the outflow that quickly becomes a pycnocline, or layer of rapid density changes. Even a strong wind cannot overturn such a stable density gradient, but the wind energy is dissipated along the interface by working against buoyancy. The hydrostatic pressure gradient of overlying brines causes solute diffusion in the direction of increasing salinity, which is the direction of increasing dynamic viscosity and of a downward density gradient. A steep vertical density gradient acts as a barrier to vertical fluid mixing and convection, but the density difference decreases as the thickness of the upper layer increases; large density differences are possible only with a shallow interface between inflow and resident brine.

Krull's model is born out by modern subtropical embayments where a surface inflow prevents a significant

lowering of the sea level whenever an evaporative water deficit is not balanced by continental drainage. The continuous outflow was deemed necessary to account for the great shortfall in salts of higher solubility if compared with the volumes of salts of next lower solubility that are present. Nonetheless, not all evaporite sequences contain salts of highest solubility, because the degree of entrance restriction dictates at what concentration of the bottom brine the surface inflow equilibrates with the intermediate or bottom outflow.

The seaward outflow of dense and anoxic bottom brines from the Mediterranean Sea today delivers a blanket of oxygen-poor and nutrient-deficient waters that extends to the coasts of Ireland and Brazil at a depth of about 1200 m beneath the ocean surface. In 1984 G. Busson suggested that an outflow of brines from extensive Upper Cretaceous gypsum precipitating basins of North Africa may have produced the anoxic event of extensive black shale deposition throughout the then much shallower central and southern Atlantic Ocean. A similar black bituminous shale, the Duvernay Formation, deposited in front of Upper Devonian reefs in Alberta, Canada, may represent the outflow from a broad anhydrite shelf, the Potlatch Evaporites, in the rear of the barrier reef. Such an outflow seriously depletes the shelf in front of the entrance sill of nutrients by washing them down the continental slope. The migration of bottom dwellers from the open ocean is prevented, while a rising salinity in the bay gradually kills off any endemic fauna.

B. Ion Imbalance

Separated from contact with the atmosphere, the bottom brines quickly turn anaerobic. Where the bottom waters reach into the photic zone because the interface is shallow enough, a pink horizon composed of prokaryote bacteria (called a "bacterial plate") develops beneath the mixing zone between oxygenated surface waters and bottom brines. Concentrated brines have a low oxygen and carbonate content because of decreased solubility of such ions. Anaerobic, sulfate-reducing bacteria as facultative autotrophs, therefore, can extract oxygen from sulfate ions, converting them to hydrogen sulfide and can utilize inorganic carbonate provided that there is a source of hydrogen as can be supplied by iron oxidation. An increasing presence of hydrogen ions raises the pH, and with it the solubility of calcium carbonate drops sharply. Only prokaryote cells can utilize inorganic energy sources directly, because the electron transport system lies in plasma membranes; eukaryotes need electron donors in solution because they house their electron-transport system in specific organelles. However, because the anaerobes are basically heterotrophs they prefer metabolizing organic matter

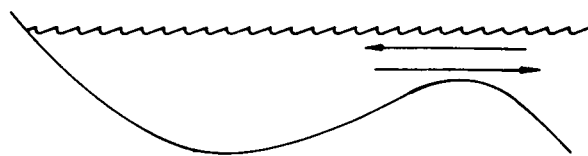


FIGURE 2 Krull's model of a barred basin with two-way flow. [Reprinted with permission from Sonnenfeld, P. (1984). In "Brines and Evaporites," Academic Press, Orlando. Copyright 1984 Academic Press.]

and thus the presence of macerated organic compounds strongly accelerates sulfate reduction.

Where sulfate ions are not supplied by incoming seawater, the bacteria eventually also scavenge oxygen from precipitated gypsum if organic matter is present. A partial destruction of gypsum laminae then leads either to ^{12}C -enriched, low magnesium calcite laminae or to magnesite, whereby huntite is a possible precursor to magnesite. As the sulfate reducers dispose of sulfate ions, the resulting excess of cations also raises the pH. The anaerobic sulfur bacteria are able to destroy more than two-thirds of all incoming sulfate ions in the anoxic bottom brines and convert them to hydrogen sulfide gas that can escape. The scavenging of sulfate ions leads to a deficit of anions and primarily a surplus of magnesium cations in inflowing seawater, at least 19.3 mol/m^3 .

In solar evaporation of a brine, the sulfate concentration will reach a maximum for a given temperature and then decline. Even the mere heating of a calcium sulfate solution above 62.5°C , a temperature readily attained in nature in concentrated brines, allows some sulfate to escape; by the time this solution reaches 99°C there is a surplus of 48.4% calcium ions present. The same separation of cations from anions is observed in a freshly mixed calcium chloride brine of density 1.39, which contains about 25 mol/m^3 of hydroxyl ions.

In a density stratified system, between the oxygenated surface waters of positive redox potential and the anaerobic bottom waters of negative redox potential there is a gradient of some 600–800 mV. This is sufficient to drive cations into the brine and extract anions, especially those that can become gases. To preserve a charge balance, the cations combine with water to generate hydroxyl ions and free hydrogen to be utilized by anaerobic bacteria.

As the salinity increases, physical parameters of the brine change: both the specific volume and the specific heat of the brine decrease, and so does its compressibility and its rate of evaporation, but its boiling point rises, as does its viscosity and surface tension and also its hygroscopy. Because of the higher refractive index of concentrated solutions, much of the sunlight is trapped and converted into heat. The temperature rise is aided by the lower specific heat of concentrating brines and by lower heat losses through reduced rates of evaporation. For every cubic meter of seawater flowing in per second, the energy trapped in the lagoon can amount to several megawatts. The shallow shelves heat up more because less brine must be heated per unit area.

The thermal diffusivity of the solute (the Soret effect) is an important factor in brine concentration. Most of the marine evaporite compounds increase their solubility with temperature and are thermophile (i.e., they wander into the warmer brine, increasing there the concentration). Ther-

mophile solutes increase the stability of density stratification, cryophyle solutes that wander into the cooler surface waters decrease it. Some solutes change their character at a given temperature. For example, sodium chloride, thermophile at ambient temperature, becomes cryophile below 12°C . Other compounds change at a given concentration (e.g., calcium sulfate solutions become exothermal above about 15.5 mmol/liter , which is close to saturation at 25°C). These temperature points are altered by the presence of other solutes.

Age dating of evaporite deposits based on the presence of radiogenic isotopes of potassium and strontium has not been very successful. The rocks have acted as open systems either continuously or episodically. Heavy losses of argon and other daughter products have led almost without exception to low values of radiometric ages.

C. Precipitation Sequence

Mere concentration of seawater to saturation leads to a relatively simple sequence of primary evaporite minerals, from aragonite or calcite to gypsum, followed only by chlorides, first halite, then sylvite or carnallite, ending with bischofite or tachyhydrite. This sequence of primary minerals is identical in all Phanerozoic marine evaporite deposits. It is evident that not only have the laws of physics and chemistry of brines been constant in the last 600–800 m.y., or that any biogenic factors in the precipitation process were present throughout this time, but also that the ionic composition of the initial brine (i.e., the seawater, whatever its salinity might have been) did not deviate far from present values. However, we have not found any marine evaporites of Archean age; the oldest bedded marine gypsum or anhydrite beds are Middle to Late Proterozoic in age, and the oldest rock salt deposits straddle the Proterozoic/Cambrian boundary. There was a significant worldwide hiatus in marine salt deposition during Middle Ordovician time. A second hiatus straddles the Cretaceous–Tertiary boundary, the very interval of rapid diversification of flowering plants and concurrent extinction of all large land and sea animals.

Calcium carbonate is the first precipitate in concentrating brines. In magnesium-rich seawater the most common form is rapidly precipitating aragonite, while slowly crystallizing calcite predominates in lacustrine environments. As the temperature of the brine rises, fewer magnesium ions are needed to subdue calcite precipitation and to foster aragonite formation; sodium ions have an opposite effect. In formation waters stripped of their magnesium content by sorption on clays or by dolomitization, aragonite recrystallizes into calcite, especially in the presence of basic or neutral amino acids. Wherever sodium carbonates are produced by bacteria they react with seawater to

form hydromagnesite that later turns into magnesite. Carbon dioxide dissolved in seawater is not only taken up by plants, by aragonite precipitation, and by increasing bacterial activity in a concentrating basin, it also escapes when its solubility is lowered by heating the brine or by increasing its salinity.

The sequence of primary deposits proceeds from calcium carbonates (aragonite and calcite) to gypsum, then to halite, and eventually to potassium and magnesium chlorides under continuing evaporation of water (Fig. 3). Primary sodium carbonates and sulfates do not occur in subtropical marine evaporite sequences because of the higher calcium/sodium ratio in normal seawater compared to most continental brines. Barite, the sulfate of barium, has a very low solubility and forms small nests in limestones. Bedded barite deposits are known from the Archean and are suspected to be replacements of gypsum. Celestite, the sulfate of strontium, precipitates when the brine is about to reach gypsum saturation. It is found together with marginal limestones or within the gypsum; its amount of precipitation decreases as the salinity further increases.

Increasing salinity means decreasing oxygen solubility and thus gradual decline in burrowers and bioturbation. The carbonates take on a finely laminated texture. Reef builders flourish around the entrance and near river mouths, as their natural enemies are gradually eliminated; syngenetic subsidence forces them to grow upward in order to keep the growing parts in the euphotic zone. Their oxygen consumption is very high, because they produce more organic matter than they consume. Since only their tops flourish in the inflow and their trunks are not alive, reefs expand around the inlet and further restrict the water exchange with the open sea. Carbonate ions, needed for algal and bacterial metabolism, must continue to be brought in by runoff.

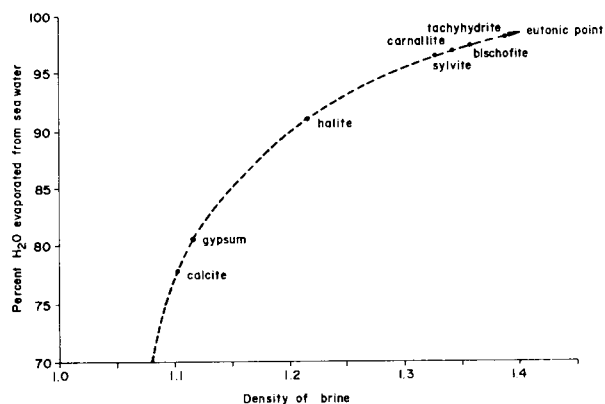


FIGURE 3 Precipitation path of an anoxic marine brine to the eutonic point. [Reprinted with permission from Sonnenfeld, P. (1984), In "Brines and Evaporites," Academic Press, Orlando. Copyright 1984 Academic Press.]

D. Saturation Shelves

Any current entering the marginal bay is deflected by the Coriolis effect, which produces in the northern hemisphere not only an anticlockwise circulation of the inflow as it glides along the shores of a marginal sea but also an interface to bottom brines tilted both westward and poleward. The progressive concentration of the longshore current leads to a loss of carbonate-ion solubility, a retreat of carbonate sedimentation near the entrance, and the continued deposition along the shores as beach rock even after the brine in the lagoon center has reached a concentration in excess of carbonate saturation. The stripping of carbonate ions aids gypsum precipitation.

Seawater contains three times as many sulfate as calcium ions, and thus could easily precipitate all calcium as gypsum. However, even very concentrated brines usually show a significant residual calcium content and a sulfate deficiency. The brine, when saturated for calcium sulfate, contains less than 4 ppm oxygen in solution, and anaerobic bacteria have to scavenge oxygen out of sulfate ions. As there are four oxygen atoms needed for each gypsum molecule, gypsum precipitates only in the oxygenated zone or where photosynthesizing bacteria living in the photozone supply new oxygen. In this zone, one also finds stromatolites, originally composed of calcium carbonate, now completely gypsified.

The shallow shelves and shoals are the sites of gradual concentration of the inflow by evaporation; they were aptly named by Richter-Bernburg in 1957 "saturation shelves." It is here that photosynthetic bluegreen algae and thiobacteria supply oxygen and convert rising hydrogen sulfide into new sulfate ions required to precipitate gypsum banks. A basin with one steep and one gentle slope would develop asymmetric saturation shelves with gypsum deposition lacking on the steep side (e.g., the Triassic Basin of North Africa).

Gypsum deposition initially spreads throughout the marine bay, but as the brine concentrates further and the continued subsidence drops the deeper parts of a basin out of the photic zone only the shallow shelves and shoals remain sites of continuing precipitation of gypsum from incoming seawater.

E. Residual Bitters

The residual brine can now slide into the deeper parts to precipitate halite, whereby the gypsum thickness then tends to vary inversely with the halite thickness. Thickest halites thus mark the centers of subsidence. In most instances brine saturation continues to increase toward precipitation of the potash minerals sylvite and carnallite. There are no known potash deposits that were not

originally encased in halite, indicating a gradual rise and eventual drop in the concentration of the brine. They occur on slopes of the ancient evaporite basin, because KCl-NaCl mixtures in brines decrease both specific gravity and solubility upon cooling and can eventually even float before precipitating.

Usiglio, conducting in 1849 a now famous and often repeated experiment, evaporated Mediterranean seawater in his well-aerated laboratory and coprecipitated first iron oxide and gypsum, then halite and magnesium sulfate. In nature, the latter two do not normally occur together, because anaerobic bacteria in the brine strip incoming seawater of its sulfate content and leave cations available as hydroxide or organic complexes. Where halophile bluegreen algae are unable to resupply sufficient oxygen to generate at least some sulfate ions, even calcium is not precipitated as gypsum but is retained in the brine to form calcium-rich formation waters or to be ultimately precipitated as tachyhydrite. Magnesium is used either to alter clays into minerals of the magnesian-chlorite group with brucite pillars or to dolomitize deposited limestones. It is significant that inside evaporite basins all carbonate intercalations, most surrounding reefs and many other limestone banks downdip from evaporite basins, show evidence of extensive secondary dolomitization.

Carnallite deposits from open brines are distinctly stratified, alternating with halite beds. Interstitial brines saturated for carnallite form with precipitated halite slush a disseminated structure with carnallite occurring in the interstices of a halite crystal matrix. Even small amounts of calcium chloride, either derived from an influx of formation waters or from a calcium residue after excessive destruction of sulfate ions, reduce the solubility of potassium chloride and even more so of magnesium chloride, thus forcing the precipitation of carnallite or the conversion of precipitated sylvite to carnallite.

Sylvite nucleates much more slowly than carnallite. However, alcohols, or nitrogen compounds derived from decaying organic matter, such as urea, ammonium chlorides, and complex cyanides, greatly reduce the solubility of KCl. Urea also increases the solubility of magnesium chloride to the point that pale yellowish sylvite becomes the preferred precipitate. Only where the brine is exposed to air and the organic matter is oxidized can carnallite precipitate. In Permian potash layers of European Russia west of the Ural Mountains, primary sylvite appears to be restricted to the area where the lagoon was covered by episodic runoff from the paleo-Ural Mountains, and carnallite occurs west of that limit.

Where the entrance restriction is extreme, further brine concentration beyond potash saturation will lead to the precipitation of bischofite or tachyhydrite, both commonly sandwiched into carnallite. However, to be preserved both

of these magnesium-chloride minerals must remain under water cover, as they decompose spontaneously when exposed to air. The presence of either of them is thus good evidence to surmise that the lagoon never dried out completely. Both minerals are usually encased in carnallite depicting the oscillation of brine concentration. Secondary bischofite can form by exposing carnallite to waters undersaturated for potassium chloride.

At first tachyhydrite was considered solely a byproduct of decomposition of carnallite or bischofite in the presence of calcium chloride containing formation waters, as it never occurs together with primary sylvite. Its occurrence in highly recrystallized Permian Zechstein evaporites in Germany for a long time caused arguments for or against a secondary origin. However, with increasing temperature of the brine, the stability field of tachyhydrite expands at the expense of both bischofite and antarcticite. Consequently, in Brazil and Thailand the tachyhydrite occurs as several bedded intercalations in carnallites and thus must be considered to be primary. Both are localities that have remained in the tropical zone since the evaporite deposition. Elsewhere, either it has never been precipitated or it has disappeared, when the lagoon dried out and the highly hygroscopic precipitate disintegrated in adsorbed atmospheric moisture and its own crystal water or when the rocks cooled below about 19°C.

F. Iron Staining

Seawater is deficient in iron, and much of it is concentrated in swept-in organisms. Bivalent iron-organic complexes are very soluble and remain dissolved until a very concentrated brine is formed. Their oxidation in brines exposed to the atmosphere leads to the inclusion in carnallite of fine needles of goethite [FeO(OH)], which are readily dehydrated to hematite (Fe_2O_3), giving the whole crystal a red color. Solubilization of the magnesium chloride by passing brines can then lead to a secondary red sylvite, and the introduction of sterile magnesium-chloride brines into primary sylvite can lead to white secondary carnallite. Red halite, often found as fracture filling in clay laminations, derived its iron from the surrounding clays.

Neither bischofite nor tachyhydrite is stained red by hematite, suggesting that organic complexes of iron did not decompose and thus were not in contact with the atmosphere.

In marginal parts of the evaporite basin, where the pH in the oxygen-deficient brine was substantially lowered, iron can substitute for magnesium in the carnallite lattice. However, even in advanced stages of brine concentration, iron very rarely forms a separate mineral rinneite ($FeCl_2 \cdot 3KCl \cdot NaCl$), which is unstable in the presence of oxygen and, therefore, absent from red carnallites. It is

commonly associated with sylvite in marginal parts of the basin farthest from the open ocean. Rinneite can also form as an early desiccation product of an iron-bearing carnallite in a hygroscopic medium but not in contact with air.

The basin tends to fill up with precipitates of progressively greater solubility, but flash floods and excessively cool seasons are prone to interrupt this process by freshening the brine temporarily and by interjecting intercalations of precipitates of lower solubility. A seasonal slight freshening of the brine allows the marginal gypsum platform to grow out onto precipitated halite as a wedge-shaped intercalation. More pronounced freshening by tropical storms (that have a nearly 10- to 12-year frequency) and temporarily increased rainfall may even allow marginal limestones, later converted to dolomites, to grow out onto the halite surface. This gives the halite a banded character. The finer gypsum laminae only become apparent when part of the halite is dissolved.

G. Depositional Fabrics

Three types of rock fabric are important to distinguish in evaporites: fabrics produced during mineral precipitation; fabrics produced by compaction and drainage of interstitial fluids; and fabrics produced by recrystallization in intercrystalline fluids, circulating hygroscopic brines, or meteoric waters. Halite develops enlarged crystals only in the absence of anhydrite. Halite crystal growth tends to be inhibited by anhydrite crystals forming on the crystal faces.

The higher the pH during gypsum crystallization, the stubbier are the crystals; alkanes, phenols, and fatty acids foster the formation of more tabular, equidimensional, or discoid-lenticular crystals. Elongate, prismatic gypsum crystals grow in low-pH environments, with or without the presence of organic matter, or in the presence of dissolved silica. Our knowledge of minute variations in fabric changes of precipitates in different types of brines is still very inadequate.

In the margins of evaporite basins occur welts of polygonal shape, called “tepee structures” (Fig. 4). These are antiform structures of slabs of precipitate propped together in overthrust pairs that circumscribe a saucer-shaped depression. They are either 0.5 to 3 m across, with very shallow central depressions and cracks no more than about 15 cm deep or 25 to 300 m across, with depressions about 1 m deep and cracks up to 15 m deep. Such tepee structures are restricted to that part of the basin rim where the water table is shallow enough that capillarity can moisten the upper reaches of the ground. They are formed by loading a heavier crust onto a precipitate-brine mush that rises during the dry season by capillary action or is squeezed up by thermal expansion and the load of the



FIGURE 4 Polygonal pattern of gypsum crusts in a gypsum- and halite-precipitating lagoon in Gran Roque, Venezuelan Antilles. The diameter of the polygons is about 1 m. [Reprinted with permission from Sonnenfeld, P. (1984). In “Brines and Evaporites,” Academic Press, Orlando. Copyright 1984 Academic Press.]

crust; at times they are sites of groundwater discharge. The upward moving brine evaporates and leaves crustal ridges that progressively thicken on their windward side and crack open parallel to the crests when the crust desiccates. Precipitation is here more rapid than removal during episodic flooding. In ancient evaporite sequences they are always underlain by coarse, recrystallized halite or by nearly vertical crystals resembling a cauliflower.

Hopper crystals and biscuits of various evaporite minerals can form at a rapidly concentrating brine surface and are held there by surface tension. Eventually they drop to the lagoon floor but are an indication that the brine was not density stratified at the time.

Nodular anhydrite can be a supratidal alteration of a gypsum crust precipitated in the capillary zone of an ancient groundwater table in the supratidal zone, an early diagenetic alteration of a semifluid gypsum/brine mush beneath the lagoon floor, a compaction texture of a still soft gypsum layer, or a later recrystallization of gypsum laminations under the influence of hygroscopic brines underneath commencing halite precipitation.

Current-deposited, cross-bedded gypsum sand (gyp-sarenite) or halite sand (haloarenite), turbidites, gravity flows, and submarine slides have been described from several evaporite sequences, (e.g., in Miocene anhydrite beds of the northern Appennines in Italy or in Permian anhydrite beds in East Germany and in Miocene halite beds from Caltanissetta in Sicily or Verotyshchensk in the Ukrainian Carpathians). In a dense brine they can occur over very gentle slopes.

H. Substitutions and Inclusions

Substitutions of cations in the crystal lattice are not uncommon. Not only does iron substitute for magnesium in

the crystal lattices of primary carnallite, bischofite, and tachyhydrite, but rubidium, cesium, thallium, or ammonia can substitute for potassium in sylvites and carnallites; only lithium remains in the brine almost to the end. Bromium substitutes in minute proportions for chlorine, but the substitution varies with brine concentration, distance from shore, brine depth and temperature, magnesium concentration in the brine, degree of recrystallization of any precipitate in the presence of passing brines, sorption by clays, scavenging by algae, and soil bacteria. Iodine, in contrast, remains in the residual brine and eventually seeps out into formation waters.

Inclusions in evaporites are voids, often in the form of negative crystals, usually filled with gaseous or liquid phases of fluids. These fluids are sodium-chloride brines, liquid and gaseous hydrocarbons, carbon dioxide, and organogenic nitrogen. Because of the difference in solubility between the warmer and colder sides of the cavity, fluid inclusions will migrate, especially under uniaxial stress. Fluid inclusions with more than 10 volume percent of gas migrate down the thermal gradient toward cooler temperatures, while those with a smaller gaseous fraction migrate in the opposite direction toward a heat source. The migration is hindered by grain boundaries that can permanently entrap the inclusion. Inclusions may coalesce during migration or be contaminated by intercrystalline moisture content. Storage of radioactive materials in salt domes would have to take into account the leakage potential through such watery conduits.

I. Clastics in Evaporites

There is a decided fining of clastics toward any evaporite basin, so that onshore sediments are frequently only red silty clays, because the surrounding land commonly has a very gentle slope. A slight rise in the sea level then inundates a large area, a slight drop in lagoon level bares large areas of shoals and new beaches and allows subaerial exposure.

The occurrence of fern pinnules, trunks of large conifers and broad-leaf trees in several marine evaporite deposits of different age indicates the nearby presence of an at least discontinuous vegetation cover, especially since the recovered, well-preserved leaves or insects would not have traveled too great a distance in a flash flood before being macerated. It further suggests a semiarid rather than an arid climate as being typical, with a great variability in annual rainfall rates, where both sandstorms and flash floods were not uncommon.

However, quartz sand or quartz silt can be found embedded only in the gypsum shelves on the basin margin; there is no evidence of detrital quartz grains within halite or within precipitates of higher solubility. Only a few detri-

tal grains of some very resistant silicates have been found, such as staurolite, tourmaline, and zircon. Discrete sand stringers encased in anhydrite occur very rarely within the halite sequence and are marks of a temporary freshening.

Surface waters of the oceans are relatively free of suspended clay particles and deliver clean water into an evaporite basin. Because of the bottom outflow, no marine clays will enter; the source of all intercalated clay beds is, therefore, not the open sea, but the surrounding shores. Clays swept in by flash floods spread out along the interface between diluted surface waters and resident brine. They can sweep brackish or freshwater faunas far into the bay where this unabraded fauna then appears intercalated into an evaporite sequence. The clays cover wide areas before settling very slowly as floccules, retaining much water in their pore spaces; with solute concentration they increase in size and amount of brine retention. Resumption of salt precipitation entraps this brine in the flocculated clays and allows the clay laminae to remain permeable. Such thin clay laminae can later act as conduits for incursions from the basin margins of lateral brine movements or diffusion of epigenetic meteoric waters, especially if they settled into very concentrated bitterns.

Concentrated, very hygroscopic brines upon contact also induce deep shrinkage cracks in clays, called syneresis cracks, that are indistinguishable from subaerial desiccation cracks and that increase the permeability of these clay laminae.

All clays become efficient ion exchangers in the hyper-saline brine and are ultimately transformed into mixed-layer varieties of the magnesian chlorite family. This suggests a large-scale liberation of hydrogen ions, dissolution of a variety of cations, insertion of magnesium-hydroxide pillars, and also some dissolution of silica. In the extreme case, if all silica is removed, a new mineral, koeneneite [$8\text{NaCl}\cdot8(\text{Mg},\text{Ca})\text{Cl}_2\cdot2\text{Mg}(\text{OH})_2\cdot8\text{Al}(\text{OH})_3$] is formed in the presence of concentrated magnesium-chloride brines in conjunction with euhedral feldspar crystals but in the absence of all clay minerals.

Sparse euhedral quartz and feldspar grains in a rock-salt sequence and the absence of all detrital quartz and feldspar indicate that most of the blown-in silica has gone into solution; further amounts in solution are derived from conversion of various clays to members of the chlorite family. Both processes indicate a very alkaline pH in the concentrating brine; the presence of even a few milligrams of ammonia or dissolved amines per cubic meter of brine suffices to raise the pH very substantially.

A tiny amount of the silica is later precipitated as authigenic quartz and feldspar crystals. The remaining dissolved silica seeps out of the basin and gives rise to frequently observed chertification features along margins of evaporite basins. Wherever wallrock dissolution can add

even small amounts of magnesium or aluminum ions to the brine, it reduces silica solubility and can instigate its precipitation.

Halloysites, kaolinite, muscovite, montmorillonite, and chlorite are thus restricted to nearshore sites, where detrital material is dumped and then quickly buried, while palygorskite is present offshore, replaced by sepiolite in areas still farther out; illites are often the later alteration product of mixed-layer varieties by descending potassium-rich brines.

J. Organic Matter in Evaporites

Concentrating brines increase their osmotic pressure and become deadly to many bottom-dwelling marine species. The concentrated, anoxic outflow prevents the migration of species from the open marine environment. While the number of species rapidly declines, the number of individuals experiences an explosive development. Organic matter is generated in evaporite basins at a rate of one to three orders of magnitude faster than in the open ocean.

Organic compounds are a very important constituent of evaporite basins; they affect the precipitation rate and are themselves affected by the precipitate. Any proteolytic solutions, naphthenic acids, amino acids, resins, sugars, or xylan, if present, retard gypsum precipitation. These organic maceration products can increase the sulfate solubility to the point where gypsum is altogether prevented from precipitating. Dissolved organic matter, however, lowers the solubility of sodium and potassium chlorides, and facilitates their precipitation. Until oxidized by contact with the atmosphere, they also keep magnesium and iron-chloride complexes in solution, hindering the precipitation of carnallites, iron-carnallites, or rinneites.

This organic matter, which cannot oxidize in an essentially anoxic brine, partly goes into solution in a sodium-enriched brine, and partly forms chloride-organic complexes with magnesium and other metals. The calcium sites in a gypsum lattice are prone to break up organic chains, while clays are known to polymerize them into larger molecules that are unable to migrate through available pore spaces. As hypersaline brines seep through an initially porous substrate of gypsum or halite slush and displace less concentrated formation waters, they carry with them dissolved organic compounds, organometallic complexes, and even broken-up polymers as finite globules or as gas.

It is a well-known observation that reefs and other porous strata around ancient evaporite basins are prime exploration targets for crude oil and natural gas, while oil shales are mostly of lacustrine origin, often associated with trona and thenardite. Moreover, a statistical evaluation of paleolatitudes of crude oil and natural gas fields

shows a prevalent occurrence in the same latitudinal belt as marine evaporites.

K. Metals in Evaporites

Base metals concentrated in the brine by a variety of planktonic organisms are in part entrapped within the gypsum and halite lattices and are then largely released either in the conversion of gypsum to anhydrite or in the recrystallization of halite. Some of the metals, such as copper, zinc, lead, and silver, remain in solution in the brine and seep into adjacent strata, apparently as chloride or chloride-organic complexes in analogy to calcium and magnesium complexing. Precipitation ensues, wherever the complexes encounter sulfuretted formation waters, often within more ancient reef complexes. The good correlation of lead-zinc deposits with ancient evaporite beds and with salt diapirs is striking. The organic fraction of the chloride complex turns into liquid petroleum that appears in fluid inclusions or in mine seeps.

L. Facies Distribution

In analogy to vertical and horizontal zonation of evaporite minerals in and around lakes, the evaporite sequences in marine embayments display a similar zonation. Lateral facies changes occur over short distances and are frequently very abrupt. Marine anhydrites often grade into lenticular near-shore limestones; the limestones grade on land into red beds with gypsum crusts in the soil. Halite and anhydrite thicknesses are in a reciprocal relationship throughout the basin. Shoreward, the total halite sequence grades into anhydrite. Each potash deposit, in turn, is encased in halite both laterally and vertically (Fig. 5).

In a vertical cross section, more soluble minerals from beds above less soluble ones. Fine laminae oscillate between two minerals of different solubility during periodic freshenings. Eventually, each deposit is capped by a reverse sequence of precipitates from progressively less concentrated brines. Vertical stacking in reverse order signals either a reduction in evaporation rates or a decrease in subsidence rates. The continued precipitation of an evaporite mineral with the next lower solubility during a prolonged period of freshening will serve as a preserver of salts of higher solubility and will shield them from redissolution.

As the Coriolis effect moves inflowing waters along the margins of circular basins; it will cause a concentric arrangement of precipitates from carbonates to anhydrite on the shelf to halite in the basin; both potash and magnesium chlorides will precipitate asymmetrically on the basin slopes. In elongate basins the bottom currents redistribute the sediments into an alignment with the basin axis.

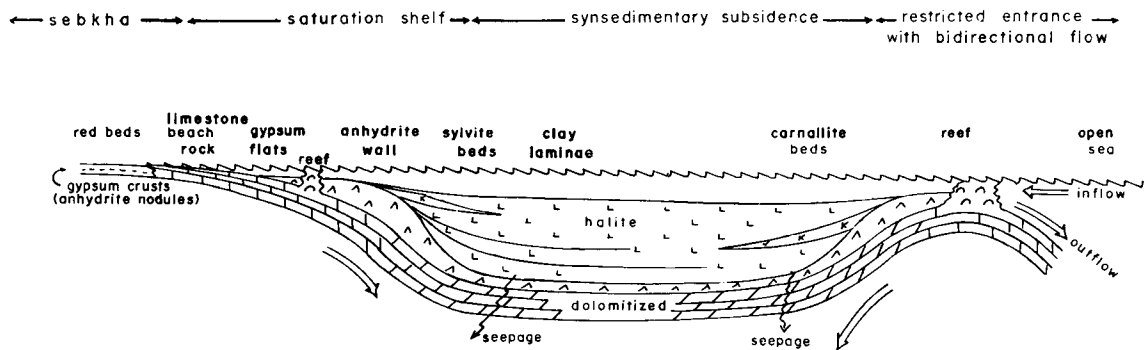


FIGURE 5 Facies relationships in an evaporite basin.

Calcite or aragonite and gypsum precipitation rates are frequently slower than rates of subsidence. Consequently, the basin progressively deepens. Gypsum precipitation rates vary but rarely exceed a few millimeters per year, while subsidence rates can be as high as 10 to 12 cm per year. As the brine saturates to the halite level and this mineral begins to precipitate, the precipitation rates overtake even excessive rates of subsidence and, in consequence, the basin shallows. Halite precipitation rates vary between 3.5 and 14 cm/yr, but halite preservation rates, and thus halite accumulation rates, are only a fraction of these figures, possibly 0.1–4.0 mm/yr. In ancient environments, the ratio between rates of subsidence of gypsum-precipitating margins and halite-precipitating deeps has often been 1 : 5 to 1 : 7. Each clay lamina, gypsum wafer, or dolomite stringer, often spaced only millimeters apart, represents a period of brine freshening, nondeposition, or even corrosion parallel to bedding planes. The ratio between elapsed times of deposition and nondeposition can be estimated to have exceeded 1 : 10.

All chloride precipitates are initially very slushy, and a fair amount of the brine can seep into the substrate and diffuse into formation waters of lesser density. In the process, the underlying precipitate is recrystallized. Descending bitterns that have surpassed the saturation for halite force the halite to salt out when they encroach upon halite-saturated interstitial brines. Preserved microfissures in underlying precipitates, cylindrical vertical voids, druses stretched out vertically, and vertical fractures filled with salts of greater solubility than the wall rock are evidence of such downward seepage. Compaction by the weight of subsequent precipitation expels most of the interstitial brine and eventually converts the slush into a solid rock.

M. Synsedimentary Subsidence

To initiate brine concentration, a gentle water-filled depression must preexist where subsidence proceeds at a

slightly faster rate than subsidence of the entrance sill or the surrounding margins (Fig. 6).

Scant runoff in a semiarid area promotes a scarcity of continental clastic intercalations in an evaporite basin, especially if this basin is not abutting hill chains. Without

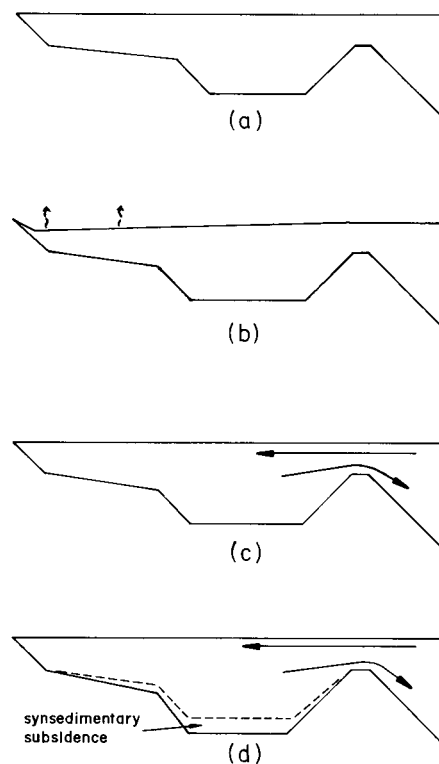


FIGURE 6 The four steps in the formation of an evaporite basin.
 (a) Bay salinity equals sea salinity. Bay level equals sea level.
 (b) Bay level depressed by evaporation. Downhill inflow begins to compensate.
 (c) Two-way flow develops in bay. Inflow salinity equals sea salinity. Increasing salinity in resident brine and in outflow. Inflow/outflow ratio increases to equilibrium: $I = E + O$ [inflow (I), outflow (O), evaporative water loss (E)].
 (d) Synsedimentary subsidence creates disequilibrium: $I > (E + O)$.

evaporite precipitation such basins would have been “starved basins” (i.e., rapidly subsiding depressions with very meager rates of sedimentation).

Inflow and outflow have a tendency to equilibrate (i.e., the salinity in the embayment stabilizes). At prevailing annual rates of evaporation and deficit in the water budget of a subtropical sea, it is impossible to concentrate seawater to halite saturation, as the inflowing and outflowing brines will find an equilibrium density ratio short of saturation. The equilibrium can be disturbed by a change in the rainfall regime of the area, by a tectonic alteration of the entrance channel, or, most effectively, by continued subsidence of the basin floor. Many basins show a synsedimentary subsidence that alters thickness ratios between shelf and basin and allows the brine to transgress over its former shoreline. Distension faults and slumping mark ancient hinge lines. Sinking can either be nonuniform or the axis of subsidence may migrate during evaporite deposition, causing an asymmetric distribution of formation thicknesses. In Permian evaporites of Germany, the axis of greatest subsidence shifted northwest during sedimentation; the greatest expanse of Triassic halite in North Africa is offset against the greatest thickness of this evaporite sequence. As the center of subsidence shifts from one depositional cycle to the next one, often closer to the periphery of the basin, the bottom currents in an elongate basin will redistribute sediments and align them with the axis.

Saline operators lead seawater through numerous concentrator pans before draining the brine into a crystallizer pan. In a natural system, the water surface has to be several times larger than the surface of halite precipitation and again even larger than the surface of precipitation of minerals of higher solubility. A sequential arrangement of interconnected basins thus facilitates the preconcentration of precipitating brines. If the frontal basins with precipitates of lower solubility have been destroyed, the sequence of evaporites has a vertical asymmetry. Triassic evaporites of North Africa and Lower Cretaceous evaporites of Brazil and Angola display a pronounced deficit of calcium carbonates and sulfates, possibly due to the destruction of their preconcentrator basins in the margins of the opening and spreading Atlantic Ocean.

Precipitation of salts is interrupted when the basin is temporarily filled. Basinwide dissolution and desiccation surfaces are the telltale signs of slowing rates of salt accumulation. Resumption of precipitation is marked by an anhydrite or carbonate bank with sharp basal contact. The carbonate bank is usually extremely uniform in thickness, indicating a temporary interruption of subsidence. The carbonate bank, often composed of algal reefs, must represent very shallow conditions, as many of the photosynthesizers could not have flourished in deeper parts of the basin.

Resumption of subsidence not only depresses the flanks of a basin, it eventually affects all the shelf areas. In a subsequent cycle of subsidence these shelves turn into subsidiary lagoons and create a series of preconcentrator depressions for moving brines. This can be documented in the Michigan Basin, the Delaware Basin of west Texas, the Elk Point Basin of western Canada, the Zechstein Basin of northwestern Europe, and in other examples.

While the basin fills with precipitates and the residual brine concentrates further, the floor of the basin is depressed allowing for greater volumes of precipitates to fill this depression. Without synsedimentary subsidence, the deposition of several hundreds of meters of rock salt on top of shallow-water gypsum beds would not be feasible; the ratio of rates of subsidence of shelf and basin areas is often more than 1 : 5.

N. Basin Depth

As the brine in the basin progressively becomes more concentrated, its density increases from an initial value of 1.0245 for ordinary seawater to 1.3995 g/cm³, at which point the brine would reach its eutonic point (i.e., the lagoon would dry out). Hand in hand with brine concentration goes an increase in the weight exerted on the substrate. By the time the brine starts precipitating halite, its weight has increased nearly 20%, and the combined weight of brine and precipitate soon exceeds 170% of the weight of the original seawater column. This must affect the isostatic equilibrium of the crust, since geodetic adjustments have been observed even after the filling of small reservoir lakes. It has to be born in mind that shortly before the onset of potash precipitation the volume of precipitated salts equals the volume of the remaining brine, and nearly three quarters of the volume of salts originally dissolved in seawater will have been precipitated.

The greater the volume of a basin, the longer it took for each salinity increment. The rate of salination is inversely proportional to the depth of the basin. The thicker the individual cycles, the longer was the time interval in which tectonic forces and climatic rates of change remained relatively stable. However, the longer the time required to bring a basin to saturation, the less probable it is that the rates of evaporation or subsidence remain constant. Evaporite cycles seem to show an upper limit of about 1000 m of halite wherever they have not been disturbed. Saturation of extensive and much deeper basins is thus very difficult to achieve. Hence, thick, multicycle evaporite sequences show evidence of synsedimentary rapid subsidence.

Basin depth estimates based on studies of halites often differ by two orders of magnitude or more from those of intercalated potash deposits. The basin floor always extends from shallower shelves to deeper parts below the

wave base of the viscous bittern, where photosynthesis beneath an interface to surface waters was inhibited. Comparison of a bittern wave base (less than 10 m) to a seawater wave base (more than 30 m) leads to overestimating basin depths.

Reverse orders of evaporite precipitation are telltale signs of temporarily slowing rates of evaporite accumulation. Dissolution and desiccation surfaces indicate that the cycle of evaporite precipitation has ended (i.e., the basin has been filled and no longer receives any inflow). Eventually, brine influx and renewed precipitation commence again when continued subsidence creates a new depression.

O. Cyclicity of Deposition

Cyclicity of deposition is evident on several orders of magnitude. The finest cycles are varve-type laminations on a millimeter to centimeter scale. These are formed by cyclic changes of brine concentration over wide areas or by episodic agitation. They extend over more than 100 km, indicating basinwide synchronous salinity fluctuations. The salinity changes are deadly to many planktonic organisms and often produce organic films at salinity thresholds.

Such laminations form only in perennially submerged parts of the basin, which are not exposed to any bioturbation or vertical discharge of brine to destroy the laminations. Alternating calcite/gypsum, gypsum/halite, or halite/sylvite couplets usually have a sharp basal contact of the less soluble member of the pair and an irregular contact on top. They cannot occur in deep water, as a rapid oscillation from supersaturation to undersaturation of the more soluble salt is only possible in a very shallow column of water.

The attempt to use laminations as indicators of elapsed time has not been successful, as couplets do not necessarily represent a daily, monthly, or seasonal record. Often every eighth to tenth varve couplet is thicker and more

pronounced, suggesting a record not of sunspot cycles, but of major storm frequency. Since storms and episodic freshenings can remove up to 80% of the varve couplets, a count does not give a realistic estimate of total elapsed time.

On a larger scale, periods of precipitating evaporites up to more than 300 m thick alternate with periods of normal salinity. There are no primary marine evaporite deposits that do not display anywhere from 3 to 4 to a score of complete cycles. A typical cycle of precipitation proceeds from salts of lower solubility to those of higher solubility, with several oscillations into and out of the saturation field of a given precipitate. If the basin then dries out, bischofite is absent from the sequence, and it is covered by an erosional surface overlain by sundry detrital rocks.

The larger the brine volume in a basin, the longer it takes for a freshened influx to readjust precipitation from one mineral to another. The ultimate dilution is faster than the original saturation, as the reverse sequence deposited from a brine being progressively freshened is usually much thinner than the sequence precipitated from a concentrating brine.

Eventually, a carbonate bank covers the evaporite deposit, often composed of varieties of algal laminations and reef detritus but generally of nearly uniform thickness throughout the basin. Renewed subsidence then starts another cycle of evaporite deposition. The transgressive nature of evaporite basins is probably best shown in the growth in volume and areal extent from one cycle to the next one. Typically, the first cycle covers a much smaller area than subsequent ones; the shelves of the first evaporite basin collapse and become additional sites of evaporite deposition in a later cycle (Fig. 7).

P. Epigenetic Alterations

Once the evaporite minerals are precipitated, they are subject to alteration by percolating brines. The initial porosity

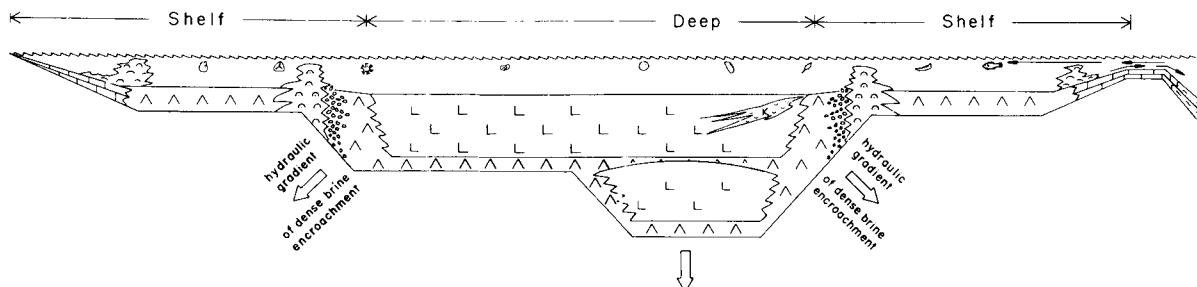


FIGURE 7 Model of an evaporite basin. Broad gypsum shelves and reefs growing into the inflow mark the margins and halite the rapidly subsiding parts of the depression; potash beds occur toward the shelf margins and slopes. Subsequent cycles expand over margins of earlier cycles. Outflow is directed partly over the entrance sill and partly seeps into the subsurface displacing less dense formation waters.

of 10 to 50% of freshly precipitated evaporites and good permeability are only gradually reduced if encased brine pockets prevent compaction. Circulating waters, be they syngenetic, more concentrated, and more hygroscopic brines, epigenetic evaporitic brines, or epigenetic meteoric waters, can enter and affect the precipitates. They can seep in from above or enter laterally and ascend as artesian waters through the initially permeable sediment.

The horizontal movement is facilitated because horizontal stresses in salt average only 80% of vertical stresses. The vertical movement of brines is attested to by crystal growth at right angles to bedding planes, such as herringbone (chevron) crystals of gypsum or halite druses stretched out vertically, separated by individual cylindrical walls. As a clean precipitate, selenitic crystals, twinned with fishtail fins pointing up, are interpreted to have grown into an open brine column as subaqueous exit points of slowly moving interstitial brines.

Brines percolating before the precipitate has been consolidated lead to recrystallization, brines percolating later lead to the formation of pseudomorphs, crystal molds, and casts. Undersaturated waters increase the plasticity of the salt, which then can drastically reduce the permeability and close any pores. Meteoric or marine waters entering laterally into an evaporite sequence can ascend through cracks and joints to find a hydrostatic equilibrium. These waters also introduce rock alterations along their pathways. It is often difficult to distinguish mineralogical alterations caused by ascending brines from those caused by descending waters, unless one has done a thorough three-dimensional study of the whole evaporite basin.

Waters entering a potash deposit leach out the sylvite or carnallite under concurrent salting out of halite and leave behind a barren recrystallized zone, called "salt horses." Descending brines produce "roof horses" or "back horses," barren areas along the hanging wall, ascending brines produce "floor horses," barren areas along the footwall. Waters rising through an evaporite deposit saturate quickly and produce brine chimneys or pipes, salt horses of exceptionally pure white halite rimmed by clays or selvage; any banding in salt will be destroyed and the insoluble clay or dolomite will be swept into interstices between crystals.

Increasing the salinity of the brine raises its hygroscopy and thus lowers the temperature range of the stability of anhydrous minerals and partially hydrated compounds. Brines saturated for sodium chloride or compounds of higher solubility are highly hygroscopic; contact with these brines will extract the crystal water from gypsum at ambient temperatures. When such brines percolate through gypsum, they convert it to anhydrite. Rising geostatic temperatures upon burial can also convert gypsum to anhydrite. Consequently, gypsum is rare in subsurface drill

cuttings, but is common in surface exposures, where either it never was turned into anhydrite or where ancient anhydrites have been rehydrated by the atmospheric humidity.

Meteoric waters are required for the conversion of anhydrite to selenite, a variety of gypsum, and affect the fabric. For instance, a porphyroblastic texture indicates volume-for-volume replacement under near-equilibrium conditions at a very early stage; an alabastine texture is formed at a later stage. The rehydration generates a large amount of heat that must be rapidly dissipated, lest it brings the interstitial brine to the boiling point.

Extraction of crystal water from the gypsum increases the pore pressure, because the resulting anhydrite and the released water together occupy a volume more than 10% larger than the original gypsum. This increased pressure is the driving force to dissipate the waters, which seem to mobilize any other trace elements that might have been initially caught in the gypsum crystal lattice, such as iron, manganese, lead, zinc, and copper, and redeposit them outside the evaporite basin. The increased volume does not create great stresses, but primarily acts to fill available voids. Overlying beds often show undisturbed laminations, indicating that the conversion to anhydrite happened before these became consolidated.

Where meteoric waters manage to enter a marine evaporite deposit, they dissolve some of the calcium sulfates and sodium chlorides and deposit sodium carbonates or sulfates in nests that invariably are a telltale mark of a meteoric incursion into the bedded evaporite deposit. Marine evaporite sequences do not contain these minerals as bedded deposits because of the higher calcium/sodium ratio in normal seawater compared to most continental brines.

Holocene anhydrite occurrences appear to be related to the presence of organic decomposition products; in inorganic environments even water salinities of 200,000 ppm cannot alter gypsum to anhydrite. Many determinations of the transition temperature from gypsum to anhydrite have been made, and the determinations seem to form clusters around 38 to 42°C and 55 to 58°C, possibly because of textural differences and the variable amount of lattice imperfections and surface-active organic matter present in gypsum samples from different sources.

Worldwide, Permian and Neogene potash deposits have largely been altered to secondary complex potassium and magnesium sulfate minerals. The source of such quantities of sulfate ions constitutes a problem, especially because no beds of other ages are affected. The conversion of basal gypsum sequences to anhydrite provides insufficient amounts, and so would an incursion of a new supply of seawater, as each meter of resulting sulfatic potassium or magnesium mineral would have required many hundreds of meters of basal gypsum thicknesses to generate the sulfatic waters necessary. Such thicknesses were not

available. The conversion may be due to the early exposure of the gypsum shelves to meteoric waters, when an ice age caused a drop in sea level. A loss of anhydrite volumes is corroborated by drastically reduced anhydrite/rock salt ratios in both Permian and Neogene evaporites compared to evaporites of other ages. Waters saturated with sulfate ions from gypsum solution were then able enter the as yet incompletely consolidated evaporite sequence. The transformation of primary marine precipitates into sulfate minerals proceeds along a very complex path of multiple alterations, in which progressively more potassium is mobilized and ultimately removed. The attendant volume reduction frequently leads to very contorted bedding planes and intraformational breccias. Calcium chloride brines derived from formation waters destabilize such secondary minerals and revert them to a second generation of chlorides and anhydrite.

A byproduct of the generation of a hypersaline brine is the eventual production of magnesium-rich, sulfate-deficient bitterns that seep into the subsurface. In the presence of decaying organic matter, especially amines, magnesium ions will affect a calcium carbonate substrate and turn it into dolomite. Most dolomite is clearly secondary, a primary limestone altered by a brine that was devoid of sulfate ions and probably carried magnesium-organic chloride complexes. Such dolomite is of fine to coarse crystallinity and has a sucrosic texture (i.e., all crystals are nearly euhedral and nearly of equal sizes). A phanerocrystalline dolomite (i.e., one with easily recognizable crystal outlines) displays the smallest crystals near the source of magnesium-rich brines and progressively becomes coarser along a paleohydraulic gradient away from an ancient evaporite basin.

Q. Salt Domes

Both the gypsum and carbonate laminae form wedges toward the basin center; their aggregate thickness increases slightly toward the basin margins. This becomes particularly noticeable when the salt is remobilized and squeezed upward into salt stocks of great vertical extent. Salt domes or diapirs are stocks primarily composed of recrystallized halite, less commonly of anhydrite, capped by a roof of gypsified anhydrites and dolomites. The carbonate and sulfate fractions, being more competent, are then separated from the recrystallized halite into a caprock of a declining thickness away from ancient basin margins.

Increasing weight of overburden plasticizes rock salt and, to a lesser extent, anhydrite. Rock salt commences to expand into voids at an overburden of 300 m, potash minerals even earlier, eliminating the original porosity and permeability. Halite becomes ductile under 12 km of overburden, sylvite under 10 km and under much less

overburden, if exposed to tectonic stresses or to regional downwarp.

Mobilized salt first produces salt pillows, then salt stocks, domes, or diapirs. A salt dome is never a singular feature; salt diapirs always occur in swarms. They commonly pierce overlying beds and upend them due to excessive pressure, wherever the crust experienced a downwarp. Many of the overlying beds are then cut by normal faults dipping into the salt stock. These fault planes allow meteoric waters to seep in, dissolve some of salt, and produce salt karst features. Bacteria may also enter, scavenge some of the available organic matter, and transform the gypsum in the caprock into native sulfur.

Examples of groups of salt domes include the margin of the Gulf of Mexico, the Arctic Archipelago of Canada, the southeast margin of the North Sea, eastern Iran, and the northwest margins of the Balearic and Levantine seas. Significantly, no salt diapirs have formed from deeply buried thick salt deposits in the central Balearic, Ionian, and Levantine seas; the Michigan, Ohio, or Elk Point Basins in North America; and many other intracratonic salt basins.

Bedded evaporites are unknown in metamorphic rock suites. Well before pressures and temperatures rise to the point of recrystallizing silicate minerals, the chlorides and sulfates become mobilized and are squeezed out. Only fluid inclusions in the metamorphic rocks then bear witness to the former presence of evaporites.

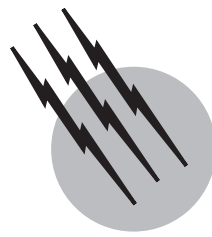
SEE ALSO THE FOLLOWING ARTICLES

CRYSTAL GROWTH • FLUID INCLUSIONS • GEOCHEMISTRY, LOW-TEMPERATURE • GEOLOGIC TIME • ROCK MECHANICS

BIBLIOGRAPHY

- Busson, G. (1984). "Relations entre les gypses des plates-formes du Nord-Quest africain et les black shales de l'Atlantique au Cénomanien inférieur moyen," *C. R. Hebd. Séances Acad. Sci. Paris*, Sec. II, **298** (18), 801–804.
- Eugster, H. P., and Hardie, L. A. (1973). "Saline lakes" in "Lakes, Chemistry, Geology, Physics" (A. Lerman, ed.), 237–293, Springer-Verlag, Berlin and New York.
- Gevantman, L. H., Lorenz, J., Haas, J. L., Jr., Clyne, M. A., Potter, R. W., II, Schafer, C. M., Tomkins, R. P. T., Shakoor, A., Hume, H. R., Yang, J. M., Li, H. H., and Matula, R. A. (1981). "Physical properties data for rock salt," *Natl. Bur. Stand. Monogr. (U.S.)*, No. 167.
- Hardie, L. A. (1984). "Evaporites: marine or non-marine?" *Am. J. Sci.* **284** (3), 193–240, and comment by Sonnenfeld, P. (1985). *Am. J. Sci.* **285** (7), 661–672.
- Krull, O. (1917). "Beitrag zur Geologie der Kalisalzlager," *Kali* **11** (14), 227–231.
- Lerman, A. (1979). "Geochemical Processes: Water Sediment Environments," pp. 481, Wiley, New York.

- Madison, R. J. (1970). "Effect of a causeway on the chemistry of a brine in Great Salt Lake, Utah," *Water-Resour. Bull. (Utah Geol. Miner. Surv.)*, No. 14, 1–52.
- Mattox, R. B., Holser, W. T., Ode, H., McIntire, W. L., Short, N. M., Taylor, R. E., and van Siclen, D. C. (1968). "Saline deposits," *Spec. Pap. Geol. Soc. Am.* No. 88.
- Ochsenius, C. (1888). "On the formation of rock salt beds and mother liquor salts," *Proc. Philadelphia Acad. Sci.*, Part 2, 181–187.
- Perthusot, J. P. (1975). "La sebkha El Melah de Zarzis. Genèse et évolution d'un bassin salin paralique," *Trav. Lab. Géol., Ec. Norm. Supér., Paris*, No. 9, 1–252.
- Richter-Bernburg, G. (1957). "Zur Palaeogeographie des Zechsteins. Atti del Convegno Milano," "I Giacimenti Gessiferi dell'Europa Occidentale," *Atti Accad. Naz. Lincei Ente Naz. Idrocarburi* 1, 87–99.
- Sonnenfeld, P. (1984). "Brines and Evaporites," Academic Press, Orlando, Florida.
- Usiglio, J. (1849). "Analyse de l'eau de la Méditerranée sur les côtes de France," *Ann. Chim. Phys.*, Sér. 3, 27(2), 97–107 and 27(3), 177–191.
- Zharkov, M. A. (1981). "History of Paleozoic Salt Accumulation," Springer-Verlag, Berlin and New York.
- Zharkov, M. A. (1984). "Paleozoic Salt Bearing Formations of the World," Springer-Verlag, Berlin and New York.



Geochemistry, Low-Temperature

C. G. Patterson

Alpine Geosciences

D. D. Runnels

Shepherd-Miller, Inc.

- I. Low-Temperature Behavior of the Elements
- II. Weathering
- III. Soils
- IV. Thermodynamic Considerations
- V. Water Chemistry
- VI. Diagenesis
- VII. Oxidation and Reduction
- VIII. Sorption and Ion Exchange
- IX. Elemental Cycling

GLOSSARY

Activity “Effective” or “reactive” amount of a solute or a solvent in solution. The activity is usually less than the total concentration, but in brines the activity may exceed concentration. Activity has no dimensional units.

Carbonates Minerals in which the characteristic framework component is the CO₃²⁻ structural group.

Complex Group of covalently bonded atoms that forms a stable dissolved species in solution. Examples include SO₄²⁻ (sulfate), CO₃²⁻ (carbonate), NO₃⁻ (nitrate), and PO₄³⁻ (phosphate).

Diagenesis Chemical and mechanical processes that take place within sediments shortly after deposition as a result of changes in temperature, pressure, and chemically active fluids.

Ion Atom or group of atoms with an electrostatic charge.

Dissolved ions with a positive charge are referred to as cations, while those with a negative charge are called anions. Examples of cations commonly found in natural waters include Ca²⁺, Mg²⁺, Na⁺, and K⁺; of anions, HCO₃⁻, Cl⁻, and SO₄²⁻.

pe A calculated term used to describe the oxidation-reduction state of natural waters and soils. High positive values represent the most oxidizing conditions. The Eh is a field-measured voltage that is comparable to pe.

$$pe = \left(\frac{Eh}{0.0592} \right) \text{ at } 298 \text{ K}$$

pH Measure of the activity of hydronium ion [H⁺] in water. Defined as the negative logarithm of the activity

of the hydronium atom. A value of 7 indicates neutral conditions at 298 K.

Regolith Blanket of loose, weathered material that covers bedrock in most regions of the earth. If the regolith contains a few percent of organic matter, it is called soil.

Saline In the context of natural waters, referring to concentrations of total dissolved solids (TDS) similar to or greater than those in ocean water.

Silicates Minerals in which the characteristic framework component is the SiO_4^{4-} structural group.

Solubility Total amount of a mineral or other substance that can be dissolved in water.

Weathering Mechanical and chemical breakdown of rock exposed at the surface of the earth under the influence of rain, changes in temperature, biologic activities, and so on.

LOW-TEMPERATURE GEOCHEMISTRY comprises the study of natural chemical processes occurring at or near the surface of the earth. The temperature and pressure are approximately 298 K and 1 atm (0.1 MPa). Of great interest in low-temperature geochemistry are the processes of chemical and mechanical weathering of bedrock and the processes of migration and cycling of the chemical elements. The discipline includes the study of the entire spectrum of natural waters, from rainwater to highly saline surface and subsurface brines. Environmental geochemistry, diagenesis of sediments, and geochemical exploration for mineral deposits are important subdisciplines.

I. LOW-TEMPERATURE BEHAVIOR OF THE ELEMENTS

A. Mobility during Weathering

Solid bedrock is under continual attack by elements of the atmosphere, hydrosphere, and biosphere. The sum of these processes is called weathering. During weathering the chemical elements that make up the original bedrock may behave very differently. Some elements, such as sodium and sulfur, tend to be dissolved during weathering and to be transported away by surface runoff and groundwater. A few elements, such as silicon, titanium, and zirconium, are relatively immobile during weathering because they occur in minerals that are extremely insoluble and resistant to weathering; the resistant minerals are called resistates. Some elements, chiefly aluminum, react with oxygen and water to form new hydroxyl-bearing minerals [such as gibbsite, $\text{Al}(\text{OH})_3$] that are then resistant to further

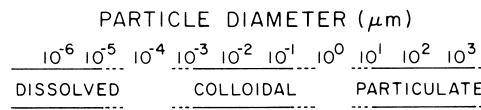


FIGURE 1 Size distribution of particulate, colloidal, and dissolved forms of the chemical elements in the processes of mechanical and chemical transport.

weathering; the new minerals are called hydrolyzates. Iron and manganese are among the elements that are oxidized under the conditions of weathering, followed by reaction with water and oxygen to form resistant oxides; examples include goethite (FeOOH) and pyrolusite (MnO_2). Elements that are essential to plant and animal life, such as carbon and phosphorus, are also released from the rock-forming minerals during weathering.

B. Particles, Colloids, and Dissolved Species

Determination of the physical form (dissolved, colloidal, or particulate) of elements in water is important in achieving an understanding of the solubility and mobility of the elements. Figure 1 shows the forms of the elements that may move through the hydrosphere, ranging from macroparticles through colloids down to individual ions and molecules.

Colloids are particles with diameters from about $1 \mu\text{m}$ down to $0.0001 \mu\text{m}$. Colloidal particles are important in the transport of organic matter in natural waters, and such elements as iron, manganese, and aluminum are transported in streams and seawater and the surface may carry a net positive or negative electrostatic charge. Some elements, such as nickel and cobalt, are probably transported in stream water chiefly as adsorbed ions on the surface of colloidal particles of iron and manganese hydroxide. In turn, the colloids themselves may form coatings on larger particles. The result is that many elements move through the hydrosphere in a combination of dissolved and adsorbed forms.

C. Forms of Dissolved Species

Dissolved chemical elements may exist in water in three principal forms: free ions, covalently bonded complexes, and electrostatically bonded ion pairs. Which form is dominant depends on the specific chemical properties of the element and the bulk chemistry of the solution. In fresh water, the free ions are most abundant, but in highly saline brines, ion pairs may dominate. In waters that are unusually rich in organic matter, such as swamp waters, metalloorganic complexes may be the most important. All three forms of dissolved elements are present in varying degrees in natural waters. The dissolved form of an element will

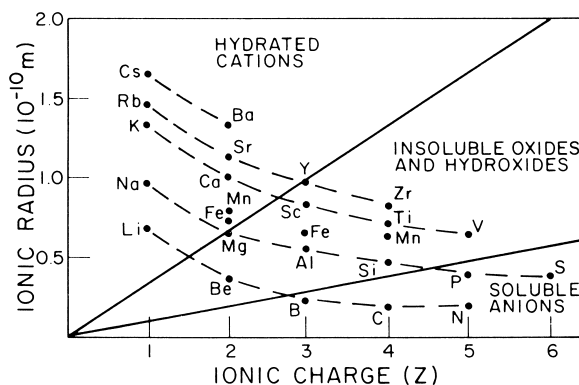


FIGURE 2 Summary of the forms in which elements may occur after reaction with water, as a function of ionic charge and ionic radius.

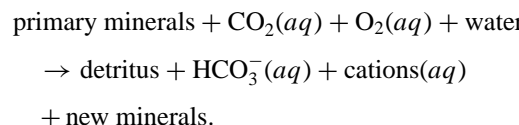
control the degree of reactivity of the element. Precipitation of a solid mineral may be prevented if the component ions are tied up in ion pairs or complexes. In terms of environmental geochemistry, the chemical form of an element is important in determining whether it will be toxic to animal or plant life. One of the most important reactions in solution occurs between cations and water molecules. the product of the reaction may be a free element surrounded by a sheath of water molecules, a solid hydroxide precipitate [e.g., $\text{Fe}(\text{OH})_3$], or a soluble oxyanion (such as SeO_4^{2-}). These possibilities are summarized in Fig. 2. The ionic radius and the valence are key parameters in describing such reactions.

II. WEATHERING

A. Mechanical and Chemical

The study of weathering is one of the most important aspects of low-temperature geochemistry. The processes of weathering produce soils residual sediments and dissolved salts. Two principal types of weathering are recognized: mechanical and chemical. Everyday terms that correspond to mechanical and chemical weathering are disintegration and decomposition, respectively.

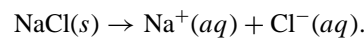
Mechanical weathering includes all processes that lead to physical breakdown of the bedrock into smaller fragments, such as the growth of ice or salt crystals, rapid changes in temperature, burrowing organisms, glacial abrasion, landslides, and abrasion by the hooves of animals and the boots of humans. These processes generate more surface area, which aids chemical weathering. In a very general way, the chemical processes of weathering can be summarized by the following simplified reaction (*aq* means aqueous):



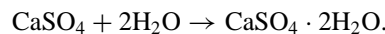
One way to visualize weathering is as an equilibration process as high-temperature and high-pressure minerals from bedrock seek to become more stable under surface conditions. Mechanical weathering forms are dominated by frost activity and therefore more prevalent in polar climates. Chemical weathering is dominant in tropical regions, where mean annual temperature and rainfall are high. Temperate climates tend to experience a mixture of mechanical and chemical weathering forms.

B. Types of Chemical Weathering

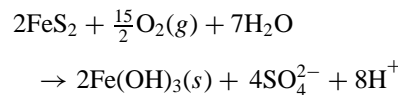
Individual processes of chemical weathering include dissolution, hydration, oxidation, carbonation, and hydrolysis. Dissolution is simply the dissolving of solid minerals. For example (*s* means solid),



Hydration is the addition of molecules of water to form new minerals. An example is the weathering of anhydrite to form gypsum, shown by



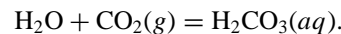
Oxidation is a process in which atmospheric oxygen oxidizes the component elements in a mineral to higher valence states. An example is the oxidation of iron and sulfur in pyrite to produce ferric hydroxide and sulfuric acid ("acid mine water"):



(*g* means gas).

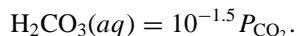
Oxidizing agents other than molecular oxygen are probably not important in weathering, although some researchers have suggested that minerals of oxidized manganese (such as MnO_2) may act as oxidizing agents. Many oxidation and reduction reactions that ordinarily proceed at a slow rate are considerably speeded up by the action of microbes in the environment.

Carbonation is the reaction of gaseous carbon dioxide with water to form carbonic acid:



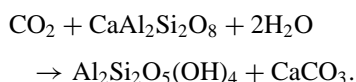
This carbonic acid may be a powerful weathering agent that can attack minerals much more effectively than pure water. In normal air the partial pressure of carbon dioxide

is 0.0003 atm (3.04×10^{-5} MPa). According to Henry's law, this partial pressure will yield a concentration of 0.00001 molal (m), as shown by

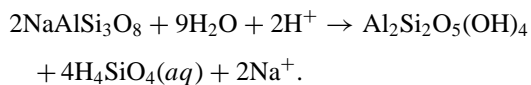


This low concentration is only slightly more effective than water at dissolving minerals. However, in soils it is not unusual for the partial pressure to approach 1 atm, resulting in a concentration of carbonic acid of 0.03 mole per kilogram of water. The carbonic acid then becomes a much more powerful agent of weathering.

In some cases one of the products of carbonation may be a new carbonate mineral. An example is the weathering of Ca-plagioclase feldspar, which can result in the formation of calcite, as shown by the following reaction for the alteration of Ca-plagioclase to kaolinite and calcite:



Lastly, hydrolysis is a weathering reaction in which the bonds of molecular water are broken, with H^+ or OH^- combining with the components of the original minerals to form new minerals. Because of the release of either H^+ or OH^- , the pH of the water undergoes a change. An example of weathering and hydrolysis of Na-plagioclase feldspar to form the clay mineral kaolinite. The OH^- in the kaolinite is produced by the addition to the silicate lattice of H^+ from the water:



The pH of the water after reaction with the feldspar will be higher because of the addition of hydroxyl to the solution.

C. Stability of Silicates

Since the 1930s, many fundamental advances have been achieved in understanding the processes of weathering. In a classic study, Goldich (1938) demonstrated that during weathering the order of stability of minerals that constitute igneous and metamorphic rocks is essentially the reverse of the order in which the minerals crystallize from a cooling magma, as shown in Fig. 3.

The inverse relationship between weathering stability and the temperature of formation is caused by differences in bonding among the silica tetrahedra that make up the framework of the silicate minerals. The tetrahedra are less extensively bonded to each other in the high-temperature primary minerals than in the minerals that form at lower magmatic temperatures.

An interesting aspect of chemical weathering is that the elements that make up a mineral may not all dissolve at

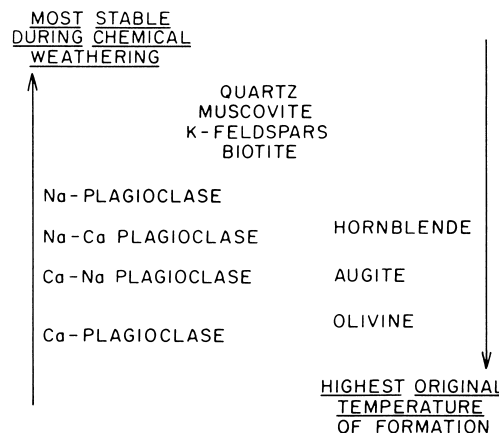


FIGURE 3 Summary of the stability of fresh igneous and metamorphic silicate minerals when exposed to the processes of weathering.

the same rate. This phenomenon is known as incongruent dissolution, and it can lead to cation-depleted or anion-depleted residue. As an example, Fig. 4 summarizes results of a set of laboratory experiments on the artificial weathering of the mineral fayalite, showing that iron, SiO_2 , calcium, and magnesium exhibit different rates of release to solution. One of the causes of the apparently incongruent dissolution of minerals is the simultaneous precipitation of new minerals, resulting in selective removal of some of the components from solution.

The concentration curves in Fig. 4 show an initially rapid rise, followed by a gradual leveling toward a nearly constant value at infinite time. Such curves are generally described as parabolic in shape, meaning that the curves

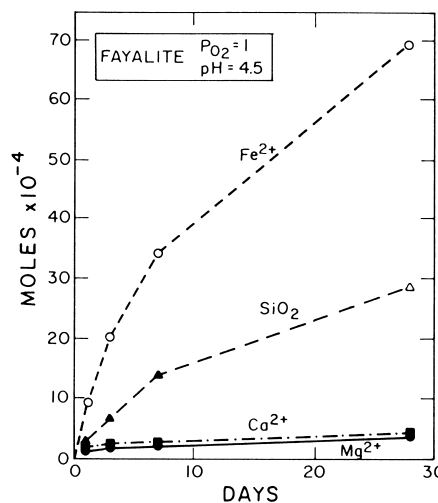


FIGURE 4 Laboratory results on the dissolution of fayalite $[(\text{Fe}, \text{Ca}, \text{Mg})\text{SiO}_4]$ in water buffered at pH 4.5 in the presence of 1 atm of oxygen gas.

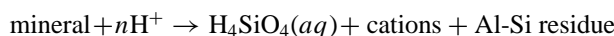
can be linearized by plotting the concentrations against the square root of time. Early interpretations of the parabolic shape hypothesized that it was the result of the formation of a relatively insoluble layer on the surface of the; the layer was thought to impose a diffusional barrier that increasingly limited the dissolution of the chemical components of the mineral with time. In fact, careful examination of deep weathering profiles in the southeastern United States shows that protective coatings are present on silicate grains collected from the thick zone of decomposed bedrock (saprolite) that underlies the true soil, whereas coatings do not form on the same minerals in the overlying leached soils. The difference is presumably due to the presence of more aggressive weathering solutions in the shallow soils than in the underlying saprolite. However, other studies have shown that dustlike particles on the surface of test grains can also lead to parabolic curves, as can preferential dissolution along imperfections and discontinuities in the crystal lattice.

Lasaga (1998) gathered together most of the quantitative information available on the rates of dissolution of silicate minerals in laboratory experiments. He showed that for dissolution experiments in which no other precipitates form, the rate of dissolution or alteration of a mineral is given by

$$\frac{dc_i}{dt} = \left(\frac{A}{V} \right) v_i k, \quad (1)$$

where c_i is the concentration of species in solution, t is the time, A is the surface area of the mineral, V is the volume of fluid in contact with the mineral, v_i is the stoichiometric content of species i in the mineral, and k is the rate constant, which may depend on pH, temperature, and other species in solution. Equation (1) shows that the rate of dissolution of component i from a mineral depends on the stoichiometric abundance of the component, the surface area of the mineral exposed to the weathering solution, and an intrinsic rate constant, k .

It is also well known that the rate of dissolution of silicate minerals depends strongly on the pH of the solution, as expressed by



The rate constant k in Eq. (1) is proportional to the activity of hydrogen ion, as shown in Eq. (2), where k is in moles per square meter per second:

$$k = (a_{\text{H}^+})^N \quad \text{where } 0 < N < 1 \quad (2)$$

The most common values of N lie between 0.5 and 1.0. Table I summarizes the values of k , from experimental N values, for a variety of silicate minerals. These values of k show the rates of dissolution of silicate minerals vary strongly as a function of the activity of H^+ ion. Potassium

TABLE I pH Dependence of Mineral Dissolution Rates in Acidic Solutions^a

Mineral	Ideal formula	k	Range
K-feldspar	KAlSi_3O_8	$(\text{H}^+)^{1.0}$	$\text{pH} < 7$
Sr-feldspar	$\text{SrAl}_2\text{Si}_2\text{O}_8$	$(\text{H}^+)^{1.0}$	$\text{pH} < 4$
Forsterite	Mg_2SiO_4	$(\text{H}^+)^{1.0}$	$3 < \text{pH} < 5$
Enstatite	Mg_2SiO_6	$(\text{H}^+)^{0.8}$	$2 < \text{pH} < 6$
Diopside	$\text{CaMgSi}_2\text{O}_6$	$(\text{H}^+)^{0.7}$	$2 < \text{pH} < 6$
Ca-plagioclase	$\text{CaAlSi}_2\text{O}_8$	$(\text{H}^+)^{0.5}$	$2 < \text{pH} < 5.6$
Quartz	SiO_2	$(\text{H}^+)^{0.0}$	$\text{pH} < 7$

^a Rate constant k in Eq. (2) in text. From Lasaga, A. C. (1984). Chemical kinetics of water–rock interactions. *J. Geophys. Res.* **89**(B6), 4009–4025, Table 2, with permission.

feldspar, Sr-feldspar, and forsterite are most sensitive to pH, whereas the rate of dissolution of quartz is independent of pH in acidic solutions.

Using the rate of release of SiO_2 as an index, Lasaga solved Eq. (1) to determine the time that would be required to dissolve a spherical grain, 1 mm in diameter, of the minerals listed in Table I at a constant pH of 5. The results (Table II) show a sequence of stability that is remarkably similar to the historical Goldich sequence of weathering described earlier. Recent studies have shown that natural rates are slightly lower than those predicted by Lasaga (Schulz and White, 1999).

Recent studies have begun to reveal the relationship between the rate of dissolution of silicate minerals and the reactions which take place on an atomic scale at the interface between the surfaces of minerals and adjacent water. For example, Brady and Walther (1989) have shown that the rate at which silica is released from a dissolving mineral into water is controlled by the rates of detachment of the component oxides as a result of reaction between

TABLE II Calculated Mean Lifetime of a 1-mm Spherical Grain at pH 5^a

Mineral	Ideal formula	Lifetime (years)
Ca-plagioclase	$\text{CaAl}_2\text{Si}_2\text{O}_8$	112
Diopside	$\text{CaMgSi}_2\text{O}_6$	6,800
Enstatite	$\text{Mg}_2\text{Si}_2\text{O}_6$	8,800
Na-plagioclase	$\text{NaAlSi}_3\text{O}_8$	80,000
K-feldspar	KAlSi_3O_8	520,000
Forsterite	Mg_2SiO_4	600,000
Muscovite	$\text{KAl}(\text{AlSi}_3)\text{O}_{10}(\text{OH})_2$	2,700,000
Quartz	SiO_2	34,000,000

^a Adapted from Lasaga, A. C. (1984). Chemical kinetics of water–rock interactions. *J. Geophys. Res.* **89**(B6), 4009–4025, Table 4, with permission.

the H⁺ and OH⁻ in water and the exposed crystal bonds. At pH values above about 8, OH⁻ appears to react with Si-OH bonds to produce H₂O plus an Si-O-bond, resulting in a weakened crystal lattice. At low pH, H⁺ may react with Al-O-bonds, causing Al-bearing oxide groups to go into solution faster than Si-bearing groups, possibly explaining why silica-rich layers are observed to form on the surfaces of feldspars in strongly acidic solutions. Brady and Walther (1989) also show that the famous Goldich sequence weathering of silicate minerals (see Fig. 3) correlates directly with the different electrostatic energies of bonding between silicon and oxygen atoms in the various minerals of the series.

III. SOILS

A. Factors Involved in Formation

Soils are the result of the weathering of bedrock. They consist of new and residual minerals, fragments of partially weathered rock, wind-blown dust, and organic matter. The organic matter is a critical component of soils. A layer of weathered bedrock without any organic matter would probably not be called a soil by most earth scientists.

The factors that determine the type and thickness of soil include climate, time, type of bedrock, topography, and biologic activity. Of these factors, climate and time are dominant. Thick soils may form on granitic rocks in a temperate climate, but under arctic conditions the same bedrock will never develop a significant cover of soil. Topography is also a significant factor; erosion prevents the development of thick soils on steep mountain slopes. Ideal conditions for the formation of soils include a long time, moderate climate, and gentle topography. These are the conditions that have formed the thick agricultural soils of the central United States.

B. Horizonation

The elements that constitute fresh bedrock are strongly segregated by the processes of weathering. In fact, the segregation of chemical elements is a distinguishing feature of soils. It is most clearly expressed in the strong vertical zoning exhibited by many soils. Figure 5 is an idealized illustration of the vertical zoning that is characteristic of a soil in a temperate climate. The lowermost zone, immediately above the bedrock, is the C horizon; it consists chiefly of decomposed fragments of the underlying bedrock. The B horizon represents a zone in which certain elements accumulate after being leached and carried down from above by percolating waters. The thickness, depth, and composition of the B horizon are strongly controlled by climate. In

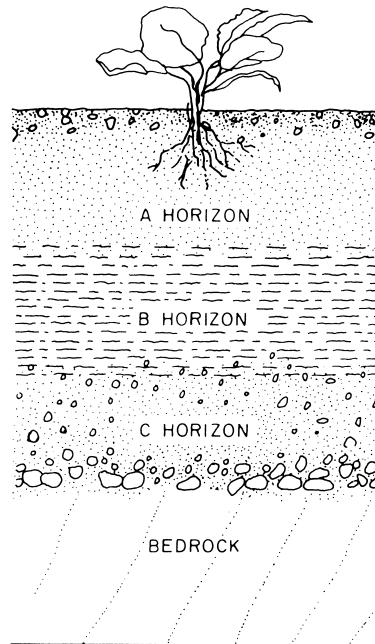


FIGURE 5 Simplified diagram showing the vertical zoning in a soil in a temperate climate.

wet, cool climates, as in the northeastern United States, the B horizon is rich in iron and clay minerals; such soils are called alfisols. In a dry temperate climate, like that of the central and southwestern United States, the B and C horizons may be characterized by an accumulation of CaCO₃, called caliche. Such soils may be classified as mollisols or aridisols. Mollisols are the great agricultural soils of the midwestern United States, Argentina, and central Asia.

The A horizon (Fig. 5) is the most important from the point of view of life on earth. It is in this zone that plants find the favorable combination of moisture and nutrients that is essential to growth. The presence of both living and dead organic matter characterizes the A horizon. The A and B horizons together are called the solum and are roughly synonymous with the word topsoil. From 10⁶ to 10⁹ microbes per cubic centimeter of soil are found in these layers. Nutrients released by the weathering of bedrock, often with the aid of these soil microbes, are adsorbed or chelated by the organic matter, and are readily available to the roots of plants.

In tropical climates the effects of abundant rainfall and high temperature combine to produce weathering that is particularly intense. The resulting soil is generally red in color and is called latisol (or laterite). A latisol represents the last insoluble residue left behind after long and intense weathering. Latisols are usually rich in iron or aluminum hydroxides, and, if very rich, may form ore deposits of these metals. Latisols are poor in organic matter

and other essential plant nutrients. In general, agricultural production from latosols is marginal and requires liberal fertilization.

Scientific study on the processes of formation of soils has been going on only for a century or so. Apart from the scientific knowledge that has been gained, it has become clear that agricultural soils are highly susceptible to damage and erosion by humans because of poor agricultural practices or urbanization and industrialization. Some of our best agricultural soils, often adjacent to large urban areas, have been taken over by suburban housing developments, shopping malls, and airports. Poor cultivation practices have resulted in soils with salinity problems, wind and slope erosion, and depleted nutrients. Thousands of years are required to develop a few centimeters of rich topsoil, but only a few years may be adequate to devastate it. Our continuing loss of agricultural soils may force some difficult social decisions in the future, as our desire to expand cities and industries continually encroaches upon this nonrenewable resource.

IV. THERMODYNAMIC CONSIDERATIONS

A. Gibbs Free Energy Function

The reactivity of geochemical species can be predicted from considerations of the Gibbs free energy function. Each solid, liquid, and aqueous species has a unique Gibbs free energy of formation. For a hypothetical reaction:



where x , y , and z represent the stoichiometric coefficients of the reactants and the products, the change in the Gibbs free energy is

$$\Delta G_f = z\Delta G_{fz} - (z\Delta G_{fx} + y\Delta G_{fy}) \quad (4)$$

where ΔG_f represents the Gibbs free energy of formation of the chemical species from the elements and ΔG_R the free energy of reaction. If the reactants and products are in the so-called standard state, Eq. (4) takes the form

$$\Delta G_R^0 = z\Delta G_Z^0 - (z\Delta G_X^0 + y\Delta G_Y^0)$$

The standard state is chosen to be at a temperature and pressure that are convenient for the problem being considered. Liquids and solids in the standard state are taken to be pure substances, gases are pure substances at a pressure of 1 bar (0.1 MPa) behaving ideally, and dissolved species are at 1 molal (1 m) concentration behaving as infinitely dilute solutions. The free energies are usually measured experimentally, although in some cases they can be calculated or estimated from basic principles. The Gibbs free energies of formation of actual solutions, gases, and min-

erals deviate from the ideal standard Gibbs free energies because of impurities.

The relationship between the Gibbs free energy of reaction and the standard free energy of reaction is

$$\Delta G_R = \Delta G_R^0 + RT \ln Q \quad (5)$$

where R is the gas constant, T the temperature of the reaction, and Q the reaction quotient for the reaction of interest. Using reaction (3) as an example, the reaction quotient is defined as

$$Q = [Z]^z / [X]^x[Y]^y$$

where $[]$ represents the thermodynamic activity of each reactant and product. (The concept of thermodynamic activity is discussed below. For very dilute solutions or gases at very low pressure and for pure solids and liquids, the activities are nearly equal to the concentrations.)

B. Equilibrium

At equilibrium the Gibbs free energy of reaction (3) is zero. A positive value of the Gibbs free energy indicates that the reaction should go to the left as written, and a negative value indicates that it should go to the right. At equilibrium, Eq. (5) becomes

$$\Delta G_R^0 = -RT \ln K_{eq} \quad (6)$$

where K_{eq} is the reaction quotient at equilibrium, now called the equilibrium constant. Tables of K_{eq} values are available in the literature for reactions involving solids, gases, and ions. However, for the great majority of reactions the K values are calculated from tabulated tables of ΔG_f^0 data.

For the dissolution of a solid, the reaction takes the general form

$$A_n B_m = nA^{m+} + mB^{n-} \quad (7)$$

$$K_{sp} = [A^{m+}]^n[B^{n-}]^m / [A_n B_m] \quad (8)$$

For pure solids $[A_n B_m] = 1$.

C. Activity versus Concentration

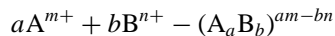
The amount of a dissolved species that is totally free and available for reaction is described as the thermodynamic activity. To illustrate the meaning of activity, let us consider the chemistry of magnesium in seawater. The total concentration of magnesium in sea water is 1292 mg/liter (0.053 m). Of this total, only a portion (0.046 m) is present as free Mg^{2+} . But not all of the free Mg^{2+} is available for reaction; the fraction that is available is the activity, with a value of 0.015 (note: activity is dimensionless). Therefore, the reactivity of magnesium in seawater is far lower

than would be suggested by a simple consideration of the total concentration.

In many situations activity can be approximated by concentration. For example, for nearly pure solids and liquids the activity is approximately equal to mole fraction X . For gases at low pressure, activity is nearly equal to partial pressure; for dilute electrolyte solutions, activity of the solute can be approximated by concentration.

D. Distribution of Aqueous Species

A chemical element dissolved in water is present in different aqueous forms. For example, in seawater over 99% of the total magnesium is present as Mg^{2+} and $MgSO_4^0$, but $MgHCO_3^+$, $MgCO_3^0$, and $Mg(OH)^+$ are also present in minor amounts. The relative abundances of the various dissolved forms depend on the constants of association K_a . Consider the reaction of species A and B to form a new dissolved species:



where a and b are the stoichiometric coefficients of the reactants, and m and n are the numbers of electrostatic charges on the reactants. For this reaction the stability of the new species is described by

$$K_a = [A_d B_b]^{am-bn} / [A^{m+}]^a [B^{n-}]^b$$

where $[]$ denotes thermodynamic activity.

Values of the association constants for magnesium include the following (expressed as \log_{10})

$Mg^{2+} + SO_4^{2-} = MgSO_4^0$	$\log K_a = 2.238$
$Mg^{2+} + HCO_3^- = MgHCO_3^+$	$\log K_a = 1.260$
$Mg^{2+} + CO_3^{2-} = MgCO_3^0$	$\log K_a = 3.398$
$Mg^{2+} + OH^- = MgOH^4$	$\log K_a = 2.600$
$Mg^{2+} + F^- = MgF^+$	$\log K_a = 1.820$

The value of K_a for $MgCO_3^0$ is larger than the value for $MgSO_4^0$; despite this, $MgSO_4^0$ is far more abundant in seawater than $MgCO_3^0$. This results from the fact that in seawater the activity of SO_4^{2-} is orders of magnitude greater than the activity of CO_3^{2-} . The reaction to form $MgSO_4^0$ is therefore driven much more strongly than the reaction to form $MgCO_3^0$.

Many comprehensive computer programs are now available to the geochemist to ease the burden of computing the multiplicity of chemical equilibria in natural waters. Some of the best known of the geochemical programs, together with the supporting institution, are EQ3/6 (Lawrence Livermore National Laboratory), WATEQ (U.S. Geological Survey), PHREEQE (U.S. Geological Survey), PATH (University of California at Berkeley),

GEOCHEM (University of California at Riverside), and MINTEQ (U.S. Environmental Protection Agency).

Many comprehensive computer programs are now available to the geochemist to ease the burden of computing the multiplicity of chemical equilibria in natural waters. Some of the best known of the geochemical programs, along with the supporting institution, are WATEQ4F (U.S. Geological Survey), MINTEQA2 (U.S. Environmental Protection Agency), NETPATH (U.S. Geological Survey), PHREEQC, PHREEQE, and PHRQPITZ (U.S. Geological Survey).

E. Activity Coefficient and Ionic Strength

The thermodynamic activity and the total concentration of an aqueous species i are related by the activity coefficient γ_i follows:

$$[i] = \gamma_i m_i \quad (9)$$

where $[]$ denotes activity and m_i is molality. At infinite dilution, activity and molality become equal; that is, γ_i goes to unity.

For very dilute solutions, γ_i can be calculated from the extended Debye–Hückel expression

$$-\log \gamma_i = \frac{Az^2 I^{1/2}}{1 + BaI^{1/2}}$$

where A and B are constants related to the density, dielectric constant, and temperature of the solvent. The terms z and a are the electrical charge and “hydrated ionic radius” of the ion, and I is the ionic strength. The ionic strength is a term that takes into account the concentrations and electrical charges of all ions in solution; it is calculated from

$$I = \frac{1}{2} \sum m_i z_i^2$$

where m_i and z_i are the molality and charge of each ion in solution. For a 1 : 1 electrolyte such as NaCl, the ionic strength is equal to the molality; $I = \frac{1}{2}[1(1)^2 + 1(1)^2] = 1$. For a 1 : 2 electrolyte such as CaCl₂, the ionic strength is 3. Thus, the ionic strength includes the effect of the concentration of solute and the electrical charge in the solution. An approximate ionic strength can be calculated for any natural water from the components listed in a comprehensive analysis. However, for a more accurate determination of the ionic strength it is necessary to compute the distribution of all aqueous species in the solution and eliminate from the calculation of ionic strength the proportion of ions that are tied up as uncharged ion pairs; this yields the “effective ionic strength” for the solution. For example, from an analysis of the total concentrations of dissolved species in seawater, an apparent ionic strength of 0.71 can be calculated. But after computer modeling to account for all of the noncharged ion pairs that form among the

dissolved components, the effective ionic strength is found to be 0.64. The latter value should be used in the Debye–Hückel and similar expressions for calculating the activity coefficients of the dissolved species.

The extended Debye–Hückel expression is valid for computing the activity coefficient of an ion up to an ionic strength of about 0.1. This covers the range of ionic strength of most natural fresh waters, such as rainwater, streams, and lakes. However, for saline waters, the Debye–Hückel expression fails to predict activity coefficients accurately. For example, in seawater, with an effective ionic strength of 0.64, the Debye–Hückel expression leads to γ_i values that may be in error by an order of magnitude.

For more saline waters, a number of semi-empirical forms of the Debye–Hückel expression have been developed. Typical of these is the following:

$$\log \gamma_i = (-) \frac{Az^2 I^{1/2}}{1 + BaI^{1/2}} + bI$$

where b is an adjustable term that is derived from experimental measurements.

Individual ion activities (and activity coefficients) cannot be measured exactly because the chemical behavior and properties of a single ion are affected by the other ions that must always be present in solution to maintain electrical neutrality. However, the mean activity coefficient γ_{\pm} can be measured for any salt. The mean activity coefficient is determined from measurements of such properties of solutions as freezing point, vapor pressure, solubility, and electrical potential. Figure 6 shows the mean activity coefficients for a number of salts as a function of molality. Note that γ_{\pm} is equal to 1.0 at infinite dilution. The curves in Fig. 6 illustrate the fact that most activity coefficients pass through a minimum and then increase at high molalities; from Eq. (9) this means that at high salinities the thermodynamic activity of a salt may be greater than the total concentration in solution.

Figure 7 summarizes the individual ion activity coefficients for several free ions, calculated from both the Debye–Hückel equation and the mean activity coefficients for individual salts.

For uncharged aqueous species such as H_2CO_3 the activity coefficient is usually approximated by an empirical expression such as

$$\log \gamma = k_m I$$

where k_m is a “salting coefficient,” which is tabulated in various standard reference books on solution chemistry, and I is the ionic strength. For H_2CO_3 , in a solution with the approximate composition of seawater the value of k_m is 0.1. For the effective ionic strength of 0.64 of seawater, this yields an activity coefficient of 1.16 for H_2CO_3 in seawater.

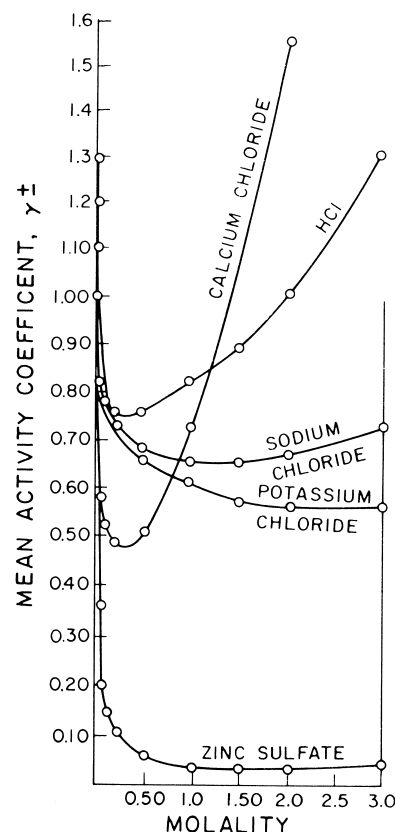


FIGURE 6 Mean activity coefficients for various salts as a function of molality.

Various approaches have been developed to model and predict mean activity coefficients in saline waters. The most successful of these is the Pitzer method, in which the mean activity coefficients are modeled by semi-empirical equations that account for all specific ion interactions except strong complexes. Data for the Pitzer equations are derived from measurements on binary and ternary systems of salts in water, then applied to any complex mixture of the same salts; this approach has been

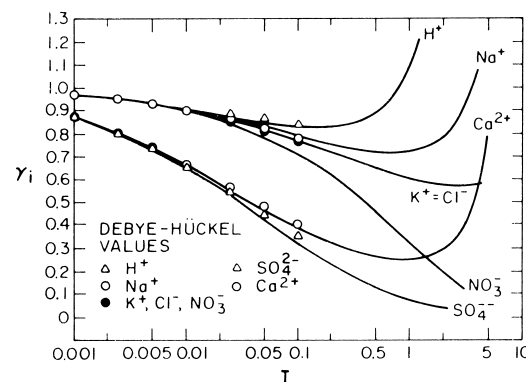


FIGURE 7 Individual ion activity coefficients, calculated from mean salt and Debye-Hückel expressions.

successful in modeling solutions up to concentrations of about 20 m.

In the absence of any theoretical basis for going from mean activity coefficients to single-ion activity coefficients, a nonthermodynamic assumption must be made to calculate the activity coefficients of individual ions. This is usually the MacInnes assumption, which states that the individual activity coefficients for aqueous K^+ and Cl^- are equal, and each is equal to $\gamma_{\pm KCl}$.

F. Saturation Index

An important aspect of low-temperature geo-chemistry is the determination of the state of saturation of natural waters with respect to minerals. For example, caves develop in limestone because the ground water is, at least temporarily, undersaturated with respect to calcite. The state of saturation of a natural water with respect to a solid mineral can be determined by combining the activities of the dissolved ions to form the ion activity product (IAP), which can then be compared to the equilibrium solubility product (K_{sp}). If the water is just at equilibrium with the mineral of interest, IAP will equal K_{sp} . For a state of supersaturation IAP will be larger than K_{sp} , and for undersaturation the IAP will be smaller than K_{sp} . As an example, the K_{sp} of calcite is $10^{-8.48}$, and in seawater the IAP of $CaCO_3$ is calculated to be $10^{-7.73}$. Thus, in normal seawater the IAP is greater than K_{sp} and the water is supersaturated with respect to calcite. The state of saturation is often expressed as the saturation index (SI):

$$\text{Saturation index} = SI = \log \frac{\text{IAP}}{K_{sp}}$$

For the example of calcite in seawater:

$$\begin{aligned} [Ca^{2+}] &= 10^{-2.65} & [CO_3^{2-}] &= 10^{-5.08} \\ \text{IAP} &= [Ca^{2+}][CO_3^{2-}] = 10^{-7.73} & (10) \\ SI &= \log \frac{10^{-7.73}}{10^{-8.48}} = (+)0.75 \end{aligned}$$

From Eq. (10), it is seen that SI is positive because the water is supersaturated with respect to the mineral. SI is zero at equilibrium and negative for undersaturation.

V. WATER CHEMISTRY

A. Rain and Snow Water

The most dilute waters in nature are rain and snow. These are the natural equivalents of distilled water in the laboratory. However, rain and snow are from pure water. They contain dissolved gases and aerosols, as well as the dissolved and solid products from reaction with atmospheric

TABLE III Composition (in mg/l, except pH) of Snow and Rain^a

Component	Snow ^b	Rain ^c	Rain ^d
Ca	0.0	0.65	1.2
Na	0.6	0.56	0.0
K	0.6	0.11	0.0
Mg	0.2	0.14	0.7
Cl	0.2	0.57	0.8
SO ₄	1.6	2.2	0.7
HCO ₃	3	?	7
NO ₃	0.1	0.62	0.2
Total dissolved solids	4.8	?	8.2
pH	5.6	?	6.4

^a From Hem, J. D. (1970). Study and interpretation of the chemical characteristics of natural water. U.S. Geological Survey Water Supply Paper 1473, 2nd ed., p. 50.

^b Spooner Summit, U.S. Highway 50, Sierra Nevada, November 20, 1958.

^c August 1962 to July 1963 (27 points in North Carolina and Virginia).

^d Menlo Park, California, January 9 and 10, 1958.

dusts. Table III shows the chemical composition of some selected samples of rain and snowmelt.

Systematic changes have been observed in the chemical composition of rainwater as a function of distance from the ocean and/or the length of time of individual storms. In general, the farther from the sea or the longer the rainfall continues, the more pure the water; this reflects a continued "rinse-out" of the aerosols and dust particles in the atmosphere.

One of the most serious environmental problems today is that of "acid rain." Research remains to be done in this area, but few would disagree with the preliminary conclusion regarding the important role of the gases of sulfur and nitrogen. These, in combination with rainfall, produce sulfuric and nitric acid, with a resultant lowering of the pH of rainfall below the value of 5.6 that would normally be imposed by the 0.0003 atm of atmospheric CO₂. It is becoming increasingly clear that gaseous emissions from automobiles, coal-fired power plants, and sulfide mineral smelters are the principal anthropogenic agents, while volcanic emissions are relatively minor and localized.

Occasionally, rainwater has a pH greater than 5.6. The higher values are attributable to aerosols of seawater or alkaline dusts from desert regions carried into the atmosphere.

B. Streams

The transition of rain and snow waters into stream waters begins as the first drops make contact with plants, soils, and bedrock. A large number of chemical and biochemical

reactions occur, adding dissolved and colloidal inorganic and organic material to the nearly pure precipitation. The amount of total dissolved solids (TDS) in rain or snowmelt can increase by an order of magnitude as waters infiltrate and percolate down through soil, shallow subsoil, or deep bedrock en route to the stream channel. As described in Sec. II, reactions such as dissolution, hydrolysis, and carbonation all contribute to the increased dissolved load in the water, as do metabolic processes of soil micro- and macro-biota, which may include both respiration and decomposition. The biochemical processes may additionally contribute dissolved gases, dissolved organic compounds, and particulate organic matter.

The chemical composition of stream waters varies greatly for different streams and for different seasons or even time of day within the same stream. For different streams, variations in chemistry depend on bedrock, climate, vegetation, and discharge. The chemical composition of a stream can vary greatly from headwaters to mouth, reflecting all these factors. Seasonal variations occur with spring flooding and resultant dilution or flushing effects. Some ions will decrease in concentration as discharge increases, indicating dilution; others will increase, indicating a flushing of soluble weathering residues from the soil. The increase peak is often quite brief, and field workers must be prepared to sample throughout the runoff period in order to capture it. Diurnal variations in pH of river water may be as much as 3 pH units, attributable to daily temperature variations and to the photosynthetic activity of aquatic plants. Typically, pH values will rise in the warmth of late afternoon, and fall in the cool, dark hours of evening. **Table IV** lists the compositions of the Mississippi River, the Amazon, and that of the “worldwide mean river water.”

In **Table IV** the differences between the Amazon and the Mississippi waters reflect the fact that the Mississippi drains the thick soils and sedimentary rocks of the central United States, whereas the Amazon drains the deeply leached lateritic soils of the Amazon rain forest. Studies of the Amazon show that the stream water carries more total dissolved solids near its headwaters, on the eastern side of the Andes. As the Amazon grows in size and flows through the Amazon basin, the lack of fresh bedrock and the enormous volume of dilute rainwater combine to make the water progressively purer as it flows toward the Atlantic.

Streams that traverse relatively insoluble crystalline rocks contain HCO_3^- as the principal dissolved anion; the HCO_3^- is derived from carbon dioxide gas in atmospheric air or soil air. If the bedrock is sedimentary, Cl^- and SO_4^{2-} are also abundant in the water.

Although K^+ is nearly as abundant as Na^+ in crustal rocks of the earth, Na^+ is far more abundant than K^+ in most stream waters. This reflects the fact that K^+ is

TABLE IV Compositions (in mg/l, except pH) of Samples of Water from the Mississippi River and the Amazon River and Worldwide Mean River Composition^a

Component	Mississippi ^b	Amazon ^c	World
Ca	42	4.3	15
Na	25	1.8	6.3
K	2.9	0	2.3
Mg	12	1.1	4.1
Cl	30	1.9	7.8
SO_4	56	3.0	11
HCO_3	132	19	58
SiO_2	6.7	7.0	13
Total dissolved solids	256	28	90
pH	7.5	6.5	—

^a From Hem, J. D. (1970). Study and interpretation of the chemical characteristics of natural waters. U.S. Geological Survey Water Supply Paper 1473, 2nd ed., p. 50.

^b October 1, 1962 through September 30, 1963. Time-weighted mean of daily samples.

^c Obidos, Brazil. High stage (7,640,000 ft³/sec), July 16, 1963.

released less readily from silicate mineral structures, once released, it is attracted more strongly than Na^+ to ion-exchange sites on clays and other fine-grained materials in stream sediments and soils, and is an essential nutrient for aquatic plants, which take K^+ up from the water. Sodium, on the other hand, tends to remain persistently soluble.

The concentration of SiO_2 is relatively constant in many stream waters of diverse origin. Its concentration appears to be controlled by the solubility of micaceous minerals and feldpars.

C. Lakes

Lakes that have surface outlets represent holding and mixing systems. Because the water moves much more slowly than in a river, geochemical reactions may approach equilibrium more closely than they do in rivers. However, mixing may not be complete in lakes, and waters may differ greatly in composition from one location to another in the same lake, or at different depths.

Thermal stratification is a significant process in many lakes. If the stratified condition persists, the deeper waters may become depleted in dissolved oxygen (anoxic) and enriched in hydrogen sulfide and methane. Lake “turnover,” with subsequent mixing of lake water strata, may occur twice a year in temperate climates as air temperatures cross 4°C. Water is at maximum density at this temperature, and surface waters can displace lower layers. Likewise, if the lake becomes isothermal, wind action on surface layers can cause mixing from bottom to top of the water column.

In lakes excessively affected by runoff containing high quantities of nutrients, overgrowth of aquatic vegetation may occur. The subsequent decomposition depletes creates anoxic conditions which extend throughout the lake; the lake is said then to be eutrophic.

Evaporation plays a major role in controlling the chemistry of lake water. Closed-basin lakes (no surface outlet) are especially influenced by evaporation. Two of the best-known closed-basin lakes are the Great Salt Lake in the United States and the Dead Sea in Israel and Jordan. These two unusual bodies of water are the result of intense evaporation of normal river water. The waters in the Great Salt Lake and the Dead Sea have roughly the ionic proportions of seawater but with about 10 times the total salinity.

Table V lists the compositions of a few lakes from closed basins in the western United States. Based on the pH values, the lake waters tend to fall into two very broad classes: saline (pH about 7.5) and alkaline (pH about 10). Studies of the chemical evolution of lake waters show that the initial composition of the dilute source water governs the final composition of the lake brine.

In **Table V** the high pH in the alkali lakes results from the fact that HCO_3^- is the dominant anion and greatly exceeds the concentration of calcium and magnesium in the fresh source streams. The low values of calcium and magnesium for Alkali Valley and Surprise Valley are caused by precipitation of calcite (CaCO_3) and a magnesium silicate [approximately sepiolite, $\text{Mg}_3\text{Si}_3(\text{OH})_2$] or magnesium carbonate. Gypsum ($\text{CaSO}_4 \cdot 2\text{H}_2\text{O}$) may also precipitate from some of the saline waters during evaporation.

TABLE V Compositions (in mg/l, except pH) of Various Lakes from Closed Basins in the Western United States^a

Component	Alkali Valley, Ore.	Surprise Valley, Calif.	Great Salt Lake, Utah	Saline Valley, Calif.
SiO_2	542	36	48	36
Ca	Trace	11	241	286
Na	117,000	4,090	83,600	103,000
K	8,850	3,890	4,070	4,830
Mg	Trace	31	7,200	552
Cl	45,700	4,110	140,000	150,000
SO_4	46,300	900	16,400	57,100
HCO_3	2,510	1,410	251	614
CO_3	91,400	664	Trace	Trace
Total dissolved solids	314,000	10,600	254,000	282,360
pH	10.1	9.2	7.4	7.4

^a From Eugster, H. P., and Hardie, L. A. (1978). Saline lakes. "Lakes: Chemistry, Geology, Physics" (A. Lerman, Ed.), Springer-Verlag, New York, p. 237–293, with permission.

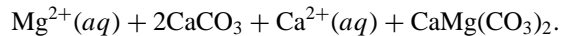
The anion chemistry is dominated by HCO_3^- – CO_3^{2-} in the alkali lakes and by Cl^- and SO_4^{2-} in the saline lakes.

D. Ground Water

Ground water is derived from precipitation that infiltrates the soil and percolates down into cracks and intergranular void spaces in either the bedrock or unconsolidated sediments. Ground water can be of excellent quality, and it is the principal water supply for most of rural America as well as such large cities as Miami, Florida, Houston, Texas, and Tucson, Arizona. For many years the extensive ground-water resources of the United States were thought to be pure and protected from pollution by the overlying layers of soil and rock. However, it is now recognized that anthropogenic contamination of ground water, particularly by organic solvents and petroleum products, is widespread.

Whereas surface streams moves at rates of a few feet per second, ground water rarely flows faster than a few feet per day. Because ground water is in intimate contact with rock minerals for much longer periods of time than streams, it is usually more saline than stream water. From the study of various radioactive isotopes, it has been determined that many ground waters are thousands of years old. For example, abundant, still potable water has been found in aquifers deep beneath the Sahara Desert, dating back to the retreat of the continental glaciers 10,000 years ago.

Deeper ground water is subject to higher temperatures and longer residence times than that in near-surface aquifers. Extensive chemical reaction with aquifer materials may occur. An example is the formation of dolomite from calcite as Mg^{2+} -rich waters migrate through a limestone:



Because of the slow kinetics of nucleation and growth of crystalline dolomite, the formation of dolomite is quite rare under near-surface conditions. However, subsurface conditions apparently allow dolomite to form in large amounts.

Waters that are produced with petroleum from deep strata may be as saline as the closed-basin lakes described earlier. Oilfield brines are thought to represent either meteoric waters that have reacted extensively with the enclosing rock strata or connate waters. Connate water may represent "fossil" water, ancient seawater from the time of formation of the rocks.

E. Seawater

The ultimate sink for dissolved elements released during weathering is the ocean. Although the absolute concentrations of elements dissolved in seawater vary from location

TABLE VI Concentrations of Major Dissolved Constituents in Seawater, with Calculated Residence Times

Component	Seawater (ppm)	Principal forms	Residence time in ocean (yr)
Na	10,556	Na ⁺ , NaCl ⁰	68,000,000
Mg	1,272	Mg ²⁺ , MgSO ₄ ⁰	12,000,000
Ca	400	Ca ²⁺ , CaSO ₄ ⁰	1,000,000
K	380	K ⁺ , KSO ₄ ⁻	7,000,000
Cl	18,980	Cl ⁻	100,000,000
S	2,649	SO ₄ ²⁻	—
C	140	HCO ₃ ⁻ , MgHCO ₃ ⁺	—
B	26	H ₃ BO ₃	18,000,000
Br	65	Br ⁻	100,000,000
F	1	F ⁻ , MgF ⁺	520,000

to location under such influences as evaporation or dilution by fresh river water, the ratio of dissolved species is remarkably constant. **Table VI** lists the major elements dissolved in seawater, the chief forms in which they occur, and the residence time for each element. The residence time is defined by is defined as the total mass of the dissolved element in the oceans divided by the amount transported in each year from the land. Some elements, such as sodium, chlorine, and sulfur, remain in a dissolved state in the ocean for long periods of time before being precipitated or incorporated in sediments or rocks. Other dissolved elements, including calcium, iron, and silicon, and the rare earth elements (REEs) quickly take part in chemical or biochemical reactions, with resulting short residence times. For example, calcium is strongly controlled by the precipitation of aragonite and calcite sediments.

The role of deep-sea hot springs at mid-ocean ridges has been shown to be much more important in controlling the residence times of some elements, particularly magnesium, than previously thought. Much research remains to be done in this area.

F. Buffering of Natural Waters

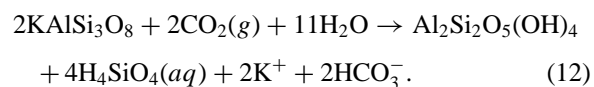
The pH of natural waters is controlled by acid–base equilibria involving dissolved species and solid compounds. Any chemical process that can add or remove H⁺ or OH⁻ in a natural water is a buffering process.

Much study has been devoted to acid–base buffering in natural systems, especially in seawater. Two major controls are recognized: water–rock interactions and ion–ion interactions. An example of the former is the reaction between acidic water and limestone:

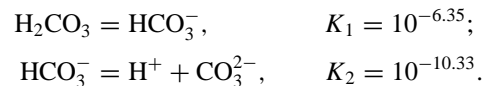


Clearly, reaction (11) has the capability of consuming and adding H⁺ to a water, thus buffering the pH. A similar reac-

tion may occur between silicate minerals and an aqueous solution; using feldspar and kaolinite as examples,



Reactions like (11) and (12) are known to be important in controlling the pH, especially over long periods of time. Short-term buffering is done by dissolved natural acids and the corresponding conjugate bases, such as H₂CO₃–HCO₃⁻–CO₃²⁻ and H₄SiO₄–H₃SiO₄⁻. Of such systems, the carbonic acid system is dominant in most natural waters. Buffering by the carbonate system is controlled by the following set of reactions (listed with the corresponding acid dissociation constants):



Most natural waters have pH values near 8, indicating that the predominant species of inorganic carbon is HCO₃⁻. **Figure 8** shows the distribution of the carbonate species as a function of pH. Note that the crossover points occur at the pH values of 6.35 and 10.33, corresponding to the pK₁ and pK₂ values; buffering is most effective at pH values near these crossover points. Similar diagrams can be constructed for H₄SiO₄, H₃BO₃, H₂S, and other natural acids.

VI. DIAGENESIS

Diagenesis is a term that describes the sum of processes that affect sediments or very young rocks, changing the composition, mineralogy, or texture. Diagenesis is characterized by low temperature and low pressure. An example of diagenesis is the reaction between seawater and fine-grained sediment carried into the ocean by fresh-water streams. Because the mineralogic debris carried in by river water, such as clays and metallic hydroxides, is out of

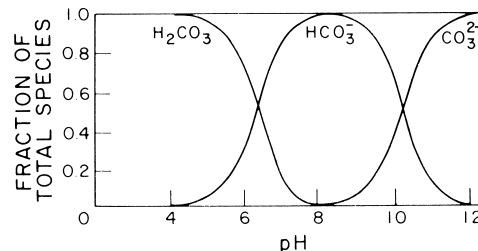
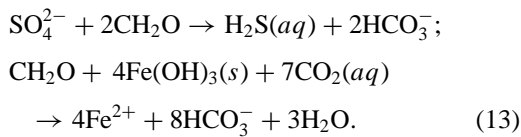


FIGURE 8 Distribution diagram for carbonic acid in water at 25°C and 1.013 bar (0.1013 mPa). Note that the crossover points occur at the acid dissociation values; buffering is most effective at these pH values.

equilibrium with seawater, there will be a tendency for reaction to occur in the new medium of seawater. Ions present in the seawater may be adsorbed on the surfaces of weathered minerals, or they may be incorporated in the structure of new minerals they may form. These early, rapid reactions are called halmyrolysis. As the sediment is gradually buried beneath the sea floor, old minerals may dissolve and new minerals may form. The final product of diagenesis will be a set of sedimentary minerals and rocks that more closely approach equilibrium with the enclosing fluids at the temperature and pressure of the new environment.

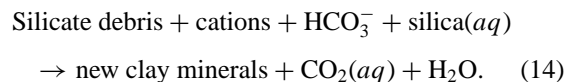
Several diagenetic reactions are reasonably well understood. Perhaps the most simple is the dissolution or recrystallization of unstable minerals into more stable forms. For example, most of the CaCO_3 deposited in modern oceans is in the form of fine-grained aragonitic mud and fragments of aragonitic shells (aragonite is the metastable orthorhombic form of CaCO_3 , calcite is the more stable rhombohedral form). Aragonite is unstable relative to calcite at the temperature and pressure of the earth's surface. Stable isotope studies using uptake of ^{44}Ca have shown the rate to be more rapid in fresh water, but still appreciable in salt water. Therefore, very early in the history of fresh-water and marine sediment, the carbonates tend to recrystallize into calcite; in some cases this results in lithification of the loose carbonate sediment into limestone. The silica derived from marine opaline diatom tests undergoes a somewhat similar reaction, resulting in hard layers of chalcedonic chert interbedded with unconsolidated sediments.

As marine sediments are buried to relatively shallow depths, the limited amount of oxygen in the pore waters is exhausted and the sediment becomes anoxic. Chemical species that are sensitive to the state of oxidation may be mobilized or immobilized by diagenetic reactions; the most notable examples are iron, sulfur, and manganese. Iron is present in most sediments as fine-grained iron hydroxide, and sulfur is present in the interstitial marine water as SO_4^{2-} ions. As the conditions become more strongly reducing, and in the presence of bacteria and organic matter, the following generalized reactions tend to occur (CH_2O represents carbohydrate):



The ferrous iron shown in reaction (13) may then react with the bicarbonate to form diagenetic siderite (FeCO_3) or with H_2S to form iron sulfide, FeS . The FeS will eventually change into the more stable form, pyrite, FeS_2 .

A third generalized type of diagenetic reaction is the so-called reverse weathering of silicates. At one time it was thought that such reactions were of primary importance in controlling the chemistry of seawater, but more recent work suggests that although reverse weathering may occur in seawater, it is probably not as important as formerly thought. The general reaction is



Reactions like (14) probably become increasingly important with increasing depth of burial of sediments beneath the sea floor.

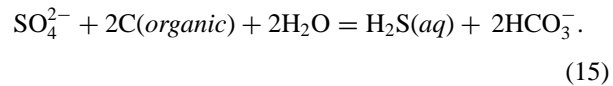
VII. OXIDATION AND REDUCTION

A. Sequence of Reactions

Many chemical elements of geochemical concern are sensitive to the oxidation-reduction (redox) status of the environment; examples include iron, sulfur, manganese, carbon, nitrogen, arsenic, chromium, copper, selenium, uranium, and vanadium. An illustration of the idealized sequence of redox-controlled changes in the chemistry of dissolved components in the interstitial water of a sediment is given in Fig. 9.

The changes shown in Figure 9 are controlled by the progressive loss of oxygen and the increasing role of anaerobic bacteria with depth in the sediment. Although the full sequence is rarely observed, portions of it are commonly present in waters of sediments, soils, and ground-water aquifers. The reactions are O_2 reduction, nitrification of organic nitrogen, nitrate reduction to nitrogen, MnO_2 reduction, Fe(OH)_3 reduction, SO_4^{2-} reduction, methane fermentation, precipitation of iron and manganese sulfides, and fixation of nitrogen. These reactions reflect the activity of bacteria in the sediment, utilizing in succession the oxygen from available solid and dissolved species. The reactions occur in the sequence predicted by standard electrochemical potentials. The bacteria serve as biological catalysts to facilitate reactions that might otherwise be kinetically slow. In general, each reaction is driven by a specific type or family of bacteria; that is, the reduction of sulfate does not occur until virtually all of the nitrate has been reduced, and methane is not generated until most of the sulfate has been reduced.

Redox reactions can be described in a variety of ways. For example, the reduction of SO_4^{2-} to aqueous H_2S can be written as



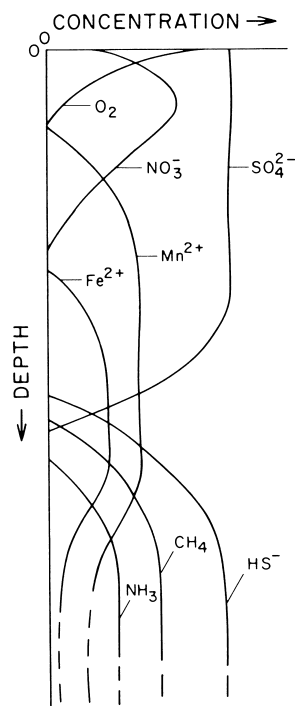
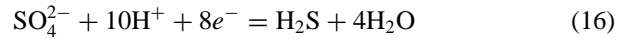


FIGURE 9 Schematic representation of changes in concentrations of redox-sensitive species to be expected in the interstitial water in a sediment with increasing depth below the sediment-water interface.

In reaction (15) the S(VI) in the SO₄²⁻ acts as the electron acceptor for the oxidation of organic matter to bicarbonate. The same reaction could be written as two half-reactions:



and



Reaction (15) is the sum of the two half-reactions (16) and (17). For this reason, it is usually convenient to write and tabulate tables of half-reactions for redox couples of interest and then add them together to describe balanced redox reactions.

B. pe-pH Diagrams

One of the most fruitful approaches to prediction of the relative stability of minerals in rocks and sediments has been the use of pe-Ph (or Eh-pH) (see Glossary) diagrams. For such diagrams a series of half-reactions are written, such as (16) or (17). Each reaction is then plotted on orthogonal graph paper, using the negative logarithm (base 10) of the H⁺ (i.e., pH) and the negative logarithm of e⁻ (i.e., pe) as master variables. The other compositional variables assigned fixed activity values.

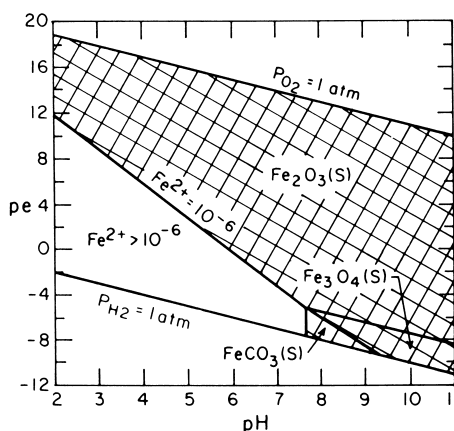


FIGURE 10 pe-pH diagram for the system Fe-O-H₂O-CO₂, assuming total dissolved CO₂ = 10⁻³ m. The solid-solution boundary for Fe²⁺ is drawn for Fe²⁺ = 10⁻⁶ m. Activities assumed to be equal to concentrations. T = 298 K and P = 1.013 bar (0.1013 mPa). Symbol (S) indicates solid compounds. The cross-hatched area indicates the fields of solids in which the activity of Fe²⁺ is less than 10⁻⁶.

A pe-pH diagram is shown in Fig. 10 for iron in water in the presence of CO₂ gas. The predictive power of such a diagram can be seen by imagining that the redox status of the water is lowered from a pe value of 12 to a pe value of -6, perhaps by adding dissolved organic matter and bacteria, while maintaining a constant pH of 8. The diagram indicates that the mineral hematite (Fe₂O₃) would be reduced to the mineral siderite (FeCO₃). If the pH were raised to about 10, the mineral magnetite (Fe₃O₄) should form at the expense of siderite. Lowering the pH would cause Fe²⁺ to go into solution at greater concentrations.

Much effort has been expended in low-temperature geochemistry in comparing thermodynamic predictions of mineral stabilities to the mineral assemblages actually found in the field. In general, the theoretical trends are observed, but with discrepancies that can usually be attributed to slow kinetics. It is also clear that the role of bacteria is profoundly important in affecting the rates of many low-temperature reactions in nature.

VIII. SORPTION AND ION EXCHANGE

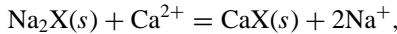
A. Types of Reactions

Sorption refers to the binding of ions and some neutral molecules to charged surfaces of minerals or colloids in sediment in contact with an aqueous solution. Ion exchange refers to the exchange of bound ions or neutral molecules with dissolved ions or neutral molecules in the aqueous solution of greater affinity to the mineral or colloid surface. Typically, the properties of sorption or ion

exchange are most exhibited by the fine-grained fraction of the sediment.

Sediments and soils commonly contain abundant fine-grained materials. The large surface areas of the fine-grained sediments are available for exchange of ions and neutral molecules between the solid substrates and the adjacent water. The attraction may result from weak electrostatic charges on the surface of the substrate or from strong chemical bonding between components of the solid and the aqueous species. Such reactions are commonly rapid, occurring in a few minutes to a few hours. The general process of attraction of the dissolved species to the surface of the solid substrate is called adsorption. A specific type of adsorption in which ions are exchanged between the surface of the solid and the aqueous solution is called ion exchange. If the sorbed species are incorporated in the interior of the solid, the process is absorption.

An example of an ion-exchange reaction, involving the exchange of Na^+ by Ca^{2+} on a substrate X, is



where X may represent any exchanging substrate.

Such reactions are described by an ion-exchange coefficient K_{ex} :

$$K_{\text{ex}} = \frac{\text{CaX}(\text{Na}^+)^2}{\text{Na}_2\text{X}(\text{Ca}^{2+})}$$

where () represents ionic concentration. In general, K_{ex} values are not constant; they vary as a function of the degree of ionic loading of the substrate, the type and concentration of competing ions in solution, other types of ions on the exchanger, and the salinity of the water. It is usually necessary to measure specific K_{ex} values for the waters and exchange substrates of interest. In soils, the cation-exchange capacity (CEC), the quantity of cations that can be held or exchanged by a given amount of soil, is measured in milliequivalents of cations per 100 g of soil (meq/g). CECs in descending order are organic material, vermiculite (hydrous mica), smectite clays, kaolinite clays, and sesquioxides (Fe, Al, Mn, and Ti oxides and hydroxides).

B. Adsorption Isotherms

Adsorption and ion exchange are often described by an empirical adsorption isotherm. In determining an adsorption isotherm, a known amount of material is added to a solution and mixed with a measured quantity of adsorbing substrate. After allowing time for adsorption to occur (at least a few hours), the amount of dissolved material is measured and the quantity lost is assigned to adsorption on the substrate. A series of experiments yields a curve (the isotherm), which can be expressed as micrograms

of material sorbed per gram of substrate. The empirical curves are described mathematically by a number of models, including the Freundlich isotherm:

$$\frac{x}{m} = kc^n,$$

where x is the mass of ion or molecule sorbed, m is the mass of the substrate, k and n are empirical constants derived from fitting the experimental curve, and c is the concentration of the dissolved species. Another model is the Langmuir adsorption isotherm:

$$\frac{x}{m} = \frac{ksc}{1 + ks}$$

where x , m , k , and n have the same meaning as in the Freundlich isotherm and s is the total sorbing capacity of the substrate per unit mass.

Much effort has been devoted to developing theoretical models for predicting sorptive processes. Some of the more fruitful results have come from consideration of the reactivity of the sorbing sites on the solid substrate. In this approach an intrinsic constant of reaction, similar to a thermodynamic constant, is assigned to each of the surface sites. The number of sites and the strength of the electrical field adjacent to the charged surfaces are then considered in calculating the extent of adsorption of species from solution. A computer code, MINSORB, a modification of MINTEQA2, successfully models various sorption processes.

IX. ELEMENTAL CYCLING

A. Carbon

If there is a “grand picture” in low-temperate geochemistry, it is the understanding of the cycling of the chemical elements through the hydrosphere, lithosphere, biosphere, and atmosphere. It is not an easy task to assemble the data required; the rates of flow of all the major rivers in the world, the concentrations of dissolved and suspended loads in the rivers, the rates of sedimentation on the sea floors, and so on. Nevertheless, many individuals have accepted the challenge.

As one example of elemental cycling, Fig. 11 illustrates the global geochemical cycle for carbon. It can be seen that the largest reservoir for carbon (10,000,000 billion metric tons) is in the rocks of the earth’s crust (chiefly in carbonates and organic-rich sedimentary rocks), followed by the oceans (35,000 billion metric tons).

The largest annual flux of carbon (100 billion metric tons per year) occurs between the oceans and the atmosphere, chiefly as carbon dioxide gas. Burning of fossil fuels contributes an anthropogenic flux of about 5 billion

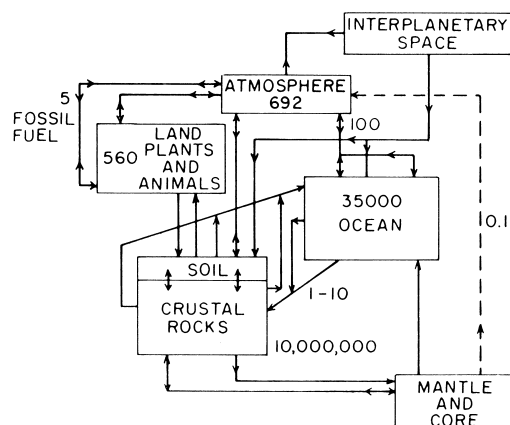


FIGURE 11 Carbon reservoirs and fluxes in the geochemical cycle. Reservoirs are in billions of tonnes (metric tons), and fluxes are in billions of metric tonnes per year.

metric tons of carbon per year, a portion of which remains in the atmosphere. Serious concern exists regarding the environmental effects of a continued buildup of carbon dioxide in the atmosphere. As the concentration of carbon dioxide increases, the so-called greenhouse effect may become important, resulting in a rise of several degrees in the average temperature of the atmosphere by the middle of the twenty-first century. Current evidence suggests that the average temperature of the Earth has been rising at the same rate as CO₂ is increasing in the atmosphere. The consequences of such an increase in temperature could include the development of deserts in the temperate agricultural areas of the world and flooding of coastal areas due to rising sea level caused by melting of the polar ice sheets. Increasing numbers of scientists are urging more reliance on alternative energy sources to avoid a possible environmental calamity.

Despite the many obvious environmental consequences of the wholesale cutting of the earth's rainforests, the main CO₂ sink is photosynthetic activity by phytoplankton in the world's oceans. An experimental effort to create more capacity to absorb CO₂ in the ocean involved fertilization of areas of the Sargasso Sea with iron, a limiting nutrient in the ocean, to stimulate the growth of phytoplankton, which would absorb more CO₂ via photosynthesis. Although the project was tentatively successful, scientists remain divided on the consequences of such massive intervention in the ocean's ecosystems.

B. Other Elements

Geochemical cycles have been worked out for most major elements and many of the nutrients and metals. It is clear that the cycles of all elements are now strongly affected by human activities, at least in the short term. For exam-

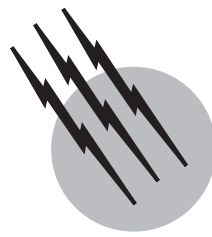
ple, the cycles of nitrogen and phosphate were altered, beginning in the 1950s and 1960s, and continuing to this day, by urban and rural runoff containing detergents and fertilizers, which contributed to eutrophication of lakes and contamination of surface and ground-water supplies in some areas. For better or worse, humans have extended their influence from the vastness of outer space to the geochemical behavior of individual atoms in the atmosphere, hydrosphere, and biosphere. Research on remedial efforts to correct these geochemical imbalances will continue to be important in the coming millennium.

SEE ALSO THE FOLLOWING ARTICLES

CARBON CYCLE • CHEMICAL THERMODYNAMICS • ELECTROLYTE SOLUTIONS, THERMODYNAMICS • ENVIRONMENTAL GEOCHEMISTRY • GEOCHEMISTRY • GEOCHEMISTRY, ORGANIC • HYDROGEOLOGY • OCEANOGRAPHY, CHEMICAL • STREAMFLOW

BIBLIOGRAPHY

- Berner, R. A. (1980). "Early Diagenesis, A Theoretical Approach," Princeton University Press, Princeton, NJ.
- Birkeland, P. W. (1999). "Soils and Geomorphology," 3rd ed., Oxford University Press, New York.
- Brady, P. V., and Walther, J. V. (1989). "Controls on silicate dissolution at neutral and basic pH solutions at 25°C," *Geochim. Cosmochim. Acta* **53**, 2833–2830.
- Chapelle, F. H. (1993). "Ground-Water Microbiology and Geochemistry," Wiley Interscience, New York.
- Drever, J. I. (1997). "The Geochemistry of Natural Waters: Surface and Ground Water Environments," 3rd ed., Prentice-Hall, Englewood Cliffs, NJ.
- Eugster, H. P., and Hardie, L. A. (1978). In "Lakes: Chemistry, Geology, and Physics" (A. Lerman, ed.), Springer-Verlag, New York.
- Faure, G. (1998). "Principles and Applications of Geochemistry," 2nd ed., Prentice-Hall, Upper Saddle River, NJ.
- Goldich, S. S. (1938). "A study in rock weathering," *J. Geol.* **46**, 17–58.
- Hem, J. D. (1992). "Study and Interpretation of the Chemical Characteristics of Natural Water," 3rd ed., U.S. Geological Survey Water-Supply Paper 2254.
- Krauskopf, K. B., and Bird, D. K. (1995). "Introduction to Geochemistry," 3rd ed., McGraw-Hill, New York.
- Langmuir, D. (1997). "Aqueous Environmental Geochemistry," Prentice-Hall, Englewood Cliffs, NJ.
- Lasaga, A. C. (1998). "Kinetic Theory in the Earth Sciences," Princeton University Press, Princeton, NJ.
- Morel, F. M. M., and Hering, J. C. (1993). "Principles and Applications of Aquatic Chemistry," Wiley Interscience, New York.
- Nordstrom, D. K., and Munoz, J. L. (1994). "Geochemical Thermodynamics," 2nd ed., Blackwell Scientific, Boston.
- Sposito, G. (1984). "The Chemistry of Soils," Oxford University Press, New York.
- Stumm, W., and Morgan, J. J. (1995). "Aquatic Geochemistry: Chemical Equilibria and Rates in Natural Waters," 3rd ed., Wiley Interscience, New York.



Geochemistry, Organic

Jürgen Rullkötter

Carl von Ossietzky University of Oldenburg

- I. Accumulation of Organic Matter in the Geosphere
- II. Transformation of Organic Matter in the Sediment
- III. Migration and Accumulation of Oil and Gas
- IV. Organic Geochemistry in Petroleum Exploration
- V. Organic Geochemical Techniques
in Paleoenvironmental and
Paleoclimatic Assessment

GLOSSARY

Biodegradation Alteration of organic matter in near-surface sedimentary rocks or of crude oil in the reservoir by microorganisms.

Biological markers Chemical compounds in sediments, crude oils, or coal with an unambiguous link to specific precursor molecules in living organisms (molecular fossils, geochemical fossils, biomarkers); among the most common biological markers are isoprenoids, steroids, triterpenoids, and porphyrins.

Bitumen Fraction of organic matter in sediments which is extractable with organic solvents.

Catagenesis Thermocatalytic transformation of organic matter in sedimentary rocks at greater burial depths (usually more than 2 km) and higher temperatures ($>50^{\circ}\text{C}$) into smaller molecules, particularly liquid and gaseous hydrocarbons which become part of the bitumen fraction.

Diagenesis Transformation of sedimentary organic matter under mild conditions (usually $<50^{\circ}\text{C}$) involving

both low-temperature chemical reactions and microbial activity.

Hydrocarbon (petroleum) potential Ability of a sediment that is rich in organic matter to generate hydrocarbons (petroleum) under the influence of geological time and temperature, expressed quantitatively in terms of milligrams of hydrocarbons per gram organic carbon (or kilograms per metric ton).

Kerogen Macromolecular organic matter in sediments that is insoluble in organic solvents and consists of structural remnants of dead organisms as well as diagenetic transformation products of various biopolymers and biomonomers.

Macerals Organic particle types specifically in coal but more generally also in dispersed sedimentary organic matter which can be recognized under the microscope and are characterized by their different structural (shape) and optical (color, reflectance, fluorescence) properties; the most common macerals are liptinite, vitrinite, and inertinite.

Maturation Thermal evolution of organic matter

(kerogen and bitumen) in the subsurface; maturity is measured by various physical and chemical maturation parameters (e.g., vitrinite reflectance, carbon preference index of *n*-alkanes, biological marker compound ratios).

Migration Movement of hydrocarbons in the subsurface from a source rock into a carrier bed (primary migration, mainly pressure controlled) and along a carrier bed into a reservoir rock (secondary migration, mainly buoyancy driven) to form a hydrocarbon accumulation.

Organic facies A mappable unit of sediment or sedimentary rock with (largely) uniform properties of its organic matter content.

Petroleum General term for fossil fuels, comprising both crude oil and natural gas.

Reservoir rock Porous rock unit (e.g., sandstone, limestone, or dolomite) suitable to contain a hydrocarbon accumulation (crude oil, gas) if structurally closed and sealed by an impermeable cap rock.

Source rock Organic matter-rich rock unit which under the influence of geological time and temperature has generated and expelled hydrocarbons (effective source rock) which may eventually have migrated into a reservoir to form a petroleum accumulation; a potential source rock (e.g., an oil shale) has not yet reached a sufficiently high maturation level for hydrocarbon generation.

ORGANIC GEOCHEMISTRY studies the distribution, composition, and fate of organic matter in the geosphere on both bulk and molecular levels, combining aspects of geology, chemistry, and biology. The biomass of decayed organisms is incorporated into sediments in the aquatic and terrestrial environment and is eventually buried to greater depth depending on the subsidence and depositional history of a sedimentary basin. Under the influence of temperature, catalysis, and (in shallow sediment layers) microbial activity, the organic matter undergoes a succession of complex chemical reactions which may ultimately lead to the formation of fossil fuels such as crude oil, natural gas, or coal.

I. ACCUMULATION OF ORGANIC MATTER IN THE GEOSPHERE

A. Bioproductivity and the Global Organic Carbon Cycle

The development of life on earth has a history of more than 3 billion years. Prokaryotic organisms started biosynthesis in the Precambrian, and remnants of their biomass still are present in ancient sedimentary rocks of that time. Mass production of organic matter did not occur, however, be-

fore oxygenic photosynthesis was established worldwide in the oceans by cyanobacteria about 2 billion years ago. At the same time, the initially reducing atmosphere gradually became enriched in free oxygen, which was the basis for the evolution of higher forms of life.

Cyanobacteria and unicellular algae prevailed until the early Paleozoic, about 550 million years (m.y.) ago. During the Cambrian, Ordovician, and Silurian, a variety of phytoplanktonic organisms evolved, and these contributed significantly to the organic carbon production on earth. At the end of the Silurian (400 m.y.), land plants started to settle the continents and spread out in the Devonian. During the Late Carboniferous (300 m.y.), the first massive woods occurred, which are documented today by a first maximum of extensive coal seams. Evolution of the terrestrial higher plant kingdom then continued in the Permian with the gymnosperms and finally during the Early Cretaceous (125 m.y.) with the angiosperms, which are the dominant species of the modern flora.

The production and decay of biomass is a cyclic process of a complex food chain in connection with the carbon dioxide (CO_2) in the atmosphere and the oceans (Fig. 1). This part of the global carbon cycle is the smaller one and has a relatively rapid turnover. It is connected via a small “leak” to the massive carbon reservoir of the lithosphere. Estimates of the mass of carbon stored in the different sections of the global carbon cycle are shown in Table I. It is evident that the world’s oceans contain the bulk of the carbon in the productivity cycle, although only about 2.5% of these 40,000 billion metric tons of carbon are organic. Carbon in the atmosphere is of the same order of magnitude as the biomass on the continents. Most of the organic carbon in the lithosphere is finely disseminated in sediments. In the most optimistic estimates, less than one-thousandth of it occurs as fossil fuels in various forms.

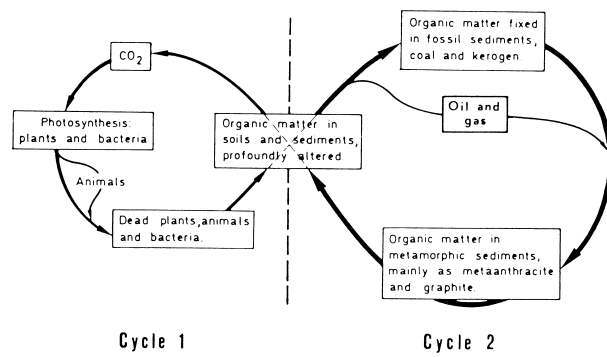


FIGURE 1 The two major organic carbon cycles on earth. Organic carbon is mainly recycled in cycle 1. The crossover from cycle 1 to cycle 2 is a tiny leak through which passes less than 0.1% of the primary organic biomass. [Reprinted with permission from Tissot, B. P., and Welte, D. H. (1984). “Petroleum Formation and Occurrence,” 2nd ed., p. 10, Springer-Verlag, Berlin and New York. Copyright 1984 Springer-Verlag.]

TABLE I Estimates of Carbon in Different Compartments of the Global Carbon Cycle^a

Compartment	Mass of carbon ($\times 10^9$ tons)
Atmosphere	700
Oceans	
Inorganic	39,000
Organic	1,000
Continents	
Biomass	600
Humic matter in soils	2,000
Lithosphere	
Inorganic	50,000,000
Organic	20,000,000
Including fossil fuels (upper limits)	
Oil, gas, tar sands	800
Coal	6,300
Oil shales	9,500

^a After Grassl, H., Maier-Reimer, E., Degens, E. T., et al. (1984). *Naturwissenschaften* **71**, 129–136.

Compared to the figures in Table I, the amount of carbon involved in the annual turnover is relatively small. The gross exchange rate between atmosphere and oceans is of the order of 80 billion metric tons/yr, whereas the annual production of biomass just exceeds 100 billion metric tons. Less than 250 million metric tons of carbon reach the marine sediments every year. The anthropogenic influence by fossil fuel consumption and cement production amounts to about 5 billion metric tons/yr.

B. Chemical Composition of the Biomass

Despite the diversity of living organisms in the biosphere, their chemical composition can be confined to a limited number of principal compound classes. Many of them are also represented in fossil organic matter, although not in the same proportions as they occur in the biosphere because of their different stabilities toward degradation during sedimentation and diagenetic transformation.

1. Nucleic Acids and Proteins

Nucleic acids, such as ribonucleic acids (RNA) or deoxyribonucleic acids (DNA), are biological macromolecules that carry genetic information. They consist of a regular sequence of phosphate, sugar (pentose), and a small variety of base units, i.e., nitrogen-bearing heterocyclic compounds of the purine or pyrimidine type. During biosynthesis, the genetic information is transcribed into sequences of amino acids which occur as peptides, pro-

teins, or enzymes in the living cell. These macromolecules vary widely in the number of amino acids and thus in molecular weight. They account for most of the nitrogen compounds in the cell and serve in such different functions as the catalysis of biochemical reactions and the formation of skeletal structures (e.g., shells, fibers, muscles).

During sedimentation of decayed organisms, nucleic acids and proteins are readily hydrolysed chemically or enzymatically into smaller, water-soluble units. Amino acids occur in rapidly decreasing concentrations in Recent and subrecent sediments, but may also survive in small concentrations in older sediments. A certain proportion of the nucleic acids and proteins reaching the sediment surface may be bound into the macromolecular kerogen network of the sediments and there become protected against further rapid hydrolysis.

2. Saccharides, Lignin, Cutin, and Suberin

Sugars are polyhydroxylated hydrocarbons which together with their polymeric forms (oligosaccharides, polysaccharides) constitute an abundant proportion of the biological material, particularly in the plant kingdom. Polysaccharides occur as supporting units in skeletal tissues (cellulose, pectin, chitin) or serve as an energy depot, for example, in seeds (starch). Although polysaccharides are largely water insoluble, they are easily converted by hydrolysis to C₅ (pentoses) and C₆ sugars (hexoses) and thus in the sedimentary environment will have a fate similar to that of the proteins.

Lignin is very common in supporting plant tissues, where it occurs as a three-dimensional network together with cellulose. Lignin essentially is a macromolecular condensation product of three different propenyl (C₃) phenols. It is fairly well preserved during sedimentation and is abundant in humic fossil organic matter.

Cutin and suberin are lipid biopolymers of variable composition which are part of the protective coatings on the outer surfaces of all higher plants. Chemically, cutin and suberin are closely related polyesters composed of various fatty and hydroxy fatty acid monomers. Both types of biopolymers are sensitive to hydrolysis and, thus, after sedimentation have only a moderate preservation potential.

3. Insoluble, Nonhydrolyzable Highly Aliphatic Biopolymers

Insoluble, nonhydrolyzable aliphatic biopolymers were discovered in higher plants and in algal cell walls as well as in their fossil remnants in sediments. These substances are called algaenan, cutan, and suberan according to their origin from algae or co-occurrence with cutin and suberin in extant higher plants. They consist of long-chain

aliphatic hydroxy esters crosslinked via ether bonds. Pyrolysis and rigorous chemical degradation methods are the only way of decomposing these highly aliphatic biopolymers. This explains why they are preferentially preserved in sediments.

4. Lipids (Monomers)

Biogenic compounds that are insoluble in water but soluble in organic solvents such as chloroform, ether, or acetone are called lipids. They are common in naturally occurring fats, waxes, resins, and essential oils but in a wider sense also include membrane components or certain pigments. The low water solubility of the lipids is responsible for their higher survival rate during sedimentation compared to other biogenic compound classes such as amino acids or sugars. The analysis of lipids and their conversion products in geological samples is a major objective of molecular organic geochemistry.

Various saturated and unsaturated fatty acids are the lipid components of fats, where they are bound to glycerol to form triglyceride esters (see Fig. 2 for examples of chemical structures of lipid molecules). In waxes, fatty acids are esterified with long-chain alcohols instead of glycerol. In addition, waxes contain unbranched, long-chain saturated hydrocarbons (*n*-alkanes) with a predom-

inance of odd carbon numbers (e.g., C₂₇, C₂₉, or C₃₁), in contrast to the acids and alcohols which show an even-carbon-number predominance.

Isoprene, a branched diunsaturated C₅ hydrocarbon, is the building block of a large family of open-chain and cyclic isoprenoids or terpenoids (Fig. 2). Monoterpene (C₁₀) with two isoprene units are enriched in essential oils of higher plants. Farnesol, an unsaturated C₁₅ alcohol, is an example of a sesquiterpene with three isoprene units. Diterpenes (C₂₀) are common constituents of higher plant resins, where they occur mostly as bi- to tetracyclic components (e.g., abietic acid; Fig. 2). The acyclic diterpene phytol is esterified to chlorophyll *a* and, thus is widely distributed in the green pigments of plants. Sesterterpenes (C₂₅) are of comparatively lower importance.

Cyclization of squalene (or its epoxide) is the biochemical pathway to the formation of a variety of pentacyclic triterpenes (C₃₀) consisting of six isoprene units. Triterpenoids of the oleanane, ursane, lupane, and other less common types are restricted to higher plants. The geochemically most important and widespread triterpenes are from the hopane series, such as diploptene, which occurs in ferns, cyanobacteria, and other eubacteria. The predominant source of hopanoids is bacterial cell wall membranes which contain bacteriohopanetetrol (and closely related molecules) as rigidifiers. This C₃₅ compound has a sugar

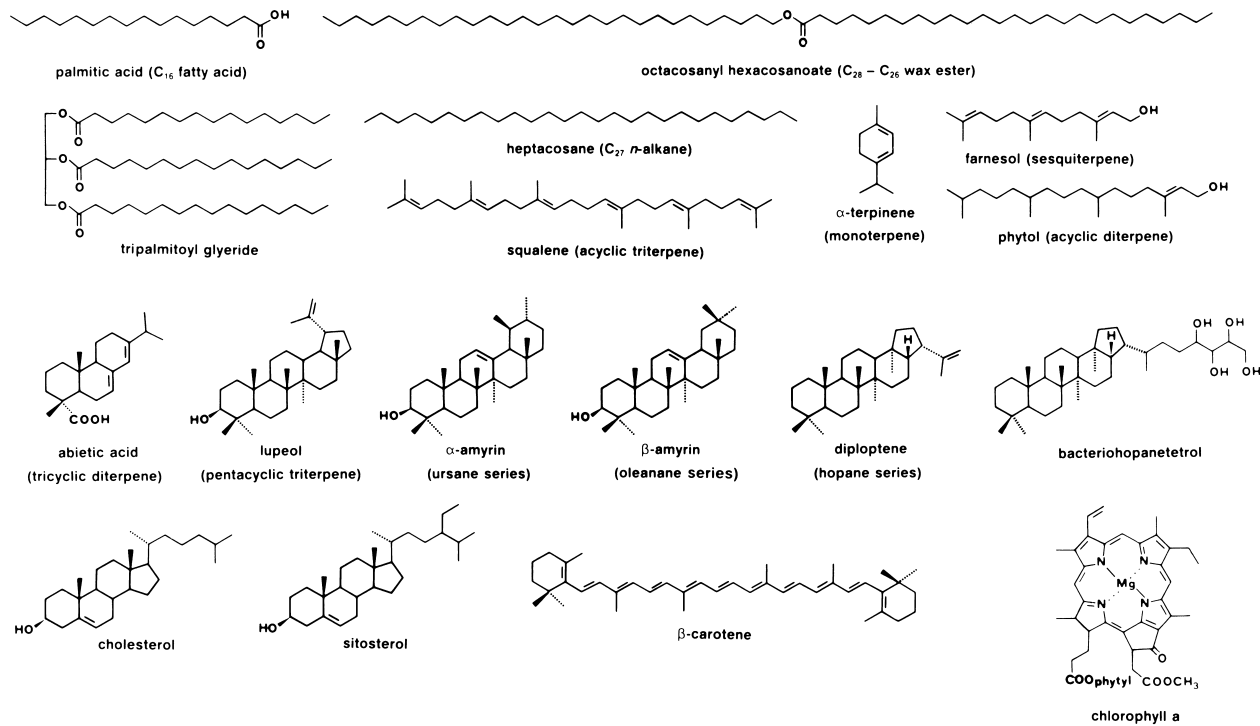


FIGURE 2 Structural formulas of representative organic lipids in living organisms and in the geosphere.

moiety attached to the triterpane skeleton (Fig. 2). The widespread distribution of bacteria on earth through time makes the hopanoids ubiquitous constituents of all fossil organic matter assemblages.

Steroids are tetracyclic compounds which are also derived biochemically from squalene epoxide cyclization, but have lost, in most cases, up to three methyl groups. Cholesterol (C_{27}) probably is the most widespread sterol in animals and many plants. Higher plants frequently contain C_{29} sterols (e.g., sitosterol) as the most abundant compound of this group. Steroids together with terpenoids are typical examples of biological markers (molecular fossils) because they contain a high degree of structural information which is retained after sedimentation. Thus, they provide an unambiguous link between the sedimentary organic matter and the biosphere. Steroids and terpenoids are among the most extensively studied classes of organic compounds in the geosphere.

Carotenoids, red and yellow pigments of algae and land plants, are the most important representatives of the tetraterpenes (C_{40}). Due to their extended chain of conjugated double bonds (e.g., β -carotene; Fig. 2), they are labile and found only in relatively small concentrations in surface sediments. Aromatization probably is one of the dominating diagenetic pathways in the alteration of the original structure in the sediment.

A second pigment type of geochemical significance are the porphyrins (tetrapyrroles) and related, not fully aromatized chlorins. Most porphyrins in sediments and crude oils are derived from the green plant pigment chlorophyll *a* and similar compounds in bacteria. It was the detection of porphyrins in crude oils and sediment extracts more in the 1930s that laid the basis for modern molecular organic geochemistry and provided the first strong molecular evidence for the biogenic origin of crude oils.

C. Factors Influencing the Preservation and Accumulation of Organic Matter in Sediments

The accumulation of sediments containing organic matter occurs primarily in the aquatic environment. The amount and composition of the organic component, i.e., the organic facies, are controlled by a number of complex, mutually dependent factors. A high primary bioproduction alone is not a sufficient criterion for the enrichment of organic matter in the sediment. Preservation of the decayed biomass is as decisive as a balance with the geological conditions and the supply of mineral components.

In a given depositional environment, organic matter may be contributed by the biomass production in the aquatic system, the transport of terrigenous organic mat-

ter from the continent by river discharge, or, usually less important, eolian dust, and by the erosion and recycling of previously deposited sediments. The relative importance of these factors will have an influence on the bulk composition of organic matter in the sediment. In the marine environment, bioproductivity is particularly high in areas of coastal upwelling, where coast-parallel winds bring cold water from deeper layers, enriched in nutrients, to the surface. This is presently significant on the western continental margins off southern California, Peru, Namibia, and on parts of the Indian Ocean margins. The supply of terrigenous organic matter to the ocean depends on the climate on the neighboring continent. A warm, humid climate supports both terrestrial vegetation and river discharge.

Consumption in the food chain or oxidation in the presence of free oxygen leads to (partial) mineralization of the organic matter and thus limits its preservation. Both processes may occur during transport to the site of deposition, during settling through the water column, and in the upper sediment layers. It is estimated that less than 0.1% of the annually produced biomass on average reaches the sediment. Different types of organic matter have different stabilities toward degradation. Marine organic matter, consisting essentially of proteins, saccharides, and lipids, is more labile than terrestrial organic matter, which contains chemically more stable compounds and lipids protected by relatively resistant supporting tissues. In fact, *n*-alkanes from higher-plant waxes frequently survive long-distance transport to remote sites in the oxic deep ocean. In oxic environments, such selective mineralization leads to an organic facies in the sediment that is not representative of the local aquatic ecosystem.

In addition to the oxygen content of the water column, water depth and sediment accumulation rates determine the preservation of organic matter. Residence time of organic particles in the water column depends on water depth as well as particle size and shape. Well-rounded large, rapidly settling particles such as fecal pellets have a great chance to reach the sediment surface even under oxic conditions. A high sedimentation rate favors organic matter preservation due to rapid burial and protection of the labile material from the oxic regime. A very high supply of mineral matter, on the other hand, may cause dilution of organic matter and thus lead to sediments with a relatively low organic matter content despite a high accumulation (preservation) rate.

Under certain conditions, an anoxic water body may develop. High surface-water bioproductivity leads to depletion of oxygen in the underlying water, because oxygen is consumed in the organic matter degradation of decayed organisms. If there is no adequate water circulation to replenish the oxygen, the whole water column down to the

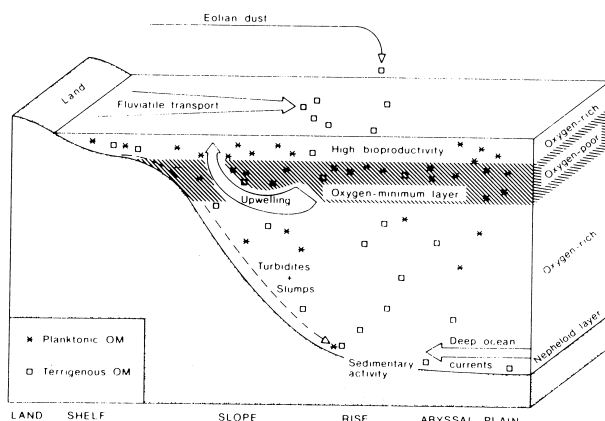


FIGURE 3 Schematic diagram showing the factors that control organic matter accumulation of marine continental shelf, slope, and rise sediments. [Reprinted with permission from Rulkötter, J., et al. (1983). In "Coastal Upwelling—Its Sediment Record, Part B" (J. Thiede and E. Suess, eds.), pp. 467–483, Plenum Press, New York. Copyright 1983 Plenum Press.]

sediment surface may become oxygen depleted. This typically happens during eutrophication of small lakes. The Black Sea is an example of a stagnant oceanic basin with an anoxic bottom water mass. A shallow sill largely separates the Black Sea from the Mediterranean Sea and suppresses the exchange of deep-water masses. In addition, density stratification due to heavy saline bottom water and lighter fresh water from river discharge at the surface prevents vertical mixing, so that over time all oxygen below a water depth of about 150 m has been consumed, and free hydrogen sulfide (H_2S) is now present in the deep anoxic waters of the Black Sea.

In the open ocean, a different process of oxygen depletion may occur (Fig. 3). A midwater oxygen-minimum layer develops in high-productivity areas, due to coastal upwelling. Where this layer impinges on the continental shelf or slope, preservation of organic matter in the sediment is highly favored. Resedimentation processes (turbidite flow, slumping) may transport such organic matter-enriched sediments down the slope to the deep, oxygenated ocean floor. Nevertheless, rapid burial of this redeposited material may protect the organic matter in it from destruction. Deep oceanic currents resuspending sediment material into a so-called nepheloid layer have an opposite effect on organic matter preservation.

II. TRANSFORMATION OF ORGANIC MATTER IN THE SEDIMENT

A. Diagenesis, Catagenesis, and Metagenesis

Organic matter that has been incorporated into a sediment will undergo a series of geochemical alterations which

are summarized schematically in Fig. 4. The microbial and chemical transformation of the original biomolecules, which started during sedimentation, is continued in the upper sediment layers. A series of still not well understood reactions, formally termed polymerization and condensation, leads to the initial "geopolymers," i.e., fulvic acids, humic acids, and humin. On a molecular level, these components are not well defined, but they are differentiated on the basis of their acid or base solubility. They are certainly not true polymers, but rather macromolecules with a variety of different building blocks which may include largely intact biopolymers. Among these, the insoluble, nonhydrolyzable, highly aliphatic biopolymers are of great importance. Kerogen is formed toward the end of the first transformation sequence, which is called diagenesis. This happens at relatively low temperatures ($<50^\circ\text{C}$) and involves the activity of microorganisms inhabiting the sediment. Kerogen is a complex organic geomacromolecule which is soluble in neither organic solvents nor in acids or bases. Its chemical composition at this stage is strongly heterogeneous and varies greatly depending on the organic facies.

A certain proportion of the organic constituents inherited from the biological system are small compounds extractable from the sediment with organic solvents. This bitumen fraction contains a number of (geo)chemical fossils,

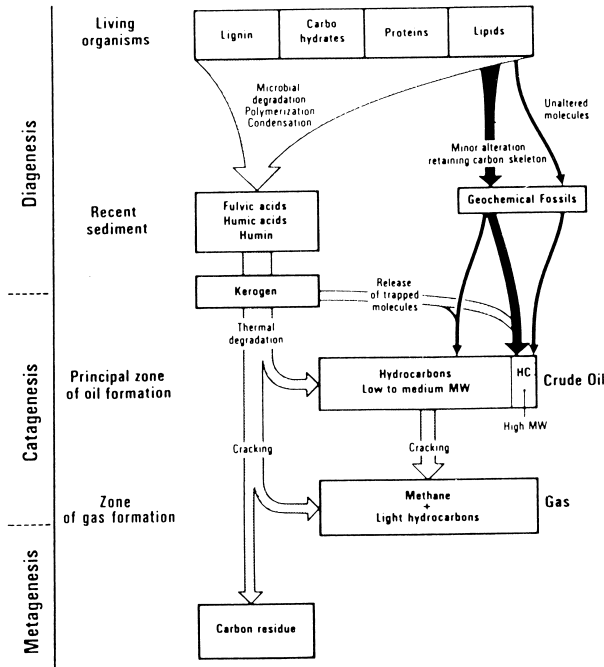


FIGURE 4 Schematic summary of geochemical transformation reactions of organic matter in the geosphere. [Reprinted with permission from Tissot, B. P., and Welte, D. H. (1984). "Petroleum Formation and Occurrence," 2nd ed., p. 94, Springer-Verlag, Berlin and New York. Copyright 1984 Springer-Verlag.]

i.e., unaltered molecules or compounds only slightly altered with essentially intact carbon skeletons compared to the precursor biomolecules. These may be hydrocarbons from higher-plant waxes or functionalized compounds such as alcohols, fatty acids, sterols, and triterpenes. The bitumen in Recent sediments accounts for only a very small portion of the total organic content.

When a sediment becomes buried more deeply in the course of continuing sedimentation and basin subsidence, it may enter the catagenesis stage, i.e., the principal zone of hydrocarbon formation (Fig. 4). Under the influence of increasing temperature ($>50^{\circ}\text{C}$) and geological time, hydrocarbons and other compounds are released from the macromolecular kerogen network, and they add to the bitumen phase. This is the process of crude oil generation. Hydrocarbons span a wide range from low to high molecular weight, and compounds containing heteroatoms (nitrogen, oxygen, and/or sulfur, i.e., other than carbon and hydrogen) can still account for a significant proportion of the total bitumen. In a later catagenesis stage, further thermal hydrocarbon generation from the kerogen as well as thermal cracking of the bitumen yields mainly gaseous hydrocarbons, at the end predominantly methane.

Finally, the organic matter in sediments may reach the metagenesis stage at great depth and very high temperatures exceeding 150°C . At this stage, only methane is stable, and the kerogen is converted to a carbon residue which may start some crystalline ordering leading ultimately to graphite.

B. Early Transformation of Kerogen and Biological Markers

1. Kerogen

The initial composition of a specific kerogen depends on the source organisms that contributed to the sediment. Because the kerogen structure is not readily accessible by conventional molecular analysis, other parameters have to be used to describe it chemically. One possibility is to measure the elemental composition in terms of carbon, hydrogen, and oxygen content. If the results are displayed in a so-called van Krevelen diagram of H/C versus O/C atomic ratios, three initial kerogen compositions (types I, II, and III) are distinguished together with three evolution pathways representing the changes in elemental composition during diagenesis and catagenesis (Fig. 5). Type I kerogen is of pure algal (and eventually bacterial) origin and rare. The very high H/C atomic ratio reflects the lipid content rich in saturated aliphatic structures. Type II kerogen is derived from other aquatic organisms such as phytoplankton and zooplankton and has an intermediate H/C atomic ratio. Terrestrial higher plant organic matter (type III) is characterized by a considerably lower H/C

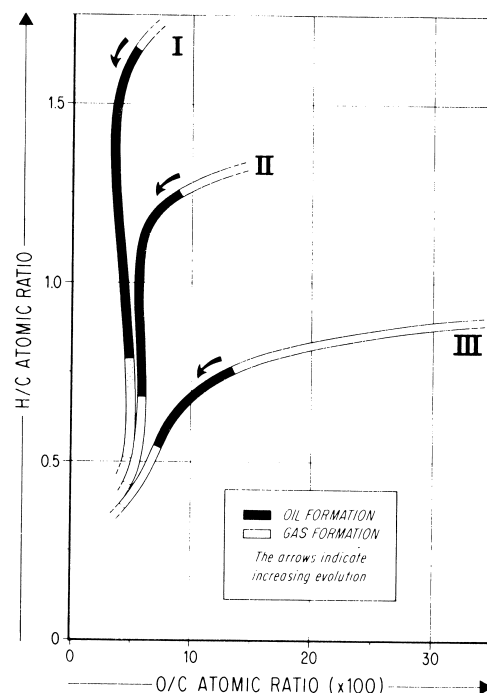


FIGURE 5 Structural evolution of various types of kerogen. [Reprinted with permission from Vandebroucke, M. (1980). In "Kerogen" (B. Durand, ed.), pp. 415–443, Editions Technip, Paris. Copyright 1980 Editions Technip.]

atomic ratio but is enriched in oxygen, as can be expected from the high cellulose and lignin contents.

The evolution pathways in Fig. 5, particularly for kerogen types II and III, show a decrease in the oxygen content in the first phase before the onset of oil generation. This represents the loss of small heteroatomic molecules such as carbon dioxide (CO_2) and water (H_2O) during the diagenesis stage. In addition, ammonia (NH_3) or hydrogen sulfide (H_2S) may be lost. The effect on the kerogen structure is a continuing condensation of the macromolecule with an increasing formation of carbon–carbon bonds.

2. Biological Markers

The developments in modern analytical techniques, particularly the combination of computerized capillary gas chromatography-mass spectrometry, allowed the identification of many of the compounds present in the complex mixture of organic molecules in sedimentary bitumen. This was used to follow the stepwise conversion of specific precursor compounds of biological origin into hydrocarbon products typically present in crude oils. The capillary gas chromatograph in this respect is used to separate the mixtures according to polarity and molecular weight by partitioning them between a gaseous phase, usually a stream of helium, and a stationary phase, usually a silicone gum coated to the inner wall of the fused silica capillary.

The effluent of the gas chromatograph enters a mass spectrometer, which generates spectra that provide information on the molecular weight and the chemical structure of the different compounds.

Molecules with a high degree of structural complexity are particularly informative and thus suitable to the study of geochemical reactions. They provide the chance of relating a certain geochemical product to a specific biological precursor. Such compounds, which retain a significant portion of their biogenic structural integrity throughout the geochemical reaction sequence, are called biological markers or molecular or (geo)chemical fossils.

The scheme in Fig. 6 illustrates the fate of sterols in sediments. Although it looks complex, Fig. 6 shows only a few selected structures of more than 200 biogenic steroids and geochemical conversion products presently known from sediments. The reaction sequence includes hydrogenation, dehydration, skeletal rearrangement, and aromatization. Steroids are only one example to illustrate these reactions, which likewise happen to many other compound classes.

The biological precursor in Fig. 6 is cholesterol (structure **1**, R=H), a widely distributed steroid in the biosphere. Hydrogenation of the double bond leads to the saturated cholestanol (**2**). This reaction occurs in the upper sediment layers or even in the water column by microbial action. Elimination of water gives the unsaturated hydrocarbon **3**. At the end of diagenesis, the former unsaturated

steroid alcohol **1** will have been transformed to the saturated sterane hydrocarbon **4** after a further hydrogenation step. An alternative route to the saturated sterane **4** is via dehydration of cholesterol, which yields the diunsaturated compound **5**. Hydrogenation of one double bond leads to a mixture of two isomeric sterenes (**6**; double-bond isomerization indicated by dots), further hydrogenation affords the saturated hydrocarbon **4**. A sterically modified form of this molecule, e.g., **7**, is formed during catagenesis at elevated temperatures. A side reaction from sterene **6** is a skeletal rearrangement leading to diasterene **8**, where the double bond has moved to the five-membered ring and two methyl groups (represented by the bold arrows) are now at the bottom part of the ring system. This reaction is catalyzed by acidic clays. Thus, diasterenes (**8**) and the corresponding diasteranes (**9**), formed by hydrogenation during late diagenesis, are found in shales but not in carbonate rocks, which lack the catalytic activity of clays.

An alternative diagenetic transformation pathway of steroids leads to aromatic hydrocarbons. The diolefin **5** is a likely intermediate on the way to the aromatic steroid hydrocarbons **10–14**. Compounds **10** and **11** are those detected first in the shallowest sediment layers. They are labile and do not survive diagenesis. During late diagenesis, the aromatic steroid hydrocarbon **12** appears in the sediments, but is also stable enough to survive elevated temperatures and to be found in crude oils. As for the

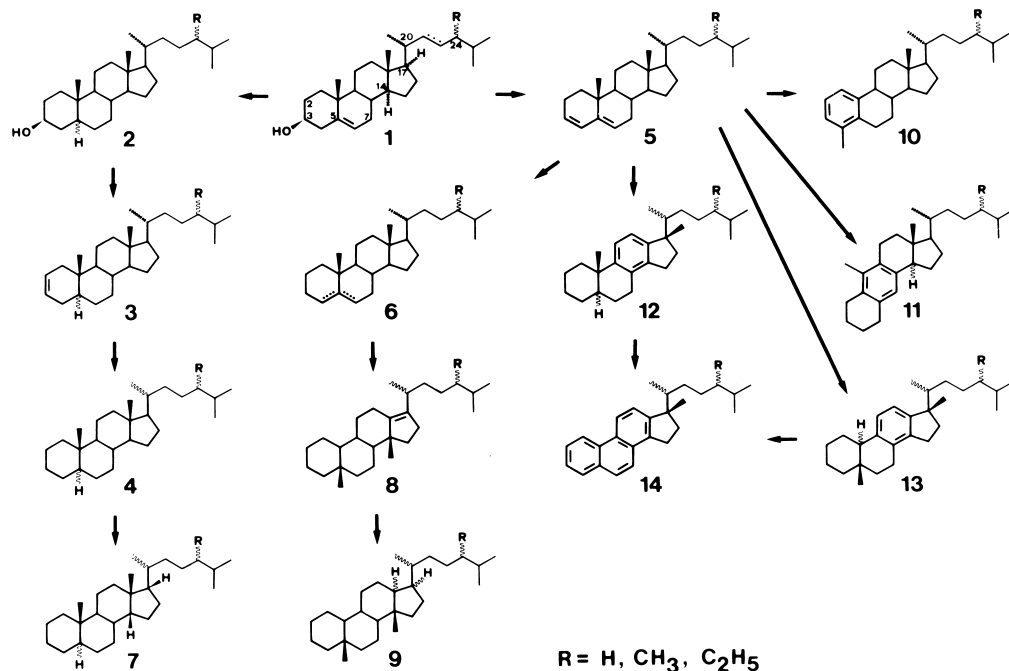


FIGURE 6 Diagenetic and catagenetic alteration of steroids.

saturated steranes, there is a corresponding rearranged monoaromatic steroid hydrocarbon (**13**). During catagenesis, the monoaromatic steroid hydrocarbons are progressively transformed into the triaromatic steroid **14** before the steroid record is completely lost by total destruction of the carbon skeleton at even higher temperatures.

Inorganic sulfur species (hydrogen sulfide, polysulfides, or elemental sulfur) play an important role in the early diagenesis of low-molecular-weight lipids carrying double bonds or alcohol groups. Common examples of such compounds known to react with sulfur are phytol (see [Fig. 2](#)), equivalent isoprenoids with two or more double bonds occurring in bacteriochlorophylls, sterols, and hopanoids (e.g., bacteriohopanetetrol; see [Fig. 2](#)). Intramolecular sulfur addition leads to the formation of thiophenes, i.e., five-membered aromatic rings with a sulfur atom in the ring system, and related saturated thiolanes (five-membered rings) or thianes (six-membered rings). Addition of more than one sulfur atom affords di- or trithianes (two or three sulfur atoms in a saturated ring) or bi- or trithiophenes (two or three thiophene units in a single molecule). Intermolecular sulfur incorporation, on the other hand, forms high-molecular-weight organic sulfur compounds. Because the inorganic sulfur species react with only a certain portion of the sedimentary lipids, the molecular geochemical information is partitioned selectively between the low-molecular-weight lipid fraction and the macromolecular sulfur species. In order to have access to the full range of biological markers, e.g., in the paleoenvironmental assessment of a sediment, it is advisable to remove the cross-linking sulfur bridges by hydrogenation with a Raney nickel or nickel boride catalyst before analysis.

Hydrogen sulfide (H_2S) is formed by microbial reduction of sulfate in seawater under strictly anoxic conditions. In clayey sediments, H_2S is preferentially trapped as pyrite (FeS_2) by reaction with Fe^{2+} ions; thus, an excess of inorganic sulfur compounds or a low iron concentration (as in carbonates) is an additional prerequisite for the diagenetic formation of organic sulfur compounds in sediments. At a later stage of organic matter transformation in sediments, organic sulfur compounds may become constituents of crude oils.

C. Thermal Hydrocarbon Generation

In the diagenesis stage, organic matter is immature with respect to hydrocarbon generation. The hydrocarbons present in the bitumen fraction, apart from methane (CH_4) formed by methanogenic bacteria in shallow sediments, largely constitute geochemical fossils inherited from the biosphere. On a molecular level, *n*-alkanes, for example, can show the typical distribution pattern of higher-plant

waxes with a maximum chain length above C_{25} and a predominance of the odd-carbon-number species. Similarly, cycloalkanes and aromatic hydrocarbons show a predominance of compounds with a close link to biogenic precursors.

The onset of oil generation occurs at the beginning of the catagenesis stage. The total amount of hydrocarbons in the sediments increases as a consequence of thermal cracking of kerogen. Initially, the weaker heteroatomic bonds are cleaved preferentially, but with increasing temperature due to deeper burial the stronger carbon–carbon bonds are broken as well. Also, relatively large units (asphaltenes) are released from the kerogen at the early catagenetic stage.

The generation of oil-type hydrocarbons goes through a maximum (“peak of oil generation”), after which gasoline-range and gaseous hydrocarbons in the wet gas zone become the main reaction products for two reasons. First of all, the kerogen during catagenesis has become depleted in large aliphatic moieties, and only the remaining smaller units can now be released. Second, the oil-type hydrocarbons in the bitumen fraction are thermally cracked into smaller, gaseous compounds.

In the dry gas zone, almost exclusively methane (CH_4) is generated from the kerogen. At the same time, methane is also the ultimate hydrocarbon product formed by cracking of oil released from the kerogen at earlier generation stages. During the oil and gas generation phase, the H/C atomic ratio of the kerogen constantly decreases as illustrated in [Fig. 5](#), and the kerogen becomes an inert carbon residue.

The amount of hydrocarbons generated from a specific source rock depends on the nature of the kerogen and on the extent to which the source rock has passed through the hydrocarbon generation zones under the given geological conditions, of which time and temperature are most important. The potential of a kerogen to generate hydrocarbons depends largely on its hydrogen richness as a limiting factor. Kerogen types I and II ([Fig. 5](#)) of dominantly aquatic origin are able to generate more hydrocarbons per unit carbon than the relatively hydrogen-poor kerogen type III.

The kerogen quality also influences the types of hydrocarbons generated. Aquatic organic matter and microbial biomass, both rich in aliphatic units, are the sources of abundant oil-type bitumen. On the other hand, coaly organic matter of terrigenous origin, which to a large extent is composed of aromatic ring systems with only short aliphatic chains, is more likely to yield predominantly gaseous hydrocarbons.

Because the rate of hydrocarbon generation is controlled by chemical reaction kinetics, both time and temperature are important for the transformation of kerogen. Although the geochemical reactions leading to the

formation of hydrocarbons may be complicated by an influence of pressure and catalytic activity of the mineral rock matrix, the general expectation is that source rocks in relatively young sedimentary basins need higher temperatures for hydrocarbon generation than those in older basins. This is confirmed by observations in nature which showed that hydrocarbon generation in the Upper Tertiary (10 m.y.) of the Los Angeles Basin starts at about 115°C, compared to 60°C in the Lower Jurassic (180 m.y.) of the Paris Basin. Since according to chemical reaction kinetics the influence of time should be linear but that of temperature exponential, the compensation of temperature by time is limited such that very old potential source rocks, which have experienced only very low temperatures, will not generate significant amounts of hydrocarbons even over very long geological times.

D. The Chemical Composition of Crude Oils Related to Geological Factors

1. Crude Oil Classification

Crude oils can be characterized by their bulk properties as well as their chemical composition. Distillation of crude oils provides fraction profiles over a certain boiling-point range. Total oils as well as distillation fractions can be described in terms of density, viscosity, refractive index, sulfur content, or other bulk parameters. A widely used parameter in the oil industry is the API gravity, which is inversely proportional to density. Conventional crude oils range from about 20 to 45° deg API gravity. Oils with lower API gravities are called heavy oils, those with higher API gravities are condensates, although these are not rigorously defined boundaries.

In organic geochemical studies, crude oils are conventionally separated into fractions of different polarities using column or thin-layer chromatography. Usually, after removal of the low-boiling components at a certain temperature and under reduced pressure ("topping"), asphaltenes (i.e., high-molecular-weight polar components) are precipitated by the addition of a nonpolar solvent (e.g., *n*-hexane). The soluble portion is then separated into saturated hydrocarbons, aromatic hydrocarbons, and a fraction containing the polar, heteroatomic compounds (NSO compounds or resins).

Of course, the gross fractions allow further subfractionation in order to facilitate subsequent studies on a molecular level using less complex mixtures. For example, the saturated hydrocarbons can be treated with 5-Å molecular sieve or urea for the removal of *n*-alkanes, leaving behind a fraction of branched and cyclic alkanes. Aromatic hydrocarbons are often further fractionated according to the number of aromatic rings.

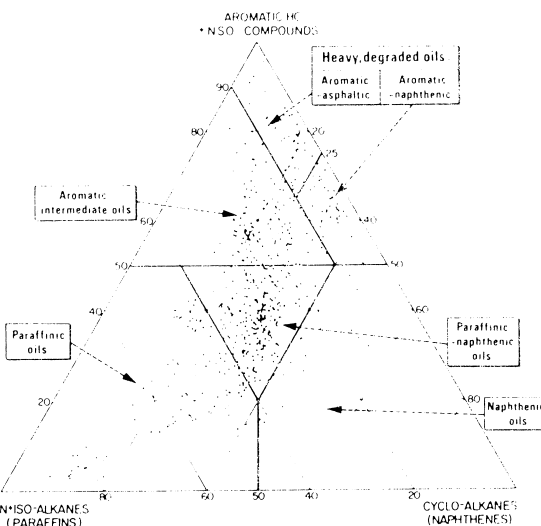


FIGURE 7 Ternary diagram showing the composition of six classes of crude oils based on the analysis of 541 oils. [Reprinted with permission from Tissot, B. P., and Welte, D. H. (1984). "Petroleum Formation and Occurrence," 2nd ed., p. 419, Springer-Verlag, Berlin and New York. Copyright 1984 Springer-Verlag.]

The ternary diagram in Fig. 7 shows the composition of six classes of crude oils based on a large number of analyses. Crude oils with more than 50% saturated hydrocarbons are called "paraffinic" or "naphthenic," depending on the relative contents of normal and branched alkanes (paraffins) and cycloalkanes (naphthenes). Paraffinic oils are light, but many have a high viscosity at room temperature due to the high content of long-chain wax alkanes. A high wax content is often an indication of a strong terrigenous contribution to the organic matter in the source rock. Such oils are commonly generated from deltaic sediments, as in Indonesia and West Africa. However, type I kerogen may also generate highly paraffinic crude oils, as is the case in the Green River Formation of the Uinta Basin, Utah. The crude oil property in the latter case is probably related to the fact that nonhydrolyzable highly aliphatic units in kerogen are derived not only from higher land plants but also from aquatic organisms (e.g., *Bottryococcus* algae; see Sect. 1.A.3). The most common oil type is paraffinic naphthenic (40% of the oils in Fig. 7), whereas naphthenic oils are scarce and often the result of microbial degradation in the reservoir (see Sect. III.C). All oils rich in saturated hydrocarbons commonly have a low sulfur content (<1%).

Aromatic intermediate oils contain 40–70% aromatic hydrocarbons and a high proportion of resins and asphaltenes. They are rich in sulfur and mostly heavy. Many crude oils from the Middle East (Saudi Arabia, Kuwait, Iraq, etc.) are included in this category, which is the second most important class in Fig. 7. The aromatic naphthenic

and aromatic asphaltic classes are represented mostly by altered crude oils. They are heavy, but the sulfur content may vary according to the original type of the crude oil. The Cretaceous heavy oils of Athabasca (Canada) are typical examples of these last two classes.

2. Geological Factors Influencing Crude Oil Composition

The depositional environment of the source rock, its thermal evolution, and secondary alteration processes are the most important factors determining the composition of crude oils. Among the environmental factors, those that influence the nature of the organic matter in the source rock and its mineral composition are of primary significance.

Although hydrocarbon source rocks are deposited under aquatic conditions, they may contain varying amounts of land-derived organic matter. The terrestrial contribution can be significant, particularly in intracontinental basins and in the deltas of large rivers, which may extend far into the open sea. Continental organic matter (type III kerogen) is rich in cellulose and lignin which, due to their oxygen content, are not considered to contribute much to oil formation. The subordinate lipid fraction together with the biomass of sedimentary microorganisms incorporated into the source rock yields crude oils which are rich in aliphatic units (from wax esters, fats, etc.), i.e., straight-chain and branched alkanes (paraffins). Polycyclic naphthenes, particularly steranes, are present in very low concentration. Total aromatic hydrocarbons are also significantly less abundant than in crude oil derived from marine organic matter, as is the sulfur content.

Marine organic matter (usually type II kerogen) produces oils of paraffinic naphthenic or aromatic intermediate type (Fig. 7). The amount of saturated hydrocarbons is moderate, but isoprenoid and polycyclic alkanes, such as steranes (from algal steroids) and hopanes (from membranes of eubacteria), are relatively more abundant than in oils from terrigenous organic matter. Kerogen derived from marine organic matter, particularly when it is very rich in sulfur, is particularly suited to release resin- and asphaltene-rich heavy crude oils at a very early stage of catagenesis. Type II kerogens are preferentially deposited where the environmental conditions are favorable for organic matter preservation (anoxic water column in silled basins or in areas of coastal upwelling) and where the continental runoff is limited for physiographical or climatic reasons.

The sulfur content of crude oils shows a close relationship to the type of mineral matrix in the source rocks. Organic matter in sediments consisting of calcareous (e.g., from coccolithophores or foraminifera) or siliceous shell

fragments (e.g., from diatoms or radiolaria) of decayed planktonic organisms and at the same time containing abundant organic matter is enriched in sulfur. The reason for this is that under the anoxic conditions which are required to preserve organic matter, sulfate-reducing bacteria form hydrogen sulfide (H_2S). This may react with the organic matter, and the sulfur will become incorporated into the kerogen. Examples are the Monterey Formation with the related crude oils produced onshore and offshore southern California and many of the carbonate source rocks of the Middle East crude oils.

In clastic rocks containing an abundance of detrital clay minerals, the iron content usually is high enough to remove most of the H_2S generated by the sulfate-reducing bacteria through formation of iron sulfides. Because terrigenous organic matter is commonly deposited together with detrital mineral matter (e.g., in deltas), waxy crude oils derived from type III kerogen usually are depleted in sulfur.

E. Coal and Oil Shales

Most organic carbon in sediments is finely disseminated. Even in hydrocarbon source rocks responsible for oil and gas accumulations, the organic carbon contents often do not exceed 10%. Apart from the secondary accumulations such as oil or gas reservoirs and tar sands, particular enrichment of organic matter in sediments occurs in the form of coal and oil shales.

1. Coal

Coal forms by the massive accumulation of land plants under a wet climate in a slowly subsiding basin. Peat formation is the first step in the process. It is essential that the decaying plant material be rapidly covered with water to prevent its oxidative decomposition. Furthermore, peat development requires the supply of plant remains over extended periods of time and a delicate balance of organic matter supply and tectonic subsidence. In terms of geological age, coal formation is possible since the advent of terrestrial higher plants in the Devonian (380 m.y. ago).

Peat formed by chemical and microbial diagenetic reactions in the first coalification step is transformed into lignite (brown coal) in the course of increasing burial. Elevated temperatures at greater depth over geological times are required to convert lignite into bituminous coals, which ultimately reach the anthracite stage at the end of the coalification process. Table II summarizes the different coalification stages together with selected physical parameters which can be used to differentiate among the coal ranks. Mean vitrinite reflectance, R_m , is the most widely used coalification parameter. It is determined on vitrinite

TABLE II Different Stages of Coalification According to the American Society for Testing and Materials (ASTM) Classification

Rank	Approximate		
	Reflectance range, R_m , (%)	Volatile matter d.a.f. (%) ^a	Carbon content d.a.f. (%) ^a
Peat	0.20–0.25	>64	<60
Lignite	0.25–0.4	55	65
Subbituminous coal (C, B, A)	0.4–0.65	48	73
High-volatile bituminous coal (C, B, A)	0.50–1.10	40	80
Medium-volatile bituminous coal	1.1–1.5	26	87
Low-volatile bituminous coal	1.5–1.9	18	89
Semianthracite	1.9–2.5	10	90
Anthracite	2.5–ca.5	5	92
Meta-anthracite	5	<3	>92

^a d.a.f. = dry and ash free.

particles (vide infra), which can be observed on polished coal surfaces under the microscope. Vitrinite reflectance is low in the peat and lignite stages; it increases from about 0.4% to 1.9% in the bituminous coal ranks, and to values in excess of 5% in the anthracite stage. At the same time, the content of volatile matter decreases drastically, and the carbon content of coals increases to more than 90%.

Coal, particularly at low ranks, is not homogeneous. This is conceivable from heterogeneity of the contributing plant materials and the variability of the chemical and microbial reactions after deposition due to changes in water coverage, acidity (pH value) or redox (Eh) potential in the depositional environment. Coal is composed of a number of organic particle types (macerals) distinguishable either macroscopically or, more importantly, microscopically.

Coal petrography, as this study is called, differentiates among three main maceral groups, each containing several macerals (Table III). The microscopic investigations are performed on polished coal surfaces in the reflected-light mode, and macerals are distinguished by their reflectance, shape, and structure. Occasionally, fluorescent light observations after ultraviolet irradiation are used to enhance the signal of low-reflecting liptinites. The same techniques are applied by organic petrographers to characterize dispersed organic particles in sediments.

Vitrinite is the most abundant maceral group in humic coals. Vitrinites are coalification products of humic substances which essentially originate from the ligno-

cellulose components of cell walls; they appear gray in reflected light under the microscope. Telinite shows cell structures of wood or bark, whereas collinite is structureless. Vitrinite in hard coals corresponds to huminite in lignite or peat, where a different terminology for the macerals and a stronger subclassification of the maceral group is used (examples are given in Table III). Small detrital particles of vitrinitic material, intimately mixed into a structureless groundmass and difficult to identify, are called vitrodetrinite.

Liptinites, less abundant in coals but major constituents of petroleum source rocks, are derived from hydrogen-rich, lipid-bearing plant materials. Among these are spores and pollen (sporinite), cuticles and cuticular layers within the outer walls of leaves or stems (cutinite), resins and waxes (resinite), and corkified cell walls of barks, roots, or fruits containing suberin as a protecting agent against dessication (suberinite). Alginite is rare in coals, with the exception of the occasionally occurring sapropelic coals, which were not deposited as peats but under more anoxic conditions as subaqueous muds rich in plankton and water plants.

Inertinites have the same biological precursors as vitrinites but when occurring in the same coal have a higher reflectivity. Fusinite and semifusinite show distinct cellular structures of wood. Many of these particles appear to be fossil equivalents of charcoal, and ancient forest fires may have contributed to their formation. Sclerotinites are mostly fungal remains, although other sources have been invoked for part of the sclerotinites, particularly in older (Carboniferous and Permian) coals. Macrinite is an amorphous substance which formed by oxidation of gelified plant material. All inertinites are highly carbonized and have no potential for hydrocarbon generation.

2. Oil Shales

Oil shales are organic matter-rich sediments which have never been buried to greater depth. They contain little extractable bitumen but generate oil when heated to

TABLE III Maceral Classification of Coals Showing Main Maceral Groups and Selected Macerals^a

Maceral group	Maceral
Vitrinite (huminite)	Telinite (ulminite), vitrodetrinite, collinite (gelinite)
Liptinite	Sporinite, cutinite, resinite, suberinite, alginite, liplodetrinite, bituminite
Inertinite	Fusinite, semifusinite, macrinite, sclerotinite, inertodetrinite

^a Special terms used for brown coals (lignite) only are given in parentheses.

temperatures of about 500°C. Oil shales may be true shales with clay minerals as the dominant inorganic component, but commonly include carbonate as well as siliceous rocks. The organic carbon content in most cases exceeds 20%, and the H/C atomic ratio is very high (close to or above 1.5).

The organic matter often consists entirely of freshwater (*Bottryococcus*) or marine (*Tasmanites*) algae and bacterial biomass (type I organic matter; cf. Fig. 5). Because oil shales have not entered the catagenetic stage, the shale oil produced by heating contains considerable amounts of sulfur- and nitrogen-bearing compounds in addition to pyrolytically formed unsaturated hydrocarbons (olefins), which are not normally present in crude oils. There is no basic geochemical difference between oil shales and petroleum source rocks. The former just have not been buried deeply enough for thermal hydrocarbon generation under natural conditions.

Oil shales were deposited in large lake basins such as the Eocene Green River shales in Utah and Wyoming, which are several hundred meters thick, in shallow seas on stable platforms such as the Permian Irati oil shale in Brazil, or in small lakes, bogs, and lagoons, where they are often associated with coal beds. Oil shales range in age from the Lower Paleozoic (Cambrian) to the Tertiary. The world's largest oil shale reserves are in the United States, Brazil, and Russia.

III. MIGRATION AND ACCUMULATION OF OIL AND GAS

A. Primary and Secondary Migration

The formation of oil and gas from kerogen occurs in relatively tight hydrocarbon source rocks. The liquid and gaseous low-molecular-weight compounds generated in this process occupy a larger volume than the solid macromolecular precursor material. Because of the generally low porosity of the source rocks, the amount of hydrocarbons that can be contained in them is limited. The generation of hydrocarbons leads to an increase in pressure that eventually causes expulsion of the hydrocarbons into more porous sediments overlying or underlying the source rock. This movement of hydrocarbons is called primary migration (Fig. 8).

The oil expelled continues its movement through the wider pores of the more permeable carrier rock. Driving forces are water flow in the subsurface and buoyancy of the hydrocarbons that have a lower density than the saline waters (brines) saturating the pores of sedimentary rocks. During this secondary migration, petroleum may ultimately reach a reservoir rock that has porosity and

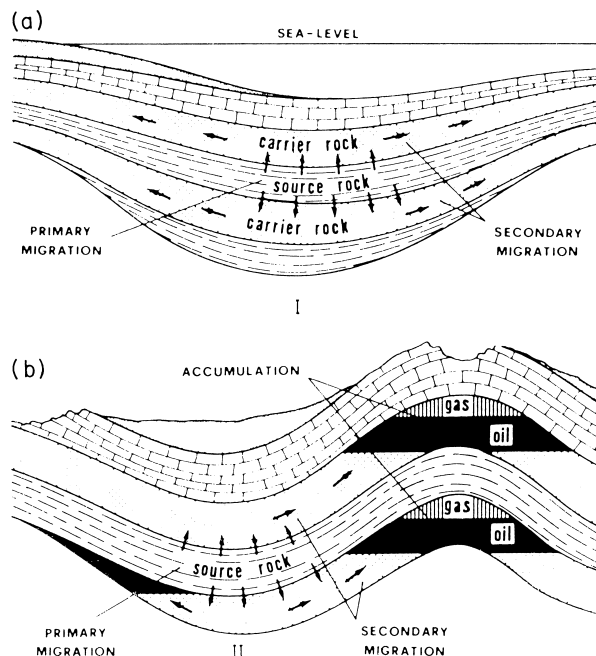


FIGURE 8 Schematic representation of primary and secondary migration leading to oil and gas accumulation: (a) initial phase and (b) advanced stage. [Reprinted with permission from Tissot, B. P., and Welte, D. H. (1984). "Petroleum Formation and Occurrence," 2nd ed., p. 294, Springer-Verlag, Berlin and New York. Copyright 1984 Springer-Verlag.]

permeability characteristics similar to those of the carrier bed but is sealed by an impermeable barrier, the cap rock (Fig. 8). In this way hydrocarbon accumulations are formed.

The most important mechanism for primary migration is transport of petroleum compounds in a continuous hydrocarbon phase with pressure as the driving force. The formation of a separate oil or gas phase in deeply buried, highly compacted sediments is favored by the fact that the amount of pore water present is low and that all or most of it is tightly bound to the mineral surface. This immobility of the pore water facilitates hydrocarbon movement. Furthermore, mineral surfaces may be covered with organic matter (kerogen network) or even be "oil wet," which further enhances transport of the apolar petroleum components. If very high pressures develop in a source rock, microfracturing may occur, which will periodically increase the migration flow toward more porous media, such as larger fractures within the source rock, or an adjacent carrier rock. Diffusion is considered an effective primary migration mechanism only in exceptional cases and mainly for gaseous hydrocarbons over short distances. Transport of hydrocarbons in aqueous solution is no longer considered a mechanism for primary migration.

Primary (and probably also secondary) migration leads to fractionation of the bitumen initially generated in the source rocks. Polar compounds tend to be preferentially retained by adsorption on mineral surfaces, and very large polar compounds such as asphaltenes may have a low chance for migration at all. Thus, crude oil in a reservoir will be depleted in polar heteroatomic compounds but enriched in hydrocarbons relative to the source rock, bitumen. The extent to which this occurs depends on the pore sizes of the migration pathway, the adsorption activity of the mineral surfaces, and the distance of migration. Fractionation among the hydrocarbons is relatively minor, as shown by numerous examples of successful oil/source rock correlation based on hydrocarbon compound ratios.

The efficiency and timing of primary migration has been a matter of debate for many years. It is now known that more than 80% of the hydrocarbons generated may be expelled during the main phase of oil formation. This contrasts sharply with the range of 10% to (exceptionally) 30% estimated in the earlier literature. Expulsion is more effective in thin source layers of a few centimeters or decimeters than in thick layers extending over several meters. In thick shales, part of the hydrocarbons retained may have to be cracked to lighter (gaseous) hydrocarbons before they get a chance to migrate out. The same occurs in rocks lean in organic matter, where the pressure buildup by liquid hydrocarbons is insufficient and not enough kerogen is present to form a continuous network supporting hydrocarbon drainage. For this reason, source rocks containing predominantly terrigenous organic matter with a low proportion of liptinite mainly generate gas, because the small amounts of liquid hydrocarbons initially formed cannot be expelled, but are later transformed into gas at higher thermal stress. Similarly, coals produce mainly gas (methane) because their microporosity and adsorption activity impede expulsion of initially formed liquid hydrocarbons. The high storage capacity of coals even for gas is well known from coal mining (pit gas).

Secondary migration of hydrocarbons through porous and permeable carrier beds and reservoir rocks is driven mainly by buoyancy due to the low densities of oil and gas. Secondary migration terminates when the retarding capillary pressures are stronger than the driving forces. If a barrier is encountered in the subsurface, then hydrocarbon accumulations will form. Otherwise, the hydrocarbons will seep out at the surface.

Oil and gas are trapped in the structurally highest position of a reservoir rock which is sealed with an essentially impermeable cap rock. Two general types of traps are commonly distinguished (Fig. 9). The sand anticline in Fig. 9a is an example of a structural trap. Other types of structural traps formed by tectonic events are associated, e.g., with salt domes, carbonate reefs, or basement highs. By far the

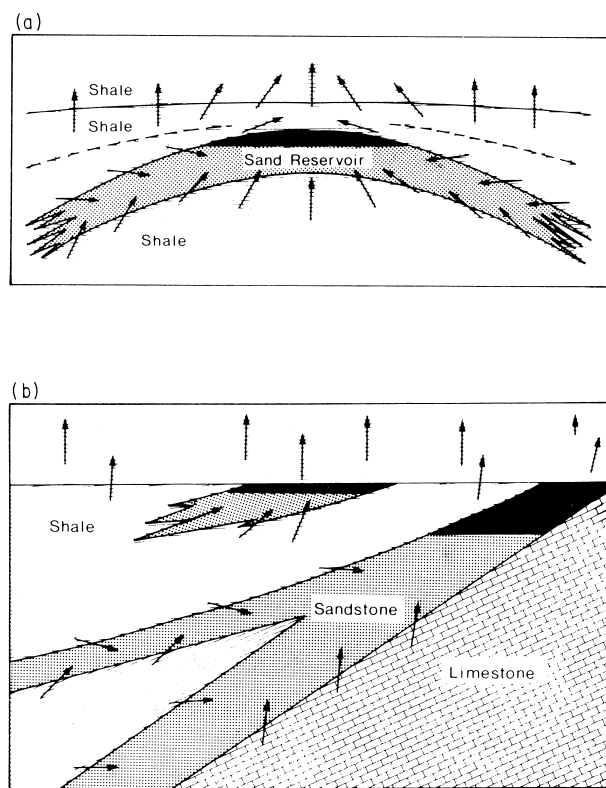


FIGURE 9 Schematic representation of two different types of hydrocarbon traps: (a) anticline as an example of a structural trap and (b) stratigraphic trap at an unconformity. [Reprinted with permission from Hunt, J. M. (1979). "Petroleum Geochemistry and Geology," pp. 223–224, Freeman, San Francisco. Copyright © 1979 W. H. Freeman and Company.]

largest amount of crude oil on earth is accumulated in anticline reservoirs, which are also the easiest to detect by geological and geophysical prospecting and are usually drilled first. The formation of stratigraphic traps is controlled by sedimentation processes. This type of trap may be associated with erosional surfaces (unconformities) as in Fig. 9b or with a change in the sediment facies (lithology). For example, when a coastal sand deposit grades into fine-grained shale farther offshore, the shale may act as a barrier to the hydrocarbons moving through the sand.

In contrast to primary migration, secondary migration may occur laterally over long distances of several tens of kilometers or even more. On the other hand, secondary migration can also be very short, e.g., from a shale source rock into an embedded sand lense. Over geological times, hydrocarbon accumulations are unstable. Tectonic events such as folding, faulting, or uplift associated with erosion can destroy hydrocarbon reservoirs completely or cause a redistribution of hydrocarbons into other reservoirs. In addition, cap rocks are not absolutely impermeable, and over

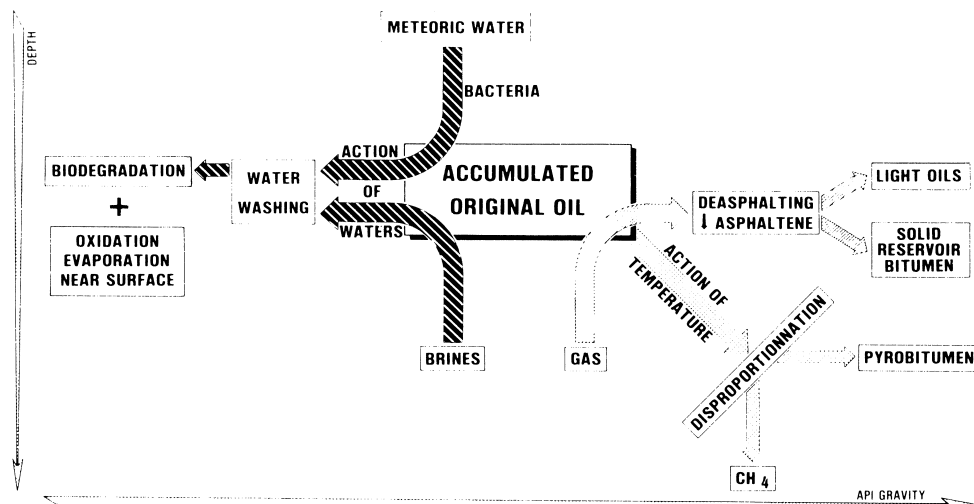


FIGURE 10 Crude oil alteration in the reservoir. [Reprinted with permission from Connan, J. (1984). In "Advances in Petroleum Geochemistry," Vol. 1. (J. Brooks and D. H. Welte, eds.), pp. 299–335, Academic Press, Orlando, FL. Copyright 1984 Academic Press.]

many millions of years the leakage rate may be sufficient to empty a reservoir.

B. Alteration of Hydrocarbons in the Reservoir

Even if reservoir conditions are tectonically stable, pooled hydrocarbons are susceptible to secondary alteration. The most important factors that can influence the chemical composition of petroleum in a reservoir are summarized in Fig. 10. Physical and chemical transformation processes will lead to either an increase or a decrease of the API gravity (or, conversely, the density). Alteration of hydrocarbons in the reservoir is quite common and is observed in many oil fields around the world. Petroleum can be altered to such an extent that the character of the source material is lost and the economic value decreases drastically.

Basin subsidence can bring a reservoir together with its accumulated hydrocarbons into a regime of higher temperature. Cracking reactions may then lead to the formation of lighter hydrocarbons (ultimately methane) and a residual pyrobitumen. Alternatively, long-term exposure of reservoir hydrocarbons to higher temperatures even without basin subsidence may cause cracking into smaller components. Within a basin this effect will be proportional to the reservoir depth.

Major amounts of gas entering a petroleum reservoir reduce the solubility of large polar compounds, and asphaltenes are precipitated in a process called desasphalting. The resulting oil is lighter than that originally present in the reservoir. The precipitated material forms a solid bitumen and may have a negative effect on the production properties of the reservoir by reducing the permeability.

Hydrodynamic flow of brines and the invasion of meteoric surface water can alter a crude oil by water washing, which removes the more water-soluble compounds from the reservoir. Meteoric water usually carries oxygen and in most cases microorganisms into the reservoir. This leads to microbial degradation of the crude oil, with a preferential removal of the readily metabolizable components. *n*-Alkanes are removed first, followed by simple branched and isoprenoid alkanes. Polycyclic saturated hydrocarbons are biodegraded less easily and at a much later stage. The biological alteration of the aromatic hydrocarbons is less well understood because the associated water washing coupled with the higher water solubility of the aromatic hydrocarbons often obscures the net effect of biodegradation. Biodegradation of crude oils in the reservoir is limited by the supply of oxygen and nutrients to the microorganisms and the maximum temperatures they can tolerate. Thus, biodegradation is rarely found at reservoir temperatures exceeding 70°C. In very shallow reservoirs, evaporation of volatile hydrocarbons to the surface strengthens the effect of biodegradation. As a result, heavy oils or tar sands may be formed, of which a famous example are the Athabasca tar sands in Alberta, Canada.

IV. ORGANIC GEOCHEMISTRY IN PETROLEUM EXPLORATION

The search for crude oil and natural gas is a costly and risky enterprise. After finding most of the easily detectable reservoirs in readily accessible areas, hydrocarbon exploration is now proceeding into new frontier areas including the deeper ocean and higher latitudes with their harsh

climate and is looking for hitherto undetected smaller traps in previously explored basins. In order to keep the economic risk of drilling within reasonable limits, as many modern techniques as possible are used by the explorationists to help them in decision making. Sophisticated geophysical measurements (seismics) and satellite imaging are almost routine. Application of the principles of organic geochemistry in this respect has become a widely used tool in petroleum exploration.

A. The Hydrocarbon Potential of Sedimentary Rocks

The initial amount and the type of organic matter in a sedimentary rock determine its hydrocarbon potential. It is a question of the thermal evolution of such a sediment, if the potential is ever used actually to generate hydrocarbons. It is not easy to define a minimum organic carbon content for a sediment to be a source rock, but commonly accepted values are 0.5% for clastic rocks (claystones) and 0.3% for carbonates. This is based on a statistical overview of a great number of suspected or proven source rock samples worldwide, which shows that carbonates on average are leaner in organic matter than clastic rocks. Carbonates, on the other hand, often contain layers of organic matter-rich material derived from algal or bacterial mats. The restrictions imposed by the mechanisms of primary migration (expulsion; see Sect. III.A), however, may require higher minimum organic carbon values, probably on the order of 1.0–1.5%. Good to excellent hydrocarbon source rocks will have more than 2% organic carbon.

It can be roughly generalized that the quality of organic matter (hydrogen richness) in sediments increases with the total organic carbon content, because once favorable conditions for organic matter accumulation have been established, the preservation of the most labile lipid-rich material is enhanced. Examples are known, however, in which an organic carbon-rich sediment has little hydrocarbon potential because the kerogen it contains is woody or highly oxidized.

While the total organic carbon content is usually measured by combustion after removal of the carbonate carbon by acid treatment, several methods are available to assess the type of organic matter in a sediment. One way is by microscopic maceral analysis in which a specific hydrocarbon potential is ascribed to different macerals. Lipitinites are believed to have a high potential for oil generation, whereas vitrinites may generate some oil but mainly gaseous hydrocarbons.

A standard pyrolysis method in petroleum geochemistry allows a quick assessment of the bulk hydrocarbon generation potential of a sediment. This so-called Rock-Eval pyrolysis uses a small amount of ground rock sample

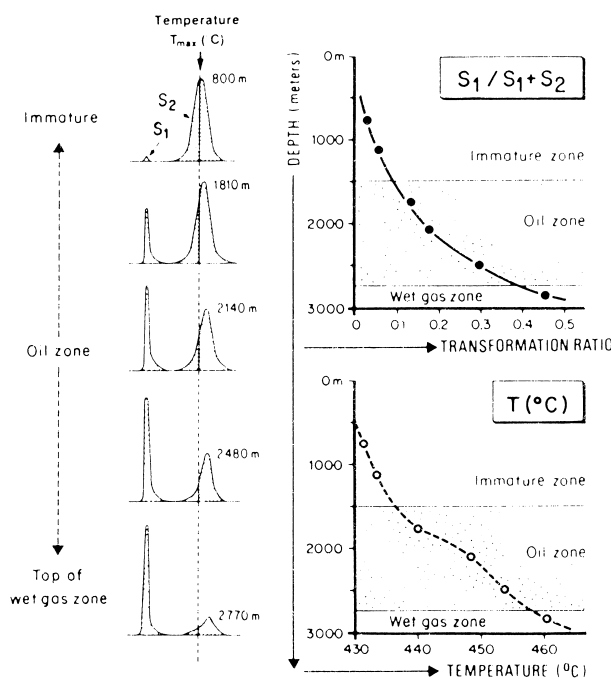


FIGURE 11 Characterization of source rocks by Rock-Eval pyrolysis. [Reprinted with permission from Tissot, B. P., and Welte, D. H. (1984). "Petroleum Formation and Occurrence," 2nd ed., p. 521, Springer-Verlag, Berlin and New York. Copyright 1984 Springer-Verlag.]

which is progressively heated to 550°C in a stream of helium. The hydrocarbon products released are monitored by combustion in a flame ionization detector. The first signal (S_1), observed at low temperature, corresponds to the volatile bitumen in the rock, whereas the second peak (S_2) in the pyrogram represents the compounds produced by thermal cleavage of the kerogen (Fig. 11, left). Separately, the carbon dioxide evolved from the kerogen during heating is also registered (not shown in Fig. 11). If S_2 and the carbon dioxide signal are normalized to the total organic carbon content of the sample, a hydrogen index and an oxygen index are obtained which are independent of the amount of organic matter in the sample and closely related to the elemental composition of the kerogen. They can be plotted in a van Krevelen-type diagram (Fig. 12). Like the H/C and O/C atomic ratios (cf. Fig. 5), which are more tedious to determine, the hydrogen and oxygen indices show the evolution pathways of different kerogen types. The quality of organic matter, i.e., the hydrocarbon potential of a source rock, is related directly to the value of the hydrogen index.

B. Maturity of Organic Matter

The thermal evolution of organic matter, a process called maturation, continuously changes the chemical

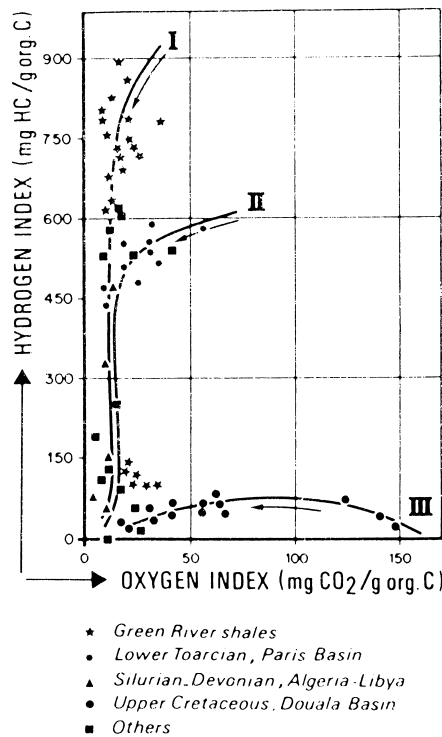


FIGURE 12 Classification of kerogen types by using hydrogen and oxygen indices from Rock-Eval pyrolysis. [Reprinted with permission from Tissot, B. P., and Welte, D. H. (1984). "Petroleum Formation and Occurrence," 2nd ed., p. 512, Springer-Verlag, Berlin and New York. Copyright 1984 Springer-Verlag.]

composition and the related physical properties. In petroleum exploration, it is important to know if a source rock has already entered the hydrocarbon generation zone or if it is above or below this zone. An immature sediment when analyzed for the quality of its organic matter will show the full hydrocarbon potential. A source rock within the generation zone will show only that potential which remained after the earlier release of hydrocarbons now present as bitumen or migrated out of the source rock. A sediment below the hydrocarbon generation zone will have a negligible residual hydrocarbon potential. To determine the thermal evolution stage of organic matter in sediments, a number of bulk and molecular parameters are available and are often used in combination with each other to account for the complexity of geochemical reactions and the time–temperature interrelationship.

1. Bulk Maturity Parameters

Rock-Eval pyrolysis in addition to information about the type of organic matter and its hydrocarbon potential also provides a sensitive measurement of the thermal history of a sediment. With increasing maturation the maximum

of the pyrolysis peak (S_2) is shifted to higher temperature values (T_{\max}) as shown in Fig. 11. At the same time, the relative proportion of the volatile material in the rock, represented by the S_1 peak, increases (Fig. 11). In most sediments there is a good correlation between the S_1 yield and the amount of extractable bitumen. The production index or transformation ratio [$S_1/(S_1 + S_2)$] is, however, affected by any hydrocarbons that have migrated out of or into the sediment, and it is recommended to study down-hole trends (Fig. 11) rather than using single measurements. The sum of S_1 and S_2 represents the total genetic potential of a rock minus the amount of hydrocarbons which have left the rock during primary migration.

Coal ranks are most satisfactorily determined by the measurement of vitrinite reflectance. This method, developed in coal petrography, has been extended to kerogen particles disseminated in sedimentary rocks in order to assess the maturity level of organic matter. From the correlation of vitrinite reflectance with hydrocarbon yields from the extraction of source rocks, but also with other maturity parameters, it has become common to define zones of hydrocarbon generation in terms of vitrinite reflectance (Table IV). The boundaries are approximate and vary with kerogen type, due to variations in the chemical composition of the respective organic matter. Another influence comes from the heating rate which the organic matter has experienced. This is due to the fact that the chemical reactions responsible for hydrocarbon generation from kerogen and for vitrinite reflectance increase have different kinetics and, thus, respond differently to temperature increase and time.

Excellent hydrocarbon source rocks often lack vitrinite particles because all their organic material consists of the remains of aquatic organisms. Also, early bitumen generation in these rocks may impregnate the few eventually present vitrinite particles, which leads to a vitrinite reflectance lower than corresponding to the actual maturation stage. In these cases, maturity assessment is made by measuring vitrinite reflectance in adjacent, less prolific rocks which contain more terrigenous organic matter or by chemical maturation parameters.

TABLE IV Approximate Boundaries for Hydrocarbon Generation Zones in Terms of Vitrinite Reflectance

Generation zone	Vitrinite reflectance for different kerogen types (%)		
	I	II	III
Onset of oil generation	0.7	0.5	0.7
Peak of oil generation	1.1	0.8	0.9
Beginning of gas zone	1.3	1.3	1.3
Dry gas zone	>2.0	>2.0	>2.0

2. Chemical Maturity Parameters

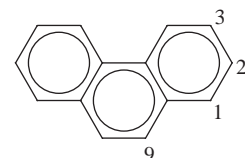
The chemical composition of bitumen is progressively changed by diagenetic and catagenetic reactions. A number of compound ratios, particularly in the hydrocarbon fractions, were found to vary systematically with increasing depth in a basin, and so these ratios can be used to measure the maturity of organic matter in a sediment. Only a few of them will be introduced here.

Because *n*-alkanes are usually the most abundant class of hydrocarbons in a sediment extract or a crude oil, much emphasis has been placed on the study of their relative compositional changes. The changes are most obvious when the sediment contains a certain amount of terrestrial higher plant material which contributes *n*-alkanes with a significant predominance of the odd carbon-number molecules that gradually disappears with increasing maturation. Several slightly differing mathematical expressions are being used to measure the maturity-dependent alteration of the *n*-alkane distribution. The most prominent among them is the carbon preference index (CPI), which uses a range of long-chain *n*-alkanes from C₂₄ to C₃₂:

$$\text{CPI} = \frac{1}{2}[(\text{C}_{25} + \text{C}_{27} + \dots + \text{C}_{31})/(\text{C}_{26} + \text{C}_{28} + \dots + \text{C}_{32}) + (\text{C}_{27} + \text{C}_{29} + \dots + \text{C}_{33})/(\text{C}_{26} + \text{C}_{28} + \dots + \text{C}_{32})] \quad (1)$$

The heights or the areas of the corresponding *n*-alkane peaks in the gas chromatograms of the saturated hydrocarbon fractions are taken to measure the ratio. The nature of the organic matter in a sediment will influence the carbon number preference, e.g., by the fact that many aquatic organisms do not synthesize long-chain *n*-alkanes, and if they do there is no predominance of either even or odd carbon numbers. Thus, in a sedimentary basin with varying organic matter supply the *n*-alkane patterns may change unsystematically and independent of the thermal evolution in closely spaced sediment layers. As a qualitative measure, however, the decrease of the carbon number predominance of *n*-alkanes has been applied successfully for maturity assessment in many cases.

More sophisticated analytical techniques are required to monitor the maturity-dependent changes of less abundant components among the hydrocarbons in the bitumen, but the specificity of the compounds and reactions studied justify these efforts. A group of compounds found to change their relative composition in a manner closely related to the increase of vitrinite reflectance through the oil generation zone and beyond are phenanthrene and the four isomeric methylphenanthrenes commonly found in sediments (**13**; numbers indicate the positions of methyl substitution).



13

With increasing depth, the relative abundances of 1- and 9-methylphenanthrene decrease and those of 2- and 3-methylphenanthrene increase due to the higher thermodynamic stability of the latter two isomers. A methylphenanthrene index (MPI) was introduced [Eq. (2); MP = methylphenanthrene, P = phenanthrene] and found to correlate positively with vitrinite reflectance at least in sediments which contain a major proportion of terrigenous organic matter:

$$\text{MPI} = 1.5[(2 - \text{MP}_3 - \text{MP}_9)/(\text{P} + 1 - \text{MP}_1 + 9 - \text{MP}_9)] \quad (2)$$

This is shown for a well in the Elmworth gas field in Western Canada in **Fig. 13**, where the measured vitrinite reflectance R_m was used to calibrate the vitrinite reflectance equivalent R_c calculated from the methylphenanthrene index:

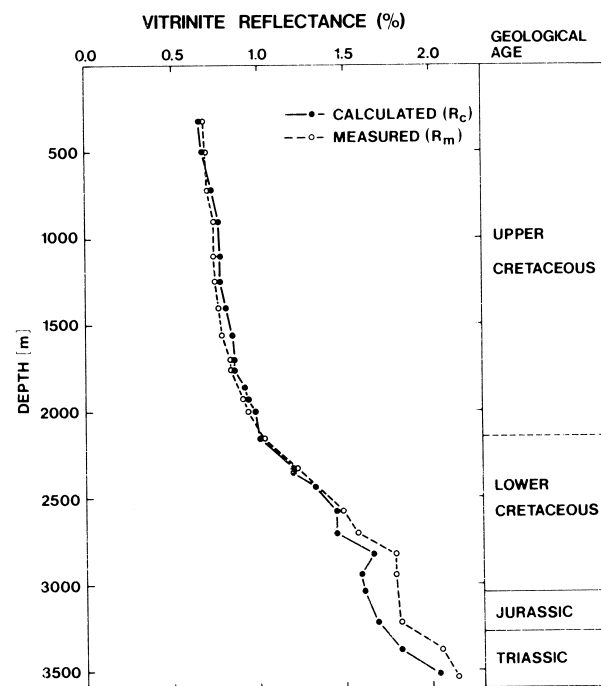


FIGURE 13 Calculated R_c and measured vitrinite reflectance R_m for selected rock samples from a well in the Elmworth gas field. [Reprinted with permission from Welte, D. H., Schaefer, R. G., Stoessinger, W., and Radke, M. (1984). *Mitteilungen des Geologisch-Paläontologischen Instituts der Universität Hamburg* **56**, 263–285. Copyright 1984 Universität Hamburg.]

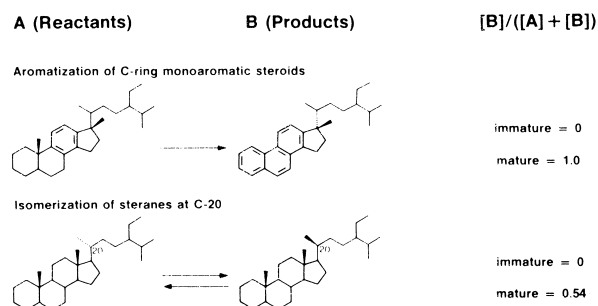


FIGURE 14 Examples of biological marker reactions used for maturity assessment of organic matter in sediments.

$$R_c = 0.60 \text{ MPI} + 0.40 \quad (3)$$

Biological marker compound ratios based on the product/reactant relationship in apparent diagenetic and cata-genetic reactions (like those illustrated in Fig. 6) are molecular maturation parameters widely applied today in petroleum geochemistry. Two of the most common examples are shown in Fig. 14. They monitor the extent of isomerization and aromatization of steroid hydrocarbons by measuring the relative concentrations of the reactants A and products B. In both cases, the initial concentration of the products is zero in immature sediments. The transformation of C-ring monoaromatic into triaromatic steroid hydrocarbons is irreversible and reaches completion within the hydrocarbon-generation zone. The isomerization of C₂₉ steranes at C-20 in the side chain is an equilibrium reaction where the natural 20R configuration inherited from the biosynthesized precursor steroids is converted to the 20S configuration. The equilibrium which is reached close to the peak of oil generation is slightly shifted to the right-hand side of the equation in Fig. 14. Both parameters are measured using peak areas (or heights) of characteristic mass spectral fragments in a combined gas chromatographic/mass spectrometric analysis.

More recently it was found, however, that the representation of biological marker reactions as in Fig. 14 is oversimplified. Although aromatization of monoaromatic steroid hydrocarbons to the triaromatic species may indeed occur as shown, the product/reactant ratio at the same time is influenced by the thermal destruction of both the reactant and the product. In fact, at high thermal stress, destruction of the triaromatic steroids is faster than that of the monoaromatic steroids, which leads to a reversal of the compound ratio trend at high maturities after having approached the predicted end value. Isomerization of steranes at C-20 appears not to happen at all in the way shown in Fig. 14. The empirically observed change in the ratio of the 20R and 20S sterane isomers with increasing thermal stress in sediments rather is the combined effect of the neoformation of mixtures of 20R and 20S steranes in the

course of thermal hydrocarbon generation from kerogen, which add to the (comparatively small amount of) 20R steranes formed diagenetically in the bitumen fraction as shown for compound 4 in Fig. 6, and the thermal destruction of both isomers at higher temperatures. The isomer ratio of the 20R and 20S sterane mixture newly formed from kerogen follows a temperature-dependent trend with a progressively increasing proportion of the 20S isomer up to the assumed equilibrium ratio also theoretically predicted by molecular mechanics calculation. The reaction rate of thermal destruction is, however, slightly faster for the 20S isomer, so again a reversal of the compound ratio trend is observed at higher maturities. If this behavior is kept in mind, biological marker compound ratios can still be applied successfully in petroleum geochemistry, although some ambiguity may occasionally arise.

C. Oil/Source Rock Correlation

The main objective of oil/oil and oil/source rock correlation is to find out the genetic origin of reservoir hydrocarbons. In a first step, usually a correlation analysis among the various oils (or condensates, gases) from different reservoirs in a producing basin is performed to see if all the oils are uniform in their composition or if they belong to several families of different genetic origin. For each type or family of oils it has to be established if they are derived from a single source rock or if a multiple origin must be considered. The composition of the crude oils will provide some basic information on the characteristics of the organic matter and on the lithology in the source rock(s) as well as on the maturity of the organic matter in the source rock(s) at the time of hydrocarbon generation. Compositional variations due to different maturities must be distinguished from those due to different sources. In a second step, a source must be identified for each oil family by comparison with samples of all possible source rocks. If the conclusion is reached that more than one source characteristic can be attributed to different oil families accumulated in a basin, organofacies variations within a single source rock layer may be the explanation, as well as two or more source rock layers of different age.

If the source(s) of crude oil in a basin are known, this can have important implications for exploration and production strategies. The information will help to define exploration targets and will influence the development of a concept for the stepwise exploration of a sedimentary basin. A mass balance calculation based on volume and thermal maturity of the known hydrocarbon source rocks and a comparison with the already-detected oil in place will help to determine if further exploration is promising. In crude oil production, oil/oil correlations can provide information about the possible communication between different productive zones.

Oil/source rock correlation is based on the concept that oil (condensate or gas) found in a reservoir was generated from kerogen disseminated in a source rock. During expulsion, only a certain proportion of the generated petroleum compounds was released and a significant proportion stayed behind. A correlation thus should be possible between the kerogen in the source rock, the bitumen extractable from the source rock, and the hydrocarbons in the reservoirs. In order to account for the complex chemical and physical processes involved in the generation, migration, and accumulation of hydrocarbons in the subsurface, as many correlation parameters as possible should be used in any correlation study, and both bulk and compositional (molecular) correlation parameters should be considered.

A number of useful correlation parameters for different types of geochemical correlation studies are compiled in **Table V**. The only bulk parameters included are carbon, hydrogen, and sulfur isotope measurements on whole samples or fractions thereof. Other bulk parameters, such as the API gravity and the distribution of distillation fractions (both for oil/oil correlation), are susceptible to severe alteration during migration and to secondary processes in the reservoir. They should nevertheless not be neglected completely, and any differences observed should be explicable in terms of the geological context of the study area.

TABLE V Correlation Parameters Useful for Different Kinds of Correlation Studies^a

Type of correlation	Correlation parameter
Gas/gas	Carbon and hydrogen isotopes ($^{13}\text{C}/^{12}\text{C}$, $^2\text{H}/^1\text{H}$)
	Ratios of light hydrocarbons (C ₂ –C ₈)
Gas/oil	Carbon and hydrogen isotopes of single <i>n</i> -alkanes
	Ratios of light hydrocarbons (C ₂ –C ₈)
Oil/oil	Carbon, hydrogen and sulfur isotopes ($^{13}\text{C}/^{12}\text{C}$, $^2\text{H}/^1\text{H}$, $^{34}\text{S}/^{32}\text{S}$)
	Ratios of specific hydrocarbons (e.g., pristane/phytane, pristane/ <i>n</i> -C ₁₇)
	Homologous series (e.g., <i>n</i> -alkane distribution)
	Biological markers (e.g., steranes, triterpanes, aromatic steroid hydrocarbons, porphyrins)
	Carbon and hydrogen isotopes
Gas/source rock kerogen	Carbon and hydrogen isotopes
Oil/source rock bitumen	Oil/oil correlation parameters
Oil/source rock kerogen	Carbon and sulfur isotopes
	Oil/oil correlation parameters applied to the products of kerogen pyrolysis

^a After Tissot, B. P., and Welte, D. H. (1984). "Petroleum Formation and Occurrence," 2nd ed., p. 548, Springer-Verlag, Berlin and New York.

Compositional correlation parameters should have characteristic compound distributions in both rocks and oils. They should be available over the proper molecular weight range (e.g., for gas/oil correlation) and possibly be present in compound classes of different polarities. They should not be too seriously affected by migration, thermal maturation, and bacterial alteration; i.e., under the given geological conditions the imprint of the source organic matter should be transferred into the hydrocarbon reservoir.

Biological markers offer one of the best correlation tools, first of all due to the high information content in their molecular structures. The characteristic distribution patterns of biological markers in crude oils often can be taken as "fingerprints" of the various organisms that contributed to the source rock. Biological markers have a narrow range of chemical and physical properties, particularly when they occur in the saturated hydrocarbon fractions. Thus, any fractionation occurring, e.g., during migration is likely to affect the whole group of biological markers and not any specific compound preferentially. In addition, biological markers are easily detected in very small concentration by the combination of computerized gas chromatography/mass spectrometry. The presence or absence of unusual biological markers in a crude oil or source rock bitumen is often highly significant, whereas other biological markers such as hopanes inherited from bacteria are ubiquitous in all geological samples and thus less specific. Many biological markers are not easily degraded in the course of microbial attack to reservoir hydrocarbons; i.e., they survive mild or even moderately severe biodegradation. The maturity effect on a great number of biological markers is known, and thus corrections and extrapolations to account for additional thermal stress are possible. There are a few disadvantages to the use of biological markers for oil/oil and oil/source rock correlation. These include the limited thermal stability of these compounds, i.e., their application is often restricted to the generation zone below the peak of oil generation. In addition, the low concentrations of the biological markers are sensitive to mixing effects in the subsurface and to contamination.

D. Experimental Simulation of Petroleum Formation

Studying the processes of petroleum formation by field observations is hampered by the fact that these processes occur in nature over periods of geological time and in an open system. Thus, many attempts were made in the past to simulate hydrocarbon generation in a well-defined confined system in the laboratory using elevated temperatures as a compensation for geological time. Hydrous pyrolysis

has turned out to be the method which appears to mimic the natural processes most closely.

In this experiment, pieces of organic matter-rich rock are heated in an autoclave in the presence of water at temperatures between about 300°C and near the critical-point temperature of water (374°C) for periods of, typically, 3 days or longer. The products are an expelled oil-type phase floating on the water and a bitumen fraction retained in the rock chips. Figure 15 summarizes the variations in the amounts of kerogen, bitumen, and expelled oils for a series of experiments at different temperatures using a sample of Woodford Shale, a Devonian-Carboniferous source rock from Oklahoma, as substrate. Physically, chemically, and isotopically, the expelled oil is similar to natural crude oils. Hydrous pyrolysis experiments in this way have not only provided useful information on the bulk processes of petroleum formation, but also on their kinetics, on thermal maturity indices, and on primary migration.

E. Modelling of Geological and Geochemical Processes

The successful application of the principles of hydrocarbon generation and migration to petroleum exploration and the increasing knowledge about the chemical and

physical parameters that determine the fate of organic matter in the subsurface have stimulated efforts in developing a more quantitative handling of the related geological and geochemical processes. A comprehensive quantitative approach in terms of a mathematical model would allow a more precise prediction of the quantities of hydrocarbons generated in a sedimentary basin and a better understanding of the timing of any event in the course of hydrocarbon generation, migration, and accumulation.

The first step in this direction was the calculation of the maturity of organic matter in a specific sediment based on reconstruction of the burial history and the knowledge (or assumption) of depth-dependent temperature variations in the basin. The basic concept was that generation of hydrocarbons follows simple first-order reaction kinetics, i.e., the reaction rate approximately doubles during each 10°C increase of temperature. The burial history curve, constructed using geological information, defines the time a sediment in the geological past spent within a certain depth (or temperature) interval. If the temperature factors for each 10°C temperature interval, increasing by exponentials of 2 in each step, are multiplied with the time (in millions of years) a time-temperature index (TTI) is obtained for each temperature interval. A summation of these index values provides a TTI value representing the total

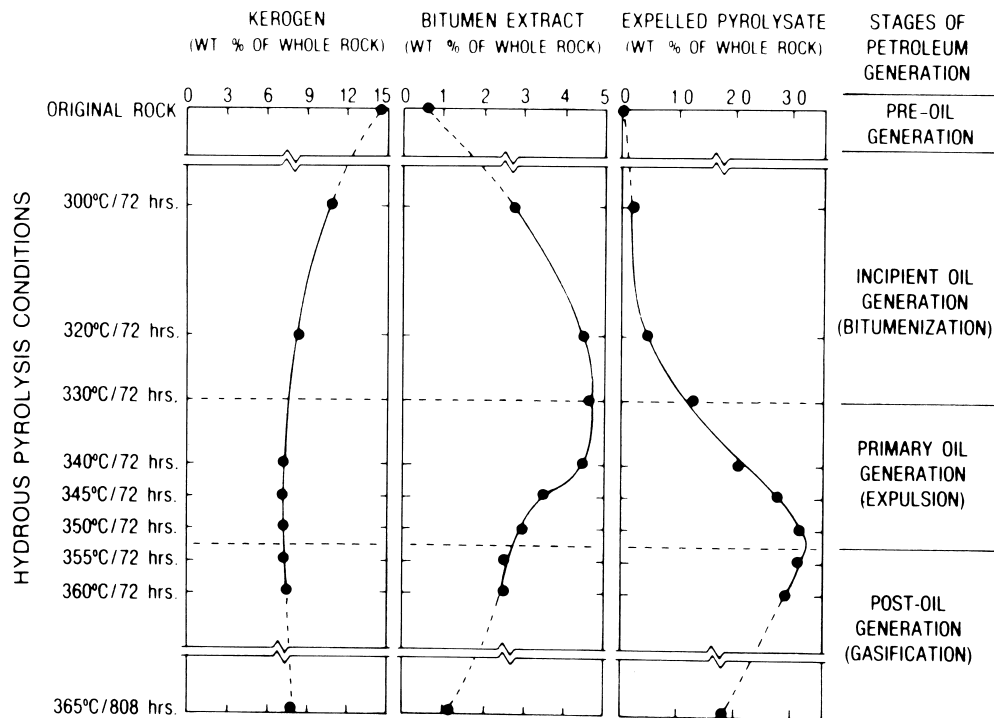


FIGURE 15 Variations in the amounts of kerogen, bitumen, and expelled oil (pyrolyzate) in series of hydrous pyrolysis experiments using Woodford Shale. [Reprinted with permission from M. D. Lewan (1983). *Geochim. Cosmochim. Acta* **47**, 1471–1479. Copyright 1983 Pergamon Press, Oxford.]

thermal evolution of the sediment. The TTI values must be calibrated against vitrinite reflectance (or hydrocarbon yields) to be a predictive, albeit simple, tool.

A considerably more sophisticated numerical treatment of hydrocarbon generation and migration starts with the three-dimensional determination of the development of a sedimentary basin using a deterministic model. Starting at a time T_0 when only the basement existed, sedimentation is followed by the model in predetermined time intervals until the present status (T_x) is reached (Fig. 16). The model continuously calculates the depth-related changes in such parameters as pressure, porosity, temperature, and thermal conductivity for each sediment layer. Mathematical equations control that a mass balance (e.g., sediment supply and water leaving the system) as well as an energy balance (e.g., heat flow from basement and energy loss to the atmosphere or as heated water) are maintained. The results of the model are compared to the real system (well and surface information), and the model approaches the real system by a series of iteration steps. As soon as the geological model is sufficiently accurate, organic matter maturity, hydrocarbon generation yields, and migration directions can be determined for each sediment layer in the basin and for each time slice in the past (Fig. 17). For this latter step a simple maturation calculation like that of the TTI values can be used. A more detailed maturation and hydrocarbon generation model will use ranges of activation energies for the different bond types in a kerogen and for different kerogen types. It will also take into account the fact that the reaction conditions will change with increasing maturation of the organic matter.

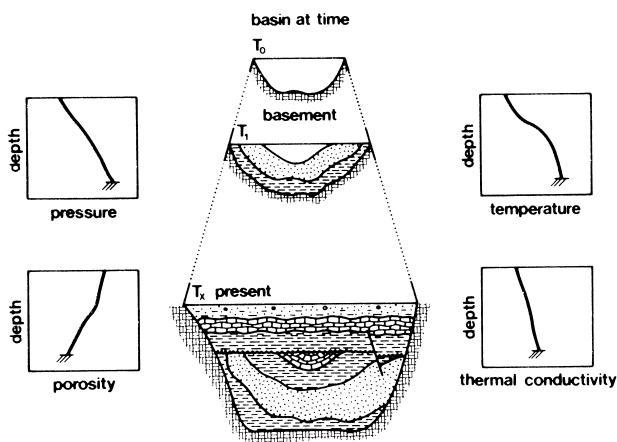


FIGURE 16 Evolution of a sedimentary basin from an initial condition at time T_0 to the present configuration at time T_x with schematic depth-related changes of physical parameters such as pressure, porosity, temperature, and thermal conductivity. [Reprinted with permission from Tissot, B. P., and Welte, D. H. (1984). “Petroleum Formation and Occurrence,” 2nd ed., p. 576, Springer-Verlag, Berlin and New York. Copyright 1984 Springer-Verlag.]

V. ORGANIC GEOCHEMICAL TECHNIQUES IN PALEOENVIRONMENTAL AND PALEOClimATIC ASSESSMENT

While organic geochemistry in petroleum exploration focuses mainly on deeply buried sedimentary rocks, shallow sediments play an important role in understanding the global organic carbon cycle and in reconstructing past climatic and oceanographic developments. Since the mid-1970s, the international Deep Sea Drilling Project and later the Ocean Drilling Program have provided the numerous sediment cores necessary to perform such studies. In the following, a few selected approaches and techniques are outlined to illustrate how organic geochemistry contributes to these interdisciplinary objectives.

A. Marine versus Terrigenous Organic Matter

Even deep-sea sediments deposited in areas remote from continents usually contain a mixture of marine and terrigenous organic matter. For any investigation of marine paleoproductivity or marine organic matter preservation, the amount of terrigenous admixture has to be known. Furthermore, global or regional climate fluctuations have changed the pattern of continental runoff and ocean currents in the geological past. Being able to recognize variations in marine and terrigenous organic matter proportions, thus, is of great significance in paleoclimatic and paleoceanographic studies.

A variety of parameters are used to assess organic matter sources. Bulk parameters have the advantage that they are representative of the total organic matter, whereas molecular parameters address only part of the extractable organic matter, which in turn is only a small portion of total organic matter. Several successful applications of molecular parameters have shown that the small bitumen fraction may be representative of the total, but there are some examples for which this is not the case. On the other hand, oxidation of marine organic matter has the same effect on some bulk parameters as an admixture of terrigenous organic matter, because the latter is commonly enriched in oxygen through biosynthesis. It is, therefore, advisable to rely on more than one parameter, and to obtain complementary information.

1. C/N Ratio

Atomic carbon/nitrogen (C/N) ratios of living phytoplankton and zooplankton are around 6, freshly deposited marine organic matter ranges around 10, whereas terrigenous organic matter has C/N ratios of 20 and above. This difference can be ascribed to the absence of cellulose in algae and its abundance in vascular plants and to the fact that algae are rich in proteins.

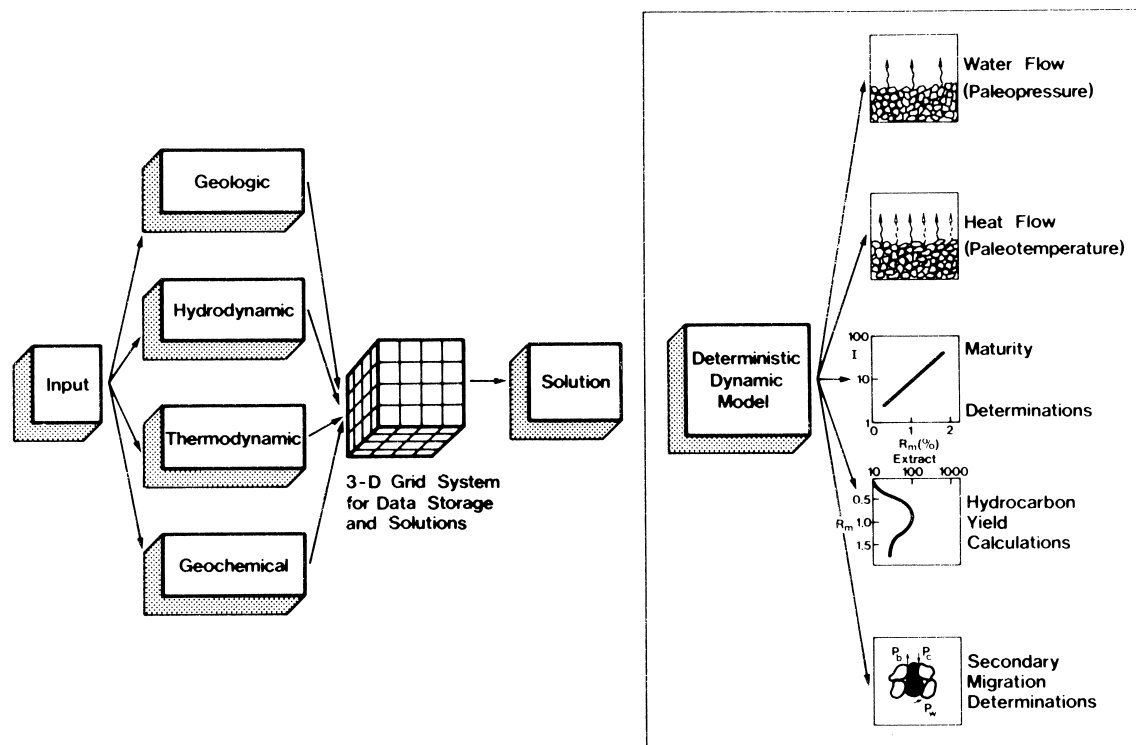


FIGURE 17 Development of a three-dimensional dynamic model. Groups of input parameters and results are schematically shown. [Reprinted with permission from Tissot, B. P., and Welte, D. H. (1984). "Petroleum Formation and Occurrence," 2nd ed., p. 578, Springer-Verlag, Berlin and New York. Copyright 1984 Springer-Verlag.]

Selective degradation of organic matter components during early diagenesis has the tendency to modify (usually increase) C/N ratios. Still, they are commonly sufficiently well preserved in shallow marine sediments to allow a rough assessment of terrigenous organic matter contribution. Care has to be taken in oceanic sediments with low organic carbon contents, because inorganic nitrogen (ammonia) released during organic matter decomposition may be adsorbed to the mineral matrix and add significantly to the amount of total nitrogen. The C/N ratio is then changed to values lower than those of the real marine/terrigenous organic matter proportions. This effect should be small in sediments containing more than 0.3% organic carbon.

2. Hydrogen and Oxygen Indices

Hydrogen indices from Rock-Eval pyrolysis (see Sect. IV.A) below about 150 mg hydrocarbons (HC)/g total organic carbon (TOC) are typical of terrigenous organic matter, whereas HI values of 300–800 mg HC/g TOC are typical of marine organic matter. Oceanic sediments rich in organic matter sometimes exhibit values of only 200–400 mg HC/g TOC, even if marine organic matter strongly dominates. Oxidation during settling through a long water

column in these cases has lowered the hydrogen content of the organic matter. Rock-Eval pyrolysis cannot be used for sediments with TOC < 0.3%, because of the so-called mineral matrix effect. If sediments with low organic carbon contents are pyrolyzed, a significant amount of the products may be adsorbed to the sediment minerals and are not recorded by the detector, thus lowering the hydrogen index.

3. Maceral Composition

If the morphological structures of organic particles in sediments are well preserved, organic petrographic investigation under the microscope is probably the most informative method to distinguish marine from terrestrial organic matter contributions to marine sediments by the relative amounts of macerals derived from marine biomass and land plants (see Sect. II.E.1). Many marine sediments, however, contain an abundance of unstructured organic matter which cannot easily be assigned to one source or the other.

4. Stable Carbon Isotope Ratios

Carbon isotope ratios are useful principally to distinguish between marine and terrestrial organic matter sources in

sediments and to identify organic matter from different types of land plants. The stable carbon isotopic composition of organic matter reflects the isotopic composition of the carbon source as well as the discrimination (fractionation) between ^{12}C and ^{13}C during photosynthesis. Most plants, including phytoplankton, incorporate carbon into their biomass using the Calvin (C_3) pathway, which discriminates against ^{13}C to produce a shift in $\delta^{13}\text{C}$ values of about $-20\text{\textperthousand}$ from the isotope ratio of the inorganic carbon source. Organic matter produced from atmospheric carbon dioxide ($\delta^{13}\text{C} \approx -7\text{\textperthousand}$) by land plants using the C_3 pathway (including almost all trees and most shrubs) has an average $\delta^{13}\text{C}$ value of approximately $-27\text{\textperthousand}$. Marine algae use dissolved bicarbonate, which has a $\delta^{13}\text{C}$ value of approximately 0\textperthousand . As a consequence, marine organic matter typically has $\delta^{13}\text{C}$ values varying between $-18\text{\textperthousand}$ and $-22\text{\textperthousand}$.

The “typical” difference of about 7\textperthousand between organic matter of marine primary producers and land plants has been used successfully to trace the sources and distributions of organic matter in coastal sediments. Unlike C/N ratios, $\delta^{13}\text{C}$ values are not significantly influenced by sediment texture, making them useful in reconstructing past sources of organic matter in changing depositional conditions. Figure 18 shows the fluctuations of organic matter $\delta^{13}\text{C}$ values in a short sediment core from a tidal flat caused by a variable admixture of eroded peat ($\delta^{13}\text{C} = -27\text{\textperthousand}$) to marine organic matter mainly from di-

atoms ($\delta^{13}\text{C} = -19\text{\textperthousand}$). If the carbon isotope values of the end members in a two-component system are known, the relative contributions can be easily determined by a simple linear mixing algorithm.

The availability of dissolved CO_2 in ocean water has an influence on the carbon isotopic composition of algal organic matter because isotopic discrimination toward ^{12}C increases when the partial pressure of carbon dioxide ($p\text{CO}_2$) is high and decreases when it is low. Organic matter $\delta^{13}\text{C}$ values, therefore, become indicators not only of the origin of organic matter but also of changing paleoenvironmental conditions on both short- and long-term scales. For example, the $\delta^{13}\text{C}$ values of dissolved inorganic carbon (DIC; i.e., CO_2 , bicarbonate, and carbonate) available for photosynthesis varies over the year with the balance between photosynthetic uptake and respiratory production. During spring and summer, when rates of photosynthesis are high, the isotope ratio of the remaining DIC is enriched in ^{13}C . In fall, when respiration is the dominant process, the $\delta^{13}\text{C}$ of DIC becomes more negative because organic matter is remineralized.

Fluctuations in the $\delta^{13}\text{C}$ values of sedimentary organic matter over the earth’s history can, thus, be interpreted in terms of the productivity in the water column and the availability of DIC in a particular geological time period. In a study of sediments from the central equatorial Pacific Ocean spanning the last 255,000 years, it has been demonstrated that the carbon isotopic composition

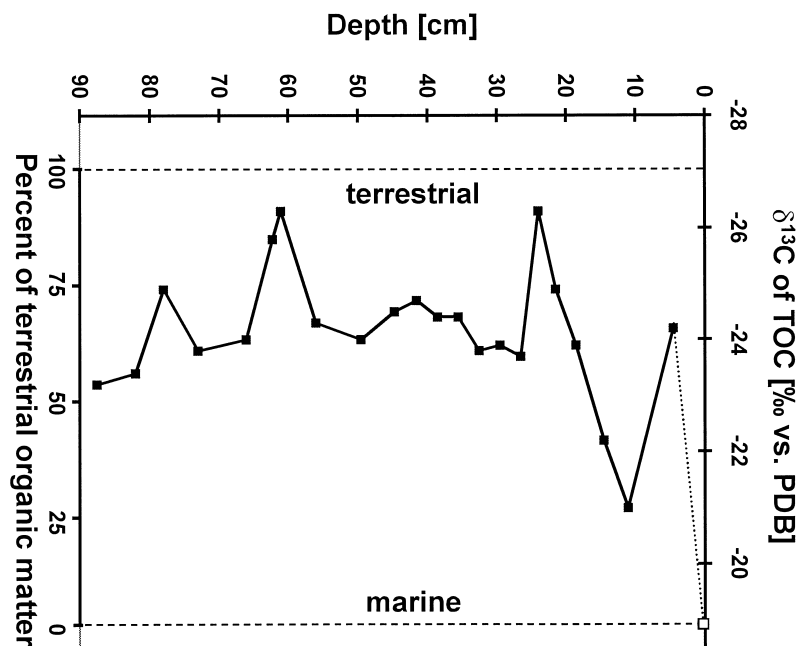


FIGURE 18 Variation of bulk $\delta^{13}\text{C}$ values of organic matter in a sediment core from a tidal flat in northern Germany. The variation is due to a variable mixture of marine organic matter ($\delta^{13}\text{C} = -19\text{\textperthousand}$) and of locally eroded peat (terrogenous organic matter; $\delta^{13}\text{C} = -27\text{\textperthousand}$). The relative percentages are calculated using a linear mixing algorithm.

of fossil organic matter depends on the exchange between atmospheric and oceanic CO₂. Changes with time can then be used to estimate past atmospheric carbon dioxide concentrations.

A new type of geochemical information became available with the development of a combined capillary column gas chromatography–isotope ratio mass spectrometry system. This instrument provides the carbon isotope signal (¹³C/¹²C) of single biological marker compounds in complex mixtures. The resulting data allows assignment of a specific origin to some of these compounds because, for example, the biomass of planktonic algae has a carbon isotope signal completely different from that of land plants or methanotrophic bacteria, due to the different carbon isotope ratios of the carbon sources used by these groups of organisms. This adds another dimension to the understanding of geochemical reaction pathways. The main advantage of the new technique is that a great number of compounds can be analyzed directly within a short time in small quantities and without the need of their tedious isolation.

B. Molecular Paleo-Seawater Temperature and Climate Indicators

1. Past Sea-Surface Temperatures (SST) Based on Long-Chain Alkenones

Palaeoceanographic studies have taken advantage of the fact that biosynthesis of a major family of organic compounds by certain microalgae depends on the water temperature during growth. The microalgae belong to the class of Haptophyceae (often also named Prymnesiophyceae) and notably comprise the marine coccolithophorids *Emiliania huxleyi* and *Gephyrocapsa oceanica*. The whole family of compounds, which are found in marine sediments of Recent to mid-Cretaceous age throughout the world ocean, is a complex assemblage of aliphatic straight-chain ketones and esters with 37 to 39 carbon atoms and two to four double bonds, but principally only the C₃₇ methylketones with two and three double bonds (14) are used for past sea-surface temperature assessment.

It was found from the analysis of laboratory cultures and field samples that the extent of unsaturation (number of double bonds) in these long-chain ketones varies linearly with growth temperature of the algae over a wide temperature range. To describe this, an unsaturation index ($U_{37}^{K'}$) was suggested, which is defined by the concentration ratio of the two C₃₇ ketones:

$$U_{37}^{K'} = [\text{C}_{37:2}] / [\text{C}_{37:2} + \text{C}_{37:3}]. \quad (4)$$

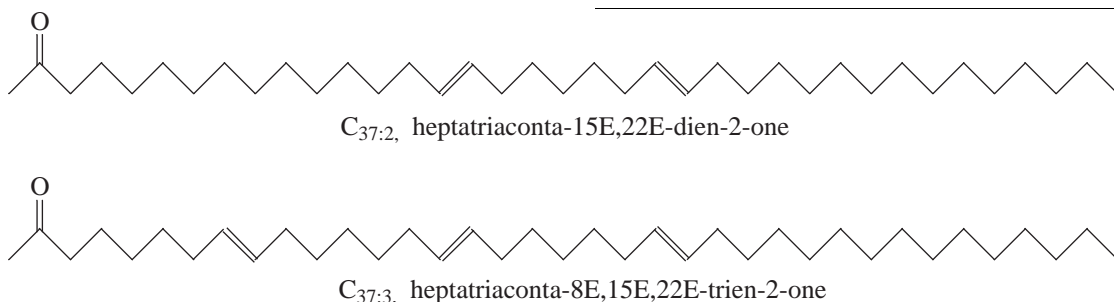
Calibration was then made with the growth temperatures of laboratory cultures of different haptophyte species and with ocean water temperatures at which plankton samples had been collected. From these data sets, a uniform calibration for the global ocean from 60°N to 60°S evolved and can be used to estimate the ocean surface temperatures in the geological past:

$$U_{37}^{K'} = 0.033T + 0.043, \quad (5)$$

where T is the temperature of the oceanic surface water (SST) in degrees Celsius. The example in Fig. 19 shows pronounced SST variations between the different oxygen isotope stages (OIS) which represent cold (even numbers) and warm periods (odd number). The last glacial maximum (18,000 yr B.P.), for example, falls into OIS 2, the present interglacial (Holocene) is equivalent to OIS 1, and the last climate optimum (Eemian, 125,000 yr B.P.) occurred early in OIS 5.

2. ACL Index Based on Land Plant Wax Alkanes

In marine sediments, higher-plant organic matter can be an indicator of climate variations, both by the total amount indicating enhanced continental runoff during times of low sea level or of humid climate on the continent and by specific marker compounds indicating a change in terrestrial vegetation as a consequence of regional or global climatic variations. Long-chain *n*-alkanes are commonly used as the most stable and significant biological markers of terrigenous organic matter supply. The odd-carbon-numbered C₂₇, C₂₉, C₃₁, and C₃₃ *n*-alkanes, major



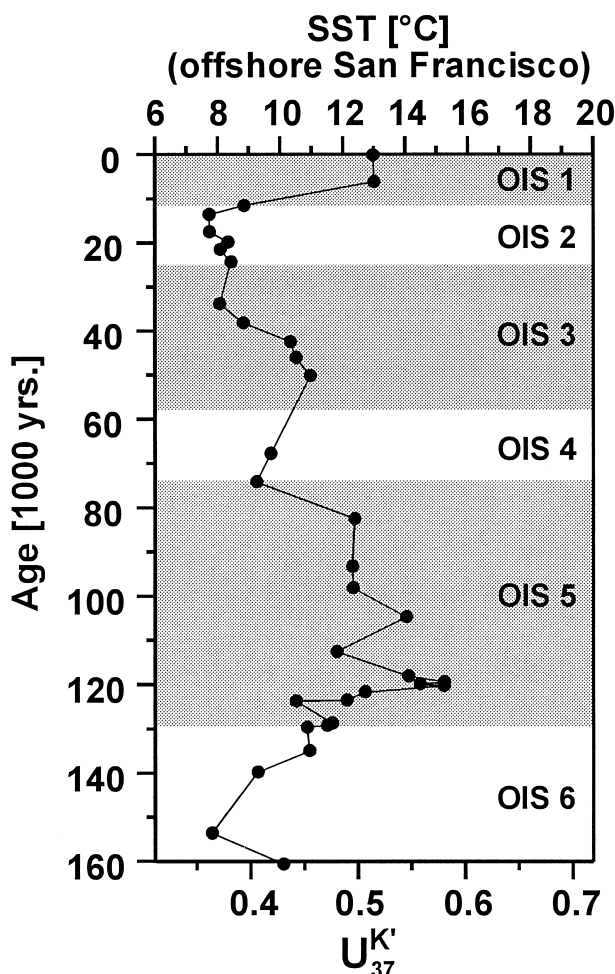


FIGURE 19 Changes of paleosea surface temperatures (SST) on the California continental margin during the last 160,000 years estimated from the relative proportions of di- and triunsaturated long-chain ketones extracted from deep-sea sediments recovered by the Ocean Drilling Program.

components of the epicuticular waxes of higher plants, are often preferentially enriched in the marine environment.

The carbon-number distribution patterns of *n*-alkanes in leaf waxes of higher land plants depend on the climate under which they grow. The distributions show a trend of increasing chain length nearer to the Equator, but they are also influenced by humidity. Based on these observations, an average chain length (ACL) index was defined to describe the chain length variations of *n*-alkanes:

$$\text{ACL}_{27-33} = (27[\text{C}_{27}] + 29[\text{C}_{29}] + 31[\text{C}_{31}] + 33[\text{C}_{33}]) / ([\text{C}_{27}] + [\text{C}_{29}] + [\text{C}_{31}] + [\text{C}_{33}]), \quad (6)$$

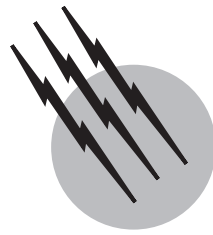
in which $[\text{C}_x]$ signifies the concentration of the *n*-alkane with x carbon atoms. Sedimentary *n*-alkane ACL values were demonstrated to be sensitive to past climatic changes. In Santa Barbara basin (offshore California) sediments from the last 160,000 years, the highest ACL values were found in the Eemian climate optimum (125,000 yr B.P.). The ACL variations recorded the climatic changes on the continent, because vegetation patterns on the continent responded rapidly to climatic oscillations, which were often characterized by drastic changes of temperature and precipitation. In addition, changes in continental precipitation significantly affected the degree of erosion and the transport of terrigenous detritus to the ocean.

SEE ALSO THE FOLLOWING ARTICLES

BIOMASS UTILIZATION, LIMITS OF • BIOPOLYMERS • CARBOHYDRATES • CARBON CYCLE • COAL GEOLOGY • COAL STRUCTURE AND REACTIVITY • ENVIRONMENTAL GEOCHEMISTRY • GEOCHEMISTRY • GEOCHEMISTRY, LOW-TEMPERATURE • PETROLEUM GEOLOGY • SEDIMENTARY PETROLOGY

BIBLIOGRAPHY

- Engel, M. H., and Macko, S. A., eds. (1993). "Organic Geochemistry—Principles and Applications," Plenum Press, New York and London.
- Hunt, J. M. (1995). "Petroleum Geochemistry and Geology," 2nd ed., Freeman, San Francisco.
- Johns, R. B., ed. (1986). "Biological Markers in the Sedimentary Record," Elsevier, Amsterdam.
- Peters, K. E., and Moldowan, J. M. (1993). "The Biomarker Guide—Interpreting Molecular Fossils in Petroleum and Ancient Sediments," Prentice-Hall, Englewood Cliffs, NJ.
- Schulz, H. D., and Zabel, M., eds. (1999). "Marine Geochemistry," Springer-Verlag, Heidelberg.
- Taylor, G. H., Teichmüller, M., Davis, A., *et al.* (1998). "Organic Petrology," Gebrüder Borntraeger, Stuttgart.
- Tissot, B. P., and Welte, D. H. (1984). "Petroleum Formation and Occurrence," 2nd ed., Springer-Verlag, Heidelberg.
- Welte, D. H., Horsfield, B., and Baker, D. H. eds. (1997). "Petroleum and Basin Evolution," Springer-Verlag, Heidelberg.



Glaciology

W. S. B. Paterson

Paterson Geophysics Inc.

- I. Introduction
- II. Features of Existing Glaciers
- III. Formation and Deformation of Glacier Ice
- IV. Glacier Flow by Ice Deformation
- V. Flow of Ice Shelves
- VI. Basal Motion and Water Flow at the Bed
- VII. Temperatures in Glaciers
- VIII. Ice Stream Flow
- IX. Growth and Decay of Glaciers
- X. Unstable Flow
- XI. Ice Core Analysis

GLOSSARY

Ablation All processes that reduce the mass of a glacier: melting followed by runoff, iceberg calving, sublimation, and snow removal by wind. Related terms are annual ablation rate and ablation area, which is the part of the glacier where there is a net loss of mass during the year.

Accumulation All processes that increase the mass of a glacier: snowfall (predominant), avalanches, rime formation, and freezing of rain in the snowpack. Related terms are annual accumulation rate and accumulation area, which is the part of the glacier where there is a net gain in mass during the year.

Calving Process of iceberg formation: ice breaks off the end of a glacier tongue into the sea or a lake.

Crevasse Large crack in the glacier surface formed by tension or shear. Depths of 20–30 m are typical.

Equilibrium line Boundary between the accumulation and ablation areas at the end of summer. Its position varies from year to year according to weather conditions.

Firn Strictly, wetted snow that has survived one summer without being transformed to ice; commonly used, as here, to mean material in the process of transformation from freshly fallen snow to glacier ice.

Grounding line Boundary between grounded and floating parts of a glacier that ends in water.

Ice cap Mass of ice that flows outward in several directions and submerges most or all of the underlying land.

Ice rise Area of grounded ice in a floating ice shelf.

Ice sheet Ice cap the size of Greenland, Antarctica, or the ice-age ice masses. A marine ice sheet is one in which most of the base is grounded below sea level.

Ice shelf Large, thick slab of ice floating on the sea but attached to land or to a grounded ice sheet. It is nearly

always nourished by both snowfall and flow from the ice sheet and sometimes also by freezing on of water at its base.

Ice stream Region in an ice sheet in which the ice flows much faster than that on either side. Ice streams often have no visible rock boundaries.

Icefall Steep, fast-flowing section of a glacier where the surface is broken up into an array of crevasses and ice pinnacles (seracs).

Mass balance Difference between annual accumulation and ablation. The term can be applied either to a whole glacier or to a point on its surface.

Temperate glacier Glacier in which all the ice is at its melting temperature, except for a surface layer, about 15 m thick, that is subject to seasonal variations in temperature. Glaciers that are not temperate are often referred to as cold, or else are called subpolar or polar according to whether or not there is surface melting in summer.

GLACIOLOGY, in the strict sense, is the study of ice in all its forms. The term is often also applied, as in this article, to the more restricted field of the study of glaciers. A glacier is a large mass of perennial ice that originates on land by the compaction and recrystallization of snow and shows evidence of past or present flow. Glaciers may be divided into three main classes: (1) ice sheets and ice caps; (2) glaciers whose paths are confined by the surrounding bedrock, called mountain or valley glaciers according to their location or piedmont glaciers where valley glaciers spread out over a coastal plain; and (3) floating ice shelves. These types frequently occur in combination; an ice cap may be drained by valley glaciers, for example.

The amount of snow falling on the surface of the higher part of a glacier each year exceeds that lost by melting and evaporation. At lower elevations, all the previous winter's snow and some glacier ice are removed by summer melting and runoff. Calving of icebergs may also result in significant loss of mass. The profile of the glacier does not change much from year to year, however, because ice flows under gravity from the accumulation area to the ablation area (Fig. 1).

I. INTRODUCTION

Glacier studies are an active research field at present for several reasons. The past 2.5 million years (Myr) have been characterized by the repeated growth and decay of continental ice sheets. At glacial maxima, ice covered almost all of Canada, the northern part of the United States,



FIGURE 1 Unnamed glaciers, Babine area, Coast Mountains, British Columbia. Lateral moraines show their recent maximum extent. The steep crevassed terminus of the right-hand glacier suggests that it may be advancing. [Photograph by Austin Post, U.S. Geological Survey.]

much of Europe, and parts of eastern Siberia. The resulting reduction in volume of the oceans caused world sea levels to fall by roughly 100 m. Ice ages alternated with interglacials, during which the extent of ice was comparable with, and sometimes less than, that of today. Switching of the climate between these states, with a regular period of roughly 100,000 years, is related to changes in the earth's orbit. Once formed, an ice sheet tends to maintain itself because of its high elevation and because a snow-covered surface reflects up to 90% of incoming solar radiation. Any explanation of ice ages must take into account both the dynamics of the ice sheet itself and its interactions with the atmosphere and ocean, topics that can best be studied on existing ice sheets.

Glaciers and ice sheets produce major changes in the landscape. Raised beaches in areas once covered by ice are evidence of the slow rise of the land after the weight of the ice was removed, a process that is still continuing in regions such as Hudson Bay and the Baltic. Most of the Canadian prairies are covered by material carried by the ice sheet, in some cases for hundreds of kilometers, and left behind when it melted. Erosion by glaciers produces the U-shaped valleys, narrow ridges, and Matterhorn-like

peaks characteristic of mountain areas. The mechanisms of erosion, transportation, and deposition can best be studied by looking at existing glaciers. An understanding of these processes is essential for the interpretation of ice-age deposits.

Recent theoretical studies have shown that glaciers possess potential sources of instability. It has been suggested that the ice sheet in West Antarctica (the part lying south of the Pacific Ocean) may be unstable and that atmospheric warming, brought on by increased consumption of fossil fuels, may trigger its complete collapse. This would raise world sea level by about 6 m, submerging the world's ports and the greater part of low-lying countries such as Holland. Assessment of the present state of the West Antarctic Ice Sheet and prediction of its future behavior is a major topic of current research.

A form of instability known to occur in some glaciers and at least two ice caps is the surge or catastrophic advance. Surges in the same glacier happen at regular intervals. Unrelated to climate, they result from some instability at the glacier bed. Moreover, the sediment in the North Atlantic contains evidence of periodic massive discharges of icebergs from the Hudson Bay sector of the Laurentide Ice Sheet during the last ice age. These so-called Heinrich events had a major effect on ocean circulation and climate. The mechanisms of these instabilities is another active branch of research.

In addition to the major growth and decay that mark the beginning and end of an ice age, glaciers also advance and retreat in response to minor changes in climate. However, the relationship is more complex than is usually assumed. Prediction of glacier advances is of practical importance in several countries where mines, highways, pipelines, and hydroelectric installations have been built near glaciers. The theory of glacier flow is now sufficiently well developed that this problem can be tackled, as can the inverse problem of making detailed inferences about past climate from geologic evidence of the former extent of glaciers.

A major recent development in glaciology has been the wealth of information about past climate and atmospheric composition obtained from analysis of drill cores from the polar ice sheets. Cores from the higher parts, where the snow never melts, have provided detailed and continuous records extending back, in one case, for about 425,000 years. Because the ratios of the concentrations of the heavy to light atoms of oxygen and hydrogen ($^{18}\text{O}/^{16}\text{O}$, $\text{D}/^1\text{H}$) in precipitation depend on the temperature, the variations of these ratios with depth may be interpreted as the variation of temperature with past time. Air bubbles in the ice provide samples of the atmosphere at the time the ice was formed and show, for example, that there was appreciably less carbon dioxide and methane during the ice ages

than there is now. The buildup of carbon dioxide since the start of the industrial era is also recorded. The ice also contains small amounts of atmospheric fallout such as wind-blown dust, volcanic ash, pollen, sea salts, and extraterrestrial particles. Major volcanic eruptions show up as highly acidic layers. Shallow cores reveal the recent increase of pollutants such as lead and sulfate in the atmosphere, while atomic and nuclear bomb tests are recorded as radioactive layers.

Glacier-fed rivers provide much of the water supply for agriculture in the Canadian prairies and central Asia and for hydroelectric power generation in several European countries. Tunnels have even been drilled underneath glaciers in the Alps and Norway to tap water from subglacial streams. Glaciers act as reservoirs that store water in solid form during the winter and release it in summer; especially large amounts are released in warm, dry summers, when flow in nonglacial rivers is low. Moreover, the annual flow of a glacier-fed river is higher in a period of glacier retreat than when the glaciers are advancing, a fact not always taken into account when planning hydroelectric schemes. Again, the sudden drainage of glacier-dammed lakes or of water stored in glaciers has caused extensive damage in countries such as Iceland, Peru, and Canada. For these reasons, the study of the flow and storage of water in glaciers, and at the glacier bed, is of considerable practical importance.

II. FEATURES OF EXISTING GLACIERS

Ice covers about 10% of the earth's land surface and stores about three-quarters of all fresh water. **Table I** shows that about 90% of this ice is in Antarctica, with most of the rest in Greenland. The range of recent estimates of the size of the Laurentide Ice Sheet in North America at its maximum extent about 20 kyr ago is given for comparison. The calculated equivalent rises in sea level make allowance for the fact that melting of ice shelves and of ice grounded below sea level changes sea level only to the extent that their thickness exceeds that for flotation.

Antarctica ([Fig. 2](#)) can be divided into three parts: the East and West Antarctic Ice Sheets, separated by the

TABLE I Ice Sheet Areas and Volumes

	Area (10^6 km^2)	Volume (10^6 km^3)	Rise in sea level (m)
Antarctica	13.6	30.1	66
Greenland	1.7	2.7	7
Rest of world	0.5	0.2	0.5
Laurentide (max.)	11.6	16–21	40–52

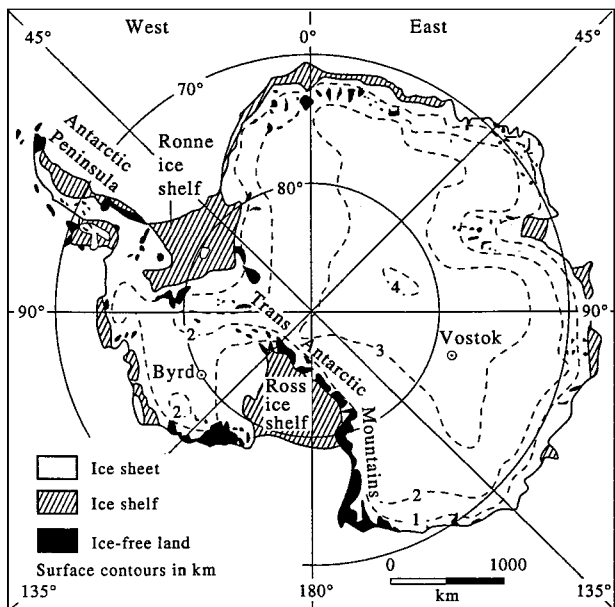


FIGURE 2 Map of Antarctica. [From Paterson, W. S. B., “The Physics of Glaciers,” 3rd ed., Elsevier, 1994. Reprinted by permission of Butterworth Heinemann Publishers, a division of Reed Educational and Professional Publishing Ltd.]

Transantarctic Mountains, and the Antarctic Peninsula, which is characterized by relatively small ice caps, valley glaciers, and ice shelves. The East Antarctic Ice Sheet, which contains about 85% of the Antarctic ice, is an elliptical dome with a maximum elevation of over 4000 m. Although the greatest ice thickness is 4800 m, this is in a narrow subglacial trench, and most of the bedrock is above sea level and has low relief. In contrast, the West Antarctic Ice Sheet has a very rugged floor, much of it well below sea level. This is reflected in a lower and much more irregular ice surface.

Ice shelves surround about half the coastline of Antarctica. They occupy all the major embayments and elsewhere appear to owe their existence to shoals on which their outer margins are grounded. The Ross Ice Shelf has the largest area; its thickness varies from about 1000 m at the grounding line to about 250 m at the outer edge, which consists of an ice cliff some 30 m high.

Annual snowfall ranges from about 25 mm, water equivalent, in the central regions of East Antarctica to about 600 mm near the coast. The mean is 170 mm, a value typical of deserts. There is virtually no surface melting even near the coast and although basal melting is significant on some ice shelves, iceberg calving accounts for nearly all the ablation. Because precipitation is low and the ice is thick, velocities ranging from a few meters per year in the central area to about 100 m/yr near the coast would be sufficient to maintain the ice sheet in a steady state. In

fact, the ice does not flow out uniformly in all directions; most of the discharge near the coast is channeled into either large valley glaciers that cut through the mountains or fast-moving ice streams. Most of these drain into the major ice shelves. Typical velocities are a few hundred meters per year in ice streams and about 1 km/yr at the outer edges of the largest ice shelves. Although the total annual accumulation on the ice sheet is reasonably known, the amount of ice lost by calving is uncertain. Thus it is not known whether the ice sheet is growing or shrinking. The extent of the ice sheet is not controlled directly by climate but indirectly by changes in world sea level, which cause the grounding line to advance and retreat. World sea level is controlled by the growth and decay of ice sheets in the Northern Hemisphere.

The surface of the Greenland Ice Sheet (Fig. 3) has the form of two elongated domes; the larger, northern dome reaches an elevation of about 3200 m. Both are displaced toward the east coast because mountain ranges reduce the outflow on that side. Maximum ice thickness is 3200 m. Bedrock is bowl-shaped; the coast is mountainous and much of the central area lies close to sea level. Most of the outflow is channeled into some 20 large outlet glaciers that penetrate the coastal mountains and discharge icebergs into the fjords. Although some of the glacier tongues are afloat, there are no ice shelves. Glaciers in West Greenland, such as Jakobshavn Isbrae, with a velocity of 7 km/yr at its terminus, are the fastest in the world. Mean annual precipitation is 340 mm/yr. Melting and runoff account for over half the total mass loss. Table II, which gives the latest (1984) estimates, shows that, as in Antarctica, the terms in the overall mass budget are not known precisely enough to determine whether the ice sheet is growing or shrinking. However, the data suggest that it is not far out of balance. A better method of finding out is to measure how the surface elevation changes with time. Such measurements reveal a complicated pattern: the central part is thickening by about 0.1 m/yr (ice equivalent thickness) on the western slope and thinning slightly in the east, while the ablation area on the west coast is thinning by about 0.2 m/yr. These measurements were made by repeated optical leveling across the ice sheet. Radar altimeter measurements from satellites indicate that the southern half of the ice sheet thickened by 0.2 m/yr, about 35% of the average precipitation rate, between 1978 and 1985. Although the precision of the radar

TABLE II Mass Budget of Greenland Ice Sheet
(km³/yr, water equivalent)

Accumulation	500 ± 100
Melting and runoff	295 ± 100
Iceberg calving	205 ± 60

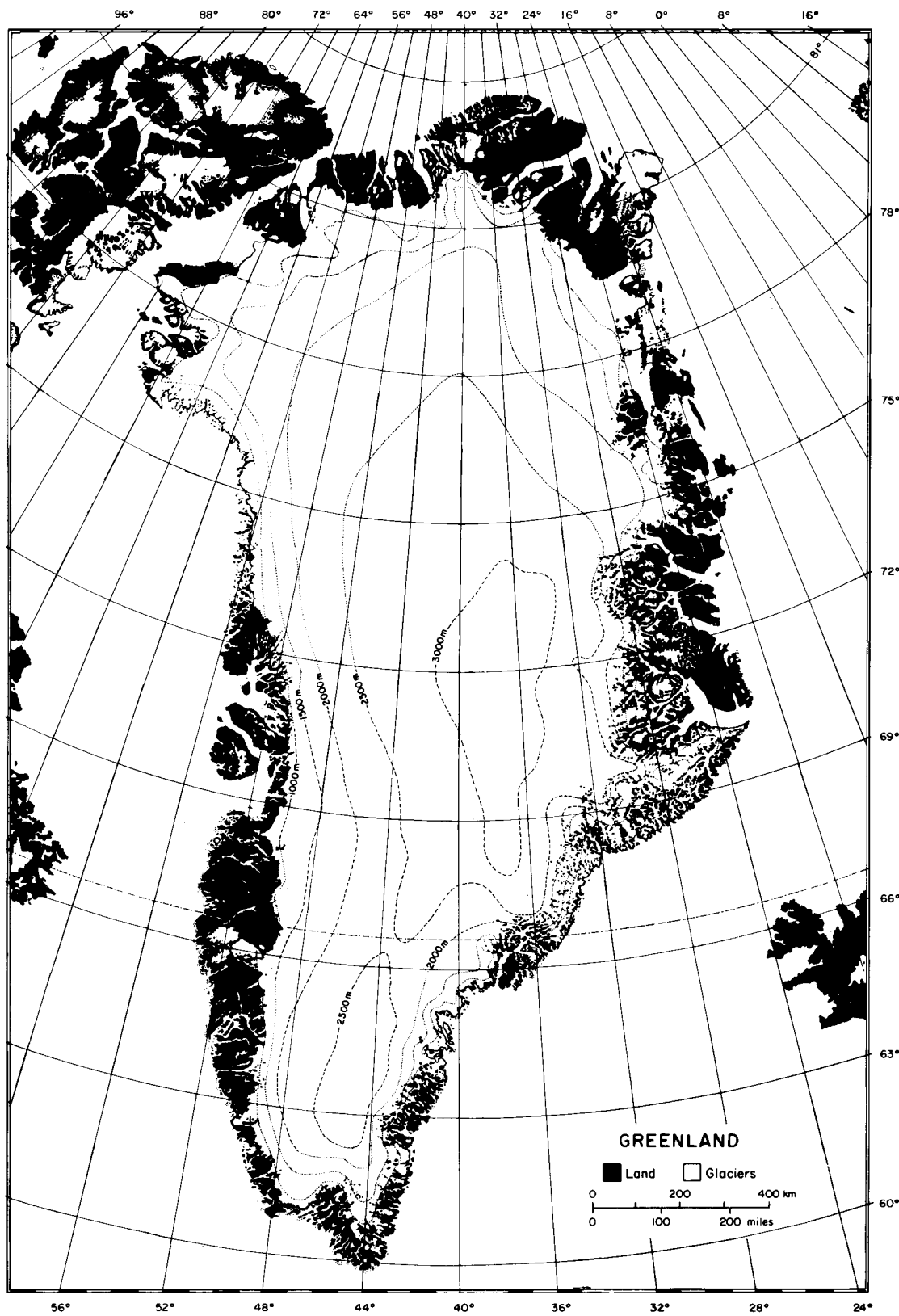


FIGURE 3 Map of Greenland. [Reprinted with permission from Colbeck, S. C. (ed.) (1980). "Dynamics of Snow and Ice Masses." Copyright 1980, Academic Press, New York.]

data has been questioned, this method or laser measurements from an aircraft with a precise three-dimensional navigation system should eventually provide an answer to the important question of the mass balance of the ice sheets.

Ice caps are found in the Canadian and Russian Arctic islands, Svalbard, Jan Mayen, Iceland, some sub-Antarctic islands, and in most major mountain ranges. The largest ice caps outside Greenland and Antarctica are in Arctic Canada where four have areas exceeding 15,000 km². Apart from some small, low-lying ice caps that disappeared during a “climatic optimum” after the end of the ice age and re-formed since, all these ice caps have existed continuously since the last ice age, and the major Arctic ice caps still contain ice dating from that time. Glaciers can exist at all latitudes, even on the Equator in the mountains of Africa, South America, and Indonesia. Mountains in some other tropical areas such as Hawaii also carried glaciers during the ice age.

III. FORMATION AND DEFORMATION OF GLACIER ICE

As fresh snow (density 50–200 kg/m³) becomes buried by subsequent falls, its density increases under the weight of the snow above. This is the first stage in its transformation to glacier ice, which takes place even in the absence of liquid water. Because, unlike other crystalline solids, natural ice is usually within 50°C of its melting point, the molecules are relatively free to move both within the lattice and over the surface of the crystal. Moreover, sublimation (direct change from solid to vapor and vice versa) can occur readily. Movement of molecules is, on average, in the direction that tends to minimize the free energy of the system. Thus snowflakes, with their complex shapes, gradually change into spherical particles, and the larger particles tend to grow at the expense of the smaller ones.

Initially, settling (rearrangement of the snow grains to reduce the air space between them) predominates. After settling has reached its limit, the grains themselves and the bonds that form between them change shape in such a way as to further increase the density. Eventually the air spaces between individual grains become sealed off, and the material becomes impermeable; air that has not escaped to the surface is now in the form of bubbles. At this point the density is about 830 kg/m³ and the firn has, by definition, become glacier ice. Compression of the air bubbles as the ice becomes more deeply buried causes a further slow increase in density up to about 910 kg/m³.

Meltwater greatly speeds up the transformation. It percolates into the snow to a depth where the temperature is

still below 0°C and refreezes, filling up the air spaces and forming lenses and sometimes continuous layers of ice. In some cases, refreezing of meltwater may transform the whole of the winter snow into ice in a single summer. Ice formed by refreezing contains few air bubbles.

Figure 4 shows typical depth-density curves for the Greenland Ice Sheet and for a valley glacier in a maritime temperate climate. Ice at the firn–ice transition is 3–5 yr old on Upper Seward Glacier but about 120 yr old at the Greenland site. Ages of 100–200 yr seem typical for much of Greenland. At Vostok Station in East Antarctica, on the other hand, where the precipitation is only 25 mm/yr and the ice temperature is –57°C, the transformation takes about 2500 yr.

Greenland and Antarctic ice cores from below a certain depth contain no visible bubbles, although air is given off when the ice is melted. The air is believed to be present as a clathrate hydrate. In a clathrate compound, the crystal lattice contains voids that can be occupied by other molecules. The term *hydrate* implies that the lattice is formed by molecules of water. The critical depth varies from 900 to 1200 m according to temperature, which corresponds to hydrostatic pressures of 8 to 10 MPa. This is the first reported natural occurrence of a clathrate hydrate on the earth, although methane hydrate forms in

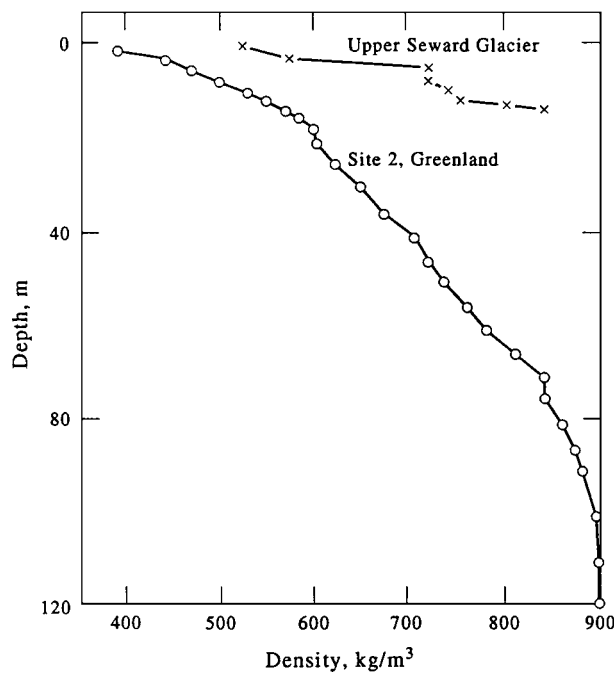


FIGURE 4 Increase of firn density with depth in Greenland Ice Sheet and Upper Seward Glacier, Yukon. [From Paterson, W. S. B., “The Physics of Glaciers,” 3rd ed., Elsevier, 1994. Reprinted by permission of Butterworth Heinemann Publishers, a division of Reed Educational and Professional Publishing Ltd.]

natural-gas pipelines and is believed to be widespread in Arctic permafrost.

Most of the properties of glacier ice depend on the structure of the individual crystals. In an ice crystal, the molecules or, more precisely, the oxygen atoms lie in layers, and within each layer the atoms are arranged hexagonally, as can be seen in the symmetry of a snow crystal. The plane of each layer is called the basal plane, and the direction perpendicular to it is the *C*-axis.

The response of ice to an applied stress is not completely elastic; that is, the sample does not return to its original shape when the stress is removed. If a large stress is applied suddenly, the ice may fracture. If stress is applied slowly, the ice becomes permanently deformed. This is the phenomenon of plastic deformation or creep; it is one process of glacier flow. (The others are sliding of ice over the bed and bed deformation.)

Plastic deformation of a single crystal of ice normally consists of the gliding, one over another, of layers parallel to the basal plane, like cards in a pack. Ice crystals can also deform in other ways, but much higher stresses than those required for basal glide are needed.

The deformation of crystals of ice and metals can be understood in terms of the movement of dislocations within the crystals. These are irregularities, formed during crystal growth and by deformation, that allow the layers of molecules to glide over each other much more readily than they could in a perfect crystal. Deformation involves the movement of dislocations. They interact with each other; in some cases they can pile up and restrict further movement until they can disperse into some more nearly uniform arrangement.

Aggregates of many crystals deform more slowly than a single crystal, because most of the crystals are not oriented for glide in the direction of the applied stress. However, other processes now come into play: displacement between crystals, migration of crystal boundaries, crystal growth, and recrystallization to form more favorably oriented crystals.

In glacier studies, the form of the relation between deformation rate and applied stress is more important than the mechanisms. The most common form of deformation experiment is to apply constant uniaxial compression, or simple shear, to an ice sample and measure how the deformation changes with time. Figure 5 is a typical result. An initial elastic deformation (OA) is followed by a period of transient creep, in which deformation rate decreases steadily. This is followed by a period during which the deformation rate remains constant (secondary creep) before starting to increase (tertiary creep). A final constant deformation rate is sometimes reached. Blocking of dislocations and interference between crystals with different orientations can explain the initial deceleration. The for-

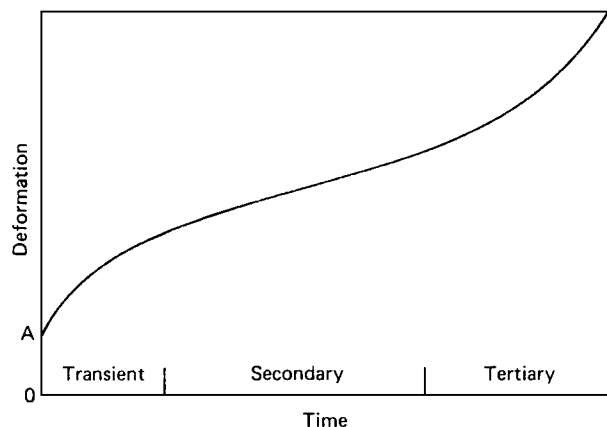


FIGURE 5 Schematic creep curve for randomly oriented polycrystalline ice under constant stress.

mation, by recrystallization, of crystals more favorably oriented for glide accounts for the increase in deformation rate in the tertiary stage. Secondary creep probably represents a temporary balance between these various processes.

For secondary creep, over the range of stresses usually found in glaciers (50–200 kPa), the relation between shear stress τ_{xy} and deformation rate or strain rate $\dot{\epsilon}_{xy}$ has the form

$$\dot{\epsilon}_{xy} = \mathbf{A} \tau_{xy}^n. \quad (1)$$

Here n is a constant, and \mathbf{A} depends on temperature, the orientation of the crystals, impurity content, and possibly other factors. A value $n = 3$ is normally used. This equation is usually called the flow law of ice, or sometimes Glen's law. For a Newtonian viscous fluid, $n = 1$, and \mathbf{A} is the reciprocal of the dynamic viscosity; ice behaves quite differently from this. It should be emphasized that Eq. (1) is not a universal law. Although the form of the relation can be explained by dislocation theory, it is essentially an empirical fit to laboratory and field data for the loading conditions and range of stresses encountered in glaciers. An engineer concerned with the bearing capacity of lake ice, for example, might well use a different relationship. The value of \mathbf{A} varies with absolute temperature T according to the Arrhenius relation,

$$\mathbf{A} = \mathbf{A}_0 \exp\left(\frac{-Q}{RT}\right), \quad (2)$$

for temperatures below -10°C . Here \mathbf{A}_0 is independent of temperature, \mathbf{R} is the gas constant (8.314 J/mol deg), and Q is the activation energy for creep (60 kJ/mol). This value implies that the deformation rate produced by a given stress at -10°C is about 5 times that at -25°C ; the speed of a glacier thus depends strongly on the temperature. The Arrhenius relation breaks down above -10°C .

because additional processes resulting from the presence of liquid water at grain boundaries begin to contribute to deformation. The effective value of \mathbf{Q} starts to increase with temperature, although current practice is to retain the form of the relation and take $\mathbf{Q} = 139 \text{ kJ/mol}$ for temperatures above -10°C .

Hydrostatic pressure does not affect the deformation rate provided that temperature is measured relative to the melting point. Hydrostatic pressure does, of course, lower the melting point; it is about -1.8°C under 2000 m of ice.

The crystals in deep samples from glaciers often have a preferred orientation, that is, a majority of the crystals have their C -axis aligned close to the normal to the shear plane. Such ice deforms more rapidly than ice with a random crystal orientation; increases by factors of up to 10 have been reported. One example is the observation that, in Greenland and Arctic Canada, ice deposited during the last ice age shears three to four times more readily than ice deposited since. This is largely because the crystals in the ice-age ice are much more strongly oriented than those in the ice above, although the higher concentration of impurities may also contribute. Impurities in glacier ice can sometimes increase its deformation rate; there is a thin layer of “soft” ice containing impurities derived from the glacier bed at the base of Meserve Glacier in Antarctica.

Whether the index n is a constant is controversial. Most of the evidence for the accepted value of 3 comes from laboratory tests at relatively high stresses or deformation measurements in temperate glaciers. Some researchers believe that a different deformation mechanism predominates at the low stresses and temperatures prevailing in the upper layers of the polar ice sheets and that the value of n should be reduced to 2 or even 1.5. The only good field data, from Dye 3 in Greenland, are consistent with any value between 2 and 3.

At most places in glaciers the ice is not deforming in simple shear, as assumed in Eq. (1); several stresses act simultaneously. If a longitudinal stress σ_x is superimposed on a shear τ_{xy} , the flow law has the form

$$\dot{\epsilon}_{xy} = \mathbf{A}\tau^{n-1}\tau_{xy}, \quad (3)$$

$$\dot{\epsilon}_{xx} = \frac{1}{2}\mathbf{A}\tau^{n-1}(\sigma_x - \sigma_y), \quad (4)$$

$$\tau^2 = \frac{1}{4}(\sigma_x - \sigma_y)^2 + \tau_{xy}^2. \quad (5)$$

Here x and y are the longitudinal and vertical coordinates, $\dot{\epsilon}$ are the deformation rates and τ is the effective shear stress. The important feature of these equations is the interaction among the different stresses; a given shear stress acting along with other stresses produces a greater deformation rate than it would when acting alone. For example, a tunnel dug in a glacier closes up under the pressure of

the ice above it. The ice at the foot of an icefall undergoes strong longitudinal compression; thus a tunnel there should close up much more rapidly than it would at the same depth in another part of the glacier. This has been observed. Note also that, at a place where $\frac{1}{2}(\sigma_x - \sigma_y)$ is large compared with τ_{xy} , the relation between shear strain rate $\dot{\epsilon}_{xy}$ and shear stress τ_{xy} will appear to be linear. This interaction between stresses, which does not occur in a Newtonian viscous material ($n = 1$), greatly complicates mathematical analyses of glacier flow.

Readers familiar with tensors will recognize that τ^2 in Eq. (5) is the second invariant of the stress-deviator tensor in the two-dimensional case. Because ice deformation is independent of hydrostatic pressure, the flow law should contain stress deviators rather than stresses. A physical property, such as the flow law, must be independent of the coordinate system and so must be expressed in terms of invariants. The most general relation between tensors, such as deformation rate and stress deviator, would involve first, second, and third invariants. The first deformation-rate invariant is zero because ice is incompressible. There is experimental evidence that the value of the third invariant does not affect the flow law. These facts, combined with the plausible assumption that corresponding deformation-rate and stress-deviator components are proportional to each other, reduce the flow law to the form given.

A useful approximation to the flow law is to regard ice as perfectly plastic. If a gradually increasing stress is applied to a perfectly plastic material, there is no deformation until a critical value, the yield stress, is reached, at which point the material deforms rapidly. This corresponds to the case $n = \infty$, as may be seen by replacing \mathbf{A} by \mathbf{A}_0/τ_0^n in Eq. (1).

IV. GLACIER FLOW BY ICE DEFORMATION

During the past 50 years, application of the methods of continuum mechanics has greatly improved the understanding of glacier flow. Continuum mechanics deals with the motion of deformable bodies whose properties, although in fact determined by their molecular structures, can be expressed in terms of a continuous theory. The simplest application, one that clarifies many of the fundamentals of glacier flow, is to consider blocks of ice in simple shapes as idealized models of glaciers. The stresses required to maintain a block in mechanical equilibrium can be calculated. Strain rates and velocities can then be calculated from the stresses by the flow law [Eqs. (3) and (4)].

Velocities of valley glaciers can be easily measured by repeated surveys, from stations on bedrock, of the

positions of stakes set in the ice. Velocities on ice sheets can be determined by the Global Positioning System, by measuring the displacement of crevasses and other identifiable features on repeated optical images from satellites, and by an interference method using the side-looking synthetic aperture radar on the ERS-1 satellite. The configuration of the ice surface can be mapped by radar altimetry, provided that the wavelength is not within the range to which ice is transparent. Shear strain rates within the ice can be found by measuring the rate at which a vertical borehole tilts. Normal strain rates at the surface are determined by measuring the rate of change of the distance between two stakes. At least two boreholes are required for measuring normal strain rates at depth; this has seldom been done. Stresses in glaciers have never been measured; they are always calculated from some simplified model.

The pattern of flow in a glacier can be deduced from the principle of mass conservation. See Fig. 6. The glacier is assumed to be in a steady state, that is, its dimensions do not change in time, and the velocity at any point, fixed in space, remains constant as the ice flows past. To maintain constant thickness in the accumulation area, ice must flow downward relative to the surface. This velocity component decreases steadily with depth, as does the surface-parallel component, and reaches zero at the bed if there is no melting there. Similarly, ice flows upward relative to the surface in the ablation area. Now consider a cross section through the glacier perpendicular to the surface and to the flow direction. To maintain a steady state, the annual flux of ice through any such cross section in the accumulation area must be equal to the total annual accumulation on the surface upstream of the cross section. Similarly, the annual flux through a cross section in the ablation area must equal the annual loss of ice between the cross section and the terminus. Thus the ice flux must increase steadily from zero at the head of the glacier to a maximum at the equilibrium line and from there decrease steadily to the terminus. Ice velocities should show a sim-

ilar trend, modified by variations in width and thickness of the glacier. In the Antarctic Ice Sheet, where nearly all the ice is lost by iceberg calving, there is no ablation area, and the velocity is greatest at the terminus.

This pattern of velocity variations means that the ice mass is being stretched in the horizontal direction in the accumulation area and compressed in the ablation area. In fact, ice is incompressible except insofar as the volume of air bubbles can be reduced. Horizontal extension must therefore be accompanied by an equal compression in the vertical direction; this is how the glacier can remain in a steady state in spite of accumulation. Similarly, longitudinal compression in the ablation area is accompanied by vertical stretching, which can keep the glacier thickness constant. This argument applies to a valley glacier in which the side walls prevent lateral extension. The general condition is not that horizontal extension must equal vertical compression, but that the algebraic sum of the deformation rates in any three mutually perpendicular directions must be zero. Where the ice is stretching/contracting in the direction of flow, it is said to be in *extending/compressing flow*. Regions of extending flow are often marked by transverse crevasses. The steady-state deformation rate can be estimated roughly from the ratio of the accumulation or ablation rate to the ice thickness. Typical values range from 10^{-2} yr^{-1} for glaciers in maritime temperate climates to 10^{-5} yr^{-1} in central Antarctica.

As a simple model of a glacier, consider a parallel-sided slab of thickness h , frozen to a plane of slope α . The length and width of the slab are much larger than h . It deforms in simple shear under its own weight. Consider a column of ice perpendicular to the plane and of unit cross section. The component of its weight parallel to the plane, the *driving stress*, is $\rho gh \sin \alpha$. (Here ρ is density and g gravitational acceleration.) This is balanced by the *basal drag*, the shear stress τ_b across the base of the column:

$$\tau_b = \rho gh \sin \alpha. \quad (6)$$

If the slab has uniform thickness, this relation holds at every point. In a real glacier h varies with x and so there are places where one term exceeds the other. In other words, there is a longitudinal stress σ_x as well as shear:

$$\tau_b = \rho gh \sin \alpha + \int_b^s \left(\frac{\partial \sigma_x}{\partial x} \right) dy. \quad (7)$$

Here s and b denote surface and bed. At most places except near an ice divide and near the terminus, the second term on the right-hand side is small compared with the first, especially if the surface slope is averaged over a distance of about $10h$. At this scale, flow is in the direction of maximum surface slope.

The value of τ_b has been calculated from measurements of thickness and surface slope on many glaciers. Most

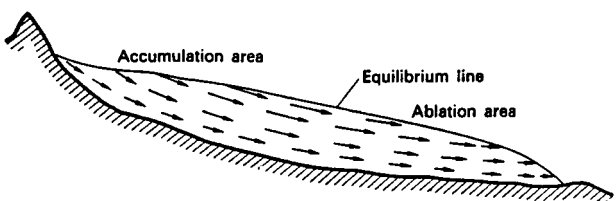


FIGURE 6 Velocity vectors in an idealized glacier. They define the flowlines. Particle paths are identical with flowlines if the glacier is in a steady state. [From Paterson, W. S. B., "The Physics of Glaciers," 3rd ed., Elsevier, 1994. Reprinted by permission of Butterworth Heinemann Publishers, a division of Reed Educational and Professional Publishing Ltd.]

values lie between 50 and 100 kPa. (Surging glaciers and Antarctic ice streams are the main exceptions, with values lower than these.) Equation (6), with τ_b constant, implies that a glacier is thin where its surface is steep and thick where the slope is small. Observations confirm this. Moreover, inflection points of the surface correspond to bedrock highs.

Because of the small variation in τ_b , a useful approximation is to regard ice as perfectly plastic. This leads to a particularly simple picture of glacier flow: the ice thickness adjusts itself so that at every point the shear stress at the base is equal to the yield stress τ_0 . This in turn leads to a simple formula for the surface profile of an ice sheet. If the bed is horizontal and the surface slope small, $\alpha = dh/dx$, and Eq. (6) can be integrated to give

$$h^2 = \left(\frac{2\tau_0}{\rho g} \right) x, \quad (8)$$

where x is distance from the edge. This is a parabola. Equation (8) with $\tau_0 = 100$ kPa correctly predicts the maximum ice thickness of 3200 m in central Greenland. This formula is frequently used to calculate the shape and volume of ice-age ice sheets from evidence of their extent provided by moraines and other glacial deposits.

The assumption that ice is perfectly plastic can also explain the maximum depth of crevasses. In the wall at the bottom of a crevasse, the weight of the overlying ice is acting downward and is not supported by any lateral pressure other than atmospheric. This vertical pressure tends to squeeze the ice downward and outward and so to close the crevasse. Below a critical depth (22 m), this happens very rapidly.

Similar, though more complicated, analyses can be made using the true flow law. According to Eq. (8), the shape of the ice sheet depends only on the plastic properties of ice, not on accumulation and ablation rates. If the flow law is used, the calculated profile is not greatly changed, and the dependence on accumulation and ablation is not a sensitive one. (Doubling the accumulation rate would increase ice thickness by 10%.) As Fig. 7 shows, many ice caps have similar, roughly parabolic, surface profiles in spite of appreciable differences in accumulation and ablation and, in some cases, in spite of mountainous bedrock topography.

How velocity varies with depth can be calculated from the flow law, Eq. (1). This is used to obtain the shear strain rate at any depth y from a formula analogous to Eq. (6). The shear strain rate is then integrated to give the horizontal velocity component u at depth y ,

$$u_s - u = \frac{2A(\rho g \sin \alpha)^n y^{n+1}}{(n+1)}, \quad (9)$$

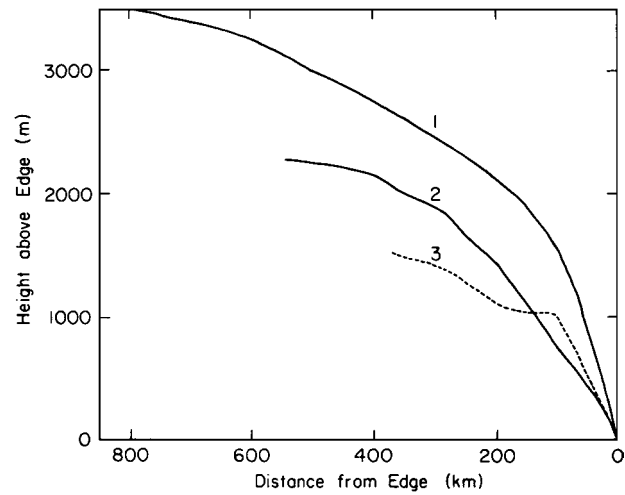


FIGURE 7 Surface profiles of ice sheets: 1, Antarctic Ice Sheet, Mirny to Komsomol'skaya; 2, Greenland Ice Sheet, west side between latitudes 69 and 71°N; 3, Greenland Ice Sheet, east side between latitudes 71 and 72°N. [Reprinted with permission from Colbeck, S. C. (ed.) (1980). "Dynamics of Snow and Ice Masses." Copyright 1980, Academic Press, New York.]

where A and n are the flow law parameters and suffix s denotes the surface value. This velocity profile is shown in Fig. 8. The velocity is greatest at the surface and decreases with depth; most of the decrease occurs near the bed. Thus perfect plasticity, for which all the deformation

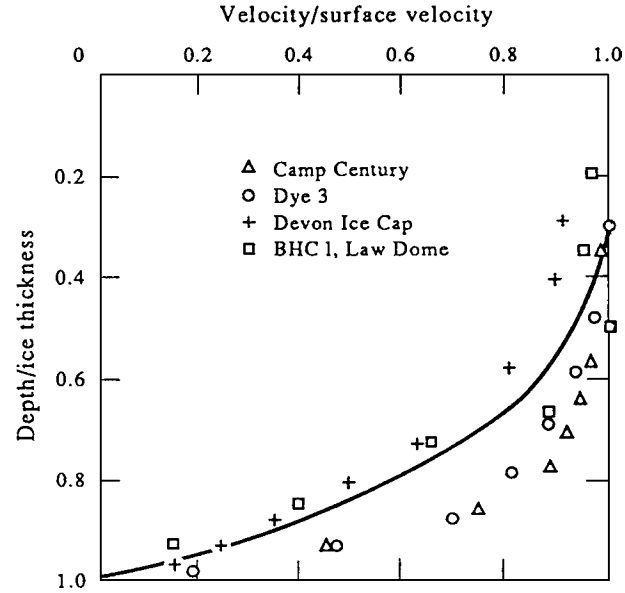


FIGURE 8 Variation of horizontal velocity with depth calculated from Eq. (9), assuming uniform temperature and $n=3$, compared with four measured velocity profiles. [From Paterson, W. S. B., "The Physics of Glaciers," 3rd ed., Elsevier, 1994. Reprinted by permission of Butterworth Heinemann Publishers, a division of Reed Educational and Professional Publishing Ltd.]

takes place at the bed, is a reasonable approximation. Except in temperate glaciers, the shear should be more concentrated near the bed than shown here, because the curve was drawn with A constant. In fact, A increases with temperature and the warmest ice is found near the bed. (See Section VII.)

In addition to adjusting the ice thickness to compensate for accumulation and ablation, extending and compressing flow enable a glacier to flow past large bumps in its bed. Crudely, the ice on top of the bump is pushed by the ice upstream and pulled by the downstream ice. More precisely, compressing flow upstream of the bump thickens the glacier there, whereas it is thinned by extending flow on the downstream side. This increases the surface slope over the bump and so provides sufficient shear stress to drive the ice over it. Again, where the valley walls converge in the direction of flow, the glacier is compressed in the transverse direction and this induces extension in the direction of flow. Similarly, there is a tendency for compressing flow where the valley widens. The combination of all these factors determines the state of flow at any point; accumulation and ablation are usually the most important.

Glacier deformation is a combination of shear and longitudinal extension and compression. Shear predominates near the bed, longitudinal stresses near the surface. Note that the longitudinal deformation rate usually varies with depth; upstream of a bedrock bump, flow near the bed will be compressing, even though the depth-averaged flow is extending when the point is in the accumulation area.

Equation (9) cannot be used for velocity calculations if there are longitudinal stresses, as there always are in a real glacier. A method based on the generalized flow law [Eqs. (3) and (4)] has to be used. As a result, shear can be either more or less concentrated in the basal layers than the simple theory predicts (Fig. 8).

Simple models that lead to equations with analytical solutions have proved successful in clarifying many fundamental aspects of glacier flow. However, many important problems, such as flow at ice divides, in and near icefalls, at grounding lines, and at glacier termini cannot be treated in this way. Moreover, dating the climatic records now being obtained from cores from polar ice sheets (Section XI) requires detailed modeling of flow upstream from the borehole. For this purpose, the velocity distribution is only the starting point; one also has to calculate particle paths, how long the ice takes to travel from the surface to a particular point in the borehole, and how the thickness of an annual layer changes as it is buried by subsequent layers. Numerical methods of obtaining approximate solutions to complicated equations have to be used in these cases. One technique is the finite-element method, developed by engi-

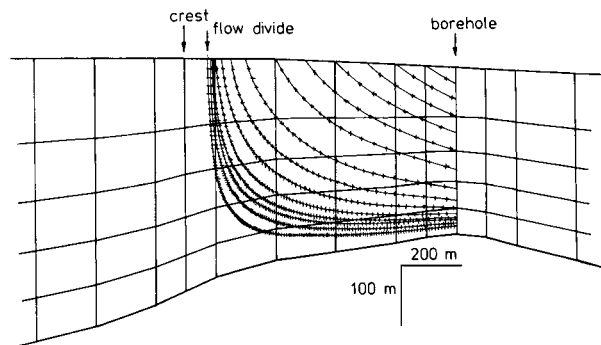


FIGURE 9 Particle paths near crest of Devon Island Ice Cap computed by finite-element modeling. The grid shows the boundaries of the elements. Ice takes 100 years to travel between two marks on a path. [Reprinted from Paterson, W. S. B., and Waddington, E. D. (1984). *Rev. Geophys. Space Phys.* **22**, 123–130. Copyright 1984, American Geophysical Union.]

neers to solve problems in structural mechanics. Figure 9 shows the results of one analysis.

The velocity distribution in real glaciers is much more complicated than the simple picture presented here. Three-dimensional effects are important. For example, ice can flow around a bedrock bump as well as over the top of it. Other observations show that the shear deformation, instead of increasing steadily with depth, can sometimes be concentrated in bands in which the orientation of crystals is particularly favorable for deformation. Again, some bedrock hollows may be filled with stagnant ice.

V. FLOW OF ICE SHELVES

Flow in ice shelves can be analyzed by similar methods. Because the shelf is floating, shear stresses are zero at the base as well as at the surface. Vertical shear is negligible, and deformation consists of uniform spreading. If the sides of the shelf are not confined by land, the spreading rate is the same in all directions, and the only restraining force is the horizontal force that seawater exerts on the edges. The spreading rate of an unconfined shelf of uniform thickness can be shown to be proportional to Ah_0^n , where h_0 is the height of the surface above sea level and A and n are the flow law parameters, A being an average value to take account of the variation of temperature with depth. An ice shelf can maintain its thickness only if spreading is counteracted by surface accumulation or by inflow from an ice sheet.

Ice shelves of significant size are found only in Antarctica. All the major ones are fed from the ice sheet and their sides are confined by bedrock or grounded ice. (See Fig. 2.)

On the Ross Ice Shelf, for instance, surface accumulation accounts for about half the mass; inflow from glaciers and ice streams provides the rest. Ice is removed mainly by calving, sometimes in the form of enormous tabular bergs. There is also some basal melt.

Deformation rates along flowlines in the Ross Ice Shelf are only about one-tenth of those calculated from the formula for the spreading rate of an unconfined shelf. This is because that analysis ignores the drag of the side walls (bedrock or grounded ice) and the restraining effect of ice rises. An ice rise has the dome-shaped profile characteristic of grounded ice and its own radial flow pattern. The shelf ice flows around it and the ice immediately upstream is relatively thick because the flow is obstructed. Because the restraining force increases with increasing distance from the calving front, the ice thickness also increases; the Ross Ice Shelf is about 250 m thick at the ice front and three to four times that at the grounding line.

Because deformation in ice shelves consists of longitudinal extension rather than shear, the velocity at any point cannot be calculated from the ice thickness and surface slope there. It has to be obtained by integrating the deformation rate from a point, usually the grounding line, where the velocity is known. Again, the vertical shear deformation characteristic of an ice sheet cannot change to longitudinal extension instantaneously at the grounding line. There must be a transition zone upstream. An ice stream, with low surface slope, low driving stress, and little vertical shear, is essentially a transition zone between the inland ice and the ice shelf. (See Section VIII.) Where an outlet glacier flows into an ice shelf, however, the extent of the transition zone is less clear.

An ice shelf exerts a back pressure on the ice flowing into it; the amount of the pressure depends on how difficult it is to push the shelf out to sea. This in turn depends on the extent of ice rises and the drag exerted by the sidewalls. This back pressure, which may be transmitted for some distance into the ice sheet, reduces the ice flow. Thinning of the ice shelf or a rise in sea level would reduce both the extent of ice rises and the area of ice in contact with the sidewalls. This would reduce the back pressure and so increase flow from the ice sheet. This is discussed further in Section VIII.

VI. BASAL MOTION AND WATER FLOW AT THE BED

Velocity at depth in a glacier can be measured by drilling a vertical hole and measuring its tilt at different depths a year later. The profile of the hole then gives the velocity-depth profile, and the surface velocity can be determined

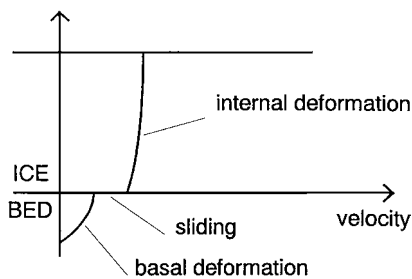


FIGURE 10 The three possible modes of glacier flow.

by standard surveying techniques. Provided that the hole extends to bedrock, this method also measures the basal motion. This can result from the glacier sliding over its bed or from deformation of the bed itself (Fig. 10). Sliding has also been measured in tunnels and by down-borehole photography and television. Sliding velocities span a much greater range than velocities produced by ice deformation. Significant sliding occurs only when the basal ice is at melting point. Bed deformation has been measured by driving a rod with strain gauges bonded to it into the subglacial sediments from the bottom of a borehole. Subglacial sediments deform only if they are saturated with water at low effective pressure, that is, the water pressure in their pores is not far below the hydrostatic pressure of the overlying ice.

How does ice, assumed to be at melting point, move past bumps in the glacier bed? Observations have confirmed that two mechanisms operate. The first is pressure melting. The resistance to motion must be provided by the upstream side of each bump. So there must be excess pressure there. Because this lowers the melting point, some ice can melt. The meltwater flows around the bump and refreezes on the downstream side where the pressure is less. The latent heat released on the downstream side is conducted through the bump and the surrounding ice to the upstream side, where it provides the heat needed for melting. This process is the same as in the classic regelation experiment, in which a wire moves through a block of ice by pressure-melting in front and refreezing behind. The process is ineffective for bumps longer than about 1 m because the heat conducted through them is negligible; nor can it take place if the ice is below its melting point. The second mechanism of sliding is enhanced plastic flow. Stress concentrations in the ice near a bump increase the deformation rate, so the ice can flow over the bump or around it. The larger the bump, the greater the area over which the stress is enhanced, and so the more effective this process will be. It follows that obstacles of some intermediate size, probably between 0.05 and 0.5 m, must provide most of the resistance to sliding.

Mathematical analysis of these processes leads to an equation for the sliding velocity:

$$u_b = B \tau_b^{(n+1)/2} R^{-n-1}. \quad (10)$$

Here B is a constant that depends on the mechanical and thermal properties of ice, $n(=3)$ is the flow law index [Eq. (1)]; τ_b is the driving stress, and R is the bed roughness (amplitude/spacing of bumps). Note the sensitivity of the sliding velocity to the roughness; doubling the roughness decreases the velocity by a factor of 16. Sliding velocities of glaciers cannot be predicted from this formula because the bed roughness is seldom, if ever, known; it is not even clear how to measure it for a real glacier bed. However, the equation, with the very dubious assumption that R is a constant, has been used extensively as a boundary condition in mathematical analyses of deformation within glaciers.

The main objection to Eq. (10) is that the effect of water at the bed is ignored. In the theory, the ice is assumed to be in contact with the rock, except for the thin water film produced in the regelation process. Large amounts of meltwater flow on the surfaces of most glaciers in summer. Most of it disappears into the ice through cracks and vertical passages called moulin, formed where water flows into a crevasse, and emerges under the terminus in one or a few large streams. Observations of increased velocity in summer, diurnal variations, and dramatic increases after heavy rain support the idea that sliding velocity is influenced by water at the bed. Short-period variations must result from sliding, because ice deformation depends on factors such as ice thickness and surface slope, which cannot change rapidly. In some cases, a rapid increase in velocity has been associated with a measurable upward displacement of the glacier surface, attributed to an increase in the amount of water at the bed.

Theoretical analyses and field observations suggest that there are two types of subglacial drainage system. One is a system of tunnels cut upward into the ice. Melting of the wall by heat generated by the friction of the water enlarges a tunnel, while ice flow tends to close it because the water pressure is normally less than the pressure of the ice above. If the flux of water increases, the increase in frictional heat increases the melting rate. To maintain a steady state, the closure rate must also increase and so, because the ice overburden pressure is fixed, the water pressure must decrease. Thus there is an inverse relation between the water flux and the steady-state water pressure in a tunnel. It follows that, of two adjacent tunnels, the larger has the lower pressure and therefore draws water from the smaller one. The system therefore develops into one or a few large tunnels. The tunnel system carries a large flux at low pressure in approximately the same direction as the ice flow.

In the second type of drainage system, often called a linked-cavity system, the water is dispersed widely over the bed in a network of interconnected passageways whose diameter varies greatly along the path. The wide parts are cavities on the downstream side of the larger bedrock bumps; the narrow parts are downstream of small bumps or are channels cut in the bed. Because the frictional heat is spread over a much larger area of the bed than it is in a tunnel, melting of the roof is not an effective way of keeping a passageway open. High water pressure is required for this. When the flux of water increases, the water pressure also increases to increase the capacity of the system by enlarging the cavities. Because water pressure increases with flux, there is no tendency for the larger passageways to grow at the expense of the smaller ones. Because the passageways tend to be on the downstream side of bedrock bumps, much of the water flow is in the cross-glacier direction. Travel times are much longer than the few hours typical of a tunnel, because the path length is much longer and the narrow sections throttle the flow. A linked-cavity system can develop only if the bed is rock rather than sediments.

The two systems are believed to exist simultaneously beneath a glacier. They expand or contract, though not instantaneously, in response to changes in the volume of water. A sudden influx, for example, may drive some of the water out of a tunnel into the linked-cavity system. In late summer, when the reduced water supply no longer fills a tunnel, it will start to close rapidly. When melting begins in spring, most of the water is probably in cavities. Once the tunnel system has developed, however, it takes over the bulk of the drainage.

Because sliding tends to keep open cavities on the downstream side of bedrock bumps, the size of a cavity increases with the sliding velocity. Conversely, the increased bed separation produced by an increase in water pressure increases the sliding velocity. Because, unlike the linked-cavity system, tunnels occupy only a small fraction of the glacier bed, the water in them has little effect on sliding.

The effect of water has been taken into account empirically by writing the equation

$$u_b = \frac{B_1 \tau_b^m}{(\rho g h - P)^p}, \quad (11)$$

where ρ is ice density, g is gravitational acceleration, h is ice thickness, P is subglacial water pressure, B_1 is a “constant” that includes the bed roughness, and m and p are positive integers. The denominator is the weight of ice reduced by the water pressure. Implicit in this equation is the dubious assumption that sliding at any point is unaffected by water conditions up- and down-stream.

A further objection to all current sliding theories is the implicit assumption that the ice rests on a rigid impermeable ("hard") bed and that the interface is well defined. In fact, parts of many glaciers and ice sheets rest on a layer of deformable sediment usually glacial till, a "soft" bed. If the sediment has a low permeability, subglacial water can, by building up pore pressure within it, make the sediment weaker than the overlying ice. In this case, bed deformation can be the major component of glacier movement. Ninety percent of the basal movement at the margin of a glacier in Iceland was found to consist not of basal sliding but of deformation in the subglacial material. Deformation of water-saturated gravel beneath the ice has also been observed in a borehole. Again, seismic measurements suggest that Ice Stream B, one of five that drain ice from the interior of West Antarctica into the Ross Ice Shelf, is underlain by about 6 m of unconsolidated sediments. Deformation in this layer could explain why the surface velocity is several hundred meters per year in spite of an extremely low driving stress. (See Section VIII.) Recent observations such as these have forced glaciologists to accept that till can, under certain conditions, deform in shear, as geologists have known for many years.

Till is a complex inhomogeneous material and a flow relation for it has not been firmly established. A relation,

$$\frac{u}{h} = B_2 \tau^a N^{-b}, \quad (12)$$

has been suggested on the basis of one set of measurements. Here u is basal velocity, h is thickness of till layer, τ is shear stress, N is effective pressure (ice overburden minus water pressure), B_2 is a constant, and a and b have values between 1 and 2. A relation of this form is an oversimplification, because the deformation rate is expected to depend on additional factors such as composition, porosity, and strain history. Equation (12) has the same form as Eq. (11). This is convenient for numerical modelers; they can use it as a boundary condition without specifying whether it represents sliding or bed deformation. In contrast, some researchers believe that till is perfectly plastic. If so, deformation cannot be pervasive; it must be confined to a thin layer at the base.

VII. TEMPERATURES IN GLACIERS

The temperature distribution in glaciers deserves study both for its own sake and for its relation to other processes. Ice velocity depends sensitively on temperature. The basal temperature is important for erosion; bedrock is protected when the ice is frozen to it. If the basal temperature of a glacier, previously frozen to its bed, were to reach melting point, the ice could start to slide; this would result in a significant advance of the terminus. Again, properties

such as the absorption of radio waves, on which the standard method of measuring ice thickness depends, vary with temperature. In particular, water in the ice scatters radio waves and greatly increases the difficulty of radar sounding.

The temperature distribution results from the interaction of many processes. Short-wave solar radiation and long-wave radiation from atmospheric water vapor and carbon dioxide supply heat to the surface, as does condensation of water vapor. The surface loses heat by outgoing long-wave radiation and sometimes by evaporation. Turbulent heat exchange with the atmosphere may warm or cool the surface according to the temperature gradient in the air immediately above. Ice deformation and, in some cases, refreezing of meltwater warm the interior while geothermal heat and friction (if the ice is sliding) provide heat at the base. Heat is transferred within the glacier by conduction, ice flow, and in some cases water flow. The interaction between ice flow and heat flow greatly complicates mathematical analyses of glacier flow.

The temperature distribution in a glacier can have one of four forms:

1. All the ice is at melting point except for a near-surface layer penetrated by a winter "cold wave," the so-called temperate glacier. Temperature decreases with increase of depth at a rate of 0.87 deg/km because of the effect of pressure on air-saturated water.
2. All the ice is below melting point.
3. The melting point is reached only at the bed.
4. A basal layer of finite thickness is at melting point. This situation depends on ice-flow conditions near the bed.

Different types of distribution can occur in different parts of the same glacier.

Seasonal variations of surface temperature are rapidly damped at depth; the temperature at a depth of 10–15 m remains constant throughout the year. In Antarctica, except near the coast, and in the higher parts of Greenland, the air temperature never reaches 0°C. The 15-m temperature is then equal to the mean annual air temperature and provides a quick way of measuring it. This temperature decreases by about 1°C per 100 m increase of elevation and 1°C for each degree increase of latitude. The 15-m temperature can vary slowly as a result of long-term climatic variations. Depth of penetration increases with the period of the change; the 100 kyr ice-age cycle penetrates through the deepest ice sheets into bedrock.

When there is surface melting, the water percolates into the snow and refreezes. Because freezing of 1 g of water releases enough latent heat to warm 160 g of snow by 1°C, this is an important means of warming the

near-surface layers of glaciers and the seasonal snowcover. The 15-m temperature may then be several degrees above mean annual air temperature. This process is self-limiting, however, because percolation stops after there is enough meltwater to form a continuous ice layer.

Thermal conditions at the base are determined mainly by the geothermal heat flux, the flow of heat produced by radioactive decay in the earth's interior. If the basal ice is below its melting point, all this heat is conducted into it. A heat flux of 56.5 mW/m^2 , the continental average, produces a temperature gradient of 2.7 deg per 100 m in ice. If the basal ice is at melting point (case 3 above), some of the heat will be used for melting and the remainder conducted into the ice. In a temperate glacier or in one with a basal layer at melting temperature, the small reversed temperature gradient prevents upward conduction of heat; all the basal heat is used for melting, about 6 mm of ice per year for an average heat flux. Frictional heat will melt the same amount if the sliding speed is about 20 m/yr.

With the upper and lower boundary conditions established, the form of the temperature distribution can be derived. Initially we consider a steady state. This means that the dimensions of the glacier do not change in time and that the velocity and ice temperature at any point, fixed in space, remain constant as the ice flows past. This is an important theoretical concept, although no real glacier is ever in this condition.

The downward component of flow in the accumulation area (see Section IV) is a much more important means of heat transfer than conduction in the upper layers. In a stagnant glacier, with no accumulation or ablation, the temperature would increase steadily with depth at a rate equal to the geothermal gradient. In a glacier with accumulation, the temperature profile still has this shape near the bed, where the vertical velocity component is very low, but temperatures in the upper layers can be nearly uniform as a result of the downward flow of cold surface ice. The higher the accumulation rate the stronger the effect. Figure 11 illustrates this. These curves are based on a simple mathematical analysis. Because the effect of the horizontal component of ice flow was ignored, they should be good approximations near the center of an ice sheet because horizontal velocities are small there.

In the ablation area, ice flows upward toward the surface, carrying warm basal ice with it; the temperature gradient in the upper layers is greater than the geothermal. Such a curve is also shown in Fig. 11. However, neglect of the horizontal velocity component in the ablation area is hard to justify.

How does the horizontal velocity affect temperatures? Figure 6 shows that with increasing depth in a borehole, the ice has originated at progressively higher elevations and thus at progressively lower temperatures. If each particle

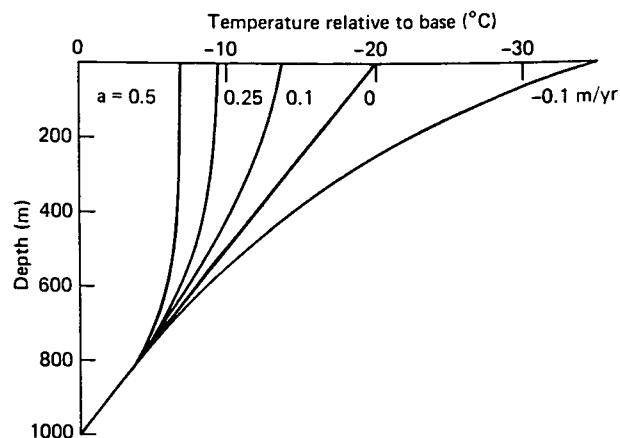


FIGURE 11 Computed temperature distribution in a steady-state ice sheet with a frozen bed for different values of ice equivalent accumulation rate (positive) and ablation rate (negative).

of ice were to retain its initial temperature, the deepest ice would be the coldest. Heat conduction changes the temperature. Nevertheless, flow of cold ice from high elevations often results in the coldest ice being found some distance below the surface. This effect should become more important with increasing distance from the ice divide. Such a temperature minimum could not occur as a steady state in a static medium.

Such negative temperature gradients (decrease of temperature with increase of depth) have been measured in many shallow boreholes in Greenland and Antarctica. However, some of the observations may have another explanation: climatic warming during the past 50 to 100 yr. In this case each snow layer is warmer than the one below, although conduction will eventually smooth out such differences.

This suggests that measurements of the present temperature profile in a borehole can be inverted to give a record of past surface temperatures, provided that the effect of flow from upstream is either allowed for or eliminated by drilling at an ice divide. The resulting record is heavily smoothed, however, and increasingly so the farther back in time it extends. Moreover, there is seldom much information about past changes in accumulation rate, ice thickness, and flow pattern, all of which affect the record. Oxygen-isotope profiles from ice cores, described in Section XI, provide much more detailed records of past surface temperatures. Borehole temperature profiles have, however, proved valuable for calibrating these records, that is, converting a given change in oxygen-isotope ratio to a temperature change. Such a calibration shows, for instance, that central Greenland was as much as 20°C colder than present at the last glacial maximum. This is about four times the difference in the tropics.

Figure 12 shows some measured temperature profiles. The simple ideas just outlined can explain the general

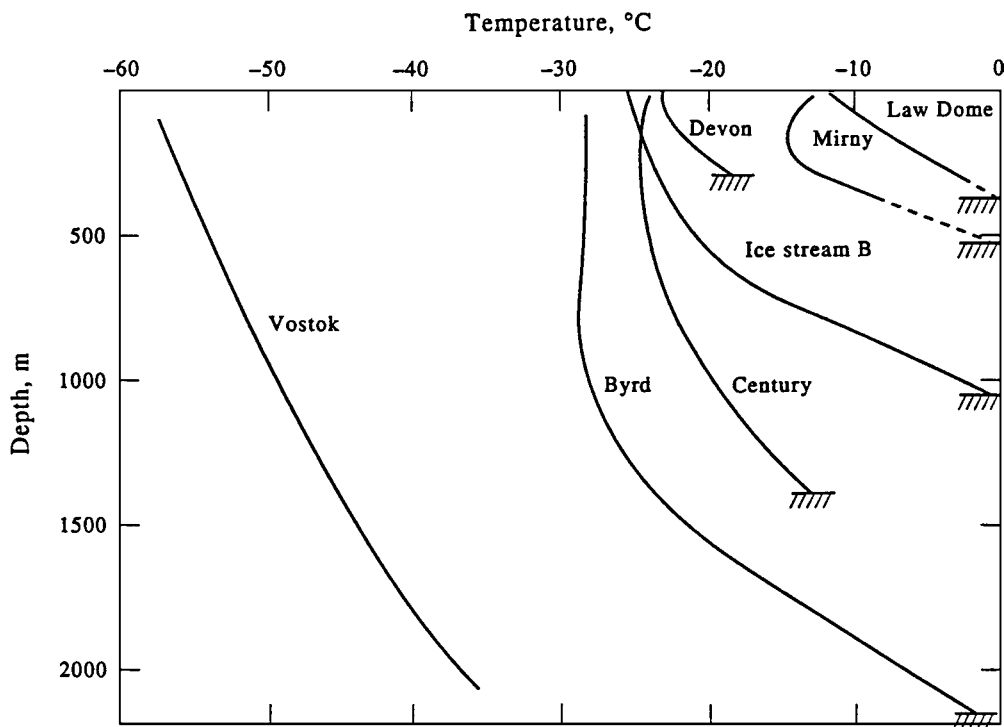


FIGURE 12 Measured temperature profiles in accumulation areas of polar ice sheets and ice caps. At Vostok, the ice is at melting point at the base (3740 m). Camp Century is in Greenland and Devon Island in Arctic Canada; the other sites are in Antarctica. [Adapted from Paterson, W. S. B., “The Physics of Glaciers,” 3rd ed., Elsevier, 1994. Reprinted by permission of Butterworth Heinemann Publishers, a division of Reed Educational and Professional Publishing Ltd.]

shapes of these curves. The details have not been successfully predicted, however, only explained afterwards on an *ad hoc* basis.

VIII. ICE STREAM FLOW

The simple picture of an ice sheet as a dome with the ice flowing out uniformly in all directions is realistic at best only in the central part. As the ice approaches the coast it is channeled, either by mountains or the nature of its bed, into fast-flowing outlet glaciers and ice streams. In Antarctica, although these comprise less than 20% of the coastline at the grounding line, they may drain as much as 90% of the accumulation from the interior. Most become part of ice shelves. Similarly, most of the discharge from Greenland is concentrated in some 20 large outlet glaciers that end as floating tongues in the fiords. The behavior of these fast-flowing outlets largely controls the state of the ice sheet.

To make a clear distinction between an ice stream and an outlet glacier is not feasible. An ice stream in the strict sense has no visible rock boundaries; heavily crevassed shear zones separate it from slow-moving ice on either

side. But Jakobshavn Isbrae in West Greenland starts as an ice stream and becomes an outlet glacier when it reaches the coastal mountains, while Rutford Ice Stream in Antarctica is bordered by mountains on one side and ice on the other.

Ice streams have various modes of flow. The outlet glaciers in Greenland and those that drain ice from East Antarctica into the Ross Ice Shelf (Fig. 2) are believed to move by ice deformation. Driving stresses are in the range 50–150 kPa and there are no seasonal variations in velocity. The situation is different on the other side of the Ross Ice Shelf, the Siple Coast, where five ice streams drain about one-third of the interior of West Antarctica. (See Fig. 13.) These ice streams are a few hundred kilometers long, 30–60 km wide, 1–1.5 km thick, and have very low surface slopes. Velocities of a few hundred meters per year are typical, apart from Ice Stream C which is almost stagnant. Shear zones, some 5 km wide, separate these ice streams from the ice ridges on either side where the velocity is less than 10 m/yr. Their beds are below sea level and would remain so, in spite of uplift, if the ice were removed.

Figure 14 shows driving stresses and velocities along a flowline that includes Ice Stream B. Contrast this with their

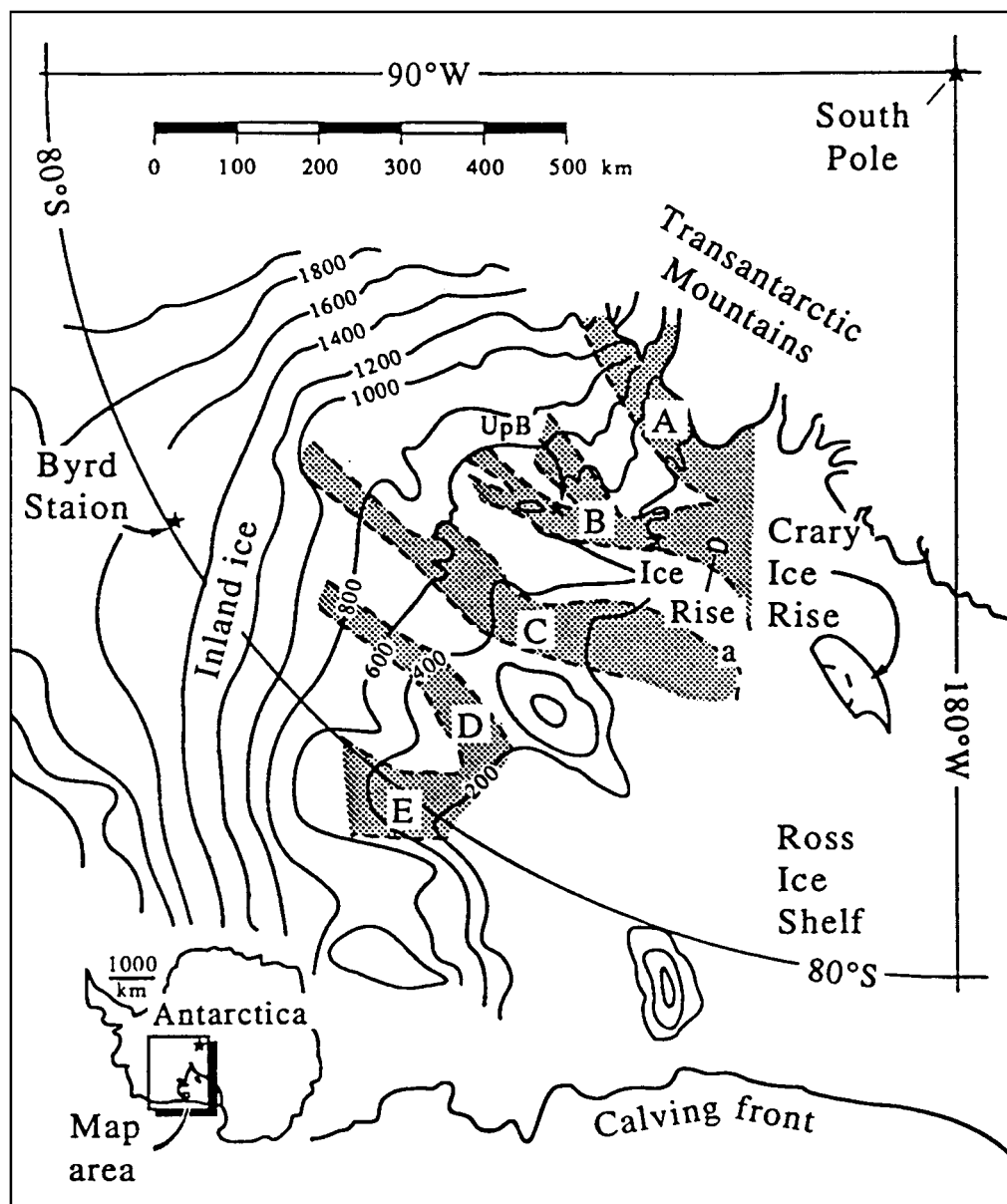


FIGURE 13 The Siple Coast region, West Antarctica, showing the ice streams. [Reprinted with permission from Alley, R. B., and Whillans, I. M. *Science* **254**, 959–963. Copyright 1991, American Association for the Advancement of Science.]

distribution along a flowline in South Greenland (Fig. 15). This has the shape expected from the discussion in Section IV. The driving stress increases from zero at the ice divide, where the surface is horizontal, to about 100 kPa at 50 km along the flowline; this value is maintained until the ice thins near the terminus. The velocity is a maximum at the equilibrium line at 165 km. Along the West Antarctic flowline, however, the ice moves fastest (up to 825 m/yr) in the ice stream although driving stresses there are so low (10–20 kPa) that ice deformation must be insignificant.

Seismic sounding, confirmed later by observations in boreholes, showed that the ice is underlain by about 6 m of water-saturated sediment. Moreover, water levels in the boreholes indicated subglacial water pressures of about 95% of those needed to float the ice. These ice streams are believed to move by bed deformation, although the possibility of a contribution from sliding has not yet been excluded by down-borehole measurements. Indeed, water-lubricated sliding is likely in the 200-km-long “transition zone” between Ice Stream B and the ice shelf.

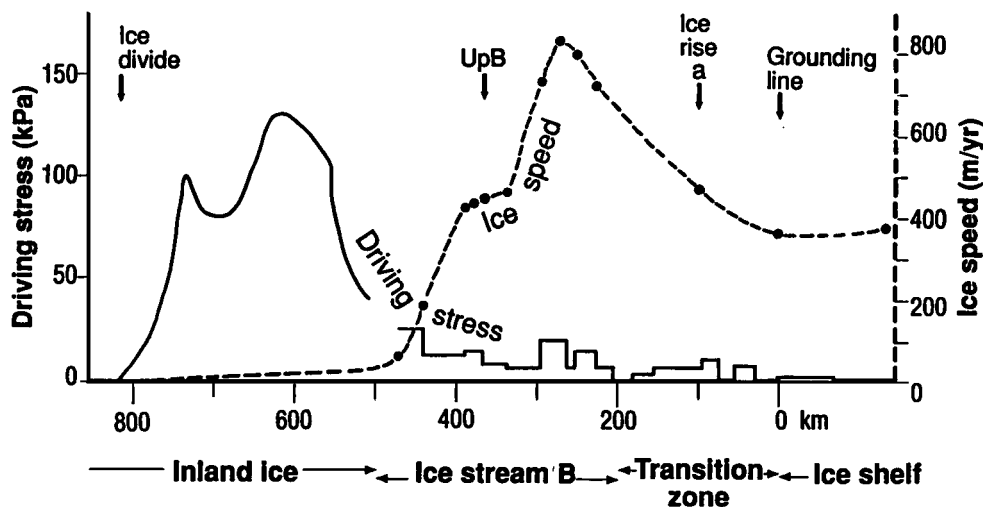


FIGURE 14 Driving stress and surface velocity along a West Antarctic flowline that includes Ice Stream B. [Reprinted with permission from Alley, R. B., and Whillans, I. M., *Science* **254**, 959–963. Copyright 1991, American Association for the Advancement of Science.]

These ice streams are not in a steady state. The head of Ice Stream B is migrating upstream by incorporating blocks of slow-moving inland ice. It is also growing wider by drawing in previously near-stagnant ice at the sides. Ice Stream A is thinning. Although Ice Stream C is stagnant at present, radar scattering has revealed extensive crevasses, indicating previous activity, buried under about 150 yr of snowfall. Capture of ice, or possibly of subglacial water, by Ice Stream B has been suggested as the cause of its shutdown. Because it is stagnant, it is now thickening at the annual accumulation rate. The ice shelf downstream is thinning, however, and the grounding line is retreating.

A marine ice sheet such as the West Antarctic Ice Sheet may be unstable against grounding-line retreat. If the sea bed slopes down toward the center of the ice sheet, any decrease in ice thickness at the grounding line will cause it to retreat into deeper water; the retreat will therefore continue. This picture is oversimplified because the back pressure of the ice shelf is ignored. (See Section V.)

An ice shelf is particularly sensitive to climatic warming because its surface is only a few hundred meters above sea level and, in addition, warming of the ocean would increase melting at its base. Ice shelves in the northern part of the Antarctic Peninsula, the warmest part of the continent and where the temperature has increased by 2°C in the last 50 yr, are already disintegrating. Could the reduction in back pressure resulting from the shrinking of an ice shelf cause an irreversible increase in flow from the grounded ice?

Near the grounding line, ice-shelf back pressure is the main restraint to flow in an ice stream. Farther upstream, however, side and basal drag are important. The amount of drag exerted by the slow-moving ice on either side can be estimated from the way in which velocity varies across the ice stream. Although the drag of water-saturated sediments must be very small, there is significant basal drag at “sticky spots” where nonlubricated bedrock projects through the sediments. The relative importance of these forces on the Siple Coast ice streams is being investigated in the field and by numerical modeling. Until more results are obtained, the extent to which a reduction in back pressure would increase flow in an ice stream, and thus whether the West Antarctic Ice Sheet may be unstable, will remain uncertain. Any disintegration would be spread over at least

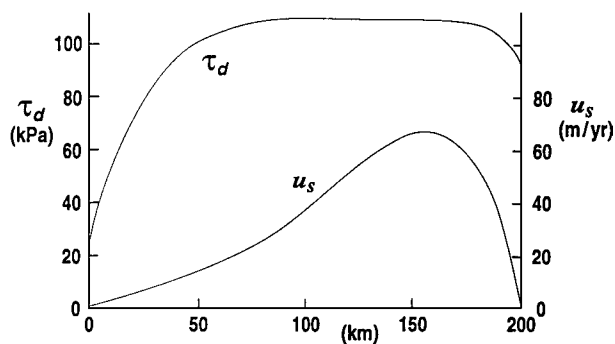


FIGURE 15 Driving stress and surface velocity along a typical flowline in south Greenland. [Reprinted with permission from Paterson, W. S. B., Some Aspects of the Physics of Glaciers. In “Ice Physics and the Natural Environment” (J. S. Wettlaufer, J. G. Dash, and N. Untersteiner, eds.), pp. 69–88, Copyright 1998, Springer-Verlag, Berlin.]

a few hundred years and no dramatic change is expected during this century.

Raised beaches and marine deposits indicate that world sea level was about 6 m higher than at present during the last interglacial about 125 kyr ago. This amount of additional water could have come only from Greenland or Antarctica. (See Table I.) West Antarctica seems the most likely source, although part of the East Antarctic Ice Sheet is also grounded below sea level and might have contributed. Disintegration of the Greenland Ice Sheet is unlikely; it is not a marine ice sheet and outflow is restricted by coastal mountains. On the other hand, a recent interpretation of some ice-core data suggests that southern Greenland was ice-free during the last interglacial. If this is correct, some ice must have remained in West Antarctica, otherwise the rise in sea level would have exceeded 6 m.

IX. GROWTH AND DECAY OF GLACIERS

Glaciers normally respond stably to small changes in climate. In a steady-state glacier, annual accumulation exactly balances annual ablation and the thickness and terminus position do not change. If snowfall increases, or summers become colder so that ablation is reduced, the glacier starts to thicken and its terminus advances because the ice flux there exceeds the ablation. In the absence of further change in climate, the glacier eventually reaches a new steady state. Similarly, reduced precipitation or increased ablation eventually leads to a new, smaller, steady-state glacier.

Advances and retreats of glaciers in any one area appear to be broadly synchronous. For example, most European glaciers attained their maximum postglacial positions in the seventeenth and eighteenth centuries, whereas the period since 1850 has been characterized by general retreat, interrupted by a few brief advances. Detailed records reveal a more complicated picture: a 1981 survey of Swiss glaciers showed that 52 were advancing, 5 were stationary, and 42 were receding. Cases are known in which one of two adjacent glaciers has the steep heavily crevassed terminus typical of an advance, while the other has the smooth gently sloping terminus that indicates stagnation or retreat. See Fig. 1. Some of these variations undoubtedly result from differences in local climates. However, glaciers differ in size, steepness, and velocity, so it is hardly surprising if they react differently, or at least at different rates, to climatic changes.

The effect of an increase in mass balance is propagated down the glacier as a bulge of increased thickness (*a kinematic wave*) moving faster than the ice itself. The existence of this type of wave is a consequence of mass conservation when there is a relation between flux (mass flowing past a

point in unit time), concentration (mass per unit distance, in this case ice thickness), and position. The concept of kinematic waves has also been useful in studying flood waves on rivers and traffic flow on highways. Kinematic waves should not be confused with dynamic waves such as ocean waves; these depend on Newton's second law, combined with a relation between force and displacement. Dynamic waves do not occur on glaciers because ice velocities are so low that the inertia term in the equation of motion can be neglected in comparison with the gravity and "viscous" terms.

The equation of mass conservation can be written as

$$\frac{\partial h}{\partial t} = b - \frac{\partial q}{\partial x}. \quad (13)$$

Here q is ice flux (ice thickness h multiplied by depth-averaged velocity u), x is distance along the glacier, t is time, and b is mass balance. This equation expresses the fact that, in a steady state, the difference between the fluxes flowing into and out of a narrow vertical column must be equal to the amount of ice added to or removed from the surface in unit time. If these terms are not equal, their difference is the rate at which the thickness of the column is changing with time. The velocity is written as the sum of ice deformation and basal motion [Eqs. (9) and (10) or (12)]:

$$u = Ch^4\alpha^3 + B(h\alpha)^2. \quad (14)$$

Here B and C are constants, α is surface slope, and a flow-law index $n = 3$ has been used. The kinematic wave equation is derived by linearizing Eqs. (13) and (14). The wave velocity is about four times the ice velocity. The dependence of ice velocity on surface slope results in diffusion of the waves. Mass balance changes are assumed to be small. Thus the theory cannot be applied to problems such as the growth and decay of ice-age ice sheets.

Have kinematic waves been observed on glaciers? Yes, but not very often. Precise measurements of surface elevation over several years are required, and because a glacier is continually adjusting to a complex series of seasonal and long-term variations, a single wave is exceptional. Moreover, diffusion lengthens the waves and reduces their amplitude.

Because the change in ice flux resulting from a change in mass balance accumulates down-glacier, the level of the upper part of the glacier does not change much whereas that of the lower part does. Lateral moraines are often close to the present glacier surface in the accumulation area, but far above it near the terminus.

Two important questions, how far the terminus moves and how long the glacier takes to adjust to the new mass balance (the *response time*), can be answered without considering how thickness changes are propagated along the

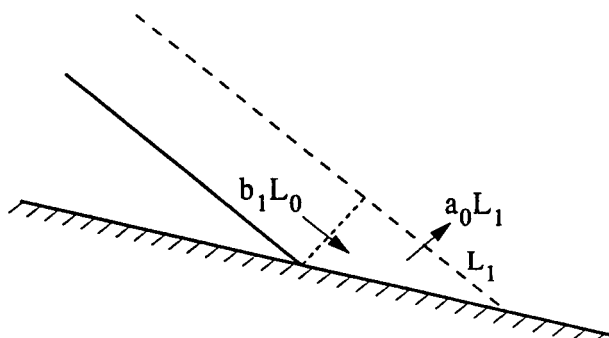


FIGURE 16 The relation between thickening and advance of a glacier terminus.

glacier. In Fig. 16, L_0 is the initial length of the glacier and $L_0 + L_1$ its length after it has adjusted to a change b_1 in mass balance. The original ablation rate at the terminus is a_0 . After the mass balance has been $b_0 + b_1$ for a long time, there will be a flux per unit width of $b_1 L_0$ at the old terminus, where b_1 is averaged over the length of the glacier. The terminus will have advanced the distance L_1 required to remove this flux by ablation. If $a_0 = -b_0(L_0)$ is the ablation rate at the terminus, then

$$\frac{L_1}{L_0} = \frac{b_1}{a_0}. \quad (15)$$

Thus if the ablation rate at the terminus is 5 m/yr, and the mass balance increases uniformly by 0.5 m/yr, the glacier's length will eventually increase by 10%. In two dimensions, the lengths L are replaced by areas S .

The response time is equal to the “filling time,” the time t that the perturbation in mass balance takes to accumulate or remove the difference V_1 between the steady-state volumes of the glacier before and after the mass-balance change. This is $V_1/b_1 S_0$. To a first approximation $V_1 = HS_1$, where H is the average thickness of the glacier. It follows from Eq. (15), written in terms of areas, that $t = H/a_0$. This formula gives response times of 15–50 yr for glaciers in temperate climates, 250–1000 yr for cold ice caps such as those in Arctic Canada, and roughly 3000 yr for the Greenland Ice Sheet. Getting data to test these predictions is difficult because any glacier is continually adjusting to a complicated history of mass-balance changes.

The general glacier response problem is to predict the ice thickness at every point and how it changes with time for a given bedrock configuration and any specified time-dependent values of accumulation and ablation. To remove the restriction to small perturbations inherent in the kinematic wave analysis, and to deal with the complicated geometry of a real glacier, numerical solutions are needed. The two-dimensional form of Eq. (13), with veloc-

ity specified by an equation such as Eq. (14), is integrated to give the ice thickness at each grid point and at each time step. Problems that have been addressed include assessing the risk that Griesgletscher in Switzerland, which ends in a lake, will advance far enough to destroy a dam, and predicting how global warming will change the amount of runoff from Hofsjökull in Iceland, which feeds a hydroelectric plant. The inverse problem, to estimate recent changes in mass balance and climate from data on glacier retreat, has also been tackled.

Only in temperate glaciers is the effect of a climatic change restricted to a change in mass balance. In cold glaciers, long-period changes in surface temperature eventually change the temperature and therefore the deformation rate of the ice at depth. Again, the position of the terminus of a tidewater glacier is affected by a change in sea level. Because each of these processes has its own characteristic response time, the overall response of the glacier is complex. All these effects have been taken into account in numerical models of the growth and decay of the Greenland and Antarctic ice sheets through a glacial cycle. Their response to global warming has also been predicted.

Figure 17 presents data on how world ice volume has varied during the past 800 kyr. Variations with periods of about 20, 40, and 100 kyr, as predicted by the *Milankovitch hypothesis*, are apparent. This hypothesis ascribes the glacial cycle to variations in the amount of solar radiation received at northern latitudes in summer. These variations result from the precession of the earth's axis (period 20 kyr), variations in the tilt of the axis relative to the plane of the earth's orbit (40 kyr), and variations in the eccentricity of the orbit (100 kyr). Although there are times when the ice sheets are growing rapidly, the general feature of Fig. 17 is a slow buildup of ice, followed by rapid decay. At the end of the last ice age, for example, world sea level rose by about 125 m in 8000 yr. This represents melting of some $57 \times 10^6 \text{ km}^3$ of ice.

The volume of an ice sheet of circular plan and parabolic profile on a horizontal base can be shown to be $0.53\pi L^2 H$ with $H = KL^{1/2}$. Here L is the radius, H is the maximum thickness, and K is a constant. If V denotes volume and t time, then

$$\frac{dV}{dL} = 1.325\pi K L^{3/2} \left(\frac{dL}{dt} \right). \quad (16)$$

But this must be equal to $\pi L^2 c$, where c is accumulation rate, assumed to be uniform over the whole ice sheet. This gives a differential equation for the growth time with solution

$$t = \frac{2.65(H - H_0)}{c}, \quad (17)$$

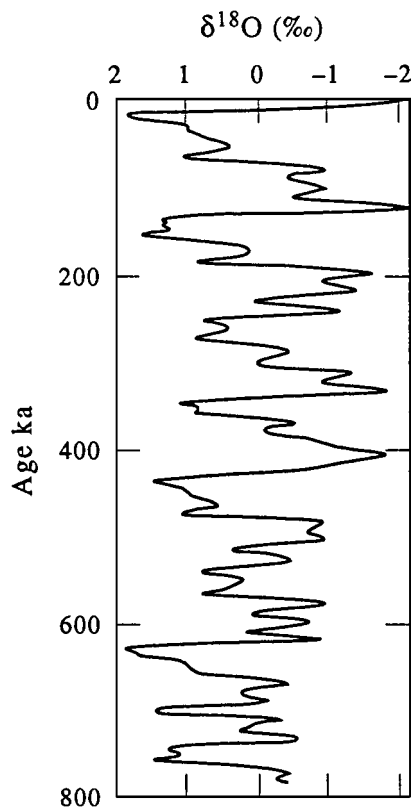


FIGURE 17 Variations in oxygen-isotope ratio in fossil foraminifera in ocean cores, a proxy for world ice volume, over the past 800 kyr. Units are standard deviations from the mean. Ice sheets are large when δ is positive. [Reproduced with permission from Ruddiman, W. F., and Wright, H. E., Jr. (eds.), “North America and Adjacent Oceans during the Last Deglaciation.” Copyright 1987, Geological Society of America.]

where subscript 0 denotes the initial value. This is a minimum growth time because it is assumed that there is no ablation. Similarly, the minimum decay time under ablation rate a is

$$t = \frac{2.65(H_0 - H)}{a} \quad (18)$$

Equation (18) predicts that to remove an ice sheet, initially 3000 m thick at the center, in 8000 yr would require an average ablation rate of 1 m/yr over the whole ice sheet, with no accumulation.

Because ablation rates are usually about three times accumulation rates on the same glacier, these equations predict that an ice sheet should take about three times as long to build up as to decay. In reality, the difference is much greater than this. Entry of the sea into Hudson Bay and the Baltic was an important factor in the decay of the Laurentide and Fennoscandian ice sheets, as was calving of icebergs into huge ice-dammed lakes around the southern margins and their catastrophic draining under the ice.

X. UNSTABLE FLOW

A few glaciers exhibit a spectacular type of instability called a surge. Unlike normal glaciers, in which the mean velocity varies little from year to year, surging glaciers alternate between an active period, usually 1–3 yr, in which they move at speeds 10–1000 times normal, and a quiescent period roughly 10 times as long. Surge velocities are so high (65 m/day briefly in one case) that they must result from basal motion. A surge transfers a large volume of ice from a reservoir area, where the surface may drop 50–100 m, to a receiving area where the ice thickens by a similar amount. These are not the same as the accumulation and ablation areas; many surges do not extend to the head of the glacier. Typically, the ice in the lower part moves forward several kilometers during a surge. This, however, represents reactivation and thickening of previously stagnant ice, not an advance beyond the previous limits of the glacier. The surface of a surging glacier is a chaotic array of crevasses and ice pinnacles, and deep longitudinal faults separate the ice from the valley walls. During the quiescent period, ice flow cannot keep pace with accumulation and ablation; the upper part of the glacier thickens while the terminal area melts down and stagnates. As a result, the surface slope steepens until a critical value, which appears to trigger the next surge, is reached. Many surging glaciers are distinguished by medial moraines that, instead of being parallel to the valley walls, are deformed into large bulblike loops formed by ice flow from a tributary while the main glacier is quiescent. The fact that surges occur at regular intervals in the same glacier suggests that they result from some internal instability.

Surging glaciers are found only in certain areas. Most of the roughly 200 in western North America lie near the Alaska–Yukon border. There are none in the United States outside Alaska, nor in the Coast, Selkirk, or Rocky Mountains in Canada. Other regions with surging glaciers include the Pamirs, Tien Shan, Caucasus, Karakoram, Chilean Andes, Iceland, Svalbard, and Greenland. The distribution of surging glaciers in any region is not random, and glaciers that originate in the same ice cap do not necessarily surge at the same time. Glaciers of all sizes can surge, although there appears to be a preponderance of relatively long glaciers.

To find one mechanism that can explain all surges may be difficult or even impossible. Surging glaciers show a variety of characteristics and only three, Medvezhiy Glacier in the Pamirs, Variegated Glacier in Alaska, and Trapridge Glacier in the Yukon, have been observed in detail. A surge apparently results from disruption of the subglacial drainage system so that water is stored at the bed, producing rapid sliding or bed deformation.

The surge of Variegated Glacier was characterized by high basal water pressure, measured by the water level in boreholes, and by greatly reduced flow in the streams at the terminus. For occasional brief periods, which coincided with pulses of exceptionally high velocity, the basal water pressure exceeded that of the overlying ice. Periodic floods from the outflow streams correlated closely with abrupt decreases in velocity. The end of the surge was marked by a particularly large flood, and the glacier surface dropped by about 0.2 m.

These observations suggest that the normal subglacial tunnel system was destroyed so that all the water was transferred to linked cavities. (See Section VI.) Accumulation of water at high pressure in cavities in the lee of bedrock bumps would permit rapid sliding. This would in turn tend to close the narrow passageways connecting the cavities and thus maintain the high water pressure. Why the tunnel system is destroyed and how it is reestablished at the end of the surge is not clear. Rapid sliding rather than bed deformation must prevail in Variegated Glacier because the driving stress remained at a normal value of around 100 kPa during the surge. This mechanism could also explain the surge of Medvezhiy Glacier. Because Variegated Glacier is temperate and the base of Medvezhiy Glacier is at melting point all the time, a thermal mechanism of surging (alternate melting and freezing of the glacier bed) cannot apply to them.

Trapridge Glacier, which has been observed only during its quiescent period, is markedly different from the other two. It is less than 100 m thick and has a "soft" bed, deformation of which contributes more than half the forward motion of the glacier. Sliding at the ice–till interface accounts for most of the remainder. At the base, a central area of melting ice is surrounded by ice frozen to the bed, a type of temperature distribution found in many nonsurging glaciers as well. Although fast flow seems unlikely unless the whole bed is at melting point, there is no evidence that the melting area is spreading. Although near-surface temperatures in the glacier range from -4 to -9°C , large quantities of surface meltwater penetrate to the bed. Thus disruption of the subglacial drainage system may still be the cause of surges in this glacier, but the detailed mechanism is unclear. A "soft" bed has no fixed bumps behind which cavities can form. Water is not being trapped at the boundary between the frozen and melting sections of the bed; it drains away through the lower unfrozen layers of till. Destruction of drainage channels within the till would increase the pore-water pressure and therefore the deformation rate. However, till is a dilatant material; deformation increases its permeability. Thus more of the water would drain away and reduce the pore pressure. It is difficult to see how fast deformation could be maintained.

Much has still to be learned about the mechanism of surging, particularly in glaciers with "soft" beds. The fact that most surging glaciers are in young mountain ranges subject to rapid erosion suggests that bed deformation may be an important factor in many surges.

Glaciers that end in fiords can also behave unstably. Shoals, headlands, and narrow parts of the channel can anchor the terminus. A slight retreat from the anchor point reduces the back pressure on the terminus, so that the ice velocity increases and the glacier thins. This can lead to a catastrophic breakup of the glacier tongue, even if the water is not deep enough to float the ice. The terminus then retreats to the next anchor point. Columbia Glacier in Alaska began such a retreat in 1983 that will, according to current estimates, amount to 30–40 km within the next few decades. The resulting icebergs are a threat to tankers at the Alaska pipeline terminal at Valdez.

Can ice sheets surge? If they do, the features may be somewhat different from those observed in glaciers in temperate and subpolar regions. In contrast to the limited reservoir area of a valley glacier, outlet glaciers and ice streams in Greenland and Antarctica may be able to keep drawing ice from an increasing area of the ice sheet. In this case their active periods would be much longer than the 1–3 yr typical of valley glaciers. Moreover, because precipitation is low, the time taken to refill the reservoir area may be hundreds or even a few thousand years. The ice-age climate in the North Atlantic region was characterized by the so-called *Dansgaard-Oeschger events*: cycles of slow cooling followed by rapid warming with periods of 500 to 2000 yr, accompanied by changes in precipitation rate. (See Section XI.) A regular interval between surges is not expected in these circumstances.

The mechanisms may also be different. A large seasonal influx of surface meltwater to the bed is an important part of the mechanism of known surges and seems to control their timing. In Antarctica, all the water at the bed of the ice sheet is generated there, presumably at a constant rate. In Greenland, although summer melting is extensive on the lower parts of the outlet glaciers, the lack of seasonal variations in their velocity suggests that surface water does not penetrate to the bed.

There is evidence that parts of the Laurentide Ice Sheet in North America behaved unstably. The sediment record from the North Atlantic between latitudes 40 and 55°N contains six layers of detrital carbonate, deposited rapidly at irregular intervals between about 65 and 14 kyr B.P. (before present) at times when the surface water was exceptionally cold and had low salinity. The layers are thick in the Labrador Sea and western North Atlantic and thin steadily further east. Their deposition is attributed to exceptionally large discharges of icebergs (*Heinrich events*) from the Hudson Bay sector of the ice sheet. These events,

each of which probably lasted not more than 1000 yr, would have a major effect on the deep-water circulation in the North Atlantic and thus on the climate of the region.

Periodic warming of the base of the ice to melting point is the likely mechanism of this instability. During the quiescent period, snow accumulation thickens the ice sheet and the basal temperature rises because the geothermal gradient at the base exceeds the atmospheric lapse rate at the surface. When the melting point is reached, water pressure builds up and permits rapid sliding and bed deformation, followed by advance of the terminus and a massive discharge of icebergs. The rapid advance thins the ice and so increases the temperature gradient in it. The increased heat conduction cools the basal ice until it eventually refreezes and the rapid flow stops. This is a plausible mechanism, although it does not apply to any current surge. A freeze-thaw cycle seems necessary to incorporate debris into the basal ice. However, the fact that some debris was carried far across the Atlantic seems to require that it was dispersed throughout the ice thickness. How this could happen is unclear.

Geologic evidence indicates that some of the southern lobes of the Laurentide Ice Sheet, which had the low surface slopes and driving stresses characteristic of glaciers moving largely by bed deformation, also made periodic rapid advances.

XI. ICE CORE ANALYSIS

A core taken from a polar ice sheet provides a record of snowfall and, through its chemistry, of past climate and also of atmospheric fallout such as windblown dust, pollen, volcanic deposits, sea salts, extraterrestrial particles, and trace elements resulting from both natural causes and pollution. In addition, the air bubbles are samples of the atmosphere at the time the ice was formed. If the core is from a region where the surface never melts, the record is continuous, except for the lowest 5–10%, which may be disturbed by folding, faulting, or movement along shear planes in the ice near the bed. Cores covering the last ice age have been recovered in Greenland and Arctic Canada, while the longest Antarctic core covers several glacial cycles. For such records to be of much value, the age of the ice at different depths (the “time scale”) must be determined.

The most important climatic parameter is the oxygen-isotope ratio ($^{18}\text{O}/^{16}\text{O}$) or, equivalently, the ratio of deuterium to hydrogen in the ice. This depends on the air temperature when the snow fell. The measure used is

$$\delta = \frac{1000(R_s - R_0)}{R_0}, \quad (19)$$

where R_s and R_0 are the ratios of the concentrations of the heavy to the light isotope in the sample and in standard mean ocean water. The relation of δ to temperature can be explained by the slight reduction in vapor pressure of the heavy components. The isotopic composition of water changes during natural cycles of evaporation and condensation because the molecules of H_2^{18}O evaporate less rapidly and condense more readily from the vapor than those of H_2^{16}O . Thus vapor evaporating from the sea surface is slightly depleted in ^{18}O . As an air mass containing ocean vapor travels toward the polar regions, it is cooled strongly and loses considerable amounts of precipitation. It therefore becomes progressively more depleted in ^{18}O , that is, δ becomes more negative. There are also seasonal variations. Figure 18 confirms that δ is correlated with mean annual air temperature in Greenland and Antarctica, although different regression lines are required for the different ice sheets, and the relation breaks down at elevations below 1000 m. The scatter of the Antarctic data arises because precipitation in different parts of the ice sheet comes from different source areas.

Variations of δ with depth are interpreted as past variations of surface temperature. The regression lines should not be used to convert δ to temperature, however, because changes in atmospheric circulation patterns, in the seasonal distribution of snow, or in the isotopic composition of the oceans can also change the value of δ . The relation between δ and temperature is derived by using the measured temperature profile in the borehole, as described in Section VII. Unless the borehole is at an ice divide, the record has to be corrected for the flow of isotopically colder ice from upstream.

Figure 19 shows the record from the highest part of the Greenland Ice Sheet. A remarkable feature of the ice-age section is the *Dansgaard-Oeschger events*: the switches of temperature by up to 10°C every 500 to 2000 yr. The change from cold to warm occurs in 100 yr or less, while that from warm to cold is more gradual. The temperature oscillations are accompanied by oscillations in precipitation rate and in concentrations of impurities in the core. The driving force may be changes in circulation and deep-water formation in the North Atlantic.

The lowest 6 m of the Summit core, not included in Fig. 19, consists of silty ice with δ values less negative (i.e., warmer) than any others in the core. This ice also contains extremely high concentrations of CO_2 (up to 130,000 parts per million by volume) and methane (up to 6000 ppmv) and levels of oxygen as low as 3%. Such concentrations preclude a direct atmospheric origin, but could result from *in situ* oxidation of organic matter. Comparable concentrations of CO_2 and CH_4 have been measured in ice layers in Alaskan permafrost. Thus it appears that this basal ice formed locally within a peat deposit in permafrost, in the

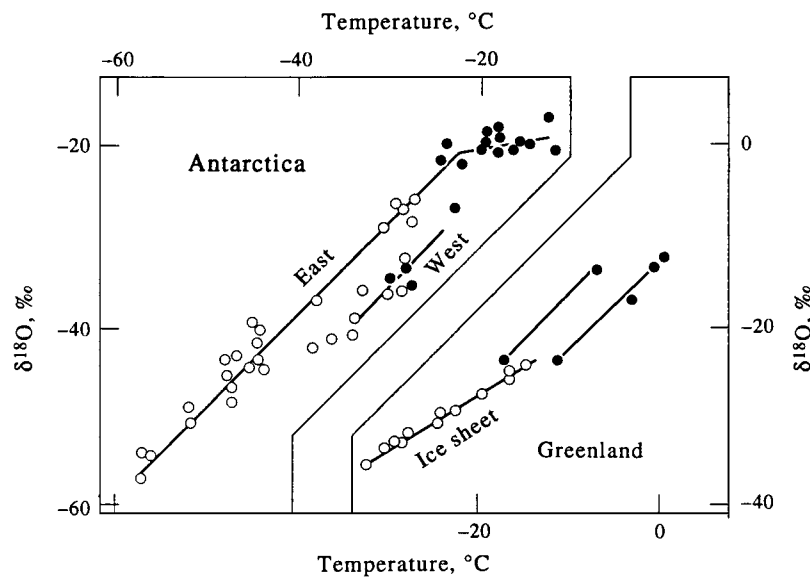


FIGURE 18 Present relation between oxygen-isotope ratio and mean annual air temperature for stations on the (a) Antarctic and (b) Greenland ice sheets. Open circles refer to elevations above 1000 m. [Adapted with permission from Dansgaard, W., et al. (1973). *Medd. Groen.* **197**(2), 1–53. Copyright 1973, Commission for Scientific Research in Greenland, Copenhagen.]

absence of an ice sheet. The glacier ice immediately above must have flowed on to the site later, probably from the mountains on the east coast. The marine-sediment record suggests that the ice sheet originated about 2.4 million years ago.

Major volcanic eruptions inject large quantities of silicate microparticles and acid gases into the stratosphere. The microparticles settle out and apparently do not reach Greenland in detectable amounts, although ash from local volcanoes has been found in Antarctic cores. Eruptions are recorded in Greenland by ice layers of increased acidity (Fig. 20). Tambora in Indonesia erupted in 1815. The acid fallout in Greenland reached a peak in 1816, which is described in historical records as “the year without a summer” in eastern North America. The cooling is believed to result from back scattering of solar radiation by a sulfate aerosol, mainly sulfuric acid, that builds up from the SO₂ produced in the eruption. Acidity measurements on Greenland cores have extended the volcanic record back to 8000 B.C. Earlier eruptions cannot be detected because the ice-age ice is alkaline. This ice contains much higher concentrations of microparticles, largely wind-blown dust rich in CaCO₃, than ice deposited since. The increase in dust has been attributed to the increased area of continental shelf exposed by the fall in sea level, combined with more vigorous atmospheric circulation.

Figure 20 shows pronounced seasonal variations in oxygen-isotope ratio and also in acidity and nitrate concentration, although these are less well defined. The dates

were obtained by counting those annual layers down from the surface.

Past changes in the amount of CO₂ and CH₄ in the atmosphere are recorded in the air bubbles in the ice. Figure 21 shows the record from Vostok, which lies at an elevation of 3490 m in the central part of East Antarctica. The record covers the Holocene, the last ice age, the preceding interglacial, and most of the previous ice-age. The temperature record shows oscillations with periods of 20 and 40 kyr and also the rapid endings of the last two ice ages roughly 100 kyr apart, as predicted by the Milankovitch hypothesis. The CO₂ record shows trends similar to the temperature record, with concentrations as low as 180 ppm during ice ages and high concentrations when it is warm. Although the increase in CO₂ was probably a result, not a cause, of the end of the ice age, the greenhouse effect would undoubtedly amplify the warming trend. Figure 21 also shows a major increase in the concentration of methane, another greenhouse gas, at the end of an ice age. Ice-core records show that the concentration of CO₂ remained at about 280 ppm between the end of the last ice age and the start of the industrial era (1750 A.D.) and has increased steadily since then. It had reached 360 ppm by 1995.

Drilling at Vostok was terminated at a depth 3623 m. Glacier ice, estimated to be about 425 kyr old, ended at 3540 m. Below that was about 200 m of ice, with crystals up to 1 m in diameter, formed by the freezing on of water from a subglacial lake. Vostok is situated over such a lake,

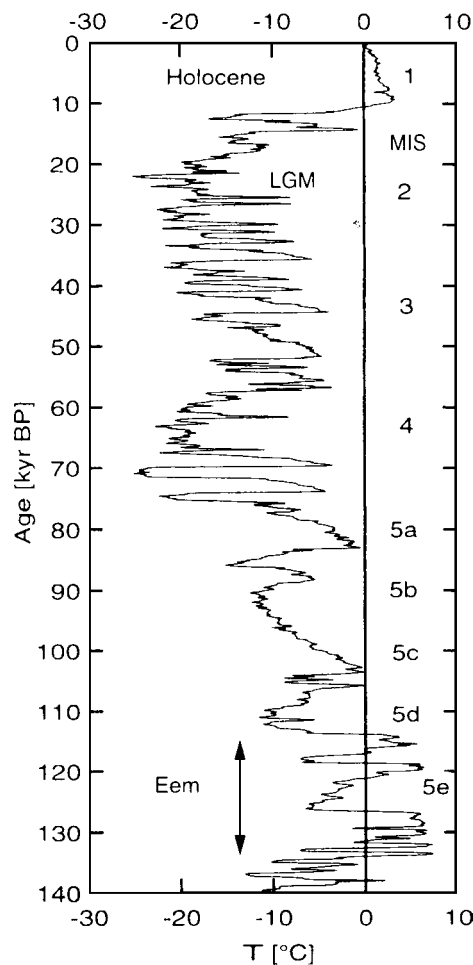


FIGURE 19 Past temperatures in central Greenland based on oxygen-isotope ratios in the 3029-m core to bedrock at Summit. The record in ice older than 110 kyr, the lowest 230 m of core, is unreliable because the stratigraphy is disrupted. The numbers on the right denote stages in the marine isotopic record. [Reprinted with permission from Johnsen, S. J., et al., “Stable Isotope Records from Greenland Deep Ice Cores: The Climate Signal and the Role of Diffusion.” In “Ice Physics and the Natural Environment” (J. S. Wettlaufer, J. G. Dash, and N. Untersteiner, eds.), pp. 89–107, [Copyright 1998, Springer-Verlag, Berlin.]

the largest of about 80 in East Antarctica, which have been discovered by radar sounding. Its area is comparable with that of Lake Ontario and it is over 500 m deep. Drilling was stopped about 120 m above the lake surface to avoid contaminating it with drilling fluid. However, plans are now being made to sample the lake for microbes and other possible forms of life.

Ice cores are valuable for pollution studies because the preindustrial background level of trace elements can be measured. The concentration of lead in northwest Greenland has increased by a factor of 3 since 1945; the source is tetraethyl lead in gasoline. Tests of atomic and nuclear bombs are recorded by radioactive layers, as is the burnup

of a U.S. satellite (SNAP-9A) containing ^{238}Pu in 1964 and the Chernobyl nuclear accident in 1986. The low radioactivity of 1976 snow, only 1.4% of the peak value, suggests that all the plutonium isotopes injected into the atmosphere by the tests have now been removed.

There are several methods of dating ice cores:

1. Counting annual layers, distinguished by seasonal variations in some property (Fig. 20).
2. Noting horizons of known age, such as acid layers from identified eruptions (Fig. 20).

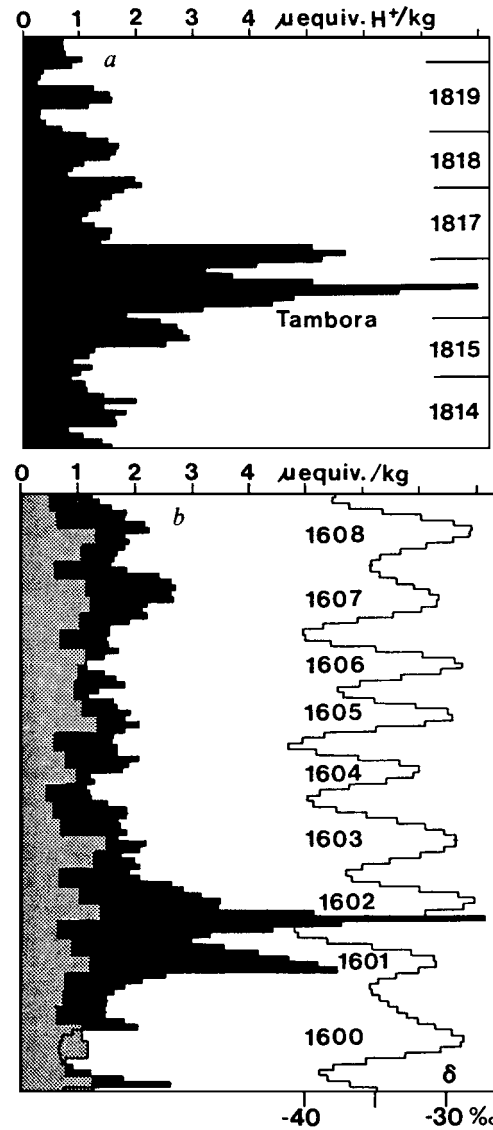


FIGURE 20 Acid fallout (black curves; scale on top) from two volcanic eruptions found in an ice core at Crête, Greenland. Seasonal variations in oxygen-isotope ratio (curve on right) and concentration of NO_3^- (shaded curve on left) are also shown in the lower diagram. [Reprinted with permission from Hammer, C. U., et al., *Nature* **288**, 230–235. Copyright 1980, Macmillan Magazines Ltd.]

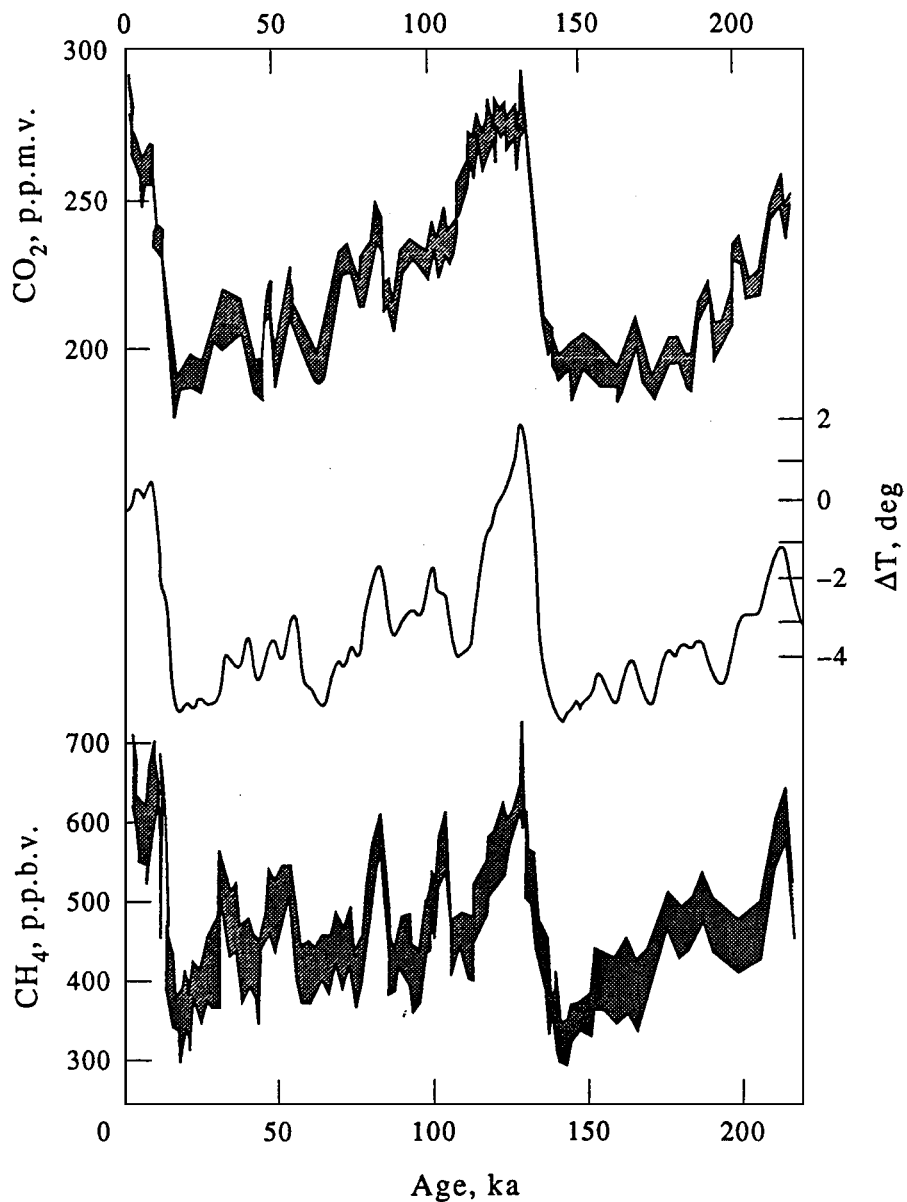


FIGURE 21 Atmospheric temperature relative to present (derived from δD) and atmospheric concentrations of CO₂ and CH₄ over the past 220 kyr measured in the core from Vostok. Shading indicates the uncertainty of the gas measurements. [Reprinted with permission from Jouzel, J., et al., *Nature* **364**, 407–412. Copyright 1993, Macmillan Magazines Ltd.]

3. Carbon-14 dating of CO₂ extracted from air bubbles in the ice.
4. Doing calculations based on ice-flow models.
5. Matching features of the oxygen-isotope record with some other dated climatic record such as an ocean-sediment core.

Counting annual layers is the most precise method. The only inaccuracy is the occasional uncertainty in identifying layers; this can usually be overcome by looking at

more than one property. Molecular diffusion smooths out variations in $\delta^{18}\text{O}$ after several thousand years, but variations in acidity and microparticle content are unaffected. However, because the layers become progressively thinner with increasing depth, a point is reached below which they cannot be distinguished. A drawback of this method is the time required; about eight samples per year must be measured. After one core has been dated in this way, however, the ages of recognizable horizons can be used to date others.

Ice-flow modeling is the most frequently used method and the only one available for planning before drilling. How the thickness of an annual layer changes with depth has to be calculated. The precision depends on the validity of the assumptions underlying the model and on how much is known about variations in accumulation rate and ice thickness in the past and upstream from the borehole. Accumulation rates are usually estimated by assuming that they are correlated with the temperatures deduced from measurements of $\delta^{18}\text{O}$.

The Summit core (Fig. 19) was dated back to 14.5 kyr B.P. by counting annual layers, and beyond that by a flow model. Parameters in the model were adjusted so that it gave correct ages for two independently dated events: the end of the Younger Dryas cold period at 11.5 kyr B.P. and the coldest part of marine isotope stage 5d at 110 kyr B.P. The comparable GISP-2 core, drilled 30 km west of Summit, was dated back to 110 kyr B.P. by counting annual layers; six properties were used to distinguish them. The precision was estimated at 1–10% down to 2500 m, where the ice is about 60 kyr old, and 20% from 2500 m to the 110-kyr horizon at 2800 m. The Vostok core (Fig. 21) was dated by a flow model, a more complicated one than that used at Summit because Vostok is not at an ice divide. The model was tuned to give correct dates at the same two

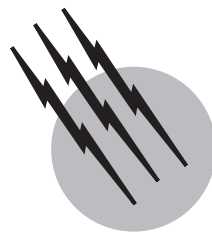
points as at Summit. The estimated uncertainty at 260 kyr B.P. is 25 kyr.

SEE ALSO THE FOLLOWING ARTICLES

CLIMATOLOGY • COASTAL GEOLOGY • GEOMORPHOLOGY • GLACIAL GEOLOGY AND GEOMORPHOLOGY • GREENHOUSE EFFECT AND CLIMATE DATA • HYDROGEOLGY • STREAMFLOW

BIBLIOGRAPHY

- Benn, D. I., and Evans, D. J. A. (1998). "Glaciers and Glaciation," Wiley, New York.
- Hambrey, M., and Aleen, J. (1992). "Glaciers," Cambridge University Press, Cambridge, U.K.
- Hammer, C., Mayewski, P. A., Peel, D., and Stuiver, M. (eds.) (1997). "Greenland Summit Ice Cores." Special volume reprinted from *J. Geophys. Res.* **102**, C12, 26315–26886, American Geophysical Union, Washington, DC.
- Paterson, W. S. B. (1994). "The Physics of Glaciers," 3rd ed., Elsevier Science, Oxford, U.K.
- Petrenko, V. F., and Whitworth, R. W. (1999). "Physics of Ice," Clarendon Press, Oxford, U.K.
- Post, A., and LaChapelle, E. R. (2000). "Glacier Ice," rev. ed., University of Washington Press, Seattle, WA.



Hydrogeology

Leslie Smith

University of British Columbia

- I. Basic Concepts of Groundwater Flow
- II. Groundwater Contamination
- III. Role of Groundwater in Geologic Processes

GLOSSARY

Aquifer Permeable geologic unit that can transmit significant quantities of water under ordinary hydraulic gradients.

Aquitard Geologic unit that, although saturated, cannot transmit appreciable quantities of water because of its lower permeability.

Hydraulic head Potential quantity controlling flow, equal to the elevation of the water level in a piezometer.

Lithostatic pressure Downward force exerted by the weight of overlying geologic units, measured at a given depth beneath the earth's surface.

Permeability Capacity of a porous medium to transmit fluids.

Piezometer Instrument installed within a borehole to measure hydraulic head.

Saturated zone Region below the water table where all voids are filled with water and fluid pressures exceed atmospheric pressure.

Vadose zone Region between the ground surface and the water table where voids contain both water and air and fluid pressures are less than atmospheric pressure.

Water table Surface separating the vadose and saturated zones; fluid pressure is equal to atmospheric pressure.

HYDROGEOLOGY is concerned with the movement of water through the subsurface geologic environment, the chemical evolution of the water along its flow path, and the influence of subsurface water on geologic and geodynamic processes occurring in the upper crust of the earth. It involves both the development of groundwater resources as water supplies and the protection of that resource from contamination. Groundwater is the source of drinking water for more than 50% of the population of the United States. The extent to which groundwater supplies have been, or potentially are, at risk to contamination by toxic chemical or radioactive wastes is a focus of considerable scientific and societal interest.

I. BASIC CONCEPTS OF GROUNDWATER FLOW

A. Principles

A basic property of both rocks and unconsolidated sediments is that they contain a network of void spaces through which water can flow. These voids may occur as pore spaces between grains and as microcracks joints or fractures. Open, well-connected voids occur with greatest frequency in the upper several kilometers of the earth's surface. As depth increases, the greater lithostatic pressure

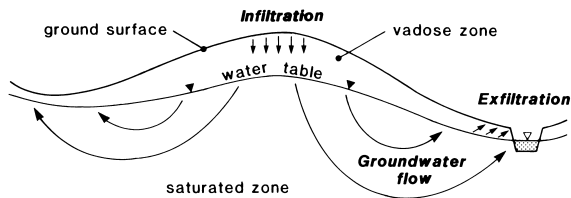


FIGURE 1 Schematic diagram of a groundwater flow system in a hillslope.

causes a reduction in the number and size of voids, but water originating at the earth's surface has been observed in boreholes that have penetrated to depths of 12 km.

Figure 1 is a schematic diagram of a vertical section through a hillslope. It is convenient to divide the subsurface into two zones, the vadose zone and the underlying saturated zone, with the water table forming the boundary between them. Below the water table, pore spaces are saturated with water and fluid pressures exceed atmospheric pressure. In the vadose zone, liquid water, water vapor, and air are present in the pore spaces. Water preferentially wets the solid matrix. The resulting interfacial tension between water and air leads to pressures in the water that are less than atmospheric in the region above the water table.

Rainfall and melting snow recharge the groundwater system by infiltration through the vadose zone in topographically higher areas of a watershed. Discharge occurs at topographically lower elevations via springs, seeps, or exfiltration through the vadose zone. A representative set of flowlines that trace the patterns of fluid flow is shown in Fig. 1. The water table is commonly observed to be a subdued replica of the surface topography. Residence times can range from periods on the orders of days to years to thousands of years, possibly even millions of years. Factors that determine the residence time include the scale of the system, the travel path from recharge to discharge areas, and the nature of the geologic units underlying the watershed. Although rates of groundwater flow are substantially smaller than those associated with surface water systems, it is appropriate to view subsurface water as a dynamic, rather than static, system.

Groundwater moves through the void spaces in response to differences in fluid pressure and elevation. Driving forces are measured in terms of hydraulic head as follows:

$$h = Z + P/\rho g, \quad (1)$$

where, P is the pressure of a fluid with constant density ρ , Z is the elevation of the measurement point above datum, and g is the acceleration caused by gravity. By convention, pressure is expressed in terms of values above atmospheric pressure. The hydraulic head at a point (x, y, z) is equal to the mechanical energy per unit weight of the fluid. Intertial effects and contributions from kinetic energy can be neglected in almost all cases. Groundwa-

ter always flows from regions where the hydraulic head is higher toward regions where it is lower. By convention, pressure is expressed in terms of values above atmospheric pressure. Defining the pressure head as

$$\psi = P/\rho g \quad (2)$$

leads to the simple relationship

$$h = Z + \psi, \quad (3)$$

where Z is the elevation head.

Hydraulic head is measured in a piezometer (Fig. 2). Standpipe piezometers are constructed by installing plastic pipe inside a borehole, with an open screen connected to the end of the casing to permit fluid inflow to the piezometer. The diameter of the standpipe is normally in the range of 4 to 6 cm, with a screen length from 1 to 3 m. Sand is placed around the screen, and the annular space between the borehole wall and the casing is backfilled to the surface with either cement or bentonite clay. In this way, an isolated measurement of fluid pressure is obtained. Equation (3) is used to calculate hydraulic head at the measurement point. Hydraulic head is sometimes referred to as the piezometric head. More sophisticated instrumentation, such as multiport piezometers with electronic data acquisition systems, is also in use.

It is not practical to describe groundwater flow in terms of the complex geometry of void spaces and their interconnecting channels. A continuum approach must be adopted where the porous medium is characterized by variables defined as average values over a representative volume of the medium. The resulting coefficients that describe the macroscopic flow of water through a porous medium are determined experimentally, as described next.

The volumetric flow rate of groundwater through a block of soil or rock is calculated using Darcy's law as follows:

$$Q_i = \mathbf{K}_{ij} A \frac{\partial h}{\partial x_j}, \quad (4)$$

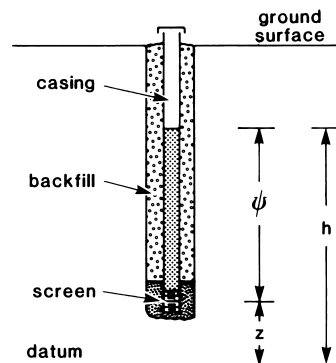


FIGURE 2 A piezometer, illustrating construction details and the measurement of hydraulic head.

where Q_i is the volumetric flow rate in coordinate direction i , A is a cross-sectional area for flow, \mathbf{K}_{ij} is the hydraulic conductivity tensor, and $\partial h / \partial x_j$ is the gradient in hydraulic head. Darcy's law is valid for laminar flow, a condition met in the great majority of hydrogeologic settings. Hydraulic conductivity characterizes the ability of the fluid to move through the interconnected void spaces in the sediment or rock; its value depends on both the properties of the medium and the fluid. To separate the effects of the medium from those of the fluid, another term is defined as follows:

$$\mathbf{K}_{ij} = \frac{\mathbf{k}_{ij}\rho g}{\mu}, \quad (5)$$

where \mathbf{k}_{ij} is permeability, μ is the viscosity of the fluid, and ρ is its density. Permeability is a property only of the porous medium. It has higher values for sands and gravels and lower values for silts and clays. Even within single geologic units, it is not uncommon for permeability to vary by several orders of magnitude over distances of several hundred meters because of spatial variations in grain size or fracture density. A number of techniques are available to estimate permeability. They include both laboratory measurements on borehole samples and *in situ* field tests. Table I is a summary of representative values of hydraulic conductivity of various geologic media, assuming water properties characteristic of near-surface environments.

If the hydraulic conductivity of a sediment or rock is independent of the direction of the hydraulic gradient, then the porous medium is isotropic and the vector describing the direction of groundwater flow is aligned with the direction of the hydraulic gradient. If the value of hydraulic conductivity is dependent on the orientation of the hydraulic gradient, then the medium is anisotropic. In an anisotropic medium, flow lines are not aligned with the direction of the hydraulic gradient but instead are rotated toward the direction of higher hydraulic conductivity.

An aquifer is a permeable geologic unit that can transmit significant quantities of water under ordinary hy-

draulic gradients. Sand and gravel deposits, sandstones, and highly fractured rocks are examples of geologic units that make good aquifers. Aquifers are valuable sources of water to meet agricultural, industrial, rural, and municipal requirements. Groundwater accounts for 35% of the water used for municipal supplies in the United States, 97% of the rural drinking water, 40% of the irrigation water, and 26% of the water used by industry (excluding thermoelectric power users).

There are two types of aquifers: unconfined aquifers and confined aquifers. The upper boundary of an unconfined aquifer is the water table. Unconfined aquifers are located close to the ground surface. Confined aquifers occur at greater depth, beneath saturated, lower permeability units. The overlying lower permeability unit is referred to as an aquitard. If pumping rates exceed long-term recharge rates to an aquifer, groundwater is effectively "mined," with a resulting decline in water levels and eventual depletion of the resource.

As groundwater moves through the subsurface, it evolves chemically as it comes in contact with different mineral species and proceeds toward chemical equilibrium. Chemical processes of importance include solution and precipitation reactions, surface reactions with clay minerals, redox reactions, and formation of neutral complexes. The solubilities of minerals that are encountered along the flow path play a major role in determining the total chemical load of the pore water. Most workers rely on equilibrium concepts to provide a framework to interpret observed patterns in chemical data. Detailed calculations, taking account of reaction kinetics, are currently limited by the complexity of the geochemical environment and the lack of data to specify reaction rates. In regions of the subsurface with very slow rates of groundwater flow, the groundwater may also be mixing with preexisting pore waters that are representative of earlier geologic environments and have yet to be flushed from the system.

The chemical characteristics of groundwater are important for two reasons. First, water quality is a primary determinant of its suitability as a potable water supply. Water pumped from wells located in the discharge areas of large-scale flow systems is typically more saline than that from wells located in either recharge areas or in the discharge areas of smaller scale flow systems. Second, chemical patterns for major ions such as Na^+ , Ca^{2+} , SO_4^{2-} , and Cl^- and concentrations of stable isotopes such as O^{18} , deuterium (^2H), and carbon-13 or radioactive isotopes such as C^{14} , tritium (^3H), and chlorine-36 can be helpful in ensuring that interpretations based on hydraulic data are consistent with chemical signatures.

In coastal and island regions, because seawater is significantly denser than fresh water, saline water will invade aquifers that are hydraulically connected to the ocean. Under natural conditions, freshwater recharge from

TABLE I Representative Values of Hydraulic Conductivity of Selected Geologic Media

Medium	Hydraulic conductivity (m sec ⁻¹)
Sands and gravels	10^{-5} – 10^{-1}
Silts	10^{-8} – 10^{-5}
Clays	10^{-12} – 10^{-9}
Sandstones	10^9 – 10^6
Shales	10^{-12} – 10^{-9}
Unfractured crystalline rock	10^{-12} – 10^{-9}
Fractured crystalline rock	10^{-8} – 10^{-4}

precipitation forms a lens that floats on top of a base of seawater. An approximate equation, known as the Ghysen–Herzberg relationship, predicts that there will be approximately 40 times as much fresh water in the lens beneath sea level as there is fresh water above the mean sea level. This freshwater lens is potentially an important source of potable water.

B. Models

Basic to most groundwater investigations is the development of a conceptual model of the flow system. [Figure 1](#) represents one such model for groundwater flow through a hillslope. To make quantitative assessments of such factors as rates and patterns of fluid flow, it is necessary to translate a conceptual model into a mathematical framework. The tool used for this purpose takes the form of a boundary value problem. A boundary value problem is set up by defining (1) the region of flow, (2) the differential equation governing fluid flow within that region, (3) hydraulic conditions on the boundaries of the flow domain and boundary values such as recharge rates or water table elevations, and (4) the values of all medium properties such as hydraulic conductivity. Two different classes of problems are encountered: those where the flow system does not vary significantly in time (steady state) and those where it does (transient). The flow of water toward a well in response to pumping is an example of a transient problem.

The governing differential equation for steady state groundwater flow in a saturated porous medium is given by the following:

$$\frac{\partial}{\partial x_i} \left(K_{ij} \frac{\partial h}{\partial x_j} \right) = 0. \quad (6)$$

This equation is a statement of mass conservation, requiring that the mass flux of water into an elemental volume equal the mass flux of water out of that volume. Equation (6) is solved to yield predictions of hydraulic head within the interior of the flow domain. Computer simulation models using numerical solution techniques are now routinely used for this purpose.

In transient problems, hydraulic head values vary in time. A change in hydraulic head coincides with a change in the total mass of water stored in the void spaces. The mass of water stored in a unit volume of a porous medium can be decreased by either expansion of the water or compression of the void space. Expansion of the water can occur because of either a reduction in fluid pressures or addition of heat to the flow system. Compression of the void space occurs if stresses acting on the solid matrix increase. Such an increase follows as a consequence of a reduction in fluid pressure, as the pore water then supports

a smaller proportion of the lithostatic load. The governing differential equation of transient groundwater flow for an isothermal system is given by the following:

$$\frac{\partial}{\partial x_i} \left(K_{ij} \frac{\partial h}{\partial x_j} \right) + W = \rho g(\alpha + n\beta) \frac{\partial h}{\partial t}, \quad (7)$$

where n is porosity, α is the bulk compressibility of the porous medium, β is the compressibility of water, and W is a volumetric flux per unit volume that represents sources and sinks of water. Porosity is defined as the volume of voids present in a unit volume of the medium. The coefficients on the right-hand side of Eq. (7) can be grouped as follows:

$$S_s = \rho g(\alpha + n\beta), \quad (8)$$

where S_s is the specific storage. This parameter defines the volume of water released from storage in a unit volume of the medium, for a unit decline in hydraulic head. Specific storage is usually estimated from observations of the response of water levels to an imposed disturbance, such as a short-term pumping test. In setting up a boundary value problem for transient flow, it is necessary to specify the initial conditions on hydraulic head. The solution of Eq. (7) yields predictions of the hydraulic head within the interior of the flow domain as a function of time.

In the case of horizontal flow through a permeable geologic layer of thickness b , two derived parameters are commonly used to define its hydraulic properties. Transmissivity is the product of hydraulic conductivity and layer thickness ($T_{ij} = K_{ij}b$), and the storage coefficient the product of specific storage and thickness ($S_s b$).

Water levels in piezometers that penetrate unconfined and confined aquifers fluctuate in response to numerous factors. These variations can occur on time scales ranging from a few minutes to hundreds of years, depending on the nature of the process that initiates fluid pressure variations in the aquifer. Short-term fluctuations can be caused by changes in barometric pressure of the atmosphere, earth tides, seismic events, and consumptive use of water by plants whose roots penetrate to the water table. Yearly cycles reflect changing wet and dry seasons and the consequent time distribution of groundwater recharge. Multiyear cycles are tied to long-term changes in precipitation patterns. Superimposed on these processes are water-level fluctuations due to varying rates of groundwater withdrawal to meet water supply demands of urban areas, agriculture, and industry.

Before a model is used for prediction it must be calibrated. Often calibration involves trial-and-error adjustment of the medium parameters and boundary conditions until the values of hydraulic head calculated by the computer model provide a satisfactory match to observed field measurements from one or more piezometers. More

sophisticated techniques are based on the concepts of inverse simulation. Here, the hydraulic parameters of the model are estimated by minimizing an objective function of the form:

$$J = (\mathbf{h} - \mathbf{h}^*)^T \mathbf{V}_h^{-1} (\mathbf{h} - \mathbf{h}^*) + \gamma (\mathbf{Y} - \mathbf{Y}^*)^T \mathbf{V}_y^{-1} (\mathbf{Y} - \mathbf{Y}^*), \quad (9)$$

where \mathbf{Y} is a vector of hydraulic conductivity estimates determined from the inverse simulation, \mathbf{Y}^* are measured values of hydraulic conductivity, \mathbf{h}^* is a vector of observed values of hydraulic head, \mathbf{h} are the values of hydraulic head calculated using \mathbf{Y} , and γ is a scaling factor that provides a relative weight to the hydraulic head and hydraulic conductivity data. The covariance matrices \mathbf{V}_y and \mathbf{V}_h contain estimates of the measurement errors in the data set. In this way, more weight can be given to the measurements of greater accuracy.

Computer models of groundwater flow are used for one or more of the following purposes: (1) as an aid in understanding the key hydrogeologic processes controlling groundwater flow within a watershed; (2) as a tool for evaluating the adequacy of, or deficiencies in, an existing database; (3) to predict values of hydraulic head at locations away from measurement points; and (4) to predict the response of the flow system to changed conditions, such as increased pumping rates.

In recent years, hydrogeology has seen a strong research focus on stochastic modeling. At the center of this effort is the recognition that hydrogeologic environments are heterogeneous and that this heterogeneity plays a key role in influencing the reliability of predictive groundwater modeling. Heterogeneity within a porous medium leads to uncertainty on the part of the analyst because only a limited amount of observational data will be available. The spatial variability of properties such as hydraulic conductivity is described using the tools of geostatistics. Hydraulic conductivity is represented by a probabilistic model, with a mean, variance, and spatial correlation structure. The stochastic approach provides estimates of both the expected behavior and the uncertainty in a model prediction. Techniques are now being developed to integrate these estimates of prediction uncertainty with decision analyses and risk assessments.

II. GROUNDWATER CONTAMINATION

A major environmental concern of the past decade has been the recognition of the extent to which groundwater supplies have been or potentially are at risk to contamination by toxic levels of both inorganic and organic chemicals. Perhaps the most widely known example of groundwater contamination occurred at Love Canal in

New York State. Contaminant migration from a chemical dump site lead to the abandonment of a neighboring community in 1978. There are a number of ways that chemical species can contaminate a groundwater flow system: seepage from unlined disposal ponds or surface impoundments; improper landfilling; failure of engineered barriers at disposal facilities; leaks from sewage lines, pipes, or storage tanks; accidental spills; or leaching of waste rock at mine sites. This list identifies point source of pollution, where the location at which contaminants enter the groundwater system is confined to a relatively small area. Distributed sources of pollution occur when the widespread use of pesticides, herbicides, or fertilizers leads to the degradation of groundwater quality over large regions of an agricultural watershed. An important contamination problem in coastal regions is the intrusion of seawater into freshwater aquifers, caused by excessive pumping of groundwater for water supplies.

Contaminants found in groundwater systems are of three general types: (1) chemical species that are miscible with the pore water and are transported as dissolved aqueous phase liquids (APLs), (2) organic liquids that are only sparingly soluble in water and move as a separate phase through the void space (nonaqueous phase liquids or NAPLs), and (3) bacteria and viruses.

A. Aqueous Phase Transport

There are four basic processes that govern solute transport in the aqueous phase:

1. Advection: transport of solutes along the flowlines of a groundwater flow system at the average groundwater velocity.
2. Dispersion: hydraulic mixing process caused by local variations in groundwater velocity.
3. Diffusion: movement of dissolved aqueous species because of a concentration gradient.
4. Reaction: all geochemical and biochemical processes that influence migration rates and concentration distributions.

The average groundwater velocity for advective transfer is calculated as follows:

$$V_i = \frac{\mathbf{K}_{ij}}{n} \frac{\partial h}{\partial x_j}. \quad (10)$$

For point sources of contamination, these processes lead to an evolving contaminant plume that migrates away from the source location in a direction governed by the hydraulic gradient within the aquifer (Fig. 3). In permeable, unconfined aquifers, advection and reaction tend to be dominant processes. Advective transport at rates ranging from 10 to

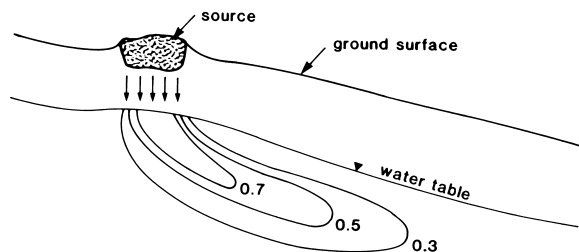


FIGURE 3 Schematic diagram of a migrating contaminant plume in an unconfined aquifer. Contours are lines of equal concentration of a specific chemical species present in the groundwater. Maximum concentration at source equals 1.0.

several hundred meters per year are typical for this environment. Within tight clays, velocities may be on the order of millimeters per year or lower.

Dispersion results in a contaminant spreading through a larger volume of the subsurface than would be predicted by advection alone, leading to reductions in peak concentration within the contaminant plume. It is caused by local variations in the groundwater velocity that originate from the spatial variability in hydraulic conductivity. The more heterogeneous a geologic unit, the greater are the effects of dispersion. Diffusion is of primary importance in low-permeability media (clays, glacial tills, and shales) and as an attenuation process in fractured media, where contaminants can be transferred from fractures into the surrounding matrix blocks in which fluid velocities may be orders of magnitude lower. Reaction includes all the chemical processes that effect the concentration of a solute species, including dissolution and precipitation, volatilization, complexation, organic reactions and biotransformation, surface reactions, redox reaction and radioactive decay. Many reactions act to retard the movement of contaminants. Because of the effects of chemical reaction, different chemical species within a contaminant plume are likely to move at different rates.

The differential equation that describes the transport of a chemical species in the aqueous phase is given by the following:

$$\frac{\partial}{\partial x_i} \left(\mathbf{D}_{ij} \frac{\partial C}{\partial x_j} \right) - V_i \frac{\partial C}{\partial x_i} - \frac{R}{n} = \frac{\partial C}{\partial t}, \quad (11)$$

where C is the concentration of the chemical species, v_i is the component of the groundwater velocity in direction i , \mathbf{D}_{ij} is the dispersion tensor, and R describes the rate at which solutes are lost from the aqueous phase because of chemical reaction. The dispersion tensor characterizes the degree to which contaminants spread in directions parallel and transverse to the groundwater flowlines. It includes terms accounting for both dispersion and diffusion. Equation (11) is used to predict how concentrations will change in time as the contaminant plume moves through a porous

medium. One such equation is written for each chemical species of interest. To complete the formulation of a boundary value problem, it is necessary to define the region of flow, constraints on concentration values at the boundaries of the domain, and initial values of concentration within the flow system. Advective velocities within the flow domain are usually obtained by first solving the boundary value problem that describes the groundwater flow system [see Eqs. (6) or (7) and (10)].

For contaminants that do not react chemically, $R = 0$. Currently, only simple models are used in practice to describe the transport of reactive contaminants. These models are of two types: one based on a first-order reaction rate equation and the other based on a partitioning of chemical species between the pore water and the solid matrix. For a first-order rate reaction, such as radioactive decay, R takes the form

$$R = \lambda C, \quad (12)$$

where λ is the decay rate. The survival of viruses in the subsurface is also modeled using this approach. In the case of sorption of metals onto surfaces of clay minerals, R takes the form

$$R = \rho_b K_d \frac{\partial C}{\partial t}, \quad (13)$$

where ρ_b is the bulk density of the medium and K_d is the distribution coefficient, defined as the mass of solute adsorbed on solids per unit mass of solids divided by the concentration of solute in pore water. The distribution coefficient can be measured in laboratory experiments by observing the amount of contaminant transferred to the solid matrix in a series of solutions of different concentrations. This model assumes that sorption is instantaneous, linear, and reversible. More general partitioning coefficients have also been proposed.

B. Immiscible Phase Transport

Leakage of gasoline or synthetic organic solvents from underground storage tanks are examples of problems that involve the migration of a contaminant as a separate phase. Because many organic liquids are slightly soluble in water, these contaminants also give rise to an aqueous phase plume that is transported by the groundwater flow system. The density of the organic liquid relative to that of the native groundwater determines migration patterns of the separate liquid phase. Liquids less dense than water, such as gasoline, infiltrate downward to the water table and then spread laterally as a lens “floating” on top of the saturated zone. Liquids having a density greater than water, such as chlorinated hydrocarbons, move vertically downward through the vadose zone and the saturated zone until they encounter a low-permeability horizon, where the liquid then spreads laterally along the contact in a down-dip

direction. Recent studies have shown that some dense organic solvents, while within the vadose zone, will evaporate to create a dense vapor, which can then flow away from the immediate source area of the solvent and transfer contaminants to a much larger surface area on the water table.

The mobility of a NAPL depends on its density, viscosity, saturation level, and the character of the geologic units. In the vadose zone, three phases fill the pore space (air, water, and NAPL), while in the saturated zone there are two phases (water and NAPL). Each phase occupies a fraction of the total porosity. Mobility of the NAPL is greater at higher NAPL saturations. Forces acting on the NAPL to control flow include gravity, fluid pressures within the NAPL phase, and capillarity. Capillarity plays a key role. A fraction of the NAPL in the descent cone beneath a spill site is retained by capillary forces; this residual NAPL is not removed by normal drainage processes. Residual saturations, measured as a mass of NAPL retained in a unit volume of soil or rock, are higher in finer grained geologic deposits, such as silts and clays. The NAPL left behind in residual saturation can only be removed by eventual dissolution into the aqueous phase, or chemical transformation. The volume of NAPL released at the source, considered in relation to its residual saturation in the surrounding geologic deposits, is an important factor in determining how far the NAPL will migrate as a separate phase. Often, organic liquid that dissolves and enters the aqueous phase spreads through a larger region of the subsurface than does the liquid phase.

A number of chemical processes are important in determining migration rates and concentration levels of organic contaminants. These processes include dissolution of the organic liquid; volatilization (evaporation), where the contaminant is in contact with the vadose zone; sorption on organic carbon naturally present within sediments and sedimentary rocks; hydrolysis; and biotransformation. The effects of hydrolysis, involving the transformation of a halogenated organic compound in the presence of water, are incorporated in Eq. (11) as a first-order rate reaction.

Sedimentary geologic deposits can contain from zero to several-percentage organic carbon by weight. Depending on the chemical affinity of an organic compound for sorption onto organic carbon, the contaminant will leave the aqueous phase to be held on the solid surfaces. This effect is incorporated in transport Eqs. (11) and (13) by defining the distribution coefficient as follows:

$$K_d = K_{oc} f_{oc}, \quad (14)$$

where K_{oc} is an experimentally determined partition coefficient between organic carbon and water and f_{oc} is the weight fraction of organic carbon in the sediment.

Indigenous microbial populations attached to solid surfaces within an aquifer have the potential to degrade a broad range of organic chemicals. The extent to which

biodegradation occurs depends on both the nature of the organic contaminants and the chemical properties of the groundwater. The redox environment is a key factor. Rates of aerobic degradation of aromatic hydrocarbons in unconfined aquifers are often limited by the concentration of dissolved oxygen within the contaminant plume rather than by characteristics of the microbial population itself. Halogenated solvents are stable in oxygenated water. In moving deeper into the saturated zone, conditions normally evolve from oxic to anoxic, as dissolved oxygen is consumed but not replenished. Methanogens (anaerobic microbes) are known to transform halogenated solvents under reducing conditions. In some instances, the products of biotransformation reactions may be as hazardous (or even more hazardous) as the original contaminant.

C. Land-Based Disposal of Hazardous Waste

Many serious groundwater contamination problems have resulted from the improper disposal of either liquid or solid chemical wastes at sites underlain by permeable, unconfined aquifers. It has only been in the past decade that regulations have been in place to strictly control site selection, facility design, and site monitoring (e.g., Resource Conservation and Recovery Act, 1976; Comprehensive Environmental Response, Compensation and Liability Act, "Superfund," 1980). Once contaminated, it is difficult, time-consuming and costly to carry out a remedial program in an attempt to restore water quality. Possible remedial techniques include the installation of impermeable barriers, drainage galleries, and purge wells; vapor extraction; excavation of contaminated material; manipulation of hydraulic gradients using injection-withdrawal wells; and enhanced biotransformation. Although more than one approach is often implemented, total cleanup is seldom achieved. The most common method of remediation is groundwater withdrawal by pumping, followed by water treatment at the ground surface. The development of management models for identifying optimal strategies for design of purge well systems is an active area of research.

While considerable attention is now focused on environmental hazards associated with groundwater contamination, it can be expected that land-based disposal of hazardous wastes will continue for the foreseeable future. Geologic media with low permeability are targeted as candidate sites for the disposal of hazardous chemical and radioactive wastes because of their association with low rates of advective contaminant transport. To illustrate current philosophies, consider the search for a repository for the permanent disposal of high-level radioactive waste generated in commercial nuclear reactors. Criteria developed by the Nuclear Regulatory Commission that guide the siting and design of the repository include specifications related to (1) radionuclide arrival

rates at the accessible environment and (2) prewaste emplacement groundwater travel times from the disturbed zone to the accessible environment. This latter requirement states that the repository site must be located so that the preemplacement groundwater travel time along the fastest path of likely radionuclide transport is at least 1000 years. In its most recent form, this regulation is interpreted in probabilistic terms, so that the probability of failing to meet the criterion must be less than some small value. These criteria are evaluated using groundwater models of the kind described in Eqs. (6), (7), and (11).

III. ROLE OF GROUNDWATER IN GEOLOGIC PROCESSES

Pore fluids are an integral part of a number of geologic and geodynamic processes that occur within the upper crust of the earth. There are several reasons why this is the case. First, fluid pressures influence the mechanical strength of sediment and rocks and thus have an impact on deformation processes such as landslides, faulting, and earthquakes. Second, fluid migration is a key process for large-scale redistribution of solutes and heat in crustal rocks.

Movement along a plane of weakness, such as a fault, is governed by the friction law as follows:

$$\tau_r = \mu_d (\tau_n - P), \quad (15)$$

where τ_r is the resistive shear strength, μ_d is the dynamic coefficient of friction, τ_n is the total normal stress across the failure plane, and P is the fluid pressure. The total normal stress is equal to the lithostatic pressure. Equation (15) indicates that higher fluid pressures reduce the shear strength of rocks.

Earthquakes occur when slip is initiated along a fault and stored elastic strain energy arising from long-term tectonic movement is abruptly released. Pore fluids, in responding to changing pressure and thermal and stress conditions associated with seismic events, can have a significant impact on faulting and earthquake processes. One possible model of fault motion proposes that a transient increase in fluid pressures due to thermal expansion caused by frictional heating within a fault zone could cause pore pressures to rise to near-lithostatic values and the fault to slip with a very low shear strength [see Eq. (15)]. This process is known as strain weakening because it leads to a progressive reduction in the frictional strength of the fault during an earthquake. Regions along the fault where rocks have higher permeability tend to retain their initial strength because the pore pressures are more easily dissipated into the surrounding region. This behavior influences the character of fault motion during the earthquake. Pore pressures may also respond to changing stress conditions prior to an earthquake. Water-level fluctuations in wells adjacent to

the San Andreas Fault in California are being monitored to examine whether such data may be useful for earthquake prediction.

Hot springs can develop if water circulates to depths of several kilometers, adsorbs heat from the rock matrix, and is then able to move relatively quickly to the ground surface, usually along fracture zones. In areas where subsurface temperatures are greatly increased by localized magmatic intrusions, hydrothermal systems may develop. The hot springs and geysers of Yellowstone National Park are a dramatic example. Buoyancy forces lead to a flow system with upward groundwater flow above the heat source and downward circulation in surrounding, cooler regions. Active hydrothermal systems are potential sources of geothermal energy. Relic geothermal systems are targets for mineral exploration. Metals such as gold, silver, or mercury may be transported by hot fluids to a location within the flow system where geochemical conditions promoted precipitation of the metals. Under favorable circumstances, this process can lead to the formation of ore deposits of economic value.

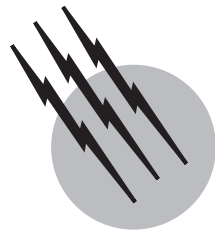
Other environments in which pore fluids play an important role in geologic processes include (1) the deformation of sediments at subduction zones where the earth's lithospheric plates are colliding; (2) circulation of seawater in basalts and sediments adjacent to oceanic spreading ridges; (3) the rise of fluid pressures in subsiding basins, such as the Gulf of Mexico, caused by sediment burial and progressive collapse of void spaces; (4) land subsidence caused by groundwater withdrawals; and (5) metamorphic reactions.

SEE ALSO THE FOLLOWING ARTICLES

COASTAL GEOLOGY • DAMS, DIKES, AND LEVEES • ENVIRONMENTAL TOXICOLOGY • HAZARDOUS WASTE INCINERATION • HYDROLOGIC FORECASTING • SOIL AND GROUNDWATER POLLUTION • STREAMFLOW

BIBLIOGRAPHY

- Back, W., Rosenschein, J. S., and Seaber, P. R., eds. (1988). *Hydrogeology*. In "The Geology of North America," Vol. O-2, Geological Society of America, Boulder, CO.
- Bedient, P. B., Rifai, H. S., and Newell, C. J. (1999). "Ground Water Contamination," 2nd ed., Prentice Hall, Upper Saddle River, NJ.
- Charbeneau, R. J. (2000). "Groundwater Hydraulics and Pollutant Transport," Prentice Hall, Upper Saddle River, NJ.
- Domenico, P. A., and Schwartz, F. W. (1998). "Physical and Chemical Hydrogeology," 2nd ed., Wiley, New York.
- Fetter, C. W. (2001). "Applied Hydrogeology," 4th ed., Prentice Hall, Upper Saddle River, NJ.
- Ingebretsen, S. E., and Sanford, W. E. (1998). "Groundwater in Geologic Processes," Cambridge Univ. Press, Cambridge, UK.



Hydrologic Forecasting

**Michael B. Butts
Jacob Hoest-Madsen
Jens Christian Refsgaard**

DHI Water & Environment

- I. Definition of Hydrologic Forecasting
- II. Hydrologic Classification of Forecast Modeling
- III. Quantitative Precipitation Forecasting
- IV. Short-Term Hydrologic Forecasting Models—River Routing
- V. Short-Term Hydrologic Forecasting Models—Rainfall-Runoff Models
- VI. Forecast Updating
- VII. Forecast Accuracy
- VIII. Long-Term (Seasonal) Forecasting

GLOSSARY

Catchment The area having a common outlet for its surface runoff. Also referred to as drainage basin or watershed.

Calibration The process where a mathematical model is fitted to observed data by adjusting the model parameters.

Flood (river or channel) routing A mathematical formulation that provides a means of estimating river flows, principally from measurements or predictions of flow at upstream sites.

Lead time The time by which the forecast of an incident precedes its occurrence (or nonoccurrence).

Rainfall-runoff model A mathematical formulation that provides a means of estimating river flows, principally from measurements of rainfall.

Runoff That part of precipitation that flows toward the stream on the ground surface (surface runoff) or within the soil and rock (subsurface runoff).

Updating A procedure for real-time correction of a forecasting model using recent measurements of water level or flow rate to adjust through a feedback process the model forecasts to match these recent observations. Updating corrects the forecasts for inaccuracy in the model and model input data such as rainfall by taking advantage of the persistence in the hydrologic flows.

I. DEFINITION OF HYDROLOGIC FORECASTING

Hydrologic forecasting is the estimation of the future states of hydrologic systems. For example, the water level (stage) in a river at 0900 hr tomorrow or the inflows to a hydropower reservoir during the next 24 hr. The time horizon over which a forecast is made is often referred to as the forecast lead time. Thus hydrologic forecasting requires estimates of future conditions at a specific future time or time interval. This should be regarded as distinct from hydrologic prediction, which is the estimation of future conditions without reference to a specific time, such as the prediction of the 100-year flood, for the design of embankment levels.

The mathematical formulation of the forecasting problem for a hydrologic variable Q can be stated simply as: Given a set of observations up to the time of forecast t_N , $Q(t_1), Q(t_2), Q(t_3), \dots, Q(t_N)$, find $Q(t_{N+1}), Q(t_{N+2}), \dots$

A. Forecast Applications

The need for hydrologic forecasting arises from a number of water management problems. The most obvious is the prediction of hydrologic extremes such as floods and droughts, indeed floods and droughts kill more people and cause more damage than any other natural disaster. By their nature floods are generated by the coincidence of several meteorological factors, heavy rainfall, snowmelt, coastal storms, etc., however, man's use of the river catchment also has an important contribution to the severity and consequences of a flood event. Associated with the almost explosive growth in urban development worldwide is the increasing need to address problems related to urban flooding. The transformation from rural to urban land use produces a significant reduction in the absorption capacity of the watershed. As a result there is an increase in the volume of runoff to streams, wetlands, and rivers and these increased volumes travel more rapidly to surface waters producing higher peak flows and velocities. Urban flooding is often the result of local heavy rains producing flash flooding with little or no warning.

Even though the investment in flood control structures has steadily increased during the second half of this century, the damage caused by floods has continued to increase dramatically. This increase is due, in part, to the increasing urban development in floodplain and flood-prone areas. Flood forecasting provides an alternative to the more traditional structural methods of flood mitigation such as the construction of dykes, polders, and embankments. In fact, in some cases, the unplanned construction or raising of embankment levels has, by confining the

floodwaters, increased the magnitude and severity of the subsequent floods rather than reducing flood damage. In addition, the environmental impact of implementing flood forecasting and warning systems is considerably less than many other flood control measures.

Forecasts are used for initiating emergency contingency plans, operating of structures and flood protection reservoirs, or the evacuation of affected areas. Forecasting also permits more effective operation of water resource systems such as water supply reservoirs, cooling water supply, hydropower schemes, water transfers, and diversions.

Hydrologic forecasting applications can be classified into three main groups according to (1) forecast purpose, (2) forecast variable, and (3) forecast period.

1. Forecast Purpose

- Flood forecasting and warning including urban and flash flooding, dam break, storm surges in estuaries, and coastal areas
- Water supply forecasts for potable water supply, hydropower production, and irrigation
- Low flow forecasts for water supply, water quality management, and habitat protection
- Navigation forecasts including operation of structures to maintain navigable levels

2. Forecasting Variables

- Water levels in rivers and the surrounding floodplains including flood depth or flood extent mapping (see Fig. 1), as well as water levels in lakes and reservoirs, and urban drainage networks
- Water quantity, e.g., discharge or reservoir inflow volumes
- Water quality, e.g., water temperature, salinity, or water pollution
- Ice formation and break-up

3. Forecast Period

- Short-term forecasts (up to two days ahead)
- Medium term (2–10 days ahead)
- Seasonal forecasts (several months ahead)

Seasonal forecasting is usually applied to water resource and drought management for the management of reservoirs. Short- to medium-term forecasts are most often used for flood warning and for the real-time operation of water resources systems such as hydropower scheduling. The most widespread use of hydrologic forecasting is in its application to flood forecasting.

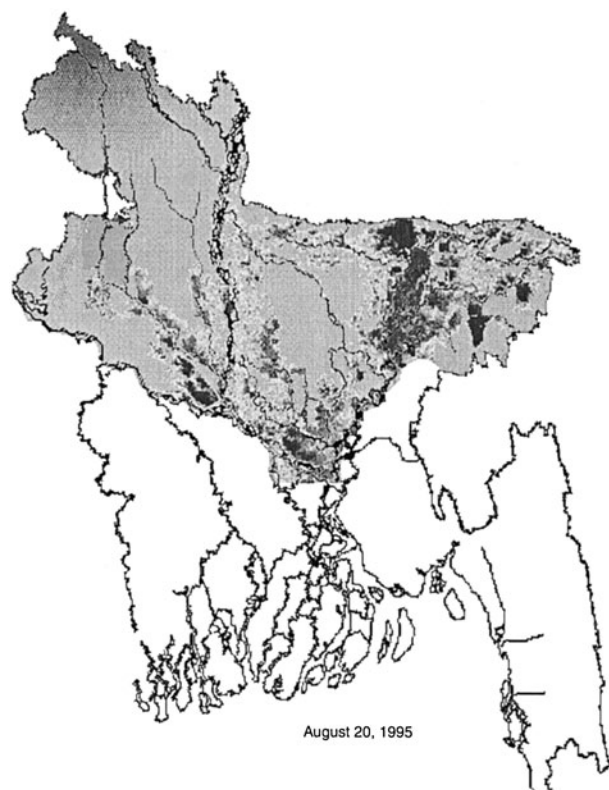


FIGURE 1 Example of a flood map showing flood extent and depth for Bangladesh during extensive flooding in 1995. The map is produced by combining river model results with a digital elevation map of topography. Courtesy of DHI Water & Environment.

B. Flood Warning and Forecast Worth

In many cases a flood forecast is converted into a flood warning issued to the appropriate authorities or the general public on the extent, severity, and timing of the flood. The benefits of flood warning depend on the response and can accrue in three main ways.

1. Evacuation of
 - People and livestock
 - Crops (by premature harvesting)
 - Sensitive and/or easily moved items (e.g., cars, electrical equipment, etc.)
2. Amelioration through
 - Temporary flood proofing (e.g., using sand bags and blankets)
 - Opportune maintenance (e.g., weed and debris clearing of culverts, etc.)
 - Early alert of emergency services
 - Orderly disruption of services (e.g., traffic diversions)
3. Control by
 - Adjusting reservoir discharges to permit flood attenuation

- Emptying storm tanks and balancing ponds prior to the arrival of floods
- Operation of flood control reservoirs and polders
- Optimal operation of river control and diversion structures

Forecast worth is the economic or other value derived from a forecast. In purely economic terms the worth can be evaluated as the net benefits obtained if a forecast is available less those that occur in the absence of a forecast. The value of flood warning depends on the action taken as a result of flood warning, which will, in turn, depend on the time available to act on a warning. The effectiveness of a flood warning will also depend on the accuracy and reliability of the flood forecast, the conversion of this forecast into a warning for the area likely to be affected, how well this warning is communicated to those affected, and the ability of those affected to usefully interpret and respond to the warning.

C. Flood Warning and Monitoring

Flood warning usually consists of severe weather or flood warnings such as bulletins describing the river status and expected levels often related to predefined warning and danger levels, (see Fig. 2). To communicate understandable levels of risk these are often in the form of color codes as shown in Fig. 3 for Bangladesh. Bangladesh is subject to regular and frequent flooding and therefore the warnings are related to the flood severity. In other countries, phased warnings are used. For example, in the U.K. flood warning codes issued to the public are “flooding possible,” “flooding expected,” or “severe flooding expected.” The basis for issuing these warning may vary considerably ranging from detailed mathematical modeling of the river system and the surrounding floodplains (see Fig. 1) to human judgment based on historical flood events and local knowledge. As an alternative to mathematical modeling, flood monitoring uses observations such as the current river level or weather radar images to directly provide early warnings. River levels or rainfall exceeding predefined thresholds trigger either an alert, an automatic flood warning, or generate a flood forecast.

II. HYDROLOGIC CLASSIFICATION OF FORECAST MODELING

Methods for forecasting floods usually include some form of mathematical model using knowledge of the past behavior of the river and a mathematical description of the processes producing the flood. The model may simply

FLOOD WARNING FOR IMMEDIATE BROADCAST	
Flood Warning is issued by Flood Forecasting and Warning Centre	
DISASTER MANAGEMENT BUREAU should IMMEDIATELY transmit this message to DISTRICTS.	
BANGLADESH RADIO and TV should broadcast this Flood Warning IMMEDIATELY and hourly on National & Local Radio and arrange for <radiostations> Radio Stations to broadcast throughout the night.	
This Warning should not be broadcast after <lasttime>	
A Warning of Severe Flooding for Districts of <districtname> was issued at <time> on <day> <date>	
<p>The BWDB Flood Forecasting & Warning Centre reports continuing heavy monsoon rainfall in <regionname> of the country and that River(s) <rivername> are flowing well above Danger Level. FF&WC forecasts predict that river levels will increase further over next few days. Flood water will rise above the BLUE zone on Flood Marker Posts and will inundate large areas of all these Districts during the next 48 hours. Flooding will occur in many rural areas and may affect some towns. Damages to property are expected. Roads, railways, embankments and bridges are likely to be washed and damaged. District flood control rooms will remain open day and night and together with local disaster preparedness committee members will issue further local advice. You should remain alert and listen to radio bulletins for further information. This bulletin will be updated at <lasttime> through <radiostations> of local radio.</p>	
A Warning of Severe Flooding has been issued for <districtname> Districts. [Message ends]	

FIGURE 2 Example of a flood warning bulletin for severe flooding issued from the Flood Forecasting and Warning Center, Dhaka. Courtesy of DHI Water & Environment.

take the form of heuristic rules and triggers for flood monitoring and warning, but usually involve precipitation forecasting, rainfall-runoff modeling, fluvial (river) forecasting, or a combination of these. In addition, updating procedures for the incorporation of real-time observations are required. Selection of the most appropriate forecasting method will depend on the forecast *lead time*. A widely accepted definition of lead time is the time between the issuance of the forecast of a hydrologic phenomena and its occurrence. This is the time available to respond to a forecast or warning. The hydrologic time scale of a forecasting problem is the time between the cause of a hydrologic phenomenon (intensive rainfall) and its occurrence. (the flood peak). The hydrologic response time of a specific catchment will depend on a number of factors; such as catchment size, catchment slope, land use, soil type, etc. In addition to these static parameters, the response time will depend on dynamic variables such as the catchment wetness, groundwater levels, the distribution of rainfall including storm type and direction, and the operation of structures such as gates, pumps, etc.

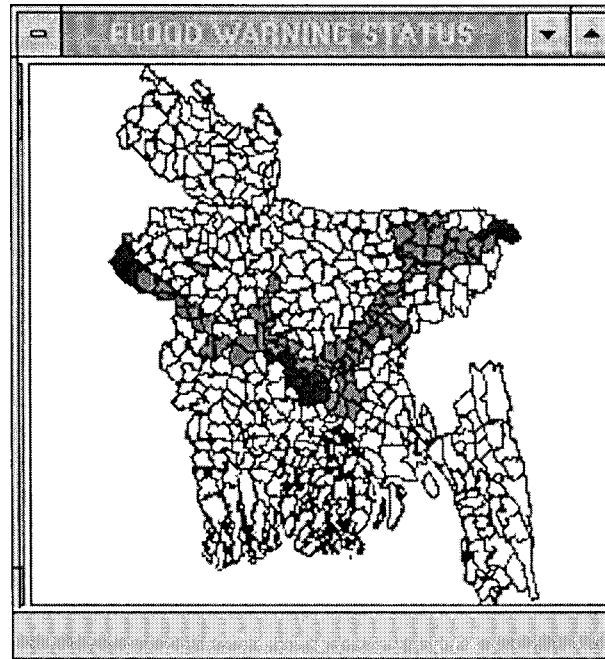


FIGURE 3 Example of a flood warning status map as issued by the Flood Forecast and Warning Center, Dhaka, Bangladesh, showing flood warning codes for each Thana (county). Gray: Danger. Black: Thanas with Severe Flooding. Courtesy of DHI Water & Environment.

A. Classification of Flood Forecasting Problems

1. Criterion 1: Time Scale of Catchment Response

The nature of the hydrologic forecasting problem can be specified by relating the forecast lead time required (T_f) to the time of concentration of the catchment at the forecast point. The time of concentration consists of the two components; the hydrologic response time of the catchment or the time between precipitation falling on the catchment and an increase in flow in the river (T_c) and the travel time through the river or channel system (T_r). This leads to the following three cases.

Case A: $T_f > T_c + T_r$ —The required lead time is larger than the time of concentration, in which case *quantitative precipitation forecasts* are required. The rainfall forecasts increase the time period over which flow forecasts can be made. In general both *quantitative precipitation forecasting* and *hydrologic forecasting* using *rainfall-runoff modeling* are required.

Case B: $T_f < T_c + T_r$, $T_c \ll T_r$ —The response time scale of the catchment/channel network is dominated by the travel (routing) time of the flood wave through the channel system. This is typical for large river systems such

as the Ganges in India and Bangladesh or the Mississippi river in the United States. This permits streamflow forecasts from observed flows (or water levels) upstream of the forecast point. In such cases it may be possible to make forecasts on *channel routing models* alone. The routing time for a river system is not a constant but depends on the size of the flood event. As the water levels approach bankfull discharge, the flood wave velocity increases with increasing discharge. However, above bankfull discharge, the flood wave velocity decreases and attenuation of the flood wave increases as water is spilled into the floodplains and flow resistance increases.

Case C: $T_f < T_c + T_r$, $T_c \gg T_r$ —The time of concentration is dominated by the hydrologic response time of the catchment but the forecast lead time is shorter than the time of concentration. Streamflow forecasts should be based on observed rainfall (from either telemetered rain gauges or weather radar) and incorporate *rainfall-runoff modeling*.

2. Criterion 2: Spatial Scale of Flood Producing Storms

When the spatial scale (L_m) of the meteorological event is significantly less than the spatial scale (L_c) of the catchment then the accuracy of forecasts assuming uniform rainfall will deteriorate. A clear distinction can be made in the case where $L_m/L_c \ll 1$. However, whenever the ratio $L_m/L_c < 1.0$ then the rainfall event will only partially cover the catchment and the accuracy of *lumped* rainfall-runoff models that assume spatially uniform rainfall will suffer. This will be the case for large catchments and for smaller catchments during intensive convective storms. The best forecasting approach in this situation will depend on the catchment response time scale, however, where the spatial distribution of the rainfall is important, a *distributed* or *semidistributed* rainfall-runoff model rather than a lumped model is required.

III. QUANTITATIVE PRECIPITATION FORECASTING

Quantitative rainfall forecasts provide valuable increases in the forecast lead time. This may be of crucial benefit for forecasting flash floods or the rapid flooding of urban catchments. Quantitative precipitation forecasts can be derived from statistical forecasting models, weather radar, synoptic forecasts, satellite-based remote sensing, or numerical weather forecasting (meteorological) models. Many of the radar-based methods are based on advective schemes that assume the rainfall storm pattern remains constant and moves at a constant velocity. Rainfall fore-

casts of this type are variously referred to as advection or feature tracing, precipitation projection, or nowcasting and are used in several countries, notably the U.K., Japan, and the United States. Experience indicates that for short lead times, the radar-based approaches provide acceptable accuracy but accuracy decreases for larger lead times (1.5–3 hr). Increasing use is being made of numerical weather forecasting models in both weather and flood forecasting as these can extend the forecast lead time considerably. However, there is an upper limit to the lead time over which weather systems can be predicted deterministically because of the turbulent and chaotic nature of meteorological flows. Numerical weather prediction models are usually meso-scale models which represent the storm process on a 15 to 20-km grid which is, in general, too coarse for many hydrologic purposes and current research has focused on developing downscaling methods and high resolution numerical modeling to represent rainfall at hydrologic scales.

IV. SHORT-TERM HYDROLOGIC FORECASTING MODELS—RIVER ROUTING

Short-term hydrologic forecasting models can be divided into two basic types using the above classification; river or channel routing and rainfall-runoff modeling. Two broad classes of channel routing exist; hydraulic models and hydrologic models

A. Hydraulic Routing (Distributed) Models

Typically hydraulic routing models divide the river or channel network into a number of computation points (see Fig. 4) and describe the flood wave movement as a numerical solution to the mathematical equations describing flow in a river channel. The models allow the water level and flow rate to be computed in both space and time.

1. One-Dimensional Dynamic Wave Methods

The routing of water down a river channel is described by one-dimensional hydrodynamic equations of unsteady flow known as the Saint-Venant equations, (see Eqs. 1 and 2). The Saint-Venant equations consist of the conservation of mass (continuity) and the conservation of momentum equations for water flow in an open channel. Derivations of the Saint-Venant equations can be found in many standard texts. General solutions of the full Saint-Venant equations are referred to as dynamic wave models. Approximations to these equations known as the kinematic and diffusion wave equations are also used. These equations are generally solved numerically.

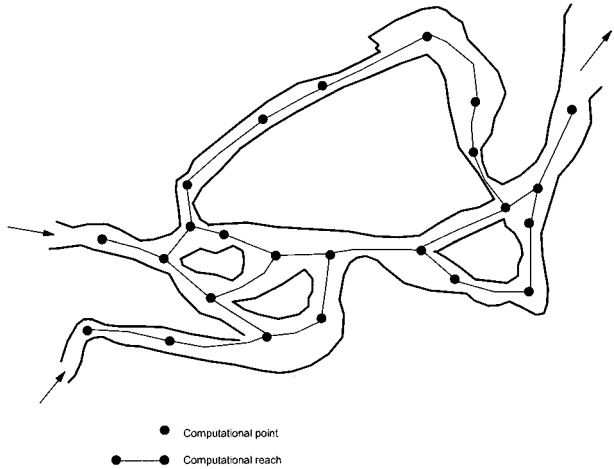


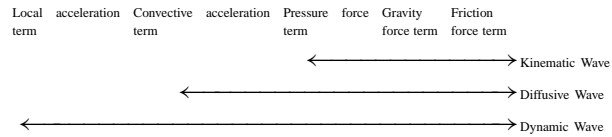
FIGURE 4 Numerical representation of a river network as computational points and computational reaches.

Continuity Equation

$$\frac{\partial Q}{\partial x} + \frac{\partial Q}{\partial t} = 0 \quad (1)$$

Momentum Equation

$$\frac{1}{A} \frac{\partial Q}{\partial t} + \frac{1}{A} \frac{\partial}{\partial x} \left(\frac{Q^2}{A} \right) + g \frac{\partial y}{\partial x} + g(S_0 - S_f) = 0 \quad (2)$$



Q is the flow or discharge in the river, A is the cross-sectional area of the river, y is the water depth, g is the gravitation constant, S_0 is the slope of the river bed, S_f is the friction slope describing the friction forces due to the roughness of the river bed, x is the distance along the channel and t denotes time.

As described in Section IV.A.2, the approximate wave solutions are suitable for certain types of applications. Dynamic wave models are generally required for the following cases:

1. Upstream movement of waves such as tidal action or storm surges
2. Backwater effects caused by downstream reservoirs and tributary flows
3. Rivers with extremely flat bottom slopes, e.g., $S \ll 0.0005$
4. Abrupt waves caused by rapid reservoir releases or dam failures or abrupt changes in velocity caused by river regulatory works

Dynamic models have the advantage of being generally applicable and can also be used for flood protection design and similar river works as well as for flood forecasting. Such models require topographical data for channel and flood plain geometry and historical or survey data for assessing roughness coefficients.

2. Approximate Wave Solutions: Kinematic and Diffusive Wave Models

For steep rivers the most important forces acting are gravity acting on the water and resistance against the flow caused by the roughness of the riverbed. The inertial and pressure terms can be neglected in the momentum equation and the momentum equation reduces to a simple balance between gravity and frictional forces. In such cases the flood wave will move without deformation downstream at a constant velocity which depends on the magnitude of the flow or depth, i.e., as a kinematic wave. The kinematic flood wave will move with a wave speed or celerity c_k given by

$$c_k = \frac{dQ}{dA} \quad (3)$$

This wave speed is the velocity at which a variation in water level or discharge moves along the channel and may be quite different from the water velocity. The kinematic wave equations can be solved using the method of characteristics and analytical solutions can be derived for a uniform river reach. The kinematic wave approximation is applicable to rivers without significant backwater effects and slopes greater than about 0.001. The diffusive wave equations are obtained by neglecting only the inertial terms in the Saint-Venant equations. A diffusive flood wave moves with a constant velocity equal to the kinematic velocity, however, the flood wave is attenuated as the wave moves downstream.

The simplified routing models are useful in understanding the physics of channel flow and appealing because of their computational simplicity, however, they are based on simplifying assumptions which limit their range of application. Dynamic routing models—the most efficient and versatile and also the most complex—are used with increasing frequency as improvements in computing power and the robustness of these models are made.

3. Two- and Three-Dimensional Hydraulic Models

A looped river network using a one-dimensional model is a simplified approximation of the two- and three-dimensional flows that actually occur in many floodplain areas (see Fig. 5), particularly in the lower reaches of many river valleys during floods. Similarly in many coastal areas

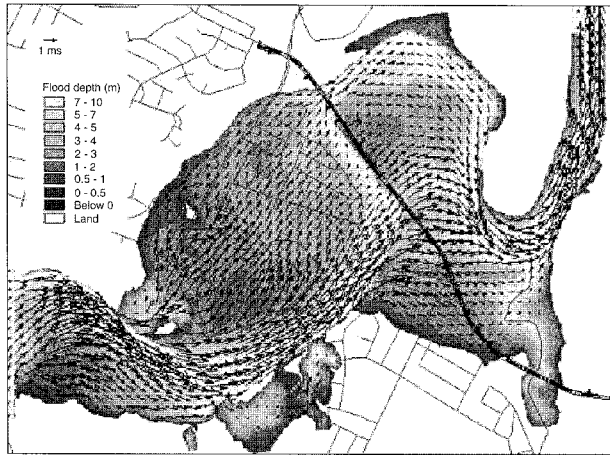


FIGURE 5 Two-dimensional model of the velocity and water depth occurring within river floodplains during a flood. Courtesy of DHI Water & Environment.

exposed to coincident river and storm surge flooding two-dimensional hydraulic modeling provides a more accurate description of the flooding pattern caused by the action of wind and waves. For river flooding two-dimensional models generally require more data for calibration and the additional accuracy does not justify their use to predict water-surface elevations and average flows in typical applications. At present most operational river forecasting models are based on the one-dimensional approximations and the two-dimensional descriptions are restricted to design and impact assessment studies where a knowledge of the velocity effects are required for hazard and damage assessment.

4. Hydrologic (Lumped) Routing Models

While hydraulic routing models divide the channel system up into a number of computational points many of the simpler hydrologic routing methods treat routing in a lumped manner, describing a single stretch of river or reach. In many of the longer rivers, satisfactory forecasts can be based on a suitable upstream gauging station and are indeed still widely used. Routing of the flood peak is determined from an empirical relation between upstream and downstream flows or water levels derived from historical data at both sites. This approach is known as station-to-station correlation or peak-to-peak correlation and is perhaps the simplest of a wide range of lumped routing methods.

Lumped flow routing methods can be categorized as (1) level-pool reservoir routing, (2) storage routing which is based essentially on the conservation of mass, and (3) linear system (impulse response) approaches. Level-pool reservoir routing is used for reservoirs assuming the water

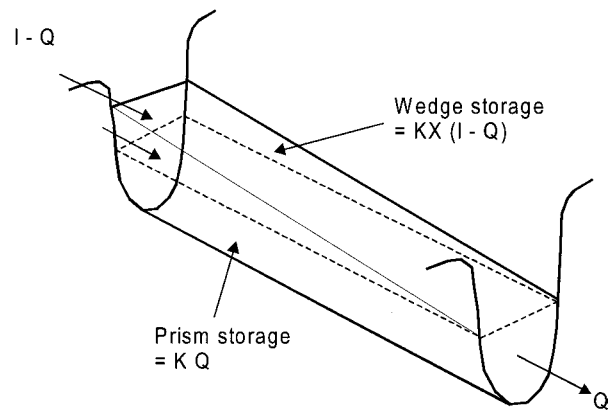


FIGURE 6 Prism and wedge storage used in deriving the Muskingum model for flood routing.

surface is level at all times and inflows do not vary significantly over time. The outflow is assumed to be a function of the water level. These assumptions mean that level-pool routing becomes less accurate as reservoir length increases, or the reservoir depth decreases or the rate of rise of the inflow hydrograph increases. Storage routing is used for rivers and considers the sloping water surface due to the passage of the flood wave. The well-known Muskingum method is a popular method of this type. The Muskingum method is kinematic in nature and can be derived from simple physical considerations. This method models the storage volume of flooding in a river channel by a combination of wedge and prism storage (see Fig. 6). During the advance of a flood wave inflow I exceeds outflow Q creating a wedge of storage in addition to the prism of storage in a uniform channel. The total storage is therefore

$$S = KQ + KX(I - Q) \quad (4)$$

This can be rearranged to give the storage for the Muskingum method

$$S = K[XI + (1 - X)Q] \quad (5)$$

The value of X lies in the range, $0 \leq X \leq 0.5$, depending on the shape of the wedge storage (typically $0.1 \leq X \leq 0.3$ in most streams). The Muskingum method has the advantage that it can be recast in an algebraic form ideally suited for flood forecasting as shown below. For routing the river reach is envisaged as a simple input output system. Defining I as the inflow to the reach and Q the outflow, their difference is related to the rate of change in storage with time dS/dt through the conservation of mass (continuity) Eq. (1) as:

$$\frac{dS}{dt} = I - Q \quad (6)$$

By considering the change in storage over a time step Δt , then the outflow at time step $j + 1$ can be related to the

previous outflows and the current and previous inflows by

$$Q_{j+1} = C_1 I_{j+1} + C_2 I_j + C_3 Q_j \quad (7)$$

Where C_1 , C_2 , and C_3 depend on K , X and the chosen time step Δt . The Muskingum method can be modified by computing the routing coefficients in a particular way, which modifies the kinematic-based Muskingum method to a diffusive wave approximation where the hydrograph is attenuated. This modification is known as the Muskingum-Cunge method.

Many of the lumped methods can be described within a linear systems framework where the routing is characterized by an impulse response function and the inflow (input)-outflow (output) relationship is defined by a convolution integral. The impulse response function relates the outflow from the reach to a unit input at the upper boundary of the reach in the same manner as the instantaneous unit hydrograph method relates a catchment hydrograph to a unit input of excess rainfall, (see below). These include methodologies based on direct estimation of the impulse response function, transfer function models, Muskingum, Muskingum-Cunge, linear reservoirs, cascades of linear reservoirs, lag, and route methods.

For a simple linear reservoir the storage function is related linearly to the outflow as a function of time,

$$S(t) = k Q(t) \quad (8)$$

And the impulse response function can be derived analytically

$$h(t) = \frac{1}{k} \exp\left(-\frac{t}{k}\right) \quad (9)$$

The lag and route method is obtained from the linear reservoir method by allowing the storage at any time be proportional to the outflow which occurs after a lag time t_L

$$S(t) = k Q(t + t_L) \quad (10)$$

And the resulting impulse response function is

$$h(t) = 0 \quad t < t_L \quad (11a)$$

$$h(t) = \frac{1}{k} \exp\left(-\frac{t - t_L}{k}\right) \quad t \geq t_L \quad (11b)$$

It is straightforward to extend the concept of a linear reservoir or lagged linear reservoirs to cascades of linear or lagged linear reservoirs to describe distributed systems. Rather than assuming the nature of the storage relationship, the impulse response function can be derived directly from observed data. The impulse response function requires continuous input, however, in forecasting applications the data are available at discrete time intervals only and the convolution for discrete times must be used.

V. SHORT-TERM HYDROLOGIC FORECASTING MODELS—RAINFALL-RUNOFF MODELS

Rainfall-runoff models describe the processes by which precipitation (rainfall or snow) generates flows in the river and drainage network of a catchment. There is a vast range of catchment models for predicting river discharge from precipitation falling on the catchment. One approach to classifying these approaches is presented in Fig. 7. These categories are by no means mutually exclusive and a particular model system may cover several categories. During the last two decades, there has been an increasing interplay between the stochastic and deterministic methods and a joint stochastic-deterministic approach provides a useful framework for addressing fundamental issues such as spatial variability (scale problems) and assessing model and forecast uncertainties.

Deterministic models can be classified according to whether the model gives a lumped or distributed description of the considered area and whether the description of the hydrologic processes is empirical, conceptual, or physically based. Distributed models take account of the spatial variability in the hydrologic processes, inputs, boundary conditions, and/or catchment characteristics. By contrast, lumped models do not explicitly take account of this variability.

A. Empirical Models

Among the earliest methods used for flood forecasting are the storage accounting methods. The idea of storage accounting is that the future runoff during the forecast period depends on the amount of water presently in storage within the catchment either as soil moisture, groundwater, snow, etc., and the amount of rainfall that has fallen on the

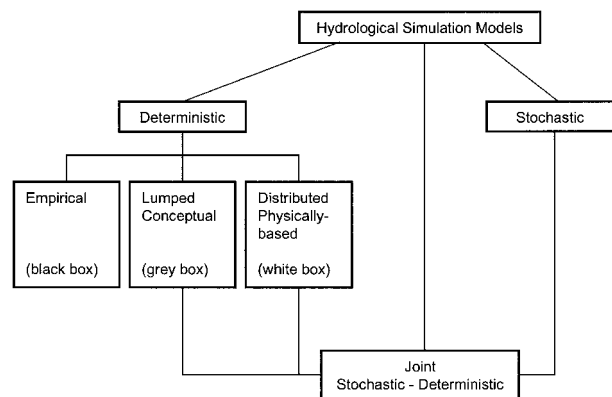


FIGURE 7 Classification of hydrologic models for rainfall-runoff modeling.

catchment. Often the forecast runoff is a linear function of the storage. In its simplest form the storage is linearly related to the runoff [see Eq. (8)] and the catchment acts as a linear reservoir. These simplified models were developed and applied before computer technology made it possible to use more physically correct and thus more complex models. Nevertheless their simplicity makes them attractive for simple forecasting applications.

The best known of the empirical methods is perhaps the unit hydrograph model and models applying similar principles. The unit hydrograph model is in fact a special case of a more general model of a hydrologic system that treats hydrologic models in a linear systems framework. The response of a linear system is uniquely characterized by the impulse response function. If a system receives a unit impulse at time T , then the response of the system at a later time t is described by the impulse response function $u(t - T)$, where $t - T$ is the time lag since the impulse was applied. For rainfall-runoff modeling the unit impulse would be 1 mm of rainfall and the response function the resulting runoff, (see Fig. 8). In the instantaneous unit hydrograph approach the discharge from a catchment is assumed to be linearly related to the effective rainfall. Effective or excess rainfall is the total rainfall minus any losses due to interception (water trapped in the vegetation), infiltration (water loss to the soil), evapotranspiration (water lost to the atmosphere), and surface storage. A unit hydrograph is defined as the direct runoff hydrograph resulting from a unit depth of excess rainfall produced by a storm of uniform intensity and specified duration. The unit of excess rainfall is taken to be 1 in. or 1 cm over the entire catchment.

The unit hydrographs are derived from the streamflow data and estimates of the excess rainfall for a particular storm or series of storms. To calculate the flood hydrograph, the unit hydrograph is applied to the excess rainfall calculated for the storm to estimate the surface runoff. The baseflow, which represents the slowly reacting component of river discharge, is then added to produce the flood hydrograph. Application of the unit hydrograph method requires estimation of the unit hydrograph, estimation of the

baseflow during the storm, and estimation of the effective rainfall.

A variety of procedures and methods have been developed for estimating the unit hydrograph. Synthetic unit hydrographs can be estimated for ungauged basins by means of relationships between the parameters of the unit hydrograph and the physical characteristics of the basin such as the SCS method derived by the U.S. Soil Conservation Service. For the widely used SCS method, a dimensionless unit hydrograph is derived from a single parameter the time to peak T_p (or the basin lag L_a) which can be related to the main catchment characteristics, soil, cover, and hydrologic condition through a curve number. Published tables of the curve number for different soil and land use types are available. The curve number also depends on the antecedent wetness of the catchment and three classes of antecedent moisture condition are defined—dry, average and wet. For more accurate flood estimates the relationships need to be derived using local data. Given times series of rainfall and catchment runoff, methods for deriving the unit hydrograph can be found using linear programming and other optimization methods based on minimizing the squared error between the observed and predicted discharge to determine the unit hydrograph parameters.

The unit hydrograph is usually derived from a number of flood or high flow events. Conditions prior to a storm event are determined by estimating the catchment wetness or antecedent moisture content for that event. Unit hydrograph methods are therefore event-based, in the sense that they are appropriate for forecasting single flood events. By contrast, continuous rainfall-runoff modeling methods, such as the lumped conceptual models described in Section V.B, maintain a running status of the water content within the catchment storages, thereby permitting forecasts over the full range of flows.

1. Statistically Based Methods

An important group of statistically based methods is the regression and correlation models. Linear regression and correlation techniques are standard statistical methods used to determine functional relationships between different data sets. Station-to-station correlation relationships are often determined by linear regression between the flood peaks of the upstream and downstream stations. The relationships are characterized by correlation coefficients and standard deviations, and the parameter estimation is carried out using rigorous statistical methods involving tests of validity and significance for the chosen model. One of the main advantages of these approaches is that it is straightforward to estimate confidence bounds on the forecast.

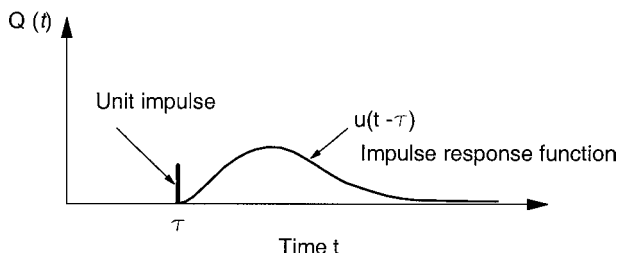


FIGURE 8 Unit pulse of rainfall and corresponding runoff response.

A number of classical stochastic time series methods used in general time series forecasting are used in hydrologic forecasting. These include autoregressive models (AR), moving average (MA) models, autoregressive with moving average terms (ARMA), and their extensions, e.g., ARIMA (autoregressive integrated moving average) models, which has been used extensively in surface water hydrology for establishing relationships between rainfall and discharge, and ARMAX (ARMA with exogenous variables).

The general AR model of order p is given by

$$Q_t = \mu + \sum_{j=1}^p \phi_j(Q_{t-j} - \mu) + \varepsilon_t \quad (12)$$

Where ε_t is an uncorrelated normal random variable with mean zero and variance σ_ε^2 .

The general ARMA (p, q) model has the form

$$Q_t = \mu + \sum_{j=1}^p \phi_j(Q_{t-j} - \mu) + \varepsilon_t + \sum_{j=1}^q \theta_j \varepsilon_{t-j} \quad (13)$$

ARMA models contain more parameters and are therefore more flexible than AR models. The ARMA(0, q) is the same as the moving average model, MA, (q). In terms of modeling it can be said that AR processes are short-term processes while ARMA processes are long-memory processes. In most practical applications the order of p and q is often very low.

2. Transfer Function Models

A more general multivariate model can be formulated using, for example, flow Q and rainfall P of the form

$$Q_t = a + \sum_{j=1}^p b_j Q_{t-j} + \sum_{j=1}^q b_j P_{t-j} + \varepsilon_t \quad (14)$$

The above relation falls into the category of a transfer function model which has been widely used in real-time forecasting applications. The model parameters are derived by fitting the relation (14) to the historical flood peaks. Linear transfer function models are widely used in flood forecasting because of their relative simplicity and the fact that they can be easily combined with forecast updating methods such as the Kalman filter technique.

3. Data-Driven Methods

Within the last few decades, a newer group of empirical modeling approaches have emerged as part of the field of hydroinformatics using techniques based on neural networks, chaos theory, nearest neighbor methods, evolutionary algorithms, and fuzzy rules. Many of these new methods exploit the dramatic expansion of digital

data acquisition and processing power to develop predictive models for streamflow dynamics for situations that are “theory-poor” and “data-rich.” This idea is by no means new and is the motivation for many of the statistical models such as the AR model. The new element in these methods is the development of new concepts (such as neural networks and phase-space reconstruction) that provide general approximations with few specific assumptions about the underlying hydrologic (dynamical) system to be modeled. The key idea is to construct a model directly from available data.

a. Chaos, phase-space and local linear models. Dynamical system theory has in recent years been applied successfully to derive phase-space-based models for characterization of chaotic time series in meteorology and time series forecasting as well as hydrology. The key assumption in this approach is that even if the exact mathematical description of the hydrologic system is not known, the state-space can be reconstructed from a single variable time series. The state-space is the multidimensional space of variables (e.g., river levels) that describe the state of a system. When the state-space is constructed from a time series rather than the actual model variables, it is referred to as a phase-space. It can be demonstrated that the phase-space retains the essential properties of the original state-space including the dimensionality. Therefore if deterministic rules can be derived for the behavior of the system in state-space then forecasts can be made of future states from the history of data embedded in the state-space. This type of model is built in two steps: (1) reconstruction of the phase-space by time delay embedding and (2) derivation of a method for state-space prediction.

It can be shown that to forecast the time series $Q(t)$, for example, a streamflow record, where the behavior of the dynamical system is described by M variables $X_k(t)$, $k = 1, M$ then the system can be equivalently described by the time series $Q(t)$ and multiple time delays up to order M . A point in this M -dimensional phase space describing the state at a time t is given by

$$\mathbf{Q}(t) = [Q(t), Q(t + \tau), Q(t + 2\tau), \dots, Q(t + \{M - 2\}\tau), Q(t + \{M - 1\}\tau)] \quad (15)$$

The choice of the time delay τ is crucial in constructing a well-behaved phase-space. A widely used option is to use the autocorrelation time scale for τ . The prediction results are sensitive to the choice of τ and M and numerous methods have been developed to determine these parameters or identify which choice provides the best predictions.

Once the phase-space representation has been made, by determining the time delay τ and the dimensionality M , this phase-space representation can be used to make

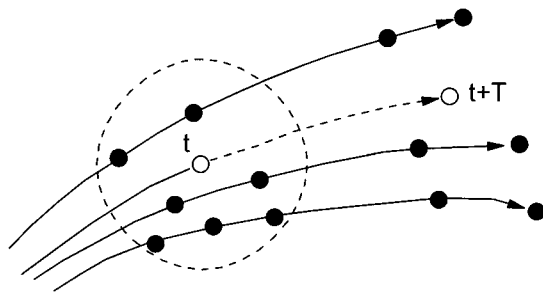


FIGURE 9 Prediction of the future behavior of a dynamical system using the nearest neighbor method for phase-space forecasting. The future state $Q(t + T)$ is derived from the current state $Q(t)$ by finding a suitable function that describes how neighbors move.

short-term predictions. The development of the system is represented by a trajectory in the phase space, (Fig. 9). By finding a suitable function that approximates the trajectory of neighboring points a forecast of the future state can be obtained. Using only the neighboring points, locally linear or locally nonlinear trajectory functions can be developed. It has been shown that local linear approximations provide better forecast accuracy for a number of controlled data sets. The nearest neighbor method is a widely used local approximation method that uses the historical values close to the current state vector to estimate the trajectory of the current state by using the trajectories of the neighboring points.

b. Neural networks. Neural networks have been widely applied to nonlinear approximation and pattern recognition. When applied to forecasting, neural networks can be regarded as a nonlinear black box (input-output) model. A neural network is simply a set of interconnected individual units called neurons. The individual neuron has a finite number of inputs and one output. Each input is associated with a weighting value. The input signals are weighted by these values and added at the summation junction. The combined signal is then passed through an activation function producing the output signal. A general neural network is a collection of interconnected neurons in several layers. A multilayer neural network with appropriate weights has been shown to be able to approximate any input-output function making it an attractive tool for modeling and forecasting.

The real benefit of a neural network in forecasting is the ability of neural networks to capture nonlinearities such as the nonlinear response of a catchment to rainfall, in which case the neuron activation function must be nonlinear. It can be shown that linear networks are equivalent to standard regression models. It should be noted that one of the advantages of neural networks is the ability to in-

clude a variety of information that is not readily included in simple linear models such as ARMA models, such as rainfall, soil moisture, etc. One of the major limitations is that it is generally recognized that while neural networks are excellent interpolators they are poor at extrapolating outside the range of calibration.

c. Fuzzy rules. Fuzzy sets were first introduced in the mid-1960s and they have been applied in many fields such as decision making and control. The application of fuzzy rules and fuzzy sets requires the specification of rule arguments and rule responses. For flood forecasting, the rule arguments consist of variables describing the present state of the catchment (e.g., rainfall, discharge), the recent evolution (changes in discharge), and other external control variables (such as temperature). The corresponding responses could be the peak discharge or water level, the forecasted discharge or water level at a given lead time, or flood volume. Formulation of the rules can be performed manually and in this manner colloquially formulated knowledge or experience can be used directly in the forecast model. Fuzziness makes it possible to treat less precisely formulated rules, such as "If the rainfall is heavy then . . ." in forecast modeling. Alternatively automatic generation of fuzzy rules can be carried out where the parameters within the possible rules are optimized to provide the best match with historical data.

d. Evolutionary algorithms. Evolutionary algorithms provide an alternative to problems solving—one in which solutions are evolved rather than being solved directly. For hydrologic forecasting, the forecasting problem becomes an identification of the nonlinear relation

$$Q(t + 1) = f(Q(t), Q(t - 1), Q(t - 2), \dots) \quad (16)$$

Using genetic programming, nonlinear forecasting relations can be developed from combinations of symbolic operators such as log, sin, $\sqrt{ }$, or *if-then-else* rules that provides the best fit to the observed data.

B. Lumped Conceptual Models

Lumped conceptual models operate with different but mutually related storages representing physical elements in a catchment. The structure of the model may be characterized as a bookkeeping system continuously accounting for the water contents in each of the storages (see Fig. 10). Due to the lumped description where all parameters and variables represent average conditions over an entire catchment, the description of the hydrologic processes cannot be based directly on physics of flow. Hence the underlying equations are semi-empirical. Therefore the

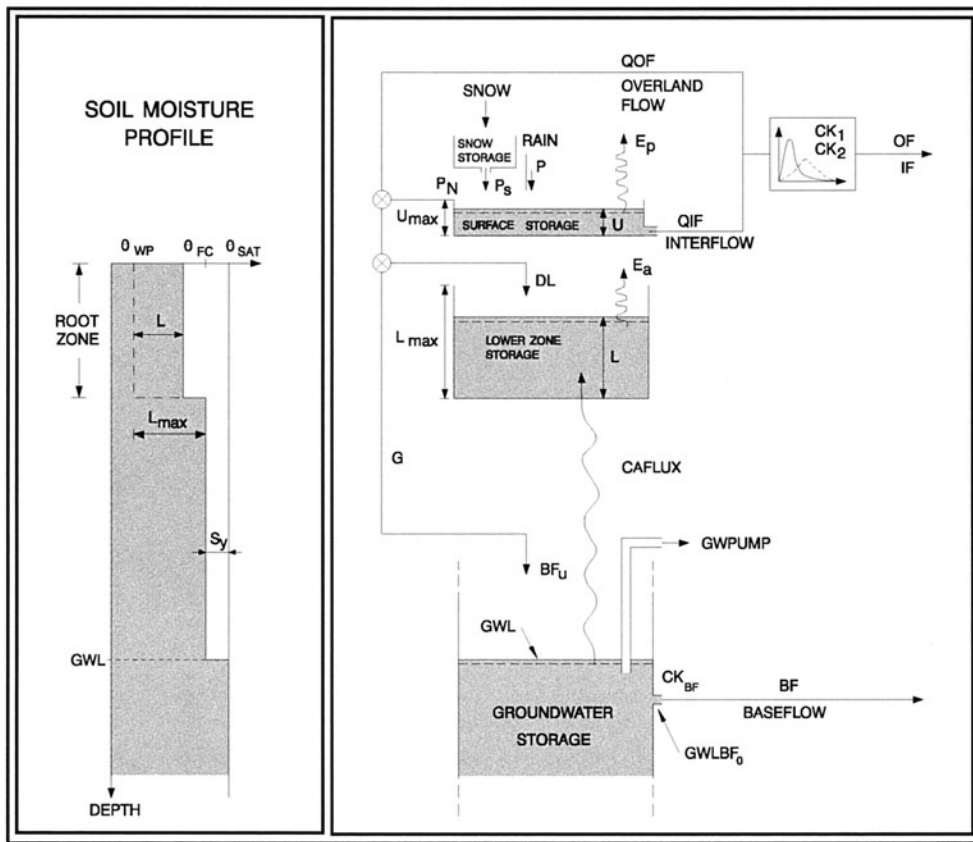


FIGURE 10 Typical structure of a lumped conceptual model illustrated by the NAM rainfall-runoff model. Courtesy of DHI Water & Environment.

parameters cannot usually be assessed from field data, but have to be obtained by a process of calibration where the parameters are adjusted until a satisfactory match is obtained between observations and model predictions. Conceptual models have successfully been applied at many different catchment sizes ranging from a few kilometers squared to more than 100,000 km². Experience indicates that some of the key parameter values are relatively stable over such a wide range of scales. Compared to empirical models, conceptual models by including a representation of the catchment behavior can be expected to provide improved accuracy for longer lead times. For short forecast lead times, the performance of these two model types is comparable.

C. Semidistributed and Distributed Models

In many conceptual models the equations and parameters of these models are representative for catchment scale conditions. Therefore, the spatial variability that catchment parameters exhibit has been built into the catchment scale equations and parameter values. Other models explicitly

include a number of zones or storages to represent the spatial distribution of soil type or altitude zones for snow storage or account for the variability indirectly through distribution functions. One of the main disadvantages of many conceptual models is their lumped description of the meteorological variables like rainfall and temperature, and hydrologic variables such as soil type and snow cover, that exhibit a high degree of spatial variability.

Theoretical studies have shown significant variations in the flood hydrograph depending on the location of the rain gauge and storm. This is also supported by more recent studies with very high resolution rainfall data in relatively small catchments that indicate that distributed models may, in certain cases, provide improved results compared to lumped models. However, the evidence is not conclusive and the physical mechanisms by which the rainfall on the catchment is transformed to discharge in a river are expected to smooth and dampen the effect of variability in space and time of the rainfall.

To address these spatial variability issues, several types of semidistributed rainfall-runoff models have been developed. One approach applicable to larger catchments is the

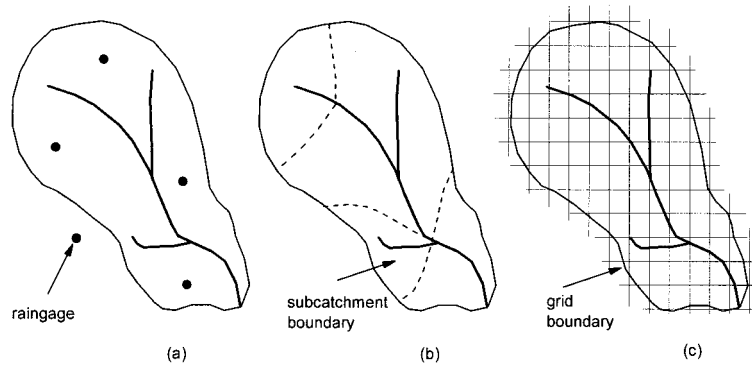


FIGURE 11 Lumped and semidistributed rainfall-runoff modeling. (a) Lumped description of a single catchment modeling using catchment average properties and meteorological inputs, (b) semidistributed modeling using subcatchment to represent spatial variability, (c) semidistributed modeling using rectangular grid to represent spatial variability in the catchment characteristics and meteorological inputs.

division or disaggregation of the catchment into a series of subcatchments connected to the river network. Each subcatchment is modeled using some form of rainfall-runoff model that provides lateral inflow or tributary flow that is then routed through the river network, (see Fig. 11). In this manner the spatial variation of both the meteorological and hydrologic variables can be captured.

A second group of models treat spatial variability by dividing the catchment into a set of hydrologic response units within a single model, often in the form of a grid or raster. Access to weather radar data has lead to the development of grid-based models that treat the surface hydrologic processes in a distributed manner designed to match the spatial resolution of satellite or weather radar (see Fig. 11). With weather radar a much finer spatial resolution of rainfall events can be obtained. The semidistributed model is based on digital terrain maps and simplified process equations discretized on the same spatial grid as the incoming radar images. The main advantage is a better representation of the spatial variability of the rainfall.

Today several general-purpose catchment models exist that use a fully distributed flow description, based on the governing partial differential flow equations for surface flow, soil moisture, and groundwater flow exist. Generally however, the detailed description of water movement in such models and the detailed treatment of the spatial variability of catchment properties (such as soil heterogeneity), are not called for in flood forecasting applications.

VI. FORECAST UPDATING

Updating or data assimilation refers to methods that take into account measurements of water level or discharge in preparing a forecast, adjusting through a feedback process the model to match the observations (see Fig. 12).

Updating is adopted for real-time forecasting to improve the initial state of the system prior to the time of forecast. Furthermore, updating is applied to model correction in the forecast period to account for any inadequacy in the model or in the input data. Updating the forecasts on observed streamflow or water levels provides a practical method of reducing the sensitivity of the flow forecasting model to uncertainties in rainfall data as well as taking advantage of the persistence in hydrologic flows to reduce prediction errors.

The hydrologic forecast model, which may be either a river routing model, a rainfall-runoff model, or a combination of these constitutes a process model. This process model consists of a set of equations that in general contains both state variables and parameters. The two quantities are distinguished by the fact that parameters remain constant while the state variables vary in time.

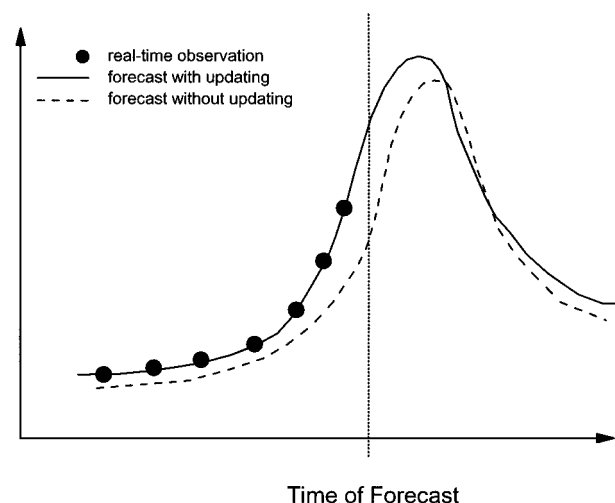


FIGURE 12 Effect of updating on flood forecasting accuracy.

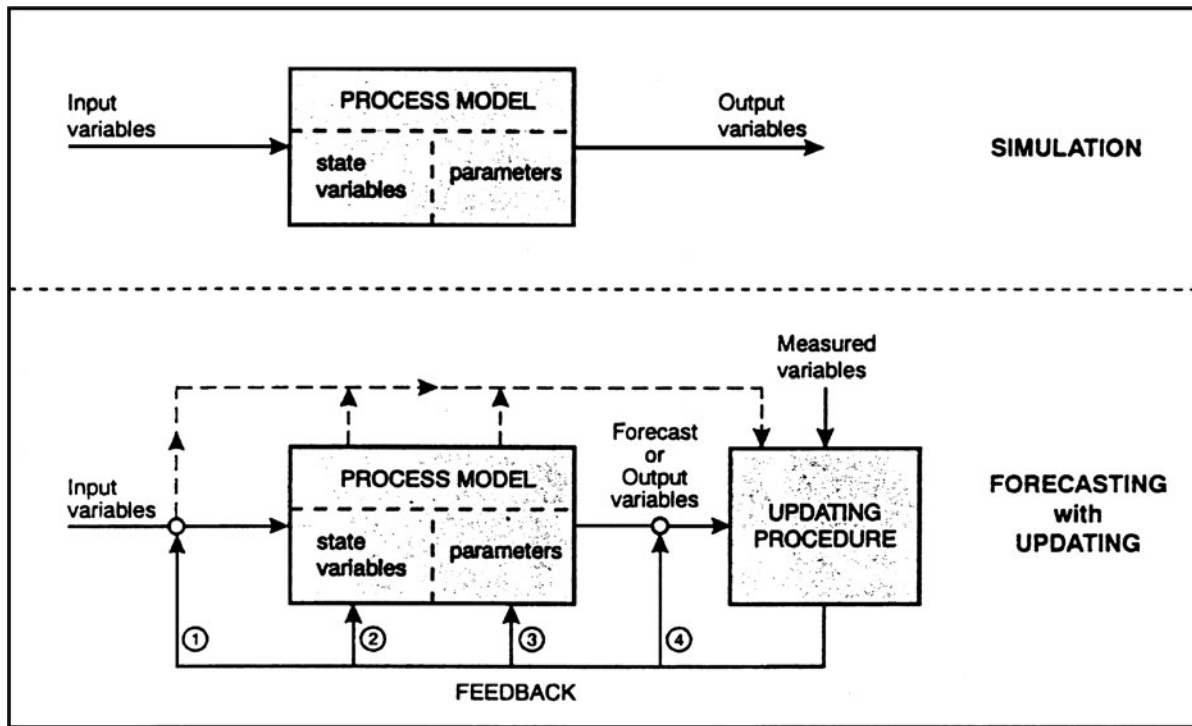


FIGURE 13 Classification of updating methods. [Reproduced with permission from Refsgaard, J. C. (1997). Validation and intercomparison of different updating procedures for real-time forecasting. *Nordic Hydrol.* **28**, 65–84, Fig. 1.]

Forecast updating procedures can be grouped according to whether the input variables (e.g., precipitation, temperature), state variables (such as water content in soil or in a linear reservoir), model parameters (such as infiltration capacity or routing constants), or output variables (discharge) are modified. In fact, operational updating methods may modify more than one of these groups. The four methodologies are illustrated in Fig. 13 and can be characterized as follows:

1. *Updating of input variables.* Updating of input variables, typically precipitation and air temperature, is justified by the fact that input uncertainties may often be the dominant error source in operational forecasting. Since input updating leads to changes in the model state, the effect may be similar to state updating.
2. *Updating of state variables.* Adjustment of state variables such as the snowpacks water equivalent and the water contents of the model conceptual storages representing the root zone, or water levels in the groundwater system or the river system can be carried out in different ways. Simple methodologies are found in some models, which enable updating of snow cover variables by observed data from snow surveys or satellites. Theoretically the most comprehensive methodology for state updating is
3. *Updating of model parameters.* In practice the use of this method is confined to statistical black box models where it may be argued that there is no clear distinction between state variable and model parameters. For other model types the model parameters are usually assessed through calibration using historical data. The value of recalibrating a model is of questionable value on the basis of the few data used in the updating period.
4. *Updating of output variables (error prediction).* The deviations between model simulations and the

based on Kalman filtering theory. Kalman filter methods are well established for linear systems and their application to linear forecast and transfer function models is straightforward as the flow forecast can usually be written as an explicit function of previous flows and the rainfall. This same theory can, with some modifications, (extended kalman filter) also provide approximate solution for nonlinear hydrologic and hydraulic systems, or using ensemble Kalman filter methods can treat nonlinear models exactly. Kalman-filtering-based updating actually allows simultaneous modification of both model states and model parameters. Kalman filter updating is based on the underlying uncertainty in the model and model inputs, however, often little is known *a priori* about these uncertainties.

3. *Updating of model parameters.* In practice the use of this method is confined to statistical black box models where it may be argued that there is no clear distinction between state variable and model parameters. For other model types the model parameters are usually assessed through calibration using historical data. The value of recalibrating a model is of questionable value on the basis of the few data used in the updating period.
4. *Updating of output variables (error prediction).* The deviations between model simulations and the

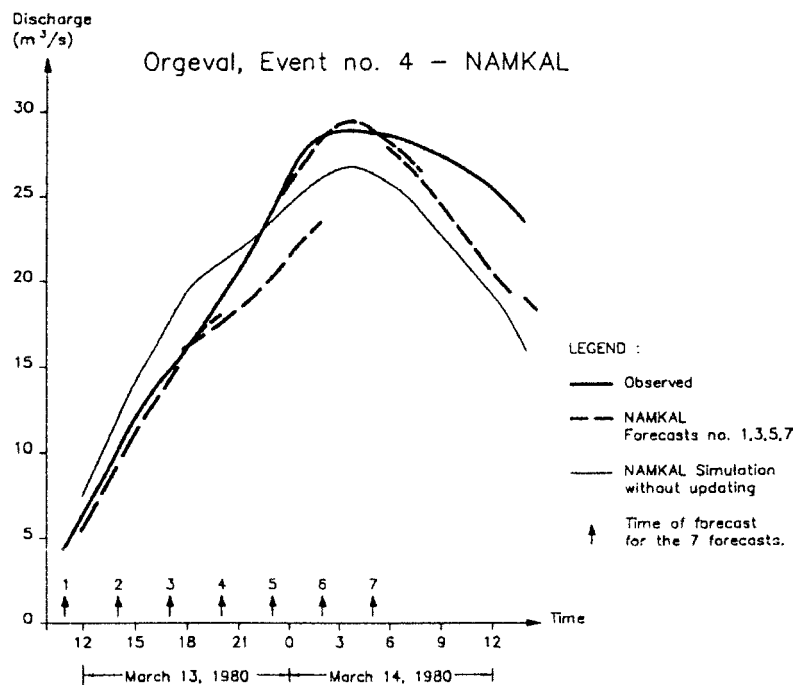


FIGURE 14 Simulation and forecasting results for the NAM model used in the 1988 WMO Simulated real-time intercomparison of hydrological models. [Reproduced with permission from Refsgaard, J. C. (1997). Validation and intercomparison of different updating procedures for real-time forecasting. *Nordic Hydrol.* **28**, 65–84, Fig. 2.]

observed river flows, i.e., the model errors, are often serially correlated. This persistence in the errors can be used to develop a forecasting procedure that consists of an initial forecast based on a hydrologic model plus a correction using the future values of these errors derived by time series models such as an AR model. This method is often referred to as error prediction and is widely used. The attraction of this method lies in its simplicity and the fact that it does not presuppose the source of the model error.

Automatic procedures are preferable in real-time forecasting because manual updating is subjective and time consuming, requiring experienced and proficient staff. Updating can substantially improve forecast accuracy for short lead-times (see Figs. 14 and 15), whereas an accurate (representative) model is necessary to achieve consistently good forecasts at longer lead times. Indeed, the model accuracy will determine the lower bound for long-term forecast error.

VII. FORECAST ACCURACY

Forecast accuracy is a measure of the forecast error, i.e., the difference between the value that is forecasted and the value actually observed. Accuracy is best assessed by a retrospective comparison of the forecast predictions and

observed flows or water levels (see Figs. 14 and 15). If this is done, then the measurement accuracy should also be included in the comparison. This is particularly relevant for discharge, which is often derived from water levels using a rating curve. Several objective measures of accuracy, commonly applied to forecasting, are given in Table I.

The bias B and the relative bias RB quantify any systematic error. The variance V reflects the random errors. A perfect forecast exists only if the bias and the variance are zero. The mean square error, root mean square error, mean absolute error, relative mean absolute error, and efficiency reflect both the random and systematic errors. Mean square error (MSE) or root mean square errors (RMSE) reflect the largest deviations, which are more critical in the case of high flow forecasting. Mean absolute error (MAE) and relative mean absolute error (RMAE) are less dominated by a small number of large errors and therefore provide a more reliable indicator of typical error magnitudes. R^2 is the square of the correlation coefficient between the observed and forecasted values. Although R^2 is widely used, care must be taken if appreciable bias is present, since R^2 evaluates the accuracy with respect to random error. For flood forecasting, these statistics should be prepared for significant flood events rather than for continuous long-term records.

In evaluating forecast accuracy it is useful to distinguish between *flood forecasting*; the calculation of high river flows and *flood warning*; the dissemination of a flood risk

ORGEVAL EVENTS 3–6

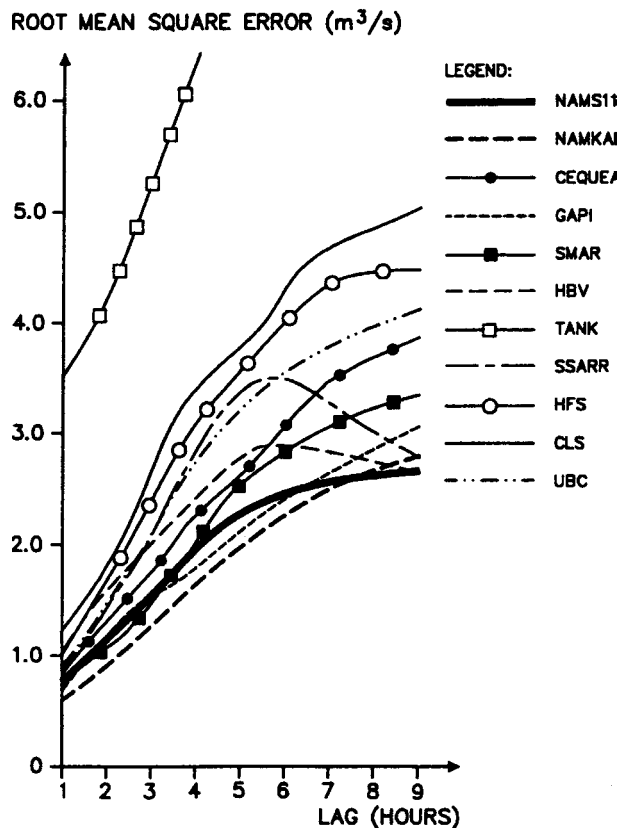


FIGURE 15 Root mean square errors (RMSE) as a function of forecast lead time for all models participating in the 1988 WMO simulated real-time intercomparison of hydrological models. [Reproduced with permission from Refsgaard, J. C., (1997). Validation and intercomparison of different updating procedures for real-time forecasting. *Nordic Hydrol.* **28**, 65–84, Fig. 4.]

estimate to those areas and people likely to be affected. The accuracy of flood warning can be assessed using simple warning statistics such as those summarized in Table II. The accuracy of the flood warning will depend to a large extent on the accuracy of the flood forecast but also on how well these forecasts can be converted into estimates of the flooded area. Essentially, this requires a relation between river levels and the area outside the river affected by flooding. This may be provided by an assessment of historical floods or by using topographical data. Accurate predictions of the flooded area may be difficult for extreme events where historical data are not available or where breaching of the confining channel occurs in an unpredictable manner.

A. Forecast Accuracy Versus Lead Time

Intuitively, the expected accuracy of a forecast will decrease (forecast uncertainty increase) with increasing lead

TABLE I Measures of Forecast Accuracy

Definition	Symbol	Equation
Forecasted flow	$Q_f(i)$	
Measured flow	$Q_0(i)$	
Number of observations	n	
	M_f	$M_f = \frac{1}{n} \sum_{i=1}^n Q_f(i)$
	M_0	$M_0 = \frac{1}{n} \sum_{i=1}^n Q_0(i)$
Measures	Symbol	Equation
Bias	B	$M_f - M_0$
Relative bias	RB	$\frac{B}{M_0}$
Mean square error	MSE	$\frac{1}{n} \sum_{i=1}^n [Q_f(i) - Q_0(i)]^2$
Root mean square error	RMSE	$(MSE)^{0.5}$
Variance	V	$MSE - B^2$
Mean absolute error	MAE	$\frac{1}{n} \sum_{i=1}^n Q_f(i) - Q_0(i) $
Relative mean absolute error	RMAE	$\frac{MAE}{M_0}$
Forecast efficiency	E	$1 - \frac{MSE}{V}$
R squared	R^2	$\frac{\left[\frac{1}{n} \sum_{i=1}^n Q_0(i)Q_f(i) - M_0M_f \right]^2}{\left[\frac{1}{n} \sum_{i=1}^n Q_0^2 - M_0^2 \right] \left[\frac{1}{n} \sum_{i=1}^n Q_f^2 - M_f^2 \right]}$

time because the forecasted streamflow in the immediate future is not expected to deviate significantly from the current situation. This arises from the persistence of river discharges. How the uncertainty increases with lead time will depend on the speed of response of the catchment as

TABLE II Measures of Forecast Warning Accuracy

	Flood warning	No flood warning
Flooding observed	A	B
No flooding	C	D
Measure	Symbol	Equation
Critical success index (threat score)	CSI	$A/A + B + C$
Probability of detection	POD	$A/A + B$
False alarm rate	FAR	$C/A + C$

well as the accuracy of the forecasting approach. The accuracy of a flow forecast depends on the following factors.

1. Accuracy and representativeness of the precipitation forecasts
2. Accuracy and representativeness of the precipitation measurements
3. Accuracy of boundary forecasts of water level and discharge
4. Accuracy of the forecasting model
5. The efficiency of the updating or data assimilation methods
6. The accuracy of flow and water level observations

The representativeness of the precipitation measurements refers to the ability of the measurement to capture the spatial and temporal variability of the flood producing rainfall. Forecast model uncertainty can arise from four main sources: uncertainty in the input data such as rainfall; uncertainty in the observations; errors due to suboptimal parameter values, i.e., inadequate model calibration; and errors due to incomplete or biased model structure, i.e., the model does not adequately represent the physical system. In general, flood routing is more accurate than rainfall-runoff modeling which is in turn more accurate

than rainfall forecasting. A retrospective assessment of forecast accuracy provides valuable information about the forecast accuracy as a function of lead time for a forecast system and can be used to identify where further improvements in forecast accuracy can be obtained. Operational experience suggests that in many cases the forecasted and observed rainfall inputs are the most significant source of forecast uncertainty. As shown in Fig. 16 the difference between forecasting and hindcasting (with perfect foreknowledge) of the rainfall and river boundaries has a dramatic effect on the forecast accuracy. The short-term accuracy in all cases is similar because updating on the river levels and discharge was used in this case to take advantage of the persistence in the flows.

It is both desirable and strongly recommended that estimates of forecast uncertainty are made as part of a forecast. Estimates of forecast uncertainty can be derived using a stochastic modeling framework such as the Kalman filter methods, which account for the input and model uncertainties. Alternatively recognizing that rainfall forecasts are often the largest source of forecast uncertainty, a range or ensemble of forecasts can be made (see Fig. 17) where different estimates of forecast rainfall are used to generate forecasts. A best estimate of the forecast can be made from the weighted mean of these forecasts, however, the

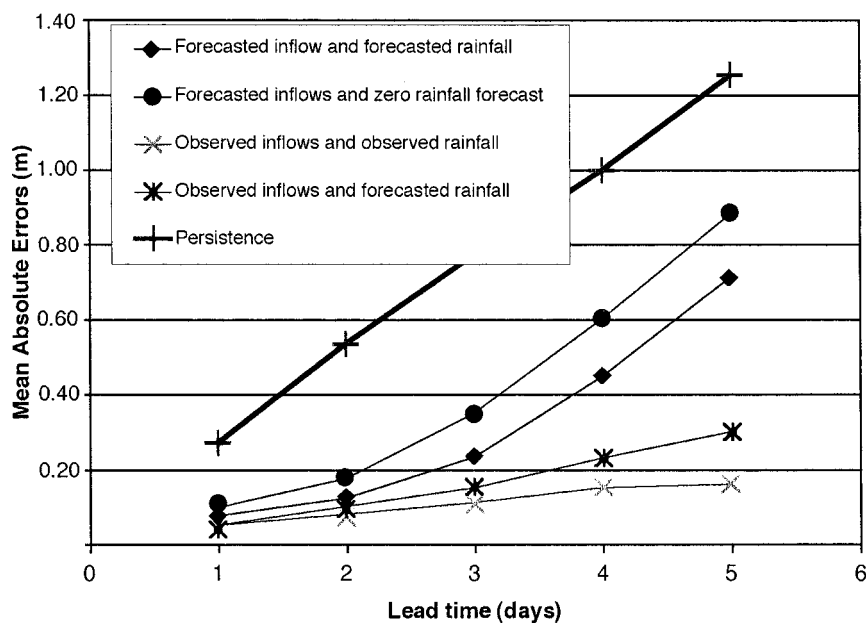


FIGURE 16 An example of an analysis of forecast accuracy as a function of lead time. Forecasts were made for the Hankou station near the city of Wuhan on the Yangtze River for the major flooding during 1998 using rainfall forecasts from a numerical weather model and forecasted inflows from regulated catchments. The forecast accuracy is compared for 4 cases. (1) Forecasted rainfall and inflows, (2) zero rainfall forecasts and forecasted inflows, (3) rainfall forecasts and observed inflows (perfect foresight) and (4) observed rainfall (perfect foresight) and observed inflows (perfect foresight). For reference simple persistence forecasts (forecast water levels = current water levels) are shown. Courtesy of DHI Water & Environment.

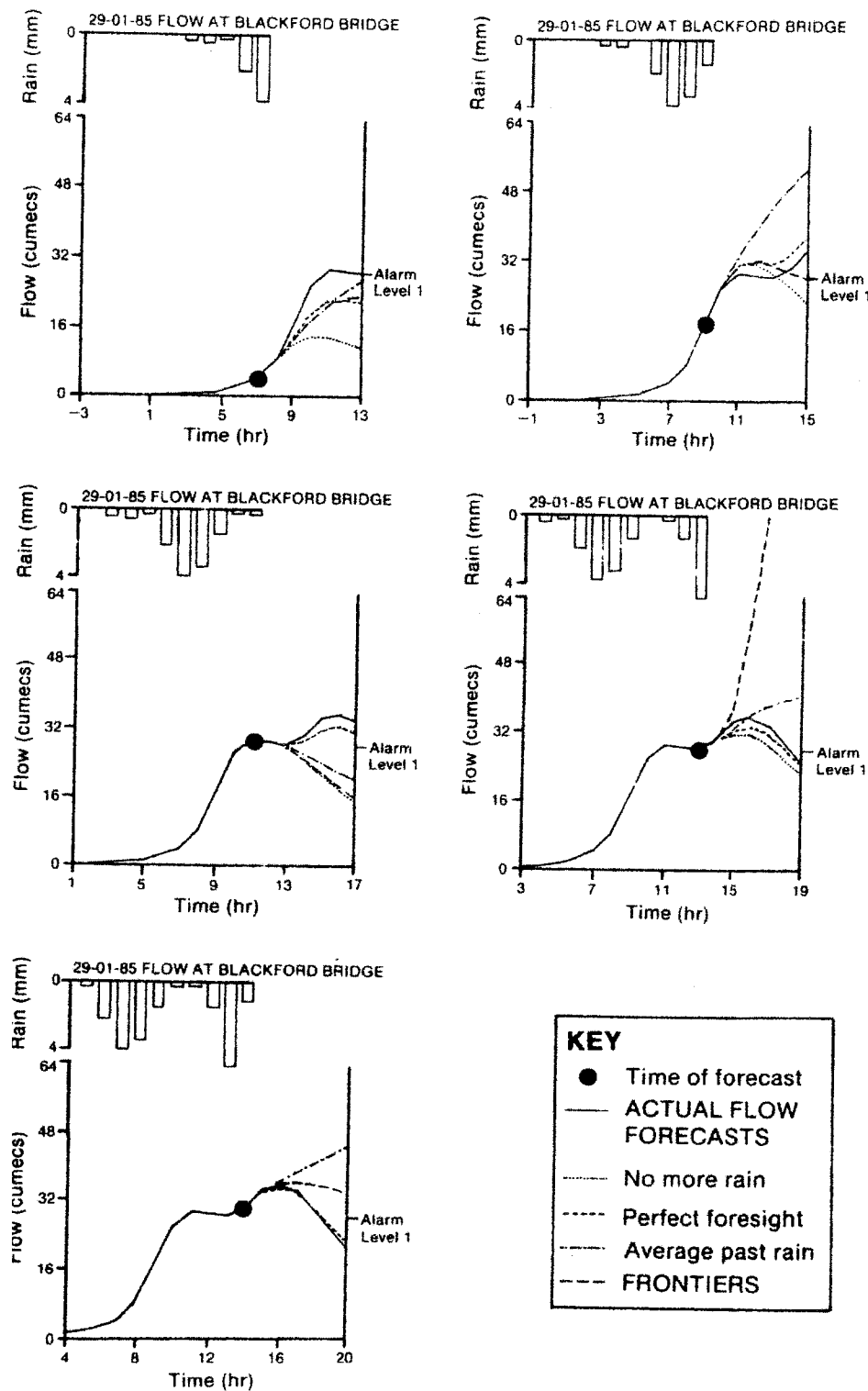


FIGURE 17 An example of ensemble forecasting using different rainfall forecasting methods. The figure shows a forecast sequence at a single site with several future rainfall scenarios. FRONTIERS is an operational forecasting system using the U.K. radar network developed by the U.K. Meteorological Office. [Reproduced with permission from Cluckie, I. D., and Owens, M. D. (1987). [Figure 12.10 Chapter 12. Real-time rainfall runoff models and use of weather radar information](#). In "Weather Radar and Flood Forecasting" (V. K. Collinge and C. Kirby, eds.), John Wiley, Chichester, Sussex.]

strength of this approach is that the ensemble provides a measure of the forecast uncertainty. The idea of ensemble forecasts can be readily extended to include forecasts using different models or updating methods.

VIII. LONG-TERM (SEASONAL) FORECASTING

Accurate long-term streamflow forecasts over a period of weeks or months are only relevant in situations where the future runoff is more strongly affected by storage of water within the catchment rather than by rainfall. For lead times of more than a few days the accuracy of meteorological forecasts is only marginally better than long-term climatological averages. Therefore only in cases where the forecast runoff is controlled by the initial catchment water storage can long-term forecasts improve on predictions based on long-term averages. This is typically the case where surface storage is controlled by lakes or reservoirs or for snowmelt forecasting where precipitation has accumulated as snow within the catchment during the winter and released during the spring thaw. Since the meteorological forecast accuracy is the limiting factor, it is important in such cases to ensure that the initial conditions within the catchment at the time of forecast are represented as accurately as possible. Therefore forecast updating may be of considerable importance in improving the forecast accuracy.

Long-term forecasting methods can be broadly classified into four main groups: index variable, storage

accounting, time series methods, and rainfall-runoff simulation.

A. Index Variable Methods

Index variable methods attempt to determine relationships between runoff during the forecast period to one or more variables that can be readily measured prior to the time of forecast. Typical index variables include current soil moisture, snow storage (as a water equivalent), accumulated precipitation, and accumulated runoff. The relationships developed are often based on well-known statistical techniques such as multiple regression and cluster analysis and therefore simple to implement. Furthermore if statistical methods are used it is straightforward to obtain confidence bounds on the forecasts. This is often more important than the estimation of a best forecast.

B. Storage Accounting Models

Storage accounting models estimate the amount of water stored in a catchment that is available for future runoff to derive a forecast that is some, usually linear, function of the estimated storage. For long-term forecasts this storage represents the water stored in large surface storages such as reservoirs or groundwater or snow. For example, the catchment storage S can be estimated at some time t as

$$S(t) = a + bP_a(t) - R_a(t) \quad (17)$$

P_a and R_a are the accumulated rainfall that has fallen on the catchment and accumulated runoff from the

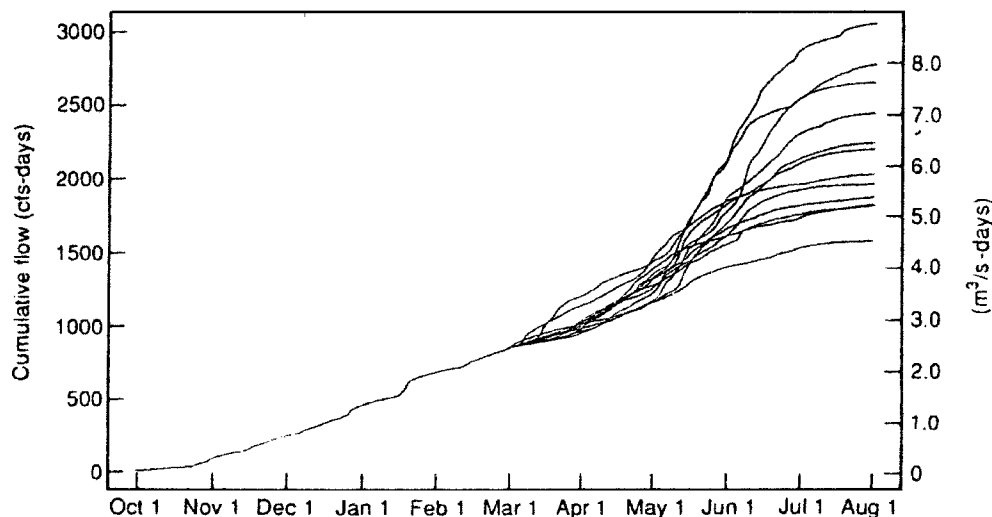


FIGURE 18 An example of extended streamflow prediction (ESP). The figure shows twelve alternate scenarios for the Rex River, Washington. The scenarios are generated from 12 years of historical data for precipitation and temperature starting from March 1. [Reproduced with permission from Lettenmaier, D. P. and Wood, E. F. (1992). Figure 26.3.2 Chapter 26 Hydrologic Forecasting, In "Handbook of Hydrology," (D. R. Maidment, ed.) McGraw-Hill, New York.]

catchment, respectively, up to the time of forecast. Assuming a linear relation between storage and forecasted discharge, then a forecast for lead time T at time t can be derived from

$$Q_f(t, T) = A(t, T)S(t) + B(t, T) \quad (18)$$

The constants A and B can be estimated by regression and are a function of both the lead time and the season.

C. Times Series Methods

Time series methods for forecasting such as the AR and MA models described earlier can also be used for long-term forecasting. It may be more appropriate in some cases to use more sophisticated models that include a time-dependent mean to account for seasonal behavior.

D. Extended Streamflow Prediction

Extended streamflow prediction (ESP) is a general approach for developing long-term forecasts based on rainfall-runoff models. The assumption is that the main contribution to the forecast uncertainty is in the long-term meteorological forecasts. First, the model is run up to the time of forecast using observed meteorological inputs, and updating should be used to ensure that the water storage (soil moisture, snow, lakes, etc.) within the catchment is represented accurately at the time of forecast. In its simplest form a long-term rainfall forecast is then used to predict the future stream forecast period. This could be a model forecast or an historical data set with similar conditions. However, one advantage of ESP is that alternative forecast scenarios can be made. This is similar to the concept of scenario forecasts. Alternative meteorological

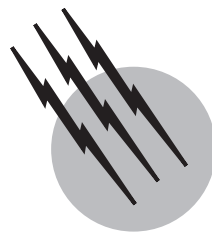
forecasts can be derived either by using all historical sequences of meteorological inputs or from synthetically generated realizations (see Fig. 18). In either case the meteorological forecast time series may be weighted according to their probabilities. From this ensemble of forecasts, a best estimate of the forecast can be made (usually the mean) and an estimate of uncertainty obtained from the distribution of forecasts.

SEE ALSO THE FOLLOWING ARTICLES

DISTRIBUTED PARAMETER SYSTEMS • ENVIRONMENTAL MEASUREMENTS • ENVIRONMENTAL OBSERVATION AND FORECASTING SYSTEMS • MATHEMATICAL MODELING • STREAMFLOW • WATER RESOURCES • WEATHER PREDICTION, NUMERICAL

BIBLIOGRAPHY

- Chow, V. T., Maidment, D. R., and Mays, L. W. (1988) "Applied Hydrology," McGraw-Hill International Editions, New York.
- Cunge, J. A., Holly, F. M., and Verwey, A. (1980). "Practical Aspects of Computational River Hydraulics," Pitman, London.
- Maidment, D. R. (1993). "Handbook of Hydrology," McGraw-Hill, New York.
- Nemec J. (1986). "Hydrological Forecasting," Reidel, Dordrecht.
- Refsgaard, J. C. (1997). Validation and intercomparison of different updating procedures for real-time forecasting. *Nordic Hydrol.* **28**, 65–84.
- Singh, V. P. (1995). "Computer Models of Watershed Hydrology" (V. P. Singh, ed.), Water Resources Publications, Colorado.
- Weigend A. S., and Gershenfeld, N. A. (1994). "Time Series Prediction: Forecasting the Future and Understanding the Past" (A. S. Weigend and N. A. Gershenfeld, eds.), Addison-Wesley, Reading, Massachusetts.



Ocean Surface Processes

James F. Price

Woods Hole Oceanographic Institution

- I. Atmospheric Forcing of the Upper Ocean
- II. Diurnal Thermal Cycle
- III. Modeling
- IV. Diurnal Current Cycle
- V. Mean Current Profile

GLOSSARY

Coriolis acceleration Apparent acceleration of a moving body that arises when the observer is on a rotating reference frame, such as the earth. The Coriolis acceleration is a function of latitude that vanishes on the equator and is maximum at the poles. At midlatitudes, Coriolis acceleration is important for ocean currents that have a time scale of several hours or more.

Density Weight per volume. Seawater density increases with increasing salinity and decreases with increasing temperature. In most open ocean regions, the temperature dependence is dominant.

Diurnal cycle Daily change in the upper ocean temperature and current that is driven by the daily variation of solar insolation.

Shear Vertical or horizontal rate of change of current with distance.

Stratification Vertical profile of density. Stratification is said to be statically stable when density increases with depth, which is almost always observed.

Wind stress Tangential force per unit area on the sea surface caused by the wind. Wind stress may be estimated from wind measurements.

I. ATMOSPHERIC FORCING OF THE UPPER OCEAN

CURRENTS AND TEMPERATURES in the upper ocean change ceaselessly in response to the time-varying forcing imposed by the atmosphere. Just how these changes occur poses an interesting problem in geophysical fluid mechanics that has important practical consequences. Short-term changes in currents can have major effects on biological processes, such as recruitment, and upper ocean temperature changes can feed back to effect the atmosphere itself. In this article, we consider some of the dynamics of the upper ocean response to local atmospheric forcing.

Atmospheric forcing of the upper ocean occurs by exchange of heat and water and by wind stress acting on the sea surface. Heat exchange is made up of four dominant terms: evaporation and sensible heat exchange, infrared radiation, and solar insolation. The first three terms generally act to cool the sea surface. Cooling at the surface tends to produce an unstable density profile, with heavier water above lighter water. This kind of static instability is quickly relieved by overturning and turbulence. Evaporation also leaves behind salt, which increases the surface

density, and wind on the sea surface produces waves and currents on a wide range of scales, all of which may eventually contribute to turbulence and vertical mixing in the upper ocean. Vertical mixing by these mechanisms often produces a surface layer that is vertically uniform and termed the surface mixed layer. The thickness of the ocean surface mixed layer is typically 30 m, but can be highly variable, as discussed later. (Mixed layers are also found within the bottom boundary layer of the ocean and in many other boundary layer flows.)

The fourth heat flux term, solar insolation, acts to warm the upper ocean. Unlike the other heat fluxes, which are absorbed within a few centimeters of the sea surface, solar insolation is attenuated more or less exponentially within an *e*-folding scale of from a few meters in very turbid coastal waters, up to 20 m in the very clear waters of the midocean gyres. Warming is concentrated near the surface and tends to produce a lighter surface layer (as does rainfall), which is statically stable and resists vertical mixing. As the heat fluxes and the winds change, the upper ocean is subject to an almost constantly changing balance between processes that act to destabilize and mix the upper ocean—heat loss to the atmosphere and the many effects of wind on the sea surface—and the stabilizing effect of solar heating and occasional rainfall. When destabilizing processes are dominant, the surface mixed layer grows thicker. When solar heating or rainfall dominates, the surface mixed layer becomes thinner, and may disappear altogether at times of intense heating or rainfall.

In most mid- and high-latitude regions, the largest temporal variations in atmospheric forcing are associated with the seasonal cycle, winter storms, and the diurnal cycle. The largest amplitude upper ocean response is generally to the seasonal cycle. For example, the seasonal cycle in the eastern North Pacific Ocean at weather station P (50 N, 145 W) has been observed over several decades, and a composite is shown in Fig. 15 of the Encyclopedia article “Ocean–Atmosphere Dynamics.” The sea surface temperature has a minimum in March of about 5°C and a maximum in August of about 13°C. The heat flux that drives this seasonal cycle in the upper ocean has an almost sinusoidal form. The heating season runs from about late March until late September with a peak in the daily average heat flux of about 160 W m⁻² in mid-June. Heat is stored in the upper ocean during the heating season and then given back to the atmosphere during the cooling season, which runs through the remainder of the year.

Heat is stored within a layer called the seasonal thermocline, which has a thickness of about 75 m at Station P, but varies over the world ocean from about 50 m to 30 m. Because the heat capacity of water is large, and because the thickness of the heat storage layer (the seasonal thermocline) is also large, the upper ocean acts as an enormous

heat reservoir for the earth’s climate (much larger than the heat reservoir of the land, where seasonal effects penetrate only a few meters, or the atmosphere, which has a thermal memory of only a few days). Thus, the seasonal cycle of the upper ocean serves to delay and moderate the seasonal change in weather.

II. DIURNAL THERMAL CYCLE

The dominant heating process, solar insolation, varies on a diurnal cycle, and the upper ocean undergoes a diurnal cycle in temperature and current that is in some ways a microcosm of the seasonal cycle. The upper ocean diurnal cycle is generally not important to weather phenomena because the amplitude of the sea surface temperature response is usually small, 1°C or less, compared with typical air–sea temperature differences. Nevertheless, the diurnal cycle is very important in some kinds of acoustic problems (the so-called “afternoon effect” of degraded acoustic detection was an important factor in World War II antisubmarine warfare), and as we will see below, the properties of the diurnal cycle contribute directly to the long-term mean state of the upper ocean. Because the diurnal cycle is relatively brief, oceanographers have been able to acquire enough separate, detailed realizations (an example of 4 days is shown in Fig. 1) to see how the diurnal cycle varies with the local weather conditions. The diurnal cycle can thus serve as a valuable test of concepts and models of the upper ocean.

The data in Fig. 1 were acquired during the spring at a site in the eastern North Pacific about 400 km west of San Diego, CA, when weather conditions were fair. Wind stress varied from a maximum on the first 2 days of about 0.12 Pa (wind speed of about 10 m sec⁻¹) and decreased to about 0.04 Pa on the second 2 days. Heat loss (the sum of evaporation, sensible heat flux, and long-wave radiation) was roughly 250 W m⁻² throughout the period (little diurnal variation of heat loss). Solar insolation had a maximum at midday of about 800 W m⁻², which varied from day to day because of variation in cloud cover. Typical of most fair weather conditions, the heat flux was positive (warming and stabilizing) during midday because of solar insolation, and thus there was an appreciable diurnal thermal cycle on each day.

Aside from a greatly reduced amplitude, the diurnal cycle of upper ocean temperature has a marked resemblance to the seasonal cycle of temperature noted for Station P. During midday, when the stabilizing effect of solar insolation is dominant, the surface mixed layer becomes thinner, and as it retreats, it leaves behind a warmed, stratified layer analogous to the seasonal thermocline. When solar insolation decreases and then stops in late afternoon, wind mixing and heat loss then become dominant and cause

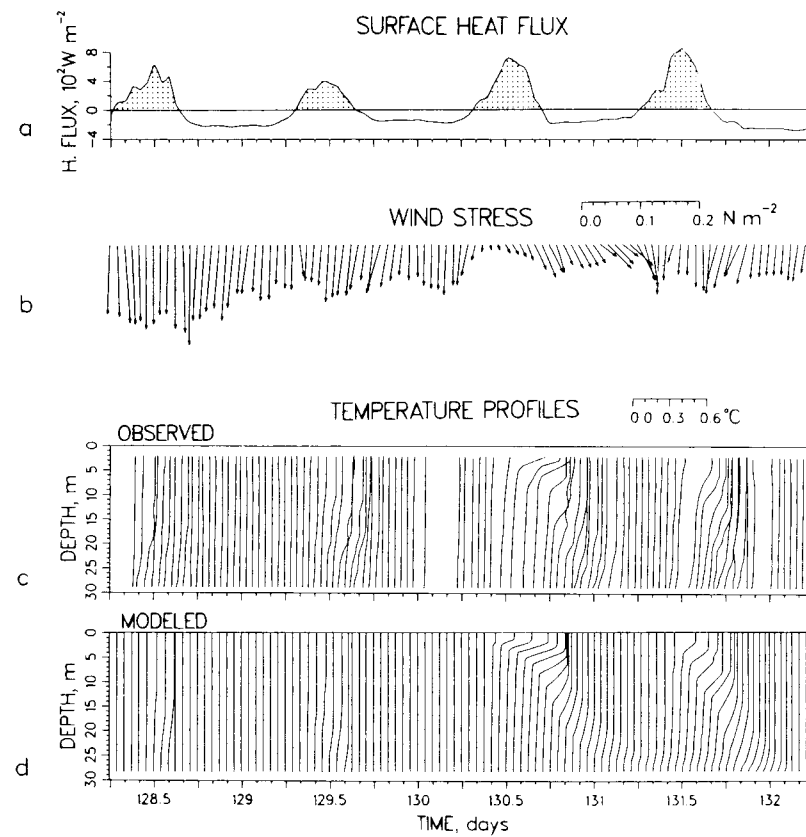


FIGURE 1 Heat flux (a), wind stress (b), and upper ocean temperature profiles (c) observed over a 4-day period of fair weather. Note the diurnal cycle of the surface mixed layer—thickening during the evenings when heat flux was negative (cooling and destabilizing) and shallowing during midday when solar insolation caused the heat flux to become positive (warming and stabilizing). The bottom set of profiles (d) is the simulated diurnal cycle from a numerical model. [From Price, J. F., Weller, R. A., and Pinkel, R. (1986). *J. Geophys. Res.* **91**, 8411–8427.]

the mixed layer to begin to grow in thickness. By early morning, continued heat loss and mixing largely erase the warming of the previous day. (If there is a net heat gain over the day, then the lower portion of the diurnal thermocline may remain; a succession of such days in late spring forms a seasonal thermocline.)

The amplitude of the surface response varied considerably over these 4 days. The diurnal increase was only about 0.1°C on the first 2 days and was about 0.4°C on the third day. The net surface heat flux changed much less than this, suggesting that the thickness of the heat storage layer (the diurnal thermocline and mixed layer) must have varied considerably from day to day. In this case, the day to day variation of the surface response is caused mainly by the variations in the wind stress amplitude. A large wind stress causes strong vertical mixing, so that the solar insolation absorbed near the surface is mixed and stored over a thicker layer on the first 2 days (midday minimum thickness) than on the next two days (midday minimum of 5 m or less). For a given warming heat flux, the amplitude of the surface response is thus considerably larger when

the wind stress is weaker, and the warming heat flux caused by solar insolation is mixed and stored over a thinner layer.

This dependence upon wind stress leads directly to an often marked spatial variation in the sea surface temperature response that can be readily observed in satellite infrared imagery. For example, regions of very large sea surface temperature response, up to 3°C , are often found to underly the major marine high-pressure systems (for example, the Bermuda high), which may cover an appreciable fraction of the midlatitude oceans during summer. This diurnal variability of sea surface temperature is for most purposes an unwanted noise. Some day it may be useful as a diagnostic of weather conditions in remote regions not sampled by conventional methods.

III. MODELING

These observations suggest some of the dynamics that have to be incorporated into a realistic model of the upper

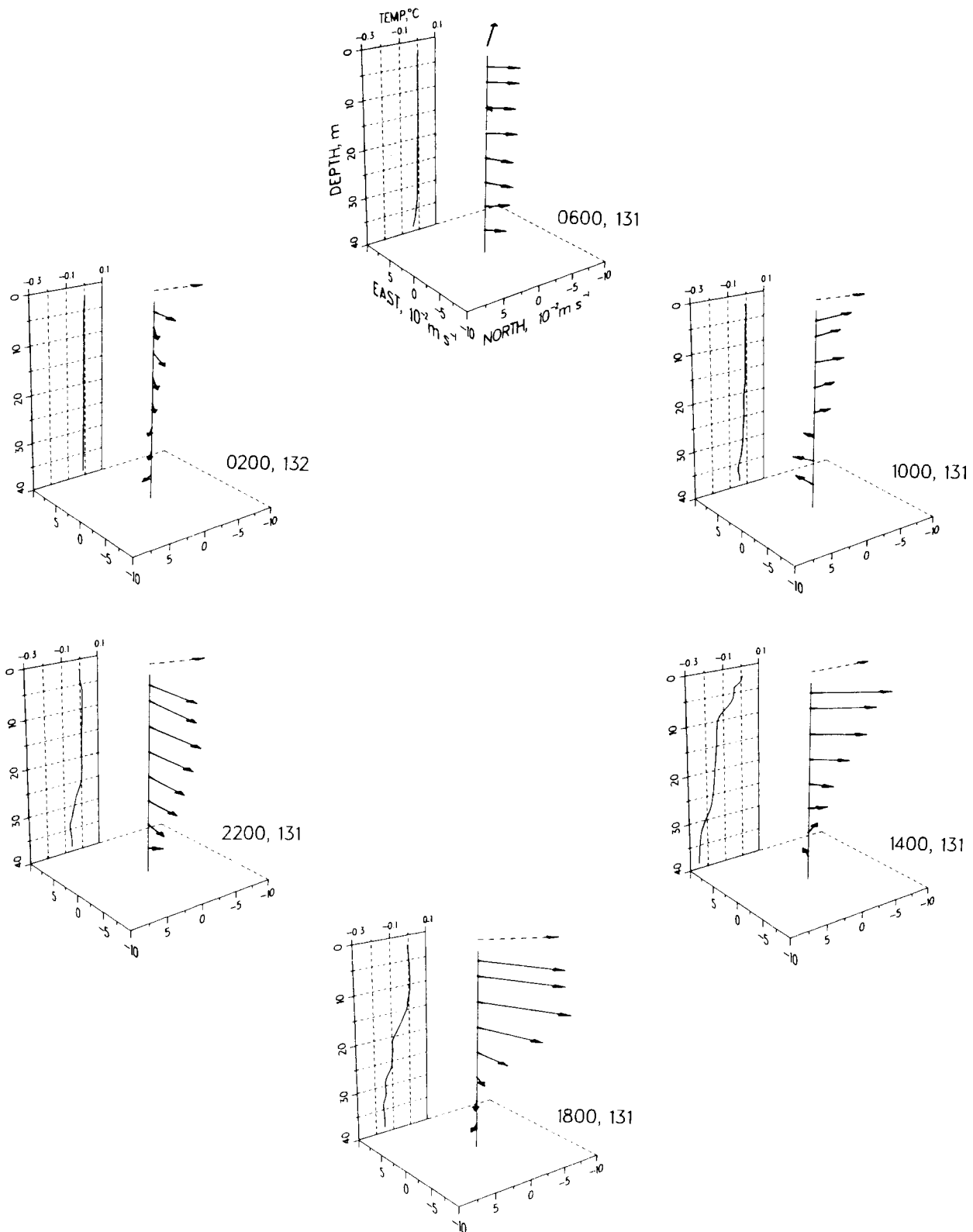


FIGURE 2 Current profiles made during the fourth day shown in Fig. 1. Note that the momentum flux supplied by the wind stress (topmost dashed vector) appears to be absorbed within the warm surface mixed layer. The clockwise rotation of the current is due to the Coriolis force. [From Price, J. F., Weller, R. A., and Pinkel, R. (1986). *J. Geophys. Res.* **91**, 8411–8427.]

ocean response to a stabilizing heat or water flux. The key problem is to estimate the depth that vertical mixing will penetrate from the surface for a given stabilizing heat flux (or rainfall rate) and a given wind stress. (A classical measure of this depth is the Obukhov length, which assumes implicitly that the primary mechanism of vertical mixing is by turbulence generated by the stress on the boundary.) Some evidence suggests that an important source of turbulent energy used for vertical mixing in the upper ocean is the vertical shear of the wind-driven current. In that case, stratification and the vertical shear of the current may be related by a Richardson number. Simulations from a numerical model built upon this hypothesis, and forced by the heat flux and wind stress shown at the top of Fig. 1, are plotted at the bottom of Fig. 1. The model simulations reproduce much of the day to day variation observed in the oceanic temperature profiles. Note that the model simulations give a very smooth, regular temperature profile since the high-frequency variability caused by internal waves is omitted.

IV. DIURNAL CURRENT CYCLE

The wind-driven current also changes on a diurnal cycle, and Fig. 2 shows the current profile observed during midafternoon on the fourth day shown in Fig. 1. The momentum flux supplied by the wind stress (the dashed vector just above the current profile) appears to be trapped within the surface mixed layer, whose thickness was about 5–10 m during midday. This current accelerates downwind during midday on account of the wind stress and is also rotated to the right by the Coriolis force. By the end of the afternoon, the diurnal current has rotated 90° to the right of the wind stress and has reached its largest amplitude, about 0.1 m sec^{-1} . Further rotation causes the current to flow into the wind, so that the wind stress then acts to retard the current. By the end of the following morning, the diurnal current from the previous day may be erased completely. Like the thermal cycle, this diurnal current cycle takes place every day under fair weather conditions. The depth and the amplitude of the midday current vary along with the thermal cycle shown in Fig. 1, and for example, the diurnal current is thicker at midday when the wind stress amplitude is greater.

V. MEAN CURRENT PROFILE

The long-term mean current profile observed during fair weather conditions has a structure that is determined to a large extent by the properties of the diurnal current cycle. An example of the mean wind-driven current acquired from the western North Atlantic during the long-term upper ocean study program (LOTUS) is shown in Fig. 3 (left).

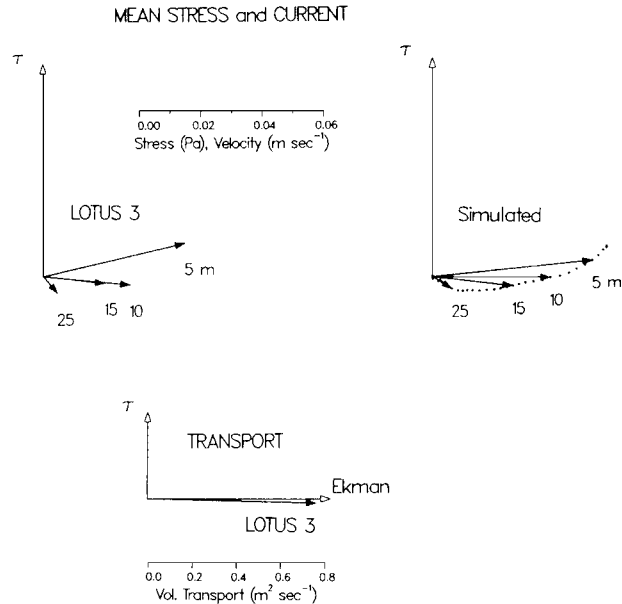


FIGURE 3 Mean current profile observed during a 6-month period of fair weather during the LOTUS 3 experiment (left) and as simulated by a numerical model (right). The lower pair of vectors is a comparison of the observed volume transport (LOTUS 3), and the transport estimated from the mean wind stress using the Ekman relation (Ekman). [From Price, J. F., Weller, R. A., and Schudlich, R. R. (1987). *Science* **238**, 1534–1538.]

These LOTUS observations span most of a heating season when diurnal thermal and current cycling were well developed. Under these conditions, the mean current profile has a spiral structure, with amplitude decreasing away from the surface where the value is about half the amplitude of the diurnal peak current (imagine calculating the time mean profile over the diurnal current cycle of Fig. 2). The mean current rotates to the right (Northern Hemisphere) with increasing depth. This spiral is at least roughly similar to an Ekman spiral, which is the theoretical profile expected if the turbulent viscosity were constant with depth. There are some differences in detail. Even very near the surface, the observed mean current flows at almost a 90° angle to the right of the mean wind stress; at that depth, the Ekman spiral would flow about 50° to the right of the wind.

The numerical model noted previously also simulates the mean current profile with some fidelity [Fig. 3 (right)]. Model results suggest that if the heat flux had been weaker (less strongly warming) or the wind stress had been stronger, then the spiral would have been less strongly trapped near the sea surface.

While the detailed structure of the mean current is different from that of an Ekman spiral, the volume transport (integrated current over the full depth of the wind-driven layer) is found to be consistent with the Ekman transport

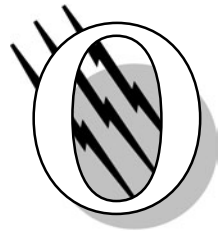
relation to within experimental error. Transport is almost 90° to the right of the mean wind stress, and its amplitude is such that the Coriolis acceleration on the integrated current is nearly equal and opposite to the wind stress acceleration on the sea surface.

SEE ALSO THE FOLLOWING ARTICLES

FLUID DYNAMICS (CHEMICAL ENGINEERING) • OCEAN-ATMOSPHERIC EXCHANGE • OCEANOGRAPHY, CHEMICAL • OCEAN THERMAL ENERGY CONVERSION • PHYSICAL OCEANOGRAPHY, OCEANIC ADJUSTMENT • PHYSICAL OCEANOGRAPHY, THERMAL STRUCTURE AND GENERAL CIRCULATION

BIBLIOGRAPHY

- Kraus, E. B. (1972). "Atmosphere–Ocean Interactions," Oxford Univ. Press (Clarendon), London and New York.
- Kraus, E. B., ed. (1977). "Modeling and Prediction of the Upper Ocean," Pergamon, New York.
- Price, J. F., Weller, R. A., and Pinkel, R. (1986). Diurnal cycling: observations and models of the upper ocean response to heating, cooling and wind mixing. *J. Geophys. Res.* **91**, 8411–8427.
- Price, J. F., Weller, R. A., and Schudlich, R. R. (1987). Wind-driven ocean currents and Ekman transport. *Science* **238**, 1534–1538.
- "Seawater" (1989). Pergamon Press, Oxford.
- Stramma, L., Cornillon, P., Weller, R. A., Price, J. F., and Briscoe, M. G. (1986). Large diurnal sea surface temperature variability: satellite and in situ measurements. *J. Phys. Oceanogr.* **16**, 827–837.
- Turner, J. S. (1973). "Buoyancy Effects in Fluids," Cambridge Univ. Press, London and New York.



Ocean-Atmospheric Exchange

Joost A. Businger

National Center for Atmospheric Research

- I. Introduction
- II. Transfer Processes Near the Interface
- III. Boundary Layers

GLOSSARY

Boundary layer Layer of fluid adjacent to the surface where the direct physical influence of the surface is felt. In the atmosphere and ocean these layers are typically turbulent, and turbulent transport to and from the surface of a number of properties is an important characteristic.

Ekman spiral Theoretical solution of the velocity profile in a laminar boundary layer over a smooth surface in a rotating coordinate system. Ekman was the first to give this solution.

Interface Surface that separates two different fluids such as air and water.

Inversion Layer where the temperature increases with height. This situation is typical at the top of the boundary layer where the transition to the free atmosphere occurs.

Molecular sublayer Layer very close to the interface where turbulence is suppressed and the molecular properties such as viscosity and thermal diffusivity become important in describing the transport processes. The molecular sublayer typically is of the order of 1 mm or less.

Rough flow When the interface is strongly modulated by the flow (e.g., a strong wind) and the molecular sublayer

characteristics very close to the interface become difficult to distinguish; the aerodynamic characteristics of the profile show a roughness length greater than corresponds to a molecular sublayer.

Roughness length Characteristic length scale in the wind profile that relates to the roughness elements of the surface.

Salinity Concentration of salt in sea water.

Smooth flow When the interface is relatively smooth and the molecular sublayer is well established; the turbulent wind profile has a specific transition to a laminar layer near the interface.

Surface layer Part of the boundary layer near the interface where the fluxes of momentum and heat are approximately constant with height or depth.

Surface renewal Model concept of what happens very close to the interface. It is assumed that fluid elements at the interface itself are replaced from time to time by fluid from layers some distance away from the interface. The new fluid elements at the surface are then at rest and modified by molecular processes until the element is replaced again.

Thermocline Transition layer at the bottom of the ocean mixed layer, which is characterized by a decrease in temperature and an increase in density with increasing depth.

OCEAN-ATMOSPHERE interaction consists of the physical processes that take place at the interface between the ocean and atmosphere and the consequences of these processes for both media. The boundary layers on both sides of the interface are a direct consequence of these physical processes and reflect the direct influence of the interface on both fluids. The interaction also includes such indirect effects as large scale circulations in both ocean and atmosphere, el niño, and even climatology, which are not discussed in this article.

I. INTRODUCTION

A. General Remarks

The atmosphere and ocean are in intimate contact at the interface. Here momentum, water, heat, and trace constituents are exchanged. Often this exchange is modest as when a light breeze strokes the surface; sometimes the processes are violent as when gale-force winds sweep up ocean spray into the atmosphere and when breaking waves engulf air. The transition between ocean and atmosphere may even become indistinct. It seems that the wind is the driving force for the exchanges, but the wind itself depends on where and when these interface exchanges took place, which is why the study of air-sea interaction is of such vital interest to both oceanographer and atmospheric scientist.

Both ocean and atmosphere are fluids that behave in a similar way in a field of forces. The main physical difference is that water is about 800 times more dense than air at sea level. The transition from ocean to atmosphere is a transition of one fluid to another with similar physical characteristics, and yet, because of the large jump in density from water to air, the interface, in most cases, may be considered a material surface; thus no turbulent transport takes place across it, except in the areas of breaking waves. On both sides of the interface the fluids are usually in turbulent motion, and properties are transported readily; but near the interface, turbulence is suppressed so that on both sides of the interface a very thin layer exists where the molecular coefficients control the transport. Consequently the interface is a barrier to the transport of heat, momentum, and trace constituents of the ocean-atmosphere system.

We are interested in a quantitative determination of the thickness of the molecular sublayers and the strength of the gradients and shears within them. Also we would like to know something about the transition to the well-mixed turbulent layers that exist beyond the molecular sublayers and the boundary layers delineating the region where the interaction at the interface may be felt.

The boundary layers are most clearly defined when the interactions at the interface are strong, for example, dur-

ing a continental cold air outbreak over a relatively warm ocean. In this case, the height of the marine boundary layer (MBL) is usually marked by a strong inversion, above which the atmosphere is relatively undisturbed. Similarly the depth of the ocean mixed layer (OML) is marked by a strong thermocline or pycnocline, below which the ocean is relatively undisturbed. When the interactions are weak, the direct effects of the transfers from the surface are often difficult to observe, and the boundary layers become less distinct.

We shall therefore focus our discussion on the well-mixed strongly interacting MBL and OML. The modeling of this type of boundary layer has progressed to the point that the scientific community has reached consensus on a number of characteristics. Of special interest in the MBL is the cloud-topped boundary layer. Whether or not a cloud forms or dissipates in the boundary layer depends on rather subtle differences in its structure; but whether or not a cloud is present has dramatic impact on the energy budget of the boundary layer in particular and on the ocean-atmosphere system in general. Boundary layer clouds, especially marine stratus, are likely to play an important role in determining the climate.

B. Basic Equations

The equations that govern the physical behavior of air, water, and the interface are the conservation equations of mass, momentum, and energy, and the equations of state for air and sea water. This set of equations is nonlinear and unstable to perturbations in media such as the atmosphere and the ocean near the interface. Consequently the flows on both sides of the interface are turbulent, and no analytical solutions to the equations are realistic, although some may have diagnostic value, such as the Ekman spiral (see below). Turbulent quantities are customarily divided into a mean and a fluctuating part. Several assumptions are involved in this manipulation of the data, which is called Reynolds averaging.

When the quantities are divided into a mean and a fluctuating part, the number of equations doubles, but the number of unknowns more than doubles because the nonlinear nature of the equations introduces correlations between fluctuating parts that are in themselves new unknowns. So we are faced with the problem that Reynold's averaging leads to a set of equations that is no longer closed. This is called the closure problem of turbulence. Many semiempirical, semitheoretical approaches have been proposed to close the set of equations, in many cases with considerable success. Finally, the assumption is made that air and water may be treated as incompressible fluids. Fluctuations in density enter only in effects of buoyancy. These assumptions are called the Boussinesq approximations.

The set of equations we are interested in may now be given as follows.

**CONSERVATION OF MASS
(CONTINUITY EQUATION)**

$$\frac{\partial U_i}{\partial x_i} = 0, \quad \frac{\partial u_i}{\partial x_i} = 0 \quad (1)$$

where U_i is the mean and u_i the fluctuating component of the wind or current. In general, a mean quantity is indicated by a capital symbol and the fluctuating part by the same symbol in lower case.

**CONSERVATION OF MOMENTUM
(EQUATIONS OF MOTION)**

$$\begin{aligned} \frac{\partial U_i}{\partial t} + \frac{\partial}{\partial x_i} [U_j U_i + \bar{u}_j u_i] \\ = -\frac{1}{\rho_0} \frac{\partial P}{\partial x_i} + \nu \frac{\partial^2 U_i}{\partial x_j^2} + g_i - 2\varepsilon_{ijk} \Omega_j U_k \end{aligned} \quad (2a)$$

$$\begin{aligned} \frac{\partial u_i}{\partial t} + \frac{\partial}{\partial x_j} [U_j u_i + u_j U_i + u_i u_j - \bar{u}_i \bar{u}_j] \\ = \frac{1}{\rho_0} \frac{\partial p}{\partial x_i} + \frac{g_i}{\rho_0} \rho' + \nu \frac{\partial^2 u_i}{\partial x_j^2} - 2\varepsilon_{ijk} \Omega_j u_k \end{aligned} \quad (2b)$$

**CONSERVATION OF ENERGY
(ENTHALPY OR HEAT CONDUCTION EQUATION)**

$$\frac{\partial \Theta}{\partial t} + \frac{\partial}{\partial x_i} [U_i \Theta + \bar{u}_i \theta] = \kappa \frac{\partial^2 \Theta}{\partial x_i^2} \quad (3a)$$

$$\frac{\partial \theta}{\partial t} + \frac{\partial}{\partial x_i} [u_i \Theta + U_i \theta + \bar{u}_i \bar{\theta}] = \kappa \frac{\partial^2 \theta}{\partial x_i^2} \quad (3b)$$

**CONSERVATION OF A TRACE CONSTITUENT
(e.g., SALINITY, WATER VAPOR, OZONE)**

$$\frac{\partial C}{\partial t} + \frac{\partial}{\partial x_i} [U_i C + \bar{u}_i c] = D \frac{\partial^2 C}{\partial x_i^2} + S \quad (4a)$$

$$\frac{\partial c}{\partial t} + \frac{\partial}{\partial x_i} [u_i C + U_i c + u_i c - \bar{u}_i \bar{c}] = D \frac{\partial^2 c}{\partial x_i^2} \quad (4b)$$

where ρ is the density, P the mean pressure, p the fluctuating part of pressure, g the acceleration of gravity, ν the kinematic viscosity, ε_{ijk} the permutation tensor, Ω the earth's rotation vector, Θ the mean temperature, θ the fluctuating part of temperature, κ the thermal diffusivity, C the mean concentration, c the fluctuating component of concentration of trace constituent, and S the source or sink.

EQUATION OF STATE FOR AIR. For the air above the interface, the equation of state for an ideal gas may be used, which may be expressed by

$$P = R_a \rho_a \Theta_v, \quad (5)$$

where R_a is the universal gas constant for dry air ($287.1 \text{ J kg}^{-1} \text{ K}^{-1}$), ρ_a the density of air, and Θ_v is the virtual temperature, which is given by

$$\Theta_v = (1 + 0.61q) \Theta_a, \quad (6)$$

where q is the specific humidity and Θ_a the actual air temperature. The virtual temperature has been introduced so that in equation of state (5) the gas constant is not dependent on humidity.

EQUATION OF STATE FOR SEA WATER. This equation of state is more complex because salinity plays also an important role. Of special interest is the density of sea water ρ_w , which determines the stratification of the ocean:

$$\rho_w = \rho_w(\Theta_w, s, P), \quad (7)$$

where Θ_w is the water temperature and s denotes salinity. Figure 1 gives the density as a function of temperature and salinity. The salinity of the world's oceans varies between about 33 and 37 parts per thousand.

C. The Ekman Spiral

In the special case that there is no turbulence, Eqs. (2a) have a steady-state analytical solution for horizontally

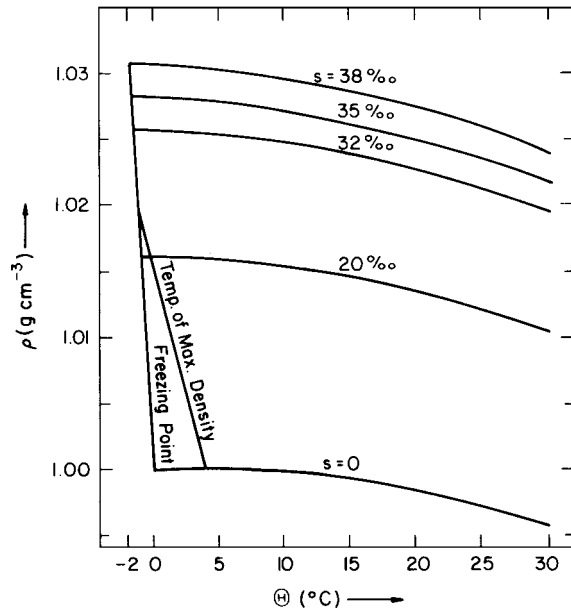


FIGURE 1 Density of water with different salinities as a function of the temperature [After Kraus, E. B., and Businger, J. A. (1994)].

uniform conditions that was first described by Ekman (1905). For this case Eq. (2a) reduces to

$$\frac{1}{\rho_0} \frac{\partial P}{\partial x} = v \frac{\partial^2 U}{\partial z^2} \quad (8a)$$

and

$$\frac{1}{\rho_0} \frac{\partial P}{\partial y} = v \frac{\partial^2 V}{\partial z^2} \quad (8b)$$

where U is the east-west component and V the north-south component of the wind. This set of equations can be applied to the boundary layers on both sides of the interface. We first observe that above the marine boundary layer (MBL), we have the geostrophic balance, which may be expressed by

$$f \mathbf{k} \times \mathbf{G} = -\frac{1}{\rho} \nabla P, \quad (9)$$

where f is the coriolis parameter and \mathbf{G} the geostrophic wind vector.

For the MBL it is convenient to choose the x -axis in the direction of the geostrophic wind. Equations (8) then may be written as

$$f V = -v \frac{\partial^2 U}{\partial z^2} \quad (10a)$$

and

$$f(U - G) = v \frac{\partial^2 V}{\partial z^2}, \quad (10b)$$

with boundary conditions $U = V = 0$ for $z = 0$ and $U = G$, $V = 0$ for $z = \infty$. The solution for this set is most easily obtained by introducing a complex velocity $W = (U - G) + iV$. Equations (10) may then be combined into

$$if W = v \frac{\partial^2 W}{\partial z^2}, \quad (11)$$

with the general solution

$$W = A e^{-(1+i)az} + B e^{(1+i)az}, \quad (12)$$

where $a = (f/2v)^{1/2}$. For $z = 0$, $A = -G$ and for $z = \infty$, $B = 0$, we find, therefore, that

$$U = G(1 - e^{-az} \cos az) \quad (13a)$$

and

$$V = G e^{-az} \sin az. \quad (13b)$$

When $az = \pi$, the velocity vector is in the direction of the geostrophic wind. The height of this point is $z = \pi(2v/f)^{1/2} \simeq 1.7$ m for $v \simeq 0.15$ cm² sec⁻¹ and $f \simeq 10^{-4}$ sec⁻¹. It is unlikely that this laminar solution has ever been observed in the atmosphere because the flow becomes unstable for $R = Gz/v > 100$. This means that a laminar Ekman spiral in the atmosphere can exist only

for $G < 10^{-3}$ m sec⁻¹. However, if we assume that v is a constant eddy viscosity of about 10 m² sec⁻¹, then this solution gives the right order of magnitude for the height of the atmospheric boundary layer.

The wind stress at the surface of an ocean at rest drives a surface current, the equations are

$$-f V = v(\partial^2 U / \partial z^2) \quad (14a)$$

and

$$f U = v(\partial^2 V / \partial z^2). \quad (14b)$$

When we choose the x -axis in the direction of the stress, the boundary conditions are $v(\partial U / \partial z)_0 = \tau_0 / \rho = u_*^2$ and $\partial V / \partial z = 0$ for $z = 0$; and $U = V = 0$ for $z \rightarrow -\infty$. In this case, we use the complex velocity in the form $W = U + iV$ and arrive again at Eq. (11). The solution is

$$U = \frac{u_*^2}{(vf)^{1/2}} e^{az} \cos(az - 1/4\pi) \quad (15a)$$

$$V = \frac{u_*^2}{(vf)^{1/2}} e^{az} \sin(az - 1/4\pi). \quad (15b)$$

As can be seen from Eqs. (15), the stress is in the direction of the surface wind which makes an angle of 45° with the geostrophic wind. Similarly, the stress makes an angle of 45° with the surface current. Consequently, the surface current is in the direction of the geostrophic wind. Thus, if we turn the coordinate system 45°, U and V in Eqs. (15) will be parallel to U and V of Eqs. (13). Furthermore, by differentiating Eqs. (13) with respect to z and setting $z = 0$, we find that

$$G = \left[\frac{u_*^2}{(vf)^{1/2}} \right]_a, \quad (16)$$

where the index a refers to air.

The difference between Eqs. (13) and (15) is that the first set of equations is in air and the second in water. The stress τ_0 at the surface is the same for water and air. Consequently the ratio

$$\frac{\left[u_*^2 / (vf)^{1/2} \right]_a}{\left[u_*^2 / (vf)^{1/2} \right]_w},$$

where the index w refers to water, determines the ratio of the velocity scales for air and water. When we assume that the ratio of the eddy viscosities $v_a/v_w \simeq u_{*a}^2/u_{*w}^2$, then we find that the drift velocity of the water surface is about $G/30$.

The coordinate system for the atmospheric spiral is moving with the drift velocity of water. This requires a

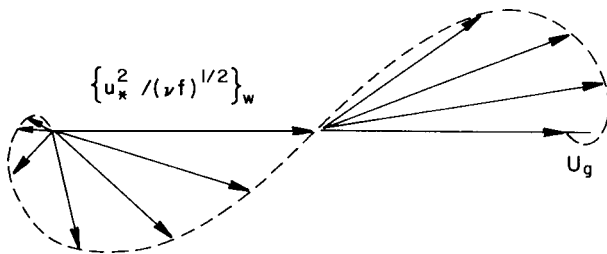


FIGURE 2 Two hodographs described by Eqs. (13) and (15). The scale of the surface drift velocity of the water has been normalized to appear to have the same magnitude as the geostrophic wind speed. The air flow in the marine boundary layer tends to have a component to the left of the isobars (parallel to the geostrophic wind), and the flow in the ocean mixed layer tends to have a component to the right of the isobars. The situation is reversed in the southern hemisphere.

small correction in Eqs. (11) and (13) which has been neglected here. From Fig. 2, we see that the ageostrophic component of the flow causes convergence in the atmosphere but divergence in the ocean when the isobars are cyclonically curved, and vice versa when the isobars are anticyclonically curved.

Although the solutions (13) and (15) have not been observed in the atmosphere or the ocean, in a qualitative sense they give considerable insight into the behavior of the boundary layers. So we recognize that when the flow in the atmospheric boundary layer is convergent, the flow in the oceanic boundary layer is divergent. This allows us to understand that the seawater in the center of the intertropical convergence zone (ITCZ) is colder than the waters north and south of it because the divergence in the ocean surface water causes upwelling of colder water. The cool ocean surface in this zone suppresses convection in the atmosphere, with the result that in the middle of the ITCZ there often is a clear band, which can be seen in the satellite picture (Fig. 3). The opposite phe-

nomenon may be observed under the subtropical high-pressure areas. Here the atmospherical flow is divergent with westerly winds to the north and easterly winds to the south. The oceanic flow is convergent: Cold water from the north is transported with a southerly component, and warm water from the south is transported with a northerly component. Consequently, a temperature front may form in the ocean under a subtropical high-pressure area. Such a frontal situation has been studied recently over the Atlantic Ocean, about 400 miles southeast of Bermuda. Figure 4 illustrates the sharpness and the location of the temperature front that was observed on Feb. 18, 1986.

Another consequence of the Ekman spiral is the so-called Ekman pumping. Consider a closed circular isobar with low pressure in the center. Near the surface there is a component of the air flow toward the center that indicates horizontal convergence. At the top of the boundary layer ($z = h$) the flow follows the isobars and is nondivergent. The vertical velocity w_h at this level can then be expressed by

$$w_h = (1/f\rho_h)\nabla \times \tau_0 \cdot \mathbf{k}, \quad (17)$$

where τ_0 is the surface stress vector and \mathbf{k} the unit vector in the vertical. In Fig. 5 the secondary flow resulting from Ekman pumping is sketched in a qualitative sense.

In the ocean the horizontal flow is diverging near the surface; therefore upwelling results near the center of low pressure. The resulting secondary flow is the mirror image of the atmospheric flow with the stream lines in opposite directions. The fact that the solutions (13) and (15) are exact solutions of the equations of motion, or Navier Stokes equations, is useful for further theoretical analysis. It has been shown that the solution is unstable to perturbations. By assuming that the fastest growing perturbation dominates the modified Ekman spiral. Brown derived modified hodographs that resemble observations

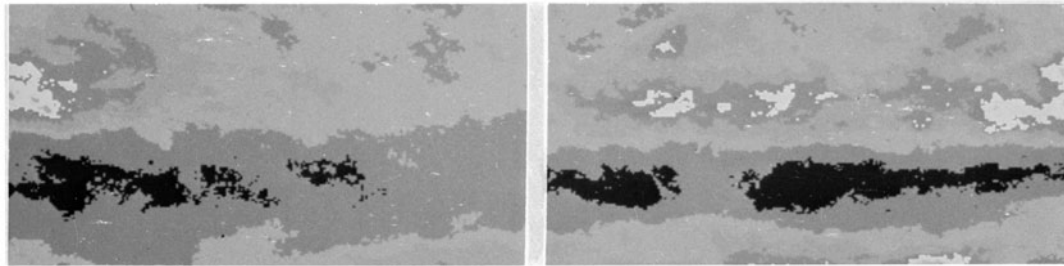


FIGURE 3 Satellite composite picture of intertropical convergence zone shows the reduction of convective activity at the equator during the month of April over the Pacific. The region depicted extends from 5°N to 10°S and from 110°W to 140°W. The left image is for April 1984 and the right for April 1985. A zone of maximum irradiance corresponds to a zone of minimum convective activity. This zone is located right at the equator where upwelling occurs associated with relatively low sea surface temperature which in turn suppresses the convection. [Courtesy Catherine Gautier, University of California, San Diego.]

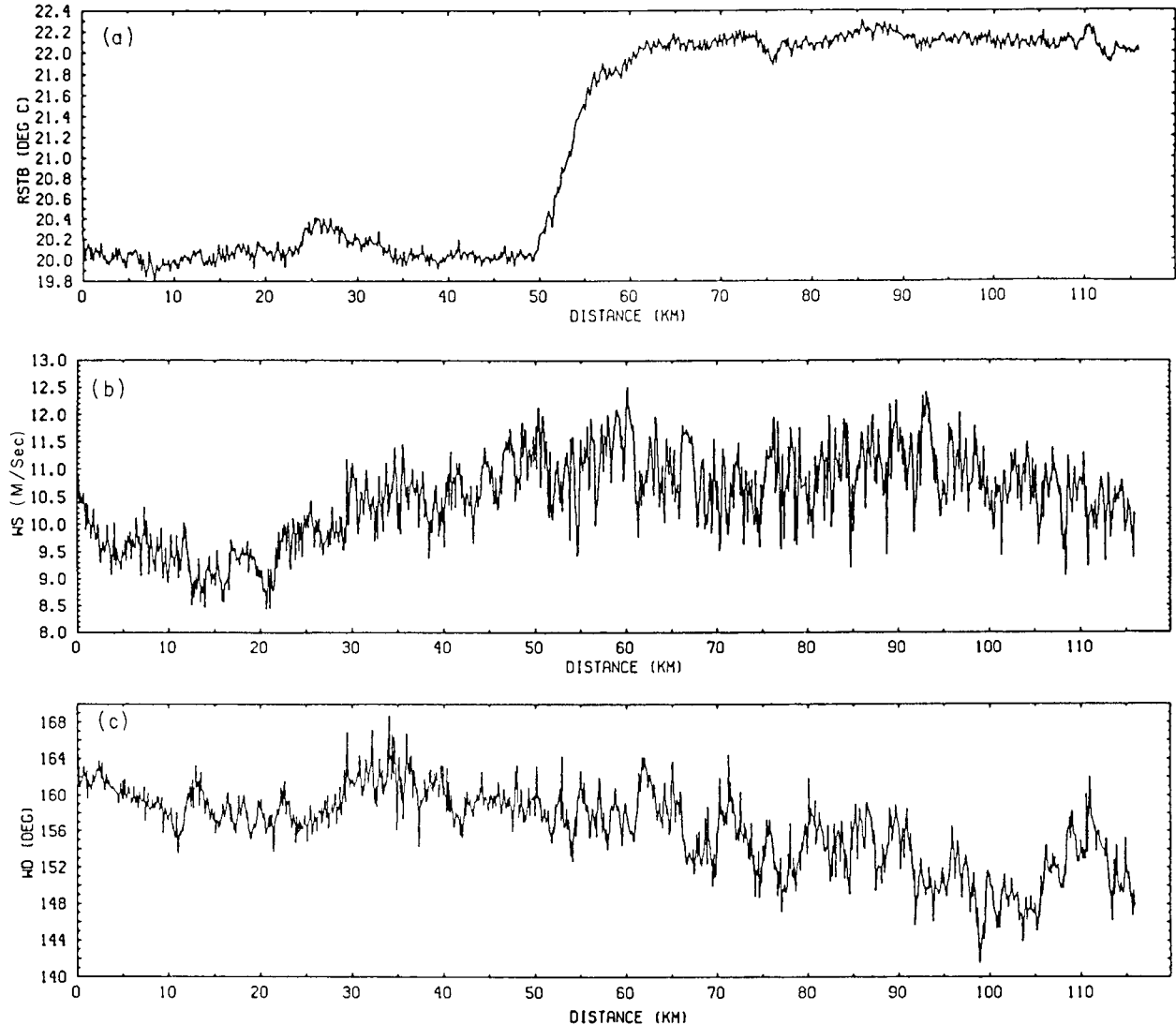


FIGURE 4 Example of an ocean surface front in the (a) surface temperature as observed remotely with the NCAR Electra flying at a height of 50 m starting at 15.51 U.T.C. (coordinated universal time) and ending at 16.12 U.T.C. The flight leg is given by the starting point at 28.72° latitude and –70.29° longitude. Also (b) wind speed and (c) direction are given. Note that the fluctuations in the wind speed increase after the aircraft passes the front. The warmer seawater enhances the buoyancy in the air, which generates more turbulence. [Courtesy Carl Friehe, University of California, Irvine.]

reasonably closely (Fig. 6). Another consequence of this study is that secondary flows develop in the boundary layers that are helical rolls with axes approximately in the direction of the mean wind. In the ocean these rolls are called Langmuir circulations.

II. TRANSFER PROCESSES NEAR THE INTERFACE

From the previous section it has become clear that the stress at the interface plays a central role in determining

the structure of the boundary layers on both sides of the interface. Similarly, the transfers of sensible and latent heat at the interface are at the core of air–sea interactions. Therefore we want to have a close look at what happens at the interface and its immediate vicinity. It is a region where in situ measurements are very difficult to obtain because the surface moves in complicated ways with the waves.

A. Profiles in the Molecular Sublayer

Very close to the interface, turbulence is suppressed because the interface itself is a material surface that is usually

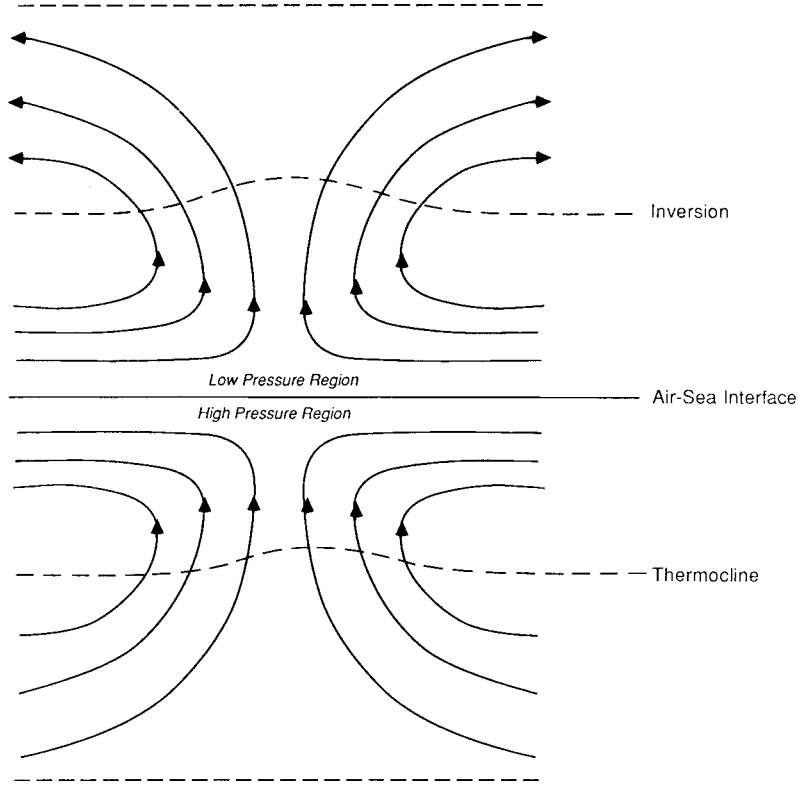


FIGURE 5 Vertical cross section through a cyclonic vortex showing schematically the stream lines of secondary flow in the Ekman layers due to Ekman pumping. The vertical scale in the ocean is about 30 times as large as the vertical scale in the atmosphere.

continuous. The interface may be locally and temporarily disrupted by breaking waves but most of the time is intact. Thus, very near the interface the flow becomes laminar, and the transport of momentum, heat, water vapor, and any other substance is controlled by the molecular coefficients and steep gradients.

The profiles indicating the transition from laminar to turbulent flow away from the interface have been successfully described for temperature with the so-called surface renewal model. It is assumed that small parcels of air or water adjacent to the interface are being replaced intermittently by air or water from the turbulent layers away from the interface.

Consider a fluid element from the mixed layer that has been moved adjacent to the sea surface. Initially, it has a uniform temperature equal to the bulk temperature. As it is exposed to the surface, which has a different temperature, thermal conduction takes place and the temperature $\Theta(z, t)$ is governed by the heat conduction equation [see Eq. (3a)],

$$\partial\Theta/\partial t = \kappa(\partial^2\Theta/\partial z^2), \quad (18)$$

where κ is the thermal diffusivity. The solution of this equation for constant initial condition $\Theta(z, 0) = \Theta_b$ and constant boundary condition $\Theta(0, t) = \Theta_s$ is given by

$$\Theta(z, t) = (\Theta_s - \Theta_b) \operatorname{erfc} \left[\frac{z}{2(\kappa t)^{1/2}} \right] + \Theta_b, \quad (19)$$

where the index s refers to the surface and b to the well-mixed interior (bulk). The corresponding heat flux density at the interface is

$$F_h(0, t) = -k(\partial\Theta/\partial z)_{z=0} = k(\Theta_s - \Theta_b)/(\pi\kappa t)^{1/2}, \quad (20)$$

where k is the thermal conductivity. We now define a distribution function $\phi(t)$ that represents the fractional area of the surface containing fluid elements that have been in contact with the interface for a time t . The average temperature and heat flux are then given by

$$\bar{\Theta}(z) = \int_0^\infty \phi(t)\Theta(z, t) dt \quad (21)$$

and

$$\bar{F}_h(0) = \int_0^\infty \phi(t)F_h(0, t) dt. \quad (22)$$

If the turbulence in the interior of the fluid provides the mechanism that replaces the surface elements, we might argue that each element has the same chance to be replaced. This may be expressed by

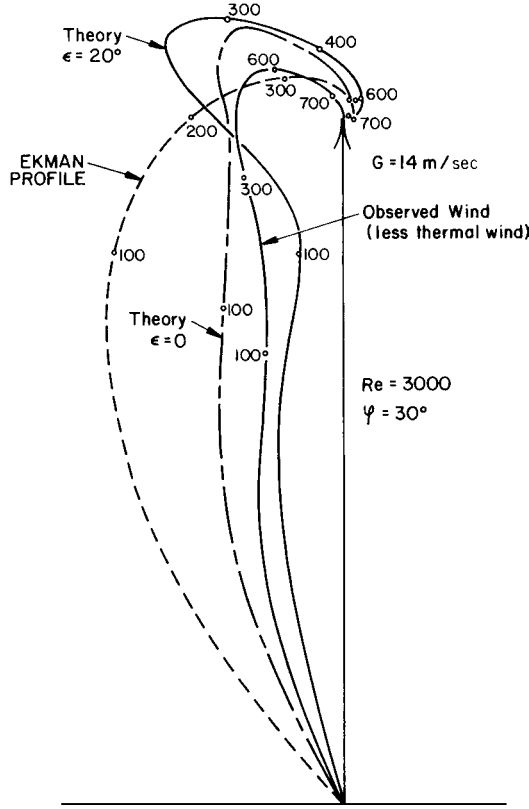


FIGURE 6 Calculated and observed hodographs in the marine boundary layer in the presence of secondary flows. The turbulent Reynolds number $Re = 3000$, the latitude $\phi = 30^\circ$, and the angle ϵ between the axis of the helical rolls and the isobars is 0° and 20° . The Ekman profile is given for comparison. The height in meters is indicated on the hodographs. [After Brown, R. A. (1974). "Analytical Methods in Planetary Modeling." Wiley, New York.]

$$d\phi(t)/dt = -s\phi(t), \quad (23)$$

where s is the fractional rate at which elements move away from the surface. Therefore,

$$\phi(t) = \phi(0)e^{-st}. \quad (24)$$

If we require $\int \phi(t) dt = 1$, we find that

$$\phi(0) = s.$$

Also $s = 1/t_*$ where t_* is the characteristic residence time of fluid parcels at the surface. Therefore Eq. (24) may be written

$$\phi(t) = (1/t_*)e^{-t/t_*}. \quad (25)$$

Substituting Eqs. (19), (20), and (25) into Eqs. (21) and (22) yields

$$(\Theta - \Theta_b)/(\Theta_s - \Theta_b) = e^{-z(kt_*)^{1/2}} \quad (26)$$

and

$$\bar{F}_h(0) = k(\Theta_s - \Theta_b)/(\kappa t_*^{1/2}), \quad (27)$$

where $(\kappa t_*)^{1/2} = z_\theta$ is a scaling length for the temperature profile. This result agrees with observations.

In a similar manner we can derive a profile for the velocity and a profile for humidity (only in the atmosphere). The only difference is that thermal diffusivity is replaced by kinematic viscosity ν for the velocity profile and by diffusivity D for the humidity profile. Therefore,

$$\frac{U - U_b}{U_s - U_b} = e^{-z(\nu t_*)^{1/2}} \quad (28)$$

and

$$\frac{q - q_b}{q_s - q_b} = e^{-z(Dt_*)^{1/2}}, \quad (29)$$

where q is specific humidity. Similarly $z_u \equiv (\nu t_*)^{1/2}$ and $z_q \equiv (Dt_*)^{1/2}$ are scaling lengths for the velocity profile and humidity profile, respectively.

B. Surface Turbulent Layers and the Transition to Molecular Sublayers

Far away from the surface in terms of the length scales z_θ , z_u , and z_q , turbulence is fully developed (the distance may not be more than a few millimeters), and the profiles behave quite differently. Yet we stay close enough to the surface that the fluxes are essentially constant with height or depth (the surface layer). In this layer, the molecular viscosity and molecular diffusivities are no longer important in the fluxes. They are replaced by eddy viscosity K_u and eddy diffusivities K_Θ and K_q . The fluxes of momentum F_u , sensible heat F_h , and latent heat F_e may be described by

$$F_u = -K_u(\partial \bar{U}/\partial z) \quad (30)$$

$$F_h = -c_p \rho K_\Theta(\partial \Theta/\partial z) \quad (31)$$

$$F_e = -L \rho K_q(\partial q/\partial z). \quad (32)$$

Prandtl developed a mixing length model that enabled him to make an accurate prediction of the profiles in this surface layer. He simply assumed that the eddy viscosity K_u is proportional to a scaling velocity u_* and a mixing length l . The mixing length was seen as the distance a turbulent eddy can travel before it loses its identity. Thus,

$$K_u \propto u_* l.$$

Furthermore he argued that the eddies are freer to move the farther they are from the surface, so that it is reasonable to assume that $l \propto z$. Using this in the above proportionality and introducing a constant of proportionality k^* , we find that

$$K_u = k^* u_* z, \quad (33)$$

where k^* is the von Karman constant. Equation (33) combined with Eq. (30) leads to

$$\frac{\partial U}{\partial z} = u_* / k^*(z + z_0), \quad (34)$$

where z_0 has been introduced so that $\partial U / \partial z$ remains finite for $z = 0$. If we require that Eq. (34) approach the limit for aerodynamically smooth flow, $\partial U / \partial z = u_* / \nu$ for $z \rightarrow 0$. This means that in this case $z_0 = \nu / k^* u_*$. Integration of Eq. (34) leads to

$$\frac{U - U_s}{u_*} = \frac{1}{k^*} \ln \frac{z + z_0}{z_0}, \quad (35)$$

where U_s is the interface velocity. For the smooth case, we find

$$\frac{U - U_s}{u_*} = \frac{1}{k^*} \ln \left(\frac{k^* u_* z}{\nu} + 1 \right). \quad (35a)$$

However, Eq. (35a) is derived for the case in which the logarithmic profile can be extended to the surface, which is not correct. The transition layer is not logarithmic and must be accounted for also. Experimental results obtained by Nikuradse more than 50 years ago suggest that a good approximation for flow over a smooth surface is given by

$$\frac{U - U_s}{u_*} = \frac{1}{k^*} \ln \frac{u_* z}{\nu} + 5.5, \quad (36)$$

which is valid only for $\zeta \equiv u_* z / \nu \gg 1$ because it does not include the transition layer. It reflects the effect of the transition layer on the logarithmic profile beyond it.

We are now in a position to match Eq. (28) to Eq. (36). From the discussion above it is clear that ν / u_* is an appropriate scaling length for the logarithmic profile as well as for the transition profile. This suggests also that ν / u_*^2 is an appropriate scaling time and that $z_u u_* / \nu \equiv \zeta_u$ and $u_*^2 t_* / \nu \equiv \delta_u^2$ are universal constants.

With the boundary condition that $U - U_s = u_* \zeta$ for $\zeta / \delta \ll 1$, Eq. (28) may be written as

$$(U - U_s) / u_* = \delta_u (1 - e^{-\zeta_u / \delta_u}). \quad (37)$$

We require that this equation and Eq. (36) match for both $(U - U_s) / u_*$ and $u_*^{-1} \partial U / \partial \zeta$. This gives us two equations and two unknowns, ζ_u and δ_u , that is,

$$\delta_u (1 - e^{-\zeta_u / \delta_u}) = (1/k^*) \ln \zeta_u + 5.5$$

and

$$e^{-\zeta_u / \delta_u} = (k^* \zeta_u)^{-1}.$$

The solution is $\delta_u = 16$ and $\zeta_u = 47$. In Fig. 7, the profiles of Eqs. (36) and (37) are compared with laboratory data by Reichardt. The fit is very satisfactory.

To get a feeling for the dimensions of the molecular transition layer we assume a friction velocity $u_* =$

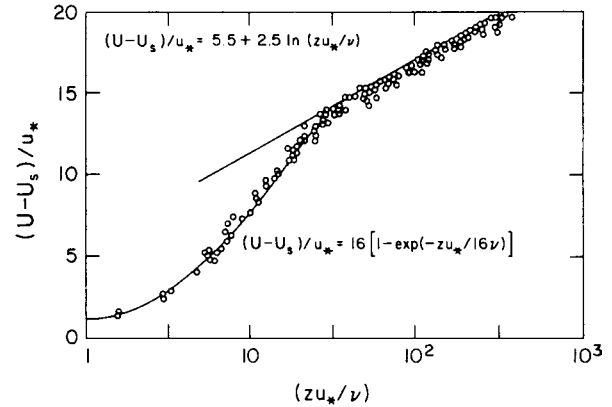


FIGURE 7 Velocity profile in the interfacial sublayer determined with the model (solid line) and measured (circles). [After Liu, W. T., Katsaros, K. B., and Businger, J. A. (1979). *J. Atmos. Sci.* **36**, 1722–1735.]

0.2 m sec⁻¹; this corresponds to a moderate windspeed of 5–6 m sec⁻¹ at 10 m height. Furthermore, the kinematic viscosity of air at 15°C is $\nu_a \simeq 1.5 \times 10^{-5}$ m² sec⁻¹. With this information, we find that the height of the transition layer is 3.5×10^{-3} m, or 3.5 mm, and the windspeed at that height is about 3 m sec⁻¹. Above this height the logarithmic profile extends to several meters above the surface.

In the ocean, the dimensions are slightly different because at the surface $\tau_a = \tau_w = \rho_w u_{*w}^2$. So if $u_{*a} = 0.2$ m sec⁻¹, $u_{*w} = (\rho_a / \rho_w)^{1/2} u_{*a} \simeq 0.035 u_{*a} = 0.7$ mm sec⁻¹. With the kinematic viscosity for water 1.05×10^{-6} m² sec⁻¹, this gives a depth of the transition of about 7 mm below the surface and the difference in surface drift and drift at this level of about 0.11 m sec⁻¹. We see that even under modest wind conditions, the molecular sub-layers are very thin, and the shears are very large.

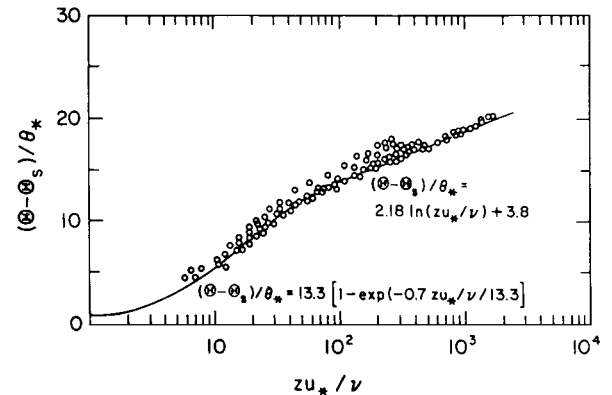


FIGURE 8 Temperature profile in the interfacial sublayer determined with the model (solid line) and measured (circles). [After Liu, W. T., Katsaros, K. B., and Businger, J. A. (1979). *J. Atmos. Sci.* **36**, 1722–1735.]

A similar matching can be achieved for the temperature profile. [Figure 8](#) shows the match with laboratory observations when we take, for the molecular sublayer,

$$(\Theta - \Theta_s)/\theta_* = \delta_\theta(1 - e^{-Pr\zeta/\delta_\theta})$$

and above it,

$$(\Theta - \Theta_s)/\theta_* = 2.18 \ln \zeta + 3.8,$$

where $Pr \equiv \nu/\kappa$, the Prandtl number: for air $Pr = 0.7$.

This combination yields $\delta_\theta = 13.3$ and $\zeta_\theta = 45$. We would expect ζ_θ in this case to be the same as for the velocity profile where $\zeta_u \approx 47$. The difference may stem from the different experiments. The ratio $\delta_\theta/\delta_u = Pr^{1/2}$.

There are no humidity observations available so close to the interface, so we cannot check the molecular sublayer and its match with the logarithmic turbulent layer for the humidity profile.

C. Transition from Smooth to Rough Flow

When the wind increases over the water starting with almost calm conditions, the following sequence of events occurs at the surface: The water surface appears initially smooth, followed by ripples of small capillary-gravity waves, larger gravity waves, breaking waves, sea spray, and more breaking waves. The air flow tends to follow the wave surface, but when the waves become very steep or break, there is flow separation at the surface. When flow separation occurs, the stress increases dramatically, and the surface is effectively rougher than in other areas. We recognize that with increasing wind more flow separation occurs, and the flow gradually becomes rough. We are interested now in specifying quantitatively where this transition from smooth to rough flow occurs. The classical study by Nikuradse was carried out in pipeflow. He found that for

$$Rr \equiv u_* z_0 / \nu < 0.13,$$

the flow is smooth, and for

$$Rr > 2.5,$$

the flow is rough, where Rr is the roughness Reynolds number.

We may assume that these limits are also valid over water. However, the roughness of the sea surface is determined by the wind stress. To account for this in a dimensionally correct way, in 1955, Charnock suggested that

$$z_0 = a u_*^2 / g, \quad (38)$$

where a is a constant of proportionality and g the acceleration of gravity. Experimental work suggests that $0.013 < a < 0.018$.

If we combine Nikuradse's criterion for rough flow with Charnock's relation (38), using $a = 0.015$, we obtain

$$Ru \equiv u_*^3 / \nu g = 167,$$

where Ru is another roughness Reynolds number. For $\nu = 1.5 \times 10^{-5} \text{ m}^2 \text{ sec}^{-1}$ and $g = 9.8 \text{ m sec}^{-2}$ we find $u_* = 0.29 \text{ m sec}^{-1}$ and $z_0 = 1.3 \times 10^{-4} \text{ m}$.

We can do the same thing for the limit of smooth flow because u_* determines Ru . In this case, we find $Ru = 8.7$ and $u_* = 0.11 \text{ m sec}^{-1}$.

Close to the surface, we may speculate that a surface renewal model will continue to hold going from smooth to rough flow. Brutsaert (1975) suggested for rough flow that $t_* \propto (\nu z_0 / u_*^3)^{1/2}$. However, when it is really rough, one would expect that the molecular viscosity no longer plays a significant role and that therefore $t_* \propto z_0 u_*$, which for a water surface becomes, after using Eq. (38),

$$t_* \propto u_* / g. \quad (39)$$

We now assume that t_* is continuous going from smooth to rough, that Eq. (28) remains valid, that in the transition zone Brutsaert's assumption holds, and that Eq. (39) is valid for fully rough flow.

Starting with $\delta_u = 16$ for smooth flow, we find that

$$t_* = 256 \nu / u_*^2.$$

This must match the transition flow, which yields

$$t_* = 656 (\nu z_0 / u_*^3)^{1/2},$$

and matching this result with the fully rough flow yields

$$t_* = 55 u_* / g.$$

If we match the rough flow to the smooth flow without a transition layer, we obtain $t_* = 26u_* / g$. It is interesting to see that t decreases with increasing u_* for smooth flow but increases with u_* for rough flow. The latter condition is a result of the fact that the roughness length increases with u_*^2 .

Although the transition layer increases in thickness with increasing u_* , there is no way yet to verify experimentally that profiles of the form of Eq. (37) are valid near the surface, because the wave height also increases with wind speed. It is very difficult to determine wind profiles at heights lower than the height of the dominant waves.

D. Rough Flow

When z_0 is entirely determined by Charnock's relation (38), the kinematic viscosity no longer plays a role in the description of the logarithmic wind profile, and we have simply

$$\frac{U - U_s}{u_*} = \frac{1}{k^*} \ln \frac{z + z_0}{z_0}. \quad (40)$$

This profile is valid for $z/z_0 \gg 1$ as we realize from the previous section. We found from the matching of the

logarithmic layer with the molecular sublayer that $\zeta_u \equiv z_u u_*/\nu = 47$. We may assume that a similar constant is valid for rough flow, that is, $\zeta_u \equiv z_u/z_0 \simeq 50$. For a strong wind with $u_* = 1 \text{ m sec}^{-1}$, $z_u \simeq 0.075 \text{ m}$ and $U \simeq 22 \text{ m sec}^{-1}$. Thus, in the range where Eq. (40) is valid, z_0 in the numerator can be neglected. Furthermore, if we use Eq. (38), this equation may be written as

$$\frac{U - U_s}{u_*} = \frac{1}{k^*} \ln \frac{zg}{u_*^2} + B, \quad (41)$$

where $B = -k^{*-1} \ln a$. For $a = 0.015$ and $B = 10.5$ this equation gives a reasonable description of the wind profile over water under neutral conditions for wind speeds $U > 8 \text{ m sec}^{-1}$.

Once we have an integrated form of the wind profile such as Eq. (41), we need to measure wind speed only at one height to determine the friction velocity and therefore the stress. If we agree on the height, say 10 m, we can standardize this procedure. In this way the drag coefficient C_d has been introduced,

$$C_d \equiv \frac{u_*^2}{(U - U_s)^2}, \quad (42)$$

so that the stress is simply given by

$$\tau = \rho C_d (U - U_s)^2. \quad (43)$$

Numerous experiments have been carried out to determine C_d . A few are summarized in Fig. 9.

Similar expressions can be given for the sensible and latent heat fluxes,

$$F_h = -c_p \rho_0 C_h (U - U_s) (\Theta - \Theta_s) \quad (44)$$

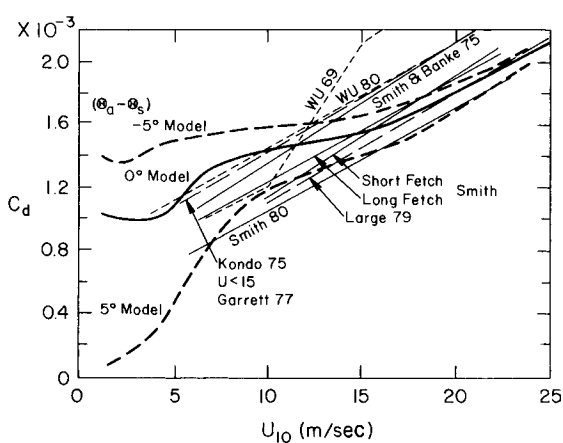


FIGURE 9 The drag coefficient as a function of the mean wind velocity at 10 m. Various experimental results are indicated. Also shown are curves recommended by Kondo; the 0° curve represents the neutral case, the -5° (and $+5^\circ$) curves, the unstable and stable cases, respectively.

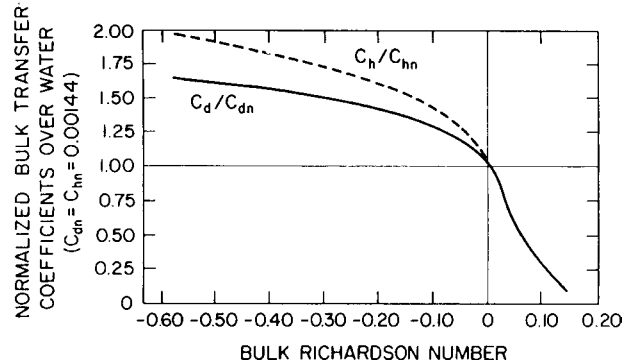


FIGURE 10 Ratios of bulk transfer coefficients to their neutral value as a function of the bulk Richardson number for a water surface. [After Fleagle, R. G., and Businger, J. A. (1980). "An Introduction to Atmospheric Physics." Academic, New York.]

and

$$F_e = -L \rho_0 C_e (U - U_s) (q - q_s), \quad (45)$$

where C_h and C_e are the bulk transfer coefficients for sensible and latent heat, respectively; c_p is the specific heat at constant pressure, and L the latent heat of vaporization.

It has usually been assumed that under neutral and stable conditions over land $C_d = C_h = C_e$, but there is some evidence that this is not the case over water. More work in this area is needed.

Figure 9 not only gives a summary of C_d as a function of wind speed under neutral conditions but also indicates the effect of stability on C_d for an air-sea temperature difference of $\pm 5^\circ\text{C}$ according to Kondo. The effect of stability has been given in Fig. 10, where the ratios of C_d/C_{dn} and C_h/C_{dn} are plotted versus the bulk Richardson number Ri_b , which is defined by

$$Ri_b \equiv \frac{gz}{\Theta_v} \frac{\Theta_v - \Theta_s}{(U - U_s)^2}. \quad (46)$$

Ri_b can be determined readily from ship observations.

The surface values U_s , Θ_s , and q_s are not easily obtained accurately. The surface drift current over the open ocean is of the order of u_* and usually can be neglected. The surface temperature is usually the bucket water temperature, which is representative of water slightly below the surface, and the surface humidity is the saturation value of humidity at the surface temperature with a small correction for salinity. With the surface renewal model it is possible to correct the bucket temperature to the surface temperature.

E. Transfer of Trace Constituents Across the Interface

An important component of the budget of many trace constituents is the exchange across the air-sea interface. This

includes naturally occurring substances as well as human-made pollutants. The measurement of the flux across the interface is notoriously difficult, not only because it is usually necessary to measure small differences of small quantities, but also because the sea surface often presents an inhospitable environment. One saving grace in this situation is the fact that scalar quantities behave similarly. This allows us to use temperature and the associated heat flux as a model for the fluxes of the other scalar quantities.

As we have seen in Section II.A, on both sides of the interface, there are very thin layers where the transport is controlled by molecular processes. However, the molecular diffusivities may be quite different on both sides of the interface. When the diffusivities are much smaller above the interface than below, the transfer is under “gas-phase control,” and when the diffusivities are much smaller below the interface, the transfer is under “liquid-phase control.” Highly soluble gases, such as SO_2 , SO_3 , NH_3 and H_2O are under gas-phase control. Less soluble, relatively inert gases, such as O_2 , N_2 , CO_2 , CO , CH_4 , and many others, are under liquid-phase control.

Gas-phase controlled transfer may be modeled by similarity to the transfer of water vapor or sensible heat from the surface to the atmosphere. The previous section has presented this case. Liquid-phase controlled transfer may be modeled to the transfer of heat, F_{hw} , in the water to or from the interface.

The flux F_c of a trace gas C at the interface may be written as

$$F_U = v_U(C_V - C_w), \quad (47)$$

where v_c is the transfer velocity and the indices w and a refer to water and air respectively. [v_c may be compared to $C_e(U - U_s)$ in Eq. (45).] The C_w must be considered the concentration in the air that is in equilibrium with the water. [The concentration of a dissolved gas in the water is usually different from C_w . For further information on this subject, the reader is referred to, e.g., [Kraus and Businger \(1994\)](#).] The main difficulty in this equation is the determination of the transfer velocity v_c .

Similarly, the heat flux from the water to the interface may be written as

$$F_{\eth V} = \rho_V c_V v_{\eth}(T_V - T_e), \quad (48)$$

where ρ_w is the density and c_w the specific heat of water. In this case, we must use the surface temperature (skin temperature) T_s rather than the bulk temperature of the air T_a , because the resistance for heat transfer in the air is much larger than in the water. (This seems in contradiction with the concept of liquid-phase control. The reason is that the heat capacity of water is more than three orders of magnitude larger than the heat capacity of air. Therefore, the thermal diffusivities in water and in air are

not strictly comparable as the diffusivities, are for gases.) To obtain complete similarity between the gas transfer and the heat transfer, C_a in Eq. (47) should have been replaced by C_s . However, because the gas transfer is liquid-phase controlled, $C_a \approx C_s$, or $C_w - C_s \gg C_s - C_a$.

The similarity between Eqs. (47) and (48) may be expressed by

$$\frac{v_U}{v_{\eth}} = \left(\frac{\text{Sc}}{\text{Pr}} \right)^{\epsilon \approx \gamma} = \left(\frac{D}{\kappa} \right)^{\epsilon \approx \gamma}, \quad (49)$$

where $\text{Sc} = D/\nu$, the Schmidt number; D is the molecular diffusivity of the gas C ; ν is the kinematic viscosity of water; $\text{Pr} = \kappa/\nu$, the Prandtl number; and κ is the thermal diffusivity of water. The exponent of 0.5 is a consequence of the surface renewal model and should be valid for light wind conditions. Combining Eqs. (48) and (49) yields

$$v_U = \frac{F_{\eth V}}{c_V \rho_V (T_V - T_e)} \left(\frac{D}{\kappa} \right)^{\epsilon \approx \gamma}, \quad (50)$$

and combining this with Eq. (47) result in

$$F_U = \frac{F_{\eth V} (C_V - C_w)}{c_V \rho_V (T_V - T_e)} \left(\frac{D}{\kappa} \right)^{\epsilon \approx \gamma}. \quad (51)$$

Thus, by measuring the heat flux, the temperature difference between the bulk water and the surface; and the concentration difference between the water and the air, the gas flux may be determined using Eq. (51). The assumption of similarity between heat conduction and diffusion in the water allows us to determine the gas transfer without needing to know the wind speed and the friction velocity.

For a complete documentation of the transfer process, it will still be essential that the wind speed and the friction velocity be known, but they are not needed for the measurement per se. The transfer velocity is related to the friction velocity by

$$v_U = D_h u_* \text{Sc}^{\epsilon \approx \gamma}, \quad (52)$$

where D_h is the bulk transfer coefficient (Dalton number) for heat below the interface. This relation may be very useful when u_* can be determined remotely from satellites.

The technique described above requires measurements of the heat flux from the water to the surface. Direct measurement of this quantity is difficult, therefore usually the energy balance at the surface is used

$$F_{\text{hw}} = F_{\text{ha}} + F_e + \Delta F_n, \quad (53)$$

where ΔF_n is that part of the net radiation that includes the absorption of the short-wave radiation at the surface. At night, $\Delta F_n = F_n$ because long-wave radiation does not penetrate the surface. In many cases, F_{hw} is the largest term in the budget. It is clearly not satisfactory to have this term as the unknown leftover in the balance.

Progress has been made in measuring F_{hw} directly. [Hauszecker and Jähne \(1995\)](#) and [Jessup and co-workers \(1995\)](#) describe active and passive techniques to obtain F_{hw} with infrared sensing of the surface. The most promising in situ technique has been developed by Suomi and colleagues (1996). The heat flux is measured by a very thin thermopile, which is imbedded in a fiberglass mesh held by a ring-shaped float. This device floats freely on the water surface and, via a buoy, may transmit its information from remote locations. At present, this device is still in the experimental stage.

The technique described here is valid under calm and light wind conditions. It is possible that it is also valid under high-wind conditions and rough seas, but it is very difficult to test this. This frontier of ocean-atmosphere exchange needs further research.

F. Comments

1. Effects of the Sea State

The sea state has usually two components: wind waves and swell. When the wind blows from the same direction over a long fetch, a quasi-steady state develops for which the bulk transfer coefficients have been derived. However, when there is a sudden change in wind direction, such as occurs with frontal passages, the fluxes may change drastically because the wind and sea state are not in equilibrium. A systematic study of these nonequilibrium conditions is needed.

Most effort over water has gone into the determination of the momentum flux from the atmosphere to the ocean. The fluxes of heat and vapor are difficult to obtain, and few good data sets exist. There is evidence however, that the profiles of temperature and humidity are not similar to the wind profile.

2. Sea Spray

In very strong winds, the turbulence near the water surface may keep water droplets that come from breaking waves in suspension. The resulting sea spray affects the fluxes of latent and sensible heat from the surface. More evaporation takes place at the cost of the sensible heat flux. Consequently the stratification above the sea spray is more stable than it would be without the spray. A good quantitative determination of this effect has been described by [Fairall et al. \(1990\)](#).

III. BOUNDARY LAYERS

So far we have directed our attention to the layers close to the interface. Now we want to extend our discussion

from the thermocline, or pycnocline, at the bottom of the ocean mixed layer to the inversion at the top of the marine boundary layer. In many cases, these two boundary layers are well mixed and are characterized by a more or less uniform vertical distribution of various conservative properties such as potential temperature and salinity. They

cesses at the interface on the ocean and atmosphere. Below the thermocline and above the inversion, the flow is more or less in equilibrium (i.e., geostrophic).

The depth of the mixed layers is strongly affected by the intensity of the transfer processes at the interface, as we have seen in a qualitative sense in the discussion following Eq. (13). The depth is also dependent on the strength of the inversion or thermocline and the strength of convection when the boundary layers are unstable. In the next sections we shall discuss these characteristics in a more quantitative manner.

A. Energetics of the Boundary Layer

The equation of turbulence kinetic energy (TKE) plays a central role in turbulent flow. It can be derived by multiplying Eq. (2b) by u_i and averaging. This yields

$$\frac{1}{2} \frac{\partial q^2}{\partial t} = -\frac{1}{2} U_j \frac{\partial q^2}{\partial x_j} - u_i u_j \frac{\partial U_i}{\partial x_j} - \frac{1}{2} \frac{\partial}{\partial x_j} \overline{u_j u_i^2} - \frac{1}{\rho_0} \frac{\partial}{\partial x_i} \overline{u_i p} - \frac{g_i}{\rho_0} \overline{\rho' u_i} - \varepsilon, \quad (54)$$

where $q^2 = \overline{u_i u_i}$ and $\varepsilon = v(\partial u_i / \partial x_j)^2$ is the dissipation. Molecular transport has been neglected. There is no coriolis term, because no work is being done by the coriolis force on the fluid parcel. In the special case of horizontal homogeneity this equation may be written in the form

$$-\frac{1}{2} \frac{\partial q^2}{\partial t} = -\overline{uw} \frac{\partial U}{\partial z} - \frac{g}{\rho_0} \overline{w\rho'} - w \left(\frac{1}{2} q^2 + \frac{p}{\rho_0} \right) - \varepsilon, \quad (55)$$

where $x = x_1$ is chosen to be in the direction of the mean wind or current. The first term on the right-hand side, the shear production term, represents the rate at which the mean flow contributes to the turbulent kinetic energy; the second term is the buoyancy production term; the third term is a combined transport and pressure term (this term does not produce or dissipate energy); and the last term represents the viscous dissipation.

The two production terms contribute energy in different ways. The shear production term contributes essentially to the u component. This term is most important near the surface, where it is always positive, and decreases rapidly with height because $\partial U / \partial z$ usually decreases rapidly. It also may be important near the thermocline or the inversion at the top of the boundary layer because these layers

often show considerable shear in the mean flow. The buoyancy production term, which can be positive or negative depending on the sign of the buoyancy force, contributes, on the other hand, to the w component, because this force is in the vertical.

The sign of the buoyancy force has a strong effect on the structure of the boundary layers. When it is positive the boundary layers are, in general, well mixed, and a simple structure emerges (see next section). When the force is negative, that is, when the buoyancy term removes energy from the reservoir of turbulent kinetic energy, the boundary layers become complex, and turbulent transfer is greatly reduced and sometimes completely suppressed. The ratio of the buoyancy term divided by the shear production term

$$R_f = \frac{g}{\rho_0} \frac{\overline{w\rho'}}{u_*^2 \partial U / \partial z}, \quad (56)$$

the flux Richardson number, is the nondimensional number that describes the stratification of the boundary layers. When $R_f \approx 0.2$, turbulence is suppressed. When $R_f < 0$, the boundary layers are usually well mixed, and turbulent transfer occurs readily.

Very near the surface, the shear production term is the dominant production term, but since this term decreases with height much more rapidly than the buoyancy term, there is usually a height above which the buoyancy term becomes the dominant term. Obukhov sensed that this height would be a useful scaling length and tried to estimate it. He assumed that near the surface the logarithmic wind profile would hold, which means that $\partial U / \partial z = u^*/kz$. Substituting in Eq. (56) and setting the ratio equal to one, he found that

$$\frac{g}{\rho_0} \frac{\overline{w\rho'} k^* z}{u_*^3} = 1,$$

where $\overline{w\rho'}$ is the buoyancy flux at the surface. This yields

$$z = L \equiv \frac{\rho_0 u_*^3}{k^* g \overline{w\rho'}}. \quad (57)$$

This length scale is called the Obukhov length.

From the preceding argument it is clear that the nondimensional height z/L can be used as a stability parameter. It has the advantage over R_f that it is a nondimensional height and provides for easy comprehension of similarity relations.

The ratio of the height h (or depth) of the boundary layer over L is a measure of whether or not the buoyancy production term is dominant in the boundary layer. Frequently $h/L \gg 1$, in which case we speak of free convection in the boundary layer, a condition that is characteristic of the well-mixed layers. Because most of the turbulent transport takes place under this condition, we shall consider the well-mixed boundary layers in some detail.

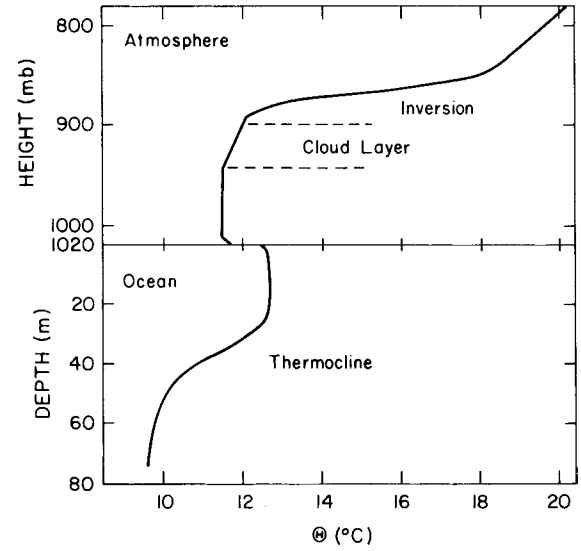


FIGURE 11 Typical profiles of potential temperature measured during the JASIN experiment (Joint Air Sea Interaction). The profiles are for 25 Aug. 1978 at latitude $\sim 59^\circ$ and longitude $\sim -12^\circ$.

B. Well-Mixed Boundary Layers

Because the boundary layers on both sides of the interface obey the same physical laws, it is not surprising that they are similar. Figure 11 gives an example of well-mixed layers on both sides of the interface. There are, of course, also substantial differences between the layers. In the MBL we find water vapor and clouds, which have no counterpart in the OML; and we find a salinity profile in the OML without a counterpart in the MBL.

The most remarkable feature of the well-mixed layers is the jump in density at the top of the MBL and at the bottom of the OML. The sharpness of the jump is related to the entrainment of relatively warm and dry air from above into the MBL and cold water from below into the OML. The details of this process are complicated; but with the help of the TKE equation (55), integrated over the entire boundary layer, we can give a reasonable description of it. If we assume quasi-steady state, the left-hand side of Eq. (55) is also negligible after integration.

For ease of argument the following discussion deals specifically with the MBL. The integral of the first term on the right-hand side may be split into three segments: the surface layer, the well-mixed region (near constant wind velocity), and the region of the top of the boundary layer where entrainment takes place. If we assume that the momentum flux is approximately constant in the surface layer, and U_1 is the wind speed at the top of the surface layer, which is the same as in the mixed layer, then the integral over the first segment yields

$$u_*^2 U_1$$

Because the shear is zero over the mixed layer, there is no contribution over the second segment. The contribution over the entrainment zone may be parameterized by assuming that the momentum transport is

$$w_e \Delta V,$$

where w_e is the entrainment velocity and ΔV the change in wind speed over the entrainment zone. Thus the integral over the third segment may be approximated by

$$w_e \Delta V^2.$$

The integral of the second term on the right-hand side of Eq. (55), the buoyancy production, can be split into a production term and a consumption term. If we assume that both production and consumption vary linearly with height, the integrals yield

$$-\frac{1}{2} \frac{g}{\rho_0} (\overline{w\rho'})_0 z_i$$

and

$$\frac{1}{2} \frac{g}{\rho_0} w_e \Delta \rho z_i,$$

where $\Delta \rho$ is the change in density over the entrainment zone. The integral over the transport term gives a negligible contribution. The integral over the pressure term yields

$$\frac{1}{\rho_0} (\overline{w\rho}) z_i.$$

This term transfers energy into gravity waves. If the inversion is strong, this transfer is a small percentage of the TKE. If the inversion is weak and the lapse rate above the inversion is only slightly stable, a substantial fraction of the energy may be radiated away from the top of the boundary layer.

The loss of TKE by dissipation, integrated over the boundary layer, balances the other terms. It is of interest to note that in the well-mixed region ε tends to be constant with height, suggesting that during the cascade process turbulent eddies are diffused throughout the boundary layer.

At this point an assumption has to be made about how much energy is available to entrainment. The simplest assumption is that a constant fraction of the production is available. Thus by neglecting the pressure-loss term, we have

$$-\frac{1}{2} \frac{g}{\rho_0} w_e \Delta \rho z_i = A \left[\frac{1}{2} \frac{g}{\rho_0} (\overline{w\rho'})_0 z_i + u_*^2 \Delta U_1 + w_e \Delta V \right]$$

and solving for w_e gives

$$w_e = \frac{A [(-g/2\rho_0)(\overline{w\rho'})_0 z_i + u_*^2 U_1]}{(-g/2\rho_0) \Delta \rho z_i - A \Delta V} \quad (58)$$

where A is the entrainment constant, which is of the order of 0.2. When buoyancy production dominates, Eq. (58) simplifies to

$$w_e = A(\overline{w\rho'})_0 / \Delta \rho. \quad (59)$$

Because in the atmosphere $\rho'/\rho_0 = -\theta/\Theta_0$ and $\Delta \rho/\rho_0 = -\Delta \Theta/\Theta_0$ at the top of the MBL, we may write

$$w_e = A \overline{w\theta} / \Delta \Theta, \quad (60)$$

where Θ is the potential temperature.

Essentially the same reasoning can be given for the OML, leading to Eqs. (58) and (59). Here the profiles of potential temperature and salinity are uniform until the thermocline is reached.

C. Cloud-Topped Marine Boundary Layer

A major dissimilarity occurs between the two boundary layers when the MBL develops a cloud layer. This is usually a stratus or stratocumulus layer. When this happens, two processes occur in the MBL that do not have a counterpart in the OML: (1) latent heat of condensation is released in the cloud layer and (2) the cloud layer absorbs and emits radiation. This means that the turbulence kinetic energy equation for the cloud-topped MBL has two more sources of energy. The latent heat release in the cloud enters the buoyant production term directly and can be simply added. The radiation effect is more complicated. The long-wave radiation is mainly emitted at the top of the cloud layer. It cools this layer and tends to destabilize the entire boundary layer. At the bottom of the cloud layer a small amount of heating occurs when the sea surface temperature is higher than the cloud-base temperature, which is usually the case. Also, the loss of energy at the top of the cloud layer tends to cool the entire boundary layer, and this enhances the cloud layer. The turbulence kinetic energy that is generated by this cooling from the top may contribute to entrainment of warm and dry air from above the cloud layer, and this tends to warm the MBL. The short-wave radiation is absorbed in the cloud layer in a more gradual way than the long-wave radiation is emitted. Its effect is to stabilize the MBL. Figure 12 illustrates the contributions of long- and short-wave radiation to the cloud layer. It shows that in mid-latitude over a 24-hr period the long-wave loss term dominates, so there is net cooling over the MBL.

Figure 13 illustrates schematically typical profiles in the MBL: q_w , the total water substance in $g \text{ kg}^{-1}$; Θ_e , the equivalent potential temperature; and the fluxes for total water, buoyancy, and equivalent potential temperature.

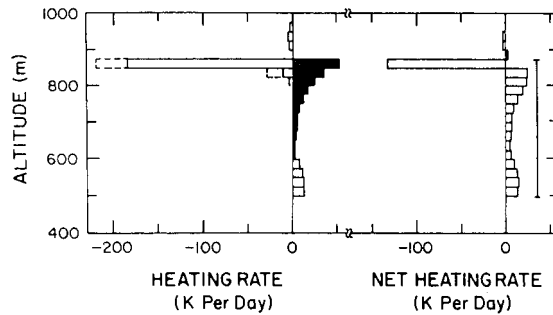


FIGURE 12 Theoretical long-wave (open), short-wave (block), and net heating rate profiles (open) at midday during the JASIN experiment. Measured heating rates near cloud top are shown dashed. [After Slingo, A., Brown, R., and Wench, C. L. (1982). *Q. J. R. Meteorol. Soc.* **108**, 407–426.]

D. Evolution of the Boundary Layers

We are now in a position to discuss qualitatively the evolution of the boundary layers. Because the oceans absorb more solar radiation than they emit long-wave radiation, there is in the average a flux of latent and sensible heat from the ocean to the atmosphere. As we have seen, the direct interactions are in the boundary layers, thus it is of interest to estimate how long it takes for the boundary layers to adjust. Assume that the ocean surface is 4°C warmer than the atmosphere and that the wind speed of the mixed layer is 10 m sec^{-1} . The e-folding time for the MBL with a height of 1000 m is then of the order of 1 day. Similarly, an estimate of the time response for the OML with a depth of 30 m is about 50 days. Therefore, whereas the MBL

adjusts itself from day to day, the OML reflects seasonal variations.

1. Cold Air Outbreak

During the winter the air moving from a continent over the ocean may have a marked difference in temperature, and strong convection may occur in both boundary layers. The land surface is considerably rougher than the ocean surface, therefore the air accelerates when it crosses the shore from land to sea. This acceleration is associated with divergence of the flow and subsidence at the top of the boundary layer. Thus, although strong heating of the MBL takes place over the water, initially the height of the MBL decreases. Further downwind, due to the strong convection, the height of the MBL increases quite rapidly at first and then more gradually. The continental air is dry and cold crossing the shore, so both the latent and sensible heat fluxes modify the MBL air. Eventually the humidity is high enough that the lifting condensation level is reached below the top of the boundary layer, and clouds form. These cold air outbreaks are often associated with relatively strong winds and the formation of helical rolls within the MBL. These secondary flows show up as cloud streets because the convection is organized that way. Figure 14 illustrates an example of cold air coming off the pack ice in the Bering Sea over the relatively warm ocean. We see that the cloud streets increase in horizontal cross-wind dimension by going downstream. This reflects the increasing depth of the convection. Also there is a tendency for the cloud streets to transform gradually into cells, reflecting the fact that

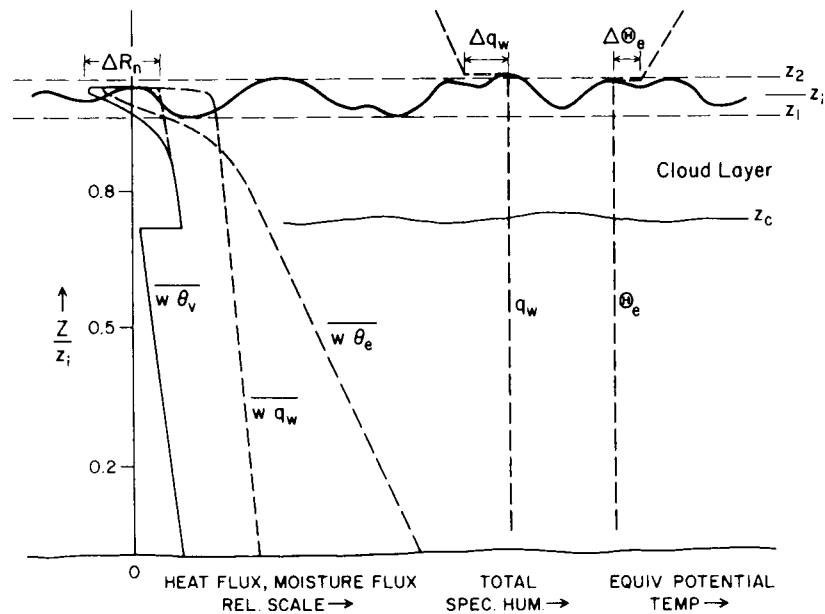


FIGURE 13 Profiles of total water content q_w , equivalent potential temperature Θ_e , vapor flux wq_w , equivalent potential temperature flux $w\Theta_e$, and buoyancy flux $w\Theta_v$, in the cloud-topped marine boundary layer.

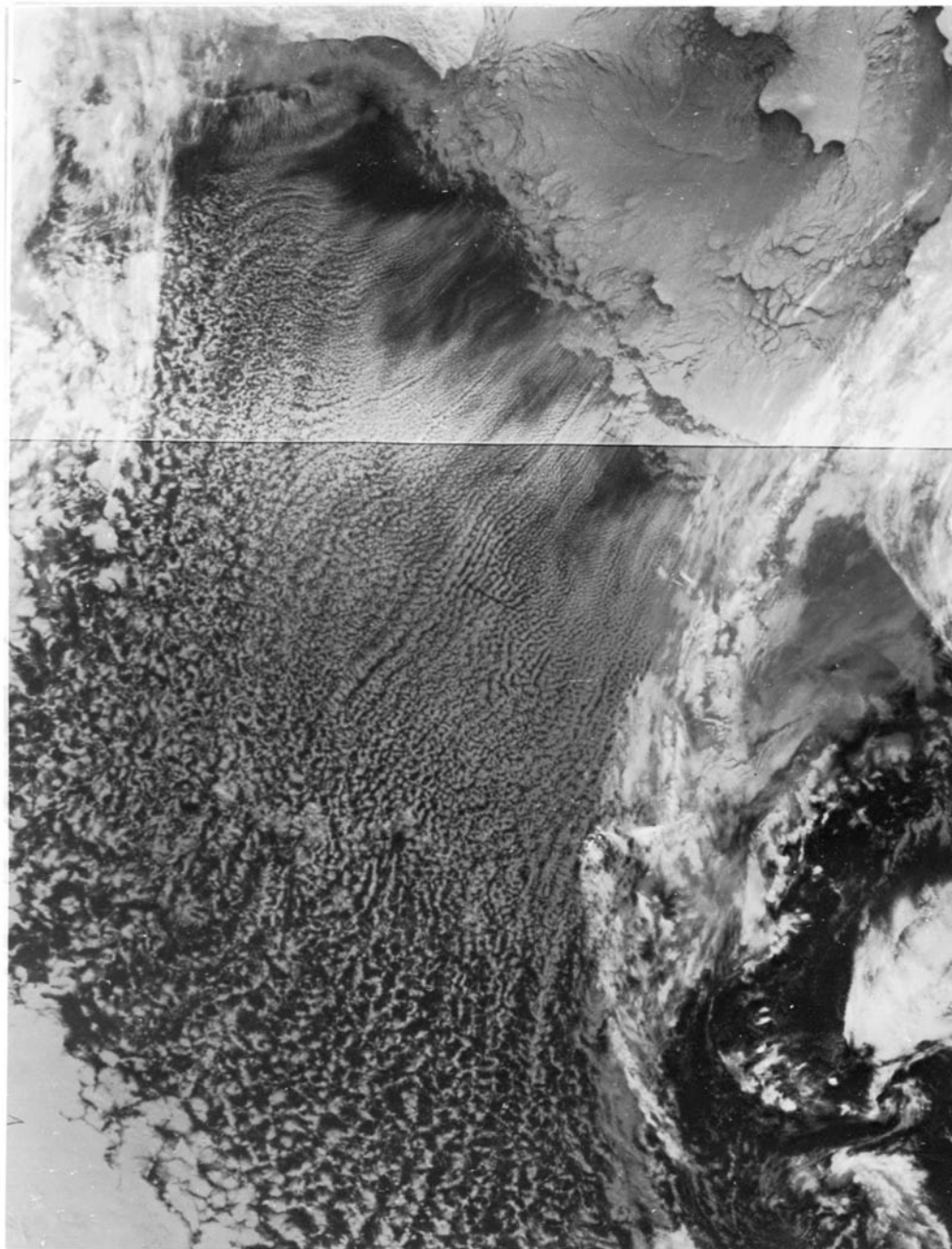


FIGURE 14 NOAA7 photograph of cloud streets in the Bering Sea. The scale is approximately $100 \times 150 \text{ km}^2$. The mean flow is from the northeast off the pack ice over the ocean. The cloud streets indicate secondary flows within the marine boundary layer and are separated by about 2 km near the ice edge and by about 6 km at 150 km downstream. [Courtesy R. A. Brown.]

the buoyancy production of TKE becomes dominant in determining the structure of the MBL.

2. Trade Winds

South of the subtropical high-pressure area the airflow over the ocean is easterly with a component to the south.

Let us assume that the MBL starts out with a layer of stratus or stratocumulus clouds. This initial condition suggests that the air-sea temperature difference is small. The air moves over gradually warmer water which enhances the convection and entrainment. In the subtropics the air above the MBL tends to be very dry, so entrainment of this air may lift the level to near the top of the MBL, and the cloud

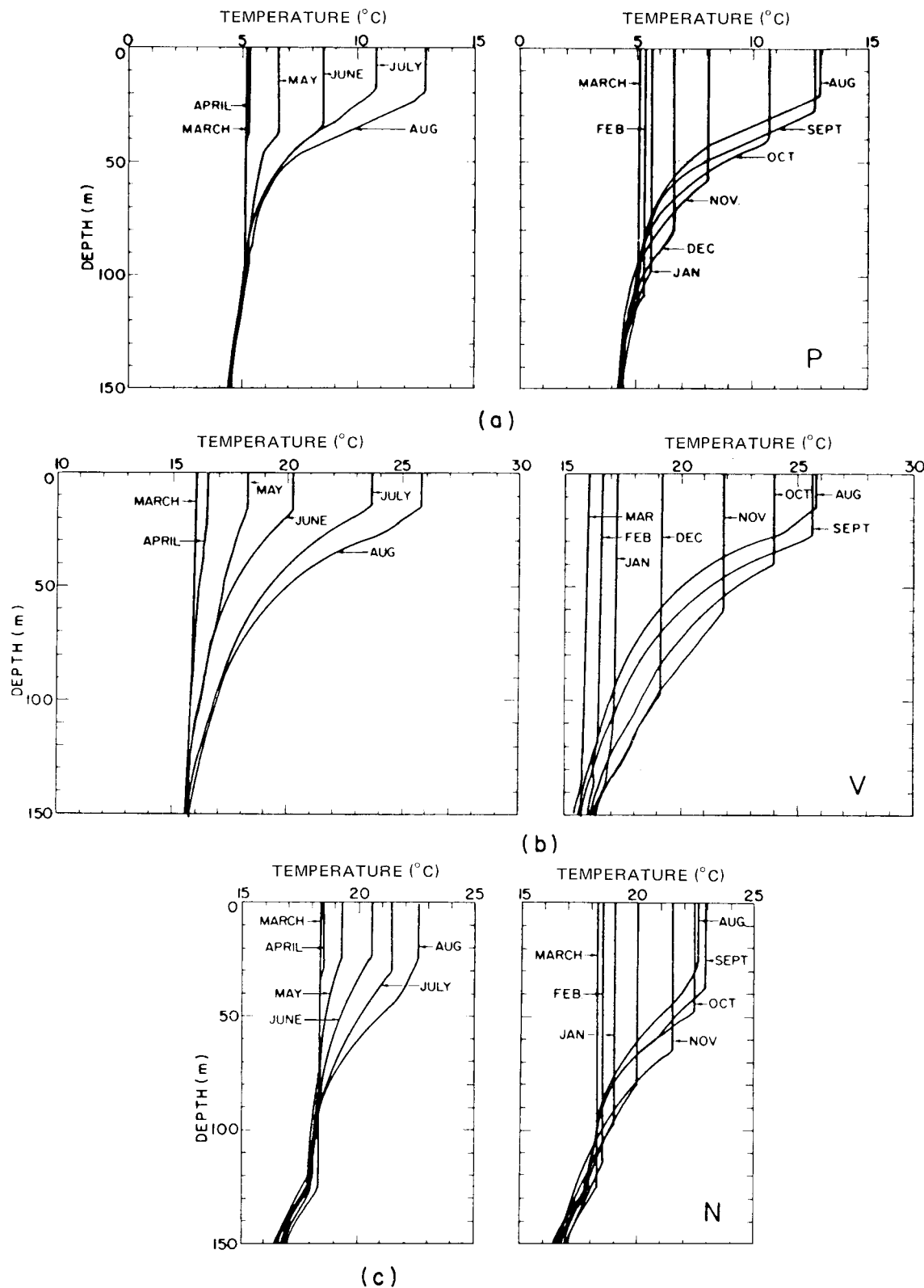


FIGURE 15 Monthly mean temperature profiles at three ocean weather stations: (a) Station P ($50^{\circ}\text{N}, 145^{\circ}\text{W}$) based on 19-yr means, 1950–1968. (b) Station V ($34^{\circ}\text{N}, 164^{\circ}\text{E}$) based on 16-yr means, 1955–1970. (c) Station N ($30^{\circ}\text{N}, 164^{\circ}\text{E}$) based on 24-yr means, 1947–1971. [Courtesy S. Tabata.]

cover may change from stratocumulus to isolated cumulus clouds and eventually may entirely disappear. The MBL moves gradually farther south, and the sea surface temperature keeps increasing. The water vapor pressure increases faster than the temperature, and the transfer of latent heat becomes the dominant flux at the interface. Consequently, the LCL lowers again, and clouds form. This time the clouds tend to penetrate deeper into the atmosphere because the equivalent potential temperature of the MBL is considerably higher. Gradually the clouds become sufficiently developed that precipitation forms, usually drizzle or light rain. Finally the MBL reaches the intertropical convergence zone (ITCZ). In this zone, boundary layer air from the north and the south converges, and intense, deep convection is generated, releasing the latent and sensible heat that has been accumulated for several thousand miles in the MBL. The latent heat is released over the entire troposphere, and this relatively warm air is then transported northward, in the upper troposphere, completing the cycle.

3. Baroclinic Zones in the Atmosphere

The deep convection in the ITCZ is one of the places where the gradually accumulated heat of the MBL is released. In mid-latitudes the processes are somewhat more complex. Again, by and large, the ocean surface is slightly warmer than the atmosphere, and the MBL tends to accumulate energy in areas of suppressed weather conditions. This energy is released not only in deep convection, as we have seen with the cold air outbreaks, but also in frontal zones that result from large-scale baroclinic instability in mid-latitude. These frontal zones tend to sweep up boundary layer air and release latent heat in organized synoptic systems (storms). There is still much research to be done on the interaction of the MBL with synoptic systems.

4. Evolution of the Ocean Mixed Layer

To a certain extent the interactions of the OML with the deeper layers of the ocean is similar to the interactions of the MBL with the free atmosphere. Deep convection occurs in a few locations where relatively dense ocean water is cooled to near the freezing point. Fronts and waves develop in baroclinic zones where the OML may be transported downward to a few hundred meters below the surface. However, in general, the OML does not interact as intensively with the deeper ocean as the MBL interacts with the free atmosphere. Consequently, the OML shows, over most of the oceans, a definite annual cycle that appears to be roughly stationary from year to year. Examples of this cycle are given in Fig. 15 where the seasonal variations of the depth of the mixed layer are given for three weather ships on the Pacific Ocean. During the fall when

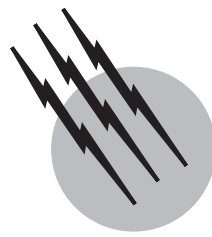
the air temperature falls below the interface temperature, the OML cools and convection occurs, besides mixing by shear of the surface current. The mixed layer cools and deepens until the spring when the air temperature rises above the interface temperature, and the heat flux reverses from upward to downward. This, combined with absorption of solar radiation in the upper part of the mixed layer, results in a stable warm layer at the top of the OML. This layer may be destroyed again in a storm accompanied by strong winds, but often it is able to grow during the summer season and form a new and shallow mixed layer near the surface, bordered by a new thermocline, which delineates the new warm water from the cold water formed in the previous winter. This continues until the cycle repeats itself.

SEE ALSO THE FOLLOWING ARTICLES

ATMOSPHERIC TURBULENCE • CLIMATOLOGY • CLOUD PHYSICS • OCEAN SURFACE PROCESSES • PHYSICAL OCEANOGRAPHY • PLANETARY WAVES

BIBLIOGRAPHY

- Brown, R. A. (1974). "Analytical Methods in Planetary Layer Modeling," Wiley, New York.
- Brutsaert, W. (1975). "A theory for local evaporation (or heat transfer) from rough and smooth surfaces at ground level," *Water Resource Res.*, **11**, 543–550.
- Charnock, H., and Pollard, R. T., eds. (1983). "Results of the Royal Society Joint Air-Sea Interaction Project (JASIN)," Royal Society, London.
- Donelan, M. (1990). Air-sea interaction. Chapter 7 in "The Sea: Ocean Engineering Science," Volume 9. Wiley, New York.
- Fairall, C. W., Edson, J. B., and Miller, M. A. (1990). Heat fluxes, white caps, and sea spray. Chapter 6 in "Surface Waves and Fluxes," Volume 1. Kluwer Academic Publishers, the Netherlands.
- Fleagle, R. G., and Businger, J. A. (1980). "An Introduction to Atmospheric Physics," Academic, New York.
- Hauszecker, H., and Jähne, B. (1995). In situ measurements of the air-sea gas transfer rate during the MBL/CoOP West Coast experiment. In "Air-Water Gas Transfer," (Jähne, B., and Monahan, L., eds.), AEON Verlag & Studio, 775–784.
- Jessup, A. T., Zappa, C. J., Hesany, V., Loewen, M. R., and Skafel, M. G. (1995). Dependence on the skin layer recovery rate on heat flux and turbulence. In "Air-Water Gas Transfer," (Jähne, B., and Monahan, L., eds.), AEON Verlag & Studio, 601–610.
- Kraus, E. B., and Businger, J. A. (1994). "Atmosphere-Ocean Interactions," Oxford University Press, New York, London.
- Nieuwstadt, F. T. M., and van Dop, H., eds. (1982). "Atmospheric Turbulence and Air Pollution Modeling," Reidel, Dordrecht, Holland.
- Suomi, V. E., Sromovsky, L. A., Anderson, J. R. (1996). "Measuring ocean-atmosphere heat flux with a new in-situ sensor," Preprints, Eighth conference on air-sea interaction, Atlanta, GA, Amer. Meteor. Soc., 38–42.
- Tennekes, H., and Lumley, J. L. (1972). "A First Course in Turbulence," MIT Press, Cambridge, MA.



Oceanography, Chemical

James H. Mathewson

San Diego State University

- I. Introduction
- II. Seawater
- III. Biogeochemical Cycles
- IV. Sampling, Analysis, and Special Methods
- V. Areas of Special Interest

GLOSSARY

Apparent oxygen utilization (AOU) Difference between the concentration of oxygen in a water sample at equilibrium with the atmosphere at the surface and the observed concentration in deeper water after oxygen depletion by respiration. The salinity and temperature (adjusted for pressure) at depth is used in determining both oxygen values.

Autotrophs Organisms that convert nutrients into biomaterials, that is, tissue mass, using light energy (photoautotrophs) or chemical energy (chemoautotrophs).

Biogenous sedimentation Formation by phytoplankton and zooplankton of skeletal “hard parts,” composed of calcium carbonate (calcite or aragonite forms) or opaline silica, which sink after the death of the organism. The deposits are referred to as calcareous oozes or muds, and siliceous oozes or muds, respectively.

Biogeochemical cycles Exchange of matter between components of ecosystems, consisting of nutrient assimilation by autotrophs, food chain transfers, losses to particulate and soluble matter, remineralization by decomposing organisms, and sedimentation.

Bottle cast Also “hydrocast” or “hydrographic station.”

A water sampling procedure in which a set of electronically actuated plastic bottles (10–30 liters) arranged in a vertical position on a circular frame (“rosette”) are lowered by a cable (“hydrowire”) at navigational positions (determined with the aid of satellite navigation). The bottles are open at each end and are closed by remote control at preselected depths. The rosette is normally fitted with a CTD (below).

Carbonate compensation depth Depth at which the rate of deposition of calcium carbonate equals the rate of dissolution.

Chlorophyll Green photoactive pigment in photosynthetic (photoautotrophic) organisms; a lipophilic tetrapyrrole containing magnesium with strong *in vivo* absorption in the violet and red.

Compensation depth Depth at which the rate of carbon assimilation (and oxygen release) by photoautotrophs equals the rate of photoautotrophic respiration.

Conservative property Property for which there are no apparent *in situ* sources or sinks and, therefore, will be additive on mixing.

Critical depth Depth at which the integrated rate of photoautotrophic growth (gross productivity) from the

surface down equals the integrated rate of photoautotroph respiration.

CTD A package of electronic sensors for conductivity (inductive salinometer), temperature (thermistor), and depth (pressure transducer). Signals are relayed to a signal processor and plotter yielding continuous profiles during bottle casts. Profiles can be generated underway with expendable probes (XCTD).

Depth The definition and measurement of depth in the ocean is not a trivial matter. Chemical oceanographers generally use the term depth to mean distance below the surface measured by a pressure transducer; but the cumulative pressure in the water column depends on density, which in turn depends on temperature, salinity, and compressibility. Depth from the surface to the bottom (bathymetry) may be obtained acoustically (echo sounding) by a precision depth recorder (PDR). Because sea level is a surface that rises or falls due to dynamic effects (e.g., currents, tides, storms) and static effects (temperature, salinity, and even gravity variations), in some applications, a sea surface reference level is required, which may be the average local surface of the Earth ("geoid") or an arbitrary plane deep in the ocean.

ENSO El Niño Southern Oscillation. Episodic (3–7 years) atmospheric forcing of the equatorial Pacific currents alternating between increased warm eastward flow (El Niño) and increased westward moving colder water ("La Niña") with attendant global weather changes due to ocean–atmosphere energy exchanges.

Euphotic zone Surface waters with sufficient light penetration to support photoautotrophic growth, i.e., productivity.

Hydrogen bonding Dipole–dipole intermolecular force formed by the close proximity of a hydrogen at the positive end of a polarized covalent bond between the hydrogen and an electronegative atom (N, O, or F) (donor dipole) to a non-bonding (unshared) electron pair on a nearby N, O, or F (the acceptor dipole).

Hydrothermal vents Also known as "geothermal vents." Deep sea hot springs associated with active tectonic zones, such as midocean ridges.

Lysocline Depth at which the dissolution of calcareous components of sediments becomes significant; lies between the saturation horizon and the carbonate compensation depth.

Net primary production Photosynthetically fixed biomaterials available to an ecosystem. "Productivity" is the *rate* of biomass accumulation in grams carbon fixed per square meter per day, usually measured by uptake of C-14 labeled bicarbonate. Traditionally, oxygen evolution has been used as a measure. Chlorophyll concentrations of the "standing crop" of autotrophs corre-

late with productivity permitting global surveys from satellites.

New production Fraction of production attributed to nutrients made available from nonlocal sources (by currents or advection) in contrast to production from locally recycled nutrients. New production equals biomass transported out of the water column ("export" production) usually by sinking below the thermocline.

Nutrients Inorganic constituents ("minerals") of seawater that support autotrophic growth. Includes those in low concentration (micronutrients) that are "biolimiting," that is, control the rate of production, such as nitrate, phosphate, and silicate. Bicarbonate, sulfate, and a number of metal ions are also nutrients. The nutrients (except the metals) exist as oxyanions in the maximum oxidation state.

Plankton Drifting microscopic organisms; "phytoplankton" are algae (photoautotrophs); "zooplankton" are animals (heterotrophs).

Productivity See "net primary production."

Redfield ratio Molar ratio of nitrate to phosphate at any location in the water column (normally 16 to 1) discovered by the late Alfred Redfield; also the molar ratios of phosphorus, nitrogen, and carbon in photoautotroph tissue and the relative moles of oxygen released in production (1P:16N:106C:138O₂).

Residence time Ratio of the total mass of a constituent of seawater to the rate of input or removal from the oceans (assuming a steady state in which the rate of input equals the rate of output).

Respiration Uptake and utilization of oxygen for the oxidative degradation of biomaterials (food) yielding the metabolic energy required by all organisms in the form of adenosine triphosphate (ATP).

Salinity Originally the mass of dissolved inorganic solids (in grams) in one kilogram of seawater, with halides measured as chloride and carbonates as oxides. The practical salinity scale is now based on a defined value of exactly 35 parts per 1000, or practical salinity units (psu), for "standard seawater" obtained from the North Atlantic that is adjusted to have a conductivity at 15°C equal to a standard KCl solution. Some oceanographic literature still contains the symbol ‰, for parts per thousand.

Saturation horizon Depth at which the conditions of carbonate concentration, temperature, salinity, and pressure just equal equilibrium calcium carbonate solubility, that is, supersaturated above and undersaturated below.

Thermocline Zone of rapid change in temperature with depth; corresponds to the zone separating the upper mixed layer with deep, slowly mixed water masses.

CHEMICAL OCEANOGRAPHY, or marine chemistry, is the study of the chemistry of the sea and is recognized as a distinct specialization in oceanography. There are journals, books, data banks, conferences, funding programs, university degrees, laboratories, and organizations dedicated to the field. Chemical oceanographers seek answers to oceanographic questions, not chemical questions. Chemical oceanographers study the composition and properties of seawater*; the associated geochemistry of ocean basins and margins, marine sediments, and hydrothermal vents; interactions between seawater and biota; atmosphere–ocean exchange; and the chemical impact of humans on the ocean including extraction of resources and pollution. Over the years, the field has borrowed ideas, methods, and terms, mainly from analytical chemistry, geochemistry, physical oceanography, and biological oceanography, but occasionally has found it necessary to develop its own equipment and methodologies to meet the challenge of data collection in a vast and dangerous environment. There are some concepts, such as salinity, that are particular to the field.

I. INTRODUCTION

Well-known chemists have made contributions to oceanography since the rise of modern science. Robert Boyle published *Observations and Experiments about the Saltiness of the Sea* in 1674 and Lavoisier investigated the composition of sea salts in the 18th century. Although chemical oceanography today remains an eclectic field, it is achieving greater coherence through integrated models, multidisciplinary research teams, and broadly based research programs. It is now well-established that we can understand the world ocean—the hydrosphere—as a chemical system only when we include the biosphere, atmosphere, and lithosphere.

The current literature in chemical oceanography is characterized by (*inter alia*): the influence of kinetic models, (continuous or compartmental); the search for meso- and microscale effects; the development of shipboard or in situ flow-through samplers and analyzers; the use of novel vehicles for data gathering including buoys, deep submersibles, remotely operated tethered vehicles and satellites; and the ubiquitous use of computers for data acquisition, modeling, and mapping. Twenty-five years ago, the dominant philosophy in the chemical modeling of the oceans was thermodynamics; but even under steady-state conditions, true thermodynamic equilibrium in nature is rare and kinetic models are now commonly used. These require the evaluation of mass and energy transfer across

*The usage of seawater as one word implies a uniquely important set of characteristics and roles in the environment for the waters of the sea.

the principal controlling discontinuities or interfaces—the ocean surface, the thermocline, and the sediment surface. The key catalytic role of organisms and their constituent enzymes in controlling water chemistry has come to be appreciated by chemists as well as biologists. Free energy differences (ΔG°) remain useful in directing our attention to energy gradients and the anticipated flow of matter and energy, that is, the theoretical “boundary conditions” and energy budgets of systems. The “master variables” pH and pE, essentially the proton and electron activities in logarithmic form, remain useful in characterizing environments.

Figure 1 shows the domains of interest to chemical oceanographers. A substantial portion of the significant chemical processes in the oceans occur in surface waters and at the natural boundaries between the atmosphere and the oceans and between the oceans and the sea floor (marked with asterisks). The use of a logarithmic depth scale (see **Depth** under “Glossary”) emphasizes the importance of processes in the euphotic zone (limit of productive light penetration), which is separated from deep water by the thermocline. Important geographic differences are found for measurements made in the coastal (littoral) zone versus the continental shelf (neritic zone) or the open ocean (pelagic zone). The oceans show long-term significant geographical variations in properties between the Atlantic, Indian, and Pacific Oceans. In “box” models, the major reservoirs are the atmosphere (to 10 km), the surface mixed layer (down to ~100 m), the deep ocean (average depth 4 km), and the sediments. We also must

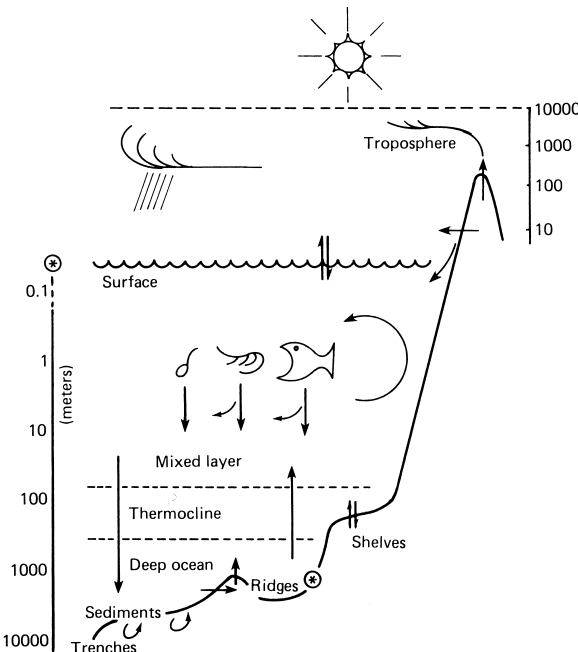


FIGURE 1 Domains of chemical oceanography.

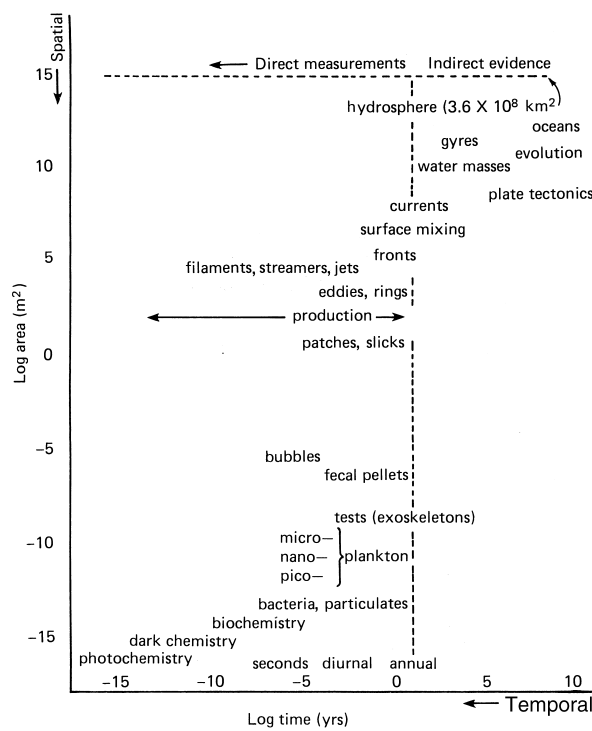


FIGURE 2 Scales for phenomena in chemical oceanography.

bear in mind that the activities of humans are concentrated on the surface and near shores where very important rate controlling processes occur.

The scope of measurements and modeling in time and space is another important aspect of investigations in chemical oceanography (Fig. 2). Laboratory science, and even quite massive industrial processes, involve much shorter times and much smaller amounts than the scale of most oceanic processes. The familiar undergraduate

exercise completed in a flask in three hours does not prepare one to think in terms of the volume of the oceans (1.4×10^9 liters) or the age of the oceans (3.8×10^9 years). On a geochemical time scale, the mixing time of the deep ocean of up to 1000 years is rapid in comparison with the residence times of major constituents. By mapping and profiling (concentration versus depth plots) the concentrations of constituents, and by determining the rates of transport and in situ production or consumption, it is possible to construct realistic (i.e., verifiable and predictive) models of the chemical processes in the world oceans as an interconnected whole. The traditional methods of chemical analysis on ships using “wet” chemistry on discrete samples collected from hydrocasts are sufficient for the construction of coarse global models, but fine-scale temporal and spatial data derived from rapid, real-time, in situ direct measurements are needed to detect fine-scale variability. The electronic instruments and automated analyzers used in chemical oceanography currently also help to minimize the errors derived from the bottles, the wire, transfer and storage, and all the attendant chemical “noisiness” of shipboard laboratories. Modern instrumentation also helps reduce random human errors caused by the abnormal physiological stress of working on a platform that undergoes multiple—sometimes severe—accelerations.

II. SEAWATER

A. Water

A discussion of seawater is invariably prefaced with a description of the special chemical and environmental characteristics of liquid water (Table I). Compared to other low molecular weight nonmetal hydrides, the properties

TABLE I Environmental Significance of Water Properties

Property	Comparisons	Significance
Density of ice < water at freezing (0.92 g cc^{-1} @ 0°C), maximum density (1.0 g cc^{-1}) @ 4°C	Lower density of solid at melting is rare	Icebergs float, fresh water bodies freeze at the surface
Heat capacity ($4.184 \text{ J g}^{-1}\text{C} @ 14.5^\circ\text{C}$)	Only liquid hydrazine, hydrogen peroxide, and liquid metals are higher	Oceans capture and distribute solar energy; limits temperature changes
Phase change energies ($\Delta H_{\text{vap}} = 40.71 \text{ kJ mol}^{-1}$)	Same as above	Ocean/atmosphere energy exchanges, temperature regulation by organisms
Surface tension ($71.97 \text{ dynes cm}^{-1}$ @ 25°C)	Same as above	Formation of fog, clouds, and bubbles; interstitial pore water and tissue water behavior
Temperatures of phase changes (m.p. = 0°C , b.p. = 100°C @ 1 atm)	High for molecular size	Water is liquid on the Earth, life requires water
Solvent properties (dielectric constant = $78.54 @ 25^\circ\text{C}$)	Best for ionic and polar materials	Salty oceans and tissues, life requires ions; transport of pollutants
Acidity ($\text{pK}_a = 15.7$); Rate of ionization ($6 \times 10^9 \text{ mol}^{-1} \text{ sec}^{-1}$)	Amphoteric behavior and high proton transfer rate	Water supports acid-base reactions; buffered oceans; bioenergetics based on proton gradients

of water are unusual, however familiar the substance may seem to us. Only very toxic and reactive materials, such as liquid hydrazine and hydrogen peroxide, have comparably high melting and boiling points, heat capacities, heats of vaporization, and surface tension. If water were not a superlative solvent, heat sink, and above all, liquid on a planet of the mass, composition, orbital radius, and radiant energy of earth, oceans and life could not exist. The properties of water depend on its tetrahedral electronic structure and strong dipole moment, which leads to strong intermolecular hydrogen bonds (defined in the glossary). The two OH dipoles and two unshared electron pairs permit water to form four hydrogen bonds (two donors, two acceptors) at each water molecule. In condensed phases (ice or liquid), the hydrogen bonds are enhanced by cooperativity, and the favorable symmetry of the molecule (point group C_{2v}) leads to the formation of interlocking rings and chains of water molecules. In ice, the stacked hexagonal rings form an open lattice with considerable open space and, consequently, a much higher molar volume (19.6 cc mol^{-1}) than close packing would predict (9 cc mol^{-1}). On melting, about 13% of the hydrogen bonds break and many of the hydrogen bonded rings contract from six to five members, reducing the molar volume to 18 cc mol^{-1} and raising the density. Hence ice floats. What would be the surreal environmental consequences if ice sank?

The strong dipole moment, hydrogen bonding propensity, and dielectric constant of water allow the solution of ionic and polar substances, causing the oceans to be salty and supporting the formation and functioning of living tissue. Water can also enclose solutes in cages formed from rings of hydrogen bonded water molecules (clathrates) solubilizing gases, such as oxygen, and macromolecules, such as proteins. The cumulative effect of so many hydrogen bonds stores vibrational energy that can absorb or release heat and must be surmounted for phase transitions. **Table I** is only a partial list of the properties of water, but the principal entries remind us that the most important single molecule in nature is water.

B. Composition and Salinity of Seawater

Seawater has constant relative composition, that is, the concentrations of the individual constituents in sea salts have fixed ratios to each other and change absolute concentrations only on mixing or from the addition or removal of water. This property is termed “conservative,” that is, there are no internal sources or sinks for the variable. Almost the entire weight of sea salts consists of just eleven constituents (**Table II**). The total dissolved salts in grams per kilogram is closely approximated by a defined parameter called salinity. (See **Salinity** in “Glossary.”)

TABLE II The Most Abundant Constituents of Seawater

Species	g kg^{-1} of 35.000 psu seawater	Milliequivalents (mEq kg^{-1})
Na^+	10.775	468.70
Mg^{2+}	1.284	105.66
Ca^{2+}	0.419	20.56
K^+	0.399	10.21
Sr^{2+}	0.0079	0.1812
Cl^-	19.353	545.88
SO_4^{2-}	2.712	56.46
HCO_3^-	0.126	2.06*
Br^-	0.0673	0.844
B(OH)_3	0.257	(0.416)
F^-	0.0013	0.068
H_2O	964.80	

* As carbonate alkalinity.

Salinity is, in principle, a simple concept, but there are difficulties in using it in practice. Sea salts decompose during evaporation from loss of HCl and CO_2 , making the direct determination of constituents exacting and time-consuming. Measurements based on the assumption of constant relative composition were developed a century ago. For the first half of the 20th century, salinity was determined by titration for halides with silver ion (Mohr method) and standardized originally against a small number of unrepresentative samples of natural seawater. The definition of salinity took on an arcane form in 1937 due to a redetermination of the atomic weight of silver. Salinity is now routinely measured by conductivity with a precision of 0.01 psu, which is limited by variations in pH and calcium ion. Salinometers are calibrated against 35 psu standard seawater samples supplied by an international service in England, and measure a conductivity ratio between the sample and the standard. The practical salinity scale was adopted in 1978 based on a defined value of exactly 35 parts per 1000, or practical salinity units (psu), for “standard seawater” obtained from the North Atlantic that is adjusted to have a conductivity at 15°C equal to a standard KCl solution. In 1981, UNESCO published standard tables relating salinity values to conductivity ratios and chlorinity (halide content) at various temperatures using empirical equations. Preservation of the continuity of historical data was a primary motivation in each of the redefinitions of salinity. Note that as a consequence, the total of the major constituents in **Table II** is 35.169 g kg^{-1} , a value larger than the nominal salinity. Electroneutrality is preserved, that is, the total milliequivalents of cations (605.31 meq/kg) equals the total for anions.

In the open ocean surface salinities vary between 32 and 38 psu and deep ocean salinities range between 34 and

35 psu. Salinity is useful primarily as a bulk determinant of density and of conservative properties. It can be used as a self-consistent parameter to identify water masses and mixing processes. It is the minor and trace constituents that provide the richest mother lode of significant data. Chemical oceanographers refer nonconservative properties to salinity and temperature in order to evaluate in situ production or removal of constituents against a background of eddy diffusion and advection. The use of conductivity–temperature–pressure sensing probes for profiling density stratification is now universal. However, careful workers still calibrate in situ values with bottle samples and reversing thermometers. As long as oceanographers recognize the inherent assumptions and limitations of the salinity concept, it will survive along with many other prepackaged parameters in science that we learn to take with a grain of salt.

The salinity concept depends on the validity of constant relative composition, which in turn is a consequence of a steady-state balance between the rate of addition of constituents to the oceans from rainout and runoff and the rate of removal by sedimentation, atmosphere exchange, and hydrothermal vent percolation. In addition, the residence times for each element (mass/flux) must be long in comparison with the ocean mixing rate, and the input and removal processes and rates must be similar in each ocean. Calcium is just on the edge of maintaining a constant ratio, with an enrichment in deeper waters of up to 0.5% due to dissolution of aragonite and calcite removed from surface waters by biogenous sedimentation.

C. Geochemical History of Seawater

The geochemical history of the oceans has been investigated extensively using radioactive tracers, isotope mass ratios, sediment cores, the chemistry of evaporites, rivers, volcanoes, and weathering. The development in the last 40 years of the concept of plate tectonics has made possible some very significant advances in understanding the processes controlling the composition of seawater. The salinity of the ocean rises as sea level falls from the formation of ice in glacial periods. The concentration of salts by evaporation in confined seas in hot, dry climates produces salt deposits (evaporites), which are significant both in the geochemical evolution of the oceans and as an economic resource. Sea salt has been a valuable commodity since prehistoric times, and it remains so today. If the salts in salt mines, salt domes, and marginal basins were all redissolved in the sea the salinity would double.

Determination of the precise salinity and composition of ancient seas must be indirect at best because of the recycling of crust through successive episodes of continental drifting, diagenesis of sediments and sedimentary

rocks, and the relatively rapid spreading rates of the sea floor (3 cm yr^{-1}). A key insight was achieved with the recognition that mid-ocean plate boundaries are the site of significant chemical modification of seawater through interaction with the basaltic crust. Percolation of seawater through hydrothermal vent systems removes magnesium and converts sulfate into sulfide, which generates ore deposits and supports unique aphotic ecosystems.

Mass spectrometry is one of the tools employed to trace various elements through geochemical cycling over huge scales of mass and time. The kinetic isotope effect causes small variations in the natural abundance of isotopes in elements when any transfer across energy barriers occurs (a kinetic or rate process). The strength of a chemical bond (or intermolecular force such as a hydrogen bond) depends on the mass of the atoms involved, and hence a rate process, such as water evaporation, will tend to fractionate molecules by mass. Water contains the major constituent atoms H-1 (hydrogen with mass of 1 atomic mass unit) and oxygen-16, but also small amounts of deuterium (H-2), tritium (H-3), O-17 and O-18. When water evaporates, the remaining liquid is enriched in deuterium and O-18. Pure D₂O (“heavy water”) can be prepared from the repeated fractionation of natural water. The isotopic composition is reported as a variation or “anomaly” from an international standard, for example Vienna Standard Mean Ocean Water (VSMOW) for water. Isotope anomalies of carbon, sulfur, nitrogen, and oxygen are important in tracing biogeochemical cycles. The emphasis in modeling these cycles is on the determination of the size and composition of reservoirs or “boxes”—primarily the oceans, biota, sediments, and the atmosphere—and the rates of exchange of elements between them.

D. The Physical Chemistry of Seawater

The physical–chemical characteristics of seawater have great significance for understanding oceanic processes and for applications in technology. The bulk pressure–volume–temperature relationships (equation of state), transport properties (viscosity, conductivity, sound transmission), and colligative properties (osmotic pressure, freezing and melting points) have clear application in the physiology of marine organisms, water recovery technology, ocean thermal energy conversion systems, echo ranging and bathymetry, and ship systems designs. Scientists have been amassing data on seawater for over a century. Measurements are usually made over a wide range of salinities (0–40 psu) and temperatures (freezing to 40°C). Some representative properties of seawater are shown in [Table III](#).

Seawater is a complex electrolyte solution of high ionic strength (0.7 m at 35 psu). The various ions of seawater,

TABLE III Representative Physical Properties of Seawater

Property	Value	Conditions ^a
Density	1027.68 kg m ⁻³	
Freezing point	-1.922°C	5.0°C not applicable
Isothermal compressibility	4.56×10^{-10} Pa ⁻¹	
Osmotic pressure	24.5 atm ^b	25°C
Reduction in volume under pressure	0.445%	1000 decibars
Refractive index	1.33977	
Solubilities of gases	O ₂ = 7.09 cc l ⁻¹ N ₂ = 12.65 cc l ⁻¹	Air at 1 atm, 100% relative humidity
Specific conductivity	33.457 millimho cm ⁻¹	
Specific heat	3.994 J kg ⁻¹ °C ⁻¹	
Thermal expansion coefficient	1.2×10^{-5} °C ⁻¹	1 bar
Vapor pressure	856 Pa	
Velocity of sound	1487.4 m sec ⁻¹	1000 dbar
Viscosity (dynamic)	1.609×10^{-3} kg m ⁻¹ s ⁻¹	
Wavelength of deepest light penetration	462 (blue)	Clearest seawater

^a Seawater at 35.00 psu, 5.0°C, and 1 atm (1.0133×10^5 Pa) unless noted.

^b Estimated from freezing point depression.

therefore, exhibit wide deviations from ideal behavior in equilibrium calculations. Models of the chemical properties of seawater require the assumption of ion pairing, for example, the formation of MgSO₄. Ion pairing is particularly significant in modeling the “speciation”—the chemical form—of trace elements in seawater. Critical variables that may contribute to the existence of a variety of forms for elements are pH, oxidation state, ion pairing, and state of aggregation.

E. Nonconservative Constituents

Dissolved gases are important constituents of seawater. They include rare gases from mantle outgassing and radioactive decay, the gaseous components or byproducts of the major biogeochemical cycles [O₂, CO, CO₂, N₂, N₂O, S(CH₃)₂], and hydrocarbons, such as methane. The global ocean is now recognized as an important source or sink for atmospheric gases that influence the chemistry and physics of the atmosphere. The most important of these are the “greenhouse” gases, principally carbon dioxide, which trap back radiation emitted by the earth in the far infrared and microwave. Carbon dioxide is consid-

ered in a separate section of this article. A final group of important nonconservative constituents—the nutrients—is discussed in the section on biogeochemical cycles.

F. Particulate and Dissolved Organic Materials

Particulates are an important class of constituents in seawater consisting of organic matter, inorganic skeletal remains, and terrigenous dusts. In recent years oceanographers have recognized the major role played by large particulates (0.1–10 mm), primarily invertebrate fecal pellets, in transporting material rapidly from surface water to deeper water and the sediment. Particles are also sites for active chemical processing in the water column, primarily from the presence of a bacterial and fungal community in the aggregates. More slowly sedimenting ubiquitous loose flocculent aggregates, broadly referred to as “marine snow,” have been observed *in situ* using scuba and deep submersibles. Oceanographers have developed sediment collectors or “traps” to establish transport fluxes, composition, and rates of particle mediated processes. A key role is played by invertebrate grazing in “packaging” finely divided suspended material, precipitates, planktonic exoskeletons, and fecal pellets into larger rapidly sinking particles.

Dissolved organic material (measured as “dissolved organic carbon” or DOC) makes up a substantial portion (over 90%) of the total of all living macroscopic and microscopic tissue and nonliving organic (carbon containing) substances. We can easily observe the presence of organics by the tendency of seawater to foam. A typical DOC deep sea concentration is 40 μmol/kg and has a C-14 age of 6000 years. The gradual conversion of these materials to refractory “humics” and “fulvics” leads to their ultimate burial in sediments and fossilization as hydrocarbons. The net removal of carbon into sediments leaves a concomitant amount of oxygen in the atmosphere that is not used in respiration. This cumulative oxygen reservoir is so vast that a complete interruption of photosynthesis and the rapid combustion of fossil fuels would not significantly deplete it for a very long time, popular myth notwithstanding.

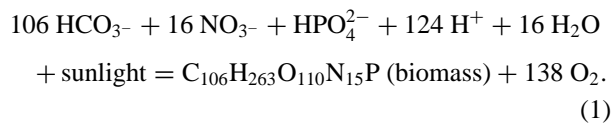
III. BIOGEOCHEMICAL CYCLES

A. The Production Equation

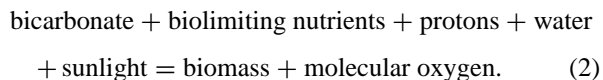
A fundamental theme in chemical oceanography is the turnover of elements in the ocean between various categories of biotic and abiotic reservoirs (biogeochemical cycles) driven by energy from the sun. Geochemical models on longer time scales also consider the evolution of the oceans and continents driven by plate tectonics. The

exchange of matter between compartments can be analyzed in terms of a single element (the carbon cycle, nitrogen cycle, etc.) and in terms of the mediating process (photoautotroph production, biogenous sedimentation, oceanic and atmospheric circulation, upwelling, weathering, and diagenesis). The processes are all interlocked in one system with multiple coupled pathways. Systems of this kind are characterized by feedback loops and inherent resistance to perturbations from a “set point,” although oscillations in internal conditions at various frequencies are the rule. The most important “pumping” input is the sun, which exhibits diurnal and seasonal cycles. Climate shifts and anthropogenic inputs are important perturbations. (The tides are a significant additional variable in estuarine, littoral, and neritic environments.)

Against a background of physical stratification and circulation, the most important chemical process in the seas is light-driven chlorophyll-dependent biological production, in which low energy oxyanions (nutrients) are incorporated into reduced, energy rich biomaterials by photoautotrophs using water as the reductant and yielding dioxygen as the product. The chemical equation is



Recast in words,



The process is usually stated as “net primary production” because the gross production is lowered by that portion of the incorporated energy used in the respiration of the photoautotrophs themselves. The term “primary” contrasts the role of autotrophs as the base of the food chain with accumulation rates for all other organisms.

The ratios of the elements in the biomass correspond to the average composition found for the metabolically active (soft parts) of marine phytoplankton; sulfur and trace metals in biota are not included in balancing the chemical equation. Note that the production equation shows the removal of protons in the reduction process resulting in a higher pH for productive seawater. The average oxidation state of carbon is zero in biomass, a median value between bicarbonate and methane. This value becomes more negative when higher ratios of fat to protein are synthesized. Nitrogen, oxygen, and sulfur are at minimum (most reduced) oxidation states in tissue, whereas phosphorus remains at +5. The oxidation state of the organic matter determines the amount of dioxygen participating in either production (photosynthetic quotient) or respiration (the respiratory quotient).

The rate of production (productivity) is chemically limited in the presence of adequate light and viable cells by the availability of nutrients. Both nitrogen and phosphorus are close to limiting concentrations in the oceans, that is, the molar ratio of nitrate to phosphate is normally 16 to 1 (the Redfield ratio) in surface waters. The average value for deep water is 14.7:1 indicating a relative loss of nitrogen from the surface layer over time. Phosphate is inherently limiting in all ecosystems, whereas nitrogen is limited by the rate of transfer into an ecosystem by fixation (from nitrogenase containing microbes and algae) and removal by denitrification (from anaerobic nitrate based microbial respiration). Under certain conditions of nutrient limitation (for example in the oligotrophic regions in the center of subtropical gyres), the availability of trace metals, principally iron, becomes limiting. A proposal by the late Prof. John Martin that oceanic productivity could be enhanced by adding iron has been successfully tested.

B. Productivity

The production equation [Eq. (1)] suggests some possible techniques for estimating productivity. Productivity is usually stated in grams carbon fixed per square meter per day (even though the ratio of carbon to total dry weight will vary) and is usually measured by the uptake of C-14 labeled bicarbonate. Oxygen evolution can be measured provided that samples do not supersaturate. Chlorophyll concentrations of the standing crop of autotrophs can be correlated with productivity permitting global surveys from satellites. The net uptake of protons is reflected in a higher oceanic pH, which can be measured on automated continuous flow-through systems with the advantage of averaging the “patchiness” of productivity. Because fresh nutrients are brought to the surface by upwelled colder water, pH, temperature, and productivity correlate in productive waters. The values of productivity observed for the world ocean can be roughly divided into the 90% of open ocean that is unproductive (oligotrophic) and the highly productive coastal regions and upwelling zones (eutrophic).

C. Chemical Effects of Vertical Mixing

Two thirds of the ocean area is permanently stratified into a relatively thin mixed surface layer (down to 50–100 meters) overlying a thermocline (to ~1000 meters) that caps off the slowly mixed cold dark depths (Fig. 1). Light penetration varies with location due to absorption and scattering but can support net production to depths of roughly 1% of the intensity of the incident surface radiation. This so-called euphotic zone may reach 100 meters in clear water. Photosynthetically active radiant energy will also undergo wavelength restrictions from the selective

absorption at the red and violet ends of the visible spectrum. Maximum photosynthesis is not found at the surface because of photoinhibition at high light intensities. At the photosynthetic “compensation depth,” gross productivity (carbon reduction rate) equals photoautotrophic respiration and net biomass accumulation ceases. If the mixed layer depth lies below the compensation depth, viable phytoplankton populations are mixed below the euphotic zone, lowering productivity. On the other hand, very shallow mixing limits the available nutrient supply from deeper water. The depth at which the integrated gross productivity, from the surface down, equals the integrated respiration is called the critical depth. Strong net productivity (a bloom) requires a mixing depth less than the critical depth. As invertebrates graze and in turn are consumed in a food chain, fecal pellets and other particulate wastes remove organic matter to deeper water depleting the surface of nutrients. This loss, called “new production,” equals between 5–15% of the surface productivity and must be balanced by advection of a resupply of nutrients. Decomposers (bacteria and fungi) remineralize the various bioelements back to the nutrient state and the cycle can continue. Steady-state in the surface layer depends on a rapid recycling before biolimiting nutrients (N and P) are lost below the thermocline. In the nutrient-poor waters of subtropical gyres, a network of extremely small photoautotrophs, grazers and decomposing microbes (“microbial loops”) rapidly recycle nutrients, limiting the losses from the mixed layer. Restoration to the surface layer of the vast store of deep nutrients occurs by slow upward advection ($\sim 4\text{--}5 \text{ m yr}^{-1}$). Upwelling from the thermocline at divergence zones and deep seasonal mixing in higher latitudes support “blooms” of larger phytoplankton and grazers that can support longer food chains and, therefore, ultimately support fisheries.

Depth profiles of the variables in the production equation reflect the vertical segregation of the chemical variables. Figure 3 shows generalized profiles for a tropical pelagic location. (Note that in the oceanographic literature the depth values increase toward the bottom—of the page or the ocean). The oxygen profile is particularly sensitive to biogeochemical cycling. Oxygen saturated seawater sinks in high latitudes (primarily the North Atlantic) and spreads laterally in the deep ocean driven by density stratification (thermohaline circulation) throughout the ocean basins. Production close to the surface produces oxygen, sometimes to supersaturation. As the biomass is recycled to yield nutrients deeper in the photic zone and in the thermocline, there is a net consumption of oxygen. The rate of respiratory depletion of oxygen declines exponentially with depth (with a significant consumption “spike” at the bottom due to sediments). The steady state oxygen profile results from the in situ consumption super-

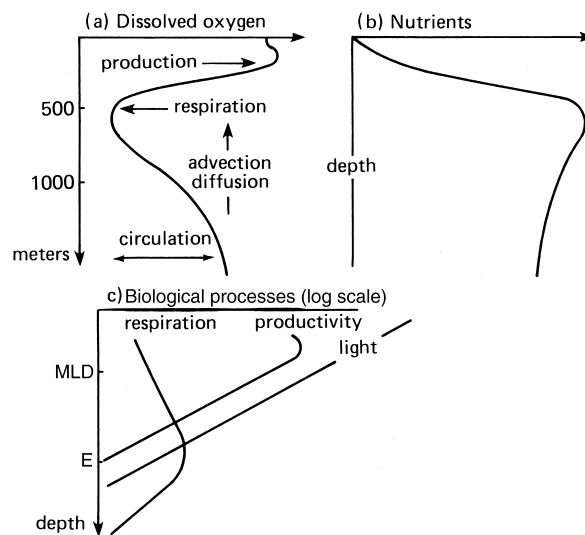


FIGURE 3 Profiles of production variables.

imposed upon the upward advection of deep “ventilated” (oxygenated) water, which is continuously mixed by eddy diffusion (Fick’s law). The in situ consumption (“apparent oxygen utilization”) correlates closely with nutrient restoration to the water column (profile b). The profile of biological processes (c) shows the respiration maximum underneath the production maximum that lies above the mixed layer depth (MLD).

When upwelled water reaches the surface, it is colder, nutrient rich, and more acidic than surrounding water. A surge of productivity occurs not in the newly upwelled water but on the margins where mixing occurs. The delay may be due to such factors as the induction of enzymes required for nutrient assimilation and photosynthesis in the inoculum (which is entrained from euphotic zone water), the formation of particulate aggregates, and the photolytic degradation of trace-metal-binding organics. Good correlation exists between temperature and chlorophyll and between temperature and pH in the productive zones. Exchange of atmospheric carbon dioxide into or out of the surface is slow in comparison with biologically induced chemistry in productive water.

D. The Nitrogen Cycle

Nitrogen is frequently biolimiting in marine ecosystems and has many observable molecular species at various oxidation states with associated rates of formation and decomposition. Figure 4 shows the forms at pH 7 and the values of the reduction potentials in millivolts at pH 7 (ΔE°) for the interconversions.

The reduction potentials show that the uptake and reduction of nitrate by phytoplankton in production is

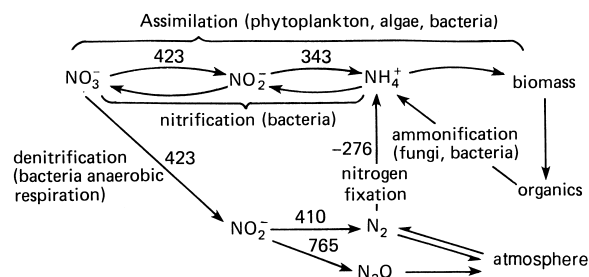
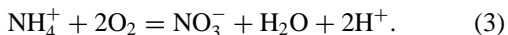


FIGURE 4 Observable nitrogen forms in seawater.

energetically favorable. Nitrate also is used as an alternative oxidant to oxygen in the respiration of bacteria in oxygen deficient waters (Black Sea, fjords, stratified trenches, East Tropical Pacific). Ammonia produced from excretion and decomposition is recycled by chemosynthetic organisms that use the energetically favorable reaction



As with all oxygen based respiration, the process is driven to the right by the heat of formation of water, reflected in the strong reduction potential of oxygen ($E^\circ = 815 \text{ mV}$). With so much nitrogen available in the atmosphere, one might expect nitrogen limitation to be rare. However, the nitrogen fixation system (nitrogenase) seems to be confined to a few species of cyanobacteria in the oceans; it is bioenergetically costly and limited by the availability of iron and molybdenum. The oceans are not in thermodynamic equilibrium with atmospheric nitrogen (0.78 mole fraction) and oxygen (0.21 mole fraction). Instead a steady-state exists in which nitrogen is recycled as rapidly as it is fixed. Denitrification may be the principal return mechanism. Hydrothermal vents may play a role in the nitrogen cycle via nitrate reduction. Some indication of the complexities in nitrogen cycling can be seen in highly productive waters, where the very rapid turnover causes buildup of ammonia and nitrite to observable levels under the euphotic zone.

E. Biogenous Sedimentation

Ocean sediments consist of biogenic silica (global average of 14%), calcite (48%), and aluminosilicate dust (abyssal clay derived from the weathering of continents) (38%). The silicic acid [Si(OH)_4] and calcium bicarbonate [$\text{Ca(HCO}_3)_2$] introduced into the oceans from rivers are removed by biogenous sedimentation. Marine plankton secrete calcareous exoskeletons (calcite or aragonite) or opaline silica. When the plant or animal is consumed or dies, its inorganic shell or skeleton ("test") drops to the bottom. In productive zones, substantial portions of the sediment are made of these remains; for example, in high latitudes silica from diatoms predominates, and in temper-

ate zones, the calcareous remains of foraminifera are important. Because seawater is undersaturated with respect to silica, dissolution occurs as the particles sink. Sediment accumulation rates depend on the rate of growth in the surface layer versus rate of dissolution at depth. Seawater is supersaturated for calcite and aragonite in surface waters but undersaturated in deeper waters. A distinct boundary for calcite disappearance is observed in ocean sediments—the "lysocline." Calcite solubility is a function of pressure, temperature, salinity, and carbonate concentration creating an equilibrium "saturation horizon" below which calcite will start to redissolve. At still lower depths, called the carbonate compensation depth, the rate of calcite return to solution equals the fall-out rate of calcite. The lysocline starts at about 4 km in the Pacific and 5 km in the Atlantic. Aragonite from pteropods is far more soluble, returning calcium to solution at 3 km in the Atlantic. Because the surface waters are actually supersaturated with calcium carbonate, and the lysoclines for calcite are deeper than the average ocean depths of 3.8 km, calcium remains close to a conservative element in seawater.

Silica is introduced into the oceans from rivers and from hydrothermal vents, and is removed by biogenous sedimentation. Diatoms (phytoplanktonic) are the principal silicic acid utilizing organisms in high latitudes. Radiolarians (zooplanktonic) also produce silica skeletons. The silica is in a hydrated amorphous form called opal. Because silica exists in low concentrations and is biologically controlled, profiles of silicic acid show the same characteristics as nutrients.

F. The Carbon Cycle and the Carbonate System

The geochemical carbon cycle (Fig. 5) can be modeled kinetically and exhibits short term steady-state conditions. The principal portions are

1. The atmosphere/hydrosphere exchange of carbon dioxide
2. The carbon dioxide/bicarbonate/ buffer system

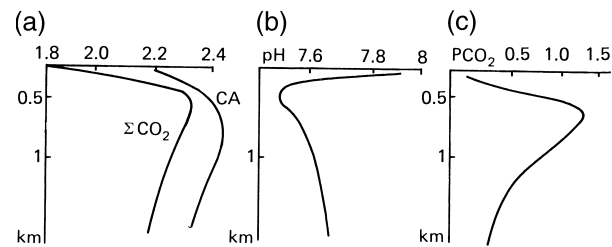


FIGURE 5 Profiles of carbon. (a) Total carbon and carbonate alkalinity (mEq kg^{-1}). (b) Hydrogen ion (pH). (c) Partial pressure of carbon dioxide (millibars).

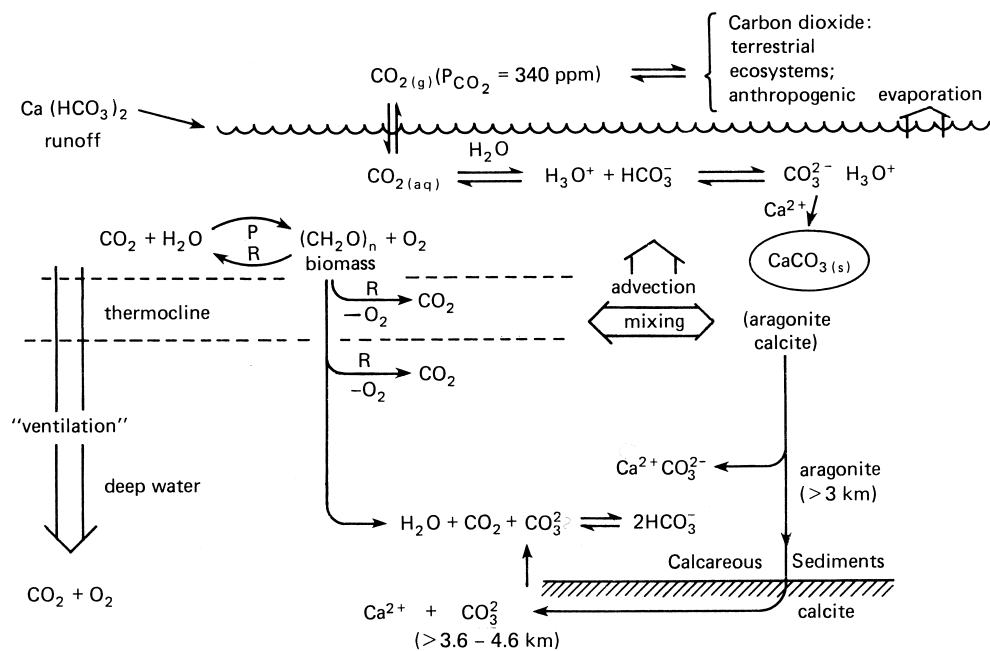


FIGURE 6 The carbonate system.

3. The production/respiration equations
4. Calcareous sedimentation and dissolution

The carbon cycle contains a massive carbonate reservoir in calcareous sediments and carbonate rocks such as limestone (the primary form of carbon on earth) undergoing net long-term accumulation on continents. The oceans and atmosphere act as a relatively rapid return loop. Atmospheric carbon dioxide mixes with the upper mixed layer of the ocean in about one year. Carbonates penetrate the thermocline with a time constant of decades, whereas centuries are required to ventilate the deep ocean with atmospheric components.

The carbon dioxide content of the atmosphere has increased from less than 250 ppm to over 360 ppm since the start of the industrial revolution from the burning of fossil fuel, the destruction of forest, and the turnover of soil carbon. This has been observed directly since 1958 at an observatory on Mauna Loa volcano in Hawaii and indirectly by analyzing gas bubbles trapped in glacial ice and from the carbon-13 to carbon-12 ratios in wood and coral. Additional verification comes from examining the decrease in atmospheric carbon-14 due to dilution with fossil fuel carbon dioxide (Suess effect). The oceans are the ultimate sink for the excess carbon dioxide but the rate of absorption does not keep pace with the rate of increase. The increase in atmospheric carbon dioxide should lead to increased heat content of the oceans (deeper mixed layer) and higher temperatures on the earth (greenhouse effect).

The carbonate system in the oceans (Fig. 6) comprises the interchange of various forms and pools of carbon at the maximum oxidation state of +4—carbon dioxide, carbonate, and bicarbonate. The system buffers the ocean, regulates the carbon dioxide content of the atmosphere, and serves as a pivotal link in the carbon cycle. Equilibrium calculations are used to characterize the acid-base behavior of the system because proton transfers are rapid. Seawater contains approximately 2.5 millimol kg^{-1} bicarbonate, which buffers the oceans at an average pH of 7.5.

Empirical first and second dissociation constants (K'_1 and K'_2) are used in equilibrium expressions

$$K'_1 = a\text{H}^+ [\text{HCO}_3^-] / [\text{CO}_2] \quad (4)$$

$$K'_2 = a\text{H}^+ [\text{CO}_3^{2-}] / [\text{HCO}_3^-]. \quad (5)$$

If the carbonate system is open to the atmosphere, the equilibrium concentration of dissolved carbon dioxide is constrained by the partial pressure of atmospheric carbon dioxide following Henry's law.

$$[\text{CO}_2] = H P_{\text{CO}_2}. \quad (6)$$

The brackets normally refer to concentrations in moles per kilogram of seawater (instead of molality or molarity). The expression $[\text{CO}_2]$ refers to the sum of the aqueous concentrations of carbon dioxide and carbonic acid. The partial pressure of carbon dioxide (P_{CO_2}) is usually given in atmospheres. The activity of protons ($a\text{H}^+$) is measured by a glass electrode calibrated against dilute standard buffers.

TABLE IV Principal Methods of Seawater Analysis

Constituent and range of values in seawater	Traditional method	Instrumental method	Precision including intercalibrations
Salinity 30–40 psu (g kg^{-1})	As chloride equivalent of halides by Ag^+ titration	Conductivity	0.01 psu
Oxygen 0–8 cc (STP) kg^{-1} 0–360 $\mu\text{mol kg}^{-1}$	Winkler titration: Alkaline Mn(II); acid, iodide; thiosulfate titration of iodine.	Polarographic electrode: Au in base covered with teflon membrane	0.03 cc kg^{-1}
Hydrogen ion (pH) 7.2–8.6	Indicator dyes (a revived technique)	Glass electrode: glass membrane enclosing Ag/AgCl electrode	0.002 pH units
Alkalinity 2.2–2.5 mEq kg^{-1}	(a) Back titration of pH 6 endpoint after acidification and CO_2 purge (b) Acidification to a precise pH (or glass electrode potential)	(c) Automated potentiometric titration with HCl (d) Automated photometric (indicator) titration with HCl	(a) 0.2% (b) 1% (c) 0.1% (d) 0.1%
Total carbonate species 1.9–2.4 mEq kg^{-1}		Acidification, CO_2 purged and measured by IR, gas chromatography or manometrically	0.1%
Nitrate 0–45 μM	Reduction to nitrite with Cd; spectrophotometric detn. of dye formed from nitrite		0.1 μM
Phosphate 0–3 μM	Spectrophotometric detn. of phosphomolybdate complex		~5%
Silicate 0–175 μM	Spectrophotometric detn. of silicomolybdate complex		~5%

Other systems for calibrating pH scales and alternative concentration units for protons are sometimes used. Values for K'_1 and K'_2 have been determined for seawater for salinities from 0–40 psu and temperatures from the freezing point to 40°C. Similar tables exist for the Henry's law solubility coefficient (H) for carbon dioxide and the dissociation constant of water required for equilibrium calculations, K_w . The carbonate system is also constrained by the carbonate alkalinity (CA)

$$\text{CA} = [\text{HCO}_3^-] + 2[\text{CO}_3^{2-}] \quad (7)$$

Other competing sources and sinks for protons, such as boric acid and bisulfate, become significant at high and low pH values. The system can be characterized by any pair of the measurable parameters pH, P_{CO_2} , CA, and total carbon ($\sum \text{CO}_2$)

$$\sum \text{CO}_2 = [\text{CO}_2] + [\text{HCO}_3^-] + [\text{CO}_3^{2-}] \quad (8)$$

Alkalinity is measured by titration (Table IV) and total carbon as carbon dioxide after acidification (Table IV). Profiles of these variables (Fig. 5) will reflect the sources and sinks for carbon shown in Figs. 6 and 7.

Representative values of the constants at 18°C (the average temperature of surface waters) and 35.00 psu are

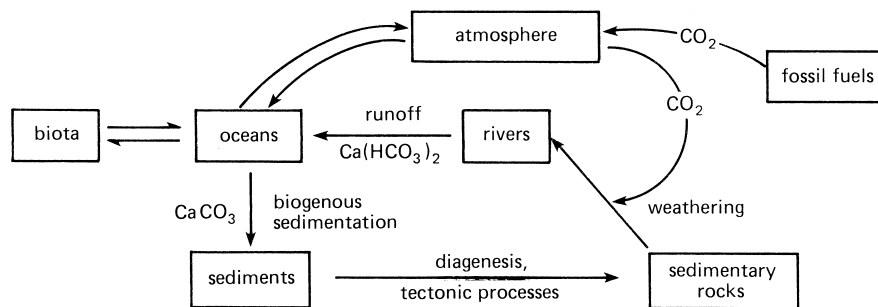
$$K'_1 = 9.08 \times 10^{-7}$$

$$K'_2 = 5.17 \times 10^{-10}$$

$$K_w = 2.38 \times 10^{-14}$$

$$H = 3.43 \times 10^{-2} \text{ mol kg}^{-1} \text{ atm}^{-1}$$

Sample calculations using these values for seawater under 381 microatmospheres carbon dioxide partial pressure and with a carbonate alkalinity of 2.25 millimol kg^{-1} yield a pH of 8.2 and a total carbon concentration of 2.07 millimol kg^{-1} (about 90% bicarbonate).

**FIGURE 7** The carbon cycle.

G. Geographical Distributions

The oceans exhibit geographic variations in the concentrations of constituents on spatial scales varying from global to very small patches and temporal scales of hours to centuries (Fig. 2). On a global scale the general deep thermohaline circulation carries deep North Atlantic water to the South Atlantic into the Indian Ocean and eventually to the North Pacific. During this slow migration, which takes up to 1000 years, the continuous rainout of particulates causes an increase in the concentrations of nutrients, decrease in oxygen, and an increase in total carbon from respiration and calcite dissolution in deep water. The horizontal movement is roughly four orders of magnitude faster than vertical mixing ($\sim 4 \text{ m yr}^{-1}$). As a result, the lowest oxygen levels and highest nutrient levels in the open ocean are observed below the thermocline in the eastern subtropical Pacific Ocean due to the cumulative effects of oxygen utilization and the high sustained productivity in surface waters off the west coasts of South America and Central America (Fig. 8).

Within ocean basins, wind patterns generate large subtropical gyres that have a central convergence zone with a deeper thermocline and lower productivity. Divergence zones with associated upwelling and higher productivity are generated at polar and equatorial current boundaries, in current eddies, and near sporadic plumes of deeper water that surface near coasts in the form of mesoscale “streamers”. These features can be observed readily from satellites, for example in the intensive study of (ENSO) events in recent years. Synoptic maps (analogous to weather maps) of the chemical constituents and physical variables (most prominently temperature) can be constructed from satellite observations combined with surface measurements (“seatruth” data) from tethered buoys and continuous underway ship observations. These observations make possible the calibration of numerical models of ocean pro-

cesses and the monitoring of production and pollution on a global scale. Long term studies are required for monitoring recurrent phenomena, such as ENSO cycles, because spectral analysis of oscillatory phenomena must have a cumulative data set over time that catches significant frequencies.

H. Additional Biogeochemical Cycles

The turnover cycles of carbon, nitrogen, and oxygen discussed in this section interlock through the common compartments of biota, sediments, the atmosphere and seawater constituents (Fig. 7). Other elements, both metals and nonmetals, such as iron, sulfur, and phosphorus, follow similar general patterns. Sulfur is particularly significant as a controlling element in the oxidation state of the oceans and atmosphere through the burial of sulfides and elemental sulfur over geologic time scales. See the bibliography for additional reading.

IV. SAMPLING, ANALYSIS, AND SPECIAL METHODS

A. Sampling

The oceanographer confronts a professional dilemma when approaching a very large ocean with an infinitesimal sampling device. How can a sufficient number of credible measurements be accomplished within practical constraints in space and time? At any location in the oceans, chemical changes are constantly occurring on all time scales (see Fig. 2) either as the result of in situ processes or from physical transport (advection and diffusion). The traditional marine chemist measures discrete seawater samples collected with bottle casts (see “Glossary”) at widely separated sites with great precision and accuracy and then extrapolates those results over large portions of the ocean. But precise chemical measurements made on a station occupied for an extended time have limited value unless they are compared with data from other locations at similar times. The modern chemical oceanographer prefers to sample those same areas continuously in “realtime” (i.e., the recording and description of events as they are actually occurring). Moving ships, autonomous underwater vehicles (AUVs), remotely operated vehicles (ROVs), staffed or machine-run submersibles, and tethered buoys become analytical tools when fitted with sensors, microprocessors, and data storage and retrieval systems, such as umbilicals and telemetry. Continuous sampling may be punctuated with bottle casts using the CTD continuous vertical profiles as baseline data. Because the time constant for vertical mixing in deep waters is much slower than the period required for deep hydrocasts (up to six hours), it is only

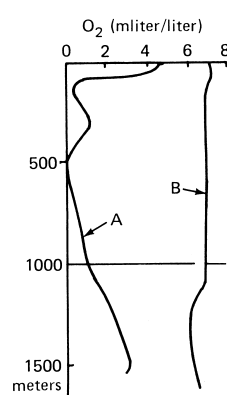


FIGURE 8 Representative oxygen profiles (A) east tropical Pacific, (B) North Atlantic.

TABLE V Comparisons of Water Sampling Methods

Method	Coverage	Strengths and limitations
Bottle	One point in time and space	Poor time and space resolution; minimum information; high accuracy
String of n bottles	Few points separated in depth	Gives coarse vertical profiles depending on bottle spacing; high accuracy
String of n bottles repeated m times	Widely spaced sets of coarse vertical profiles; variable temporal coverage	Some spatial and temporal resolution; physical and logistic limitations
Shipboard pumped systems or towed sensor packages	Nearly continuous horizontal resolution	Good two-dimensional resolution; shallow depths only; limited geographic and synoptic coverage; high accuracy (frequent calibration)
Remote sensing (AUVs, ROVs, buoys, submersibles)	Local high spatial and temporal resolutions	Limited range; frequent calibration for high accuracy
Satellites and aircraft	Global or regional range	Maximum spatial/temporal coverage; no depth penetration; requires “sea-truth” data and atmosphere corrections

necessary to duplicate deep measurements (>1000 meters) for verification and self-consistency. **Table V** compares the coverage and limitations of sampling methods. The methods selected have to be geared to the particular study undertaken. Ship operations are very expensive, which makes the use of satellites and tethered instrument platforms carrying automated instruments and telemetry cost effective.

B. Remote Sensing and Satellite Chemical Oceanography

Previous sections pointed out the importance of satellite observations in oceanography. Satellites have clearly shown that the surface of the ocean, particularly along coasts and along intertropical convergence zones, is composed of countless mesoscale (~ 100 km) features, such as rings or eddies, plumes, and jets. The boundaries of these features are known as fronts and are the locations of energy and mass transfer between adjoining formations and between deeper water and the surface. Mesoscale features clearly show up in thermal and color (visible) satellite imagery but neither can be said to be a measure of a chemical constituent (except chlorophyll). On the other hand, measurements of constituents with classical bottle casts will miss the overall pattern of mesoscale structures. The solution to the dilemma is the combination of satellite observations, which give maximum spatial and temporal coverage, with shipboard, buoy, AUV and ROV sampling using sensors, sampling bottles, or pumped systems to provide “sea truth” data. In effect, the radiation in the microwave, infrared, or visible region of the electromagnetic spectrum detected by the satellite is correlated with temperature, salinity, chlorophyll, and chemical concentrations actually measured at sea. For example, underway observations in some tropical systems demonstrate that the pH

of surface seawater correlates with sea surface temperature (SST) on large spatial scales. It is possible, therefore, to infer pH from satellite observations of SST (by infrared). Because productivity correlates with pH and chlorophyll, global estimates of oceanic productivity can be generated by satellite. The rapidity of satellite observations assures synopticity of measurements.

C. Analytical Methods and Instrumentation

Modern chemical oceanography has been characterized by a substantial increase in the development and use of electronic instrumentation. However, the funding for instrumentation in oceanography generally lags behind related efforts in space research and biotechnology, forcing oceanographers to adapt “off the shelf” systems to the special conditions of pressure and salinity in the ocean. Traditional solution chemistry methods of chemical analysis on discrete samples collected from sampling bottles remain as the primary methodology, but are being replaced with automated (microprocessor controlled) analyzers. The reliability of any analytical procedure depends on three factors: sample acquisition, handling, and storage; the analytical procedure; and calibration and standardization. The precision (reproducibility) and accuracy of measurements in marine chemistry usually depend on the first category, assuming adherence to high standards of practice in the other areas. A good example of these problems is provided by the analysis for dissolved oxygen. Most chemical oceanographers (and other environmental chemists) still use a thiosulfate titration, developed originally by L. W. Winkler in 1888, in which the dissolved oxygen reacts with Mn(II) and the resulting oxide is converted to an equivalent amount of iodine with iodide. The method is quite sensitive and precise down to 0.1 ppm. Scientists interested in measuring trace quantities of oxygen, at the

boundaries of anoxic layers, for example, find the principal error in trapping and handling the sample. Transferring the sample from the sampling bottle to the analytical vessel can add oxygen from the atmosphere. Withdrawing samples by suction (by syringe, for example) may actually remove gas from solution. To increase precision in the analysis of trace gasses or metals, very large samples are desirable. For some constituents of seawater, the wire holding the sampler, the sampling bottle, and the associated mechanisms can add contamination. This is an especially severe problem in trace metal analysis.

Collection of chemically labile samples is another severe hurdle. A good example is the determination of sulfides (and other constituents) in the effluents from hydrothermal vents. In 1986, the first direct measurements of sulfide were made at a site in the Pacific from the submersible *Alvin* using flow injection analysis. Techniques that can make in situ measurements are increasingly significant including spectrophotometers and fluorometers that use fiber optic cables connected to a cell or sensor below the surface.

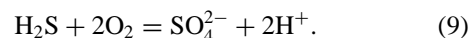
Table IV lists some seawater constituents together with the techniques normally used and the precision of measurement.

D. Biochemical Oceanography

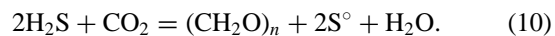
Biochemical techniques have important applications in chemical oceanography. Studies of the biochemistry and biophysics of photosynthesis in marine organisms have remained a major concern in oceanography for half a century. Recent work has been centered on the effects of anthropogenically altered global conditions, such as increased atmospheric carbon dioxide, increased surface temperatures, and increased surface ultraviolet radiation in high latitudes. Remineralization of biomass is an example of a major chemical process that must be approached as a problem in microbial ecology and physiology as well as oceanography since energy that flows through most marine ecosystems is carried predominantly by very small unicellular organisms, both at the first trophic level and at the decomposer level. The in situ rates of cycling of carbon, nutrients, and oxygen can be obtained by using sensitive techniques for measuring the rate limiting enzymes in crucial metabolic pathways. For example, a tetrazolium dye assay for the electron transport system that mediates oxidative phosphorylation in virtually all organisms can be used to estimate oxygen consumption rates in the water column after direct or indirect calibration. Bioenergetic rates may also be evaluated by the turnover of the nucleotide phosphate pool (ATP). Polynucleotide (DNA, RNA) synthesis rates can be assayed as a measure of the growth of microbial communities that correlates with cell

division and protein synthesis. Nitrogen cycling rates can be estimated from enzymatic assays such as glutamine synthetase (nitrogen assimilation) and nitrogenase (nitrogen fixation). The responses of organisms to pollution includes the induction of lysozyme, metal binding protein (metallothionein), and many other adaptative reactions. Adaptations to hyperbaric conditions and deep cold have also been investigated.

A dramatic development in biochemical oceanography in recent years has been the discovery of entire ecosystems in the vicinity of mid-ocean ridge hydrothermal vents that are based on chemosynthetic autotrophic growth. The energy is derived from the oxidation of the hydrogen sulfide in the vent water



The H_2S also serves as a reductant for autotrophic growth



A very close mutualism is observed in which organisms, such as tube worms and bivalves, have lost digestive mechanisms and rely entirely on endosymbiont bacterial populations for energy. The organisms actually hold H_2S on a sulfide binding protein to concentrate and transport this otherwise extremely toxic substance.

E. Trace Metals, Isotopes, and Radionuclides

Until quite recently, trace metal concentrations (less than 1 mg kg^{-1}) in seawater were of interest primarily to geochemists for calculations of residence times and global fluxes. Usually only average values were available and these were highly suspect due to sample contamination from samplers, hydrowires, ships, and laboratories. The development of modern methods—sophisticated and sensitive instrumentation, preconcentration techniques, and “clean” sampling and handling procedures—have begun to yield reliable results that make some modeling of trace element dynamics possible. **Figure 9** shows the

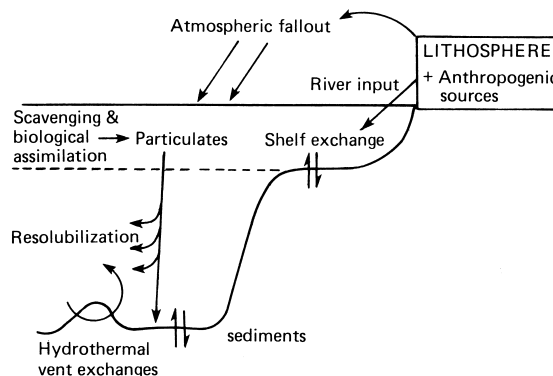


FIGURE 9 Trace element dynamics.

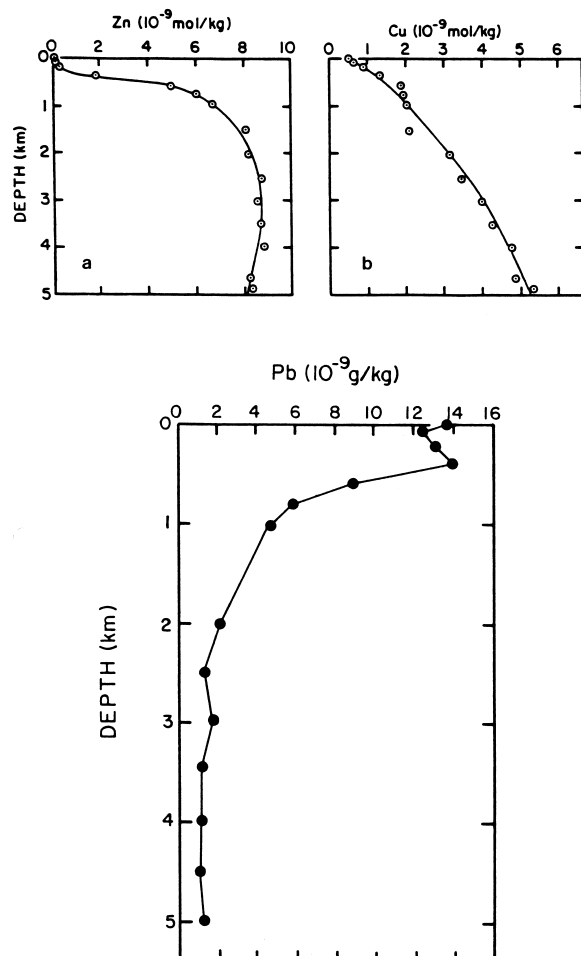


FIGURE 10 (a,b) Plots of dissolved Zn and Cu as a function of depth in the central North Pacific. These results were obtained by Bruland and coworkers at the University of California at Santa Cruz. (c) Distribution of dissolved lead with depth in the north temperate Pacific Ocean. The excess for the upper waters is thought to represent pollution, for example, lead from gasoline. These measurements were made by Patterson and Schaeffer at California Institute of Technology. [Reprinted from Broecker, W. S., and Peng, T. H. (1982) "Tracers in the Sea." Eldigia Press, Palisades, New York.]

principal pathways for trace metal mobilization in the oceans.

The chemical nature of a given trace element, together with the relative rates of the processes in Fig. 9 and the physical processes of mixing and circulation, produce several types of trace element profiles (Fig. 10).

1. Conservative: Concentrations exhibit a strong coherence with salinity; for example, cesium.
2. Nutrient-like: Surface depletion and enrichment in deeper waters, with strong correlations to biolimiting nutrients; for example, zinc.
3. Surface enrichment and depletion at depth due to rapid scavenging. An example is lead.

Some profiles show maxima or minima due to oxygen deficiency in the water column or hydrothermal-vent activity. Copper profiles are atypical in showing scavenging into particulates throughout the water column together with a remobilization into the bottom of the water column from the sediments.

Radionuclides and the variations in stable isotope ratios, for example, C-12:C-13 and O-16:O-18 provide uniquely sensitive tracers for the mixing and circulation processes in the oceans and the long-term sedimentary cycling reflecting climatic shifts, such as ice ages. Because the decay rates of radionuclides are invariant with temperature and chemical speciation, they may be used for dating materials. One of the most striking examples of the use of radionuclides comes from the relatively sudden introduction of C-14 and tritium into the surface waters from atmospheric nuclear detonations. These anthropogenically induced radionuclides have now penetrated temperate zone waters to approximately 1000 m following isopycnal (equal density) surfaces. The stable isotopes of carbon and C-14 have also enabled us to evaluate the capacity for the oceans to absorb the huge excess of carbon dioxide generated by humans since the industrial revolution. The oceans can, in fact, absorb the carbon dioxide, forming bicarbonate from carbonate and dissolving calcareous sediments, but the rates of these processes are insufficient to maintain a steady-state atmospheric concentration of carbon dioxide. Carbon dioxide will, therefore, increase in the atmosphere from two to five times over the next two centuries and actually alter global climate patterns due to the "greenhouse effect." It turns out that other anthropogenic atmospheric constituents also contribute to climate alteration.

V. AREAS OF SPECIAL INTEREST

The literature of chemical oceanography contains substantial material on some well-defined topics of special interest. These include marine electrochemistry, marine photochemistry, the chemistry of anoxic basins, marine pollution, dissolved and suspended organic matter, the formation of hydrogenous sediments (most notably ferromanganese nodules), spectral analysis of oscillatory phenomena, and chemical resources in the sea, such as magnesium, seaweed extracts, and natural products of pharmacological significance. Most of these topics are discussed in the sources listed in the bibliography.

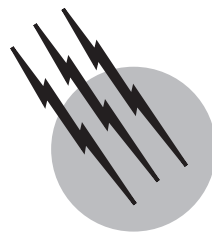
SEE ALSO THE FOLLOWING ARTICLES

CARBON CYCLE • ENVIRONMENTAL GEOCHEMISTRY • GAS HYDRATE IN THE OCEAN ENVIRONMENT • NITROGEN CYCLE, ATMOSPHERIC • OCEAN-ATMOSPHERIC EXCHANGE • OCEAN SURFACE PROCESSES • OCEAN

THERMAL ENERGY CONVERSION • PHYSICAL OCEANOGRAPHY, OCEANIC ADJUSTMENT • PHYSICAL OCEANOGRAPHY, THERMAL STRUCTURE AND GENERAL CIRCULATION • PLATE TECTONICS

BIBLIOGRAPHY

- Bearman, G., (ed.). (1995). "Seawater: Its Composition, Properties and Behaviour," 2d ed. Butterworth Heinemann & The Open University, Oxford.
- Bearman, G., (ed.). (1989). "Ocean Chemistry and Deep-Sea Sediments," The Open University and Pergamon, London.
- Broecker, W. S., and Peng, T. H. (1982). "Tracers in the Sea," Lamont Doherty Geological Observatory, Columbia Univ., Eldizia Press, Palisades, New York.
- Falkowski, P. G., and Woodhead, A. D., (eds.). (1992). "Primary Productivity and Biogeochemical Cycles in the Sea," Plenum, New York.
- Grasshoff, K., Ehrhardt, M., and Kremling, K. (1983). "Methods of Seawater Analysis," 2d ed. Verlag Chemie, Weinheim.
- Libes, S. M. (1992). "An Introduction to Marine Biogeochemistry," Wiley, New York.
- Millero, F. J. (1996). "Chemical Oceanography," 2d ed. CRC Press, New York.
- Morel, F. M. M., and Hering, J. G. (1993). "Principles and Applications of Aquatic Chemistry," Wiley, New York.
- Pilson, M. E. Q. (1998). "An Introduction to the Chemistry of the Sea," Prentice Hall, Upper Saddle River, NJ.
- Riley, J. P., and Skirrow, G., (eds.). (1975–1990). "Chemical Oceanography," 2d ed., vols. 1–9. Academic Press, London.
- Schlesinger, W. H. (1997). "Biogeochemistry: An Analysis of Global Change," 2d ed. Academic Press, San Diego, CA.
- Singer, S. F., (ed.). (1990). "The Ocean in Human Affairs," Paragon House, New York.
- Stillinger, F. H. (1980). Water revisited. *Science* **209**, 451–457.
- Stumm, W., and Morgan, J. J. (1996). "Aquatic Chemistry: Chemical Equilibrium and Rates in Natural Waters," 3d ed. John Wiley, New York.
- Zirino, A., ed. (1985). "Mapping Strategies in Chemical Oceanography" (Advances in Chemistry No. **209**). American Chemical Society, Washington.



Physical Oceanography, Oceanic Adjustment

Ping Chang

Texas A&M University

- I. An Overview of the Physics of Ocean General Circulation
- II. Adjustment in Extratropical Wind-Driven Circulation
- III. Adjustment of Tropical Wind-Driven Circulation
- IV. Adjustment of Thermohaline Circulation

GLOSSARY

Ekman drift or transport A direct wind-driven flow integrated over the mixed layer—a thin top layer of the ocean. The flow is to the right (left) of the local wind in the Northern (Southern) Hemisphere.

Ekman pumping or suction Vertical movement of water resulting from convergence or divergence of the Ekman drift.

Equatorial wave guide A narrow equatorial zone within which planetary waves and inertial gravity waves co-exist and wave energy is trapped.

Kelvin waves Special long gravity waves generated by the earth's rotation. These waves are trapped either along boundaries of the oceans or along the equator.

Potential vorticity A dynamical quantity that gives a measure of the spin of a fluid column bounded by two constant-density surfaces. The quantity is conserved following a fluid parcel in a nondissipative flow.

Rossby waves Planetary-scale waves that owe their exis-

tence to the latitudinal variation of the Coriolis parameter. The dynamics of these waves obeys the conservation of potential vorticity.

Sverdrup flow A steady oceanic flow induced by changes in the depth of the water column in the ocean interior due to Ekman pumping or suction to conserve potential vorticity.

OCEANIC ADJUSTMENT refers to dynamical processes responsible for ocean circulation changing from one state to another in response to changes in forcing. The oceans are primarily forced by the atmosphere and the gravitational attraction of the moon and sun. The atmospheric forcing consists of momentum flux generated by wind stress on the ocean surface and heat flux generated by radiation, evaporation, and air-sea temperature difference. In contrast to the atmosphere, which is forced from below through radiative forcing, the oceans are forced from above. The solar radiation heats the surface of the

oceans, creating a stably stratified fluid layer over much of the global oceans except in a few isolated polar regions. Therefore, to a first-order approximation, ocean circulation can be described by an appealingly simple model of a two-layer fluid system. The motion of the upper layer is primarily driven by momentum flux, i.e., surface wind stress. This part of the circulation is referred to as the wind-driven circulation. In contrast, the motion of the lower layer, which represents the abyssal ocean circulation, is primarily driven by deep convection caused by heat loss to the atmosphere in high latitudes. This part of the circulation is called the thermohaline circulation. The interface dividing the wind-driven and thermohaline circulation layer is called the thermocline of the ocean, and is characterized by a strong vertical density gradient. The discussion here is not on how the thermocline is formed, but on how ocean circulation adjusts to a change in atmospheric forcing for a given thermocline structure.

Ocean circulation is subject to considerable variability over a broad time scale due to tremendous variability in the atmospheric forcing. Well-known phenomena caused by rapid oceanic adjustment to large-scale changes in the surface wind forcing are, for example, the sudden appearance of the Somali Current along the eastern coast of Africa shortly after the onset of the Asian–Australian monsoon in late spring, and El Niño in the tropical Pacific Ocean. The latter can be considered, strictly from an oceanic perspective, as the equatorial ocean response to interannual changes in trade wind strength associated with the Southern Oscillation phenomenon in the atmosphere.

Adjustment time scales in the oceans vary considerably from location to location. The adjustment of the upper ocean proceeds much faster than that in the interior of the oceans. In fact, the ocean surface currents adjust almost instantaneously to changes in local wind forcing, whereas the adjustment of abyssal circulation can take hundreds of years. The adjustment in low-latitude oceans also proceeds much faster than that in high latitudes. For example, a low-latitude western boundary current, such as the Somali Current, can be generated within a matter of weeks after the onset of the monsoon, whereas a midlatitude western boundary current, such as the Gulf Stream, has a response time on the order of a decade. Two major factors influencing how oceanic adjustment proceeds are intrinsic time scales determined by internal ocean dynamics and extrinsic time scales imposed by forcing fields.

I. AN OVERVIEW OF THE PHYSICS OF OCEAN GENERAL CIRCULATION

Within the top 50 m or so of the oceans, known as the mixed layer, there is a direct local wind-driven current

called Ekman flow. This flow results from a local balance between the Coriolis force and the frictional force generated by the turbulent stresses associated with wind forcing. The water within this layer is transported by wind stresses to the right (left) of the local wind in the Northern (Southern) Hemisphere, and adjusts nearly instantaneously to changes in local wind stresses. Integrating Ekman flow over the mixed layer gives the Ekman drift or transport, which flows perpendicular to the local wind.

Below this stress-carrying layer, relationships between currents and local winds are problematic because the circulation in the interior of the ocean is not directly driven by the local wind, but rather by the convergence of the stress-driven Ekman drift in the mixed layer. The Ekman drift convergence and divergence produce upward (Ekman suction) and downward (Ekman pumping) motion, respectively, at the base of the mixed layer. The maximum Ekman pumping occurs along the latitudes where the tropical trade winds and midlatitude westerlies winds meet (approximately at 30°S and 30°N), where water is being pushed below the mixed layer, causing the interior water column to contract (shrink). The maximum Ekman suction occurs along the equator and along the latitudes where the midlatitude westerlies meet the polar easterlies (50°N–55°N). In these divergent regions, water is being drawn from the interior of the ocean into the mixed layer, causing the interior water column to expand (stretch).

In the interior of the ocean, where frictional effects are generally small, a water column of depth H conserves its potential vorticity f/H , where f is the Coriolis parameter, which increases from zero at the equator to twice the earth angular velocity at the poles. The potential vorticity can be thought of as the spin angular momentum of a small cylinder of fluid. When the cylinder is stretched (contracted), it spins faster (slower). It follows that in the midlatitudes, where Ekman pumping causes the interior water column to contract (decreasing H), the water must move equatorward (decreasing f) to conserve potential vorticity, whereas in the high latitudes, where Ekman suction causes the interior water column to expand (increasing H), the water must move poleward (increasing f) to conserve potential vorticity. Therefore, there are two wind-driven circulation gyres in the North Pacific and Atlantic Oceans. The subtropical gyres are driven by Ekman pumping and circulate clockwise, whereas the subpolar gyres are driven by Ekman suction and circulate anticlockwise. Thus, potential vorticity dynamics is at the core of the extratropical wind-driven circulation.

Conservation of potential vorticity can also be used to explain thermohaline circulation in the abyssal oceans. Here the stretching of the interior water column is caused by a different physical mechanism. Heat loss to the atmosphere in the polar region produces intense cooling at

the ocean surface, giving rise to the formation of dense water, which sinks to a great depth. To balance this water mass in the abyssal ocean, water elsewhere must upwell gradually. This gradual upwelling induces stretching of the water column in the abyssal oceans. Conservation of potential vorticity then requires that these waters in both hemispheres move poleward, forming thermohaline circulation cells. Therefore, potential vorticity is crucial to understanding the ocean general circulation, and oceanic adjustment relies on dynamical processes that can carry and modify potential vorticity in the oceans. Among these processes, global-scale planetary waves known as Rossby waves are of prime importance.

Within the equatorial oceans, the adjustment process is further complicated by the existence of equatorial Kelvin waves—a special gravity wave trapped along the equator. The vanishing Coriolis parameter at the equator makes the equatorial oceans a trapping zone for oceanic waves. Adjustment processes in this part of the oceans obey dynamical constraints in addition to those of potential vorticity dynamics.

II. ADJUSTMENT IN EXTRATROPICAL WIND-DRIVEN CIRCULATION

In the open oceans, thermocline depth typically ranges from 100 m in the tropics to 1000 m in the extratropics. This depth is quite shallow compared to the total depth of the oceans, which is on the order of 4000–5000 m. The difference in the thicknesses of the two layers allows the adoption of a reduced-gravity assumption, wherein the lower layer of the ocean is assumed to be infinitely deep. It must also be motionless to ensure a finite kinetic energy in the system. Under this approximation, the wind driven circulation is decoupled from the thermohaline circulation and obeys linear shallow-water dynamics. On a local Cartesian coordinate system fixed on the rotating earth with an angular velocity Ω , momentum and mass conservation can be expressed mathematically as

$$u_t - fv = -g'\eta_x + \tau^x/H, \quad (1)$$

$$v_t + fu = -g'\eta_y + \tau^y/H, \quad (2)$$

$$\eta_t + c^2/g'(u_x + v_y) = 0, \quad (3)$$

where η represents a departure from the mean depth of the thermocline and is linearly related to the pressure perturbation from the hydrostatic pressure, u and v are the zonal and meridional components of the ocean currents, respectively τ^x and τ^y are the respective wind stresses acting as a body force within a constant depth layer of H (H is sometimes referred to as the equivalent forcing depth), g' is the reduced gravity [given by $g' = g\Delta\rho/\rho$, where g is gravity,

$\Delta\rho$ is the density difference between the upper and lower layers, and ρ is the mean density], and c is the characteristic gravity wave speed. The Coriolis parameter f is given by $f = 2\Omega \sin \theta$, with θ the latitude. To simplify the mathematics, f is often approximated by its first-order Taylor expansion around a local latitude θ_0 , i.e., $f = f_0 + \beta y$, where $f_0 = 2\Omega \sin \theta_0$ is the local inertial frequency and $\beta = 2\Omega \sin \theta/a$ describes change of the rotation due to curvature of the earth, assuming that the earth is a sphere of radius a . This approximation is called the β -plane approximation. Setting the latitude to that of the equator, i.e., $\theta_0 = 0$, gives the equatorial β -plane approximation.

A. Quasigeostrophic Dynamics

The above shallow-water system (1)–(3) contains two set of wave motions: inertial gravity or Poincaré waves, whose restoring force is gravity, and planetary or Rossby waves, whose restoring effect is the latitudinal gradient of planetary potential vorticity f/H . The gravity wave frequencies always exceed the local inertial frequency f_0 and dominate high-frequency fluctuations. For motions with frequency lower than the local inertial frequency, Rossby waves dominate transient dynamics. Furthermore, if the horizontal scale of the motion is larger than the Rossby radius of deformation c/f , a length scale at which rotation effects become as important as buoyancy effects, then the flow obeys the quasigeostrophic potential vorticity equation:

$$(\psi_{xx} + \psi_{yy} - f_0^2/c^2\psi)_t + \beta\psi_x = H^{-1}\text{curl}_z\tau, \quad (4)$$

where ψ is a streamfunction such that $u = -\psi_y$ and $v = \psi_x$, and $\text{curl}_z\tau$ is the vertical component of the wind stress, $\text{curl}\text{curl}\tau \cdot \mathbf{k}$. The streamfunction ψ is linearly related to the thermocline depth perturbation η . One important consequence of the quasigeostrophic approximation is that inertial gravity waves are filtered out and only Rossby waves remain in the system.

In the steady state, a simple balance emerges from Eq. (4):

$$\beta v H = \text{curl}_z\tau. \quad (5)$$

This balance is called the Sverdrup flow. Physically, Eq. (5) states that the wind stress $\text{curl}\text{curl}_z\tau$ produces Ekman pumping (or suction) at the base of the mixed layer, which causes planetary vortex filaments to contract ($\text{curl}_z\tau < 0$) or stretch ($\text{curl}_z\tau > 0$) in the ocean interior. Conservation of potential vorticity then requires the water to move equatorward (or poleward). Therefore, the Sverdrup balance is simply a manifestation of potential vorticity conservation as a dynamical constraint for wind-driven circulation. It is important to note that the Sverdrup balance breaks down at the equator because the

quasigeostrophic approximation is no longer valid when f approaches zero.

B. Extratropical Planetary Waves

The Sverdrup flow represents a steady-state balance between local wind stress curl and oceanic response. To achieve this steady-state response, the ocean must undergo an adjustment from an initial unbalanced state to a final balanced state. The adjustment relies on Rossby waves, whose dynamics obey the conservation of potential vorticity, i.e., the homogenous part of (4). Assuming a wave solution of the form $\psi = \psi_0 \cos(kx + ly - \omega t)$, we obtain for the homogenous part of (4) the following wave dispersion relation:

$$\omega = -\beta k / (k^2 + l^2 + f_0^2/c^2), \quad (6)$$

where ω is the wave frequency and k and l are the zonal and meridional wave numbers, respectively. Note that the wave frequency ω and zonal wave number k are of opposite sign, which means that the Rossby wave always has a westward phase propagation. In other words, wave crests always move from east to west regardless of wavelength. This is not the case for wave energy propagation, which is given by the wave group velocity. The zonal and meridional components of the wave group velocity are obtained by differentiating wave frequency ω with respect to wave numbers k and l , respectively:

$$\begin{aligned} \omega_k &= \beta(k^2 - l^2 - f_0^2/c^2) / (k^2 + l^2 + f_0^2/c^2)^2 \\ \omega_l &= 2kl\beta / (k^2 + l^2 + f_0^2/c^2)^2. \end{aligned} \quad (7)$$

For Rossby waves whose zonal wavelength is much greater than the Rossby radius of deformation, i.e., $k \ll f_0/c$, the zonal group velocity is negative and independent of zonal wave number k . This means that in the long-wave limit, wave energy propagates westward at the same rate for all the waves and thus the long Rossby waves are able to keep their initial shape during propagation. These waves are called nondispersive waves. In contrast, for short Rossby waves, $k \gg f_0/c$, the zonal group velocity is positive and decreases like k^{-2} as k increases. These short Rossby waves move energy eastward at a much slower rate than the long waves and are highly dispersive.

Figure 1 illustrates the dispersion relation for a typical Rossby wave. Note that the highest possible wave frequency, $\omega_{\max} = \beta c / 2f_0$, occurs at zonal wave number $k = f_0/c$ (assuming $l = 0$) with zero group velocity. Since the Coriolis parameter f_0 increases poleward, the maximum frequency of a Rossby wave in high latitudes is lower than in low latitudes. The zonal group velocity ω_k at the long-wave limit $k = 0$, given by $\omega_k = \beta c^2/f_0^2$ (assuming $l = 0$) also decreases with an increase in latitude. This

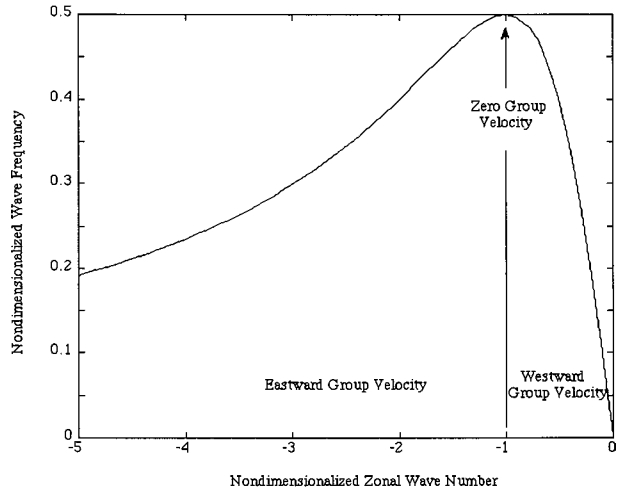


FIGURE 1 A dispersion diagram for Rossby waves with a zero meridional wave number $l = 0$. The zonal wave number is nondimensionalized in terms of the radius of deformation c/f_0 . The wave frequency is nondimensionalized in terms of $\beta c/f_0$. The slope of the dispersion curve gives the zonal group velocity, which changes from negative values (westward propagation) for $k < f_0/c$ to positive values (eastward propagation) for $k > f_0/c$. The zonal group velocity vanishes at $k = f_0/c$, where the wave frequency is maximum.

means that the westward energy transport by the waves in the high-latitude oceans is much slower than that at low latitudes. On the other hand, the group velocity for the short waves is independent of latitude.

In a closed ocean basin, wave reflection takes place as a wave reaches a boundary. At the western boundary an incoming long Rossby wave converts its energy into a short Rossby wave of the same frequency but with much shorter zonal wavelength and slower eastward energy propagation. This means that western boundaries of the oceans are regions where wave energy accumulates. This wave energy can be transferred into mean flow energy through frictional effects. This is one of reasons for the existence of intense western boundary currents in the oceans. At northern and southern boundaries incoming and reflected Rossby waves are of the same frequency and wavelength, and consequently are propagating at a same speed but in the opposite direction. Superposition of these waves forms standing waves or modes. Therefore, in the presence of northern and southern boundaries, a set of discrete standing Rossby waves, instead of a continuum of waves, emerges. Mathematically, these meridional modes are solutions of the following eigenvalue problem:

$$\phi_{yy} - (\beta k/\omega + k^2 + f_0^2/c^2)\phi = 0$$

with boundary conditions

$$\phi = 0 \quad \text{at} \quad y = 0 \quad \text{and} \quad y = L.$$

The resultant eigenvalues are given by

$$\omega_n = -\beta k / [k^2 + (n\pi/L)^2 + f_0^2/c^2], \quad n = 0, 1, 2, \dots,$$

and the corresponding eigenfunctions are given by

$$\phi_n = \sin(n\pi y/L), \quad n = 0, 1, 2, \dots$$

These eigenfunctions form a complete set of orthonormal vector basis. The excitation of these waves depends on the meridional structure of the forcing. Since the meridional scale of high-order modes is smaller than that of low-order modes, a broad-scale forcing excites mostly low-order modes. A narrow forcing, on the other hand, excites a broad spectrum of modes.

C. Extratropical Ocean Adjustment

In extratropical regions, the adjustment of wind-driven circulation is achieved through Rossby wave propagation. Consequently, how these waves are excited by the winds has a direct impact on the adjustment process. The wave excitation depends not only on the spatial structure of the wind forcing, but also on the temporal variability. If the winds fluctuate at a frequency ω higher than local inertial frequency f_0 , then only inertial gravity waves are excited. In this case, the Ekman pumping produces a local vorticity response and steady-state Sverdrup balance will not be possible. Mathematically, the solution is governed by a balance between the first term on the left-hand side and the term on the right-hand side of (4), i.e.,

$$(\psi_{xx} + \psi_{yy} - f_0^2/c^2\psi)_t = H^{-1}\text{curl}_z\tau. \quad (8)$$

This response is the local Ekman drift. In the other extreme case, where the winds vary at an exceedingly low frequency, a quasi-steady Sverdrup balance holds, i.e., the response is governed by a balance between the second term on the left-hand side and the term on the right-hand side of (4). In more general case where winds fluctuate between these frequencies, the response is nonlocal and Rossby wave adjustment comes into play.

The adjustment of the ocean in this case occurs in two stages. During the initial stage, the response is dominated by the local Ekman drift, where the local Ekman pumping (suction) causes changes in the thermocline depth. Since the time rate of change of the thermocline depth is given by the local wind stress curl [see Eq. (8)], the response of the thermocline depth lags the local winds by a quarter of the forcing period. In the idealized case where a uniform Ekman pumping is suddenly switched on at $t = 0$ and then retains a constant value, the initial response shows a steady increase of thermocline depth with time everywhere, i.e., $\psi = -(c^2 H^{-1} \text{curl}_z \tau / f_0^2)t$.

During the second stage of the adjustment, Rossby waves excited by the wind stress curl come into play.

These waves are excited along the eastern and western boundaries. Of particular importance are the long Rossby waves. The role of these waves is to bring the unsteady Ekman drift to the steady Sverdrup flow in its wake. Excessive energy and potential vorticity produced by local Ekman pumping are now being carried toward the western boundary by the long waves. Since the long Rossby waves are initiated along the eastern boundary of the oceans, the regions close to the eastern boundary adjust to equilibrate with the wind forcing much faster than in the ocean interior. At the western boundary, the waves available for adjustment are the short Rossby waves. These waves transport energy eastward at a rate that is nearly an order of magnitude slower than the long Rossby waves (see Fig. 1). Adjustment in this region proceeds at a much slower pace than at the eastern side of the basin. This slow adjustment causes energy to accumulate along the western boundary. Additionally, the reflection of the long Rossby waves at the western boundary further enhances energy accumulation. This eventually causes inviscid, linear theory to break down. Therefore, adjustment near the western boundary cannot be simply explained in terms of linear wave dynamics. Nonlinearity and dissipation are important parts of adjustment processes along the western boundary.

Figure 2 gives a schematic illustration on how the adjustment process takes place along a given latitude as a function of time in response to a sudden onset of Ekman pumping. The propagation of long and short Rossby waves is indicated by two wave characteristics in the time-longitude space. The region between the two wave characteristics is occupied by the initial Ekman drift, where the depth of the thermocline increases steadily with time. The region above the long-wave characteristics emanating from the eastern boundary is where steady Sverdrup flow is achieved.

From the above discussion, it is evident that the time needed for a linear, inviscid ocean to adjust to equilibrium in the extratropics is essentially determined by the time taken for a long Rossby wave to propagate across the basin. Since the long Rossby wave speed decreases rapidly with increase of latitude, the adjustment time scale can increase by a few order of magnitude from low-latitude oceans to high-latitude oceans. This offers a simple explanation as to why response time for the Somali Current is so different from that for the Gulf Stream. Under a periodic forcing, such as the seasonal variation of the winds, the response of the ocean can vary considerably from low latitudes to high latitudes because of the different adjustment times. In low latitudes, where the adjustment time scale is shorter than the forcing period, changes in ocean circulation are governed by the Sverdrup balance. In contrast, at high latitudes, where the adjustment time is much longer than the forcing period, response is dominated by

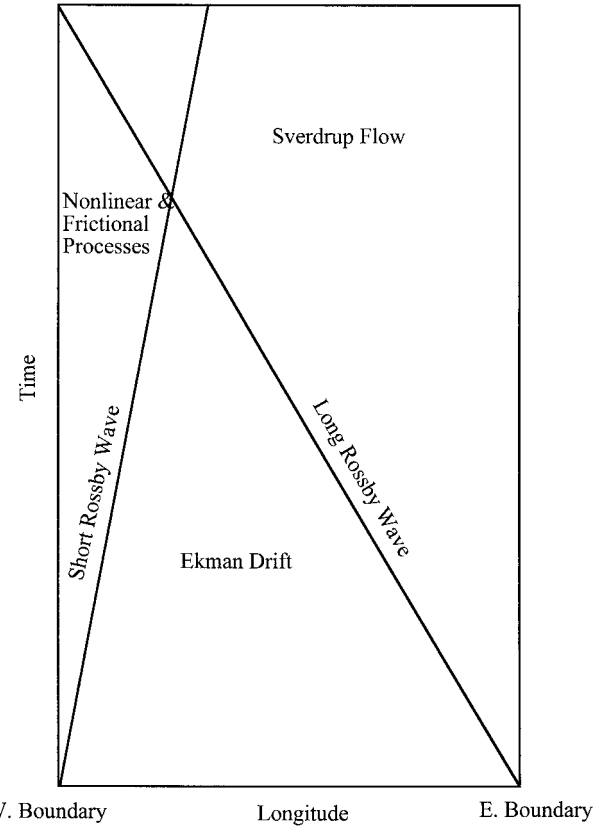


FIGURE 2 An illustration of Rossby wave adjustment in a quasi-geostrophic ocean in terms of a time–longitude plot. The forcing is a sudden-onset Ekman pumping. Two straight lines indicate long and short Rossby waves emanating from the eastern and western boundaries. At a given location of the ocean, the response is governed by an Ekman drift before the arrival of the long Rossby wave. In the wake of the long Rossby wave, the response is given by Sverdrup flow. The adjustment near the western boundary is dominated by nonlinear and friction effects.

local Ekman drift. In the subtropics, where the adjustment time is comparable to the forcing period, both the Rossby waves and local Ekman drift are important. To illustrate this point, Fig. 3 shows a comparison between the measured seasonal variation of the thermocline depth in the subtropical North Pacific Ocean and the computed thermocline variation based on a model ocean similar to Eq. (4). The agreement between the measurement and simulation is remarkable, given the simplicity of the physics included in the dynamical model. If the Rossby wave contribution is removed from the calculation, the remaining response, i.e., the Ekman drift, differs considerably from the observation. This result supports the linear theory and points to the importance of the long Rossby waves in the adjustment of the subtropical ocean.

Rossby waves are not the sole contributor to the adjustment of the oceans. Advective and dissipative processes also contribute. These processes generally adjust

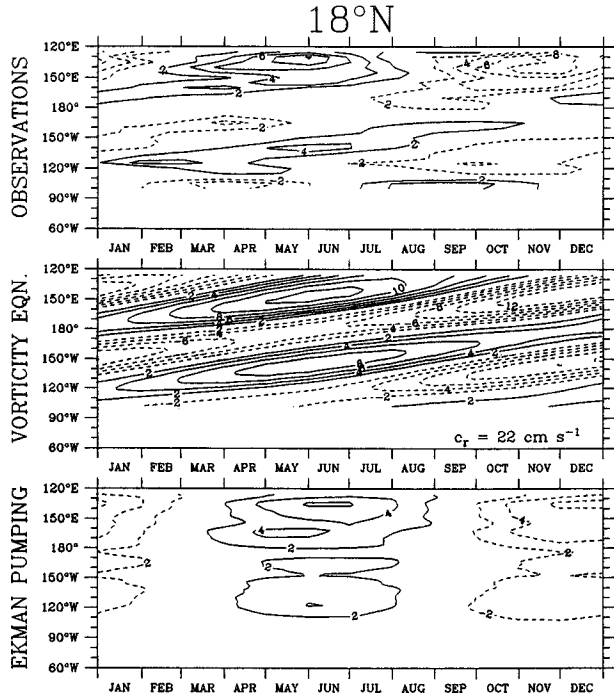


FIGURE 3 A comparison between the measured (upper panel) and computed (middle panel) seasonal variation of the thermocline depth along 18°N in the subtropical Pacific Ocean. The computed variation is based on a simple model similar to the one described by Eq. (4). The local Ekman drift is shown in the bottom panel. [From Kessler (1990).]

the oceans at a much slower rate than the waves, and become important in regions where nonlinear processes are strong, such as the western boundary regions. In these regions, time-variable currents are generally much larger than the mean flow. A large portion of the energy of the time-varying flow comes from instability of the western boundary currents. The instability process gives birth to mesoscale eddies in the ocean by drawing energy from the mean flow maintained by the atmospheric forcing. Eddies then transfer momentum vertically into the deep ocean, forming a deep recirculation gyre at the northwestern part of the subtropical wind-driven gyre. The adjustment of the circulation in this region is governed by dissipation rather than Rossby waves.

III. ADJUSTMENT OF TROPICAL WIND-DRIVEN CIRCULATION

The potential vorticity dynamics given by Eq. (4) is not appropriate to describe equatorial adjustment because f_0 vanishes at the equator and the quasigeostrophic approximation breaks down. This may be explained in terms of time scales of inertial gravity and Rossby waves: Recall

that the lowest allowable frequency of an inertial gravity wave is the local inertial frequency f_0 , whereas the highest frequency of a Rossby wave is given by $\omega_{\max}^2 = \beta c / 2 f_0$. Sufficiently far away from the equator, the local inertial frequency is much higher than the highest allowable Rossby wave frequency. Therefore, inertial gravity waves are well separated from Rossby waves in frequency space, which allows the application of the quasigeostrophic approximation to filter out gravity waves in the extratropics. Near the equator, the inertial frequency f approaches zero and the Rossby wave frequency increases. This substantially reduces the frequency gap between gravity and Rossby waves, making it more difficult to separate them in the equatorial region. Therefore, the equator is a special location where low-frequency gravity waves and Rossby waves can coexist.

A. Equatorially Trapped Waves

Linear equatorial wave dynamics can be conveniently studied using a single equation for the meridional component of the velocity v deduced from the homogeneous part of the shallow-water system (1)–(3) on an equatorial β -plane,

$$(v_{xx} + v_{yy})_t + \beta v_x - c^{-2} v_{ttt} - f^2 c^{-2} v_t = 0, \quad (9)$$

where $f = \beta y$. Assuming a wave solution of the form $v = \phi(y) e^{ikx - i\omega t}$, then the governing equation for equatorially trapped waves is given by

$$\phi_{yy} + (\omega^2 c^{-2} - k^2 - \beta k \omega^{-1} - \beta^2 c^{-2} y^2) \phi = 0. \quad (10)$$

Note that the coefficient of this equation changes from positive to negative values poleward of latitudes $\pm y_t$, where y_t is given by

$$y_t^2 = \omega^2 \beta^{-2} - k^2 c^2 \beta^{-2} - c^2 \beta^{-1} k \omega^{-1}.$$

This means that the solution to (10) changes from wave-like to exponentially decaying behavior poleward of $\pm y_t$. Physically, these latitudes act like walls on both sides of the equator, bouncing poleward-propagating wave energy back toward the equator. Therefore, these latitudes are called turning latitudes. They trap the wave energy in a narrow equatorial zone and act like a tunnel guiding the wave along the equator. The region between the turning latitudes is called the equatorial wave guide, and its width depends on the zonal wave number and wave frequency. For low-frequency planetary waves, the width of the wave guide is inversely proportional to the wave frequency. This means that the lower frequency planetary waves can penetrate deeper into the higher latitudes than can the higher frequency waves.

The equatorial wave guide allows for the formation of standing meridional modes. These modes are obtained as

eigensolutions to Eq. (10) with boundary condition $\phi = 0$ as $y \rightarrow \pm\infty$. The eigenvalues are determined by the wave dispersion relation:

$$c^{-2} \omega^2 - k^2 - \beta k \omega^{-1} = \beta c^{-1} (2n + 1), \quad n = 0, 1, 2, \dots \quad (11)$$

As in the midlatitude case, two types of wave modes, the inertial gravity and Rossby waves, are included in (11), with frequencies of the former higher than those of the latter. Additionally, two new waves have emerged as a result of vanishing Coriolis parameter at the equator. The first wave corresponds to $n = 0$ in Eq. (11) and has an antisymmetric meridional structure about the equator. The dispersion relation of this wave is such that it approaches the gravest inertial gravity wave as $\omega \rightarrow \infty$ and $k \rightarrow \infty$, and the gravest short Rossby wave as $\omega \rightarrow 0$ and $k \rightarrow -\infty$. Since the mode has the mixed nature of both the inertial gravity and Rossby waves, it is referred to as the mixed Rossby-gravity mode. This mode has an eastward group velocity. For low-frequency equatorial adjustment it is relatively unimportant because it resembles short Rossby waves at low frequency.

The second wave has zero meridional velocity, and thus is not included in Eq. (11). Its solution can be obtained from (1)–(3) directly by setting $v = 0$. The resultant wave has the form of

$$u = g' c^{-1} h = A(x - ct) \exp(-2\lambda^{-2} y^2), \quad (12)$$

where λ , given by $c^{1/2} \beta^{-1/2}$, is the equatorial radius of deformation, and A is an arbitrary function. Clearly, this wave is nondispersive and symmetric about the equator; it is known as the equatorial Kelvin wave. The Kelvin wave is a special gravity wave and has an eastward-propagating group velocity. These two waves along with the inertial gravity and Rossby waves form a set of complete eigenfunctions. For equatorial adjustment, the Kelvin and long Rossby waves are of prime importance.

Because of the presence of equatorial Kelvin waves, the reflection of Rossby waves incident on the western boundary in the tropical oceans differs from that in the extratropical oceans. If the incoming long Rossby wave is symmetric about the equator, the Kelvin wave can return up to 50% of the incoming energy eastward depending on the properties of the incoming Rossby waves. The remaining energy is carried by the short Rossby and mixed Rossby-gravity waves. Since the Kelvin wave efficiently transports the incoming energy away from western boundary, energy accumulation near the tropical western boundary is generally much weaker than in the midlatitudes. This means that the western part of the equatorial oceans behaves more linearly than the counterparts in the extratropical oceans.

Reflection of a Kelvin wave incident on the eastern boundary depends on the frequency of the wave. If the

incident wave has a frequency close to $(\beta c)^{1/2}$, which corresponds to a period between 1 week and 1 month, the reflected waves consist of a pair of coastally trapped Kelvin waves propagating poleward in both hemispheres at a speed c . The incoming wave energy leaks along the eastern boundaries toward the poles. At lower frequencies, a finite number of long Rossby waves is also excited in addition to the pair of coastal Kelvin waves. These long Rossby waves carry a portion of the incoming wave energy toward the western boundaries. This means that a certain portion of the incoming wave energy is reflected back into the interior of the ocean. The lower the incident wave frequency, the more incoming wave energy is reflected.

B. Equatorial Adjustment

As the equilibrium response of the extratropical ocean is described by the Sverdrup flow, the equatorial equilibrium response to an impulsively switched-on uniform zonal wind is governed by a simple balance between the zonal wind stress and an east–west pressure gradient, with the ocean approaching a state of rest, i.e., a steady-state solution to the shallow-water system (1)–(3) is given by

$$\eta_x = (Hg')^{-1} \tau^x. \quad (13)$$

This can be thought of as a degenerate Sverdrup balance at the equator. The dynamical processes responsible for bringing the ocean from an initial state to this equilibrium state are equatorial Kelvin and Rossby waves, provided that the time scale of the winds is longer than 1 week so inertial gravity waves are not excited by the winds.

Equatorial adjustment proceeds as follows: Immediately following the onset of an easterly (westerly) wind, poleward (equatorward) Ekman flow develops off the equator. The flow diverges (converges) at the equator, producing equatorial upwelling (downwelling). This causes a steady decrease (increase) of the thermocline depth at the equator. The shoaling (deepening) equatorial thermocline induces an equatorward (poleward) pressure gradient which drives a westward (eastward) jet at the equator according to the geostrophic balance:

$$fu + g' \eta_y = 0. \quad (14)$$

At the equator, where $f = 0$, the zonal momentum equation (1) reduces to a simple balance between acceleration of zonal current u_t and the local wind forcing $H^{-1} \tau^x$, giving rise to an accelerating jet in the direction of the wind, i.e.,

$$u = H^{-1} \tau^x t. \quad (15)$$

Therefore, the initial equatorial ocean response to a sudden-onset uniform zonal wind consists of an accelerating westward (eastward) jet and a rising (deepening) ther-

mocline as well as a steady divergent (convergent) Ekman flow. This current system is referred to as a Yoshida jet, and its width is determined approximately by the equatorial radius of deformation $(c/\beta)^{1/2}$, which is about 250 km in the oceans. This initial response can be thought of as a degenerate Ekman drift. Figure 4a gives a schematic illustration of the initial response.

In a zonally unbounded ocean, the Yoshida jet will continuously gain strength until nonlinearity becomes important. In a bounded ocean, however, long Rossby and Kelvin waves are excited at the eastern and western boundaries. These nondispersing waves propagate along the equatorial guide as pressure fronts. The sharp pressure gradients, initially introduced by the winds along the eastern and western boundaries, move eastward at speed c as the Kelvin wavefront and westward at speeds $c/3, c/5, \dots$ as the long Rossby wavefronts. In the wake of these wavefronts, the acceleration of the Yoshida jet is arrested due to the pressure gradients introduced by the waves. This happens in stages. First comes the Kelvin wave, in the wake

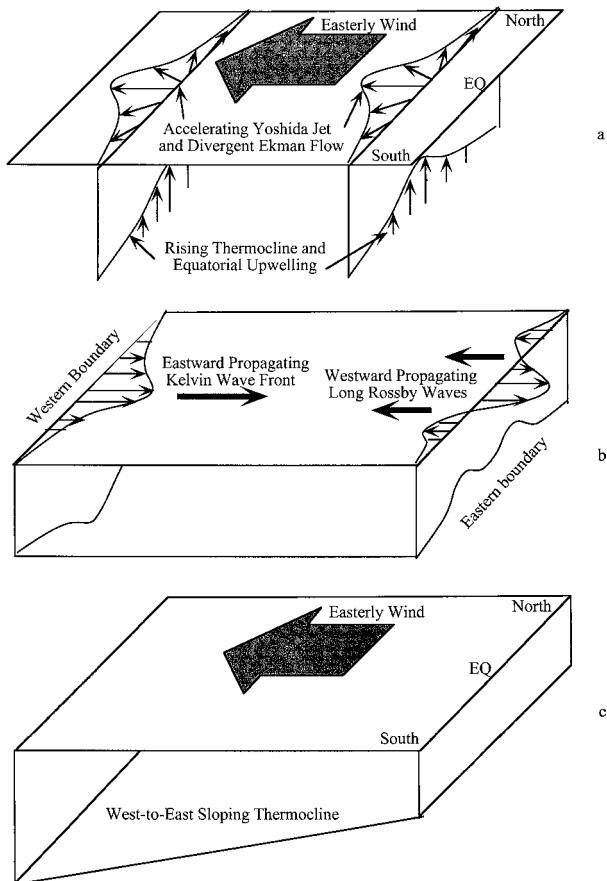


FIGURE 4 A schematic illustration of an equatorial adjustment in response to a sudden-onset easterly wind. (a) Initial response, (b) Kelvin and Rossby wave adjustment, and (c) a steady state.

of whose front the acceleration of the jet and the change of the equatorial thermocline depth are reduced substantially. Because of its narrow meridional extent, the Kelvin wave only affects the flow confined close to the equator within the equatorial radius of deformation. Next comes the first meridional Rossby mode, followed by the second-, third-, . . . , and higher order Rossby modes, each of which acts to further reduce the local acceleration. The higher is the order of the Rossby mode, the longer is the adjustment time and the further away from the equator can the wave influence the adjustment. Moreover, wave reflection at the western and eastern boundaries further complicates the adjustment process. As mentioned previously, upon reaching the eastern boundary the low-frequency Kelvin wave converts a portion of its energy into long Rossby waves, which continue to participate in the adjustment process of the interior ocean. The long Rossby waves, upon impinging on the western boundary, transfer some energy to Kelvin waves, which in turn influence the equatorial adjustment. These wave adjustment processes are depicted in Fig. 4b.

If dissipation in the ocean interior is very weak, this adjustment process will persist until the waves lose all their energy in the tropical ocean. In this case, the loss of wave energy comes from two major factors: a poleward transfer of Kelvin wave energy along the eastern boundary to coastally trapped Kelvin waves and a transfer of long Rossby wave energy to short Rossby waves along the western boundary. The equilibrium response is a state of no motion with a zonal pressure that balances the winds (13). Since the Kelvin wave and low-order Rossby waves propagate much faster than the high-order Rossby waves, the equatorial zone adjusts much more rapidly than the high-latitude oceans. The further away from the equator, the longer it takes to bring the ocean to equilibrium. The adjustment time of the equatorial ocean is essentially determined by the time it takes for the Kelvin wavefront and first long Rossby wavefronts to propagate across the ocean basin. Since Kelvin and long Rossby waves propagate at speeds c and $c/3$, respectively, the equatorial adjustment time is roughly $4L/c$, with L the width of the ocean basin. For the Pacific basin, this turns out to be about 1 year, which is considerably shorter than the corresponding adjustment time in midlatitudes. The fully adjusted ocean response to a sudden onset of a uniform zonal wind is shown in Fig. 4c.

If dissipation is important in the ocean interior, then the equilibrium response is no longer a state of no motion described by (13). This is because the wave energy is quickly dissipated as the wave propagates across the basin, so that the pressure gradient associated with the wave is too weak to balance the zonal wind stress τ^x . Of the two possible dissipation mechanisms, i.e., momentum and heat dissipa-

tion, the latter has a much stronger effect on equatorial waves and consequently adjustment.

In reality the winds in the tropics vary in both space and time. The response of the ocean therefore depends on the spatial structure and temporal variability of the winds. Of particular interest is the response of the tropical ocean to a patch of oscillating zonal wind centered at the equator in the middle of basin. This wind forcing, to a first order of approximation, represents changes in wind forcing during El Niño in the tropical Pacific. Understanding the forced oceanic response thus provides insight into the role of ocean adjustment in the evolution of El Niño. Assuming that the forcing period is sufficiently long (for El Niño the forcing period is about 3–4 years), the response of the ocean can be divided into three regions: Within the forcing region, the response is nearly in equilibrium with the local forcing given by (13). Except for a minor phase difference, the perturbation of thermocline depth to the east of the center of the forcing is almost out of phase with that to the west. In other words, the thermocline varies like a seesaw within the forcing region: when the thermocline shoals in the east in response to an increase in easterly wind, the thermocline in the west deepens, and vice versa. This quasi-equilibrium response results from a rapid adjustment due to Kelvin and Rossby waves. These waves are excited along the eastern and western boundaries, where large pressure gradients exist.

To the east of the forcing region, the equatorial response is strongly influenced by the two eastward-propagating Kelvin waves excited at the eastern and western forcing boundaries. The former initiates the oceanic response in the eastern forcing-free region, producing a zonally independent thermocline perturbation which increases with time. The latter reduces the increase of the thermocline perturbation and adjusts the ocean toward an equilibrium state. As time progresses, the thermocline perturbation expands gradually poleward in the vicinity of the eastern ocean boundary. Since the Kelvin wave adjustment proceeds very rapidly, the response in the eastern basin is practically in an equilibrium with the forcing, and can be seen as a uniform eastward extension of the equilibrium thermocline response in the forcing region. Therefore, for an easterly (westerly) wind, the thermocline shoals (deepens) uniformly to the east of the forcing.

To the west of the forcing, the adjustment is more complicated. It involves the two Rossby waves excited along the western and eastern forcing boundaries as well as the reflected Kelvin waves. Initially, the response in the western forcing-free region is influenced by the Rossby waves excited at the western edge of the forcing. These waves generate maximum thermocline perturbations off the equator which have opposite sign to those generated by the Kelvin waves in the eastern basin. In other words, if

the wind is an easterly (westerly), the initial thermocline perturbation in the western basin will be a downwelling (upwelling) signal, whereas the signal to the east is an upwelling (downwelling) signal. After reaching the west coast, the downwelling (upwelling) Rossby waves convert a portion of energy into a downwelling (upwelling) Kelvin wave. The reflected Kelvin wave contributes to the adjustment both within the forcing region and in the eastern forcing-free region. For example, it acts to further reduce the upwelling (downwelling) induced by the initial Kelvin wave in the eastern basin. The Rossby waves excited at the eastern forcing edge enter the western forcing-free region after propagating across the forcing region and contributing to the adjustment within that region. These waves play an important role in adjustment of the off-equatorial ocean in the western basin. Furthermore, through reflection at the western boundary, they produce an equatorial Kelvin wave, which, in turn, can influence ocean response in the eastern basin. Because the Rossby waves propagate relatively slowly compared to the Kelvin waves, the response in the western forcing-free region is not quite in equilibrium with the forcing. Figure 5 shows the evolution of thermocline perturbation in a linear shallow-water model of an idealized Pacific Ocean forced by a patch of oscillating zonal wind stress. The wind has a period of 3 years and is centered at the date line (180°W). Within the forcing region, the response is marked by a strong zonal thermocline gradient with opposite sign on each side of the date line. To the east of the forcing region, the thermocline response is essentially independent of longitude with poleward expansions along the eastern boundaries. To the west of the forcing region, the response is dominated by the two large thermocline perturbations off the equator. This pattern of

response contains two parts, one consisting of free Rossby waves not in equilibrium with the forcing and another consisting of equilibrium response to the forcing. It is worth emphasizing that the total response is a superposition of a large number of equatorial wave modes and should not be interpreted as an individual wave.

One of the most important properties of the equatorial ocean response to changes in winds is that the response at a given location and time not only is affected by the local wind at the present time, but can be affected by a signal excited by a forcing several months ahead of the current time that propagates a great distance to the current location. A good example is the response at the eastern edge of the forcing, which contains a local forced part plus a remote part that comes from long Rossby waves propagating westward and reflecting into an eastward-propagating Kelvin wave. In other words, the ocean can “memorize” the local forcing and produce a delayed response. This “ocean memory” effect plays a central role in the coupled ocean–atmosphere dynamics that is responsible for the El Niño in the tropical Pacific. In more general terms, the “ocean memory” can be defined as the part of ocean response not in equilibrium with the local forcing. From the above discussion, it is evident that much of the “ocean memory” resides in the off-equatorial regions of the western basin of the tropical oceans.

IV. ADJUSTMENT OF THERMOHALINE CIRCULATION

Below the thermocline lies the abyssal region of the oceans, where the temperature is much lower and variability generally much weaker than in the upper ocean. The

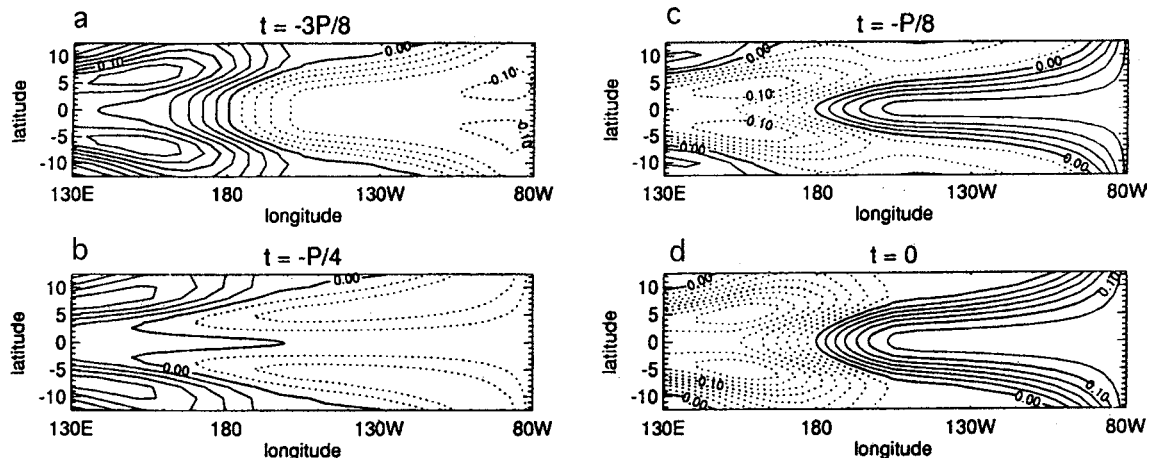


FIGURE 5 Response of a linear, shallow model of the tropical Pacific Ocean to a patch of oscillating zonal wind stress centered along the date line (180°W) with a period of $P=3$ years. Shown is the response at different phases of the forcing cycle. The strongest easterly wind occurs at $t=-P/2$, whereas the strong westerly wind occurs at $t=0$ (panel d). The transition phase of the forcing occurs at $t=-P/4$, where the wind stress is zero everywhere.

average temperature is approximately 3.5°C. These cold waters result from the cooling of water masses by the atmosphere in polar regions. The cold and dense waters sink to the bottom of the oceans, filling the abyssal basins and gradually rising to the surface, replacing the sinking waters formed in polar regions and forming a global circulation cell. This thermally driven abyssal circulation is called the thermohaline circulation. Much of our understanding of this circulation is derived from the Stommel–Arons theory, which shares the same dynamical core—potential vorticity conservation—as the Sverdrup theory for the wind-driven circulation. The key difference between the wind-driven and thermohaline circulations is the physical processes that give rise to the vertical motion responsible for stretching the water column. For the wind-driven circulation, the vertical velocity is given by the Ekman pumping, which provides the driving force for the thermocline. For the thermohaline circulation, the vertical velocity is determined from a balance between the downward heat diffusion at the base of the thermocline and an upward transport of heat due to the rising cold water below the thermocline, i.e.,

$$w\theta = \kappa\theta_z,$$

where $\theta = \kappa T_z$ is the downward heat flux and κ is the vertical diffusivity. Since the vertical diffusivity κ is very difficult to measure, determining w for the thermohaline circulation is far more difficult than determining the Ekman pumping velocity for the wind-driven circulation, which can be calculated directly from the surface wind stress curl. In the Stommel–Arons theory, w is assumed to have a fixed structure (for example, geographically uniform) and does not depend on the abyssal circulation. If the locations of deep-water formation are specified, a global thermohaline circulation is determined. This consists of a poleward interior flow induced by vortex stretching due to a slow uniform upwelling w throughout the oceans and a deep western boundary current balancing the poleward interior flow.

An alternative to specifying the horizontal structure of the interior upwelling is to assume that the upwelling depends entirely on the abyssal circulation, such that the upwelling is internally determined as a part of the abyssal circulation solution. This allows for a delineation of the adjustment process of the abyssal circulation in the context of a shallow water system similar to Eqs. (1)–(3). Here, the active layer is assumed to be beneath a motionless upper layer. τ^x and τ^y are set to zero because wind forcing has no direct impact on the abyssal circulation. Instead, a source of deep water Q is introduced into the linearized equation of mass conservation (3) at the northern latitude to represent a flux of water from upper ocean into the abyssal oceans. This water mass flux must be balanced by a slow upwelling w assumed to be linearly proportional

to the departure of the interface from its rest position, i.e., $w = \mu\eta$, where μ can be interpreted as a thermal dissipation parameter. When these additional processes are taken into consideration, the mass conservation equation (3) must be modified to include a source term Q and a sink term $-w = -\mu\eta$. The resulting shallow-water equations represent a self-contained dynamic system with Q being the only external forcing. This simple system can be used to depict the time evolution of the abyssal circulation in response to changes in deep-water source Q .

Considering a deep-water source Q which is turned on at time $t = 0$ and then kept steady, the response of the abyssal ocean to this sudden-onset deep water source can be described as follows: Initially, the sudden onset of the deep-water source sends off a pressure front in the form of a coastally trapped Kelvin wave whose properties are similar to those of the equatorial Kelvin wave. This wave moves rapidly toward the equator at the speed of the characteristic gravity wave speed c and is trapped along the western boundary with an e -folding scale of the radius of deformation $\lambda = c/f$. In the wake of the wave, a southward boundary current is developed. As the wave approaches the equator, it turns away from the western boundary because linear dynamics does not permit a southward-traveling wave in the Southern Hemisphere along the western boundary. The coastal Kelvin wave is diffracted into an equatorial Kelvin wave as well as short Rossby and mixed Rossby–gravity waves. The energy carried by the equatorial Kelvin wave propagates rapidly across the basin along the equator and splits evenly into two poleward-propagating coastal Kelvin waves along the eastern boundary. These Kelvin waves, while propagating poleward, emanate long Rossby waves, which then carry energy westward and gradually set up flow in the interior of the deep ocean basin. It is particularly interesting to note how the western boundary current is established in the Southern Hemisphere. It is established indirectly through the propagation of Kelvin and Rossby waves. In other words, the Southern Hemisphere western boundary flow does not result from a direct cross-equatorial flow from the Northern Hemisphere, but rather is generated indirectly by the Kelvin and Rossby wave propagation.

In summary, the adjustment process can be described in three stages: The first stage involves the fast propagation of Kelvin waves responsible for setting up the pressure and upwelling signals along the equator and the eastern boundaries in both hemispheres. The second stage involves long Rossby waves emanating from the eastern boundaries which are responsible for setting up upwelling signal in the interior. The final stage involves a gradual basin-wide stretching of water columns to establish a balance between upwelling and deep-water product. [Figure 6](#) gives a schematic illustration of the adjustment process.

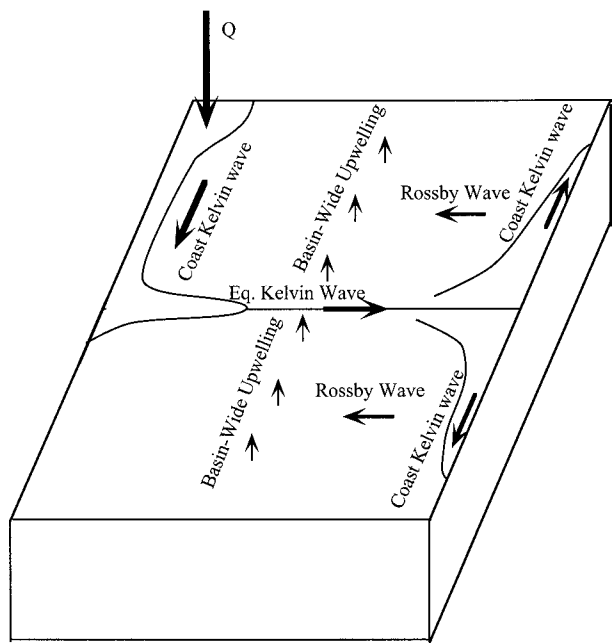


FIGURE 6 A schematic illustration of the adjustment of thermohaline circulation to a sudden-onset deep-water source Q . The adjustment takes place in three stages. The first stage involves fast propagation of Kelvin waves. The second stage involves long Rossby waves emanating from the eastern boundaries. The final stage involves a gradual basin-wide stretching of the water column to establish a balance between upwelling and deep-water production.

The above result implies that the structure of the abyssal circulation depends critically on the underlying wave dynamics in this linear model. The ability of waves to propagate in the deep ocean is strongly affected by dissipation. This is particularly true for the Rossby waves because these waves propagate slower than the Kelvin waves. Therefore, it is anticipated that the final structure of the abyssal circulation depends on the thermal dissipation parameter μ . The strength of this dissipation can be conveniently measured by a parameter δ given by the ratio between the distance the long Rossby wave can travel over the damping time scale μ^{-1} and the basin width, i.e., $\delta = c_R \mu^{-1} / L$, where c_R is the long Rossby wave speed and L is the width of the basin. If $\delta \ll 1$, then the thermal damping μ is so strong that the long Rossby wave energy is quickly dissipated and the wave is effectively prohibited from propagating in the ocean interior. In this case, the pressure signal from the Northern Hemisphere can only be found along the equator and along the eastern boundaries in both hemispheres as a consequence of the fast-propagating Kelvin wave. Therefore, upwelling into the thermocline occurs only in these regions and the interior circulation is practically nonexistent owing to the absence of the long Rossby wave. A major portion of the signal is confined along the equator. Note that western

boundary currents in the Southern Hemisphere are also absent in this case because the signal cannot directly cross the equator. In the opposite limit where $\delta \gg 1$ the thermal damping μ is so weak that the long Rossby wave can reach across the basin and the flow field fills the whole basin in both hemispheres. The pressure and upwelling signals are more uniformly distributed in space and the spatial concentration of the upwelling region does not exist. This limit is consistent with the uniform-upwelling assumption in the Stommel–Arons theory, and the resultant circulation pattern is in agreement with the Stommel–Arons solution.

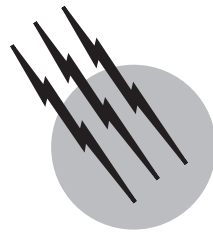
It is worth emphasizing that the above treatment of the abyssal circulation is based on two major simplifications: (1) flat bottom topography and (2) decoupling between the wind-driven circulation and thermohaline circulation. Neither of these assumptions holds in the real ocean. Pronounced abyssal bathymetry can significantly modify the simple theory presented here. Recent observations suggest that strong vertical mixing can exist near a steep bottom topography. This intense mixing can produce strong upwelling, which causes interactions between the wind-driven and thermohaline circulations. In this case the dynamics of the wind-driven and thermohaline circulations can no longer be separated and must be treated jointly. A unified theory for a combined treatment of both wind-driven and thermohaline circulation is lacking. Meanwhile, the simple linear theory provides a basic view on how large-scale ocean circulation adjusts to changes in forcing conditions.

SEE ALSO THE FOLLOWING ARTICLES

OCEAN-ATMOSPHERIC EXCHANGE • OCEANOGRAPHY, CHEMICAL • OCEAN SURFACE PROCESSES • PHYSICAL OCEANOGRAPHY, THERMAL STRUCTURE AND GENERAL CIRCULATION • POLLUTION, AIR • POLLUTION, ENVIRONMENTAL • WAVE PHENOMENA

BIBLIOGRAPHY

- Abarbanel, H. D. I., and Young, W. R. (1986). "General Circulation of the Ocean," Springer-Verlag, New York.
- Cushman-Roisin, B. (1994). "Introduction to Geophysical Fluid Dynamics," Prentice-Hall, Englewood Cliffs, NJ.
- Gill, A. E. (1982). "Atmosphere–Ocean Dynamics," Academic Press, New York.
- Kessler, W. S. (1990). "Observations of long Rossby waves in the northern tropical Pacific," *J. Geophys. Res.* **95**, 5183.
- Kawase, M. (1987). "Establishment of deep ocean circulation driven by deep-water production," *J. Phys. Oceanogr.* **17**, 2295.
- Neelin, J. D., et al. (1998). "ENSO theory," *J. Geophys. Res.* **103**, 14, 167.
- Pedlosky, J. (1996). "Ocean Circulation Theory," Springer-Verlag, Berlin.
- Philander, S. G. H. (1990). "El Niño, La Niña, and the Southern Oscillation," Academic Press, San Diego, CA.



Physical Oceanography, Thermal Structure and General Circulation

Anand Gnanadesikan

Princeton University

Robert Hallberg

NOAA Geophysical Fluid Dynamics Laboratory

- I. Watermass Structure of the Ocean
- II. Physical Balances Governing Large-Scale Ocean Flow
- III. Models of the Thermocline
- IV. Conclusions

GLOSSARY

Coriolis force An apparent force arising from the imbalance amongst gravitational acceleration, pressure forces, and the acceleration required to keep a body moving in a straight line with respect to a point on the rotating earth.

Ekman flow Flow in which the balance is between frictional forces and the Coriolis force.

General circulation The circulation of the ocean responsible for setting the thermal and chemical structure on spatial scales of hundreds of kilometers and time scales of tens to thousands of years.

Geostrophic flow Flow in which the balance is between pressure gradient forces and the Coriolis force.

Isopycnal surface A surface along which particles may be exchanged without changing the local density.

Pycnocline A region of the ocean where there is a vertical gradient in density.

Thermocline A region of the ocean where there is a vertical gradient in temperature.

PHYSICAL OCEANOGRAPHY is concerned with the study of the physical processes which control the spatiotemporal structure of such fields as density, temperature, and velocity within the ocean. A major thrust of this field is the development of an understanding of the general circulation, namely the circulation of the ocean on large scales (of order 100–10,000 km) and over long times (decades to millenia). The general circulation is what determines the large-scale chemical and thermal structure of the ocean and plays a major role in global climate and biogeochemistry. The large-scale circulation can be

broken down into three cells, a surface cell where wind driving is important, a deep cell where mixing is important, and an intermediate cell where potentially both wind and mixing are important. This article discusses the physical framework necessary to understand these circulations and presents standard models which explain some key features of the large-scale structure.

I. WATERMASS STRUCTURE OF THE OCEAN

During the 1700s, observations with early versions of the thermometer showed that the deep ocean in the tropics was extremely cold, with temperatures reaching as low as 4°C. Since such cold waters are never found at the surface in the tropics, it was recognized that their presence along the equator was the signature of a global-scale circulation which transported water masses laterally. Characterizing the various branches of this large-scale circulation and understanding how they are maintained constitutes one of the major tasks of the discipline of physical oceanography. While the outline of a comprehensive picture of the large-scale circulation has emerged over the past 75 years, many of the details of how the oceans transport heat, salt, and chemical constituents remain controversial. This article

represents an attempt at a synthesis of some of the major pieces of the circulation.

Starting with the *Challenger* expedition in the 1870s, oceanographers have mapped out the distribution of temperature, salt, and various dissolved constituents with increasing levels of detail and accuracy. One of the early advances was made by realizing that the *in situ* temperature of a parcel of seawater is not a good indicator of its origin, as it rises when sinking water parcels are compressed. Oceanographers therefore use the potential temperature θ , the temperature of a water parcel raised to the surface of the ocean without exchanging heat with its surroundings. Early in the century, it was also realized that the composition of biologically inert dissolved solute in various parts of the ocean was relatively constant, though the total concentration of these solutes varied spatially and temporally. Oceanographers have defined the salinity S as the total dissolved solute in grams per kilogram. Figures 1 and 2 show contours of θ and S in the Atlantic and Pacific.

Among the dissolved solutes which do vary greatly from location to location are certain dissolved nutrients which are taken up by microscopic marine organisms in the upper ocean. When these organisms die some portion of these nutrients are exported to the deep ocean in the form of particulate matter. Once in the deep ocean most of the nutrients go back into solution. Figure 3 shows

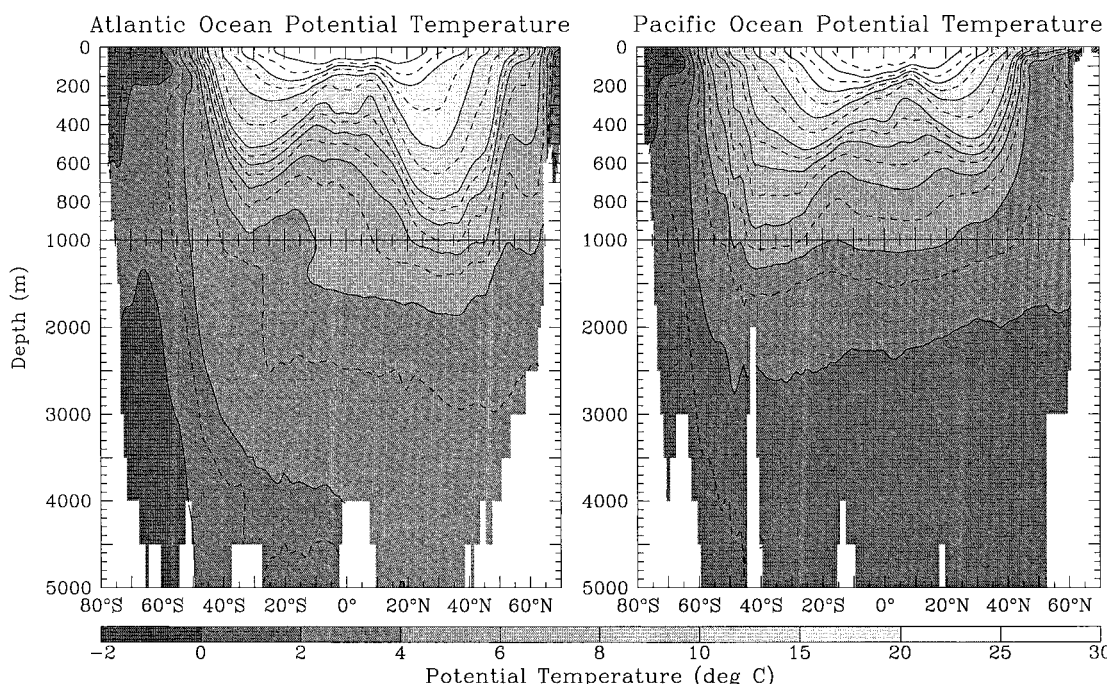


FIGURE 1 Climatological cross sections of potential temperature in the Atlantic (left) and Pacific (right) Oceans. The Pacific profile is the average between 170°W and 170°E. The Atlantic profile is the average over a 20-deg-wide swath around a line extending along 30°W from the south to the equator, then to 60°W 25°N, to 30°W 45°N, and continuing north along 30°W. The dashed lines represent the midpoint of each temperature class.

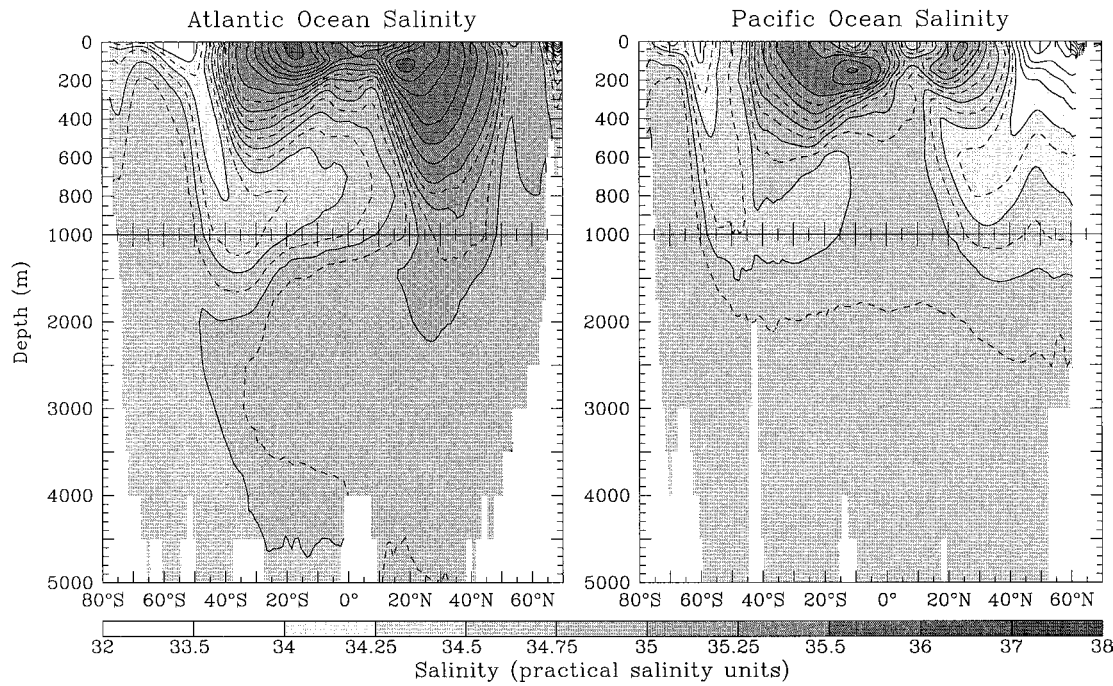


FIGURE 2 Climatological cross-sections of salinity in the Atlantic (left) and Pacific (right) Oceans. The averaging longitudes are the same as in Fig. 1. The units here, practical salinity units, are close to salt concentrations in parts per thousand. Dashed lines represent the midpoint of each salinity class.

contours of one such nutrient (silicic acid) in the Atlantic and Pacific oceans. In general, the longer water spends away from the surface, the higher its nutrient concentration becomes.

The large-scale tracer distributions contain a number of features which reflect the large-scale circulation. There are five features which are of particular importance in the context of this article.

- *The low-latitude thermocline.* A region with a strong gradient in temperature is known as a thermocline. A permanent thermocline is found in the low latitudes of all three ocean basins. The depth of the thermocline is not constant. If one follows a given temperature surface (say the 14°C contour), it can be seen to touch the surface in high latitudes (polewards of about 45 deg), slope down to a maximum depth at about 30 deg, and then slope back upward towards the equator. Similar patterns are seen in the salinity and silicate distributions, with salinities being high in midlatitudes and silicate being low.

- *The intermediate waters.* Immediately below the warm, low-latitude thermocline waters a tongue of low-salinity water can be seen extending northward from the Southern Ocean. This water mass is known as the Antarctic Intermediate Water. In the Atlantic it is associated with a weak maximum in silicate, though not in the Pacific and

Indian Oceans, where the deep waters are more enriched in nutrients. In the Pacific, there is another low-salinity tongue of water associated with North Pacific Intermediate Water. In the North Atlantic, the intermediate waters are significantly saltier than elsewhere in the global ocean as the result of an outflow of very salty water from the Mediterranean Sea.

- *The North Atlantic Deep Water.* The salinity structure of the Atlantic clearly shows a mass of relatively salty (34.8 psu) water with low nutrients centered at a depth of 2000 m. This water mass can be traced by its high salinity into the South Atlantic, and by its low silicate content into the Indian and Pacific Oceans, where it shows up as a wedge of low-nutrient water south of 30°S. As the deep water is carried around the Antarctic continent it mixes with high-nutrient, lower salinity waters to the north and south.

- *Antarctic Bottom Water.* In the deep Atlantic, there is a clear signature of waters which are colder (less than 1°C), fresher (around 34.7 psu), and more enriched in nutrients than North Atlantic Deep Water overlying this water mass. The source of this water is the shelves around the Antarctic continent. This water can also be seen as cold, low-silicate water in the Pacific.

- *Common Deep Waters.* In the deep Pacific, Indian, and Southern Oceans, a vast volume of water exists which is relatively cold (1–2°C) and with a salinity around 34.7

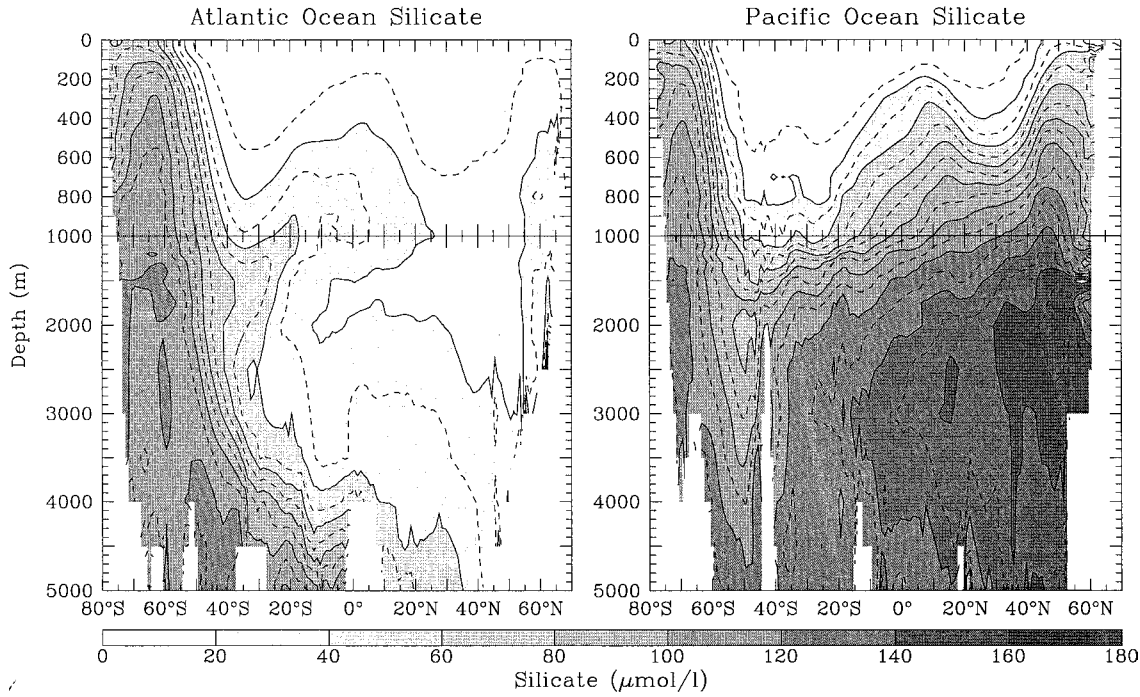


FIGURE 3 Climatological cross sections of silicate in the Atlantic (left) and Pacific (right) Oceans. The averaging longitudes are the same as in Fig. 1. Silicate is used by certain marine organisms to make their shells. These shells dissolve at depth after the organisms die, resulting in a subsurface source of silicate.

(similar to the Antarctic Bottom Water and fresher than the North Atlantic Deep Water). This is the most abundant of all water masses; its salinity is close to the average ocean salinity. It is not formed directly at the surface, but as a result of the slow mixing between other deep, intermediate, and bottom waters. Transient tracers and nutrients show that Common Deep Waters have been largely isolated from the influence of the surface for many hundreds of years. Common Deep Waters feed much of the upwelling in the Southern Ocean.

The temperatures and salinities associated with these different classes of water are the result of surface fluxes of heat and freshwater. Averages of these fluxes along latitude circles are shown in Fig. 4. The heat flux shows the expected pattern of warming in the low latitudes (where incoming solar radiation exceeds outgoing long-wave radiation, evaporative cooling, and sensible cooling by the atmosphere) and cooling in the high latitudes (where the cooling terms are stronger and the incoming solar radiation is weaker). The water flux shows three separate maxima, in the tropical rain belts (equatorward of about 10 deg) and the midlatitude storm tracks (poleward of 40 deg). These regions are associated with rising air. In between, the atmospheric circulation is dominated by sinking, which brings dry air into the lower atmosphere. This process suppresses precipitation and increases evapora-

tion. Consequently, in midlatitude bands between about 10 and 40 deg evaporation exceeds precipitation, and the ocean loses freshwater to the atmosphere. This in turn results in the high-salinity regions seen between 20 and 40 deg latitude in Fig. 2. The atmospheric circulations which produce these patterns also result in the pattern of winds shown in Fig. 4c, with easterly (westward) winds along the equator and westerly (eastward) winds poleward of 30 deg latitude. The strongest winds are found at about 50 deg latitude in both the Northern and Southern Hemispheres.

The general circulation can be thought of as three separate cells involving the five classes of water listed above. Oceanographers quantify transport in units of Sverdrups, where $1 \text{ Sv} = 10^6 \text{ m}^3/\text{sec}$ of flow. For comparison, the Amazon River has a flow of about 0.15 Sv. The uppermost cell consists primarily of low-latitude thermocline waters. It is characterized by upwelling along the equator and downwelling between 20 and 40 deg latitude. This cell involves a lot of water, with longitudinally summed fluxes in the three ocean basins reaching up to 80 Sv.

The equatorial cell is relatively limited in its geographic extent. More important for the global circulation is the *global overturning circulation*, a schematic of which is shown in Fig. 5. This comprises two separate cells. The first involves downwelling of Antarctic Intermediate Water in the Southern Ocean, upwelling of this water

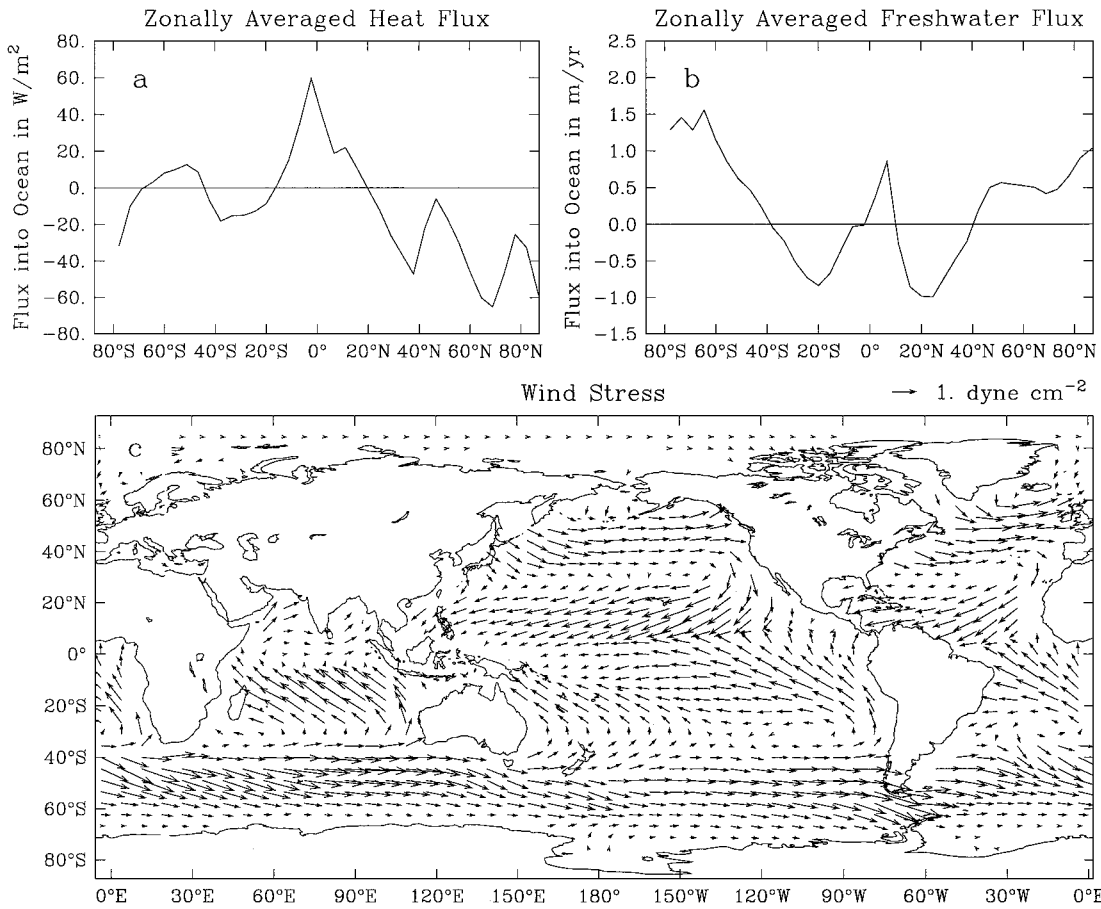


FIGURE 4 Heat, moisture, and momentum fluxes into the ocean. Upper left panel shows the heat flux taken from a climatological dataset produced by A. M. Da Silva of the National Oceanic Data Center. Upper right panel shows the moisture flux from the same dataset. Lower panel shows wind stresses from a dataset compiled by S. Hellermann.

mass in the low latitudes, where it becomes warm and salty (denoted by the conversion of dark gray arrows to black), followed by transport into the high-latitude North Atlantic, where it is cooled to form the North Atlantic Deep Water (denoted by the conversion of black arrows to light gray), and upwelling of this water mass in the Southern Ocean, where it is freshened and moves northward to feed the Antarctic Intermediate Water (denoted by the conversion of light gray arrows to dark gray arrows). This cell has a flow of about 20 Sv. It transports a great deal of heat and is thought to be a major driver of long-term variations in the earth's climate.

The final cell of importance involves the downwelling of Antarctic Bottom Water along the Antarctic continent, its flow northward into the ocean basins, where it mixes with North Atlantic Deep Water and Antarctic Intermediate Water and is returned to the south as high-nutrient deep waters from the Indian and Pacific Oceans. This is shown as closed loops in light gray in the Indian and Pacific Oceans in Fig. 5. The magnitude of this cell is

highly controversial, but it is probably about 10 Sv in each basin.

The ocean circulates horizontally as well as vertically, with the most prominent expression of this being the wind-driven gyres and Circumpolar Current (Fig. 6). In latitudes between about 23 and 45 deg, the interior circulation is equatorward and the boundary currents are poleward. These are the *subtropical gyres*. Between about 45 and 70 deg latitude the interior circulation is poleward and the boundary currents flow equatorward. These are the *subpolar gyres*. The gyre circulations involve slow interior flows with velocities of order 1 cm/sec and strong boundary currents (such as the Gulf Stream in the North Atlantic and the Kuroshio in the North Pacific) where flow speeds are of order 1 m/sec. The gyres transport up to 100 Sv of fluid apiece, 600 times the transport of the Amazon River. However, a certain amount of the gyre circulation involves the motion of fluid along isopycnal surfaces (surfaces of constant potential density) with relatively little transformation of water from one density class to another implied.

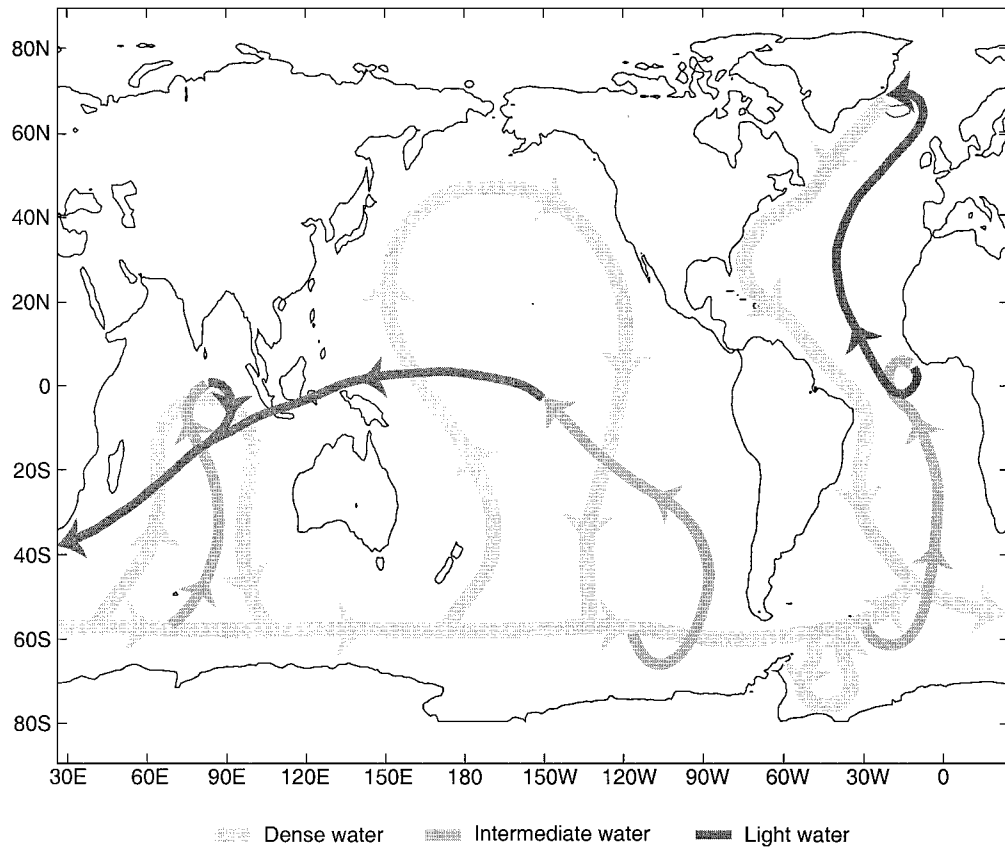


FIGURE 5 Schematic of the overturning component of the thermohaline circulation. Shading indicates different densities, with the lightest shading indicating the densest water and the dark shading indicating the lightest water.

The physics responsible for these gyres is discussed in Section III.A.

In addition to the gyre circulations, there is a significant flow of water (100–150 Sv) around the continent of Antarctica. This Antarctic Circumpolar Current can be seen in both Figs. 5 and 6 as a west-to-east flow of water in latitudes to the south of 40°S. The dynamics involved in determining the magnitude of this current are still very much in question, though Southern Ocean winds are thought to play a key role.

The gyre circulations are closely connected to the overturning circulation. For example, the location of the sinking of the lightest cell is dictated by convergent near-surface wind-driven flows. The equatorial upwelling is entirely due to the divergent Ekman transport driven by westward winds. In the northern sinking regions of the intermediate-deep water cell, the wind brings intermediate-density waters to the surface, permitting surface cooling to form the very dense water. Moreover, even though the formation of the densest waters in marginal Arctic and Antarctic seas is strongly influenced by geography, the return of the Common Deep Waters is strongly

tied to the spatial pattern of surface winds in the Southern Ocean.

II. PHYSICAL BALANCES GOVERNING LARGE-SCALE OCEAN FLOW

A. Equations of Motion

Before discussing the observed oceanic thermal structure and the theories explaining this structure, it is worth briefly describing the equations governing the oceanic circulation and the leading-order balances that are frequently encountered. A more extensive discussion of these equations and balances can be found in a number of introductory texts on oceanography. The careful and extremely readable text of Gill (1982) is particularly recommended, as is the book of Pedlosky (1996). The reader not as deeply interested in the mathematics of the problem should nonetheless read the subsection on Ekman and geostrophic flow, and on potential vorticity constraints on the ocean circulation.

The ocean flow is governed by the Navier–Stokes equations in a rotating coordinate frame:

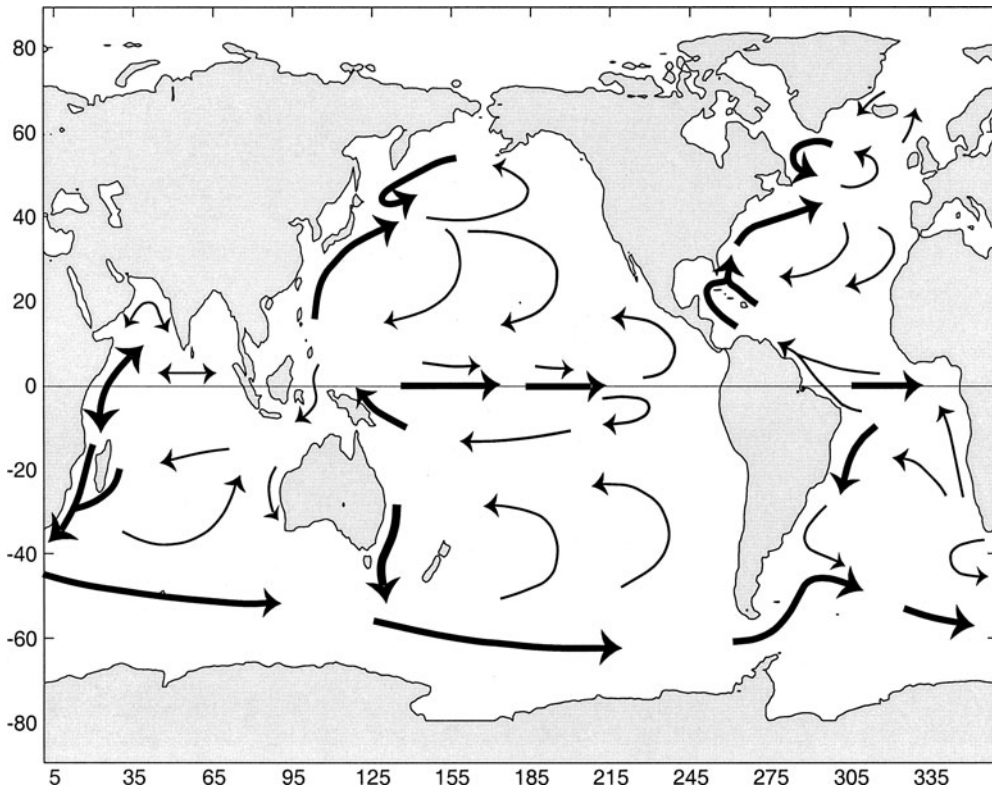


FIGURE 6 Schematic of the gyre components of global ocean circulation. Thick lines are concentrated flows involving tens of Sverdrups ($1 \text{ Sv} = 10^6 \text{ m}^3/\text{sec}$). Thin lines are either more diffuse or involve far less volume flux.

$$\frac{\partial \mathbf{U}}{\partial t} + \mathbf{U} \cdot \nabla \mathbf{U} + 2\boldsymbol{\Omega} \times \mathbf{U} = -\frac{1}{\rho} \nabla p - g\hat{z} + \frac{1}{\rho} \nabla \cdot \tilde{\tau}. \quad (1)$$

Here \mathbf{U} is the three-dimensional fluid velocity, $\boldsymbol{\Omega}$ is the earth's rotation vector, p is pressure, ρ is density, g is the gravitational acceleration at the surface of the earth, and $\tilde{\tau}$ is the stress tensor. The gravitational acceleration includes the effects of both the actual gravitational attraction of the earth and the velocity-independent centrifugal force, and the direction of that acceleration defines the vertical direction. In general, the equations are cast in a form such that \hat{x} is a unit vector pointing eastward, \hat{y} is a unit vector pointing northward, and \hat{z} is a unit vector pointing upward.

The Navier-Stokes equation is essentially just Newton's second law of motion, $\mathbf{F} = m\mathbf{a}$, following a fluid parcel. Without rotation, this interpretation is particularly clear. The first two terms on the left-hand side are just the acceleration of the fluid parcel, while the terms on the right-hand side are surface and body forces acting on that parcel, divided by the mass of the parcel. These so-called "forcing terms" act to change the momentum of a parcel as it moves through the ocean. The effects of rotation can be derived fairly easily by noting that the time derivative of a vector in a rotating reference frame is related to the time derivative in a fixed reference frame by

$$\frac{d\mathbf{A}_f}{dt} = \frac{d\mathbf{A}_r}{dt} + \boldsymbol{\Omega} \times \mathbf{A}_r, \quad (2)$$

where \mathbf{A}_f is the vector in the fixed reference frame and \mathbf{A}_r is the vector in the rotating reference frame. Applying this relationship twice to the position vector \mathbf{x} gives

$$\begin{aligned} \frac{d^2\mathbf{x}_f}{dt^2} &= \frac{d}{dt} \left(\frac{d\mathbf{x}_r}{dt} + \boldsymbol{\Omega} \times \mathbf{x}_r \right) + \boldsymbol{\Omega} \times \left(\frac{d\mathbf{x}_r}{dt} + \boldsymbol{\Omega} \times \mathbf{x}_r \right) \\ &= \frac{d^2\mathbf{x}_r}{dt^2} + 2\boldsymbol{\Omega} \times \frac{d\mathbf{x}_r}{dt} + \boldsymbol{\Omega} \times (\boldsymbol{\Omega} \times \mathbf{x}_r). \end{aligned} \quad (3)$$

Using the definition of velocity gives

$$\frac{d\mathbf{U}_f}{dt} = \frac{d\mathbf{U}_r}{dt} + 2\boldsymbol{\Omega} \times \mathbf{U}_r + \boldsymbol{\Omega} \times (\boldsymbol{\Omega} \times \mathbf{x}_r). \quad (4)$$

The last, centripetal acceleration, term is relatively uninteresting because it can be combined with the gravitational potential to give the geopotential. The gradient of the geopotential is the gravitational acceleration. The ocean's surface closely approximates a geopotential surface, bulging 21 km further from the center of the earth at the equator than at the poles.

The *Coriolis acceleration* term, $2\boldsymbol{\Omega} \times \mathbf{U}$, has a profound effect on the low-frequency ocean circulation (that occurring on time scales longer than a pendulum day).

This term causes particles moving relative to the rotating earth to turn to the right in the Northern Hemisphere and to the left in the Southern Hemisphere. Additionally, it allows a steady balance between a force acting on the fluid and a flow at right angles to that force.

When the horizontal length scales of interest are much larger than the vertical scales, the vertical momentum equation is well approximated by the *hydrostatic balance* between vertical pressure gradients and gravitational accelerations,

$$\frac{dp}{dz} = -g\rho. \quad (5)$$

Essentially, this implies that the pressure at a given point within the ocean is just the atmospheric surface pressure plus the weight of the water overlying that point. This balance applies both to the horizontal mean, dynamically inert pressure as well as to the dynamically active pressure anomalies (those which have gradients in the horizontal plane). Using the hydrostatic equation involves discarding a number of other terms from the vertical momentum equations, in particular the vertical component of the Coriolis force. In order to prevent this modification from introducing nonconservation of energy it is necessary to modify the horizontal momentum equations as well, eliminating a term involving the horizontal component of the earth's rotation vector times the vertical velocity.

In addition to the momentum equation, conservation of mass gives

$$\frac{\partial \rho}{\partial t} + \nabla \cdot (\mathbf{U}\rho) = 0. \quad (6)$$

But when averaged over periods longer than a few seconds, density is well described by an empirical *equation of state*, which expresses density as a function of pressure, temperature (or preferably potential temperature θ), and salinity S ,

$$\rho = \rho(S, \theta, p). \quad (7)$$

Over these same periods, the mass conservation equation is well approximated by the incompressibility equation

$$\nabla \cdot \mathbf{U} = 0 \quad (8)$$

Making the incompressibility approximation is equivalent to filtering out sound waves by setting the speed of sound in the ocean to be infinite. Since flow speeds are typically three to six orders of magnitude smaller than the roughly 1500 m sec^{-1} speed of sound, this is a very good approximation. It is worth noting that while the full density conservation equation (6) is prognostic (it can be integrated forward in time), the incompressibility equation contains no time derivatives and is thus purely diagnostic. Usually the vertical velocities are diagnosed from a known horizontal velocity field since the time derivatives of the

vertical velocities are discarded by making the hydrostatic approximation.

Salinity is the concentration of sea salt. (The ratios of the ions which constitute sea salt do not vary substantially within the open oceans.) Salinity is conserved under material advection, except for the effects of mixing (which invariably reduces the variance of salinity), and the dilution or concentration of salt at the surface by the imbalance between evaporation (E) and precipitation (P) and the freezing (F_{ice}) and melting (M_{ice}) of sea ice. The salinity conservation equation is

$$\frac{\partial S}{\partial t} + \mathbf{U} \cdot \nabla S = \nabla \cdot \mathbf{F}_S, \quad (9)$$

where \mathbf{F}_S is the flux of salinity with boundary conditions

$$\mathbf{F}_S \cdot \hat{n} = 0 \quad \text{at the seafloor} \quad (10)$$

and

$$\mathbf{F}_S \cdot \hat{n} = S(E - P + F_{\text{ice}} - M_{\text{ice}}) \quad \text{at the surface.} \quad (11)$$

Temperature is not conserved in the ocean due to the compressibility of seawater but it is possible to define an empirical potential temperature that is conserved under adiabatic compression. The potential temperature conservation equation is given by

$$\frac{\partial \theta}{\partial t} + \mathbf{U} \cdot \nabla \theta = \nabla \cdot \mathbf{F}_\theta + \frac{Q}{\rho c_p}. \quad (12)$$

Here Q is an internal heating rate (in W m^{-3}), c_p is the (empirically determined) heat capacity of sea water, and \mathbf{F}_θ is the turbulent or diffusive flux of heat. The heating rate can be quite large near the surface due to exchange with the atmosphere. Infrared heating and cooling and latent heat loss due to evaporation occur within a few millimeters of the ocean surface, and can have magnitudes integrated through the near-surface region of order 200 W m^{-2} . Incident solar radiation is absorbed with extinction length scales of up to tens of meters, depending on wavelength. It is not surprising, then, that there is typically a strongly turbulent *mixed layer* at the surface of the ocean with typical vertical scales of tens of meters due to both the unstable heating/cooling profile and wind- and surface wave-induced turbulence. In the ocean interior, heat sources are very weak due, for example, to the conversion of kinetic energy to internal energy and to radioactive decay of trace elements. At the sea floor there is sometimes a locally substantial geothermal heat source, but the average magnitude of this heating is fairly modest, of order 0.05 W m^{-2} . Thus, to good approximation, potential temperature is often treated as conserved away from the surface.

The density of seawater varies from its mean value of about 1030 kg m^{-3} by a few percent due to compressibility,

and at any given pressure it varies by a few parts per thousand due to temperature and salinity variations over most of the ocean. For this reason, the *Boussinesq approximation* is very often made in studying the dynamics of the ocean, in which density in the Navier–Stokes equation is replaced by its mean value ρ_0 except within the hydrostatic equation (5).

The large-scale dynamics of the ocean is approximately governed by the *primitive equations*, which include (5), (8), and the horizontal momentum equations

$$\frac{\partial \mathbf{u}}{\partial t} + \mathbf{U} \cdot \nabla \mathbf{u} + f \hat{z} \times \mathbf{u} = -\frac{1}{\rho_0} \nabla_H p + \frac{1}{\rho_0} \nabla \cdot \tilde{\tau}, \quad (13)$$

where \mathbf{u} is the horizontal velocity vector, the subscript H with the gradient emphasizes that only the horizontal components are of interest, and $f \equiv 2|\Omega| \sin(\text{latitude})$ is the vertical component of the earth's rotation vector. The primitive equations are often used in computer simulations to describe the ocean circulation.

B. Ekman and Geostrophic Flow

For low frequencies compared to the inertial period ($1/f$) and horizontal length scales longer than the few kilometers which oceanic currents can cover within an inertial period, the horizontal velocities are in *geostrophic balance* with the horizontal pressure gradients. Under these conditions, the horizontal momentum equations (13) are well approximated as

$$f \hat{z} \times \mathbf{u} = -\frac{1}{\rho_0} \nabla_H p. \quad (14)$$

Instead of producing a continually accelerating flow, pressure gradients are opposed by the Coriolis acceleration of the horizontal velocities. This results in horizontal circulation which proceeds clockwise around centers of high pressure in the Northern Hemisphere and counterclockwise around centers of high pressure in the Southern Hemisphere (Fig. 7). To the extent that f is constant, these geostrophic velocities are nondivergent, and no vertical velocities result from the incompressibility equation (8).

One region where the geostrophic balance does not hold is very near the surface. Winds impart significant horizontal stresses to the ocean at the surface. Averaging the velocities over a time longer than the inertial period leads to a balance between the Coriolis acceleration due to an ageostrophic velocity and an acceleration due to vertical divergence of the stress. Integrating these velocities from the surface down to a depth where the stress becomes insignificant leads to a net transport at right angles to the wind stress:

$$\int \mathbf{u} dz = \frac{1}{f} \hat{z} \times \tau_{\text{Sfc}}, \quad (15)$$

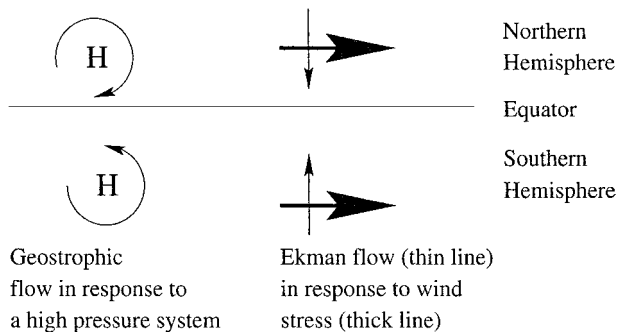


FIGURE 7 Schematic of geostrophic and Ekman flows. Left-hand side shows the flow around high-pressure systems associated with geostrophic flows in the Northern and Southern Hemispheres. The right-hand side shows the Ekman flows associated with wind stresses.

where τ_{Sfc} is the surface stress. This is known as the *Ekman transport*, and was first described theoretically by V. W. Ekman in 1905. It was developed as an explanation for the observation during the *Fram* expedition that the mean ice drift was always at a significant angle to the right of the winds in the Northern Hemisphere. Similarly, in the Southern Hemisphere, an applied wind stress leads to an Ekman flow to the left of the wind (Fig. 7).

If the wind stress is spatially variable, there will be convergences and divergences in the Ekman transport. Conservation of mass then implies upwelling and downwelling at the base of the wind-driven layer. The resulting vertical velocity (which is of order tens of meters/year), known as the *Ekman pumping velocity*, is largely responsible (along with the basin geometry) for setting much of the pattern of the gyre circulations in Fig. 6. We will later denote this pumping velocity as W_e .

The geostrophic momentum equations can be combined with the hydrostatic equation to give the *thermal wind* equations:

$$f \hat{z} \times \frac{d\mathbf{u}}{dz} = \frac{g}{\rho_0} \nabla_H \rho. \quad (16)$$

The name of the thermal wind equations derives from their atmospheric origin, in which case the right-hand side can be written in terms of temperature alone. In the ocean it has long been possible to measure density [by measuring pressure, temperature, and conductivity to infer salinity and using (7)], and the thermal wind equations permit an accurate estimate of the vertical velocity shear. However, the calculation of the exact velocity from such hydrographic measurements requires knowledge of the absolute velocity at some depth. It is only recently that accurate acoustic Doppler current profiler measurements have provided sufficient accuracy for the actual ocean currents to be calculated except for those few cases when they can be referenced to isolated current meters.

C. Potential Vorticity

Although the geostrophic momentum equations and the hydrostatic equations (and their offspring, the thermal wind equation) provide an accurate description of the dynamic balances in the ocean, they are purely diagnostic equations. They inform the physical oceanographer about how the flow responds to changes in temperature and salinity as these produce changes in pressure. They do not, however, allow for the calculation of whether such flows are capable of maintaining the temperature and salinity structures which sustain them. In order to answer this question it is necessary to extend the equations to include time derivatives, which enter only at the next level of approximation. At that next level of approximation, the momentum and continuity equations can be combined into a single prognostic equation for the conservation of *potential vorticity* (PV). Ertel's PV (Π) is defined, starting from the full compressible Navier–Stokes equations, as

$$\Pi = \frac{\nabla \times \mathbf{U} + 2\Omega}{\rho} \cdot \nabla R, \quad (17)$$

where R is any materially conserved quantity which is a function of pressure and density only. Density corrected for compressibility (the so-called *potential density*) is close to being such a quantity in the ocean but there is no perfect quantity, given the ocean's complicated equation of state. If sources and sinks of R and frictional stresses acting on the fluid are negligible, Π satisfies the equation

$$\frac{\partial \Pi}{\partial t} + \mathbf{U} \cdot \nabla \Pi = 0. \quad (18)$$

In other words, PV is materially conserved (i.e., conserved by fluid parcels subject to advection), except for diabatic or viscous mixing or forcing terms. The full, compressible, nonhydrostatic version of potential vorticity is presented here to emphasize that the discussion which follows does not depend substantially on the simplifications that have been made. For the large-scale ocean circulation on scales of tens to hundreds of kilometers, Π can be approximated by

$$\Pi \approx (f + \hat{z} \cdot \nabla \times \mathbf{u}) \frac{1}{\rho_0} \frac{\partial \rho_{\text{pot}}}{\partial z}. \quad (19)$$

On even larger horizontal scales the $\hat{z} \cdot \nabla \times \mathbf{u}$ which corresponds to the relative vorticity associated with energetic, swirling flows can be dropped. In this case

$$\Pi \approx \frac{f}{\rho_0} \frac{\partial \rho_{\text{pot}}}{\partial z}. \quad (20)$$

The horizontal scales for which the relative vorticity is much less important in the calculation of potential vorticity than variations in stratification are those scales which are much larger than the *deformation radius*. The inter-

nal deformation radius is the distance that internal gravity waves can propagate in an inertial period, and is given by

$$\lambda = \frac{1}{f\pi} \int_{-D}^0 \sqrt{\frac{g}{\rho_0} \frac{\partial \rho_{\text{pot}}}{\partial z}} dz, \quad (21)$$

where D is the depth of the fluid. In midlatitudes, the internal deformation radius is typically several tens of kilometers. The internal deformation radius is also approximately the dominant scale of the rich eddy field in the ocean.

For flow that is independent of depth, an appropriate version of potential vorticity is

$$\Pi \approx \frac{f + \hat{z} \cdot \nabla \times \mathbf{u}}{D}. \quad (22)$$

The external deformation radius $\lambda_{\text{ext}} = \sqrt{gD}/f$ is the appropriate length scale for determining whether relative vorticity is more important than potential vorticity anomalies due to deflections of the free surface. Since this length scale is thousands of kilometers in the deep ocean, relative vorticity cannot be neglected compared to variations in the surface height for flow that is independent of depth. Topographic variations are extremely important in the potential vorticity balance of many flows that are independent of depth, but as they are fixed, relative vorticity cannot be neglected compared with topographic variations. However, the flows of greatest interest tend to exhibit strong vertical shears, and it is the smaller, internal deformation radius (ranging from 10 to 200 km) which is most important in such cases.

The discussion which follows is largely cast in terms of layers of fluid, mostly for simplicity, but the conclusions about the circulation would still be valid if a continuously stratified formulation were retained.

D. A Layered Description of the Flow

It is often useful to describe the ocean in terms of a stack of constant-density layers rather than as a continuously stratified fluid. This is a sensible procedure for much of the ocean, given that processes which involve crossing density surfaces (so-called *diapycnal* processes) are much less efficient than processes involving the motion of fluid along density surfaces (so-called *isopycnal* processes). While this is not an accurate description of the ocean, it is a physically realizable system whose behavior is qualitatively similar to that of the real ocean. When there are relatively few layers, the system can be much easier to think about than the real ocean, and when there are many layers this physical model becomes an increasingly accurate description of the real ocean.

The horizontal gradient of the dynamically active pressure is vertically constant within each layer. The *Montgomery potential*, the horizontal gradient of which within

a layer equals the horizontal gradient of the dynamically active pressure divided by the mean density, can be calculated from the hydrostatic equation as

$$M_k = M_{k-1} + \frac{g(\rho_k - \rho_{k-1})}{\rho_0} \eta_{k-1/2}, \quad (23)$$

where $\eta_{k-1/2}$ is the height of the interface between layers k and $k-1$. The gradient of the Montgomery potential is just the opposite of the acceleration due to pressure gradients. At the surface, if the atmospheric sea level pressure is p_{atm} ,

$$M_1 = \frac{p_{\text{atm}}}{\rho_0} + g\eta_{1/2}. \quad (24)$$

Thus the primitive equations (13) can be written within each layer k as

$$\begin{aligned} \frac{\partial \mathbf{u}_k}{\partial t} + (f + \zeta_k) \hat{z} \times \mathbf{u}_k \\ = -\nabla_h \left(M_k + \frac{1}{2} \mathbf{u} \cdot \mathbf{u} \right) + \frac{1}{h_k} \nabla_h \cdot (h_k K_h \nabla_h \mathbf{u}_k) \\ + \frac{\tau_{k-1/2}^V - \tau_{k+1/2}^V}{h_k}, \end{aligned} \quad (25)$$

where \mathbf{u}_k is the horizontal velocity vector in layer k and h_k is the thickness of layer k . Here $\zeta_k \equiv \hat{z} \cdot \nabla \times \mathbf{u}_k$ is the vertical component of relative vorticity, the stress tensor has been separated into the horizontal and vertical fluxes of horizontal momentum, and a Fickian form has been assumed for the horizontal stresses. The cross-interface advection of momentum is typically so small that it has been neglected.

The continuity equation, written in terms of the layer thickness h_k , is

$$\frac{\partial h_k}{\partial t} + \nabla \cdot (\mathbf{u}_k h_k) = \omega_{k+1/2} - \omega_{k-1/2}. \quad (26)$$

The diapycnal velocities ω are due solely to vertical diffusion of density or internal buoyancy sources.

The momentum and continuity equations can be combined to give the potential vorticity equation by subtracting $(f + \zeta)/h^2$ times the continuity equation from the curl of the momentum equations divided by the thickness. This gives

$$\begin{aligned} & \left(\frac{\partial}{\partial t} + \mathbf{u}_k \cdot \nabla \right) \left(\frac{f + \zeta_k}{h_k} \right) \\ &= \frac{K_h}{h_k} \nabla^2 \zeta_k + \frac{\nabla \times (\tau_{k-1/2}^V - \tau_{k+1/2}^V)}{h_k^2} \\ & - \left(\frac{f + \zeta_k}{h_k^2} \right) (\omega_{k+1/2} - \omega_{k-1/2}), \end{aligned} \quad (27)$$

where the gradients of the thicknesses have been neglected in the viscous terms compared to the gradients of the

stresses, and the horizontal viscosity K_h has been assumed to be constant. Note that all of the terms on the right-hand side of this equation are either viscous or diabatic. Layer potential vorticity is conserved following a fluid parcel in the absence of these terms. Also, the pressure field (or Montgomery potential) is absent from the potential vorticity equation.

On scales that are larger than the internal deformation radius (21) relative vorticity ζ_k can be neglected for flows with substantial thermal wind shears, as can horizontal turbulent momentum transport. The actual diapycnal velocity $\omega_{k+1/2}$ can be combined with the curl of the vertical stress at the surface of a layer to give an effective vertical velocity (positive upward):

$$W_{k+1/2} = \omega_{k+1/2} + \nabla \times \tau_{k+1/2}^V / f. \quad (28)$$

The large-scale, steady potential vorticity equation is then

$$\mathbf{u}_k \cdot \nabla \frac{f}{h_k} = \frac{f}{h_k^2} (W_{k-1/2} - W_{k+1/2}). \quad (29)$$

E. Potential Vorticity Constraints on Flow

The steady, large-scale PV conservation equation (29) imposes strong constraints on the ocean circulation. As these constraints will be used extensively in Sections III.A and III.B it is important to develop a better physical insight into the meaning of this equation. If there are no interfacial frictional fluxes or diapycnal mass fluxes, then the effective vertical velocity $W_{k\pm 1/2}$ is identically 0 for all k . In such cases

$$\mathbf{u}_k \cdot \nabla \frac{f}{h_k} = 0 \quad (30)$$

and the flow must follow lines of constant f/h_k . This means that if a parcel moves poleward (causing the magnitude of f to increase), then the thickness of that parcel must increase as well. This constraint can essentially be interpreted as a constraint on the angular momentum of a parcel. As a parcel moves poleward, its spin relative to that of the earth underneath it increases. Much as an ice skater pulls his or her arms inward in order to spin faster, the parcel must contract in the horizontal and stretch in the vertical direction in order to match its spin to that of the earth underneath it. An example of this is seen in the northeastern Pacific (Fig. 8). The thickness of the layer bounded by isopycnal surfaces with potential densities of 1026.5 and 1027.0 kg m^{-3} varies in this region from 150 to 400 m. However, the potential vorticity of this layer scarcely varies at all between 20°N and 40°N. Within this latitude range, then, it will be relatively easy to drive flow in any direction. To the north of 40°N and to the south of 20°N, however, the potential vorticity of the layer has considerable structure, and it will be difficult to drive flow

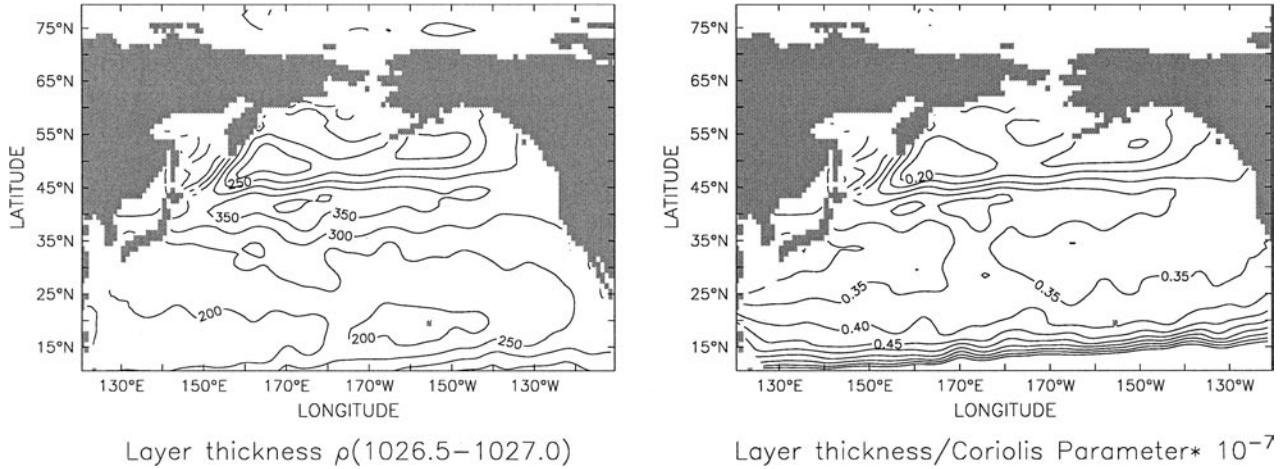


FIGURE 8 Layer thickness and potential vorticity in the North Pacific. Left: Thickness of layer with density between 1026.5 and 1027.0 kg m⁻³. Notice that there are strong gradients between 15° and 45°N, with the thickness varying between 150 and 400 m. Right: Layer thickness divided by Coriolis parameter (inverse of the potential vorticity) and scaled by 10⁻⁷ sec⁻¹ m⁻¹. Note that this parameter varies much less between 15° and 45°N, only ranging between 0.35 and 0.4.

across these gradients without significant forcing to make $W_{k\pm 1/2} \neq 0$.

Insight into why potential vorticity must be conserved along lines of steady flow driven only by pressure gradients can be gained by looking at the equations for such flow in more detail. In particular, when the flow is geostrophic

$$fv_k = \frac{\partial M_k}{\partial x}, \quad fu_k = -\frac{\partial M_k}{\partial y}, \quad (31)$$

where f is the Coriolis parameter, v_k is the north-south velocity within layer k , u_k is the east-west velocity, and M_k is the Montgomery potential in layer k . Note that this implies that the flow lies along lines of constant M_k . If the layer is to remain at a constant thickness, the flow must be nondivergent. This can only happen if

$$\begin{aligned} \frac{\partial}{\partial x}(u_k h_k) + \frac{\partial}{\partial y}(v_k h_k) &= -\frac{\partial}{\partial x} \frac{h_k}{f} \frac{\partial M_k}{\partial y} + \frac{\partial}{\partial y} \frac{h_k}{f} \frac{\partial M_k}{\partial x} \\ &= \mathbf{u}_k \cdot \nabla \frac{h_k}{f} = 0. \end{aligned} \quad (32)$$

This will only be true if $h_k/f = F(M)$. Geostrophic flow which crosses lines of f/h_k will thus fail to satisfy (32) unless there is some other forcing which can balance the resulting convergence and divergence of mass.

Either diapycnal mass fluxes (which remove mass from a layer) or horizontal gradients in the wind stress (which essentially change the vorticity of the layer) can provide such a balance. Consider the case where a layer is forced only from above and h_k is constant along the direction of flow. In this special case, (29) becomes

$$\beta v_k h_k = f W_{k-1/2}, \quad (33)$$

where $\beta \equiv df/dy$ is the northward gradient of the Coriolis parameter and $v = \mathbf{u} \cdot \hat{\mathbf{y}}$ is the northward velocity. When the forcing is due to the curl of the wind stress, (33) is known as the *Sverdrup relation*. The following section will consider two special cases of this equation, one in which the $W_{k-1/2}$ is the result of wind stress and a second in which it is the result of diapycnal velocities.

F. Small-Scale Mixing

The molecular viscosities and diffusivities of heat and salinity are so small as to have negligible effects on the large-scale velocities and thermal structure. However, small-scale three-dimensional turbulence can break larger scale gradients into smaller and smaller filaments until gradients occur on fine enough scales for the molecular viscosity and diffusion to be effective. As a result, one of the key processes involved in setting the large-scale temperature structure is small-scale mixing.

Because the ocean is stratified, a parcel of fluid moved upward will be denser than the fluid around it and will tend to return to its initial level. As a result of this restoring force, the ocean can support internal gravity waves. Current understanding holds that a major source for such waves is the interaction of ocean tides with small-scale (2–5 km) hillocks on the ocean. As the waves generated by this mechanism move upward in the water column they break, resulting in vertical mixing on scales of a few meters. Other mixing processes (such as instabilities caused by differential diffusion of salt and heat) may be important in some areas of the ocean but they are not thought to play a primary role in generating mixing.

The cumulative effect of many such breaking events can be parametrized in terms of a mixing coefficient K_v . The flux of temperature F_T caused by such mixing is then

$$F_T = -K_v \frac{\partial T}{\partial z}. \quad (34)$$

If this flux changes in the vertical direction, it causes a temperature tendency,

$$\frac{dT}{dt} = -\frac{\partial F_T}{\partial z} = \frac{\partial}{\partial z} K_v \frac{\partial T}{\partial z}. \quad (35)$$

Two sorts of measurements are currently used to estimate the magnitude of the diffusion coefficient K_v , with consistent results. The first is to make centimeter-scale measurements of the temperature gradients and velocity shears from which mixing rates can be inferred. This method has been used in a wide range of oceanographic conditions. The second method is to inject some tracer (usually a chlorofluorocarbon) which can be detected at very low concentrations into the thermocline. A general solution of the (35) assuming constant K_v and starting with an infinitesimally compact tracer concentration is

$$C(t) = \frac{1}{\sqrt{K_v t}} \exp\left(\frac{-z^2}{K_v t}\right), \quad (36)$$

where t is time and z is the vertical distance from the injection depth. In 1993, a project directed by J. Ledwell of the Woods Hole Oceanographic Institution injected 300 kg of sulfur hexafluoride into the pycnocline at a depth of 300 m in the Eastern Atlantic. Over 2 years, the spread of this tracer gave a vertical diffusivity of 0.1–0.15 cm²/sec, consistent with small-scale turbulence measurements made in the same region by J. Toole, R. Schmitt, and K. Polzin, also at Woods Hole. More recent studies over rough topography in the Brazil Basin in the South Atlantic by the same group of investigators found higher values (of order 1 cm²/sec) in the deep ocean.

In contrast with vertical mixing, there is no restoring force for fluid displacements along surfaces of constant potential density (isopycnals). As a result, the ubiquitous eddy field in the ocean is able to homogenize gradients along isopycnals much more easily than in the cross-isopycnal direction (which is nearly vertical). Tracer-release-based estimates of the tracer mixing rates along isopycnals are of order 1000 m²/sec in relatively quiet regions, fully eight orders of magnitude larger than in the cross-isopycnal direction! While a Fickian diffusive description of the eddy fluxes of tracers along isopycnals may not be strictly accurate, these estimates of mixing rates explain why vertical tracer gradients in the ocean are very much larger than the along-isopycnal gradients.

III. MODELS OF THE THERMOCLINE

A. Surface Wind-Driven Thermocline

The near-surface circulation and density structure are dominated by the wind-driven circulation. The vertically integrated wind-driven gyres are qualitatively described by the Sverdrup relation (33). Although there is some modification to the circulation in the Atlantic, for example, because the seafloor is not flat and the velocities do not vanish at the seafloor, this is a detail that is not important for understanding the density structure associated with the surface gyres.

Considerable insight can be gained from the simplest version of the layered model, that with a motionless deep layer, a single interior layer governed by the Sverdrup relation, and a surface layer in which the wind stress drives an Ekman flux. If one makes the assumption that diapycnal fluxes at the surfaces bounding the interior layer are zero and that one can consider the map of an ocean basin on a spherical earth to a plane tangent to the sphere, (33) becomes

$$\beta v_1 h_1 = f W_e \quad (37)$$

where W_e is the Ekman pumping velocity from the surface layer to the interior layer.

This equation can be integrated to find the steady-state density structure which is consistent with such a flow. The assumption of a motionless deep layer means that in this layer the total pressure gradient must be zero. This in turn means that any pressure gradient associated with changes in the surface height must be compensated by changes in the internal interface height, as illustrated in Figure 9. In this case, following (23),

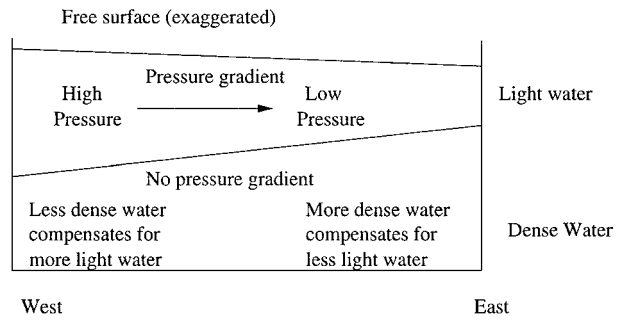


FIGURE 9 Schematic of how changes in internal interface can compensate pressure gradients associated with changes in surface height. In the upper layer, pressure is high where the surface is high and low where it is low. In the lower layer, pressure is constant as the changes in the amount of light water are compensated by changes in the amount of dense water overlying a particular point.

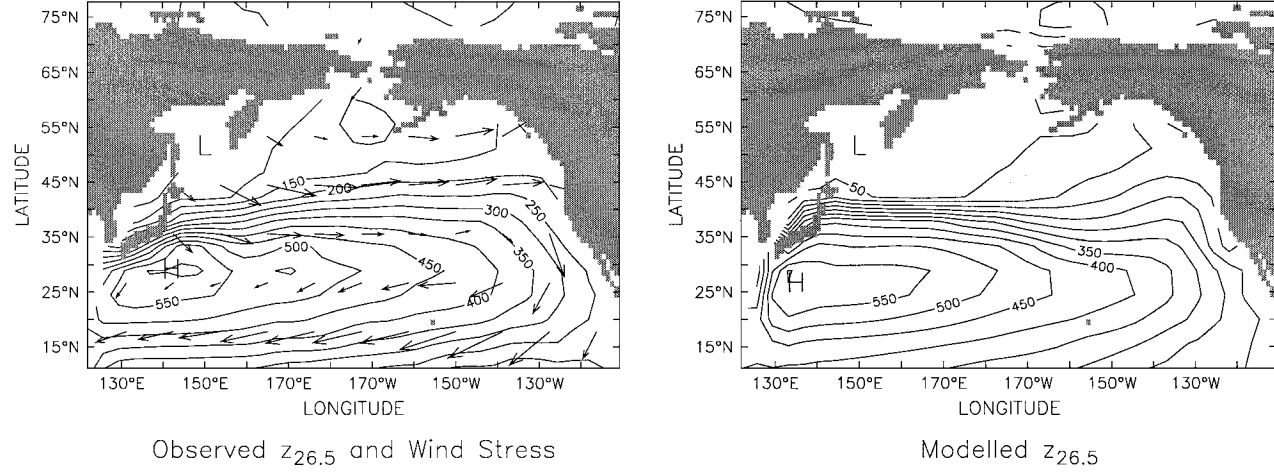


FIGURE 10 Shape of the North Pacific thermocline. Left: Depth of layer with potential density equal to 1026.5 kg m^{-3} . Notice that there is a high in the subtropics and a low in the subpolar zone, with both high and low shifted to the western part of the basin. The wind stress at the surface is shown by the vectors. Right: Depth of same density surface in a numerical model in which the dynamics is dominated by Sverdrup balance. Notice the broad agreement between the modeled and observed field.

$$g\eta_{1/2} + \frac{g(\rho_2 - \rho_1)}{\rho_0}\eta_{3/2} = \text{const.} \quad (38)$$

Given that the density differences between oceanic layers is much smaller than the density difference between the water and atmosphere, changes in the depth of the internal interface height $\eta_{3/2}$ will be much larger than changes in the surface height. This means that the changes in the layer thickness will be dominated by changes in the internal interface height ($\nabla_H \eta_{3/2} = -\nabla_H h_1$) and thus

$$g\nabla_H \eta_{1/2} = -\frac{g(\rho_2 - \rho_1)}{\rho_0}\nabla_H h_1 \equiv -g'\nabla_H h_1 = -\frac{\partial M_1}{\partial x}, \quad (39)$$

where h_1 is the height of the interior layer and $g' \equiv g(\rho_2 - \rho_1)/\rho_0$ is called the *reduced gravity* across an interface. Assuming that the flow is geostrophic, so that the pressure gradient is balanced only by Coriolis forces,

$$v_1 = \frac{g'}{f} \frac{\partial h_1}{\partial x}. \quad (40)$$

Substituting into (37), we find that

$$\frac{g'\beta}{f} h_1 \frac{\partial h_1}{\partial x} = \frac{g'\beta}{2f} \frac{\partial h_1^2}{\partial x} = f W_e. \quad (41)$$

This equation can be easily solved to yield

$$h_1^2(x) = h_1^2(x = x_e) - (x_e - x) \frac{2f^2 W_e}{g'\beta}. \quad (42)$$

Thus when W_e is negative (winds cause convergence of water in the Ekman layer), the upper layer thickness thins toward the east. As discussed in Section II.D, this height difference leads to equatorward geostrophic flow. In order to conserve potential vorticity, the resulting divergence

in the geostrophic flow is supplied by convergence in the Ekman flow. In regions where W_e is positive, (winds cause a divergence in the Ekman layer) isopycnals will slope down toward the east. An illustration of this is shown in Fig. 10, in which the depth of the surface with potential density of 1026.5 kg m^{-3} in the real North Pacific Ocean is compared with that in a general circulation model. The dominant picture that emerges from the observations is that this density surface has a maximum depth in the western subtropical Pacific and a minimum in the western subpolar Pacific, with intermediate values found in the eastern Pacific. The model captures this broad-scale behavior (and indeed is quantitatively quite accurate, especially in the subtropics). Similar depressions in the depth of this density surface are reflected in the upper ocean temperature, salinity, and silicate fields in Figs. 1–3.

When geostrophic flows are sufficiently large, the isopycnal surfaces associated with these flows exhibit large deformations. This means that the potential vorticity contours in deeper layers are then affected by the structure of the surface layers. Thus the potential vorticity structure of the density layer in Fig. 8 is affected strongly by the shape of the isopycnal surface shown in Fig. 10. Geostrophic flow must be along potential vorticity contours in the absence of frictional forcing. This means that as a column of fluid moves northward or southward, it must be stretched or compressed. As the surface atop an interior layer is deformed in the east–west direction, it tends to make the contours of the potential vorticity in the interior layer run in the north–south direction. If the upper layer height goes to zero, certain contours of potential vorticity within an interior layer will intersect the

surface at some latitude. Flow along these contours may then be directly forced at the surface by the winds. If the Ekman pumping (which is proportional to the curl of the wind stress) is downward, flow is forced into the layer which outcrops at this point. This process is thought to set the structure of the so-called *ventilated thermocline*, that part of the density and temperature field associated with downward-bowing of surfaces of constant temperature or density in subtropical gyres and upward bowing of such surfaces in subpolar gyres. By contrast, PV contours that are further east or on denser surfaces may intersect the eastern boundary while still submerged. Flow tends to be nearly stagnant in this *shadow zone* since there is no physical mechanism to cause it to cross contours of PV. The original paper describing these ideas mathematically and physically was published in by Luyten *et al.* (1983).

Further west, there may be PV contours [which are also characteristics of (29)] which both emanate from and return to the western boundary without ever encountering the ocean's surface. Fluid may flow freely along these contours, closing the circulation within intense western boundary currents, but is insulated from direct forcing near the surface. Within these regions, fluid may circulate many times before it is exchanged with fluid from outside of these closed contours. P. Rhines of the University of Washington and W. Young of Scripps Institution of Oceanography suggested that within these isolated regions, PV may become homogenized. The signature of such homogenization can be seen in Fig. 8. When com-

bined with the ventilated thermocline theory of Luyten *et al.*, the entire structure of the wind-driven thermocline in certain idealized instances can be calculated semianalytically by the method of characteristics for a given wind stress pattern and assumptions about the density distribution both at the surface and at the eastern boundary.

There is compelling observational evidence to support this depiction of the ventilated thermocline. Some of this evidence comes from the distribution of chemically inert anthropogenic trace gases such as chlorofluorocarbons, whose surface concentrations have increased at known rates over the past few decades. The observed thermal and density structure is largely consistent with the homogenization of PV in the deep western portions of the subtropical gyres.

The interior flow associated with the ventilated thermocline is balanced by boundary currents such as the Gulf Stream. In these boundary currents frictional forces allow the potential vorticity to change and the Sverdrup relation (33) does not hold. The strongest boundary currents tend to be located on the western side of ocean basins. This can be understood through the physical argument illustrated in Fig. 11. In terms of the conservation of potential vorticity f/h_k , the clockwise wind stress field reduces the potential vorticity, requiring a decrease in f and thus a southward flow. The frictional stress produced by a northward boundary current on the western side of the basin opposes this wind stress field, allowing for an increase in f within the boundary current (corresponding to a northward flow) and a potential vorticity balance for the basin as a whole. The

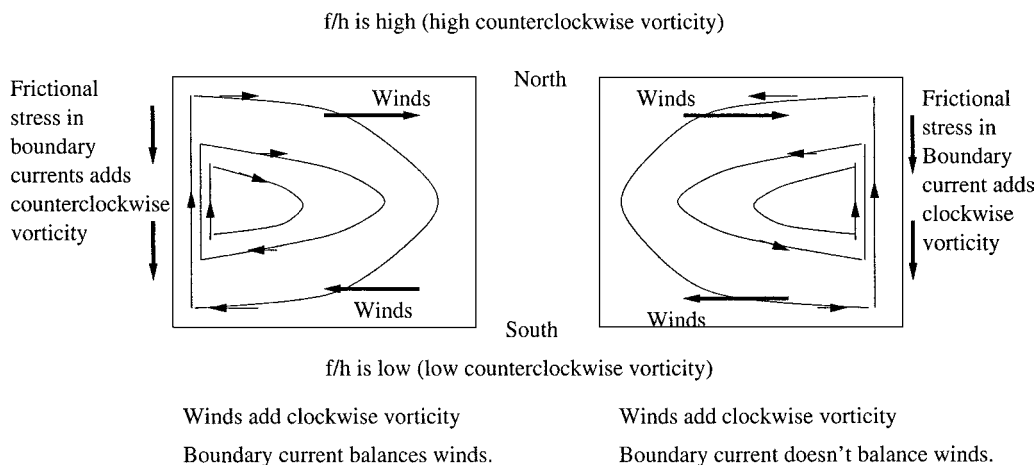


FIGURE 11 Schematic illustrating how vorticity constraints determine the structures of the wind-driven gyres. In both left and right-hand panels the assumption is made that the bottom of the ocean is flat, so that f/h is high in the north and low in the south, and that the winds swirl in a clockwise direction. In the ocean interior this produces a decrease in the potential vorticity and a southward interior flow. On the left-hand side the boundary current is on the west. The boundary located to the west of the fluid exerts a stress which tends to make fluid rotate in the counterclockwise direction, counteracting the wind stress and allowing for parcels of water to move to the north. On the right-hand side, the boundary current is on the east. In this case, the boundary adds vorticity of the wrong sign to make the ocean come into balance or to allow fluid parcels to increase their counterclockwise vorticity as they move northward.

frictional stress produced by a northward boundary current on the eastern side of the basin, by contrast, would be in the same sense as the wind stress field. This would tend to require a decrease in f and a southward flow, inconsistent with the requirement of a northward-flowing boundary current.

There are limitations to the theory of the ventilated thermocline. It applies most clearly to those density surfaces which are at the surface, where the curl of the wind stress tends to drive fluid downward, as in the subtropical gyre. In the subpolar gyre, the appropriate characteristics would emanate from the western boundary currents. While there have been attempts to extend the theory of the ventilated thermocline to the subpolar gyre, the processes by which potential vorticity is set in the streamlines which flow through the dynamically rich western boundary region are complicated and not fully understood. Without a robust theory describing how the characteristics are determined, extension of a ventilated thermocline-type theory to the subpolar gyre will be incomplete.

In addition, the ventilated thermocline theory assumes that essentially laminar dynamics govern the interior ocean circulation. However, an inevitable feature of surface-intensified subtropical gyres where PV is conserved along streamlines is the development of meridional PV gradients which oppose the planetary PV gradients due to the steady northward increase of the Coriolis term. A change in sign of the PV gradient is a well-known necessary (and in some instances sufficient) condition for the growth of unstable eddies, whose dynamics are analogous to the high- and low-pressure systems that dominate the weather of the midlatitudes. Eddy activity is, in fact, ubiquitous both in oceanic observations and in sufficiently high resolution numerical simulations of the ocean's dynamics. Eddies inevitably alter the generally correct structure arising from the laminar theory of the ventilated thermocline.

The ventilated thermocline and PV homogenization theories explicitly assume that vertical diffusion is not important. However, even in the limit of very weak diffusion, there may be portions of the thermocline which are strongly modified by diffusion. R. Samelson and G. Vallis have pointed out that there may be a density discontinuity which develops between the wind-driven ventilated thermocline and deeper, convectively ventilated thermocline. Diffusion will act to moderate this discontinuity, and diffusive fluxes across this discontinuity may be significant. Density profiles do tend to show two regions of greater stratification, one at the surface and the other at the base of the directly ventilated fluid, supporting the interpretation that there will be regions of the thermocline in which diffusion is significant, even if the upper thermocline as a whole is largely shaped by the winds.

B. The Deep Thermocline and the Importance of Small-Scale Mixing

In the presence of mixing, water in the ocean interior can change its density. In the deep ocean, both geothermal heating through the ocean bottom and diffusive heating from above cause the deep water to become lighter. In the absence of circulation, this would imply that a layer of dense water near the ocean bottom would tend to become thinner and thinner. In the early 1960s, H. Stommel and A. Arons of the Woods Hole Oceanographic Institution proposed that this thinning of deep layers could be balanced by a circulation in which the geostrophic circulation was divergent. Essentially, this theory is analogous to the thermocline theory developed in the previous subsection, except that the forcing term in the Sverdrup relation (33) arises from a diapycnal velocity ω rather than wind stress. Assuming a motionless interior layer $k - 1$ overlying a deep dense layer k , one has a pressure gradient in the dense layer

$$\nabla_H M_k = g \frac{\rho_k - \rho_{k-1}}{\rho_k} \nabla_H h_k \equiv g'_d \nabla_H h_k, \quad (43)$$

where g'_d is the reduced gravity across a deep interface. The Sverdrup relation in the deep layer then becomes

$$-\frac{g'_d \beta h_k}{f} \frac{\partial h_k}{\partial x} = f \omega, \quad (44)$$

leading to the solution of h_k

$$h_k^2 = h_e^2 - \frac{2f^2}{\beta g'_d} \omega(x_e - x), \quad (45)$$

where h_e is the layer height on the eastern boundary. Given that mixing produces $\omega > 0$, the height of the dense bottom layer would be expected increase toward the east, with warmer water in the interior. The flow is fed from the western boundary through a strong boundary current as shown in Fig. 12. The solution is nonintuitive in that throughout most of the ocean interior the flow is toward the polar regions, which serve as a source of dense water, with flow away from these regions only in the boundary currents. The flow can be broken down into an east–west part which is convergent and a north–south part which is divergent. The convergent part dominates, resulting in a circulation that is capable of supplying the required upwelling across any given deep isopycnal.

The Stommel–Arons solution for abyssal circulation remains a standard part of the physical oceanography curriculum for two reasons. The first is that it predicted the existence of a strong, deep, western boundary current before such boundary currents were actually discovered. The second is that it can be easily verified in a laboratory setting. However, finding evidence for such circulations in the real ocean has proven more difficult. Figure 13 shows

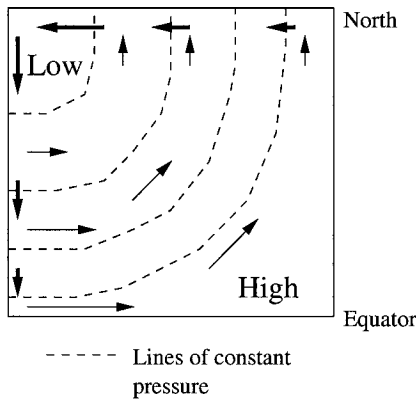


FIGURE 12 Schematic of the deep circulation proposed by Stommel and Arons. Dashed lines show lines of constant pressure. Thin vectors show the velocities associated with the geostrophic interior flow.

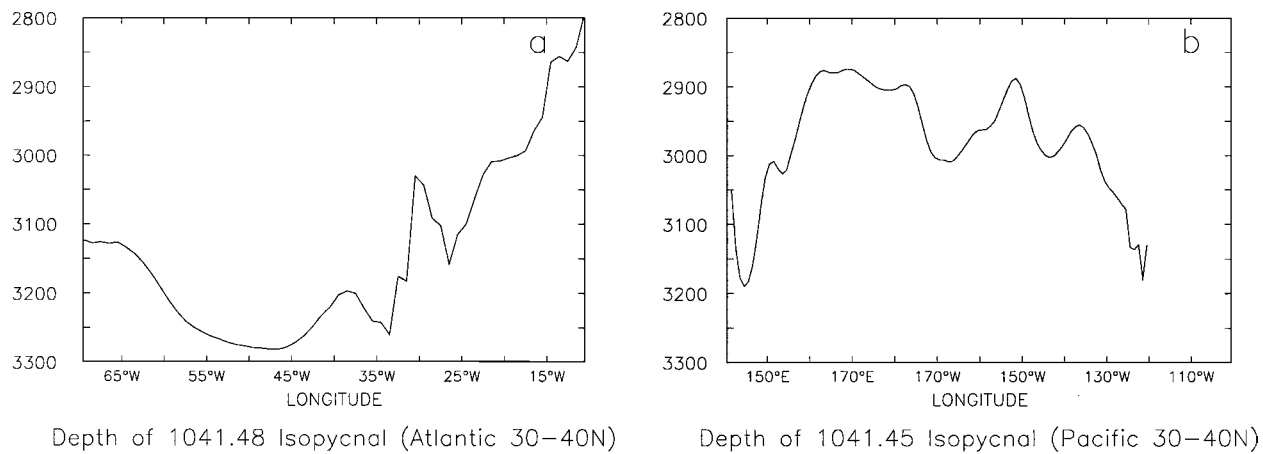
plots of the depths of two isopycnal surfaces at nominal depths around 3000 m in the North Atlantic and North Pacific. In the North Atlantic, the climatology shows a clear low in the interior of the basin, consistent with the theory of Stommel and Arons and Fig. 12. However the center of this gyre is not shifted as far toward the western boundary as would be expected from Stommel–Arons theory (and as is the case for the wind-driven gyres).

The North Pacific shows a very different picture. In the Pacific, the isopycnal surfaces are actually higher in the basin interior than on the edges, the opposite of the prediction made by Stommel and Arons. This implies a circulation which is clockwise with northward-flowing currents along the western boundary and southward-flowing currents along the eastern margin of the basin. Measure-

ments of the concentration of radiocarbon and silicate support this picture. Younger waters associated with higher values of radiocarbon and lower values of dissolved silicate are found along the equator and a plume of this water appears to penetrate into the northwest Pacific along the western boundary. As it does, the radiocarbon concentration slowly decreases, consistent with a picture in which water moves slowly clockwise around the basin.

There are two likely reasons for the failure of the Stommel–Arons solution to explain the circulation in basins such as the North Pacific. The first is the presence of bottom topography. When there is substantial bottom relief, the potential vorticity distribution of the bottom layer may be substantially altered, developing closed contours along which the geostrophic flow may proceed without barriers. This does not alter the sense in which the flow will proceed (if upwelling and diffusion are removing fluid from the interior of a basin, there will still be a low in the interior). However, it does alter the dynamics which supplies this upwelling. Instead of the divergence of geostrophic mass transport playing a critical role, bottom stresses working against the strong geostrophic flows generate Ekman fluxes which converge mass into the interior.

A second shortcoming of the Stommel–Arons circulation is that it assumes a spatially constant diapycnal velocity, which corresponds to assuming spatially constant diapycnal mixing. In fact, it is known that mixing in the deep ocean is highly variable spatially, with high values occurring over rough topography and lower values (in general) over abyssal plains. This means that large diapycnal velocities could well be concentrated over the part of the basin where topographic gradients are the strongest. A localized upwelling will tend to generate a circulation



Depth of 1041.48 Isopycnal (Atlantic 30–40N)

Depth of 1041.45 Isopycnal (Pacific 30–40N)

FIGURE 13 Abyssal density in the Atlantic and Pacific Oceans. Plotted are the depths of surfaces of potential density referenced to a depth of 3000 m (the density a parcel would have if taken to 3000 m without exchanging heat or salt with its surroundings) averaged from 30°N to 40°N. (a) Depth of the 1041.48 potential density surface in the North Atlantic. Note the low in the interior of the basin as predicted from theory. (b) Depth of the 1041.45 potential density surface in the Pacific. Note the high in the interior of the basin, opposite to the predictions of Stommel and Arons.

known as a “beta-plume” consisting of a plume of low pressure radiating along lines of constant potential vorticity with high potential vorticity to the right. If such a plume were located in a region with strong topographic gradients (such as the margin of the Pacific), the result would be the creation of a low along the boundaries and a clockwise circulation around the basin.

C. Intermediate-Depth Circulation

While there is widespread agreement that the shape of the main thermocline can largely be explained in terms of wind forcing and that the deep thermocline is strongly affected by mixing, there remains considerable disagreement about the intermediate cell. A schematic of this flow is shown in Fig. 14. The question of what drives this flow can be broken down into two parts:

- What sets the rate of formation of North Atlantic Deep Water in the North Atlantic, involving a transformation of light waters to dense waters?
- How do these dense waters get transformed back to light water?

A number of investigators have linked the formation rate of North Atlantic Deep Water to the large-scale pressure gradient between low and high latitudes. This linkage was first proposed by H. Stommel in the 1960s and tested in a general circulation model by a number of investigators, most notably F. Bryan at Princeton University and T. Hughes at McGill University. Their results can be summarized in terms of the density difference between the light and dense waters $\delta\rho$ and the depth of the pycnocline D . In general they found that the Northern Hemisphere overturning circulation M_n scaled as the square of the pycnocline depth D ,

$$M_n = \frac{g\delta\rho D^2}{\rho_0\epsilon}, \quad (46)$$

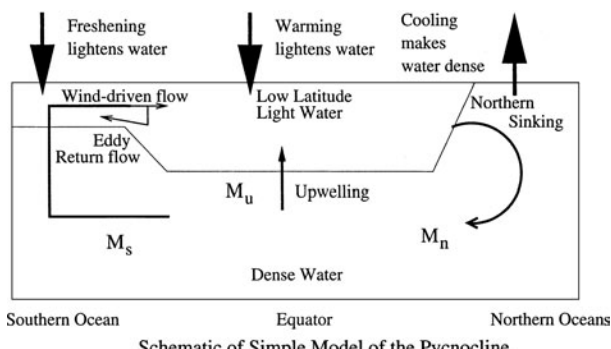


FIGURE 14 Schematic of intermediate-depth circulation driven either by Southern Ocean winds or by low-latitude diffusion.

where $1/\epsilon$ is a characteristic time scale. Y.-G. Park and J. Whitehead at Woods Hole showed that this relationship also holds in a laboratory model of the pycnocline.

There is a relatively simple physical argument why such a relationship should hold. Insofar as the coupled atmosphere–ocean system acts to maintain a relatively fixed temperature gradient between the low and high latitudes, some portion of the geostrophic flow of light water into the North Atlantic will automatically be converted into dense water and downwelled. The pressure difference which drives this flow is δp , given by

$$\delta p \sim \frac{g\delta\rho}{\rho_0} D = g'D. \quad (47)$$

All velocities in the system, whether the eastward flow within the gyres or the boundary current flow which feeds this eastward flow, will tend to scale as this pressure difference over some characteristic length scale L , which will be different for boundary layers and interior flows,

$$U \sim \frac{1}{\rho_0 f} \nabla p = \frac{g'D}{fL},$$

where U is a characteristic velocity scale. The mass transport associated with these flows will scale as

$$M_n = C * U * L * D = C * \frac{g'D^2}{f}, \quad (48)$$

where C is a constant of proportionality. Letting $\epsilon = f/C$ gives Eq. (46). Given $M_n = 18$ Sv, D of 600 m, and $\delta\rho/\rho$ of approximately 0.002 gives an ϵ of 0.005 sec⁻¹.

In order to truly understand how this system is driven, it is necessary to understand how the dense water is converted back into light water and how this process may itself depend on the pycnocline depth. There are essentially two possibilities. The first is that the dense water can upwell in low latitudes, experiencing as it does so a warming from the downward diffusion of heat. This would make the intermediate-depth circulation physically similar to that within the deep ocean. In this case the temperature balance would be

$$w \frac{\partial T}{\partial z} = K_v \frac{\partial^2 T}{\partial z^2}, \quad (49)$$

where w is the vertical velocity. This equation has a solution for constant w and K_v of

$$T = T_d + \delta T \exp(wz/K_v), \quad (50)$$

where T_d is the temperature of the abyss and δT is the difference between this temperature and the surface temperature. For such a solution, the pycnocline depth D scales as $D = K_v/w$. If one assumes uniform upwelling over the area A of the low-latitude pycnocline, then the upwelling transport is $M_u = wA$ and

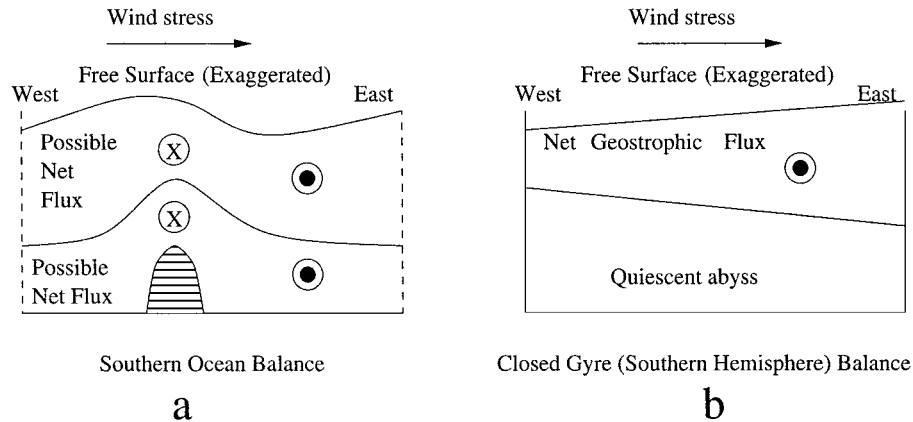


FIGURE 15 Illustration of how the open latitudes of the Southern Ocean are different from closed gyres. (a) Southern Ocean. Eastward winds drive a northward flux of water in the surface layer. This can be balanced by a geostrophic flow within the surface layer associated with surface pressure gradients (as shown) in which eastward pressure forces drive northward flow over ridges, where the layer is thin, and westward pressure forces drive southward flows over abyssal plains, where the layer is thick. Insofar as this is also true for the lower layer, this wind-driven flow can supply dense water to the Southern Ocean, which must then be converted to light water through freshening. (b) A contrasting case from the subtropical gyres. Here, the wind stress can pile up light fluid in the upper layer against one boundary, so that the winds need not be associated with any flow in the lower layer.

$$M_u = \frac{K_v A}{D}. \quad (51)$$

In the event that the temperature and salinity differences between low and high latitudes are fixed (the case when this is not true is considered later in this section), equating Eqs. (46) and (51) implies that

$$D \propto (\delta\rho)^{-1/3} K_v^{1/3}, \quad M \propto (\delta\rho)^{1/3} K_v^{2/3}, \quad (52)$$

so that the transport of the overturning is closely related to the magnitude of the diffusion coefficient. Given the area of the low-latitude ocean (approximately $2.4 \times 10^{14} \text{ m}^2$), the depth of the pycnocline (approximately 600 m), and an overturning of approximately 18 Sv, it is possible to use (51) to estimate the required diffusion coefficient as around $0.43 \text{ cm}^2/\text{sec}$. This value is approximately three times that found by tracer release experiments in the pycnocline.

An alternative approach is to assume that the transformation of light to dense water primarily occurs in the Southern Ocean. This idea has been championed by J. R. Toggweiler of the NOAA Geophysical Fluid Dynamics Laboratory and is increasingly gaining credence in the general community. The Southern Ocean is a special region for one main reason. At the latitudes of the Drake Passage, between the southern tip of South America and the Antarctic Peninsula, it is possible to follow a latitude circle around the world without encountering topography above a depth of 2000 m or so. This means that if one integrates the velocity along a latitude circle at some depth above 2000 m, the mean geostrophic velocity must in-

tegrate out to zero. However, because there are westerly winds at these latitudes, there is a strong Ekman transport in the northward direction, so water is being exported from the system. This flow must be compensated somehow.

Figure 15 illustrates how this compensation occurs. The surface and internal interfaces deform in the vicinity of topography, resulting in flows in both the upper and lower layers. Depending on the phasing of the interfacial flows, these flows may result in net transport in either the upper or the lower layer. If the internal interface is aligned with the topography so that the thickness of the lower layer is constant, no net flux of water will occur within this layer. As shown in the figure, northward flow will then occur within the upper layer where it is thin, and southward flow will occur within the upper layer where it is thick, resulting in a net transport of fluid to the south. On the other hand, if the internal interface is aligned with the surface so that the upper layer height is constant, the same process will occur in the lower layer. The northward Ekman flow can then be supplied by upwelling which has its roots deep in the water column, thus allowing for relatively dense deep waters to be brought to the surface. This means that within the Southern Ocean, in contrast with the low-latitude gyre circulation discussed in the previous subsection, the effects of wind forcing are felt all the way to the bottom.

Reality probably lies somewhere between the two extremes discussed above. It is unlikely that the entire Ekman flux is supplied from the deep ocean, and implicitly from the North Atlantic Deep Water. Estimates of the Ekman flux at the northern tip of Drake Passage are between 30 and 40 Sv, about twice the magnitude of the flow of North

Atlantic Deep water. The remainder must be supplied by lighter waters.

Theoretical studies support the idea that this flow of light water is intimately linked to transient eddies. Such eddies tend to homogenize the potential vorticity field, which over short distances corresponds to homogenizing layer thickness. This is associated with a pressure stress exerted between layers in which pressure gradients in the upper layer act across minima or maxima in upper-layer thickness. It has been hypothesized that the transient eddy mass flux might be represented as a diffusion of layer thickness

$$M_{\text{eddy}} = A_I L_x D / L_y^s, \quad (53)$$

where A_I is a diffusion coefficient, L_x is the length of a circumpolar transect, and L_y^s is the length scale over which the pycnocline shoals in the south. It is possible that A_I itself may depend on the local slope of the pycnocline; for example, in one proposed closure

$$A_I = ANDL_y^s, \quad (54)$$

where A is a dimensionless constant and $N = \sqrt{(g/\rho)\partial\rho/\partial z}$ is the buoyancy frequency (the frequency at which parcels moved vertically in the water column will tend to oscillate). If an overall mass balance holds, then

$$\begin{aligned} M_n &= \frac{g\delta\rho}{\rho} \frac{D^2}{\epsilon} = \frac{K_v A}{D} + L_x \left(\frac{\tau_s}{\rho|f_s|} - \frac{A_I D}{L_y^s} \right) \\ &= M_u + M_{\text{ekman}} - M_{\text{eddy}}, \end{aligned} \quad (55)$$

where τ_s and f_s are the wind stress and Coriolis parameter in the Southern Ocean. Equation (55) gives a cubic equation in the pycnocline depth D . As seen in Fig. 16, the solutions of this equation result in an overturning circulation of about the right magnitude either with strong Southern Ocean eddies and high diffusion (in which case all the transformation of water occurs at low latitudes) or

with low diffusion and Southern Ocean eddies (in which case all the transformation of water occurs in the Southern Ocean). Based on the best available estimates of water flow and diffusion, it is probable that the Southern ocean pathway accounts for about two-thirds of the transformation of dense water. It is thus likely that Southern Ocean winds play an important role in driving the overturning circulation.

The situation is somewhat complicated by the fact that the density gradient itself is a function of the flow. A simple way of thinking about this is as follows. The radiative balance between incoming solar and outgoing infrared radiation might be thought of as restoring the temperature gradient between low and high latitudes. If $\Delta T = T_l - T_h$, then one can think of the equation for the gradient as

$$\frac{\partial}{\partial t} \Delta T = \gamma(\Delta T_0 - \Delta T) - \frac{M_n}{V} \Delta T, \quad (56)$$

where γ is a restoring rate, ΔT_0 is the temperature difference between low and high latitudes at radiative equilibrium, and V is some characteristic volume. Similarly, if $\Delta S = S_l - S_h$, the equation for δS can be written

$$\frac{\partial}{\partial t} \Delta S = F_w S_0 - \frac{M_n}{V} \Delta S, \quad (57)$$

where F_w is the net flux of freshwater and S_0 is an averaged salinity. In general, the freshwater flux tends to oppose the overturning circulation, while the heat fluxes tend to reinforce it.

At steady state

$$\frac{\delta\rho}{\rho} = \tilde{\alpha} \Delta T + \tilde{\beta} \Delta S = \frac{\tilde{\alpha} \Delta T_0}{1 + M_n/V\gamma} + \frac{\tilde{\beta} F_w S_0 V}{M_n}, \quad (58)$$

where $\tilde{\alpha}$ and $\tilde{\beta}$ are the expansion coefficients for heat and salinity. Thus as the overturning increases, the temperature and salinity gradients driving it tend to decrease.

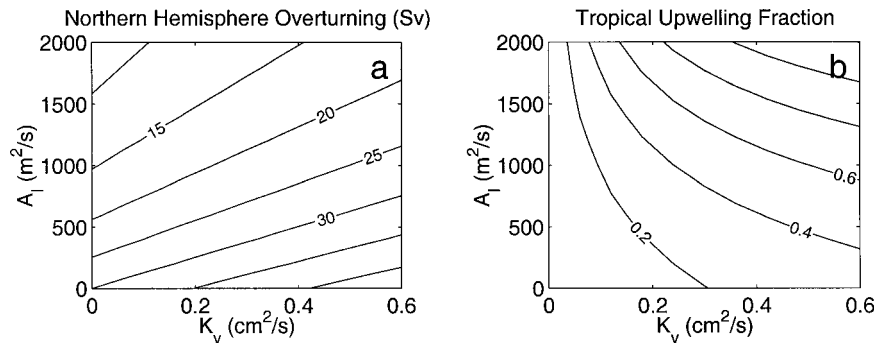


FIGURE 16 Solutions of (55) for an Ekman flux of 30 Sv ($1 \text{ Sv} = 10^6 \text{ m}^3/\text{sec}$) for different values of Southern Ocean eddy mixing (A_I) and vertical diffusion within the low-latitude pycnocline (K_v). (a) Northern Hemisphere overturning in Sverdrups (estimates from data are between 15 and 20). (b) Fraction of this upwelling which goes through the tropical pycnocline.

It is possible to generalize Eq. (55) to include this feedback. Two limits of the resulting solution are of particular interest. The first is one where the mixing is stipulated to fix the pycnocline depth D and the radiative forcing is very strong so that $\gamma \gg M_n/V$ and the temperature gradient is essentially fixed. In this limit, first explored by H. Stommel in 1961, the following relationship between overturning circulation and freshwater flux can be derived:

$$M_n^2 - \frac{gD^2}{\epsilon}(\tilde{\alpha}\Delta T_0)M_n = \frac{gD^2}{\epsilon}(\tilde{\beta}S_0F_wV), \quad (59)$$

so that M_n is a parabolic equation in F_w . When there is no freshwater flux, the heat fluxes drive an overturning with transport $M_T = gD^2(\tilde{\alpha}\Delta T)/\epsilon$. As the freshwater flux increases, the overturning circulation decreases. The decrease is quadratic rather than linear, as the weakening overturning circulation allows for stronger and stronger salinity gradients to build up. When the overturning reaches one-half its value in the absence of freshwater forcing, it collapses and the overturning circulation reorganizes as a circulation which has sinking in the salty tropics and upwelling in the fresh poles. It has been argued that such a pattern of ocean circulation was actually found in the real ocean during the early Cretaceous, though this is still controversial.

The second limit is one in which the wind-driven flux from the south is fixed, but low-latitude diffusion and eddy mixing are zero. In this limit, the overturning flux in the north must equal the upwelling in the south, as long as the water in the north can become denser than the surface water in the south. In this limit, the depth of the pycnocline will increase as the freshwater flux into the Northern Hemisphere increases, but the overturning will remain constant until the freshening of the water in the north is strong enough that the North Atlantic Deep Water becomes lighter than Antarctic Intermediate Water. At this point the thermohaline circulation undergoes a catastrophic reorganization.

The question of whether it is broadly distributed diapycnal diffusion or wind-driven upwelling and surface processes in the Southern Ocean that is predominant in governing the conversion of dense waters back into intermediate waters has profound implications for the dynamics of the ocean. Much of the deeper diapycnal mixing is now thought to be due to internal waves and turbulence-generated deep tidal flows over rough topography. As both tidal forcing and abyssal topography change only over geologic time scales, it might be reasonable to expect that this mixing should itself be relatively invariant with time. If, on the other hand, the conversion is largely mediated by the Southern Ocean wind and buoyancy fluxes, much greater variability can be expected. In particular, the possibility of very low frequency coupled ocean-atmosphere

fluctuations emerges, with time scales governed by the slowness with which the deep ocean is flushed. Low-frequency oscillations, with time scales of decades, have been described both observationally and in models as arising from the dynamics of the sinking regions. However, ocean models which have been run for the required hundreds of years have invariably been much more diffusive than the real ocean, and it is a matter of continuing research how wind-driven control of upwelling may help explain the past variations of the earth's climate system.

IV. CONCLUSIONS

This article has described the dynamical processes which control the large-scale structure of the temperature, salinity, density and nutrient fields in the global ocean. To summarize, the ocean circulation can be broken up into three regimes

1. A surface, wind-driven regime characterized by upwelling at high latitudes and along the equator and wind-driven downwelling at midlatitudes. This circulation accounts for the bowl-shaped masses of warm, salty, nutrient-poor waters found in midlatitudes and for the horizontal, gyral circulations around these water masses. Circulation models do a reasonably good job at capturing this regime, and its dynamics are reasonably well understood.

2. A deep regime in which diapycnal mixing and bottom topography play important roles. Although many of the physical processes which must be involved in driving these deep circulations are well known, the exact ways in which these processes combine to produce the large-scale thermal structure of the deep ocean remain obscure. In particular, an understanding is only beginning to emerge of how the location of diapycnal mixing and the associated transfers of mass between density classes may be correlated with bottom topography and the large-scale circulation.

3. An intermediate regime in which either diapycnal mixing or wind driving (or both) can play an important role. Although there is considerable disagreement about which physical mechanism dominates, there is increasing evidence that the wind driving is important. The major piece of physics which is not understood in this respect is the role played by mesoscale eddies in returning the light surface waters which flow northward in the Ekman layer above the depth of the pycnocline. A particular question is the interaction of these eddies with large-amplitude bottom topography.

As this article makes clear, there are many unanswered questions regarding the physics which set the large-scale

structure of the ocean. These can be grouped broadly into three areas, which are anticipated to be major themes for the large-scale physical oceanography community. The first is the importance of understanding how the ocean interacts with the land beneath it. Bottom relief plays a major role in setting the location of diapycnal mixing (as internal waves tend to be more energetic near topography) and mixing associated with mesoscale eddies (which also tend to be more energetic downstream of topography). General theories for these processes remain to be developed. It is also unclear how fluid which is in contact with the bottom actually propagates into the ocean interior and how its potential vorticity changes as it does so.

A second area where more remains to be done is a development of a better understanding of how the oceanic circulation interacts with the atmosphere above it. This was hinted at in the final section for the thermohaline circulation, but the actual physics involved in this problem is likely to be much more complicated than discussed there, involving the details of geography, sea ice, atmospheric thermodynamics, and the ocean's nonlinear equation of state. The dynamics of coupling between the midlatitude ocean and the atmosphere remains controversial as well. The midlatitudes are particularly difficult to study because it is unclear how changes in ocean temperature affect atmospheric circulation. Even in the tropics, where such relationships can be found and are reasonably robust, coupled models are not always able to predict important phenomena such as the Southern Oscillation (discussed in more detail elsewhere in this work).

A final area for future research is the role of mesoscale eddies. As seen in Section III.C, these eddies can play a significant role in the circulation of intermediate water, and they are also probably responsible for the homogenization of the potential vorticity field seen in Fig. 8. The

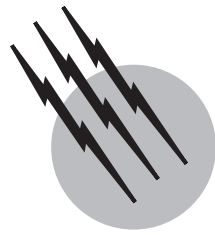
basic kinematics of these eddies is only starting to become apparent as variations in sea surface height are measured using satellite altimeters. Observationally, the effect of such eddies on the potential vorticity field and circulation remains to be characterized, especially in such key regions as the Southern Ocean. The interaction of eddies with the surface and bottom is also a subject about which much remains to be understood.

SEE ALSO THE FOLLOWING ARTICLES

- FLUID DYNAMICS • GAS HYDRATE IN THE OCEAN ENVIRONMENT • OCEAN-ATMOSPHERIC EXCHANGE
- OCEANOGRAPHY, CHEMICAL • OCEAN SURFACE PROCESSES • OCEAN THERMAL ENERGY CONVERSION
- PHYSICAL OCEANOGRAPHY, OCEANIC ADJUSTMENT • STREAMFLOW

BIBLIOGRAPHY

- Gill, A. E. (1982). "Atmosphere Ocean Dynamics," Academic Press, New York.
- Gnanadesikan, A. (1999). "A simple model for the structure of the oceanic pycnocline," *Science* **283**, 2077–2079.
- Ledwell, J. R., Watson, A. J., and Law, C. S (1993). "Evidence for slow mixing across the pycnocline from an open-ocean tracer-release experiment," *Nature* **364**, 701–703.
- Luyten, J. R., Pedlosky, J., and Stommel, H. M. (1983). "The ventilated thermocline," *J. Phys. Oceanogr.* **13**, 292–309.
- Macdonald, A. M., and Wunsch, C. (1996). "An estimate of global ocean circulation and heat fluxes," *Nature* **382**, 436–439.
- Pedlosky, J. (1996). "Ocean Circulation Theory," Springer-Verlag, Heidelberg.
- Samelson, R., and Vallis, G. K. (1997). "Large-scale circulation with small diapycnal diffusivity: The two-thermocline limit," *J. Marine Res.* **55**, 1–54.



Soil Mechanics

John T. Christian

Consulting Engineer, Waban, Massachusetts

- I. Basic Relations and Classification
- II. Flow Through Porous Media
- III. Settlement and Consolidation
- IV. Strength
- V. Special Soils

GLOSSARY

- Atterberg limits** Water contents at which the soil changes behavior.
- Coefficient of consolidation** Coefficient in consolidation equation.
- Compression index** Slope of $e - \log p$ line.
- Consolidation** Decrease of volume due to expulsion of water from the pores.
- Effective stress** Total stress minus the pore fluid pressure in a saturated soil.
- Hydraulic conductivity** Ratio between approach velocity and hydraulic gradient.
- Maximum past pressure** Maximum vertical effective stress to which a soil has been loaded in the past.
- Mohr-Coulomb strength** Shear strength expressed as a function of apparent cohesion and the tangent of a friction angle.
- Normal consolidation** Situation in which the present effective vertical stress is the maximum past pressure.
- Overconsolidation** Situation in which the present effective vertical stress is less than the maximum past pressure.
- Pore pressure** Pressure in the fluid in the pores of a soil (usually water).

Relative density Relative value of void ratio between maximum and minimum values.

Total stress Stress evaluated across the entire area of the soil regardless of pores and grain contacts.

Void ratio Ratio between volume of voids and volume of solids.

Water content Ratio between the weight of water in the pores and weight of solids.

SOIL MECHANICS deals with the mechanical behavior of soils—those naturally deposited and those placed by human agencies during construction. It provides the mechanical basis for geotechnical engineering. Its emphasis on the engineering behavior of soils distinguishes it from the related fields of soil physics, pedology, agronomy, and geology, although all these disciplines overlap at the edges. Because of the importance of both static and flowing water in soil mechanics, the field shares many interests with ground water hydrology. The principal applications of soil mechanics are in the design and construction of foundations, dams and levees, underground facilities, and other engineered facilities built on, in, or out of soil.

Almost all the problems that soil mechanics addresses fall into one or more of three categories: flow through

porous media, deformation and settlement, or strength and stability. Examples of the first group include the seepage of water through or under dams and transport of pollutants by groundwater flow. The leaning tower of Pisa is a classic illustration of excessive settlement, as are the subsidence problems in Mexico City and Venice. Landslides are well-known examples of instability. Some situations fall into two or all three categories. The following sections deal with each category in turn.

In all three types of problems, the analyst begins by developing a mechanical or physical model and then determines the relevant mechanical properties. Traditional methods of solving the resulting formulations were either analytical or graphical; many are identical to solutions used in other fields of science and engineering. Digital computers have now allowed numerical methods to supplant many traditional approaches. Furthermore, advances in laboratory modeling—especially centrifuge testing—have made physical modeling an attractive alternative for many complicated problems. Regardless of the methods used to attack a particular problem, the underlying physical principles remain the same.

I. BASIC RELATIONS AND CLASSIFICATION

In addition to basic definitions and relations among the parameters describing a soil, engineers have developed index properties, which are relatively simple measurements that can be related empirically to mechanical properties. The wide variability of soils and the difficulty in obtaining sufficient quantities of good direct measurements of mechanical properties have made index properties essential tools for practical work.

A. Relations among Soil Phases and Unit Weights

Soil mechanics is concerned primarily with inorganic soils. A soil consists of three phases: solid matter, liquid (usually water), and gas (usually air). In the majority of cases, these phases are distinct, but some minerals, such as gypsum and halloysite, include water in their crystal structures, and the different phases must be identified with care. It is convenient to imagine an element of soil with unit cross-sectional area and with different phases segregated into three zones (Fig. 1). The weights of solids and water are designated W_s and W_w , respectively. The weight of air is neglected. The following definitions apply:

$$e = \text{void ratio} = V_v/V_s \quad (\text{dimensionless})$$

$$n = \text{porosity} = V_v/V_t = e/(1+e) \quad (\text{dimensionless})$$

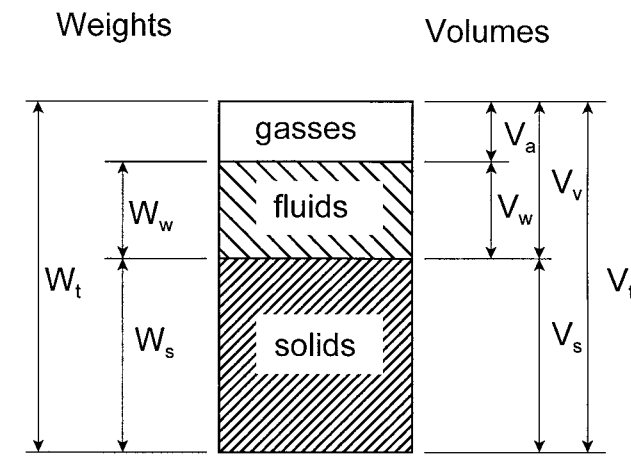


FIGURE 1 Soil phases and corresponding notation.

w = water content

$$= W_w/W_s \quad (\text{usually expressed as a percentage})$$

S = saturation

$$= V_w/V_v \quad (\text{usually expressed as a percentage})$$

$$\gamma_w = \text{unit weight of water} = W_w/V_w \quad (\text{N/m}^3)$$

$$\gamma_s = \text{unit weight of solids} = W_s/V_s \quad (\text{N/m}^3)$$

$$G = \text{specific gravity of solids} = \gamma_s/\gamma_w \quad (\text{dimensionless})$$

$$\gamma_t = \text{total unit weight} = (W_w + W_s)/V_t \quad (\text{N/m}^3)$$

G is 2.65 for quartz, the most common soil mineral, and has approximately the same value for most other soil-forming minerals. From Fig. 1 and the previously cited definitions,

$$\gamma_t = \frac{G + Se}{1 + e} \gamma_w.$$

The dry unit weight, γ_d , is the unit weight that would exist if all the water were removed with no change in volume:

$$\gamma_d = \frac{G}{1 + e} \gamma_w.$$

The buoyant unit weight, γ_b , is the apparent unit weight of a fully saturated soil submerged in water:

$$\gamma_b = \gamma_t - \gamma_w = \frac{G - 1}{1 + e} \gamma_w.$$

Reference to Fig. 1 and the previously cited definitions yields other useful relations, including

$$Gw = Se.$$

For granular soils, especially sands, the *relative density*, D_r , indicates how the actual void ratio compares to the maximum and minimum values that the soil can exhibit:

$$D_r = \frac{e_{\max} - e}{e_{\max} - e_{\min}} \times 100\% \\ = \frac{\gamma_{d\max}}{\gamma_d} \times \frac{\gamma_d - \gamma_{d\min}}{\gamma_{d\max} - \gamma_{d\min}} \times 100\%.$$

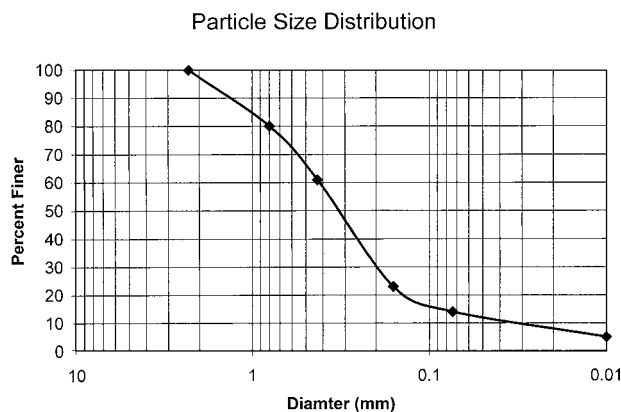


FIGURE 2 Particle size distribution from sieve analysis.

B. Grain Size Distribution

The relative amounts of different sizes of grains in a soil are determined by shaking a sample of the soil through a stacked series of sieves with progressively smaller openings. The percentage by weight retained on each sieve is calculated and the cumulative results plotted in the manner of Fig. 2. The data points tend to fall on an inverted “S” curve. The symbol D_x denotes that x percent of the soil is finer than diameter D . By convention, the *uniformity coefficient* of the soil (C_u) is

$$C_u = D_{60}/D_{10}.$$

A soil with a limited range of grain sizes has a low C_u (<2) and is said to be *uniform*. A soil with a wide range of grain sizes is said to be *well graded*. Types of granular soils are identified by their ranges of particle sizes, as shown in Table I. The numbers in parentheses are the openings in the #4 (4.76-mm) and #200 (0.074-mm) sieves, which are often used as alternate practical boundaries between soil types. When it is necessary to describe the grain size curves for material smaller than the #200 sieve, a technique using a hydrometer and based on Stokes’ Law is used.

The distinction between clays and other types of soils arises primarily from differences in mineralogy rather than grain sizes. Silts, sands, and gravels are usually composed

TABLE I Grain Size Ranges

Name	Particle sizes
Boulder	>12 in.
Cobble	6 to 12 in.
Gravel	2.0 mm (4.76 mm) to 6 in.
Sand	0.06 to 2.0 mm (or 0.074 to 4.76 mm)
Silt	0.002 to 0.06 mm (0.074 mm)
Clay size	<0.002 mm

of quartz, feldspars, and other blocky minerals. Clays are made up of small plates of complex layered silicates such as kaolinite, illite, and montmorillonite or smectite. Therefore, the last entry in Table I is identified as “Clay Size” to indicate the usual size of clay minerals rather than a criterion for distinguishing clays.

C. Atterberg Limits

The behavior of fine-grained soils is determined more by their colloidal chemistry than by their grain sizes. The most useful practical indices of the behavior of clays and silts are the Atterberg limits, which are water contents at which the soil changes character. The *plastic limit*, w_p , is the water content at which the soil can just be rolled out in a thread 1/8 in. in diameter. The *liquid limit*, w_l , is the water content at which the soil loses enough of its strength to begin behaving like a liquid. The determination is done by specially designed laboratory devices—either a falling cone that penetrates the soil to a prescribed depth or a falling cup device containing a sample of soil cut into a prescribed slope that closes after a number of calibrated blows. Two very useful parameters derived from the Atterberg limits are:

$$\text{Plasticity Index, } I_p \text{ or P.I.} = w_l - w_p$$

and

$$\text{Liquidity Index, } I_l \text{ or L.I.} = w - w_p$$

where w is the natural water content.

D. Classification

Several systems exist for classifying soils, most developed for specific purposes such as pavement design. The most widely used system is the Unified Soil Classification System (USCS). Two upper-case letters identify the soil. The first identifies the most important component according to the following convention:

G	Gravel
S	Sand
M	Silt
C	Clay
O	Organic soil

Gravels and sands are further separated into two categories, depending on whether the content of fines (silts or clays) is significant. Clean gravels and sands (those with low fines content) are then identified by a second letter W if they are well graded or P if they are poorly graded. Gravels and sands with significant fines content are identified by a second letter M if the fines are primarily silts

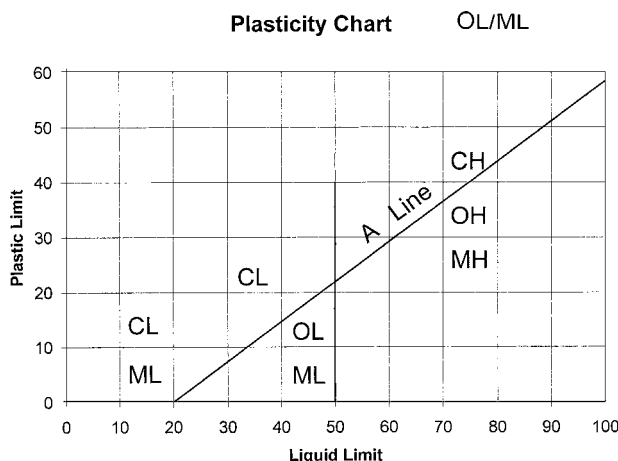


FIGURE 3 Plasticity chart.

or C if the fines are primarily clay. Thus, GW indicates a clean, well-graded gravel, and SC indicates a sand with significant clay content. Clays, silts, and organic soils are separated into those with high plasticity (denoted by H as the second letter) and those with low plasticity (denoted by L). Thus, CH indicates a highly plastic clay, and ML indicates a silt of low plasticity. The distinction between these categories of silts, clays, and organic soils is usually done by finding the appropriate region on the plot of liquid limit and plasticity index in Fig. 3. Most soils fall close to the "A" line. Finally, a special category is reserved for highly organic soils such as peat; these are labeled Pt.

E. Total Stresses, Pore Pressures, and Effective Stresses

The total stress at a point in a mass of soil is simply the Cauchy stress tensor for the soil treated as a continuum. Various notations are used in the literature. Sometimes a component of stress is identified by a doubly subscripted σ (e.g., σ_{xy}); sometimes a singly subscripted σ is used for a normal component (e.g., σ_x) and a doubly subscripted τ for shear components (e.g., τ_{xy}). The notations σ_v and σ_h are used to denote the vertical and horizontal normal components, respectively. When special notation is used, the meanings are usually clear from the context. Because almost all problems in soil mechanics deal with compression, it is customary to treat compression as positive. This is the reverse of the usual convention in engineering mechanics, and the sign convention for shear stress is usually reversed at the same time.

In a saturated soil, the pore pressure is the actual pressure in the pore fluid. It is usually denoted by the symbol u , except when confusion with symbols for displacement

requires using some other symbol such as p . Compression is positive.

By definition, the effective stress is the difference between the total stress and the pore pressure. It is denoted by a prime or a bar over the symbol for the normal component of stress. Thus

$$\bar{\sigma}_x = \sigma_x - u$$

or

$$\sigma'_x = \sigma_x - u.$$

The pore pressure affects only the normal components of the stress, not the shear components, so the total and effective shear stresses are identical.

A basic principle of soil mechanics is that the mechanical behavior of soil is controlled by effective stress, not total stress. The effective stress represents the effect of that portion of the total stress transmitted by forces between the particles. However, it is not a direct measure of the contact forces. The equation for effective stress assumes that the soil is saturated. If it is not, an equivalent relation involving the gas as well as liquid phases must be used, but there is not consensus on the precise form such a relation should assume in all cases.

II. FLOW THROUGH POROUS MEDIA

The flow of a liquid—usually water—through a porous medium is essentially a field problem and can be approached by the same mathematical techniques used to solve other field problems such as those in electromagnetism and heat flow. The basic formulation derives from Bernoulli's energy equation. The geotechnical engineer deals with problems of seepage and is often most interested in the pore fluid pressures. The groundwater hydrologist deals with problems of groundwater flow and is most interested in the quantities and patterns of flow. Both are working in the same technological area and with essentially the same tools.

A. Heads

A datum is an arbitrary elevation from which all other elevations and distances are measured. At any point in a water-saturated soil three heads are defined:

h_e —the elevation head—the vertical distance between the point in question and the datum, positive upward

h_p —the pressure head $= u/\gamma_w$ —the fluid pressure divided by the unit weight of the fluid

h_t —the total head $= h_e + h_p$

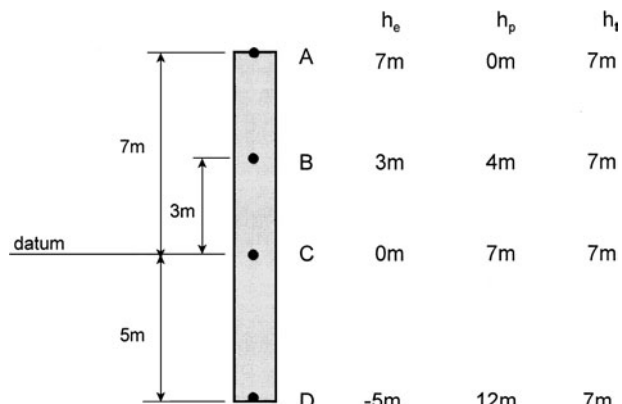


FIGURE 4 Definitions of heads.

Because the seepage velocities are low, the velocity head can be ignored. Figure 4 applies these definitions to several points along a standing column of water saturated soil.

B. Darcy's Law

Darcy's Law is the basic relation describing flow through a porous medium. For the conditions in Fig. 5, and with the assumption that flow is slow enough that contributions due to velocity heads and turbulence can be ignored, it states that

$$v = -ki,$$

where v is the approach velocity explained further below, k is a coefficient, and i is the gradient in the total head. A more general set of expressions for the components of flow in an isotropic material is

$$v_x = -k \frac{\partial h_t}{\partial x}$$

$$v_y = -k \frac{\partial h_t}{\partial y}$$

$$v_z = -k \frac{\partial h_t}{\partial z}$$

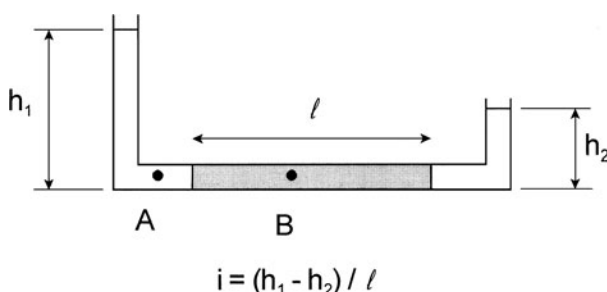


FIGURE 5 Definitions for Darcy's Law.

The terms in Darcy's Law require some explanation:

1. The velocity v is the *approach velocity*. That is, it describes the velocity of fluid as it approaches the porous medium at, say, point A in Fig. 5. Once the fluid enters the porous medium, the solids force the fluid to accelerate to the *superficial velocity* v_s , which is what an external observer would see at, say, point B. Continuity requires that the two velocities be related by $v_s = v/n$. Actually, v_s is an average velocity; the individual fluid particles follow tortuous paths among the solid grains so that the instantaneous velocity of a particle varies erratically in magnitude and direction.
2. The coefficient k has units of velocity. It is now called the *hydraulic conductivity*, but earlier texts referred to it as the *permeability*. The term permeability (sometimes specific or intrinsic permeability) is now reserved for a measure of the grain structure that has units of distance squared. If this permeability is κ and the dynamic viscosity of the fluid is μ , then $k = \kappa \gamma_w / \mu$. It should be noted that k includes the contribution of both the grain structure and the fluid properties and it is necessary to account for this when doing similitude calculations. There are three ways to determine k . The first is to use empirical correlations, such as Hazen's relation $k = 0.01 D_{10}^2$, where k is in m/sec and D_{10} in mm. The second is to test the material in the laboratory. The third is to run field tests such as pumping tests.

In the general anisotropic case, k is not a scalar but has different values in different directions. With the convention that $f_{,x}$ means $\partial f/\partial x$ and dropping the subscript t from the total head, the general anisotropic form of Darcy's Law becomes, in matrix notation,

$$\begin{Bmatrix} v_x \\ v_y \\ v_z \end{Bmatrix} = - \begin{bmatrix} k_{xx} & k_{xy} & k_{xz} \\ k_{yx} & k_{yy} & k_{yz} \\ k_{zx} & k_{zy} & k_{zz} \end{bmatrix} \begin{Bmatrix} h_{,x} \\ h_{,y} \\ h_{,z} \end{Bmatrix}.$$

The matrix of k 's must be symmetric. Furthermore, a great many practical cases involve horizontally bedded soils, for which the principal axes must be horizontal and vertical. Then

$$v_x = -k_{xx}h_{,x} \quad v_y = -k_{yy}h_{,y} \quad v_z = -k_{zz}h_{,z}.$$

A further simplification occurs when there is no flow in one coordinate direction, say z :

$$v_x = -k_{xx}h_{,x} \quad v_y = -k_{yy}h_{,y}.$$

C. Laplace's Equation and Its Solution

In the isotropic case, continuity of flow in and out of an elemental volume leads to Laplace's equation:

$$\frac{\partial^2 h}{\partial x^2} + \frac{\partial^2 h}{\partial y^2} + \frac{\partial^2 h}{\partial z^2} = \nabla^2 h = 0,$$

or, in two dimensions,

$$\frac{\partial^2 h}{\partial x^2} + \frac{\partial^2 h}{\partial y^2} = \nabla^2 h = 0.$$

This is the form that is usually solved. The boundary conditions can be of three types: (a) h specified, (b) normal gradient of h specified, and (c) linear combination of h and its gradient specified. In practice, the first two are the most common, and type (b) usually is expressed as a condition of no outward flow.

Figure 6a shows a typical problem; seepage occurs under a dam with a partial cutoff below the dam. Along AB, h_t is 10 m. Along GH, h_t is 0 m. The boundaries BCDEFG and IJ have conditions of no flow across the boundary. A classical method of solution is the *flow net*, illustrated in **Fig. 6b**. The region is divide by two sets of lines, which must satisfy the following conditions:

- a. The boundaries with specified constant h_t are equipotentials.
- b. The boundaries with no flow across them are stream lines.
- c. Equipotentials and stream lines must intersect orthogonally.
- d. The curvilinear quadrilaterals defined by a pair of adjacent stream lines and a pair of adjacent equipotentials must be equidimensional (i.e., "curvilinear squares").

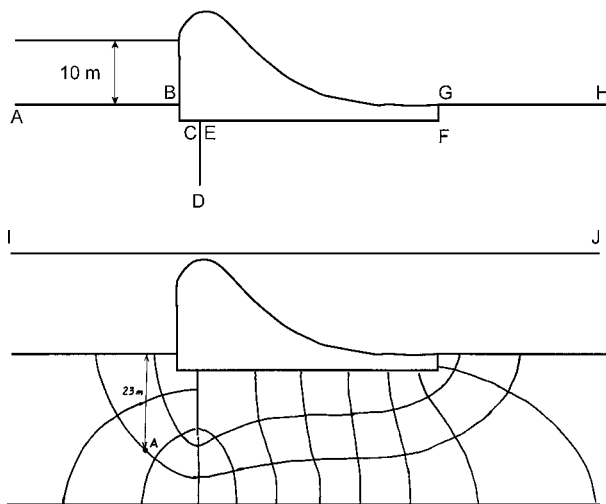


FIGURE 6 Seepage under the cross-section of a dam with a cutoff. (a) Problem geometry, (b) flow net solution.

With practice, flow nets can be drawn quickly for most practical isotropic cases. Sometimes it is not possible to draw a net with an integral number of stream paths and head drops and partial "quadrilaterals" must be used. However, the proportions of the partial figures must remain constant.

If the number of stream paths (paths between stream lines) is n_f and the number of head drops (spaces between equipotentials) is n_d , the total flow through a section 1 unit thick into the paper is

$$Q = k \cdot \frac{n_f}{n_d} \cdot \Delta h,$$

where Δh is the total head drop across the region and the ratio n_f/n_d is called *the shape factor*. For the problem in **Fig. 6**, n_f is 3, n_d is 10.4, and Q is approximately $2.88k$. To compute the fluid pressure at a point one first finds the total head by counting the number of head drops to the point, subtracting the elevation head, and multiplying the result by the unit weight of the fluid. For example, at point A in **Fig. 6b**,

$$h_t = \left(\frac{10.4 - 1.7}{10.4} \right) \cdot 10 \text{ m} = 8.84 \text{ m}$$

$$h_e = -23 \text{ m}$$

$$h_p = 8.84 - (-23) = 31.84 \text{ m}$$

$$u = (31.84 \text{ m})(10^4 \text{ N/m}^3) = 3.184 \times 10^5 \text{ N/m}^2 \\ = 0.32 \text{ MPa.}$$

A frequently encountered case is one in which the top surface (the phreatic surface) is unconstrained. It is both a steam line and a boundary along which $h_p = 0$, but its location is initially unknown. The solution is obtained by adjusting the flow net until the change in elevation for each head drop along the phreatic surface is the same. The quantity of flow and the pressure anywhere in the region are found in the same way as in the case of confined flow.

If $k_x \neq k_y$, a flow net can still be drawn by transposing the geometry into new coordinates (u, v) :

$$u = \sqrt{\frac{k_v}{k_h}} \cdot x \quad v = y.$$

The isotropic flow net is drawn in the transformed space and then transformed back into the original geometry of the problem. Again the pore pressures are found as in the isotropic case, and

$$Q = k_{\text{eff}} \cdot \frac{n_f}{n_d} \cdot \Delta h,$$

where $k_{\text{eff}} = \sqrt{k_h k_v}$.

Today, numerical methods, especially the finite element method, are commonly used to solve steady-state flow

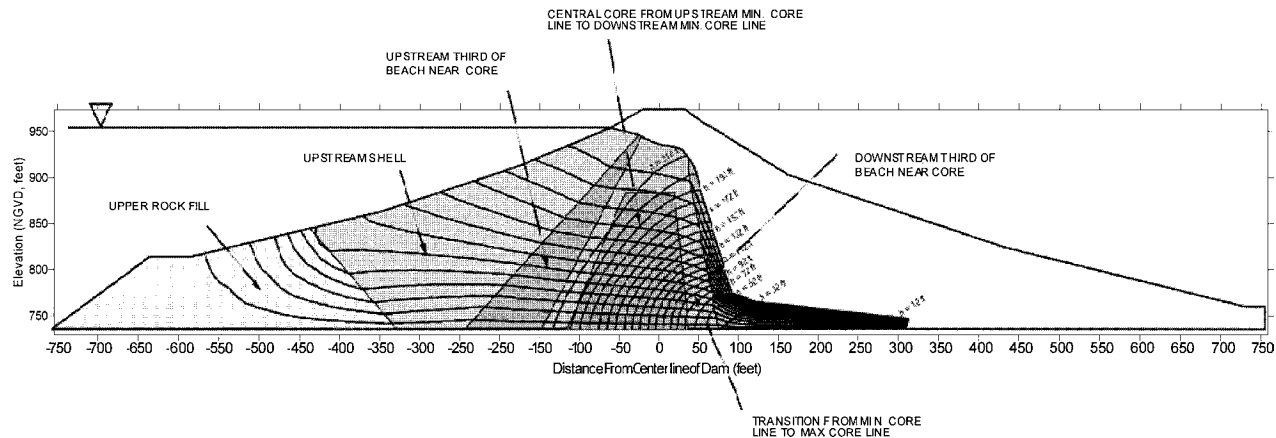


FIGURE 7 Flow net for seepage through a dam with anisotropic, inhomogeneous properties, and a phreatic surface.

problems. Almost all commercially available finite element programs can plot the equipotentials; a few can also plot the stream lines as well to give a full flow net. Numerical methods are especially useful when there are several regions with different hydraulic conductivities and when anisotropy is present. Figure 7 shows a flow net drawn by a finite element program for the principal cross section of a dam with anisotropic, inhomogeneous conductivities and a phreatic surface. Numerical methods are also the tools of choice for problems in three dimensions or those in which it is necessary to compute the transient development of the flow regime.

III. SETTLEMENT AND CONSOLIDATION

The most important deformations that the geotechnical engineer must address are the settlements of structures founded on or near the surface. There are two parts to this problem: estimating the total settlements and estimating the rate at which the settlements will occur. Most practical settlement analyses are carried out using extensions of linear elastic theory, but modern numerical methods now include nonlinear, elastoplastic constitutive relations that provide better estimates of deformations.

A. Compression Relations

Experimental observations reveal that the load-deformation behavior of a soil follows the general pattern illustrated in Fig. 8. If a horizontal soil layer is placed in a confining ring and loaded vertically, void ratio decreases gradually until the effective stress reaches a critical level. As the load increases beyond this level, the incremental change in void ratio increases dramatically. In a plot of void ratio e versus the logarithm (base 10) of the effective vertical stress, the downward slope of the relation is

called the *compression index*, C_c . Sometimes the plot is not a straight line, so C_c is said to vary with the applied load or the void ratio. Since the load applied in the laboratory is often designated by the letter p , a plot like Fig. 8 is called an “ $e - \log p$ plot.”

Figure 8 further shows that if the load is carried up to some level, then reduced, and then reapplied, only a portion of the compression is recovered during rebound. Some of the decrease in volume is retained, and the shape of the recompression curve resembles that of the original loading curve. The effective stress at which the reversal occurred is called the *maximum past pressure*. A soil that exists at its maximum past pressure (i.e., a soil that has never been loaded beyond the present level) is said to be *normally consolidated* and to lie on the virgin compression curve. A soil loaded at level lower than the maximum past pressure is said to be *overconsolidated*, and the ratio between its maximum past pressure and the present vertical effective stress is the *overconsolidation ratio* (OCR).

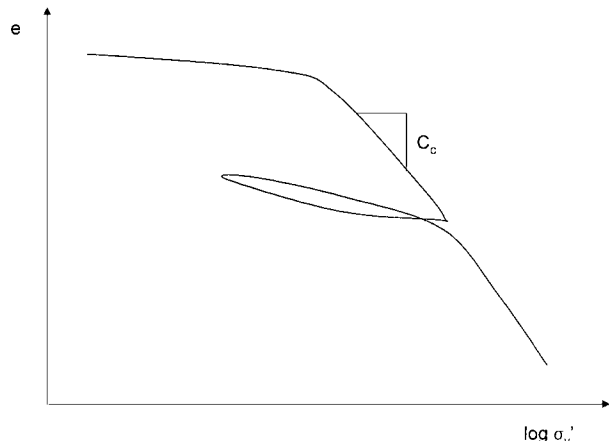


FIGURE 8 Loading, unloading, and reloading of a compressible soil.

Determining the maximum past pressure from tests on samples of a soil can be difficult. Disturbance during sampling operations tends to make the break in the compression curve less distinct. The most common procedure, developed by A. Casagrande is to find the point of maximum curvature and draw a tangent and a horizontal line through that point. The angle between the two lines is bisected. The intersection between the bisector and the extension of the virgin line defines the maximum past pressure. Other, sometimes more accurate, constructions have also been proposed.

The apparent shape of the compression curve and its location on the plot are affected by the way the test is run. If the load increments are left on longer or applied more slowly, the measured void ratio is smaller for a particular value of effective vertical stress. One convention is to load the sample by doubling the load at each increment and leaving each load on for a predetermined time such as 24 hr. Another approach that is increasingly favored is to compress the sample at a constant, slow rate of strain and to measure the corresponding pore pressure and applied load.

B. Secondary Compression

When a sample is tested in one-dimensional compression, the deformation versus time for a given load increment does not follow the pattern of Fig. 9a predicted by linear consolidation theory. Instead it exhibits a continuing deformation after the excess pore pressure has largely dissipated (Fig. 9b). This is called *secondary compression* and is usually considered to be linear with the logarithm of time.

The proper treatment of secondary compression is the subject of some controversy. It is clearly a viscous component of behavior that continues to occur after the elastic and plastic deformations have taken place. One position is that the secondary compression—or viscous component—is present throughout the consolidation process. The relative contributions of the viscous and elastic—plastic components are determined by the relative rates of deformation allowed by the viscous constitutive relation and by hydraulic dissipation. Another view is that secondary compression occurs only after the excess pore pressure has dissipated—the so-called “end of primary” consolidation. Most researchers adhere to the former view, but there is a strong minority that holds to the latter. If viscous behavior occurs throughout the consolidation process, it explains a great deal of the influence of loading rates and loading increments.

Secondary compression occurs in all soils. It is most important in clays because the magnitude of the compression can be large. However, the ratio of secondary to primary compression can be just as large in sand. It is usually

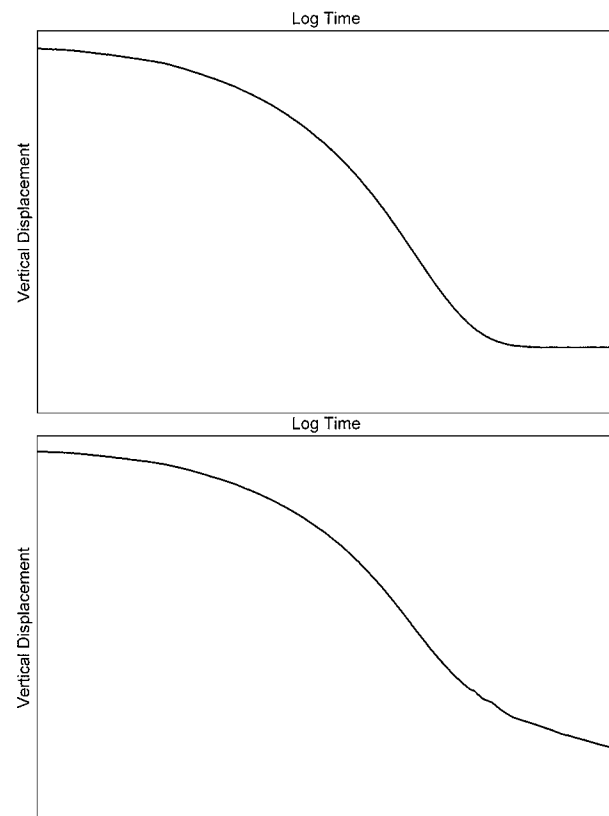


FIGURE 9 Consolidation deformation versus time. (a) Without secondary compression, (b) with secondary compression.

neglected in sands because the primary and secondary settlements tend to be small.

C. Settlement Analysis

The most important use of compression and consolidation theory is in the analysis of settlements, both in the design of new structures and in the evaluation of existing facilities. It is a major analytical component of foundation engineering. The general procedure is as follows:

1. Divide the compressible soils into several layers for computational purposes.
2. Evaluate the distribution of initial void ratio (e_0), vertical total stress, pore pressure, and vertical effective stress (σ_v^*) in the various layers of the profile before the new foundation loads are applied.
3. Evaluate the increment of vertical stress ($\Delta\sigma_v$) in each layer caused by the new loading.
4. At each layer determine whether the existing vertical effective stress plus the increment of vertical stress is greater or less than the maximum past pressure.
5. If the result of Step 4 is less than the maximum past pressure, compute the vertical strain in that layer

- according to the recompression part of the curve of Fig. 8.
6. If the result of Step 4 is greater than the maximum past pressure, compute the vertical strain in that layer as the sum of the strain computed along the recompression curve from $\bar{\sigma}_{v0}$ to the maximum past pressure and the strain computed along the virgin curve from the maximum past pressure to the final value of vertical effective stress.
 7. Add the contributions of all layers to obtain the final settlement.

To obtain an estimate of the development of the settlement versus time, it is necessary to estimate the excess pore pressure caused by the application of the load. In many cases this is equal to the vertical load increment. Once the initial excess pore pressure is known, consolidation theory gives an estimate of the development over time. Often the solution for a uniform layer with uniform initial excess pore pressure gives adequate results, but the actual situation may be more complicated. Numerical methods are often employed in the latter case.

D. Linear, One-Dimensional Consolidation

In soil mechanics, “consolidation” refers to the compression of a soil over time as fluid is expelled from the pores. Terzaghi’s formulation and solution of this problem in the 1920s is usually taken to mark the beginning of modern soil mechanics. Figure 10 illustrates a typical situation. A wide load q is placed over a deposit that includes a layer of clay that is much more compressible and less permeable than the layers above and below it. Since the clay is saturated and the pore fluid is much less compressible than the soil skeleton, the load must initially be carried by the pore fluid. Thus, there is an initial *excess pore pressure* $u_e = q$. (Note that there already is a hydrostatic pressure in the pore fluid, but this does not affect the following analysis.) Let the increment of vertical strain in an element of

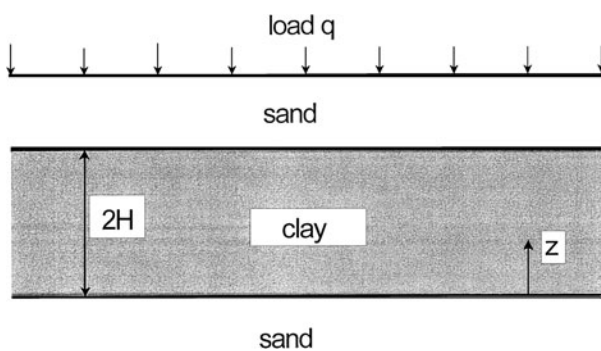


FIGURE 10 Geometry for one-dimensional consolidation.

the clay, $\Delta\varepsilon_v$, be related to a change in vertical effective stress, $\Delta\sigma_v$, by

$$\Delta\varepsilon_v = m_v \Delta\bar{\sigma}_v \quad (\text{compression positive}).$$

Because the load and the layering extend widely in all horizontal directions, all flow and deformation can be assumed to be vertical. Continuity of vertical flow v requires that

$$\frac{\partial v}{\partial z} = \frac{\partial \varepsilon_v}{\partial t} - k \frac{\partial^2 h_t}{\partial z^2} = m_v \frac{\partial \bar{\sigma}_v}{\partial t} = m_v \left(\frac{\partial \sigma_v}{\partial t} - \frac{\partial u}{\partial t} \right).$$

The total vertical stress component must remain constant once the load has been applied, so dropping the subscript e for convenience and simplifying leads to

$$\frac{k}{\gamma_w} \frac{\partial^2 u}{\partial t^2} = m_v \frac{\partial u}{\partial t}$$

or

$$\frac{\partial^2 u}{\partial z^2} = c_v \frac{\partial u}{\partial t} \quad c_v = \frac{km_v}{\gamma_w}.$$

The term c_v is called the *coefficient of consolidation*. This is the classic linear diffusion equation. The boundary conditions are that, at $z = 0$ and at $z = 2H$, $u = 0$. The initial condition is that, for all values of Z , $u = q$. The general solution is expressed in terms of dimensionless variables

$$Z = \frac{z}{H} \quad T = \frac{km_v}{\gamma_w}.$$

The solution is

$$u = \sum_{m=0}^{\infty} \frac{2q}{M} \sin MZ \exp(-M^2 T), \quad M = \frac{\pi}{2}(2m + 1).$$

Figure 11 shows the values of excess pore pressure u at several values of T .

The average degree of consolidation is defined by

$$U = 1 - \frac{\int_0^{2H} u \, dx}{\int_0^{2H} u_{\text{initial}} \, dx},$$

where the subscript “initial” is used to indicate any initial distribution of excess pore pressure. For the present case of uniform initial excess pore pressure

$$U = 1 - \sum_{m=0}^{\infty} \frac{2}{M^2} \exp(-M^2 T).$$

For $T \leq 0.3$, a very close approximation is

$$U \approx 2\sqrt{\frac{T}{\pi}} \quad T \leq 0.03,$$

and for $T \geq 0.2$ an approximate solution is

$$U \approx 1 - \frac{8}{\pi^2} \exp\left(-\frac{\pi^2}{4} T\right) \quad T \geq 0.2.$$

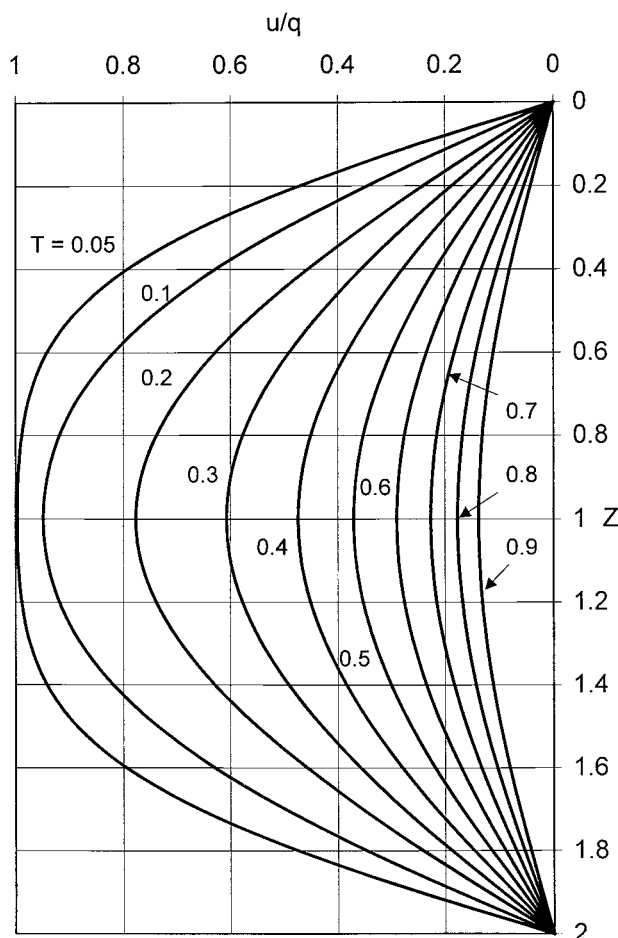


FIGURE 11 Dissipation of excess pore pressure for initially uniform distribution.

Figure 12 shows the exact solution and the two approximations. The approximation for small times (U proportional to \sqrt{T}) applies until 60% of the consolidation occurs.

E. Extensions to Consolidation Theory

The previous section describes the classic case of linear, one-dimensional consolidation at small strain with a constant applied load. By relaxing any or all of the assumptions, the theory can be extended to other conditions. In some cases the extensions lead to formulations that are different from linear diffusion equations. In particular, the following situations have received serious attention:

1. Time varying loading. If the other assumptions are retained, the solution for a load that varies with time or for excess pore pressures generated within the soil mass over time can be obtained by direct application of Duhamel's integral.

2. Two- or three-dimensional geometry. If the flow or deformation is not restricted to one spatial dimension, the basic consolidation equation must be reformulated into two or three simultaneous equations. One complication is that the total stress at a point, which is constant in the one-dimensional case, is not necessarily constant in the two- or three-dimensional case, even when the applied load is constant. One simplification is to assume that the total stress does remain constant, and the formulation becomes that for two- or three-dimensional linear diffusion. The resulting solution overestimates the rate of consolidation in most cases.
3. Large strains and nonlinear properties. When the analysis deals with very loose soils such as slurries, it is necessary to consider that the deformations are large and the relations between stress and strain are not linear. A restatement of the basic consolidation equation becomes necessary. Analytical solutions become very difficult, so numerical methods are used routinely. One interesting result of these analyses is that high fluid gradients near the boundaries can cause rapid local consolidation leading to the formation of a dense cake that retards further dissipation of excess pore pressure.

IV. STRENGTH

The third major division of soil mechanics concerns the strength of soils. This is a complicated subject. Because the strength of a soil depends on the effective stress and also on its stress history, aspects of the theories of flow through porous media and consolidation become part of an extended treatment of the strength of soil. Nevertheless, the basic principles underlying the shear strength of soil are summarized in the following sections.

A. Coulomb Relation

The classic description of the shear strength of a soil derives from Coulomb's work in the 18th century. The basic relation is

$$\tau = \bar{c} + \bar{\sigma} \tan \bar{\phi},$$

in which τ is the shear strength on a plane of sliding, $\bar{\sigma}$ is the normal effective stress on that plane, and \bar{c} and $\bar{\phi}$ are parameters defining the shear strength in terms of effective stress. The first parameter is called the cohesion and the second is the friction angle. Although the cohesion and friction angle are sometimes treated as though they actually described cohesive and frictional behavior, a

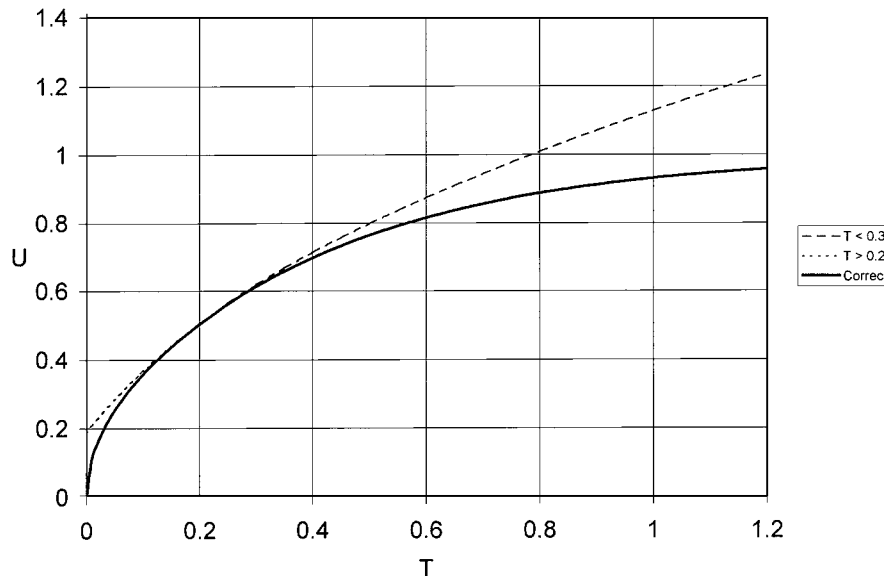


FIGURE 12 Development of settlement over time for initially uniform case.

more accurate view is that they are simply parameters that define the observed values of shear strength.

B. Mohr's Circle

To deal with a more general state of stress, Mohr's circle of stress is employed. For a two-dimensional case there are three components of stress at a point: σ_x , σ_y , and τ_{xy} . They can be plotted in the format shown in Fig. 13. The sign conventions are that compression is positive and shear stresses are positive if they tend to cause counter-clockwise rotation of the element. It can be shown that the numerical values of the components of stress for any

other orientation of the coordinate planes plot on a circle. If the angle defining the orientation of such a plane is θ , the corresponding angle for Mohr's circle is 2θ . Thus, Fig. 13 shows the orientation of the major principal stress σ_1 and the corresponding construction on Mohr's circle.

A triaxial testing cell is a device that allows the vertical stress to be varied independently of the horizontal stresses (which are maintained equal). If several samples of a soil are tested by first consolidating them in such a device at different but isotropic confining stresses and then are failed by increasing the vertical load, the results can be plotted as shown in Fig. 14. Each circle represents a different sample. The confining stresses are the minor principal stresses σ_3 , and the major principal stresses, σ_1 ,

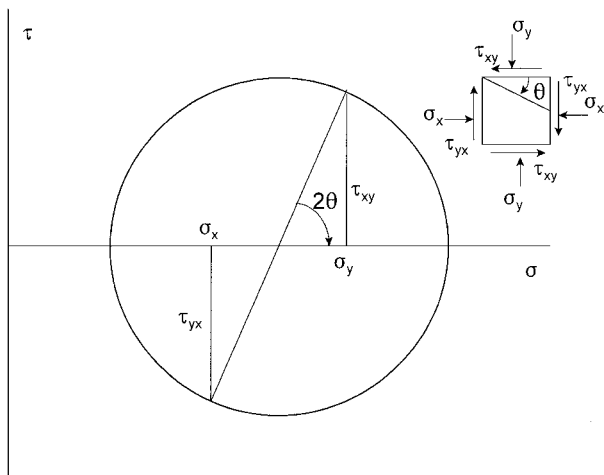


FIGURE 13 Mohr's circle of stress.

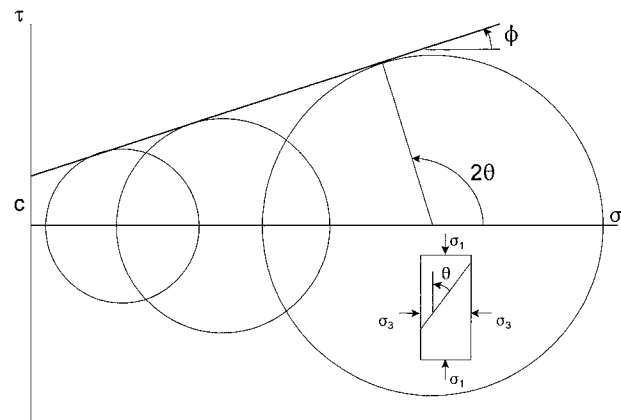


FIGURE 14 Mohr's circles for results of triaxial strength tests.

are the vertical stresses at failure. Stresses on other planes are described by the Mohr's circle. The Coulomb strength relation can then be interpreted as a line that is tangent to the set of Mohr's circles. In some cases, the tangent will be curved, but the straight line is a good approximation in most cases. As the figure shows for the largest circle, the orientation of the plane on which failure occurs is determined from the Mohr construction. This description of the strength of a soil is called the *Mohr–Coulomb relation*.

C. Undrained Strength

The Mohr–Coulomb relation is generally considered to be a valid description of the ultimate strength of a soil if the stresses are effective stresses. In many practical cases there are significant pore pressures, and these must be subtracted from the total stresses before the effective stress Mohr–Coulomb relation can be used. Unfortunately, the delays in adjustment of pore pressures due to consolidation effects may make it difficult to predict the actual pore pressures that will exist during a failure. To deal with this difficulty, an alternative to the effective stress analysis is often used. In this approach, called the “ $\phi = 0$ ” or “undrained” approach, it is assumed that the pore pressures do not dissipate during the failure process. Based on laboratory tests on samples that are not allowed to drain and accounting for the effects of prior stress history, relations are established between the states of stress prior to loading and the available shear strength.

D. Modern Constitutive Theory

For many nonfrictional materials the strength describes the conditions at which irreversible or plastic strains start to occur, and it is said to be a yield criterion. In many materials experiment shows further that the increments of plastic strain are proportional to the outward normal to the yield criterion. If such a *normality condition*, or *associated flow rule*, applies, many useful results follow, including many solutions used in practice. However, if the Mohr–Coulomb relation is treated as a yield criterion with normality, the theory predicts continuous volumetric strains that are very much larger than anything observed experimentally. The Mohr–Coulomb relation, or a three-dimensional generalization of it, must not be a yield criterion, but it may represent some sort of limit state. Finding appropriate constitutive relations that do describe soil behavior has been a major focus of research in soil mechanics.

Many of the most successful modern constitutive models are the so-called capped models, and the most popular

are versions of the critical state model. These start by observing that a soil loaded isotropically along the virgin compression curve develops irreversible volumetric strains. In other words, there is volumetric plastic flow with no shear stress present. The models assume that there is a yielding surface. If the stress is below this surface, behavior is elastic. If it is on this surface, plastic strains occur. The yield surface includes the state of isotropic stress so that the surface forms a sort of “cap” over the open end of the Mohr–Coulomb relation. The plastic strain increments are normal to this surface, and there is a critical state at which the plastic volumetric strain is zero. This is called the critical state line. The yield surface moves (“hardens”) as a function of the plastic strains.

To use the models in practice, the analyst must incorporate them into a numerical procedure such as a finite element program. This has been done for many of them. In particular, the Modified Cam Clay model has been implemented in several commercially available programs and used to analyze complicated problems of excavation and loading of soil. One of the major benefits of such models is that they make it possible to deal rationally with cases in which the soil is both loaded and unloaded during construction.

E. An Example—The Infinite Slope

Figure 15 shows a uniform slope that is so long that it can be considered infinite. Because the slope is infinite, the stresses are the same along any vertical plane must be the same as those along any other vertical plane. If there is no seepage of water and the soil has no cohesion, the analysis proceeds as follows. The weight of the small section in the figure is

$$W = \gamma_t az \cos \theta,$$

and it follows that, along an inclined plane at depth z

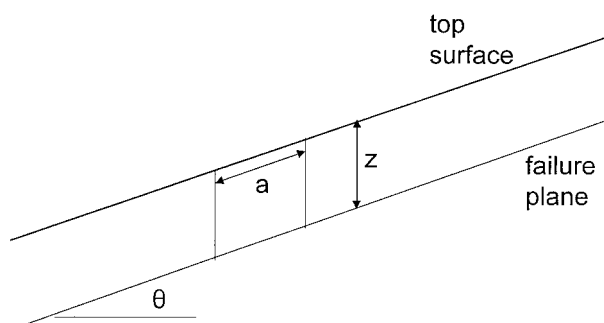


FIGURE 15 The infinite slope in a cohesionless soil with no seepage.

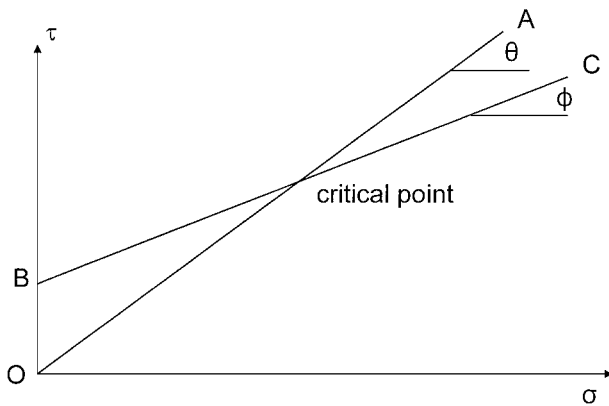


FIGURE 16 Strength and stresses in an infinite slope in a cohesive soil.

$$\bar{\sigma}_n = \gamma_t z \cos^2 \theta$$

$$\tau = \gamma_t z \cos \theta \sin \theta.$$

The subscript n indicates that the stress is the normal stress on the plane. The available shear strength $\bar{\sigma}_n \tan \phi$, so the factor of safety is

$$F = \frac{\gamma_t z \cos^2 \theta \tan \phi}{\gamma_t z \cos \theta \sin \theta} = \frac{\tan \phi}{\tan \theta}.$$

This implies that the slope is stable as long as its angle of inclination is less than the friction angle of the soil and that a pile of dry soil will come to rest at a slope equal to the friction angle, also known as the angle of repose.

When the soil has cohesion, line BC in Fig. 16 represents the relation between the normal stress on an inclined plane at a depth z and the shear strength. Line OA represents the relation between the shear and normal stresses on the plane. Clearly, if the friction angle is greater than the inclination of the slope, the slope will always be stable. If the friction angle is less than the slope angle, the slope will still be stable for the portion of the lines lying below and to the left of their intersection. The critical depth H at which this happens is defined by the stability number:

$$\frac{c}{\gamma H} = \cos^2 \theta (\tan \theta - \tan \phi).$$

Figure 17 illustrates the case of cohesionless soil with seepage occurring parallel to the slope. All the stream lines must be parallel to the slope, and the equipotentials must be perpendicular to it. Since the total head is constant along an equipotential, it follows that the pore pressure at depth z must be $\gamma_w z \cos^2 \theta$. Then, the components of stress along an inclined plane at depth z are

$$\bar{\sigma}_n = \gamma_b z \cos^2 \theta$$

$$\tau = \gamma_t z \cos \theta \sin \theta$$

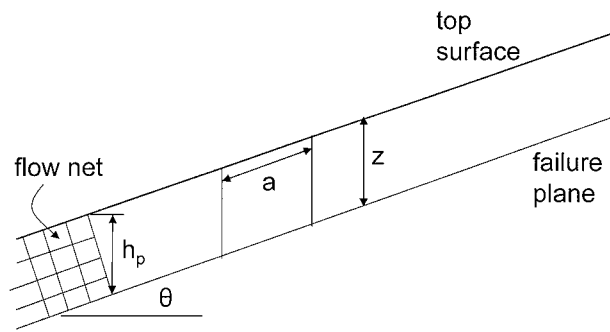


FIGURE 17 The infinite slope in a cohesionless soil with seepage parallel to the slope.

The critical angle at which the slope becomes unstable is

$$\theta = \tan^{-1} \left(\frac{\gamma_b}{\gamma_t} \tan \phi \right).$$

More complicated situations require the use of more sophisticated analytical techniques. Nevertheless, this simple example illustrates how stability calculations are carried out and shows the interaction between stability analysis and analysis of flow through porous media.

V. SPECIAL SOILS

Soil mechanics has historically dealt primarily with saturated inorganic soils. While this has led to many advances, it ignores many categories of soils that may represent the majority of conditions encountered in practice. In particular, organic soils, residual soils, and unsaturated soils are not as well understood as the conventional saturated sands and clays.

Organic soils have significant amounts of organic material. In the extreme they are peats, but many otherwise ordinary deposits contain organic material. The organic material causes significant complications in the behavior of the soil. Not only is the soil likely to be more compressible and deformable but also the decay of organic material over time introduces additional uncertainty and complications.

Residual soils are the result of in place weathering of rocks. In many cases the deposit shows the relict structure of the original rock, the grain size distribution shows significant amounts of large particles, but the behavior of the soil is determined largely by the clays in the matrix. Because they have not been sorted and redeposited, they tend to be quite heterogeneous. Such soils are particularly common in tropical regions and in the southeastern United States. There is not at this time a consistent set of theories to deal with these materials, and engineers must rely heavily on local experience.

Residual soils are often unsaturated, but many conventional soils are also. The most widely observed examples are soils compacted by construction equipment. Although some compacted soils become saturated during the life of the constructed facility, many do not. Usually engineers deal with compacted soils by testing samples of the actual soil formed in the laboratory or extracted in the field. While the effective stress principle is a valuable tool for dealing with saturated soils, its extension to unsaturated soils is still the subject of controversy. Most unsaturated soils must be treated on a case by case basis.

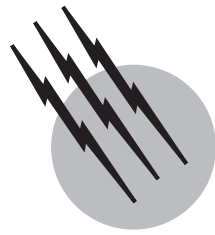
SEE ALSO THE FOLLOWING ARTICLES

DAMS, DIKES, AND LEVEES • EARTHQUAKE ENGINEERING • FOUNDATIONS • GEOENVIRONMENTAL ENGINEER-

ING • ROCK MECHANICS • SEISMOLOGY, ENGINEERING • SOIL AND GROUNDWATER POLLUTION • SOIL PHYSICS • STOCHASTIC DESCRIPTION OF FLOW IN POROUS MEDIA

BIBLIOGRAPHY

- Holtz, R. D., and Kovacs, W. D. (1981). "An Introduction to Geotechnical Engineering," Prentice-Hall, Englewood Cliffs, NJ (new edition in preparation).
- Lambe, T. W., and Whitman, R. V. (1969). "Soil Mechanics," Wiley, New York.
- Mitchell, J. K. (1993) "Fundamentals of Soil Behavior," 2nd edition, Wiley, New York.
- Terzaghi, K., Peck, R. B., and Mesri, G. (1996). "Soil Mechanics in Engineering Practice," 3rd edition, Wiley, New York.
- Taylor, D. W. (1948). "Fundamentals of Soil Mechanics," Wiley, New York (paperback reprint issued in 2000).



Soil Physics

Daniel Hillel

Goddard Institute for Space Studies

- I. General Physical Characteristics of Soil
- II. Texture, Particle Size, and Specific Surface
- III. Soil Structure and Aggregation
- IV. Soil Water: Content and Potential
- V. Flow of Water in Saturated Soil
- VI. Flow of Water in Unsaturated Soil
- VII. Soil Air and Aeration
- VIII. Soil Temperature and Heat Flow

GLOSSARY

Clay Fraction of the soil consisting of the finer (colloidal) particles. Clay is the active fraction of the soil, since it exhibits high specific surface area and such phenomena as cation adsorption and exchange, hydration, and swelling and shrinkage. Clay minerals (such as the aluminosilicates) may form in the soil as a result of the slow dissolution of primary minerals and their reprecipitation as secondary minerals in the course of soil formation.

Darcy's law Equation relating the rate of flow of water (the volume flux) to the effective hydraulic potential gradient. The ratio of the flux to the gradient is termed the hydraulic conductivity.

Drainage Removal of excess water, either from the soil surface (surface drainage) or from within the soil profile (internal drainage or groundwater drainage). Poorly drained (water-logged) soils are generally unsuited for crop production and require artificial drainage by means of ditches or subsoil tubes. Drainage is particularly

important in irrigated soils in arid regions, where high water-table conditions may result in soil salinization due to the capillary rise and evaporation of salt-bearing groundwater reaching the soil surface.

Infiltration Entry of water into the soil, generally from the surface downward. The rate of infiltration depends of the soil's conductivity, particularly at the surface. A high infiltration rate promotes absorption of rainfall, whereas restricted infiltration may cause runoff and soil erosion.

Neutron moisture meter Instrument to measure the volume content of soil water and its distribution in depth. It consists of a probe (which can be lowered into a vertical access tube inserted into the ground) with a radioactive source emitting fast neutrons and a detector of slow (attenuated) neutrons scattered within the soil as a consequence of the presence of the hydrogen nuclei contained in water.

Soil Natural body occurring over the earth's continental surface, consisting of fragmented mineral matter (formed by the weathering of rocks) with an admixture

of organic matter (the residues of biological activity). The soil is the principal medium for the growth of higher plants (including crops), as well as for the recycling of organic waste products.

Soil aeration Process by which soil air is exchanged with the external atmosphere through convection and diffusion. When aeration is impaired (e.g., in saturated or highly compacted soils), the respiration of plant roots and aerobic microbes is restricted and anaerobic conditions develop.

Soil profile Vertical cross section of the soil exhibiting a succession of layers (horizons), which may differ in texture, structure, chemical composition, water content, and other characteristics.

Soil structure Arrangement and orientation of soil particles in space and their association into aggregates. Soil structure can be more or less stable if the aggregates are internally cemented (generally by organic matter), or it can be unstable (in which case the aggregates break down when wetted or when subjected to mechanical manipulation).

Soil texture Array of particle sizes constituting the soil. If relatively coarse particles predominate, the soil is called sandy; if relatively fine (colloidal) particles predominate, the soil is called a clay; and if a more or less balanced mixture exists, it is called a loam.

Soil water potential Energy state of soil moisture, a measure of the amount of energy per unit mass of water that must be invested to transform soil moisture into pure, free water at a specified elevation. Soil moisture potential is also expressed in terms of soil moisture tension, being a measure of the tenacity with which water is retained in the soil. The lower the soil water content, the lower the soil water potential and the higher the tension with which it is held (in capillary pores and as films over soil particles).

Tensiometer Instrument to measure soil moisture tension in the field. It consists of a water-filled porous cup placed within the soil and connected to a manometer indicating the subpressure (tension) of soil moisture relative to the reference atmospheric pressure.

SOIL PHYSICS can be described as the branch of soil science dealing with the physical properties of soil, as well as with the measurement, prediction, and control of the physical processes taking place in and through the soil. As physics deals with the forms and interrelations of matter and energy, so soil physics deals with the state and movement of matter and with the fluxes and transformations of energy in the soil.

On the one hand, the fundamental study of soil physics aims at achieving a basic understanding of the

mechanisms governing the behavior of the soil and its role in the biosphere, including such interrelated processes as the terrestrial energy exchange and the cycles of water and transportable materials in the field. On the other hand, the practice of soil physics aims at the proper management of the soil by means of irrigation, drainage, soil and water conservation, tillage, aeration, and regulation of soil heat, as well as the use of soil material for engineering purposes. Soil physics is thus seen to be both a basic and an applied science with a very wide range of interests, many of which are shared by other branches of soil science and by other interrelated sciences including terrestrial ecology, hydrology, microclimatology, geology, sedimentology, botany, and agronomy. Soil physics is likewise closely related to the engineering profession of soil mechanics, which deals with soil mainly as a building and support material.

I. GENERAL PHYSICAL CHARACTERISTICS OF SOIL

A. Soil as a Disperse Three-Phase System

The three phases of ordinary nature are represented in the soil as follows: the solid phase constitutes the soil matrix; the liquid phase consists of soil water, which always contains dissolved substance so that it should properly be called the soil solution; and the gaseous phase is the soil atmosphere. The solid matrix of the soil includes particles that vary in chemical and mineralogical composition as well as in size, shape, and orientation. It also contains amorphous substances, particularly organic matter, which is attached to the mineral grains and often binds them together to form aggregates. The organization of the solid components of the soil determines the geometric characteristics of the pore spaces in which water and air are transmitted and retained. Finally, soil water and air vary in composition, both in time and in space.

The relative proportions of the three phases in the soil vary continuously and depend upon such variables as weather, vegetation, and management.

B. Volume and Mass Relationships of Soil Constituents

Figure 1 is a schematic representation of a hypothetical soil showing the volumes and masses of the three phases in a representative sample. The masses of the phases are indicated on the right-hand side: the mass of air M_a , which is negligible compared to the masses of solids and water; the mass of water M_w ; the mass of solids M_s ; and the total mass M_t . These masses can also be represented by

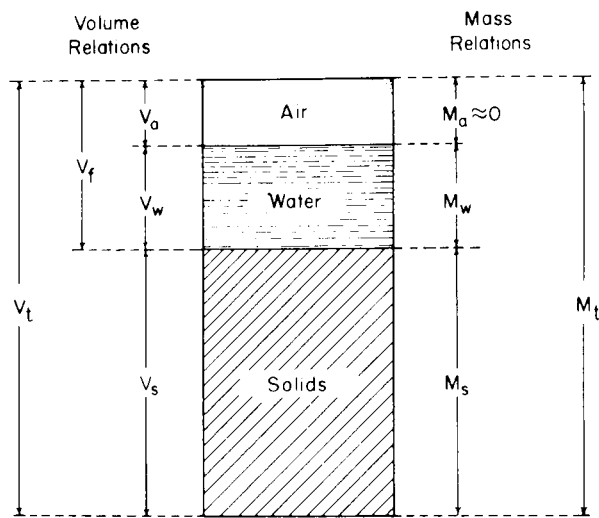


FIGURE 1 Schematic diagram of the soil as a three-phase system. [Reprinted with permission from Hillel, D. (1982). "Introduction to Soil Physics," Fig. 2.2, p. 8. Copyright 1982 by Academic Press, New York.]

their weights (the product of the mass and the gravitational acceleration). The volumes of the same components are indicated on the left-hand side of the diagram: volume of air V_a , volume of water V_w , volume of pores $V_f = V_a + V_w$, volume of solids V_s , and the total volume of the representative soil body V_t .

On the basis of this diagram, we can now define terms that are generally used to express the quantitative interrelations of the three primary soil constituents.

1. Density of Solids ρ_s (Mean Particle Density)

In most mineral soils, the mean density of the particles is about 2.6 to 2.7 g/cm³ and is thus close to the density of quartz, which is often prevalent in sandy soils. Aluminosilicate clay minerals have a similar density. The presence of iron oxides, and of various heavy minerals, increases the average value of ρ_s , whereas the presence of organic matter lowers it.

$$\rho_s = M_s / V_s. \quad (1)$$

2. Dry Bulk Density ρ_b

The dry bulk density expresses the ratio of the mass of dried soil to its total volume (solids and pores together). Obviously, ρ_b is always smaller than ρ_s , and if the pores constitute half the volume, ρ_b is half of ρ_s , namely, 1.3–1.35 g/cm³. In sandy soils, ρ_b can be as high as 1.6, whereas in aggregated loams and in clay soils, it can be as low as 1.1 g/cm³. The bulk density is affected as by the structure of the soil, that is, its looseness or degree

of compaction, as well as by its swelling and shrinkage characteristics, which are dependent upon clay content and wetness.

$$\rho_b = M_s / V_t = M_s / (V_s + V_a + V_w) \quad (2)$$

3. Porosity f

The porosity is an index of the relative pore volume in the soil. Its value generally lies in the range 0.3 to 0.6 (30–60%). Coarse-textured soils tend to be less porous than fine-textured soils, though the mean size of individual pores is greater in the former than in the latter. In clayey soils, the porosity is highly variable as the soil alternately swells, shrinks, aggregates, disperses, compacts, and cracks.

$$f = V_f / V_t = (V_a + V_w) / (V_s + V_a + V_w) \quad (3)$$

4. Void Ratio e

The void ratio is also an index of the fractional volume of soil pores, but it relates that volume to the volume of solids rather than to the total volume of soil. The advantage of this index over the previous one (f) is that a change in pore volume changes the numerator alone, whereas a change of pore volume in terms of the porosity will change both the numerator and the denominator of the defining equation. Void ratio is the generally preferred index in soil engineering and mechanics, whereas porosity is the more frequently used index in agricultural soil physics. Generally, e varies between 0.3 and 2.0.

$$e = (V_a + V_w) / V_s = V_f / (V_t - V_f) \quad (4)$$

5. Soil Wetness

The wetness, or relative water content, of the soil can be expressed in various ways: relative to the mass of solids, relative to the total mass, relative to the volume of solids, relative to the total volume, and relative to the volume of pores. The various indexes are defined as follows (the most commonly used are the first two).

a. Mass wetness w . This is the mass of water relative to the mass of dry soil particles, often referred to as the gravimetric water content. The term dry soil is generally defined as soil dried to equilibrium in an oven at 105°C.

$$w = M_w / M_s \quad (5)$$

b. Volume wetness θ . The volume wetness (often termed volumetric water content or volume fraction of soil water) is generally computed as a percentage of the

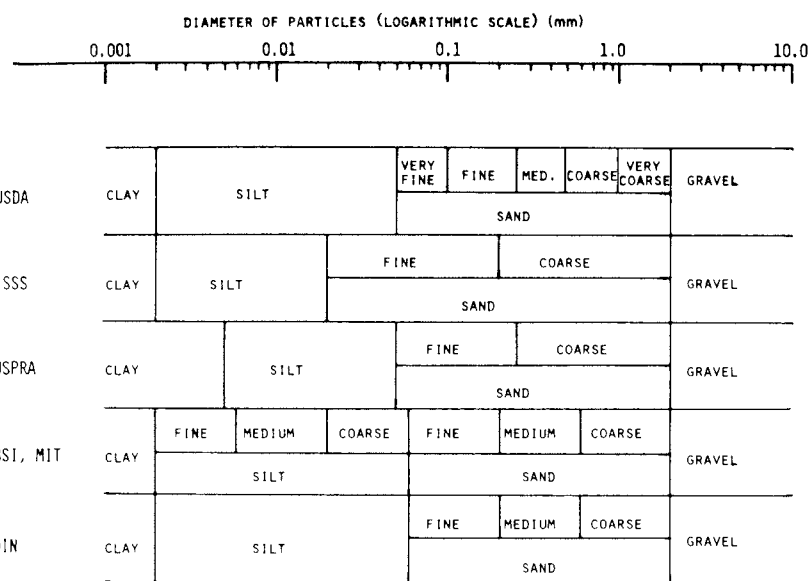


FIGURE 2 Several conventional schemes for the classification of soil fractions according to particle diameter ranges: U.S. Department of Agriculture (USDA); International Soil Science Society (ISSS); U.S. Public Roads Administration (USPRA); German Standards (DIN); British Standards Institute (BSI); Massachusetts Institute of Technology (MIT). [Reprinted with permission from Hillel, D. (1982). "Introduction to Soil Physics," Fig. 3.1, p. 23. Copyright 1982 by Academic Press, New York.]

total volume of the soil rather than on the basis of the volume of particles alone.

$$\theta = V_w/V_t = V_w/(V_s + V_f) \quad (6)$$

c. Degree of saturation s. This index expresses the volume of water present in the soil relative to the volume of pores. The index *s* ranges from zero in dry soil to unity (or 100%) in a completely saturated soil.

$$s = V_w/V_f = V_w/(V_a + V_w) \quad (7)$$

6. Air-Filled Porosity f_a (Fractional Air Content)

This is the measure of the relative air content of the soil, and as such it is an important criterion of soil aeration. The index is related negatively to the degree of saturation *s* (i.e., $f_a = f - s$).

$$f_a = V_a/V_t = V_a/(V_s + V_a + V_w) \quad (8)$$

II. TEXTURE, PARTICLE SIZE, AND SPECIFIC SURFACE

A. Definition of Soil Texture

The term soil texture refers to the size range of particles in the soil, that is, whether the particles of which a particular soil is composed are mainly large, small, or of some intermediate size or range of sizes.

The traditional method of characterizing particle sizes in soils is to divide the array of possible particle sizes into three conveniently separable size ranges known as textural fractions or separates, namely, sand, silt, and clay. The actual procedure of separating out these fractions and of measuring their proportions is called mechanical analysis, for which standard techniques have been devised. The results of this analysis yield the mechanical composition of the soil, a term that is often used interchangeably with soil texture.

Several of the often-used particle-size classification schemes are compared in Fig. 2.

B. Nature of Clay

The term clay designates not merely a range of particle sizes but also a large group of minerals, some of which are amorphous but many of which occur in the form of highly structured microcrystals of colloidal size. The clay fraction thus differs mineralogically, as well as in particle sizes, from sand and silt, which are composed mainly of quartz and other primary mineral particles that have not been transformed chemically into secondary minerals as is the case with clay. The various clay minerals differ greatly in properties and prevalence.

The most prevalent clay minerals are the layered aluminosilicates. Their crystals are composed of two basic structural units, namely, a tetrahedron of oxygen atoms surrounding a central cation, usually Si^{4+} , and an octahedron

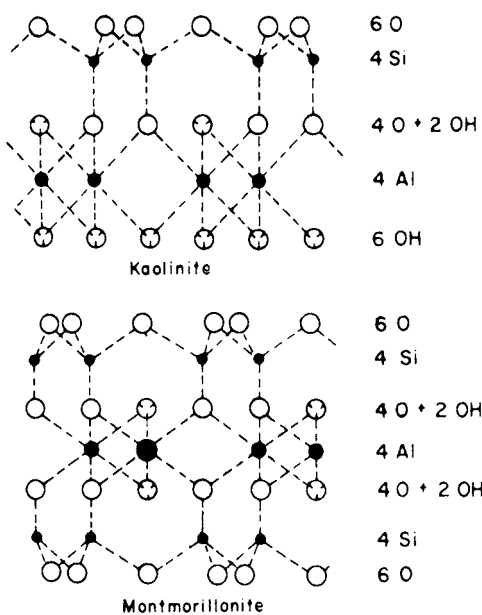


FIGURE 3 Schematic representation of the structure of aluminosilicate minerals. [Reprinted with permission from Hillel, D. (1982). "Introduction to Soil Physics," Fig. 3.3, p. 26. Copyright 1982 by Academic Press, New York.]

of oxygen atoms or hydroxyl groups surrounding a larger cation usually Al^{3+} or Mg^{2+} . The tetrahedra are joined at their basal corners and the octahedra are joined along their edges by means of shared oxygen atoms. Thus, tetrahedral and octahedral layers are formed.

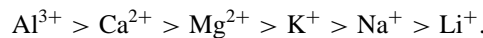
The layered aluminosilicate clay minerals are of two main types, depending upon the ratios of tetrahedral to octahedral layers, whether 1:1 or 2:1. (See Fig. 3.) In the 1:1 minerals such as kaolinite, an octahedral layer is attached by the sharing of oxygens to a single tetrahedral layer. In the 2:1 minerals such as montmorillonite, it is attached in the same way to two tetrahedral layers, one on each side. A clay particle is composed of multiply stacked composite layers (or unit cells) of this sort, called lamellae.

A hydrated clay particle forms a colloidal micelle, in which the excess negative charge of the particle is neutralized by a spatially separated swarm of cations. Together, the particle surface and the neutralizing cations form an electrostatic double layer. The cation swarm consists partly of a layer more or less fixed in the proximity of the particle surface (known as the Stern layer) and partly of a diffuse distribution extending some distance away from the particle surface. Just as cations are adsorbed positively toward the clay particles, so anions are repelled, or adsorbed negatively, and relegated from the micellar to the intermicellar solution.

The quantity of cations adsorbed on soil-particle surfaces per unit mass of the soil under chemically neutral

conditions is nearly constant and independent of the species of cation, and it is generally known as the cation exchange capacity. Soils vary in cation exchange capacity from nil to perhaps 0.60 mEq/g.

The attraction of a cation to a negatively charged clay micelle generally increases with increasing valency of the cation. Thus, monovalent cations are replaced more easily than divalent or trivalent cations. Highly hydrated cations, which tend to be farther from the surface, are also more easily replaced than less hydrated ones. The order of preference of cations in exchange reactions is generally



C. Soil Classes

The overall textural designation of a soil, called the textural class, is conventionally determined on the basis of the mass ratios of the three fractions. Soils with different proportions of sand, silt, and clay are assigned to different classes, as shown in the triangle of Fig. 4.

D. Mechanical Analysis

Mechanical analysis is the procedure for determining the particle-size distribution of a soil sample. The first step in this procedure is to disperse the soil sample in an aqueous suspension. The primary soil particles, often naturally aggregated, must be separated and made discrete

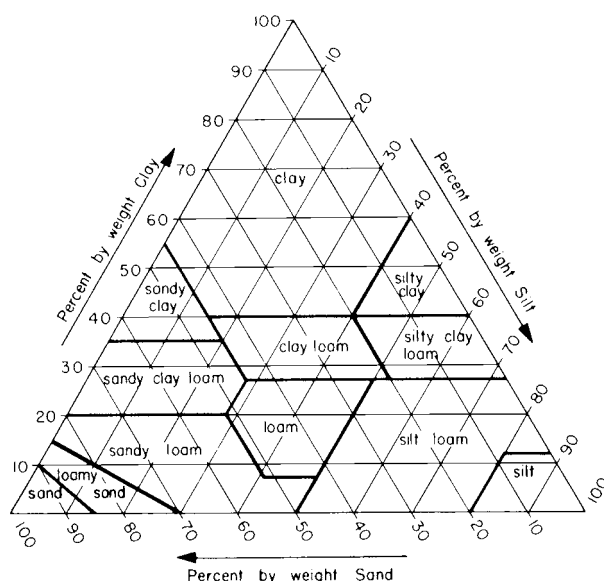


FIGURE 4 Textural triangle, showing the percentages of clay (below 0.002 mm), silt (0.002–0.05 mm), and sand (0.05–2.0 mm) in the basic soil textural classes. [Reprinted with permission from Hillel, D. (1982). "Introduction to Soil Physics," Fig. 3.5, p. 29. Copyright 1982 by Academic Press, New York.]

by removal of cementing agents (such as organic matter, calcium carbonate, or iron oxides) and be deflocculating the clay. Removal of organic matter is usually achieved by oxidation with hydrogen peroxide, and calcium carbonate can be dissolved by addition of hydrochloric acid. Deflocculation is carried out by means of a chemical dispersing agent (e.g., sodium hexametaphosphate) and by mechanical agitation (shaking, stirring, or ultrasonic vibration). The function of the dispersing agent is to replace the cations adsorbed to the clay, particularly divalent or trivalent cations, with sodium, which has the effect of increasing the hydration of the clay micelles, thus causing them to repel each other rather than coalesce, as they do in the flocculated state.

Actual separation of particles into size groups can be carried out by passing the suspension through graded sieves, down to a particle diameter of approximately 0.05 mm. To separate and classify still finer particles, the method of sedimentation is usually used, based on measuring the relative settling velocity of particles of various sizes from the aqueous suspension.

E. Specific Surface

The specific surface of a soil material can variously be defined as the total surface area of particles per unit mass a_m or per unit volume of particles a_v or per unit bulk volume of the soil as a whole a_b :

$$a_m = A_s / M_s \quad (9)$$

$$a_v = A_s / V_s \quad (10)$$

$$a_b = A_s / V_t, \quad (11)$$

where A_s is the total surface area of a mass of particles M_s having a volume V_s and contained in a bulk volume V_t of soil.

Specific surface is commonly expressed in terms of square meters per gram or per cubic centimeter of particles. It depends in the first place upon the size of the particles. It also depends upon their shape. Flattened or elongated particles obviously expose greater surface per volume or per mass than do equidimensional (e.g., cubical or spherical) particles. Since clay particles are generally platy, they contribute even more to the overall specific surface area of a soil than is indicated by their small size alone. In addition to their external surfaces, certain types of clay crystals exhibit internal surface areas, such as those that form when the open lattice of montmorillonite expands on imbibing water. Whereas the specific surface of sand is often less than $1 \text{ m}^2/\text{g}$, that of clay can be as high as several hundred square meters per gram. Therefore, it is the clay fraction, its content and mineral composition, that largely determines the specific surface of a soil.

III. SOIL STRUCTURE AND AGGREGATION

A. Definition of Soil Structure

The arrangement and organization of the particles in the soil is called soil structure. Since soil particles differ in shape, size, and orientation and can be variously associated and interlinked, the mass of them can form complex and irregular configurations that are in general exceedingly difficult if not impossible to characterize in exact geometric terms. A further complication is the inherently unstable nature of soil structure and hence its inconstancy in time, as well as its nonuniformity in space. Soil structure is strongly affected by changes in climate, biological activity, and soil management practices, and it is vulnerable to destructive forces of a mechanical and physicochemical nature. For these reasons, we have no truly objective or universally applicable method to measure soil structure per se, and the term soil structure therefore denotes a qualitative concept rather than a directly quantifiable property.

B. Types of Soil Structure

In general, we can recognize three broad categories of soil structure: single grained, massive, and aggregated. When particles are entirely unattached to each other, the structure is completely loose, as it is in the case of coarse granular soils or unconsolidated deposits of desert dust. Such soils were labeled structureless in the older literature of soil physics, but since even a loose arrangement is a structure of sorts, we prefer the term single-grained structure. On the other hand, when the soil is tightly packed in large cohesive blocks, as is sometimes the case with dried clay, the structure can be called massive. Between these two extremes, we can recognize an intermediate condition in which the soil particles are associated in quasi-stable small clods known as aggregates or peds. This last type of structure, called aggregated, is generally the most desirable condition for plant growth, especially in the critical early stages of germination and seedling establishment. The formation and maintenance of stable aggregates is the essential feature of soil tilth, a qualitative term used by agronomists to describe that highly desirable, yet unfortunately elusive, physical condition in which the soil is an optimally loose, friable, and porous assemblage of aggregates permitting free movement of water and air, easy cultivation and planting, and unobstructed germination and root growth.

A complex interrelationship of physical, biological, and chemical reactions is involved in the formation and degradation of soil aggregates. An important role is played by the extensive networks of roots that permeate the soil and tend to enmesh soil aggregates. Roots exert pressures

that compress aggregates and separate between adjacent ones. Water uptake by roots causes differential dehydration, shrinkage, and the opening of numerous small cracks. Moreover, root exudations and the continual death of roots and particularly of root hairs promotes microbial activity, which results in the production of humic cements.

C. Characterization of Soil Structure

Soil structure, or fabric, can be studied directly by microscopic observation of thin slices under polarized light. The structural association of clay can be examined by means of electron microscopy, using either transmission or scanning techniques. The structure of single-grained soils, as well as of aggregated soils, can be considered quantitatively in terms of total porosity and of pore-size distribution. The specific structure of aggregated soils can, furthermore, be characterized qualitatively by specifying the typical shapes of aggregates found in various horizons within the soil profile or quantitatively by measuring their sizes. Additional methods of characterizing soil structure are based on measuring mechanical properties and permeability to various fluids. None of these methods has been accepted universally. The shapes of aggregates observable in the field are illustrated in Fig. 5.

D. Stability of Soil Aggregates

Soils vary, of course, in the degree to which they are vulnerable to externally imposed destructive forces. Aggre-

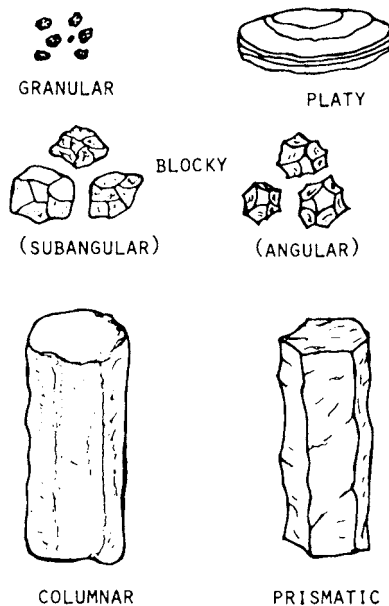


FIGURE 5 Observable forms of soil aggregation. [Reprinted with permission from Hillel, D. (1982). "Introduction to Soil Physics," Fig. 4.3, p. 47. Copyright 1982 by Academic Press, New York.]

gate stability is a measure of this vulnerability. More specifically, it expresses the resistance of aggregates to breakdown when subjected to potentially disruptive processes.

To test aggregate stability, soil physicists generally subject samples of aggregates to artificially induced forces designed to simulate phenomena that are likely to occur in the field. The nature of the forces applied during such testing depends on the investigator's perception of the natural phenomenon that is to be simulated, as well as on the equipment available and the mode of its employment. The degree of stability is then assessed by determining the fraction of the original sample's mass that has withstood destruction and retained its physical integrity or, conversely, the fraction that appears, by some arbitrary but reproducible criterion, to have disintegrated.

The classical and still most prevalent procedure for testing the water stability of soil aggregates is the wet sieving method. A representative sample of air-dry aggregates is placed on the uppermost of a set of graduated sieves and immersed in water to simulate flooding. The sieves are then oscillated vertically and rhythmically, so that water is made to flow up and down through the screens and the assemblage of aggregates. In this manner, the action of flowing water is simulated. At the end of a specified period of sieving, the nest of sieves is removed from the water and the oven-dry weight of material left on each sieve is determined.

E. Soil Crusting

It is the aggregates exposed at the soil surface that are most vulnerable to destructive forces. The surface aggregates, which collapse and slake down during wetting, may form a slick layer of dispersed mud, several millimeters or centimeters thick, which clogs the surface macropores and thus tends to inhibit the infiltration of water into the soil and the exchange of gases between the soil and the atmosphere (aeration). Such a layer is often called a *surface seal*. Upon drying, this dispersed layer shrinks to become a dense, hard crust that impedes seedling emergence by its hardness and tears seedling roots as it cracks, forming a characteristic polygonal pattern.

IV. SOIL WATER: CONTENT AND POTENTIAL

A. Importance of Soil Water

The variable amount of water contained in a unit mass or volume of soil and the energy state of water in the soil are important factors affecting the growth of plants. Numerous other soil properties depend very strongly upon water content. Included among these are mechanical properties

such as consistency, plasticity, strength, compactibility, penetrability, stickiness, and trafficability. In clayey soils, swelling and shrinkage associated with addition or extraction of water change the overall specific volume (or bulk density) of the soil as well as its pore-size distribution. Soil water content also governs the air content and gas exchange of the soil, thus affecting the respiration of roots, the activity of microorganisms, and the chemical state of the soil (e.g., oxidation-reduction potential).

B. Measurement of Soil Water

1. Sampling and Drying

The traditional (gravimetric) method of measuring mass wetness consists of removing a sample by augering into the soil and then determining its moist and dry weights. The moist weight is determined by weighing the sample as it is at the time of sampling, and the dry weight is obtained after drying the sample to a constant weight in an oven. The more or less standard method of drying is to place the sample in an oven at 105°C for 24 h.

2. Electrical Resistance

The electrical resistance of a soil volume depends not only upon its water content but also upon its composition, texture, and soluble-salt concentration. On the other hand, the electrical resistance of porous bodies placed in the soil and left to equilibrate with soil moisture can sometimes be calibrated against soil wetness. Such units (usually called electrical resistance blocks) generally contain a pair of electrodes embedded in gypsum, nylon, or fiberglass.

3. Neutron Scattering

First developed in the 1950s, neutron scattering has gained widespread acceptance as an efficient and reliable technique for monitoring soil moisture in the field. Its principal advantages over the gravimetric methods are that it allows less laborious, more rapid, nondestructive, and periodically repeatable measurements, in the same locations and depths, of the volumetric wetness of a representative volume of soil. The method is practically independent of temperature and pressure. Its main disadvantages, however, are the high initial cost of the instrument, low degree of spatial resolution, difficulty of measuring moisture in the soil surface zone, and the health hazard associated with exposure to neutron and gamma radiation.

4. Other Methods

Additional approaches to the measurement of soil wetness include X-ray absorption, the dependence of soil thermal properties upon water content, and the use of ultrasonic

waves, radar waves, and dielectric properties. Some of these and other methods have been tried in connection with the remote sensing of land areas from aircraft or satellites.

C. Energy State of Soil Water

Soil water, like other bodies in nature, can contain energy in different quantities and forms. Classical physics recognizes two principal forms of energy, *kinetic* and *potential*. Since the movement of water in the soil is quite slow, its kinetic energy, which is proportional to the velocity squared, is generally considered to be negligible. On the other hand, the potential energy, which is due to position or internal condition, is of primary importance in determining the state and movement of water in the soil. The concept of soil-water potential is a criterion, or yardstick, for this energy. It expresses the specific potential energy of soil water relative to that of water in a standard reference state. The standard state generally used is that of a hypothetical reservoir of pure water, at atmospheric pressure, at the same temperature as that of soil water (or at any other specified temperature), and at a given and constant elevation. Since the elevation of this hypothetical reservoir can be set at will, it follows that the potential that is determined by comparison with this standard is not absolute, but by employing even so arbitrary a criterion we can determine the relative magnitude of the specific potential energy of water at different locations or times within the soil.

Soil water is subject to a number of force fields, which cause its potential to differ from that of pure, free water. Such force fields result from the attraction of the solid matrix for water, as well as from the presence of solutes and the action of external gas pressure and gravitation. Accordingly, the total potential of soil water can be thought of as the sum of the separate contributions of these various factors:

$$\phi_t = \phi_g + \phi_p + \phi_o + \dots, \quad (12)$$

where ϕ_t is the total potential, ϕ_g is the gravitational potential, ϕ_p is the pressure (or matric) potential, ϕ_o is the osmotic potential, and the ellipsis signifies that additional terms are theoretically possible.

D. Soil-Water Characteristic Curve

In saturated soil at equilibrium with free water at the same elevation, the actual pressure is atmospheric, and hence the hydrostatic pressure and the suction (or tension) are zero.

If a slight suction (i.e., a water pressure slightly sub-atmospheric), is applied to water in a saturated soil, no outflow may occur until, as suction is increased, a certain critical value is exceeded, at which value the largest pore at

the surface begins to empty. This critical suction is called the air-entry suction.

As suction is further increased, more water is drawn out of the soil and more of the relatively large pores, which cannot retain water against the applied suction, will empty out. Recalling the capillary equation ($-P = 2\gamma/r$), we can readily predict that a gradual increase in suction will result in the emptying of progressively smaller pores until at high suction values only the very narrow pores retain water. Similarly, an increase in soil-water suction is associated with a decreasing thickness of the hydration envelopes covering the soil-particle surfaces. Increasing suction is thus associated with decreasing soil wetness. The amount of water remaining in the soil at equilibrium is a function of the sizes and volumes of the water-filled pores, and hence it is a function of the matric suction. This function is usually measured experimentally, and it is represented graphically by a curve known as the soil-moisture retention curve or the soil-moisture characteristic.

The amount of water retained at relatively low values of matric suction (say, between 0 and 1 bar of suction) depends primarily upon the capillary effect and the pore-size distribution, and hence it is strongly affected by the structure of the soil. On the other hand, water retention in the higher suction range is due increasingly to adsorption and is thus influenced less by the structure and more by the texture and specific surface of the soil material (Fig. 6).

E. Hysteresis of Soil Water

The relation between matric potential and soil wetness can be obtained in two ways: (1) in desorption, by taking an

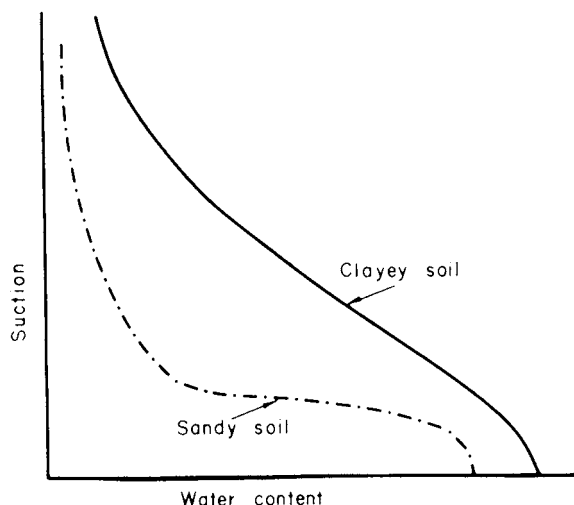


FIGURE 6 The effect of texture on soil-water retention. [Reprinted with permission from Hillel, D. (1982). "Introduction to Soil Physics," Fig. 5.6, p. 76. Copyright 1982 by Academic Press, New York.]

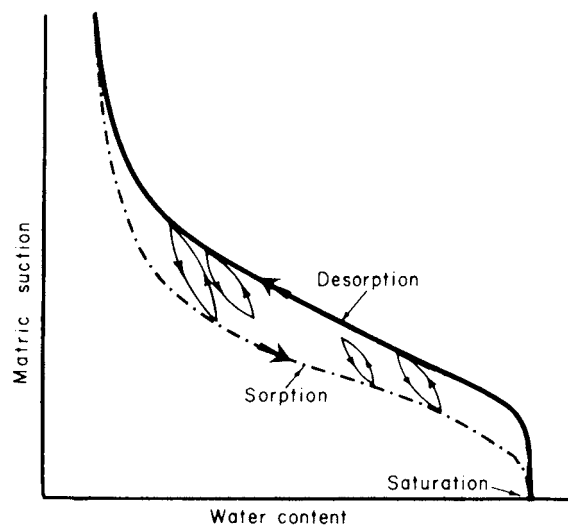


FIGURE 7 The suction-water content curves in sorption and desorption. The intermediate loops are *scanning curves*, indicating transitions between the main branches. [Reprinted with permission from Hillel, D. (1982). "Introduction to Soil Physics," Fig. 5.8, p. 78. Copyright 1982 by Academic Press, New York.]

initially saturated sample and applying increasing suction to gradually dry the soil while taking successive measurements of wetness versus suction; and (2) in sorption, by gradually wetting up an initially dry soil sample while reducing the suction. Each of these two methods yields a continuous curve, but the two curves will in general not be identical. The equilibrium soil wetness at a given suction tends to be greater in desorption (drying) than in sorption (wetting). This dependence of the equilibrium content and the state of soil water upon the direction of the process leading up to it is called hysteresis (Fig. 7).

F. Measurement of Soil-Water Potential

1. The Tensiometer

The essential parts of a tensiometer are shown in Fig. 8. The tensiometer consists of a porous cup, generally of ceramic material, connected through a tube to a manometer, with all parts filled with water. When the cup is placed in the soil where the suction measurement is to be made, the bulk water inside the cup comes into hydraulic contact and tends to equilibrate with soil-water suction through the pores in the ceramic walls. The subpressure is indicated by a manometer, which may be a simple water- or mercury-filled U tube, a vacuum gauge, or an electrical transducer.

A tensiometer left in the soil for a long period of time tends to follow the changes in the matric suction of soil water. As soil moisture is depleted by drainage or plant uptake, or as it is replenished by rainfall or irrigation,

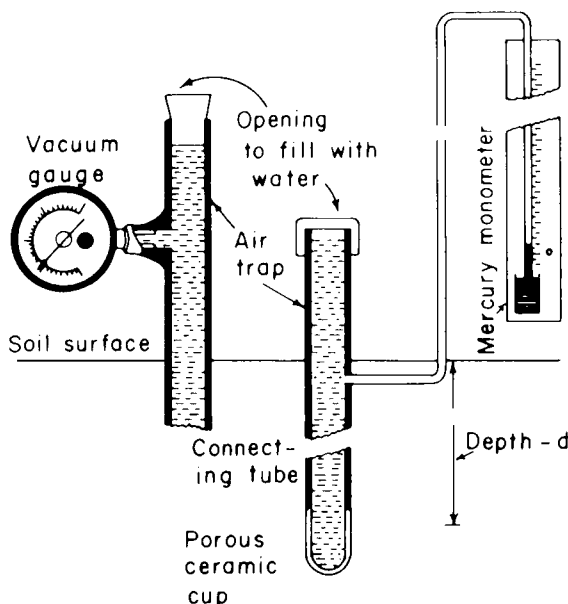


FIGURE 8 Schematic illustration of the essential parts of a tensiometer. [Reprinted with permission from Hillel, D. (1982). "Introduction to Soil Physics," Fig. 5.10, p. 82. Copyright 1982 by Academic Press, New York.]

corresponding readings on the tensiometer gauge occur. Because of the hydraulic resistance of the cup and the surrounding soil, or of the contact zone between the cup and the soil, the tensiometer response may lag behind suction changes in the soil. Tensiometers are generally limited to the suction range of 0 to 1 atm.

2. The Thermocouple Psychrometer

The soil psychrometer consists of a fine-wire thermocouple, one junction of which is equilibrated with the soil atmosphere by placing it inside a hollow porous cup embedded in the soil, while the other junction is kept in an insulated medium to provide a temperature lag. During operation, an electromotive force (emf) is applied so that the junction exposed to the soil atmosphere is cooled to a temperature below the dew point of that atmosphere, at which point a droplet of water condenses on the junction, allowing it to become, in effect, a wet bulb thermometer. This is a consequence of the so-called Peltier effect. The cooling is then stopped, and as the water from the droplet reevaporates, the junction attains a wet bulb temperature that remains nearly constant until the junction dries out, after which it returns to the ambient soil temperature. While evaporation takes place, the difference in temperature between the wet bulb and the insulated junction serving as dry bulb generates an emf that is indicative of the soil moisture potential.

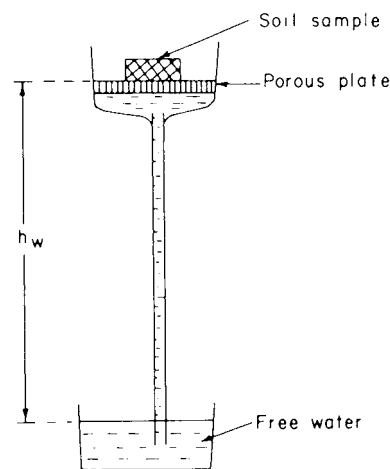


FIGURE 9 Tension plate assembly for equilibrating a soil sample with a known matric suction value. This assembly is applicable in the range of 0–1 bar only. [Reprinted with permission from Hillel, D. (1982). "Introduction to Soil Physics," Fig. 5.12, p. 85. Copyright 1982 by Academic Press, New York.]

3. Measurement of the Soil-Moisture Characteristic Curves

The fundamental relation between soil wetness and matric suction is often determined by means of a tension plate assembly (Fig. 9) in the low suction (<1 bar) range and by means of a pressure plate or pressure membrane apparatus (Fig. 10) in the higher suction range. These instruments allow the application of successive suction values and the repeated measurement of the equilibrium soil wetness at each suction.

The maximum suction value obtainable by porous-plate devices is limited to 1 bar if the soil air is kept at atmospheric pressure and the pressure difference across the plate is controlled either by vacuum or by a hanging water

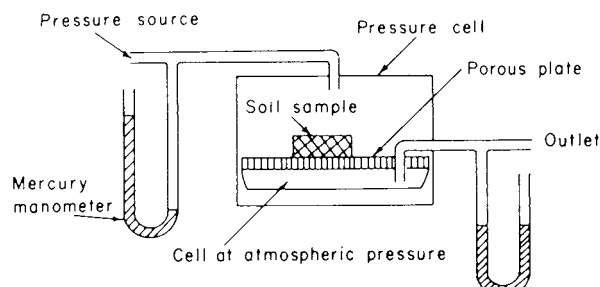


FIGURE 10 Pressure plate apparatus for moisture characteristic measurements in the high-suction range. The lower side of the porous plate is in contact with water at atmospheric pressure. Air pressure is used to extract water from initially saturated soil samples. [Reprinted with permission from Hillel, D. (1982). "Introduction to Soil Physics," Fig. 5.13, p. 86. Copyright 1982 by Academic Press, New York.]

column. Matric suction values considerably greater than 1 bar can be obtained by increasing the pressure of the air phase. This requires placing the porous-plate assembly inside a pressure chamber, as shown in Fig. 10. The limit of matric suction obtainable with such a device is determined by the design of the chamber (i.e., its safe working pressure) and by the maximal air-pressure difference the saturated porous plate can bear without allowing air to bubble through its pores. Ceramic plates generally do not hold pressures greater than about 20 bars, but cellulose acetate membranes can be used with pressures exceeding 100 bars.

V. FLOW OF WATER IN SATURATED SOIL

A. Darcy's Law

Were the soil merely a bundle of straight, parallel, smooth tubes, each uniform in radius, we could assume the overall flow rate of water in the soil to equal the sum of the separate flow rates through the individual tubes. Knowledge of the size distribution of the tube radii would then enable us to calculate the total flow through a bundle caused by a known pressure difference:

$$Q = \pi R^4 \Delta p / 8vL. \quad (13)$$

This equation, known as Poiseuille's law, indicates that the volume flow rate Q is proportional to the pressure drop per unit distance ($\Delta p/L$) and the fourth power of the radius of the tube, v being the viscosity.

Unfortunately, from the standpoint of physical simplicity, however, soil pores do not resemble uniform, smooth tubes, but are highly irregular, tortuous, and interconnected. Flow through soil pores is limited by numerous constrictions, or necks, and occasional dead-end spaces. Hence, the actual geometry and flow pattern of a typical soil specimen is too complicated to be described in microscopic detail, as the fluid velocity varies drastically from point to point, even along the same passage. For this reason, flow through complex porous media is generally described in terms of a macroscopic flow velocity vector, which is the overall average of the microscopic velocities over the total volume of the soil. The detailed flow pattern is thus ignored, and the conducting body is treated as though it were a uniform medium, with the flow spread out over the entire cross section, solid and pore space alike.

Figure 11 shows a horizontal column of soil through which a steady flow of water is occurring from left to right, from an upper reservoir to a lower one, in each of which the water level is maintained constant.

Experience shows that the discharge rate Q , which is the volume V flowing through the column per unit time, is directly proportional to the cross-sectional area and to the hydraulic head drop ΔH and is inversely proportional to the length of the column L :

$$Q = V/t \propto A\Delta H/L. \quad (14)$$

The head drop per unit distance in the direction of flow ($\Delta H/L$) is the hydraulic gradient, which is, in fact, the driving force. The specific discharge rate Q/A (i.e., the

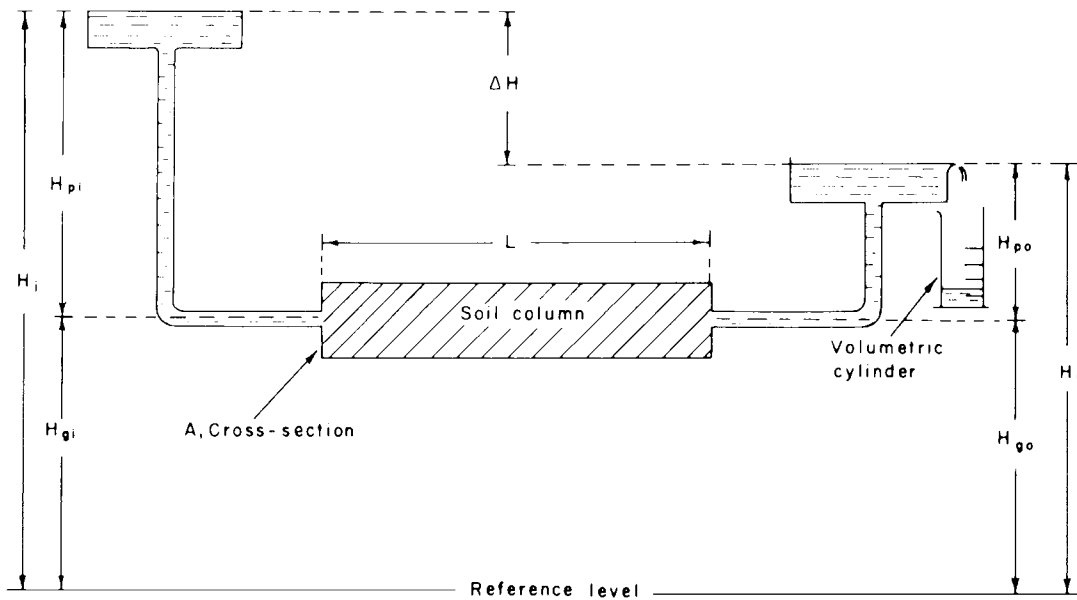


FIGURE 11 Flow in a horizontal saturated column. [Reprinted with permission from Hillel, D. (1982). "Introduction to Soil Physics," Fig. 6.3, p. 94. Copyright 1982 by Academic Press, New York.]

volume of water flowing through a unit cross-sectional area per unit time t) is called the flux density (or simply the flux) and is indicated by q . Thus, flux is proportional to the hydraulic gradient or

$$q = Q/A = V/At \propto \Delta H/L. \quad (15)$$

The proportionality factor K is generally designated as the hydraulic conductivity:

$$q = K \Delta H/L. \quad (16)$$

This equation is known as Darcy's law, after Henri Darcy, the French engineer who discovered it over a century ago in the course of his classic investigation of seepage rates through sand filters in the city of Dijon.

Where flow is unsteady (i.e., the flux changes with time) or the soil nonuniform, the hydraulic head may not decrease linearly along the direction of flow. Whenever the hydraulic head gradient or the conductivity is variable, we must consider the localized gradient, flux, and conductivity values rather than overall values for the soil system as a whole. A more exact and generalized expression of Darcy's law is, therefore, in differential form

$$q = -K \nabla H, \quad (17)$$

in which ∇H is the gradient of the hydraulic head in three-dimensional space.

In a one-dimensional system, Eq. (17) takes the form

$$q = -K dH/dx. \quad (18)$$

Water flow in a horizontal column occurs in response to a pressure head gradient. Flow in a vertical column can be caused by gravitation as well as by pressure. The gravitational head H_g at any point is determined by the height of the point relative to some reference plane, while the pressure head H_p is determined by the height of the water column resting on that point.

The total hydraulic head H is composed of the sum of these two heads:

$$H = H_p + H_g. \quad (19)$$

B. Flux, Flow Velocity, and Tortuosity

As stated earlier, the flux density (hereafter, simply flux) is the volume of water passing through a unit cross-sectional area (perpendicular to the flow direction) per unit time. The dimensions of the flux are

$$q = V/At = L^3/L^2T = LT^{-1},$$

that is, length per time (in cgs units, centimeters per second). These are the dimensions of velocity, and yet we prefer the term flux to flow velocity, the latter being an ambiguous term. Since soil pores vary in shape, width, and direction, the actual flow velocity in the soil

is highly variable (e.g., wider pores conduct water more rapidly, and the liquid in the center of each pore moves faster than does the liquid in close proximity to the particles). Strictly speaking, therefore, one cannot refer to a single velocity of liquid flow, but at best to an average velocity.

Yet, even the average velocity of the flowing liquid differs from the flux, as we have defined it. Flow does not in fact take place through the entire cross-sectional area A , since part of this area is plugged by particles and only the porosity fraction is open to flow. Since the real area through which flow takes place is smaller than A , the actual velocity of the liquid must be greater than the flux q . Furthermore, the actual length of the path traversed by an average parcel of liquid is greater than the soil column length L , owing to the labyrinthine, or tortuous, nature of the pore passages.

Tortuosity can be defined as the average ratio of the actual roundabout path to the apparent, or straight, flow path; that is, it is the ratio of the average length of the pore passages (as if they were stretched out in the manner one can stretch out a coiled or tangled telephone wire) to the length of the soil specimen. Tortuosity is thus a dimensionless geometric parameter of porous media that, although difficult to measure precisely, is always greater than 1 and may exceed 2. The tortuosity factor is sometimes defined as the inverse of what we defined as the tortuosity.

C. Hydraulic Conductivity

With the dimensions of flux being LT^{-1} , those of hydraulic conductivity depend on the dimensions assigned to the driving force (the potential gradient). In the preceding section, we showed that the simplest way to express the potential gradient is by use of length, or head, units. The hydraulic head gradient H/L , being the ratio of a length to a length, is dimensionless. Accordingly, the dimensions of hydraulic conductivity are the same as the dimensions of flux, namely, LT^{-1} . (See Fig. 12).

In a saturated soil of stable structure, as well as in a rigid porous medium such as sandstone, for instance, the hydraulic conductivity is characteristically constant. Its order of magnitude is about 10^{-1} to 10^{-3} cm/s in a sandy soil and 10^{-4} to 10^{-7} cm/s in clayey soil.

In many soils, the hydraulic conductivity does not in fact remain constant. Because of various chemical, physical, and biological processes, the hydraulic conductivity may change as water permeates and flows in a soil. Changes occurring in the composition of the exchangeable-ion complex, as when the water entering the soil has a different composition or concentration of solutes than the original soil solution, can greatly change the hydraulic conductivity. In general, the conductivity decreases with

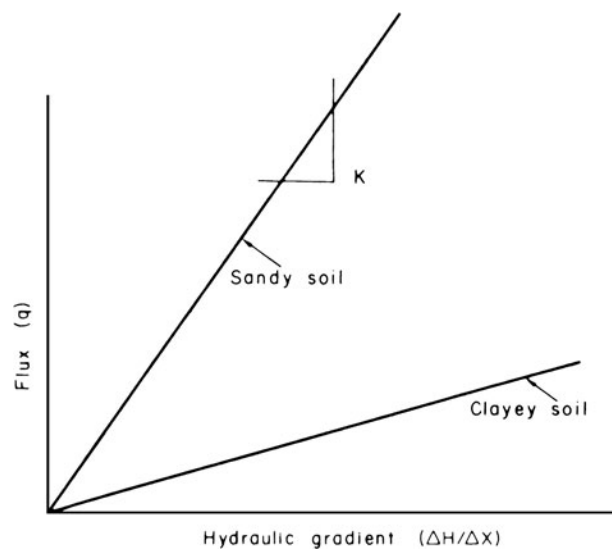


FIGURE 12 The linear dependence of flux upon hydraulic gradient, the hydraulic conductivity being the slope (i.e., the flux per unit gradient). [Reprinted with permission from Hillel, D. (1982). "Introduction to Soil Physics," Fig. 6.8, p. 101. Copyright 1982 by Academic Press, New York.]

decreasing concentration of electrolytic solutes, due to swelling and dispersion phenomena, which are also affected by the species of cations present. Detachment and migration of clay particles during prolonged flow may result in the clogging of pores. The interactions of solutes with the soil matrix and their effect on hydraulic conductivity are particularly important in saline and sodic soils.

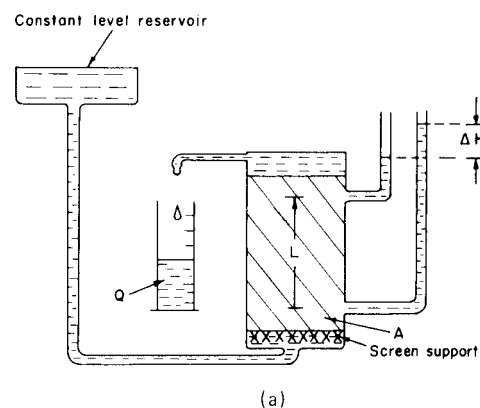
D. Measurement of Hydraulic Conductivity

Methods for measuring hydraulic conductivity in the laboratory are illustrated in Fig. 13. Numerous methods have been proposed for measuring hydraulic conductivity in the field, but no single method has yet been adopted universally as standard.

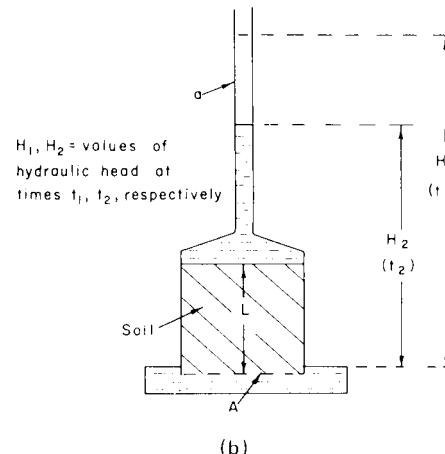
VI. FLOW OF WATER IN UNSATURATED SOIL

A. Flow in Unsaturated versus Saturated Soil

The moving force in a saturated soil is the gradient of a positive pressure potential. (We shall disregard, for the moment, the gravitational force, which is completely unaffected by the saturation or unsaturation of the soil.) On the other hand, water in an unsaturated soil is subject to a subatmospheric pressure, or suction, which is equivalent to a negative pressure potential. The gradient of this potential likewise constitutes a moving force.



(a)



(b)

FIGURE 13 (a) The measurement of saturated hydraulic conductivity with a constant head permeameter; $K = VL/At\Delta H$. (b) The measurement of saturated hydraulic conductivity with a falling head permeameter; $K = [2.3aL/A(t_2 - t_1)](\log H_1 - \log H_2)$. H_1 and H_2 are the values of hydraulic head at times t_1 and t_2 , respectively. [Reprinted with permission from Hillel, D. (1982). "Introduction to Soil Physics," Figs. 6.10 and 6.11, pp. 103 and 104. Copyright 1982 by Academic Press, New York.]

Perhaps the most important difference between unsaturated and saturated flow is in the hydraulic conductivity. When the soil is saturated, all of the pores are water filled and conducting, so that continuity and hence conductivity are maximal. When the soil desaturates, some of the pores become air filled and the conductive portion of the soil's cross-sectional area decreases correspondingly. Furthermore, as suction develops, the first pores to empty are the largest ones, which are the most conductive, thus leaving water to flow only in the smaller pores. The empty pores must be circumvented, so that, with desaturation, tortuosity increases. In coarse-textured soils, water sometimes remains almost entirely in capillary wedges at the contact points of the particles, thus forming separate and discontinuous pockets of water (see Fig. 14).

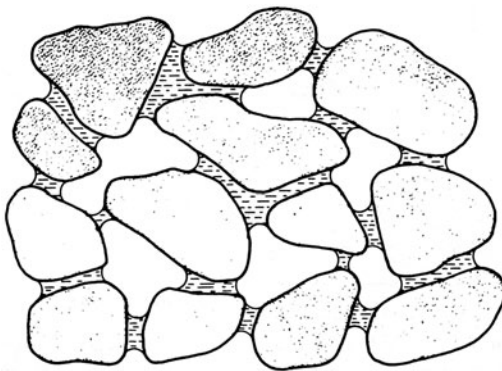


FIGURE 14 Water in an unsaturated coarse-textured soil. [Reprinted with permission from Hillel, D. (1982). "Introduction to Soil Physics," Fig. 7.1, p. 109. Copyright 1982 by Academic Press, New York.]

In aggregated soils, too, the large interaggregate spaces that confer high conductivity at saturation become (when emptied) barriers to liquid flow from one aggregate to its neighbors.

For these reasons, the transition from saturation to unsaturation generally entails a steep drop in hydraulic conductivity, which may decrease by several orders of magnitude (sometimes down to 1/100,000 of its value at saturation) as suction increases from 0 to 1 bar. At still higher suctions, or lower wetness values, the conductivity may be so low that very steep suction gradients, or very long times, are required for any appreciable flow to occur.

At saturation, the most conductive soils are those in which large and continuous pores constitute most of the overall pore volume, while the least conductive are soils in which the pore volume consists of numerous micropores. Thus, as is well known, a saturated sandy soil conducts water more rapidly than a clayey soil. However, the very opposite may be true when the soils are unsaturated. In a soil with large pores, these pores quickly empty and become nonconductive as suction develops, thus steeply decreasing the initially high conductivity. In a soil with small pores, on the other hand, many of the pores retain and conduct water even at appreciable suction, so that the hydraulic conductivity does not decrease as steeply and may actually be greater than that of a soil with large pores subjected to the same suction.

Figure 15 shows the general trend of the dependence of conductivity on suction in soils of different texture. [K versus suction curves are usually drawn on a log-log scale, since both vary over several orders of magnitude within the suction range of general interest (say, 0–10,000 cm of suction head).] It is seen that although the saturated conductivity of the sandy soil K_{S1} is typically greater than that of the clayey soil K_{S2} , the unsaturated conductivity of

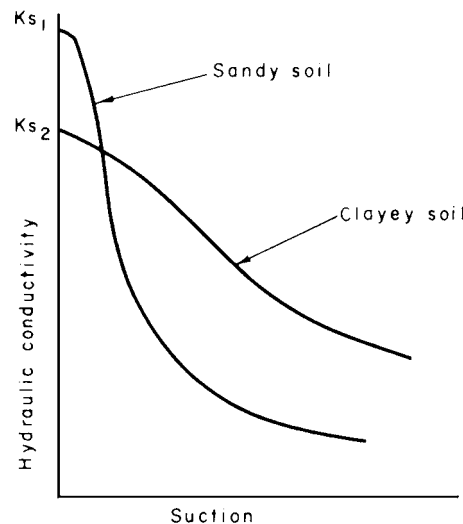


FIGURE 15 Dependence of conductivity on suction in soils of different texture (log-log scale). [Reprinted with permission from Hillel, D. (1982). "Introduction to Soil Physics," Fig. 7.5, p. 113. Copyright 1982 by Academic Press, New York.]

the former decreases more steeply with increasing suction and eventually becomes lower.

B. General Equation of Unsaturated Flow

Darcy's law, although originally conceived for saturated flow only, has been extended to unsaturated flow, with the provision that the conductivity now be a function of the matric suction head:

$$q = -K(\psi)\nabla H, \quad (20)$$

where ∇H is the hydraulic head gradient, which may include both suction and gravitational components.

Equation (20) is difficult to apply, because the $K(\psi)$ function may be highly hysteretic. However, the relation of conductivity to volumetric wetness $K(\theta)$ or to degree of saturation $K(s)$ is affected by hysteresis to a much lesser degree than is the $K(\psi)$ function. Thus, Darcy's law for unsaturated soil can be written as

$$q = -K(\theta)\nabla H, \quad (21)$$

which, however, still leaves us with the problem of dealing with the hysteresis between ψ and θ .

To obtain the general flow equation and account for transient as well as steady flow processes, we must introduce the continuity equation, which embodies the conservation of mass law in mathematical form:

$$\partial\theta/\partial t = -\nabla \cdot q. \quad (22)$$

Thus,

$$\partial\theta/\partial t = \nabla \cdot [K(\psi)\nabla H]. \quad (23)$$

Remembering that the hydraulic head is, in general, the sum of the pressure head (or its negative, the suction head ψ) and the gravitational head (or elevation) z , we can write

$$\partial\theta/\partial t = -\nabla \cdot [K(\psi)\nabla(\psi - z)]. \quad (24)$$

Since ∇z is zero for horizontal flow and unity for vertical flow, we can rewrite (24) as

$$\frac{\partial\theta}{\partial t} = -\nabla \cdot [K(\psi)\nabla\psi] + \frac{\partial K}{\partial z} \quad (25)$$

or

$$\begin{aligned} \frac{\partial\theta}{\partial t} = & -\frac{\partial}{\partial x} \left(K \frac{\partial\psi}{\partial x} \right) - \frac{\partial}{\partial y} \left(K \frac{\partial\psi}{\partial y} \right) \\ & - \frac{\partial}{\partial z} \left(K \frac{\partial\psi}{\partial z} \right) + \frac{\partial K}{\partial z} \end{aligned} \quad (26)$$

Processes may also occur in which ∇z (the gravity gradient) is negligible compared to the strong matric suction gradient $\nabla\psi$. In such cases,

$$\partial\theta/\partial t = \nabla \cdot [K(\psi)\nabla\psi], \quad (27)$$

or in a one-dimensional horizontal system,

$$\partial\theta/\partial t = (\partial/\partial x)[K(\psi)(\partial\psi/\partial x)]. \quad (28)$$

C. Laboratory Measurement of Unsaturated Conductivity

Knowledge of the unsaturated hydraulic conductivity at different suction and wetness values is generally required before any of the mathematical theories of water flow can be applied in practice. Since there is as yet no universally proven way to predict these values from more basic or more easily obtainable soil properties, K must be measured experimentally. In principle, K can be obtained from either steady-state or transient-state flow systems. In steady flow systems, flux, gradient, and water content are constant in time, while in transient flow systems, they vary. In general, therefore, measurements based on steady flow are more convenient to carry out and are often more accurate. The difficulty, however, lies in setting up the flow system, which may take a very long time to stabilize. Conductivity is usually measured by applying a constant hydraulic head difference across the sample and measuring the resulting steady flux of water. Soil samples can be desaturated either by tension-plate devices or in a pressure chamber. Measurements are made at successive levels of suction and wetness so as to obtain the functions $K(\psi)$, $K(\theta)$. The $K(\psi)$ relationship is hysteretic, and, therefore, to completely describe it, measurements should be made

both in desorption and in sorption, as well, perhaps, as in intermediate scanning. This is difficult, however, and requires specialized apparatus, so that all too often only the desorption curve is measured (starting at saturation and proceeding to increase the suction in increments).

Such laboratory techniques can also be applied to the measurement of undisturbed soil cores taken from the field. This is certainly preferable to measurements taken on fragmented and artificially packed samples, though it should be understood that no field sampling technique yet available provides truly undisturbed samples. Moreover, any attempt to represent a field soil by means of extracted samples incurs the problem of field soil heterogeneity as well as the associated problem of determining the appropriate scale (i.e., the representative volume) for realistic measurement of parameters.

D. Field Measurement of Unsaturated Conductivity

Application of the theories of soil physics to the description or prediction of actual processes in the field (e.g., processes involved in irrigation, drainage, water conservation, groundwater recharge and pollution, as well as infiltration and runoff control) depends upon knowledge of the pertinent hydraulic characteristics of the soil, including the functional relation of hydraulic conductivity and of matric suction to soil wetness as well as the spatial and temporal variation of these in the often heterogeneous field situation. Hence it is necessary to devise practical methods for measuring soil hydraulic conductivity on a macroscale *in situ*. Among the methods proposed are the following: (1) using sprinkling infiltrometers, (2) performing infiltration through an impeding layer (crust), and (3) monitoring the internal drainage of soil profiles in the absence of evaporation. These methods are described in standard texts on soil physics.

VII. SOIL AIR AND AERATION

A. Importance of Soil Aeration

The process of soil aeration is one of the most important determinants of soil productivity. Plant roots adsorb oxygen and release carbon dioxide in the process of respiration. In most terrestrial plants (except such specialized plants as rice), the internal transfer of oxygen from the parts above the ground (leaves and stems) to those below the ground surface (roots) cannot take place at a rate sufficient to supply the oxygen requirements of the roots. Adequate root respiration requires that the soil itself be aerated, that is, that gaseous exchange take place between soil air and the atmosphere at such a rate as to prevent

a deficiency of oxygen and an excess of carbon dioxide from developing in the root zone. Soil microorganisms also respire, and, under conditions of restricted aeration, might compete with the roots of higher plants.

Impeded aeration resulting from poor drainage and waterlogging, or from mechanical compaction of the soil, can strongly inhibit crop growth. In particular, the problem of soil compaction seems to have worsened in recent decades, along with the growing trend to use larger and heavier machinery and the tendency to tread over the field repeatedly. It seems likely that root systems are commonly restricted in extent by the progressive decrease of aeration in the deeper regions of the soil profile.

Anaerobic conditions in the soil induce a series of reduction reactions, both chemical and biochemical. Included among these reactions are denitrification (the processes by which nitrate is reduced to nitrite, thence to nitrous oxide and eventually to elemental nitrogen: $\text{NO}_3^- \rightarrow \text{NO}_2^- \rightarrow \text{N}_2\text{O} \rightarrow \text{N}_2$), manganese reduction from the manganic to manganous form, iron reduction from the ferric to the ferrous form, and sulfate reduction to form hydrogen sulfide.

B. Composition of Soil Air

With good aeration, the composition of soil air remains close to that of the open atmosphere. Not so in a poorly aerated soil. Over time and depth, soil air is much more variable than the atmosphere. In particular, the concentration of carbon dioxide (the principal product of aerobic respiration by roots and microbes) can be 10 or even 100 times greater in the soil than in the atmosphere. A rise in CO_2 concentration is generally associated with a drop in O_2 concentration. In extreme cases of aeration restriction, O_2 levels can fall to near zero. Prolonged anaerobic conditions can result in the development of a chemical environment characterized by reduction reactions such as denitrification, the evolution of such gases as hydrogen sulfide (H_2S), methane (CH_4), and ethylene, and the reduction of mineral oxides such as those of iron and manganese.

C. Convective Flow of Soil Air

The exchange of air between the soil and the atmosphere can occur by means of two different mechanisms: convection and diffusion. Each of these processes can be formulated in terms of a linear rate law stating that the flux is proportional to the moving force. In the case of convection, also called mass flow, the moving force consists of a gradient of total gas pressure, and it results in the entire mass of air streaming from a zone of higher pressure to one of lower pressure. In the case of diffusion, on

the other hand, the moving force is a gradient of partial pressure (or concentration) of any constituent member of the variable gas mixture that we call air, and it causes the molecules of the unevenly distributed constituent to migrate from a zone of higher to lower concentration even while the gas as a whole may remain isobaric and stationary.

A number of phenomena can cause pressure differences between soil air and the external atmosphere, thereby inducing convective flow into or out of the soil. Among these phenomena are barometric pressure changes in the atmosphere, temperature gradients, and wind gusts over the soil surface. Additional phenomena affecting the pressure of soil air are the penetration of water during infiltration, causing displacement of antecedent soil air downward, and the extraction of soil water by plant roots. Short-term changes in soil air pressure can also occur during tillage or compaction by machinery.

Notwithstanding the differences between water flow and air flow, it is possible to formulate the convective flow of air in the soil as an equation analogous to Darcy's law for water flow:

$$q_v = -(k/\eta)\nabla p, \quad (29)$$

where q_v is the volume convective flux of air (volume flowing through a unit cross-sectional area per unit time), k is permeability of the air-filled pore space, η is viscosity of soil air, and ∇p is the three-dimensional gradient of soil air pressure. In one dimension, this equation takes the form

$$q_v = -(k/\eta)(dp/dx). \quad (30)$$

If the flux is expressed in terms of mass (rather than volume) per unit area and per unit time, then the equation is

$$q_m = -(\rho k/\eta)(dp/dx), \quad (31)$$

where q_m is the mass convective flux and ρ is the density of soil air.

Recalling that the density of a gas depends on its pressure and temperature, we shall now assume that soil air is an ideal gas in which the relation of mass, volume, and temperature is given by the equation

$$pV = nRT, \quad (32)$$

where p is pressure, V is volume, n is number of moles of gas, R is the universal gas constant per mole, and T is absolute temperature. Since the density $\rho = M/V$ and the mass M is equal to the number of moles n times the molecular weight m , we have

$$\rho = (m/RT)p. \quad (33)$$

We now introduce the continuity equation (conservation of mass) for a compressible fluid as

$$\frac{\partial \rho}{\partial t} = -\frac{\partial q_m}{\partial x}. \quad (34)$$

Substituting the expression for ρ from Eq. (33) and the expression for q_m from Eq. (31) into Eq. (34), we obtain

$$\frac{m}{RT} \frac{\partial p}{\partial t} = \frac{\partial}{\partial x} \left(\frac{\rho k}{\eta} \frac{\partial p}{\partial x} \right). \quad (35)$$

If $\rho k/\eta$ are more or less constant (i.e., the pressure differences are small), we can write

$$\frac{\partial p}{\partial t} = \alpha \frac{\partial^2 p}{\partial x^2}, \quad (36)$$

where $\alpha = RTk/m$, a composite constant. This is an approximate equation for the transient-state convective flow of air in soil. An assumption underlying the use of this equation is that flow is laminar, which it was indeed shown to be for small pressure differences.

D. Diffusion of Soil Air

The diffusive transport of gases such as O₂ and CO₂ in the soil occurs partly in the gaseous phase and partly in the liquid phase. Diffusion through the air-filled pores maintains the exchanges of gases between the atmosphere and the soil, whereas diffusion through water films of various thickness maintains the supply of oxygen to, and disposal of CO₂ from, live tissues, which are typically hydrated. For both portions of the pathway, the diffusion process can be described by Fick's law as

$$q_d = -D \frac{dc}{dx}, \quad (37)$$

where q_d is the diffusive flux (mass diffusing across a unit area per unit time), D is the diffusion coefficient (generally having the dimensions of area per time), c is the concentration (mass of diffusing substance per volume), x is the distance, and dc/dx is the concentration gradient. If partial pressure p is used instead of concentration of the diffusing component, we get

$$q_d = -(D/\beta) \frac{dp}{dx}, \quad (38)$$

where β is the ratio of the partial pressure to the concentration.

Considering first the diffusive path in the air phase, we note that the diffusion coefficient in the soil D_s must be smaller than that in bulk air D_0 owing to the limited fraction of the total volume occupied by continuous air-filled pores and also to the tortuous nature of these pores.

Having established the variable nature of D_s , we now return to the mathematical formulation of diffusion processes. To account for transient conditions, we must once again introduce the continuity principle

$$\frac{\partial c}{\partial t} = -\frac{\partial q_d}{\partial x}, \quad (39)$$

which states that the rate of change of concentration with time must equal the rate of change of diffusive flux with distance. The foregoing assumes that the diffusing substance is conserved throughout. As O₂ and CO₂ diffuse through the soil, however, O₂ is taken up and CO₂ is generated by aerobic biological activity along the diffusive path. To take account of the amount of a diffusing substance added to, or subtracted from, the system per unit time, we add a $\pm S$ term to the right-hand side of Eq. (39). Note that a positive sign represents an increment rate (source) and a negative sign represents a decrement rate (sink) for the substance considered. Accordingly,

$$\frac{\partial c}{\partial t} = -(\frac{\partial q_d}{\partial x}) \pm S(x, t). \quad (40)$$

The designation $S(x, t)$ implies that the source–sink term is a function of (i.e., varies with) both space and time.

We next substitute Eq. (37) into Eq. (40) and consider only the vertical direction z (depth) to obtain

$$\frac{\partial c}{\partial t} = \frac{\partial}{\partial z} \left(D_s \frac{\partial c}{\partial z} \right) \pm S(z, t). \quad (41)$$

In the event that D_s is constant, Eq. (41) simplifies to

$$\frac{\partial c}{\partial t} = D_s (\frac{\partial^2 c}{\partial z^2}) \pm S(z, t). \quad (42)$$

In aggregated soils, gaseous diffusion can be expected to take place rapidly in the interaggregate macropores, which quickly drain after rain or irrigation and form a network of continuous air-filled voids. On the other hand, the intraaggregate micropores can remain nearly saturated for extended periods and thus restrict the internal aeration of aggregates.

VIII. SOIL TEMPERATURE AND HEAT FLOW

A. Importance of Soil Temperature

Soil temperature, its value at any moment and the manner in which it varies in time and space, is a factor of primary importance in determining the rates and directions of soil physical processes and of energy and mass exchange with the atmosphere, including evaporation and aeration. Temperature also governs the types and rates of chemical reactions that take place in the soil. Finally, soil temperature strongly influences biological processes, such as seed germination, seedling emergence and growth, root development and respiration, and microbial activity.

Soil temperature varies in response to changes in the radiant, thermal, and latent energy exchange processes that take place primarily through the soil surface. The

effects of these phenomena are propagated into the soil profile by a complex series of transport processes, the rates of which are affected by time- and space-variable soil properties. Hence the quantitative formulation and prediction of the soil thermal regime can be a formidable task. Even beyond passive prediction, the possibility of actively controlling or modifying the thermal regime requires a thorough knowledge of the processes at play and of the environmental and soil parameters that govern their rates.

B. Conduction of Heat in Soil

The first law of heat conduction, known as Fourier's law, states that the flux of heat in a homogeneous body is in the direction of, and proportional to, the temperature gradient:

$$q_h = -\kappa \nabla T, \quad (43)$$

where q_h is the thermal flux (i.e., the amount of heat conducted across a unit cross-sectional area in unit time), κ is thermal conductivity, and ∇T is the spatial gradient of temperature T . In one-dimensional form, this law is written as

$$q_h = -\kappa_x dT/dx$$

or

$$q_h = -\kappa_z dT/dz. \quad (44)$$

Here dT/dx is the temperature gradient in any arbitrary direction designated x and dT/dz is, specifically, the vertical direction representing soil depth ($z = 0$ being the soil surface).

If q_h is expressed in calories per square centimeter per second and the temperature gradient in degree kelvin per centimeter, κ has the units of calories per centimeter degree second. If, on the other hand, the thermal flux is given in watts per meter and the gradient in degrees per meter, the thermal conductivity assumes the units of watts per meter degree.

Equation (43) is sufficient to describe heat conduction under steady-state conditions, that is, where the temperature at each point in the conducting medium and the flux remain constant in time. To account for nonsteady or transient conditions, we need a second law analogous to Fick's second law of diffusion. To obtain the second law of heat conduction, we invoke the principle of energy conservation in the form of the continuity equation, which states that in the absence of any sources or sinks of heat the time rate of change in heat content of a volume element of the conducting medium (in our case, soil) must be equal to the change of flux with distance:

$$\rho c_m \partial T / \partial t = -\nabla \cdot q_h, \quad (45)$$

where ρ is mass density and c_m is specific heat capacity per unit mass (called simply specific heat and defined as the change in heat content of a unit mass of the body per unit change in temperature). The product ρc_m (often designated C) is the specific heat capacity per unit volume, and $\partial T / \partial t$ is the time rate of temperature change. Note that the symbol ρ represents the total mass per unit volume, including the mass of water in the case of a moist soil.

By combining Eqs. (43) and (45), we obtain the desired second law of heat conduction as

$$\rho c_m \partial T / \partial t = \nabla \cdot (\kappa \nabla T), \quad (46)$$

which in one-dimensional form is

$$\rho c_m \frac{\partial T}{\partial t} = \frac{\partial}{\partial x} \left(\kappa \frac{\partial T}{\partial x} \right). \quad (47)$$

Sometimes we may need to account for the possible occurrence of heat sources or sinks in the realm where heat flow takes place. Heat sources include such phenomena as organic matter decomposition, wetting of initially dry soil material, and condensation of water vapor. Heat sinks are generally associated with evaporation. Lumping all these sources and sinks into a single term S , we can rewrite the last equation in the form

$$\rho c_m \frac{\partial T}{\partial t} = \frac{\partial}{\partial x} \left(\kappa \frac{\partial T}{\partial x} \right) \pm S(x, t), \quad (48)$$

in which the source-sink term is shown as a function of both space and time.

C. Volumetric Heat Capacity of Soils

The volumetric heat capacity C of a soil is defined as the change in heat content of a unit bulk volume of soil per unit change in temperature. Its units are calories per cubic centimeter per degree (Kelvin) or joules per cubic meter per degree. As such, C depends on the composition of the soil's solid phase (the mineral and organic constituents present), bulk density, and the soil's wetness.

The value of C can be calculated by addition of the heat capacities of the various constituents, weighted according to their volume fractions, as

$$C = \sum f_{s_i} C_{s_i} + f_w C_w + f_a C_a. \quad (49)$$

Here, f denotes the volume fraction of each phase: solid (subscripted s), water (w), and air (a). The solid phase includes a number of components, subscripted i , such as various minerals and organic matter, and the symbol \sum indicates the summation of the products of their respective volume fractions and heat capacities. The C value for water, air, and each component of the solid

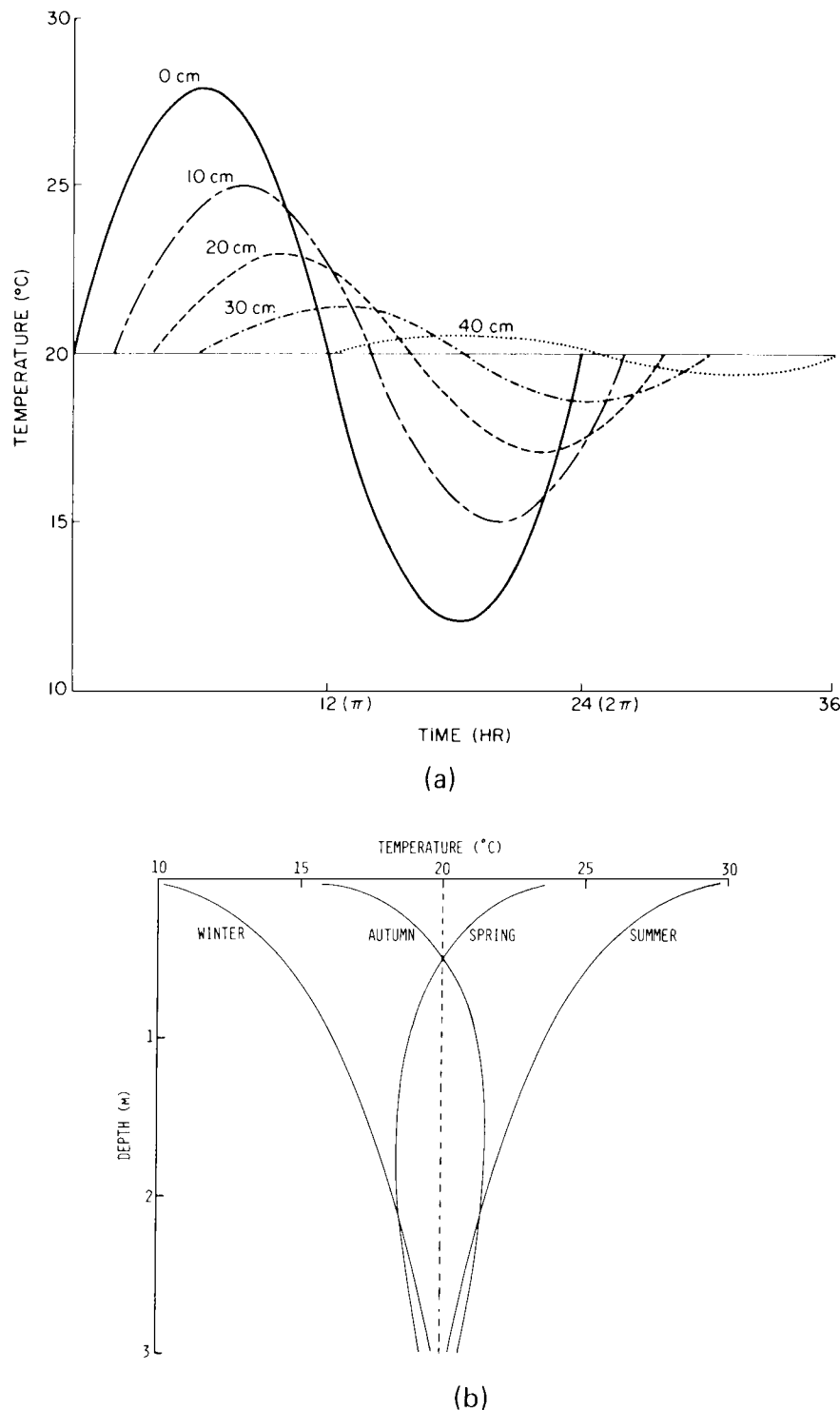


FIGURE 16 (a) Idealized variation of soil temperature with time for various depths. Note that at each succeeding depth the peak temperature is damped and shifted progressively in time. Thus, the peak at a depth of 40 cm lags about 12 h behind the temperature peak at the surface and is only about $\frac{1}{16}$ of the latter. In this hypothetical case, a uniform soil was assumed, with a thermal conductivity of 4×10^{-3} cal/cm s deg and a volumetric heat capacity of 0.5 cal/cm³ deg. (b) The soil temperature profile as it might vary from season to season in a frost-free region. [Reprinted with permission from Hillel, D. (1982). "Introduction to Soil Physics," Figs. 9.3 and 9.4, pp. 169 and 170. Copyright 1982 by Academic Press, New York.]

phase is the product of the particular density and specific heat per unit mass.

D. Thermal Conductivity of Soils

Thermal conductivity, designated κ , is defined as the amount of heat transferred through a unit area in unit time under a unit temperature gradient. The thermal conductivities of specific soil constituents differ very markedly. Hence the space-average (macroscopic) thermal conductivity of a soil depends upon its mineral composition and organic matter content, as well as upon the volume fractions of water and air. Since the thermal conductivity of air is very much smaller than that of water or solid matter, a high air content (or low water content) corresponds to a low thermal conductivity. Moreover, since the proportions of water and air vary continuously, κ is also time variable. Soil composition is seldom uniform in depth, hence κ is generally a function of depth as well as of time. It varies with temperature.

E. Thermal Regime of Soil Profiles

In nature, soil temperature varies continuously in response to the ever-changing meteorological regime acting upon the soil-atmosphere interface. That regime is characterized by a regular periodic succession of days and nights and of summers and winters. Yet the regular diurnal and annual cycles are perturbed by such irregular episodic phenomena as cloudiness, cold waves, warm waves, rainstorms, snowstorms, and periods of drought. Add to these external influences the soil's own changing properties (i.e., temporal changes in reflectivity, heat capacity, and thermal conductivity as the soil alternately wets and dries, and the variation of all these properties with depth), as well as the influences of geographic location and vegetation.

The simplest mathematical representation of nature's fluctuating thermal regime is to assume that at all depths in the soil the temperature oscillates as a pure harmonic (sinusoidal) function of time around an average value. (See Fig. 16.)

Now let us assume that although soil temperature varies differently at different depths in the soil, the average temperature is the same for all depths. We next choose a starting time ($t = 0$) such that the surface is at the average temperature. The temperature at the surface can then be expressed as a function of time as

$$T(0, t) = \bar{T} + A_0 \sin \omega t, \quad (50)$$

where $T(0, t)$ is the temperature at $z = 0$ (the soil surface) as a function of time t , \bar{T} is the average temperature of the surface (as well as of the profile), and A_0 is the amplitude of the surface temperature fluctuation [the range from

maximum (or minimum) to average temperature]. Finally, ω is the radial frequency, which is two times the actual frequency. In the case of diurnal variation, the period is 86,400 s (in 24 h) and so $\omega = 2\pi/86,400 = 7.27 \times 10^{-5}/s$. Note that the argument of the sine function is expressed in radians rather than in degrees.

Equation (50) is the boundary condition for $z = 0$. For the sake of convenience, let us assume that at infinite depth ($z = \infty$) the temperature is constant and equal to \bar{T} . Under these circumstances, temperature, at any depth z and time t , is also a sine function of time:

$$T(z, t) = \bar{T} + A_z \sin[\omega t + \varphi(z)], \quad (51)$$

in which A_z is the amplitude at depth z . Both A_z and $\varphi(z)$ are functions of z but not of t . They can be determined by substituting the solution of Eq. (49) in the differential equation $\partial T/\partial t = D_h(\partial^2 T/\partial z^2)$. This leads to the solution

$$T(z, t) = \bar{T} + A_0 [\sin(\omega t - z/d)]/e^{z/d}. \quad (52)$$

The constant d is a characteristic depth, called the damping depth, at which the temperature amplitude decreases to the fraction $1/e$ ($=0.37$) of the amplitude at the soil surface A_0 .

The annual variation of soil temperature down to considerable depth causes a deviation from the simplistic assumption that the daily average temperature is the same for all depths in the profile. The combined effect of the annual and diurnal variation of soil temperature can be expressed by

$$T(z, t) = \bar{T}_y + A_y \frac{\sin(\omega_y t + \varphi_y - z/d_y)}{\exp(z/d_y)} + A_d \frac{\sin(\omega_d t + \varphi_d - z/d_d)}{\exp(z/d_d)}, [2pt] \quad (53)$$

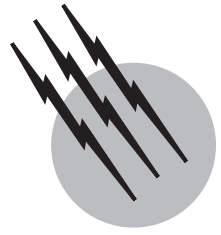
where the subscripted indices y and d refer to the yearly and daily temperature waves, respectively. Thus, \bar{T}_y is the annual mean temperature. The daily cycles are now seen to be short-term perturbations superimposed upon the annual cycle. Vagaries of weather (e.g., spells of cloudiness or rain) can cause considerable deviations from simple harmonic fluctuations, particularly for the daily cycles.

SEE ALSO THE FOLLOWING ARTICLES

ENVIRONMENTAL GEOCHEMISTRY • GEOCHEMISTRY, ORGANIC • HEAT FLOW • SOIL AND GROUNDWATER POLLUTION • SOIL MECHANICS • STREAMFLOW • WATER RESOURCES

BIBLIOGRAPHY

- Baver, L. D., Gardner, W. R., and Gardner, W. H. (1973). "Soil Physics," Wiley, New York.
- Campbell, G. S. (1985). "Soil Physics with BASIC," Elsevier, Amsterdam.
- Hanks, R. J., and Ashcroft, G. L. (1980). "Applied Soil Physics," Springer-Verlag, Berlin.
- Hillel, D. (1971). "Soil and Water: Physical Principles and Processes," Academic Press, New York.
- Hillel, D. (1977). "Computer Simulation of Soil-Water Dynamics," International Development Research Center, Ottawa.
- Hillel, D. (1980). "Fundamentals of Soil Physics," Academic Press, New York.
- Hillel, D. (1980). "Applications of Soil Physics," Academic Press, New York.
- Hillel, D. (1982). "Introduction to Soil Physics," Academic Press, New York.
- Kirkham, D., and Powers, W. L. (1972). "Advanced Soil Physics," Wiley (Interscience), New York.
- Koorevaar, P., Menelik, G., and Dirksen, C. (1983). "Elements of Soil Physics," Elsevier, Amsterdam.
- Marshall, T. J., and Holmes, J. W. (1979). "Soil Physics," Cambridge Univ. Press, Cambridge and London.
- Soil Science*, 75th Anniversary Issue, **151**(1), January 1991.



Stochastic Description of Flow in Porous Media

Ghislain de Marsily

*Université Pierre et Marie Curie and
Ecole des Mines de Paris*

- I. Definition of the Average Properties of a Porous Medium
- II. Darcy's Law and Averaging Permeabilities in Heterogeneous Porous Media
- III. Estimation by Kriging of Heterogeneous Permeability Fields
- IV. Stochastic Flow Equations, Analytical and Numerical Solutions

GLOSSARY

Averaging Estimating physical quantities defined at a macroscopic scale for a continuum from microscopic measurements. Spatial averaging is done by integration over space and ensemble averaging by integration over the space of realizations.

Conditional simulation See simulation.

Covariance Second moment of a stationary random function.

Ergodicity Assumption that the spatial distribution of a realization of a stationary random function has the same probability distribution function as the ensemble of realizations of the same random function.

Geostatistics A theory that applies to variables extending over space, which are spatially correlated. Most

geologic quantities (thickness of a layer, concentration of an element in the rock or the water, permeability, porosity, etc) display such spatial correlation. Geostatistics offer the means to estimate the value of the variable in space, based on local measurements (see kriging) or to simulate the value of the variable in space (see simulations and conditional simulation).

Kriging A geostatistical technique that is used to estimate the value of a Random Function (e.g., a parameter such as the permeability) in space, based on a set of local measurements. Kriging produces contour maps of the parameter and can be extended to generate conditional simulations of the same parameters.

Macroscopic scale Level at which the porous medium is considered as an equivalent continuum without distinguishing between the pores and the grains.

Microscopic scale Level at which the pores and the grains of a porous medium are distinguished and their respective roles analyzed.

Random function (RF) Function $Z(x, \xi)$ of both the spatial coordinates x and a state variable ξ . For each value ξ_i of the state variable, the spatial function $Z(x, \xi_i)$ is completely defined in space. Each value of ξ_i represents a different spatial function; for a position x_j , $Z(x_j, \xi)$ is a random variable.

Random variable Variable Z , which can take an infinite number of values. In general, the statistical properties of these values are defined: mean, variance, probability density function.

Realization of an RF Spatial function $Z(x, \xi_i)$ for a given value of the state variable ξ_i .

Simulation of an RF To simulate an RF is to produce a (large) number of realizations of the spatial function $Z(x, \xi_i)$ (i.e., for different ξ), which have the correct statistical properties of Z (same mean, variance, covariance). A **conditional simulation** is a simulation that has not only the correct statistical properties of Z , but also takes the measured values Z_i of Z at a discrete set i of measurement points.

Stationarity Assumption that any statistical property of a random function $Z(x, \xi)$ (e.g., mean, variance, covariance, higher-order moments or probability distribution functions) is stationary in space (i.e., does not vary with a translation).

THE STOCHASTIC DESCRIPTION of porous media is an approach that has been developed in recent years to take into account the very complex nature of the void space in such media and to derive an exact phenomenological description of the macroscopic flow, coherent with the classical empirical approach represented by Darcy's law. On a larger scale, it makes it possible to quantify the uncertainty in the macroscopic flow predictions, given the inherent uncertainty and spatial variability of the properties of porous media in natural systems. The concepts of the change from the microscopic pore scale to the macroscopic one are outlined and followed by a description of the mathematics of developing Darcy's law and the flow equation, and of the estimate of average properties of porous media in one, two, or three dimensions in spatially variable systems. The problem of estimating spatially variable parameters, generally known as Geostatistics, is then summarized for the example of permeabilities; kriging equations are given and simulation methods are outlined. Stochastic partial differential flow equations are presented and analytical or numerical techniques to solve them are briefly discussed.

I. DEFINITION OF THE AVERAGE PROPERTIES OF A POROUS MEDIUM

A porous medium is a very complex assembly of grains, solids, and pores containing fluids. The major conceptual obstacle to the understanding of the porous medium behavior is that of change of scale: at the microscopic pore scale, the physics of the interactions between the fluid and the solid are relatively well understood and documented, but at any larger scale, it is necessary to perform an integration in order to define the "average" properties of the porous medium, regarded as a continuum. This problem of scale change is discussed in the following.

A. Representative Elementary Volume

The classical approach is that of the representative elementary volume (REV) (see, e.g., Bear, 1972, 1979). Consider the case of one very simple property of a porous medium, its porosity ω , defined as the ratio of the pore volume to the total volume of a sample. If a porous medium is regarded as a continuum, we must be able to define its porosity at a point x in space. The REV method consists in saying that we give to the mathematical point x the porosity $\langle \omega \rangle$ of a certain volume of material surrounding this point, the REV, which will be used to define (and possibly measure) the "average" property of the volume in question. Here, $\langle \cdot \rangle$ stands for "volume average." Conceptually, this definition involves integration in space or taking a representative sample of the medium to measure the property. The size of the REV is constrained in two ways.

The first one assumes that the REV is sufficiently large to contain a sufficiently great number of pores to allow us to define a mean global property, while ensuring that the effects of the fluctuations from one pore to another are negligible. One may, for example, take 1 cm³ or 1 dm³.

The second one assumes that the REV is small enough for the parameter variations from one domain to the next to be approximated by continuous functions, so that we may use infinitesimal calculus, without introducing any error that may be picked up by the measuring instruments at the macroscopic scale, where meters and hectometers are the usual dimensions.

The size of the REV (e.g., measured by one of its characteristic dimensions l , such as the radius of a sphere or the side of a cube) is determined by a flattening of the curve representing the variation of the porosity with l (Fig. 1). However, nothing allows us to assert that such a flattening always exists, and the size and existence of a REV is thus quite arbitrary. A further limitation of this concept is that it gives no basis for studying the variation of the porosity in space.

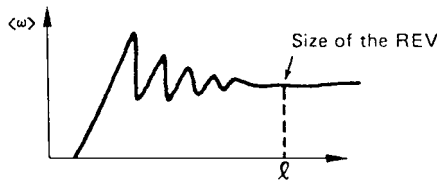


FIGURE 1 Porosity (ω) as a function of the dimension 1 of the sample. [From G. de Marsily (1986). “Quantitative Hydrogeology, Groundwater Hydrology for Engineers,” Academic Press, Orlando, FL.]

B. Stochastic Approach

The most recent definition of the average properties of a porous medium is the stochastic approach (e.g., Dagan, 1989; Gelhar, 1993). The microscopic porosity $\omega(x)$ is then considered as a random function (RF). This approach consists in saying that the studied porous medium is a “realization” of a random process.

Let us try to visualize the concept. Suppose that we create, in the laboratory, several sand columns, each one filled with the same type of sand. Each column represents the same porous medium but is somewhat different from the others. Each column is a “realization” of the same porous medium, defined as the ensemble of all possible realizations (infinite in number) of the same process.

A property such as the porosity can then be defined, at a given geometrical point in space, as the average over all possible realizations of its point value (defined as zero in a grain and one in a pore). One speaks of “ensemble averages” instead of “space averages.” For the previously mentioned sand columns, it is obvious that the ensemble average (or expected value E) of these point porosities will be identical to the space average defined by taking the column itself as the REV. Furthermore, this ensemble average will be the same for any point of the column. We will define later the conditions necessary for this to be true.

In more general terms, a property Z will be called a random function (RF) $Z(x, \xi)$ if it varies both with the spatial coordinate system x and with the “state variable” ξ in the ensemble of realizations. Then, $Z(x, \xi_1)$ is a realization of Z ; $Z(x_0, \xi)$ is a random variable (i.e., the ensemble of the realizations of the RF Z at location x_0); and $Z(x_0, \xi_1)$ is the single value of Z at x_0 for realization ξ_1 . To simplify the notations, the variable ξ is generally omitted.

A more realistic example of realizations of random porous media is given by sand dunes in a desert: each of the dunes can be seen as a “realization” of the same process, which here is genetically the accumulation of grains of sand transported by the wind. It would be meaningful to describe the properties of the dunes statistically (ensemble averages), as their number can indeed be very large.

The immense advantage of the stochastic approach over the REV concept is that one can study other statistical properties of the porous medium in the ensemble of realizations than just the expected value. One very often uses the variance of the property, which characterizes the magnitude of the fluctuations with respect to the mean, and the autocovariance (or simply covariance), which characterizes the correlation between the values taken by the property at two neighboring points in space.

However, when a given real porous medium is studied, there will be only one realization of the conceptual random medium. Some assumptions are necessary to make this concept useful. The most common ones are stationarity and ergodicity.

Stationarity assumes that any statistical property of the medium (mean, variance, covariance, or higher-order moments, defined by the “ensemble averaging” concept) is stationary in space (i.e., does not vary with a translation): it will be the same at any point of the medium. Weak stationarity refers to a medium where only the first two moments are stationary: if $Z(x)$ is the studied property, where x is the coordinates in one, two, or three dimensions and the state variable ξ is omitted, the random function (RF) $Z(x)$ satisfies: (1) expected value:

$$E[Z(x)] = m$$

not a function of x , and (2) covariance:

$$E\{[Z(x) - m][Z(x + h) - m]\}$$

not a function of x , but a function of only the lag h , a vector in two or three dimensions. By developing and labeling this covariance $C(h)$,

$$C(h) = E[Z(x) - Z(x + h)] - m^2$$

By definition,

$$C(0) = E[(Z(x) - m)^2] = \sigma_z^2$$

is the variance of Z .

In more rigorous terms, true stationarity means that all the probability distribution functions (PDF) of the random function $Z(x)$ are invariant under translation, whether we consider one point $p[Z(x)]$ or n points $p[Z(x_1) \dots Z(x_n)]$.

Ergodicity implies that the real unique realization available behaves in space with the same PDF (and with the same moments) as the ensemble of possible realizations. In other words, by observing the variation in space of the property on the only available realization, it is possible to determine the PDF of the random function for all realizations. This is called the “statistical inference” of the PDF of the RF $Z(x)$.

In the vocabulary of stochastic processes, a phenomenon that is “stationary” and “ergodic” is called

“homogeneous.” We would then use “uniform” to describe a medium in which a property does not vary in space. Geologists traditionally call it “homogeneous.” Other, less stringent hypotheses, can also be defined (e.g., stationarity of increments of Z).

II. DARCY'S LAW AND AVERAGING PERMEABILITIES IN HETEROGENEOUS POROUS MEDIA

A. At the Microscopic Level

Darcy's law is an empirical linear relationship between the macroscopic filtration velocity $\langle u \rangle$, and the macroscopic pressure gradient $\langle \text{grad } p \rangle$: $\langle u \rangle = -(k/\mu) \langle \text{grad } p \rangle$. Here, $\langle \cdot \rangle$ stands for a spatial or an ensemble average. k is called the permeability, a parameter specific to each soil or rock, which can be a scalar or a second-order tensor if the medium is anisotropic, and μ is the dynamic viscosity. Physically, Darcy's law is the result of the integration of the Navier–Stokes equations in the very complex geometry of the pore space. Navier–Stokes is the general equation of fluid mechanics for Newtonian fluids. However, since this pore geometry is, in general, unknown, it is impossible to systematically derive Darcy's law and the value of the tensor k from Navier–Stokes, except when a very simple geometry of the pore space is assumed (e.g., cylindrical tubes or fissures of constant aperture (see, e.g., Marsily, 1986). The dimension of k is length (squared).

The general linear form of Darcy's law, and some properties of the permeability tensor k , can, however, be rigorously established. This is done for an incompressible fluid in steady-state flow while assuming that the microscopic velocity u is small enough to neglect the inertial term in the Navier–Stokes equations (this is quite acceptable in practice since the flow velocity in porous media is, in general, very small). Furthermore, these equations are written without the body forces F , only for the sake of simplicity. Navier–Stokes then reduces to

$$\mu \nabla^2 \mathbf{u} = \text{grad } p \quad \text{and} \quad \text{div } \mathbf{u} = 0.$$

Here, ∇^2 is the Laplace differential operator $\sum_i \partial^2 / \partial x_i^2$, p is the microscopic fluid pressure, and \mathbf{u} the microscopic fluid velocity vector. Let the porous medium be considered as a stationary and ergodic random ensemble, and let $\omega(x)$ be the microscopic porosity ($\omega(x) = 1$ in the pores and 0 in the grains). The solution of the microscopic flow problem in the entire domain can be described as finding a stationary random velocity $\mathbf{u}(x)$ that satisfies

$$\begin{aligned} \mu \nabla^2 \mathbf{u} &= \omega(x) \text{grad } p; & \text{div } \mathbf{u} &= 0 \\ \mathbf{u}(x) &= \omega(x) \mathbf{u}(x); & E(\mathbf{u}) &= \langle \mathbf{u} \rangle. \end{aligned}$$

To establish the existence and uniqueness of this solution, Matheron (1967) proposed the use of a variational principle to represent the energy dissipation by the viscous forces. The power per unit volume of this energy at the microscopic level is

$$W = -\mathbf{u} \cdot \text{grad } p.$$

It is then possible to show that the random velocity \mathbf{u} , which minimizes the mathematical expectation $E(W) = -E(\mathbf{u} \cdot \text{grad } p)$ while satisfying $\text{div } \mathbf{u} = 0$ and $\mathbf{u}(x) = \mathbf{u}(x)\omega(x)$, is also the solution of the Navier–Stokes equation. If \mathbf{u} is then extended to the grains ($\mathbf{u} = 0$ in the grains), the relationship $E(W) = -E(\mathbf{u} \cdot \text{grad } p) = -\mu E(\mathbf{u} \cdot \nabla^2 \mathbf{u})$ can be extended over the whole space. Furthermore, for a stationary $\text{grad } p$ and a stationary \mathbf{u} with $\text{div } \mathbf{u} = 0$, we have

$$E(\mathbf{u} \cdot \text{grad } p) = E(\mathbf{u}) \cdot E(\text{grad } p).$$

Then

$$E(W) = -E(\mathbf{U} \cdot \text{grad } p) = \langle \mathbf{u} \rangle \cdot \langle \text{grad } p \rangle,$$

which means that the averaging conserves the energy: the average of the microscopic energy dissipation is equal to the energy dissipation at the macroscopic level.

It can then be shown that the macroscopic Darcy law $\langle \mathbf{u} \rangle = -(k/\mu) \langle \text{grad } p \rangle$ derives from the linearity of the Navier–Stokes equation $\mu \nabla^2 \mathbf{u} = \text{grad } p$ and from this conservation of energy. Furthermore, it can be shown that the permeability tensor k is symmetric and positive definite.

B. At the Macroscopic Level

At the macroscopic level, the permeability $k(x)$ can also be regarded as a RF, for studying the behavior of heterogeneous porous media where the macroscopic parameter $k(x)$ varies in space. It is then of interest to again average the permeability in order to obtain the equivalent homogeneous permeability at a larger scale. Again, using the variational principle, it is possible to give an upper and a lower bound to this average permeability $\langle k \rangle$ at the large scale:

$$[E(k^{-1})]^{-1} < \langle k \rangle < E(k).$$

Expressed in words, the average $\langle k \rangle$ always lies between the harmonic and the arithmetic mean of the local permeability value. The harmonic mean is the obvious average for one-dimensional flow.

Furthermore, it is possible to show (Matheron (1967) for porous media; Landau and Lifschitz (1960) in electrodynamics) that, in two dimensions, and for macroscopic parallel flow conditions, the average permeability $\langle k \rangle$ is exactly the geometric mean if the probability distribution function of k is log-normal:

$$\ln\langle k \rangle = E(\ln k).$$

The geometric mean, which is an arithmetic averaging in the log space, always lies between the harmonic and the arithmetic means. This result has been extended to three dimensions, using a perturbation approach, initially as a conjecture, e.g., by King (1987), Dagan (1993), Indelman and Abramovich (1994), de Wit (1995), and now demonstrated by Noetinger (2000). The general expression for the average value of a log-normal permeability distribution is thus, for an isotropic medium in one, two, or three dimensions :

$1/\langle k \rangle = \langle 1/k \rangle$	in 1-D, the harmonic mean
$\ln\langle k \rangle = \langle \ln k \rangle$	in 2-D, the geometric mean
$\langle k \rangle = \langle k^{1/3} \rangle^3$	in 3-D, a power average with exponent 1/3

Most field studies show that the experimental PDF of the permeability of rocks is indeed log-normal, therefore these expressions are commonly used. For radial flow systems, or for transient conditions, average permeabilities have not yet been established theoretically but the previous results have been shown to be applicable by numerical experiments with flow models. See also Renard and Marsily (1997), Meier *et al.* (1998), and Dagan (2001), for the problem of up-scaling permeabilities.

III. ESTIMATION BY KRIGING OF HETEROGENEOUS PERMEABILITY FIELDS

Kriging, which is a part of the theory of Geostatistics, is a very powerful tool for estimating random functions (RF), which are defined by a set of local measurements and by their statistical properties (mean, variance, covariance), see, e.g., Matheron (1973), Journel and Huijbregts (1978), Marsily (1986), Deutsch and Journel (1992), Chilés and Delfiner (1999). We will restrict this presentation to the case of a second-order stationary random function Y with a constant mean, a constant variance and a stationary covariance. We consider the hydraulic conductivity $K = k\rho g/\mu$, where k is the macroscopic, spatially variable permeability, g is the acceleration due to gravity, and μ the dynamic viscosity or, in two dimensions, the transmissivity $T = K e$ of an aquifer, with e the thickness of the aquifer. As already stated, K or T are generally log-normally distributed, so that we will first transform them into their logarithm Y , which will be the RF on which we will work. Kriging is indeed a better estimator if the variable to be estimated is approximately normally distributed, although this is not an absolute requirement. Let us assume that a set of N measurements of Y have been made at N locations x_i in space. We call them Y_i . Here, x_i

represents the one, two or three coordinates in space of point i .

The problem that we want to solve is to *estimate* the value of Y at locations x_j , which have not been measured, based on the knowledge of the N measurements Y_i of Y and of the statistical properties of Y . These estimations are noted $Y^*(x_j)$, and will always be an approximation of reality. Kriging is a method for estimating Y^* ; it is both an *unbiased* and an *optimal* estimator. “Unbiased” means that the error of estimation will be, on average, zero (no systematic underestimation or over-estimation). “Optimal” means that the variance of the estimation error will be minimum. Lastly, Kriging is a linear estimator. It is written:

$$Y^*(x_j) = \sum_i \lambda_i Y_i,$$

where the summation over i is, generally, extended to all the N measurements Y_i , but in some cases only to a subset of measurements surrounding the point x_j to be estimated (e.g., if the number N is very large). The $N \lambda_i$'s are the “kriging weights,” they are the unknowns of the kriging problem, which we will now calculate. There are as many kriging equations as there are locations x_j where Y^* will be estimated and for each such location, the N weights λ_i will be different. In general, kriging is performed on a regular square grid, and the set of estimated values on that grid is used, e.g., as input in a flow model or for automatic contouring of the field Y .

The set of weights λ_i are determined by successively applying the two conditions defined above: (1) Unbiased estimation: one writes that $E[Y^*(x_j)] = Y'$, where Y' is the true (unknown) mean of the RF Y . By developing the kriging equation:

$$E[Y^*(x_j)] = Y' = E[\sum_i \lambda_i Y_i] = \sum_i \lambda_i E[Y_i] = \sum_i \lambda_i Y'$$

or

$$\sum_i \lambda_i = 1.$$

(2) Optimal estimation: one writes that the variance of the estimation error is minimum, i.e., $\text{Var}[Y^*(x_j) - Y(x_j)]$ minimum, which, since $E[Y^*(x_j) - Y(x_j)] = 0$, is written: $E[(Y^*(x_j) - Y(x_j))^2]$ minimum.

By substituting the kriging equation and after some rearranging, one gets

$$\begin{aligned} E[(Y^*(x_j) - Y(x_j))^2] &= \sum_i \sum_k \lambda_i \lambda_k E[(Y_i - Y(x_j)) \\ &\quad \times (Y_k - Y(x_j))]. \end{aligned}$$

By definition, the covariance of Y is defined as $E\{[Y(a) - Y'][Y(b) - Y']\} = C(a-b)$, where a and b are the coordinates of any points in space, and $(a-b)$ the distance (or vector) between these two points. We can rewrite $E[(Y^*(x_j) - Y(x_j))^2]$ with the objective of developing it in terms of the covariance function C :

$$\begin{aligned} E[(Y^*(x_j) - Y(x_j))^2] &= \Sigma_i \Sigma_k \lambda_i \lambda_k E\{[(Y_i - Y') \\ &\quad - [Y' - Y(x_j)])([Y_k - Y'] - [Y(x_j) - Y'])\}, \end{aligned}$$

which, after some developments and taking into account that $\Sigma_i \lambda_i = 1$, gives

$$\begin{aligned} E[(Y^*(x_j) - Y(x_j))^2] &= \Sigma_i \Sigma_k \lambda_i \lambda_k [C(x_i - x_k) \\ &\quad - 2C(x_i - x_j) + C(0)] \\ &= \Sigma_i \Sigma_k \lambda_i \lambda_k C(x_i - x_k) \\ &\quad - 2\Sigma_i \lambda_i C(x_i - x_j) + C(0). \end{aligned}$$

This is where the major “trick” of kriging comes in: the expression which gives the variance of the estimation error is no longer a function of the unknown “real” value $Y(x_j)$ but only of the covariance function C of the RF Y . The rest of the story is straightforward. The variance of the estimation error subject to the constraint that $\Sigma_i \lambda_i = 1$ is minimized with the Lagrange multiplier method: one minimizes $E[(Y^*(x_j) - Y(x_j))^2] + 2\mu[\Sigma_i \lambda_i - 1]$. Here, μ is the Lagrange multiplier and the factor 2 is just used to simplify the result. The minimization of this quadratic form in λ is obtained by setting to zero all its partial derivatives with respect to the N λ ’s and μ , which provides a linear system with $N + 1$ equations and $N + 1$ unknowns:

$$\begin{aligned} \Sigma_k \lambda_k C(x_i - x_k) + \mu &= C(x_i - x_j) \quad \text{for } i = 1, \dots, N \\ \Sigma_i \lambda_i &= 1. \end{aligned}$$

Once this linear system is solved, e.g., by Gauss elimination, the λ s can be used to estimate $Y^*(x_j)$ with the first kriging equation and furthermore, it is possible to estimate the variance of the estimation error by some simple substitutions of the expression given previously:

$$\text{Var}[Y^*(x_j) - Y(x_j)] = C(0) - \Sigma_i \lambda_i C(x_i - x_j) - \mu.$$

In the next section, we will describe how a variable can be simulated rather than just estimated. We conclude this section by some indications on how to determine the statistical properties of a variable Z , which has been measured in the field at N different locations. This step is called the “statistical inference.” The type of PDF can be estimated by building the histogram of the observed values and trying to fit it with a usual PDF (e.g., normal). On a normal distribution paper, this histogram should plot as a straight line; one can see how much the data deviate from this line. The mean can be estimated by averaging the data, in some cases with weighting coefficients, to eliminate clustering effects. A kriging equation can also be written to estimate the mean. Once the mean is known, the calculation of the experimental variance is straightforward. The covariance is more elaborate. The N measurement points are grouped into pairs, there are $N(N - 1)/2$ pairs that can be built

with N points. Let a_i and b_i be the two points of pair i . These pairs are then grouped into classes of distances, i.e., $h_i = a_i - b_i$ falls into a class of distance h_k . For each distance class h_k , the value of the experimental covariance C^* is estimated as

$$C^*(h_k) = (1/N_k) \{ \Sigma_i [Z(a_i) \cdot Z(b_i)] - Z'^2 \},$$

where N_k is the number of pairs a_i and b_i in the class of distance h_k , and Z' is the mean of Z . The experimental covariance C^* is plotted versus the distances h_k , and a general function $C(h)$ is fitted on the experimental covariance C^* , e.g., an exponential function, etc. Any function cannot be used to represent a covariance; it has to be a positive definite function (see, e.g., [Matheron, 1973](#); [Chilès and Delfiner, 1999](#)).

A more common approach to kriging and statistical inference is to assume that Z is not necessarily stationary, but that the first-order increments of Z are stationary; this is called the intrinsic hypothesis. One then defines a new function, the variogram of Z , which is more general than the covariance, and is written:

$$\gamma(h) = \frac{1}{2} E\{[Z(x + h) - Z(x)]^2\}.$$

It can be shown that, when both functions exist, the variogram γ is related to the covariance C by

$$\gamma(h) = C(0) - C(h).$$

Kriging equations can be written by using the variogram rather than the covariance and the inference of γ is easier than that of C as the mean Z' does not need to be known (see, e.g., [Marsily, 1986](#); [Chilès and Delfiner, 1999](#)).

IV. STOCHASTIC FLOW EQUATIONS, ANALYTICAL AND NUMERICAL SOLUTIONS

The diffusivity equation in hydrogeology is the result of combining (i) the macroscopic mass-balance equation, (ii) the macroscopic Darcy law, and (iii) the state equations for both the fluid and the porous medium, involving the compressibility of the fluid and that of the medium. Expressed in terms of the hydraulic head H rather than of the pressure p , it is similar to the heat equation:

$$\text{div}(K \text{grad } H) = S_s \partial H / \partial t,$$

where H is the hydraulic head, equal to $p/\rho g + z$ (p is the fluid pressure, ρ is the fluid mass per unit volume, z is the elevation above the datum, e.g., the mean sea level); K is the macroscopic hydraulic conductivity, equal to $k \rho g / \mu$; k is the macroscopic permeability, g is acceleration due to gravity, and μ the dynamic viscosity; S_s is the specific storage coefficient equal to $\rho \omega g (\beta + \alpha / \omega)$, with ω

the macroscopic porosity, β the compressibility of water, and α the compressibility of the porous medium; t is time.

This equation can be solved analytically, when the parameters K and S_s are constant over space (or when equivalent average parameters are used), and when the boundary and initial conditions are sufficiently simple. In more complex or heterogeneous cases, numerical solutions (finite differences, finite elements, boundary element, etc.) are commonly used (see e.g., [Anderson and Woessner, 1992](#); [Kinzelbach, 1986](#); [Marsily, 1986](#)). However, when the parameters of this equation are considered as random functions, the method of solution is quite different from the usual approach. Two methods of solving this problem are described below.

A. Analytic Solutions of the Stochastic Diffusivity Equation

The stochastic definition of the properties of porous media has led to the concept in which the diffusivity equation is considered as a stochastic partial differential equation (PDE). The parameters (K and S_s) of the equation are considered as stationary random functions, and therefore the solution H of the diffusivity equation is also an RF. Solving the stochastic PDE means determining the statistical properties of the solution H , given the statistical properties of the parameters K and S_s .

The advantage of this approach is that it makes it possible to take into account, in the field, the spatial variability and the uncertainty in the values of the parameters of the diffusivity equation. Local measurements of these parameters in the field (e.g., on samples or through local *in situ* hydraulic tests) show that they are, in general, highly variable in natural media. Rather than attempting to estimate them deterministically at all locations in the domain of interest, it is more relevant to try to estimate their variability statistically and to relate this variability to the uncertainty of the solution of the stochastic PDE.

We shall give a simple example of one method for solving analytically a stochastic PDE, namely the method of perturbation. This method is only valid if the variance of the stochastic process of interest is small. We shall solve a one-dimensional steady-state flow equation, without any source term, written as

$$d/dx[K(x)dH/dx] = 0.$$

The hydraulic conductivity $K(x)$ is assumed to be a stationary RF, the first two moments of which are known

$$E(K) = K'$$

$$E\{[K(x+s) - K'][K(x) - K']\} = C_K(s).$$

The variance of K , $C_k(0)$, is assumed small. Since K is stationary, K' is not a function of x , and $C_K(s)$, the covariance of K is only a function of the lag vector s , not of x . The stochastic PDE will be solved if we can determine the same first two moments of the solution H , its mean and covariance. To use the method of perturbation, one assumes that both K and H can be decomposed into a mean plus a perturbation:

$$\begin{aligned} K &= K' + k & \text{with } E(K) = K', E(k) = 0 \\ H &= H' + h & \text{with } E(H) = H', E(h) = 0. \end{aligned}$$

K and H are then developed to the first order (i.e., by adding to K' and H' a small fraction β of their fluctuation, which thus requires the perturbation to be small, i.e., the variance of K is small):

$$K = K + \beta k \quad \text{and} \quad H = H + \beta h.$$

We introduce this definition into the original PDE, develop in β and disregard terms in β^2 :

$$\begin{aligned} K' d^2H'/dx^2 + \beta[K' d^2h/dx^2 + dk/dx \cdot dH'/dx \\ + k d^2H'/dx^2] = 0. \end{aligned}$$

If this is to hold for any small β , each one of the two terms must be equal to zero:

$$(i) \quad K' d^2H'/dx^2 = 0$$

i.e.,

$$dH'/dx = 2q/K' \quad \text{and} \quad H' = 2qx/K' + a,$$

which gives us the required first moment of H , which, in this case, is not stationary. The two constants q and a are determined by the boundary conditions.

$$(ii) \quad K' d^2h/dx^2 + dk/dx \cdot dH'/dx + k d^2H'/dx^2 = 0$$

substituting the solution H' in this equation gives

$$d^2h/dx^2 = (q/K'^2)dk/dx$$

or

$$dh/dx = (q/K'^2)k + b$$

where b is a constant. We take the expected value of this expression:

$$E[dh/dx] = d/dx[E(h)] = (q/K'^2)E(k) + E(b).$$

As $E(h) = E(k) = 0$, we can see that $E(b) = b = 0$.

Then the relation

$$dh/dx = (q/K'^2)k$$

gives directly:

$$C_{dh/dx}(s) = (q^2/K'^4)C_k(s) = (q^2/K'^4)C_K(s).$$

However, for a stationary RF with a differentiable covariance, one can write

$$C_{dh/dx}(s) = -d^2/ds^2[C_h(s)].$$

Thus, if we can assume that

$$d/ds[C_h(s)]|_{s \rightarrow -\infty} = 0 \quad \text{and} \quad C_h(s)|_{s \rightarrow -\infty} = 0.$$

Then with two integrations, we find

$$C_h(s) = -(q^2/K'^4) \int_{-\infty}^s \int_{-\infty}^y C_k(u) du dy.$$

If we take, for instance, a modified exponential covariance for K :

$$C_k(s) = \sigma_K^2 \exp(-|s|/l)(1 - |s|/l),$$

where l is a characteristic length and σ_K^2 is the variance of K , then we find, by integration,

$$C_h(s) = l^2(q^2/K'^4)\sigma_K^2 \exp(-|s|/l)(l + |s|/l).$$

We can, for instance, determine the variance of h :

$$\sigma_h^2 = C_h(0) = l^2(q^2/K'^4)\sigma_K^2.$$

We have thus found the first two moments of the solution H of the stochastic PDE. Other methods for solving the stochastic PDE are the spectral method (see, e.g., [Gelhar, 1993](#)) and the Monte Carlo simulation method (see following, and in, e.g., [Delhomme, 1979; Freeze, 1975; Lavenue et al., 1995; Ramarao et al., 1995; Rubin and Gomez-Hernandez, 1990; Smith and Freeze, 1979](#)).

B. Monte Carlo Simulation Method for Solving the Stochastic Flow Equations

This is probably the most powerful method, where fewer assumptions are required. However, it is a numerical method that may require much central processing unit (CPU) time and a careful examination of the results. The principle of the method is very simple. Let $Z(x, \xi)$ be a stochastic process, x being the coordinates in space and ξ the state variable, for instance, the permeability. One first builds a numerical model of the problem, in each mesh of which a value of the permeability Z is required to solve the diffusivity equation. One then generates "simulations" $Z(x, \xi_i)$ of Z in the probabilistic sense, i.e., values of $Z(x_j, \xi_i)$ for each mesh x_j of the numerical model. A large number N of realizations ξ_i , $i = 1, \dots, N$, of Z are generated. To do so, one must know the probability distribution function of Z , its mean and its variance and covariance (if Z is spatially correlated). Note that the knowledge of the probability distribution function of Z was not necessary in the previous analytical method, only the mean, variance and covariance. Then for each of these realizations ξ_i , the parameter represented by $Z(x_j, \xi_i)$ in each mesh of the model is completely determined and known (e.g., the permeability). Thus, the diffusivity equation representing the flow in the porous medium can be solved numerically for each realization, providing the value of the dependent variable [e.g., $H(x_j, \xi_i)$ for the same realization ξ_i and

for all the x_j meshes]. It is then possible to statistically analyze the ensemble of calculated solutions $H(x, \xi_i)$ for $i = 1, \dots, N$: expected value of H at any location x_j , variance, histogram, and distribution function. It is no longer necessary to assume that H is stationary; these statistics can be calculated at each point. The covariance can also be determined if H is found to be stationary.

There are, however, some difficulties associated with the simulation method. First, a large number N of realizations is necessary in order to get meaningful statistics: from 50 to several hundreds or thousands. Second, as N is necessarily finite, one can always calculate an experimental variance or covariance, even for a phenomenon where they do not exist. It is preferable to check that when N increases, these statistics become, in fact, constant. Third, the solution can be a function of the mesh size: because the numerical solution requires that an average of $Z(x, \xi_i)$ be estimated over a mesh, this estimate becomes less variable as the mesh size increases, simply because of the spatial integration over each mesh. Thus, the variability of the solution $H(x, \xi)$ will also be affected. Furthermore, one must realize that if C_Z is the correlation structure of Z in space, then the correlation structure of the average of Z over a mesh will be the integral of C_Z over the mesh.

To generate realizations of $Z(x, \xi_i)$, several methods are available. Let us first assume that Z is stationary with a given PDF, but that Z is not spatially correlated. Most computer software provides a random number generator, which usually gives real numbers with a uniform distribution between 0 and 1, with mean 0.5 and variance 1. Standard routines can be used to transform these numbers into random numbers with a given PDF (e.g., normal), with mean 0 and variance 1. Let us call such random numbers z_j with, e.g., a normal PDF, mean 0 and variance 1. Let us assume that the parameter Z that we want to simulate is the permeability, which has a log-normal distribution, i.e., $Y = \ln Z$ is normal with mean Y' and variance σ_Y^2 . The uncorrelated values of Y and thus of Z at each mesh x_j ($j = 1, \dots, M$, with M the number of meshes of the model) for a realization ξ_i are simply generated by

$$\begin{aligned} \text{For } j = 1, \dots, M: \quad Y(x_j) &= Y' + z_j \sigma_Y \\ \text{and thus} \quad Z(x_j) &= \exp[Y(x_j)]. \end{aligned}$$

For a new realization ξ_k , a new set of M random numbers z_j are used. Note that in the case of permeability, the value of Z is simply the exponential of Y , with no additional term to account for the variance of Y , as is sometimes done for such a transformation (see, e.g., [Marsily, 1986](#)).

Let us now assume that Y is spatially correlated. The simplest method for generating an RF Y with a spatial correlation is called the Nearest Neighbor (e.g., [Smith and](#)

(Freeze, 1979). First an uncorrelated RF Y is generated, as outlined above. Then, in each mesh of the model, the correlated RF X is calculated as the weighted mean of the values of Y at mesh x_j and at surrounding meshes of x_j : for instance, on a regular square grid, the four meshes above, below, to the right, and to the left. Such averaging will keep the mean of Y , change the variance and generate a spatial correlation, i.e., a covariance for X . This covariance can be determined experimentally; it is a function of the number of neighbors used and of the weights assigned to each neighbor. By trial and error, one can very approximately fit a given covariance function and variance to X . Z is then again generated as $Z = \text{Exp}[X]$. But there are more elaborate methods that can generate directly correlated RFs with a prescribed covariance, e.g., the turning bands method (Matheron, 1973; Mantoglu and Wilson, 1982), the spectral method (e.g., Gelhar, 1993), the Cholesky decomposition of the covariance matrix (e.g., Neuman, 1984) or the sequential simulation (e.g., Deutsch and Journel, 1992).

Conditional simulations of $Z(x, \xi_i)$ instead of simple simulations can also be generated. This is a great improvement on the Monte Carlo method for practical problems. Indeed, the stochastic process Z is then said to be conditioned by the measurements $Z(x_j)$ in space if all the realizations $Z(x, \xi_i)$ have the measured values $Z(x_j)$ at each point x_j , where a measurement has been made. In nonconditional simulations, as discussed earlier, there is no way of insuring that the random value $Z(x)_j$, generated by the algorithm in mesh x_j , has the desired observed value. The method used to generate these conditional simulations is based on kriging, as shown in Section III, and works as follows.

Let us take the example of permeabilities Z , where $Y = \text{Ln}[Z]$ is a normal RF with a given mean and covariance. First, given the measurements Y_i , a kriged field Y^* is calculated in each mesh x_j of the model, using ordinary kriging:

$$Y^*(x_j) = \sum_i \lambda_i Y_i.$$

Then, an unconditional simulation $U(x_j)$ of a new RF U is generated in each mesh x_j of the model, with the same mean and covariance as Y , using one of the standard methods presented above. At each location x_i , where a measurement of Y is available, a fictitious "measurement" is taken of U ; let us call these measurements U_i . It is then possible to produce a kriged field U^* of U , based on the "measurements" U_i only:

$$U^*(x_j) = \sum_i \lambda_i U_i.$$

The conditional simulation of Y is then given by

$$Y(x_j) = Y^*(x_j) + [U(x_j) - U^*(x_j)].$$

This expression holds because the deviation $U - U^*$ (or $Y - Y^*$) around the kriged estimate U^* (or Y^*) is independent of U^* (or Y^*). An alternative to this "double kriging" method is the sequential simulation algorithm (e.g., Deutsch and Journel, 1992).

Nonconditional simulations are suitable for studying the theoretical variability of a process: the statistics of Z are assumed to be known, but no measured values are available. On the contrary, conditional simulations take the measured values into account and the considered variability and uncertainty are only those stemming from the residual uncertainty in the estimation of Z between measurement points.

The stochastic approach outlined here for the single-phase flow problem, can be extended to multiphase flow or to multi-component single-phase flow (i.e., petroleum reservoir engineering, hydrodynamic dispersion and pollution problems (see, e.g., Dagan, 1989, Gelhar, 1993 Lavenue *et al.*, 1995).

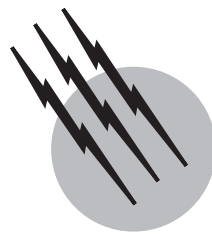
SEE ALSO THE FOLLOWING ARTICLES

HYDROGEOLOGY • MESOPOROUS MATERIALS, SYNTHESIS AND PROPERTIES • SOIL MECHANICS • SOIL PHYSICS • STOCHASTIC PROCESSES O STREAMFLOW

BIBLIOGRAPHY

- Anderson, M. P., and Woessner, W. W. (1992). "Applied Groundwater Modeling: Simulation of Flow and Advective Transport," Academic Press, San Diego, CA.
- Bear, J. (1972). "Dynamics of Fluids in Porous Media," American Elsevier, New York.
- Bear, J. (1979). "Hydraulics of Groundwater," McGraw-Hill, New York.
- Chilès, J. P., and Delfiner P. (1999). "Geostatistics: Modeling Spatial Uncertainty," Wiley, New York.
- Dagan, G. (1989). "Flow and Transport in Porous Formations," Springer-Verlag, New York.
- Dagan, G. (1993). "High-order correction of effective permeability of heterogeneous isotropic formations of lognormal conductivity distribution," *Transp. Porous Media* **12**, 279-290.
- Dagan, G. (2001). "Effective, equivalent and apparent properties of heterogeneous media." "Proc. 20th Intern.Congress of Theoretical and Applied Mechanics" (H. Aref and J. W. Phillips, eds.), Kluwer Academic Press, Dordrecht, The Netherlands.
- Delhomme, J. P. (1979). Spatial variability and uncertainty in groundwater flow parameters: a geostatistical approach. *Water Resour. Res.* **15**(2), 269-280.
- Deutsch, C. V., and Journel, A. (1992). "GSLIB, Geostatistical Software Library and Users' Guide," Oxford University Press, New York.
- de Wit, A. (1995). "Correlation structure dependence of the effective permeability of heterogeneous porous media," *Phys. Fluids* **7**(11), 2553-2562.
- Freeze, R. A. (1975). "A stochastic-conceptual analysis of one-dimensional groundwater flow in non-uniform homogeneous media," *Water Resour. Res.* **11**(5), 725-741.

- Gelhar, L. W. (1993). "Stochastic Subsurface Hydrology," Prentice-Hall, Englewood Cliffs, NJ.
- Indelman, P., and Abramovich, B. (1994). "A higher order approximation to effective conductivity in media of anisotropic random structure," *Water Resour. Res.* **30**(6), 1857–1864.
- Journel, A., and Huijbregts, C. (1978). "Mining Geostatistics," Academic Press, New York.
- King, P. (1987). "The use of field theoretic methods for the study of flow in heterogeneous porous media," *J. Phys. A. Math. Gen.* **20**, 3935–3947.
- Kinzelbach, W. (1986). "Groundwater Modeling," Elsevier, Amsterdam, The Netherlands.
- Landau, L. D., and Lifschitz, E. M. (1960). "Electrodynamics of Continuous Media," Pergamon Press, Oxford, United Kingdom.
- Lavenue, A. M., Ramarao, B. S., Marsily, G., de, and Marietta, M. G. (1995). "Pilot point methodology for an automated calibration of an ensemble of conditionally simulated transmissivity fields," *Appl. Water Resour. Res.* **31**(3), 495–516.
- Mantoglu, A., and Wilson, J. L. (1982). "The turning bands method for the simulation of random fields using line generation by a spectral method," *Water Resour. Res.* **18**(5), 645–658.
- Marsily, G. de (1986). "Quantitative Hydrogeology, Groundwater Hydrology for Engineers," Academic Press, Orlando, FL.
- Matheron, G. (1967). "Eléments pour une théorie des milieux poreux," Masson, Paris.
- Matheron, G. (1973). "The intrinsic random functions and their applications," *Adv. Appl. Prob.* **5**, 438–468.
- Meier, P. M., Carrera, J., and Sanchez-Vila, X. (1998). "An evaluation of Jacob's method for the interpretation of pumping tests in heterogeneous formations," *Water Resour. Res.* **34**(5), 1011–1025.
- Neuman, S. P. (1984). "Role of geostatistics in Subsurface Hydrology. In Geostatistics for Nature Resources Characterization, NATO-ASI" (Verly *et al.*, eds.), Part 1, pp. 787–816, Reidel, Dordrecht, The Netherlands.
- Noetinger, B. (2000). "Computing the effective permeability of log-normal permeability fields using renormalization methods," *C.R. Acad. Sci. Paris/Earth Plan. Sci.* **331**, 353–357.
- Ramarao, B. S., Lavenue, A. M., Marsily, G., de, and Marietta, M. G. (1995). "Pilot point methodology for an automated calibration of an ensemble of conditionally simulated transmissivity fields. 1. Theory and computational experiments," *Water Resour. Res.* **31**(3), 475–493.
- Renard, P., and Marsily, G. de (1997). Calculating equivalent permeability: A review. *Adv. Water Resour.* **20**(5–6), 253–278.
- Rubin, Y., and Gomez-Hernandez, J. (1990). "A stochastic approach to the problem of upscaling the conductivity in disordered media: Theory and unconditional numerical simulations," *Water Resour. Res.* **26**(3), 691–701.
- Smith, L., and Freeze, R. A. (1979). "Stochastic analysis of steady-state groundwater flow in a bounded domain. 1. One-dimensional simulations. 2. Two-dimensional simulations," *Water Resour. Res.* **15**(3), 521–528; **15**(6), 1543–1559.



Streamflow

A. I. McKerchar

National Institute of Water and Atmospheric Research Ltd.

- I. Streamflow Measurement
- II. Streamflow Data Archives
- III. Streamflow in the Hydrological Cycle
- IV. Streamflow Variability
- V. Importance of Streamflow
- VI. Hazards of Extreme Streamflow
- VII. Conclusion

GLOSSARY

Current meter A precision instrument with a rotating propeller or set of cups for measuring velocity at a point in flowing water. The speed of rotation is proportional to the mean velocity at the point.

Discharge The total volume of water flowing past a point in a river at a specified time. Discharge is measured as volume per unit time.

River basin The area of land draining to a particular location on a river. Synonymous terms are “catchment” and “watershed.”

Runoff The average depth of water yielded from the catchment in a specified time interval, expressed in the same units as precipitation and evaporation. Runoff is calculated by dividing the average discharge issuing from a catchment for a specified time interval by the area of the catchment.

Streamflow The flow of water in a stream or river.

STREAMS of flowing water are a visible and enduring feature of the hydrological cycle. Streams provide ready

sources of freshwater that are essential for communities and, in inland areas, are typically the receivers of wastewaters.

In hydrological terms, streamflow is an outflow from a catchment. The inflow is provided by precipitation (rain and snow) received over the area of the catchment. The water provided by precipitation moves through the catchment, some seeping into deep groundwater, some evaporating from the vegetation canopy or from the ground surface, and some being held in the soil from where it meets the transpiration requirements of plants. Streamflow is the residual after the demands for seepage, evaporation, and transpiration have been met.

I. STREAMFLOW MEASUREMENT

Quantitatively, streamflow rate is measured as discharge in units of volume per unit time. The most common units are cubic meters per second (m^3/s , also known as cumecs) and liters per second (L/s) for smaller streams. Time units of seconds are appropriate because streamflow can vary over short time intervals. Other units include megaliters

per day (ML/day) and, in the United States, cubic feet per second (ft^3/s or cusecs) and acre-feet per hour.

Runoff expresses discharge as an average depth of water running off over the area of the river basin. It is calculated by dividing discharge by the area of the catchment. Runoff can be compared with the mean annual precipitation averaged over catchment. The precipitation should be greater by an amount depending on the losses to groundwater and to evaporation and transpiration. In areas where rain gauges are sparse, or where precipitation varies, especially in hilly and mountainous terrain, the runoff derived from streamflow measurements with an estimate of mean evaporation and transpiration can be a useful indicator of the mean precipitation over the river basin.

Streamflow is measured using a two-step process. First, the water level, or stage, (defined as height above a datum) is measured at regular time intervals. Then the series of stage values are converted to a series of discharges using a transformation that relates stage level to discharge. The transformation is termed a stage/discharge rating curve. A series of measurements of discharge, typically using current meters, must be undertaken to establish the stage/discharge rating. The shape of this curve is determined by the hydraulic conditions at the measurement site on the stream channel.

The site for measurement of stage, commonly termed a gauging station, must be carefully selected to ensure that the downstream hydraulic conditions will be suitable. The prime attributes sought are stability and sensitivity. Typically, stability is provided by a rock bar across the stream, or a gorge section. Stability of the site ensures that the hydraulic relationship represented by the rating curve is well defined and does not have to be continually recalibrated. This can be particularly difficult to achieve in rivers that convey substantial sediment loads and suffer periodic aggradation and scour of the channel. The second attribute required is sensitivity, such that a measurable change in stage is accompanied by a measurable change in discharge. Other desirable attributes are ease of access, even in extreme flood conditions; freedom from aquatic and terrestrial vegetation; and freedom from variable backwater effects (due to tides or high water levels in tributaries or lakes or reservoirs downstream).

A desirable feature sought for the discharge measurement site is relatively uniform flow across the river channel, and this is normally achieved in a long, straight section of channel. Areas of high velocity, changing current angles, and rapid changes in depth of water should be avoided.

On smaller streams and rivers, weirs or flumes with known stage/discharge rating curves are often used for flow measurement. Weirs and flumes have the advantages that once installed, and once the calibrations have been

verified, the data can be more reliable. However, regular checks are still necessary to ensure that flow through the structure is not impeded by sediment deposits or by vegetation growth. Dams and hydroelectric power stations also provide stable hydraulic conditions that enable reliable measurement of flow.

A. Measurement of Stage

Early measurements of water level, typically at daily intervals, were made using a staff gauge fixed in a secure position. With water level recorders, a stilling well, connected to the river or lake by narrow pipes, is commonly used to provide a calm, undisturbed area of water to enable a reliable measurement. A float is connected to a rotating shaft on the recorder by a metal tape or chain. Early recorders used pens drawn across a clock-driven chart. These have been largely replaced by electronic recorders that store regular values for the stage, as determined by the rotation of the float-driven shaft. These modern measurement methods have better resolution than charts and avoid the labor-intensive work necessary to digitize charts.

Typically, the recording interval used is 15 min, but a finer time resolution may be necessary on small, fast responding streams and on lakes and reservoirs where seiching, i.e., oscillations of the water surface caused by wind or barometric pressure gradients, is of interest. An example of a stage record for a river over a 2-month period is shown in Fig. 1A.

Other devices for water level measurement include pressure transducers and gas-purge manometers. Experience with pressure transducers shows that because their calibration is prone to drift over long time periods, they are not a suitable primary sensing mechanism for water level measurement. Nevertheless, they can provide measurements of the rate of change of water level, which is useful for flood warning purposes.

B. Measurement of Discharge

To establish the stage/discharge rating curve, discharge measurements must be carried out for a range of river levels. Measurement of discharge is an exacting task if good quality measurements are to be achieved. Commonly, these measurements are undertaken by dividing a river cross section into 20 or more panels, each of similar area, and measuring the velocity through each of the panels. Total discharge is assessed as the sum of the product of the panel area multiplied by the mean velocity across the panel.

The width of each panel is measured with a tape stretched across the river, and the depth is determined by

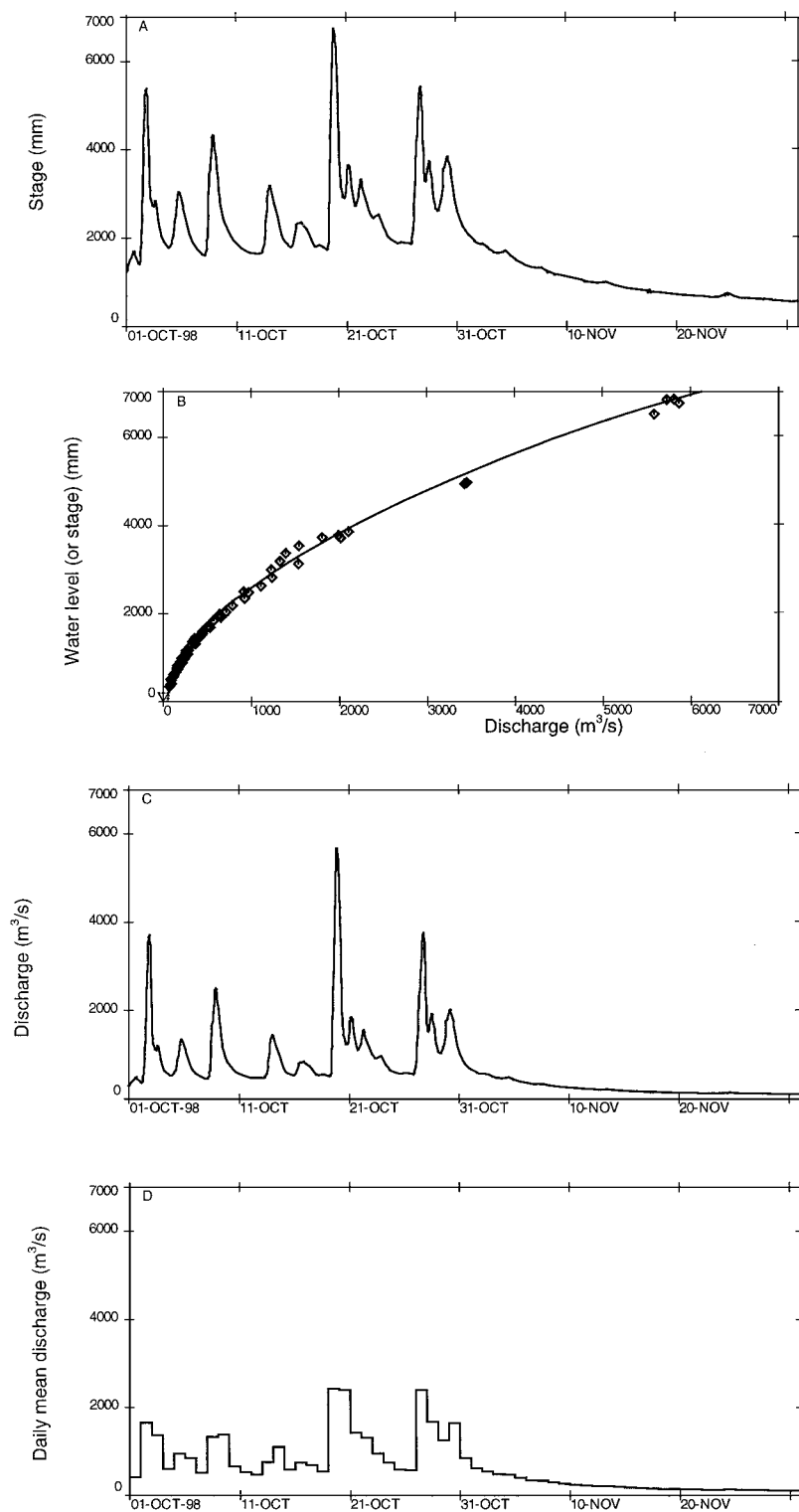


FIGURE 1 Illustration of the measurement of streamflow data for a 2-month interval for the Grey River near Greymouth, New Zealand. (A) Stage data recorded at 15-min intervals. (B) Stage/discharge rating curve used to transform the stage data to discharge, with the calibration measurements (obtained over a period of years using current meters) plotted. (C) Discharge hydrograph resulting from application of the rating curve in B to the stage data in A. (D) Daily mean discharge series calculated from C. Note that the daily averaging eliminates much of the detail of the floods.

sounding with a weight or, in the case of a small stream that can be waded, with a rod. The velocity at points within each panel is measured with a current meter. Typically, in shallow streams, the velocity measured at 0.6 of depth provides a reasonable estimate of the mean velocity in the cross section. In deeper rivers, the mean of the velocity at 0.2 and 0.8 of depth is used as an estimate of the mean velocity for the cross section.

Current meters have propellers or cups with rates of rotation proportional to the water velocity. In small streams that can be waded, the current meter can be mounted on a rod. In larger rivers, current meters are suspended with winches from cableways, bridges, or boats. The meters are precision instruments that require regular maintenance and calibration in special towing tanks.

Other less frequently used methods for discharge measurement include the use of floats (which enable assessment of velocity on the surface), ultrasonic equipment, chemical methods based on determining the extent of dilution of a concentrated solution, and measurement of volume change.

Measurement of the rate of volume change is useful for calibrating very low flow rates, provided the streamflow can be diverted into a container, and for assessment of total streamflow into lakes. In the case of lakes, it can be impractical to measure flows in all the streams entering the lake. If the total inflow for all streams is of interest, this can be assessed from the rate of change of the lake volume and the outflow. The rate of change of volume is estimated as the rate of change of lake level multiplied by the lake surface area. Precise measurement of the lake level is necessary to assess the changes in level and to distinguish these changes from the effects of seiching, which is the oscillation of the lake surface caused by wind blowing over the lake or by barometric pressure gradients.

C. Stage/Discharge Rating Curve

The quality of the stage/discharge rating curve (see example in Fig. 1B) determines the reliability of the streamflow record. Ideally, the calibration measurements should cover a full range of flow conditions from droughts to floods to ensure that extrapolation of the curve beyond the range of supporting measurements is minimized. However, achieving gaugings over a full range of flows is difficult where the gauging site is remote or where the river basin is small so that the river responds rapidly to infrequent storms. For this reason some degree of extrapolation of the rating curve is often necessary. Extrapolation tends to introduce error, and, consequently, larger measurement errors generally accompany estimates of flood flows.

D. Calculation of Streamflow Record

Application of the rating curve (Fig. 1B) to the record of stage (Fig. 1A) yields the record of flow (Fig. 1C). Although the flow data are of prime interest and are used for a wide range of purposes, there are reasons (see below) why the archives of data should retain the original measurements of stage.

II. STREAMFLOW DATA ARCHIVES

Streamflow is a natural phenomenon. It is not controllable in the same way that a laboratory experiment is controllable. When extremes of flood and drought occur, only one opportunity is presented to measure the event, and that is as it happens. Thus, measurements of streamflow and especially measurements of extremes are critically important because they cannot be repeated. Ready access to records of extremes is essential to ensure that societies adequately manage the risk of extremes.

Most countries have recognized the importance of archives of hydrologic data. National hydrometeorological services have been established to gather records of streamflow and to maintain and review archives to ensure that the data collected are correct and are securely archived and that copies are available for use.

With the advent of computers, archiving operations have moved from the publication of yearbooks to reliance on electronic data held in computer archives. Desirable features of the archives and the computer software used to submit and retrieve data include:

1. The inclusion of the original field measurements (stage, rating curves, calibration gaugings) in the archive: This offers the advantages that the details of flow hydrographs can be retrieved, the quality of rating curves and the extent of extrapolations can be assessed, and the rating curves can be adjusted retrospectively as new measurements of extreme discharge come to hand. These advantages are lost when the data are archived in a processed form, for example, as daily mean discharge. Compare the detail of Fig. 1C (based on 15-min data) with daily mean discharges for the same period in Fig. 1D: the flood peak that occurred was $5670 \text{ m}^3/\text{s}$, whereas the maximum daily mean is only $2400 \text{ m}^3/\text{s}$.

2. The ability to resolve units of time over hundreds of years to minutes or seconds: Details of extreme flood measurements retain their importance and validity over long periods, and accurate timing detail is necessary for detailed hydraulic study of the movement of flood waves.

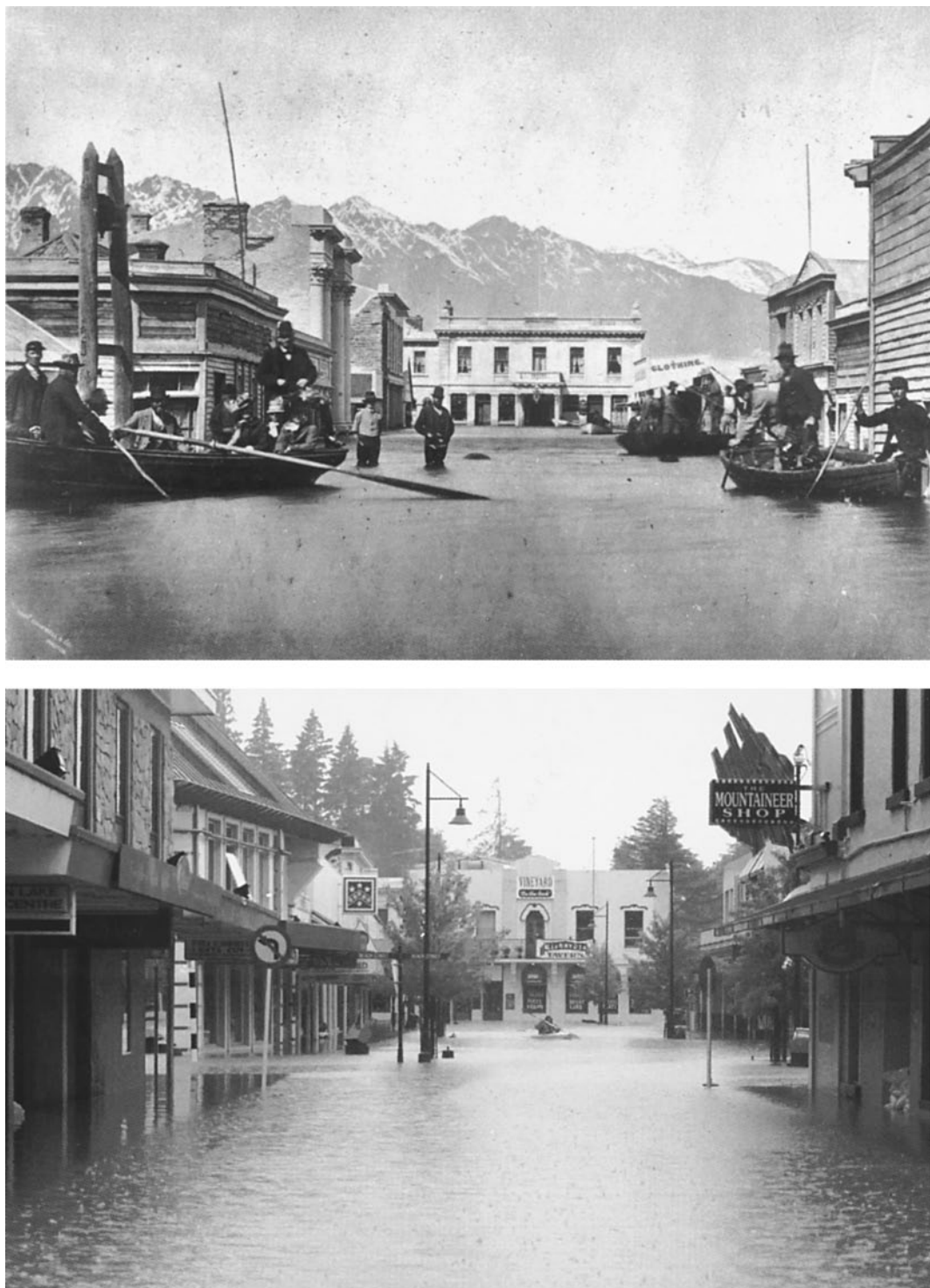


FIGURE 2 Rees Street in Queenstown on 29 September 1878 (above) and 16 November 1999 (below). In both cases, the water level is nearly at the windowsills of the hotel in the center of the photographs. The maximum lake level in 1999 was 15 cm above the 1878 maximum. The mountain range in the background of the 1878 photograph is obscured by clouds in the 1999 picture. (Photos: Otago Daily Times Dunedin, New Zealand.)

3. Ready access to the archive: In some countries this is being achieved by making streamflow data available through the Internet.

4. Timeliness: Use of data for forecasting and management during floods and droughts requires data up to the present time. The facility for the archive to be regularly updated with the most recent data is highly desirable. This access to data in near real time requires an electronic system for retrieval of data from remote stations. American data provided by the U.S. Geological Survey are available via the Internet (website: <http://water.usgs.gov/realtime.html>).

Archives are important. This is illustrated by the pair of photographs in Fig. 2 which show flooding of the town of Queenstown in New Zealand in 1878 and 1999. Better use of knowledge that the site is flood prone could have guided the development of the town since 1878 to lessen the impact of the 1999 flood.

III. STREAMFLOW IN THE HYDROLOGICAL CYCLE

A. Simple Water Budget

The entry of water into a catchment and the movement through it to become streamflow is indicated in the schematic diagram in Fig. 3, which represents the terrestrial phase of the hydrological cycle. Precipitation (rain, snow, hail, dew) arriving at the catchment surface can be intercepted by the vegetation canopy and then can evaporate back to the atmosphere or drip through onto the ground.

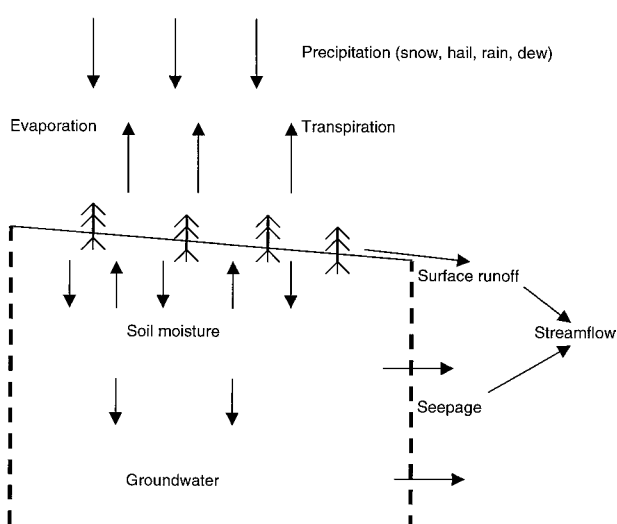


FIGURE 3 Schematic diagram to show the movement of water through a catchment to produce streamflow.

Water arriving at the ground surface can evaporate, infiltrate into the soil, or flow over the ground surface into a stream channel if it cannot infiltrate.

Water seeping into the soil forms a reservoir of soil moisture. This is depleted by losses to groundwater, abstractions by plant roots, and capillary action moving water to the ground surface where it evaporates.

Streamflow is supplied by surface and near-surface runoff and by seepage from groundwater. During high flows and floods, surface and near-surface runoff supplies most of the water appearing as streamflow, whereas in the absence of precipitation, flows are sustained largely by seepage from groundwater.

The size of flood peak flows is determined by

- The size of the catchment
- The intensity of the storm rainfall and its distribution over the catchment
- The vegetation cover
- The hydraulic properties of the soil of the catchment
- The status of the soil moisture storage at the start of the storm
- The geometry and hydraulic properties of the stream channel network of the catchment

Low flows occurring during prolonged dry spells when the soil moisture becomes depleted are dictated mainly by the rate at which seepage occurs from groundwater. This is determined by the nature and size of the groundwater reserves and by the extent to which the groundwater zones are intercepted by the stream channels. These, in turn, are set by the geological conditions. The magnitudes and rates of recession of low streamflows are indicators of the soil moisture and groundwater conditions.

Understanding, quantifying, and modeling the translation of water through a catchment to become streamflow is a challenging task that forms much of the science of hydrology. It is particularly difficult to define and deal with the spatial variation of the catchment processes described above. With the ready availability of powerful computers that provide access to databases which characterize the surface shape of large land areas, modeling methods have advanced dramatically in recent years. Such models are critically important for assessing extreme flood size, developing flood forecasts, predicting the effects of land use changes, and quantifying the components of the hydrological cycle to assess impacts of climate variability and change.

When studying catchments and comparing rainfall and streamflow, it is useful to convert streamflow from the units of discharge measurement (volume per unit time) into runoff (average depth of water per unit time flowing from the catchment area). For example, the Grey River near Greymouth on the west coast of New Zealand has a

mean discharge of 364 m³/s. At the stream gauge the catchment area is 3830 km², and the catchment is hilly to mountainous. The average annual runoff rate is calculated as

$$\begin{aligned}\text{Runoff} &= 364 \text{ m}^3/\text{s} \times 86,400 \text{ s/day} \\ &\quad \times 365 \text{ day/year}/(3830 \times 10^6 \text{ m}^2) \\ &= 3.00 \text{ m/year} \\ &= 3000 \text{ mm/year}.\end{aligned}$$

From Fig. 3, a simple budget for the inputs and outputs to a catchment can be expressed as

$$P = E + T + \Delta S + \Delta G + \Delta L + R, \quad (1)$$

where

P = precipitation

E = evaporation

T = transpiration

ΔS = change in soil moisture storage

ΔG = change in groundwater storage

ΔL = loss of deep groundwater out of the catchment

R = runoff

Over a time interval of 1 year, the changes in soil moisture and groundwater storage ($\Delta S + \Delta G$) typically may be negligible compared with the first three terms in Eq. (1). Also, if the loss to deep groundwater (ΔL) is minimal, Eq. (1) simplifies to

$$P = E + T + R, \quad (2)$$

which can be rewritten as

$$R = P - (E + T). \quad (3)$$

This emphasizes that runoff is the residual term after the demands of evaporation and transpiration have been satisfied. Evaporation and transpiration are determined by the solar radiation, the wind, the relative humidity, the roughness of the vegetation surface, the vegetation type, the soil type, and the rooting depth. It varies widely. Values range from more than 2000 mm/year in arid subtropical zones to less than 200 mm/year in high-latitude regions. In dry regions where evaporation and transpiration are high, runoff may be only a few millimeters per year and highly variable from year to year.

For much of New Zealand, evaporation and transpiration is thought to be in the range 500–800 mm/year. For the Grey catchment, runoff of 3000 mm/year implies that average precipitation should be about 3500–3800 mm/year.

Only 1 of the 11 long-term rain gauges in the Grey catchment has a mean rainfall approaching these figures. This is because the mountainous high rainfall zones in the catchment are sparsely inhabited and have few rain gauges: most of the gauges are in the drier areas where

people live. This illustrates a widespread problem of adequately sampling rainfall in hilly and mountainous areas. In fact, the streamflow record for the Grey River is a better indicator of the total precipitation received by the catchment than the estimate inferred from the network of rain gauges. For this reason, investing in streamflow measurement rather than rainfall measurement can be a prudent use of limited resources.

IV. STREAMFLOW VARIABILITY

A. Scales of Time Variability

Streamflow varies at different time scales, and all these scales are of interest. Graphs are an excellent way to display the variability of streamflow. As examples, Figs. 4–6 show the variability of a single streamflow record at three different time scales: short, medium, and long. At each scale there are interesting features that have an impact on a range of issues. The streamflow record used is from the Clutha River at Balclutha in New Zealand. The catchment area for this river is 20,582 km² and the streamflow record commenced in 1954. Upstream of the recorder there are two hydroelectric dams and one controlled lake that provides limited regulation of the streamflow, storing water in summer for release during winter. Several other small hydroelectric developments have negligible influence on the flows in the main river. There are also minor withdrawals for irrigation in spring and summer.

1. Short-Term Variation

At a time scale of hours, Fig. 4 shows an example of the variation of flows at the stream gauge. The flow has a daily (diurnal) cycle caused by the daily variation of power generation at the hydroelectric stations, the first of which is 90 km upstream of the recorder. Typically, the hydroelectric station has a fairly constant minimum outflow in the early morning from 12 AM to 7 AM. The downstream data recorded at Balclutha data show that the daily minima occurs as a distinct minima at about 9 PM, reflecting the attenuation of the changing flow as it moves down the river to the gauge at Balclutha. The hydrograph is modified in the translation down the river channel, with the higher flows moving more quickly and gradually overtaking the slower moving lower flows and eliminating the 7-h interval of low flow.

In the case of the Clutha River, the diurnal variations in streamflows in the river have adverse consequences for

- Instream biota which tend to favor relatively constant flows

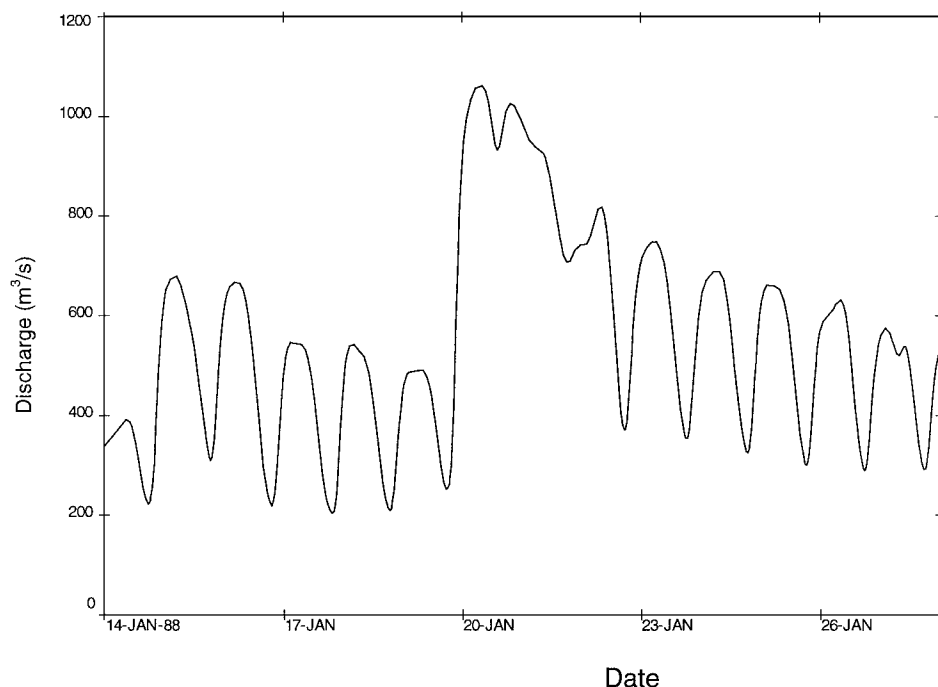


FIGURE 4 Example of short-term streamflow variations caused by the daily variations in generation of a hydroelectric power station (Clutha River at Balclutha, New Zealand).

- The stability of the river bank which suffers greater erosion as a result of constantly fluctuating flows and levels
- The opening and closing of the mouths of the branches of the river as it enters the sea; increased occurrences of mouth closure have impeded drainage of productive low-lying land near the river mouth.

2. Seasonal Variation

Seasonal variation is evident in most streamflow records and occurs because of seasonal variations in the precipitation, evaporation and transpiration, and soil moisture and groundwater levels. Snow and ice accumulation in winter and snowmelt in spring and summer contribute to the seasonal variation in cooler regions. Where rivers are sources of water for irrigation, the abstractions typically have a strong seasonal pattern, which impacts on the flow remaining in the river. Other human impacts are regulating reservoirs that store water at times of high flows for release when natural flows are lower.

All these factors contribute to the seasonal variations. For the Clutha River, seasonal variation is displayed as the distributions of monthly mean flows in Fig. 5. This figure is a boxplot of the monthly mean flows for each month from 1955–1999. For each month it shows the minimum monthly mean streamflow, the value exceeded in 75, 50, and 25% of years, and the maximum monthly

mean streamflow. (The 50 percentile value is also known as the median.) The seasonal variation is modest, but the austral winter values (in June, July, and August) are typically lower than the austral spring and summer values (in September, October, November, December, January, and February). The lower winter flows and the higher spring and summer flows are due primarily to winter snow accumulation and spring and summer snowmelt.

3. Long-Term Variation

Annual mean flows for the Clutha River are displayed in Fig. 6. These means display an interesting pattern of variability. The year 1958 had exceptionally high flows, but otherwise the flows up to and including 1978 tended to be less than those after 1978. The mean for the whole series is $572 \text{ m}^3/\text{s}$, and the standard deviation is $112 \text{ m}^3/\text{s}$. The ratio of the standard deviation to the mean, known as the coefficient of variation, is 0.195. (This dimensionless quantity is useful because it enables comparison of the variability of the series for different rivers.)

Means for the two periods shown on Fig. 6 differ by 16%. This difference is so large that it is very unlikely to arise through chance variation on the expectation that mean flow in every year is the same. The difference is consistent with fluctuations noted in some long-term rainfall records, and it appears to be related to the frequencies of occurrence of phases of the El Niño Southern

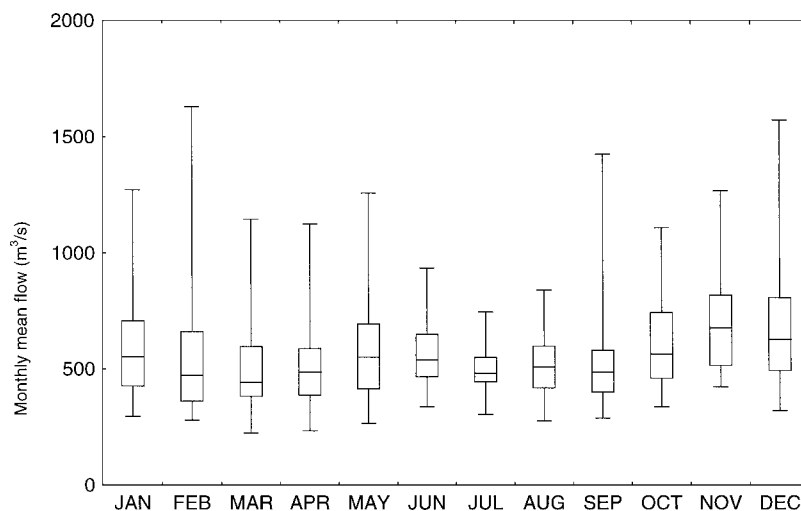


FIGURE 5 Seasonal variation in streamflow illustrated using boxplots of monthly mean flows for the Clutha River at Balclutha, New Zealand, for 1954–1999. For each month, the plots show the minimum monthly streamflow, the value exceeded in 75, 50, and 25% of years, and the maximum monthly streamflow.

Oscillation phenomenon. These appear to have changed in 1978.

Climate change studies examine long time series to detect shifts and trends. The apparent shift in Fig. 6 raises interesting questions about the causes of fluctuations in long-term records.

B. Variability between Rivers

The mean annual discharge varies greatly between river basins. The variation is driven primarily by the difference between total precipitation and the evaporation and transpiration occurring over the basin. Any thorough assessment of streamflow has to look beyond the mean annual discharge to the expected variation in annual discharge and the expected variation in seasonal streamflow.

Seasonal variation is driven by the seasonal variability in the water balance. In tropical areas and subtropical conditions, the patterns are driven largely by seasonality in rainfall, and in monsoon-type climates, most of the stream-

flow occurs over a few months, with low flows occurring for the remainder for the year. In mid- and high-latitude zones, seasonality may or may not be present in precipitation, but it occurs in streamflow because of the strong seasonal patterns affecting transpiration of plants and evaporation. In colder continental climates and in mountainous areas, snow accumulation in winter and snowmelt in spring and summer are primary sources of seasonal variation.

To illustrate the contrasts experienced in a small country, Fig. 7 shows the monthly flow regime for another New Zealand river basin that experiences conditions differing from the Clutha River. This river is the Motu, in the North Island. The catchment area is 1393 km², and the influence of snow is negligible. Figure 7 shows that the highest monthly flows tend to occur in the (austral) winter (June, July and August) and that the lowest flows tend to occur in the late (austral) summer and early fall (January, February, March). Higher winter flows occur partly because rainfall is somewhat higher in winter, but

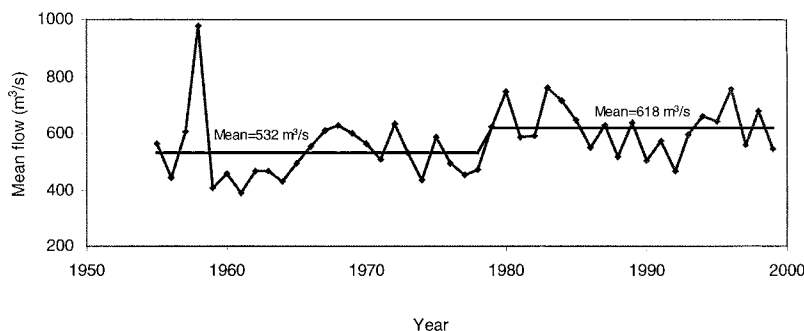


FIGURE 6 Annual mean flows for the Clutha River at Balclutha, New Zealand, for 1954–1999. The mean for the whole record is 572 m³/s.

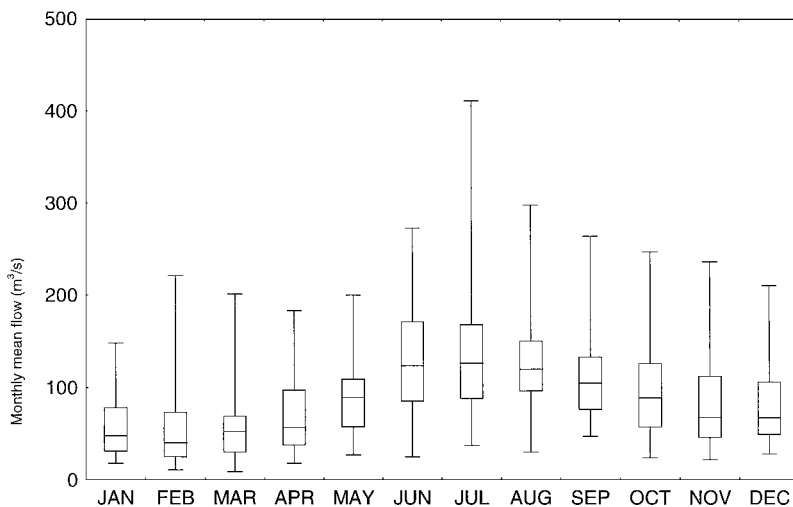


FIGURE 7 Seasonal variation in streamflow illustrated using boxplots of monthly mean flows for the Motu River, New Zealand, for 1957–1999. For each month, the plots show, the minimum monthly streamflow, the value exceeded in 75, 50, and 25% of years, and the maximum monthly streamflow.

mainly because evaporation and transpiration demands are suppressed. The mean annual discharge is 92 m³/s, the runoff is 2080 mm/year, and the coefficient of variation for annual streamflow is 0.210. Although the coefficient of variation is practically identical to the Clutha River, the seasonal patterns differ significantly. Higher streamflow in winter would be important if, for example, this river basin was to be developed for hydroelectric power generation. High winter flows would tend to match the peak energy demand in winter for heating, whereas, without construction of a storage dam, the relatively lower summer flows reduce the attractiveness of the river as a source of irrigation water. This contrasts with the Clutha River, where the high season flows are out of phase with the seasonal energy loads.

Global runoff studies use long streamflow records from around the world to examine runoff patterns. The coefficient of variation of annual discharge is an indicator of the expected year-to-year variation of streamflow. In general, a spatial averaging applies, with larger river basins having lower coefficients of variation than smaller basins. The relationships differ by continental regions, with characteristically higher values in Australia and Southern Africa. The higher values relate to the general aridity of these regions and indicate that they are relatively more prone to extremes of streamflow.

V. IMPORTANCE OF STREAMFLOW

A. Spiritual and Cultural

Streamflow has always been important for people, and many of the great civilizations of the world, e.g., Egypt,

Mesopotamia, India, and China, have been located by large rivers.

In the Judeo-Christian tradition, streamflow figures prominently in the historical narrative of the Israelite people. For example, the 7 years of plenty followed by 7 years of famine in the Exodus story relate to the annual flow volumes of the Nile River (Genesis 41). (It is now known that a portion of the Nile River flow variability is determined by the state of the El Niño Southern Oscillation phenomenon.) The plagues that were experienced in Egypt as a prelude to the release of the enslaved Israelites also appear to relate to abnormal Nile River flows, which were followed by a set of environmental catastrophes stemming from a toxic algal bloom in the river (Exodus 7).

Other groups, who determine their identity in relation to the country and the landscape, see streamflow differently. For example, the Maori people of New Zealand define their identity in relation to particular mountains and rivers of their traditional tribal area. Rivers, and the streamflow they convey, are seen as having a life force contributing to personal and tribal identity and status. In addition, the river is a provider of food from the fish and bird life and a traditional route for navigation by canoe.

Water resource developments have often upset this relationship between people and rivers. Damming of rivers and impeding access for migrating fish, manipulating river flows and diverting them to other catchments, and discharging effluents into rivers are all at variance with this life view. Some conventional developments can thereby ignore and belittle these deeply held views.

Resolving development with these alternative views will be a significant challenge for river basin management

in the 21st century. An example of resolving these issues is the disposal of sewage effluent of an inland city by spray irrigation in a forest, rather than into a river noted for its eel fishery. Other examples include the construction of an artificial wetland to remove contaminants from stormwater drainage from an industrial site before it enters an estuary used for gathering shellfish and the provision of fish passes to enable elvers to migrate upstream over dams.

B. Water Supply and Effluent Disposal

Every community needs a clean water supply and safe effluent disposal. Streamflow is frequently used as a water source. Determining whether a river has the capacity to meet a demand requires analysis of the streamflow records to establish the low-flow characteristics of the stream. Specific quantities of interest are the low flows expected in the stream, their probabilities of occurrence, and the residual flows required to be maintained in the stream after abstractions have occurred. The study of low flows will determine whether a storage is needed to sustain a supply during dry periods.

A reliable record covering a number of years is necessary to provide a comprehensive understanding of the seasonal and year-to-year variability of low flows. Where no such record exists, hydrological models that encapsulate the dynamics of water movement through the catchment, as illustrated in Fig. 3, can be used with long records of rainfall to extend streamflow records. This presumes that suitably representative long rainfall records are available. Constructing, calibrating, and verifying a hydrological model normally requires that at least a short-term measured streamflow record is available.

Disposal of sewage is a complement of water supply. Communities normally dispose of sewage by treating it to various levels. The treated effluent, or wastewater, is then disposed of into a suitable stream, lake, estuary, or the sea. Varying levels of treatment are available, but even highly treated effluent can have elevated levels of nitrates and phosphates. The nutrients can lead to enhanced growth of aquatic plants in the receiving water. The eventual die-off and decay of these plants causes depleted dissolved oxygen levels, leading to the die-off of fish populations.

Analysis of low streamflow quantities and the quality characteristics of the water, such as the nitrate levels, the biochemical oxygen demand, and the dissolved oxygen levels, assist in determining the capacity of a stream to receive treated effluents.

Where water supplies are sparse, or where effluent disposal into receiving water is offensive to a section of the

community, on-land disposal by irrigation or by recharge of groundwater aquifers may sometimes be a viable solution.

C. Irrigation

Streamflow is a primary source of water for irrigation. Where streamflows are highly variable, storage reservoirs are often necessary to sustain flows for irrigation during dry periods.

Careful design and operation of irrigation schemes are necessary to manage the delivery of water. Excessive water supplied for irrigation can lead to high water tables and waterlogging, which causes a range of adverse effects. Drainage of surplus irrigation water back into the stream can convey contaminants into the stream below the irrigation area. In the lower Murray River in Australia, for example, elevated levels of salt, due partially to drainage of water from irrigation areas, limits the usefulness of the river water.

Depletion of streamflows due to irrigation abstractions can also affect a river as a biological habitat. Prominent effects include

- Reduction of the areas of water with depths and velocities suitable for fish habitat
- Alterations to algal communities, with changes from thin diatom layers to thick growths of filamentous algae
- Alterations to invertebrate and, ultimately, fish communities
- Disturbance of the movement of migratory fish (e.g., salmon)
- Elevated water temperatures

The impacts of these deleterious effects can be managed when streamflow data are readily available and when a community has agreed on rules about reducing irrigation abstractions when streamflows become low.

D. Energy Generation

1. Hydroelectric Power

Hydroelectric power development is an attractive source of renewable energy. Hydroelectric power generation does not have the emissions that accompany fossil-fueled thermal power stations or the waste-disposal problems that accompany nuclear power stations. The “fuel,” the flowing water, is continually replenished, though its supply is subject to the variability described above. In a sense the water is free, but it can have a value imputed to it on the basis of its potential energy, which is given by prevailing

energy prices. On the other hand, when areas of land are flooded during the filling of reservoirs, methane, a powerful greenhouse gas, is released by decaying vegetation.

Hydroelectric power stations can have very long lifetimes. Many stations constructed early in the 20th century generate power today and will do so for the foreseeable future.

Conventional hydroelectric developments normally require large dams to provide the head of water for generation. Large dams are expensive to construct, and the economics can be marginal if the transmission line losses are high because the center for electricity demand is a long distance from power station.

Streamflow data are necessary to establish the patterns of generation that will be available from the station. It is highly desirable that the streamflows are well sustained in dry periods. This is illustrated in Fig. 8, which compares the flow variability for two contrasting rivers, the Clutha and the Motu. Figure 8 plots the cumulative flows for the two rivers, as percentages of their respective means, against the probability of flow being greater than a given value. For example, the plot shows that for the Clutha River

the flow exceeded 80% of the time is 63% of the mean, whereas for the Motu River the corresponding figure is only 30% of the mean. In other words, the Motu River flows are much more variable than the Clutha River. The lower variability of the Clutha River occurs because of three large natural lakes, one with controlled outflows, in the headwaters that moderate the flow extremes. No such moderation of the Motu River flows occurs, and, not surprisingly, hydroelectric development of the Motu River has not proceeded.

Consequences of the changes in streamflow regime caused by hydroelectric power development can be severe. They can include

- The loss of wild and scenic features when reaches of a river are inundated by a reservoir.
- The loss through inundation of productive land and the forced relocation of communities.
- The restriction of access to the river system for fish such as salmon and eels whose life cycle is spent partially in the sea. Fish passages typically present only partial solutions.

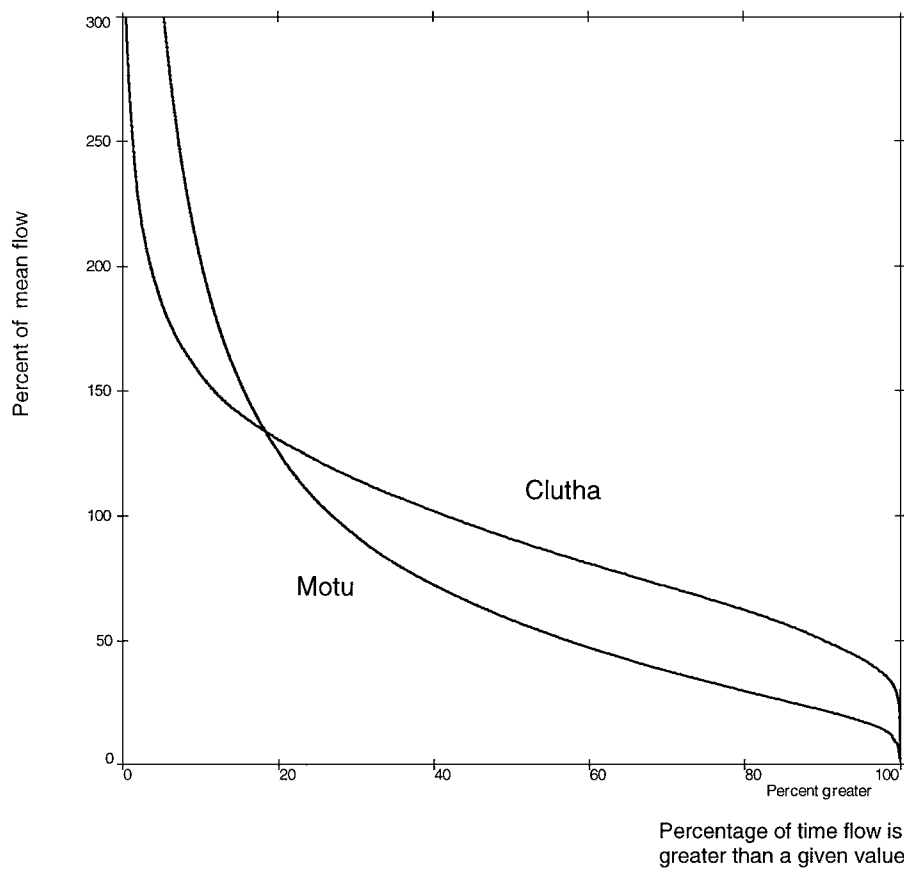


FIGURE 8 Cumulative percentage of flow for two contrasting rivers, expressed as a percentage of the mean, plotted against the probability of flow being greater than a given value.

- The reduction of downstream sediment loads, resulting in increased channel scouring and bank erosion. Furthermore, the reduction of sediment entering the coastal zone can result in shifts in the coastal geomorphology.
- The diminution of floods that have periodically flushed sediment and reshaped and redefined the river channel.

Where the environmental costs are seen as being too high, the desire to restore a river to a more natural flow regime has resulted in the closure and removal of some early hydroelectric schemes where the power output is relatively small.

2. Cooling Water

Rivers are also used as sources of cooling water for thermal power stations, both fossil fueled and nuclear. The capacity of the streamflow to receive waste heat from these plants is determined by the discharge in dry conditions, the prevailing stream temperatures, and the maximum temperature desired for the stream. In cases where low river flows occur at times of high power demands, the capacity of the river to receive waste heat can be a constraint on the operation of the plant.

E. Aquatic Habitat

Many biological communities live in flowing water. The composition and structure of these communities are affected by many aspects of streamflow, including the water quality and the nutrients and sediments that it carries, the temperature, and the scales of variability in the streamflow quantities.

The scales of variation are conveniently considered as large (macro) scale, medium (meso) scale, and small (micro) scale.

1. Large-Scale Flow Variation

Large-scale variations in flows regimes caused by seasonal and annual variability affect populations at a community level and are the ultimate regulators of species composition. Communities in a particular flow regime with regular seasonal variability tend to have become adapted to that regime, whereas erratic patterns of flood flow can cause considerable disturbance to a community.

The number of high-flow events and the durations between events are useful measures in assessing biological habitats. In streams that flood frequently, smaller “weedy” taxa tend to dominate among aquatic plant species, whereas larger more competitive taxa prefer environments that flood rarely, such as the outflows from lakes.

Low flows also affect biological communities. Algal growth commonly increases during low-flow episodes, and algal communities change from thin diatom films to thick growths of filamentous algae. These thick growths tend to smother instream habitats and have adverse impacts on invertebrate and fish communities. Other deleterious effects are a reduction in stream habitat by exposure and desiccation of a normally inundated streambed. Consideration of these impacts is necessary to establish the residual flows required to maintain the health of the stream when use of a stream is being considered for water supply, effluent disposal, irrigation, or hydroelectric power generation.

2. Medium-Scale Flow Variation

The variability encountered along individual reaches of streams, with the length scales in the range of meters to kilometers, exerts influences over the composition of local populations of biota and often dictates the differences observed in species composition along a stream. An individual stream reach can be classified into riffles, runs, and pools, and the differing hydraulic properties (depths and velocities) and the differing substrate composition are important factors determining the biological variability. Algal and invertebrate communities differ between riffles, pools, and runs.

Substrate stability is also important for stream communities. Stability is determined by the composition of the substrate (silt, sand, gravel), the flow velocity, imbrication, and the relative bed roughness. Macrophytes (larger aquatic plants) and bryophytes (mosses) can stabilize substrates in lowland and upland streams, respectively, and thereby play an important role in determining the structure and function of other instream components.

The hydraulic habitat conditions for plants are controlled by flood frequency, the velocities occurring between spates, and substrate stability. Invertebrate communities often respond to similar variables.

3. Small-Scale Flow Variation

Small spatial scales (millimeters to meters) are important for the control that they exert on the generation and dissipation of turbulence. The extent of flow velocity variation and the associated turbulence directly influences individual organisms in streams and is often responsible for the observed inherent variability of populations in streams.

Turbulence is manifest as the variation over short time scales of velocity in a steady flow. The variability of the three spatial components of flow velocity with time can now be measured with acoustic Doppler velocity meters. On a fixed streambed, the velocity must be zero, and in

the zone near the bed (the boundary layer), the velocity changes rapidly. Measurements of velocity close to the bed of a stream provide a measure of the near-bed stream turbulence. Understanding the near-bed turbulence is necessary to estimate the fluxes of oxygen and nutrients available to biota within the slow-flowing, near-bed boundary layer. Organisms that grow too large and intrude into faster flowing water can get washed away. Small-scale variability in invertebrate and algal communities often reflects changes in the velocity and turbulence regimes. The growth of organisms on stream boundaries can also affect the turbulence in streams.

VI. HAZARDS OF EXTREME STREAMFLOW

Unusually high streamflows are described as floods. The area of land beside a river inundated during floods is termed the floodplain. Floodplains are naturally fertile and are often the most productive land in a region. When inundation occurs on floodplains that are closely settled, the damage and suffering can be enormous. Most countries have developed a suite of measures to limit flood damage, including regulations and rules that keep people away from flood-prone areas and controls and structures such as levees and control dams that keep the flood water away from people. On large river basins, where severe precipitation can take days to weeks to progress down a river system to cause flooding, national hydrometeorological services can provide forecasts, enabling some reduction in damages.

Rivers draining mountainous areas tend to have steep channels where water flows swiftly. The response times are short, and flooding can occur within hours of the heavy rain. So-called flash-flood forecasting is a challenging area.

VII. CONCLUSION

Fresh, clean water is essential for life. Streamflow is a major source of this water, and streams are a vital resource.

Understanding streamflow, quantification of its magnitude, and variability is essential for sustainable utilization of this precious natural resource.

ACKNOWLEDGMENT

Funding of the streamflow data used in the figures is from the Foundation for Research Science and Technology, contract CO1815 (Information on New Zealand's freshwater). I thank Dr A. Suren and other colleagues of the National Institute of Water and Atmospheric Research, Christchurch, New Zealand, for advice and support.

SEE ALSO THE FOLLOWING ARTICLES

COASTAL GEOLOGY • DAMS, DIKES, AND LEVEES • DRINKING WATER QUALITY AND TREATMENT • FLOW VISUALIZATION • GLACIOLOGY • HYDROGEOLOGY • HYDROLOGIC FORECASTING • SOIL AND GROUNDWATER POLLUTION • STOCHASTIC DESCRIPTION OF FLOW IN POROUS MEDIA • WATER RESOURCES

BIBLIOGRAPHY

- Ackers, P., White, W., Perkins, J., and Harrison, A. (1978). "Weirs and Flumes for Flow Measurement," Wiley, Chichester.
- Harper, D., and Ferguson, A. (eds.). (1995). "The Ecological Basis for River Management," Wiley, Chichester.
- Herschy, R. (1985). "Streamflow Measurement," Elsevier, London.
- Herschy R. (1998). "Hydrometry: Principles and Practices," 2nd ed., Wiley, Chichester.
- Hosking, J., and Wallis, J. (1998). "Regional Frequency Analysis: An Approach Based on L-Moments," Cambridge Univ. Press, Cambridge, UK.
- Maidment, D., ed. (1993). "Handbook of Hydrology," McGraw-Hill, New York.
- McMahon, T., Finlayson, B., Haines, A., and Srikanthan, R. (1992). "Global Runoff: Continental Comparisons of Annual Flows and Peak Discharges," Catena Verlag, Cremlingen-Destedt.
- Sutcliffe, J., and Parks, Y. (1999). "The Hydrology of the Nile," International Association of Hydrological Sciences, Wallingford.